SPRINGER SERIES IN COMPUTATIONAL NEUROSCIENCE

Dynamic-Clamp

From Principles to Applications

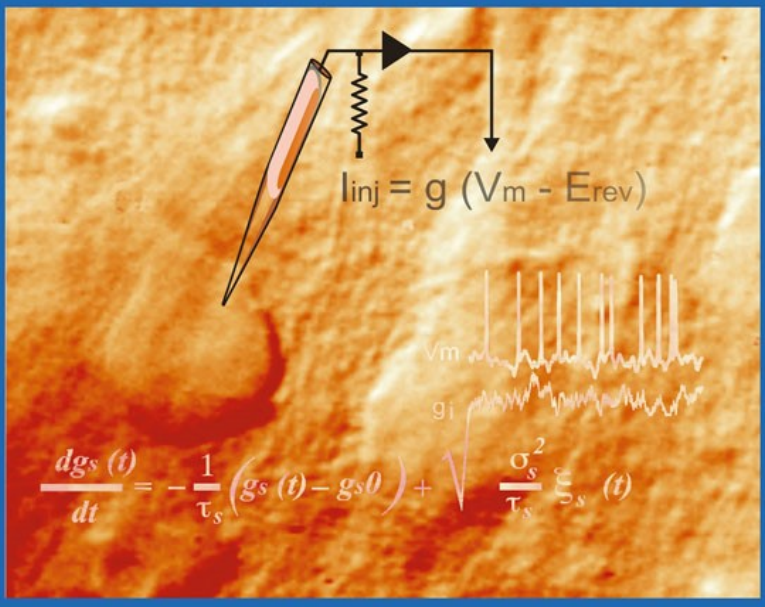

Alain Destexhe • Thierry Bal
Editors

Springer

Springer Series in Computational Neuroscience

Volume 1

Series Editors
Alain Destexhe
Unité de Neurosciences Intégratives et Computationnelles (UNIC)
CNRS
Gif-sur-Yvette
France

Romain Brette
Equipe Audition (ENS/CNRS)
Département d'Études Cognitives
École Normale Supérieure
Paris
France

For other titles published in this series, go to
www.springer.com/series/8164

Alain Destexhe · Thierry Bal
Editors

Dynamic-Clamp

From Principles to Applications

Springer

Editors
Alain Destexhe
Unité de Neurosciences Intégratives
et Computationnelles,
CNRS, 91198 Gif-sur-Yvette
France

Thierry Bal
Unité de Neurosciences Intégratives
et Computationnelles,
CNRS, 91198 Gif-sur-Yvette
France

ISBN 978-0-387-89278-8 e-ISBN 978-0-387-89279-5
DOI 10.1007/978-0-387-89279-5

Library of Congress Control Number: 2008942719

Printed on acid-free paper

springer.com

Preface

This book intends to provide an overview of different approaches using the "dynamic-clamp" technique. This technique was introduced many years ago (see "Introduction" for an historical perspective) and enables one to inject artificially generated conductances in living neurons. Because the quantity physically injected by the electrode is a current, which is the product of the conductance with the membrane potential (Ohm's law), and because the membrane potential itself changes if a current is injected, one needs to continuously update the current to be injected as a function of the changing membrane potential of the recorded cell. Injecting a conductance thus requires to establish a real-time loop between the device which calculates the current (usually a computer) and the recorded membrane potential. This real-time loop is at the heart of the dynamic-clamp technique, as illustrated in the chapters of the book. The different chapters cover topics ranging from cardiac physiology, dendritic recordings, single-neuron recordings, as well as circuits or networks interactions. We refer to the introductory chapter for a description of these chapters, as well as a detailed introduction of the dynamic-clamp technique.

The many authors who have contributed to this book are not only among the initiators of the technique, and among the researchers who have published the most prestigious articles on dynamic clamp, but they also collectively illustrate the great power and the variety of paradigms in which the dynamic-clamp technique is used. These paradigms range from injecting artificial conductances in cardiac cells, neurons or dendrites, artificially connect different neurons, create "hybrid" networks of real and artificial cells, re-create in vivo conditions by providing a synthetic synaptic background activity, as well as use the dynamic clamp to correct the recording according to a computational model of the electrode. These paradigms show that computational models directly interact with living neurons, which is perhaps one of the most spectacular progress that has happened in the interaction between theory and experiments in biology. Our hope is that this book will provide an overview of these progress and convince the reader that theory and experiments have never been so close.

Alain Destexhe
Gif-sur-Yvette, France Thierry Bal

Contents

Associating Living Cells and Computational Models: an Introduction to Dynamic Clamp Principles and its Applications 1
Zuzanna Piwkowska, Alain Destexhe, and Thierry Bal

Dendritic Dynamic Clamp – A Tool to Study Single Neuron Computation 31
Stephen R. Williams

Synaptic Conductances and Spike Generation in Cortical Cells 49
Hugh P.C. Robinson

Simulating In Vivo Background Activity in a Slice with the Dynamic Clamp 73
Frances Chance and Larry F. Abbott

Impact of Background Synaptic Activity on Neuronal Response Properties Revealed by Stepwise Replication of In Vivo-Like Conditions In Vitro 89
Steven A. Prescott and Yves De Koninck

Testing Methods for Synaptic Conductance Analysis Using Controlled Conductance Injection with Dynamic Clamp 115
Zuzanna Piwkowska, Martin Pospischil, Michelle Rudolph-Lilith, Thierry Bal, and Alain Destexhe

In Vivo Dynamic-Clamp Manipulation of Extrinsic and Intrinsic Conductances: Functional Roles of Shunting Inhibition and I_{BK} in Rat and Cat Cortex 141
Lyle J. Graham and Adrien Schramm

Functions of the Persistent Na^+ Current in Cortical Neurons Revealed by Dynamic Clamp 165
J.F. Storm, K. Vervaeke, H. Hu, and L.J. Graham

Using "Hard" Real-Time Dynamic Clamp to Study Cellular and Network Mechanisms of Synchronization in the Hippocampal Formation 199
John A. White, Fernando R. Fernandez, Michael N. Economo, and Tilman J. Kispersky

Unraveling the Dynamics of Deep Cerebellar Nucleus Neurons with the Application of Artificial Conductances 217
Dieter Jaeger and Risa Lin

Intrinsic and Network Contributions to Reverberatory Activity: Reactive Clamp and Modeling Studies 237
Jean-Marc Fellous, Terrence J. Sejnowski, and Zaneta Navratilova

Dynamic-Clamp-Constructed Hybrid Circuits for the Study of Synchronization Phenomena in Networks of Bursting Neurons 261
Carmen C Canavier, Fred H. Sieling, and Astrid A. Prinz

Using the Dynamic Clamp to Explore the Relationship Between Intrinsic Activity and Network Dynamics 275
Anne-Elise Tobin, Rachel Grashow, Lamont S. Tang, Stefan R. Pulver, and Eve Marder

Re-Creating In Vivo-Like Activity and Investigating the Signal Transfer Capabilities of Neurons: Dynamic-Clamp Applications Using Real-Time Neuron 287
Gerard Sadoc, Gwendal LeMasson, Bruno Foutry, Yann Le Franc, Zuzanna Piwkowska, Alain Destexhe, and Thierry Bal

Using the Dynamic Clamp to Dissect the Properties and Mechanisms of Intrinsic Thalamic Oscillations 321
Stuart W. Hughes, Magor Lörincz, David W. Cope, and Vincenzo Crunelli

Dynamic Clamp with High-Resistance Electrodes Using Active Electrode Compensation In Vitro and In Vivo 347
Romain Brette, Zuzanna Piwkowska, Cyril Monier, José Francisco Gómez González, Yves Frégnac, Thierry Bal, and Alain Destexhe

Key Factors for Improving Dynamic-Clamp Performance 383
Robert Butera and Risa Lin

Development of a Genetically Engineered Cardiac Pacemaker: Insights from Dynamic Action Potential Clamp Experiments 399
Arie O. Verkerk, Jan G. Zegers, Antoni C.G. van Ginneken, and Ronald Wilders

Index 417

Contributors

Larry F. Abbott Center for Neuroscience, Department of Physiology and Cellular Biophysics, Columbia University College of Physicians and Surgeons, New York, NY 10032-2695, USA

Thierry Bal Unité de Neurosciences Intégratives et Computationnelles (UNIC), CNRS, 91198 Gif-sur-Yvette, France, thierry.bal@unic.cnrs-gif.fr

Romain Brette Equipe Audition (ENS/CNRS), Département d'Études Cognitives, École Normale Supérieure, F-75230 Paris Cedex 05, France, romain.brette@di.ens.fr

Robert Butera Laboratory for Neuroengineering, School of ECE, Georgia Institute of Technology, Atlanta, GA, USA, rbutera@gatech.edu

Carmen C. Canavier Neuroscience Center of Excellence, Louisiana State University Health Sciences Center, New Orleans, LA, USA, ccanav@lsuhsc.edu

Frances Chance Department of Neurobiology and Behavior, University of California, Irvine, CA 92697, USA, frances.chance@uci.edu

David W. Cope School of Biosciences, Cardiff University, Cardiff CF10 3US, UK

Vincenzo Crunelli School of Biosciences, Cardiff University, Cardiff CF10 3US, UK

Alain Destexhe Unité de Neurosciences Intégratives et Computationnelles (UNIC), CNRS, 91198 Gif-sur-Yvette, France, destexhe@unic.cnrs-gif.fr

Michael N. Economo Department of Bioengineering, Brain Institute, University of Utah, Salt Lake City, UT, USA; Department of Biomedical Engineering, Boston University, Boston, MA, USA

Jean-Marc Fellous Department of Psychology and Program in Applied Mathematics, ARL Division of Neural Systems, Memory and Aging, University of Arizona, Tucson, AZ 85724, USA, fellous@email.arizona.edu

Fernando R. Fernandez Department of Bioengineering, Brain Institute, University of Utah, Salt Lake City, UT, USA

Bruno Foutry INSERM E358 Institut Magendie, Université Bordeaux 2, Bordeaux, France

Yann Le Franc Unité de Neurosciences Intégratives et Computationnelles (UNIC), CNRS, Gif sur Yvette; INSERM E358 Institut Magendie, Université Bordeaux 2, Bordeaux, France

Yves Frégnac Unité de Neurosciences Intégratives et Computationnelles (UNIC), CNRS, 91198 Gif-sur-Yvette, France

Antoni C.G. van Ginneken Department of Physiology, Academic Medical Center, University of Amsterdam, Amsterdam, 1105 AZ, The Netherlands

José Francisco Gómez González Unité de Neurosciences Intégratives et Computationnelles (UNIC), CNRS, 91198 Gif-sur-Yvette, France

Lyle J. Graham Neurophysiology of Visual Computation Laboratory, Laboratory of Neurophysics and Physiology, CNRS UMR 8119, Université Paris Descartes, 45 rue des Saint-Pères, 75006 Paris, France, lyle@biomedicale.univ-paris5.fr

Rachel Grashow Volen Center and Biology Department, MS 013, Brandeis University, Waltham, MA 02454-9110, USA, rgrashow@brandeis.edu

H. Hu Department of Physiology at Institute of Basal Medicine, and Centre of Molecular Biology and Neuroscience, University of Oslo, PB 1103 Blindern, N-0317 Oslo, Norway

Stuart W. Hughes School of Biosciences, Cardiff University, Cardiff CF10 3US, UK, hughessw@Cardiff.ac.uk

Dieter Jaeger Department of Biology, Emory University, Atlanta, GA 30322, USA, djaeger@emory.edu

Tilman J. Kispersky Department of Bioengineering, Brain Institute, University of Utah, Salt Lake City, UT, USA; Program in Neuroscience, Boston University, Boston, MA, USA

Yves De Koninck Unité de Neurobiologie Cellulaire, Centre de Recherche Université Laval Robert-Giffard, Québec, Québec, G1J 2G3, Canada, yves.dekoninck@crulrg.ulaval.ca

Risa Lin Laboratory for Neuroengineering, School of ECE, Department of Biology,Georgia Institute of Technology, Emory University, Atlanta, GA 30322, USA, risa@gatech.edu

Magor Lörincz School of Biosciences, Cardiff University, Cardiff CF10 3US, UK

Eve Marder Volen Center and Biology Department, MS 013, Brandeis University, Waltham, MA 02454-9110, USA, marder@brandeis.edu

Gwendal Le Masson INSERM E358 Institut Magendie, Université Bordeaux 2, Bordeaux, France

Cyril Monier Unité de Neurosciences Intégratives et Computationnelles (UNIC), CNRS, 91198 Gif-sur-Yvette, France

Zaneta Navratilova ARL Division of Neural Systems, Memory and Aging, University of Arizona, Tucson, AZ 85724, USA, zanetan@email.arizona.edu

Zuzanna Piwkowska Unité de Neurosciences Intégratives et Computationnelles (UNIC), CNRS, 91 198 Gif-sur-Yvette, France; Institute of Higher Nervous Activity, Russian Academy of Science, 117 865 Moscow, Russia, piwkowska@unic.cnrs-gif.fr

Martin Pospischil Unité de Neurosciences Intégratives et Computationnelles (UNIC), CNRS, 91198 Gif-sur-Yvette, France

Steven A. Prescott Department of Neurobiology, University of Pittsburgh, Biomedical Science Tower, W1455, 200 Lothrop Street, Pittsburgh, PA 15213, USA, prescott@neurobio.pitt.edu

Astrid A. Prinz Wallace H. Coulter Department of Biomedical Engineering, Georgia Institute of Technology and Emory University; Department of Biology, Emory University, Atlanta, GA 30332, USA

Stefan R. Pulver Volen Center and Biology Department, MS 013, Brandeis University, Waltham, MA 02454-9110, USA, srpulver@brandeis.edu

Hugh P.C. Robinson Department of Physiology, Development and Neuroscience, University of Cambridge, Cambridge CB2 3EG, UK, hpcr@cam.ac.uk

Michelle Rudolph-Lilith Unité de Neurosciences Intégratives et Computationnelles (UNIC), CNRS, 91198 Gif-sur-Yvette, France

Gerard Sadoc Unité de Neurosciences Intégratives et Computationnelles (UNIC), CNRS, Gif sur Yvette, France, sadoc@unic.cnrs-gif.fr

Adrien Schramm Neurophysiology of Visual Computation Laboratory, Laboratory of Neurophysics and Physiology, CNRS UMR 8119, Université Paris Descartes, 45 rue des Saint-Pères, 75006 Paris, France

Terrence J. Sejnowski Computational Neurobiology Laboratory, Howard Hughes Medical Institute, The Salk Institute for Biological Studies, La Jolla, CA 92037, USA, terry@salk.edu

Fred H. Sieling Wallace H. Coulter Department of Biomedical Engineering, Georgia Institute of Technology and Emory University, Atlanta, GA 30332, USA

J.F. Storm Department of Physiology at Institute of Basal Medicine, and Centre of Molecular Biology and Neuroscience, University of Oslo, pb 1103 Blindern, N-0317 Oslo, Norway, j.f.storm@medisin.uio.no

Lamont S. Tang Volen Center and Biology Department, MS 013, Brandeis University, Waltham, MA 02454-9110, USA, lamont@brandeis.edu

Anne-Elise Tobin Volen Center and Biology Department, Brandeis University, Waltham, MA 02454-9110, USA, atobin@brandeis.edu

Arie O. Verkerk Department of Physiology, Academic Medical Center, University of Amsterdam, Amsterdam, 1105 AZ, The Netherlands

K. Vervaeke Department of Physiology at Institute of Basal Medicine, and Centre of Molecular Biology and Neuroscience, University of Oslo, PB 1103 Blindern, N-0317 Oslo, Norway

John A. White Department of Bioengineering, Brain Institute, University of Utah, 20 S. 2030 E., Salt Lake City, UT 84112, USA, john.white@utah.edu.

Ronald Wilders Department of Physiology, Academic Medical Center, University of Amsterdam, 1105 AZ Amsterdam, The Netherlands, r.wilders@amc.uva.nl

Stephen R. Williams Neurobiology Division, Medical Research Council Laboratory of Molecular Biology, Hills Road, Cambridge CB2 0QH, UK, srw@mrc-lmb.cam.ac.uk

Jan G. Zegers Department of Physiology, Academic Medical Center, University of Amsterdam, Amsterdam, 1105 AZ, The Netherlands

Associating Living Cells and Computational Models: an Introduction to Dynamic Clamp Principles and its Applications

Zuzanna Piwkowska, Alain Destexhe, and Thierry Bal

Abstract The dynamic-clamp electrophysiological technique allows the mimicking of the electrical effects of arbitrary ion channels, controlled by the experimentalist, activating and inactivating into the membrane of an intracellularly recorded biological cell. Dynamic clamp relies on the establishing of a loop between the injected current and the recorded membrane potential. In this introductory chapter, we first present the principles of the technique, starting by recalling the basis of the equivalent electrical circuit representation of a cellular membrane. We then briefly list some of the issues encountered in the practical implementation of the dynamic-clamp loop. Finally, we overview the numerous applications of the method to the study of neurons, other excitable cells and networks of cells: these include the manipulation of intrinsic ion channels and of single or multiple synaptic inputs to a cell, as well as the construction of whole hybrid networks in which the biological cell interacts with model cells simulated in real time using a digital or analog system. Many of the applications briefly presented here are the subject of the following chapters.

Dynamic clamp is an electrophysiological technique for "injecting conductance" (Robinson and Kawai 1993) into an intracellularly recorded cell. Different other terms have been used to describe what it is the dynamic clamp is doing: it has been called a "virtual knock-in" that "introduces a conductance" in the membrane (Dorval and White 2005), a "conductance clamp" (Reyes et al. 1996), a way of "creating artificial conductances in neurons" (Sharp et al. 1993, who also introduced the "dynamic-clamp" name; Prinz et al. 2004), of "changing the membrane resistance" (Le Masson et al. 1995), of "introducing an artificial conductance" (Schreiber et al. 2004), of "applying a conductance waveform" (Gauck and Jaeger 2000), as well as a "partial voltage-clamp"

Z. Piwkowska (✉)
Unité de Neurosciences Intégratives et Computationnelles (UNIC), CNRS, 91 198 Gif-sur-Yvette, France
e-mail: piwkowska@unic.cnrs-gif.fr

A. Destexhe, T. Bal (eds.), *Dynamic-Clamp*, Springer Series in Computational Neuroscience 1, DOI 10.1007/978-0-387-89279-5_1,

(Jaeger and Bower 1999). All these terms are different shorthand ways of saying something along the following lines: dynamic clamp reproduces the electrical effects of the opening of ion channels in the membrane of the cell at the site of the recording. In order to clearly explain how this can be achieved, it is useful to first recall the *equivalent electrical circuit* description of a cellular membrane.

1 Principles of the Technique

1.1 The Equivalent Electrical Circuit of the Membrane

The two essential circuit components used in this description are capacitors and resistors. The double layer of phospholipids composing most of a cell's membrane constitutes an electrical insulator between the intracellular and extracellular conductive media. This insulating sheet is very thin (6–8 nm, Siegelbaum and Koester 2000) so that the electrical charges on both sides, although separated, interact across the membrane: it acts like a capacitor, storing charges of equal magnitude but opposite polarity on each side, which gives rise to a difference of potential V_C . The progressive storage of charges during flow of a current I_c leads to a progressive change of V_C across the capacitor, expressed by the equation[1] (Fig. 1a)

$$C\frac{dV_C}{dt} = I_c$$

The bigger the capacitance C, the slower the change of V_C: this parameter is proportional to the membrane area, which corresponds to the fact that for a bigger membrane area, the charges flowing into the capacitor can "spread" more, and so more of them are needed to produce the same difference of potential in each point across the insulating lipid bilayer.

On the other hand, ion channels inserted in this lipid bilayer are, when open, conductive elements through which electrical charges – that is, ions – flow. This current flow I is proportional to the difference of electrical potential V between both sides of the channel: the channel acts like a resistor, the proportionality law being known as Ohm's law, $I = g \times V$. The coefficient of proportionality, or conductance g, quantifies how easy it is for the charges to move across the channel (with the resistance $R = 1/g$ quantifying how difficult it is, $V = R \times I$ being the more traditional formulation of Ohm's law): for this reason, *conductance* is often used to simply mean *ion channel*, as in some of the dynamic-clamp vocabulary cited above. The direction of current flow is such as to restore

[1] Note that this equation assumes an "ideal" capacitance, in which the charges are re-equilibrated instantaneously. Cable models have been proposed based on "non-ideal" capacitances, which do affect the high-frequency response of the membrane (see Bedard and Destexhe 2008), but such effects will not be considered here.

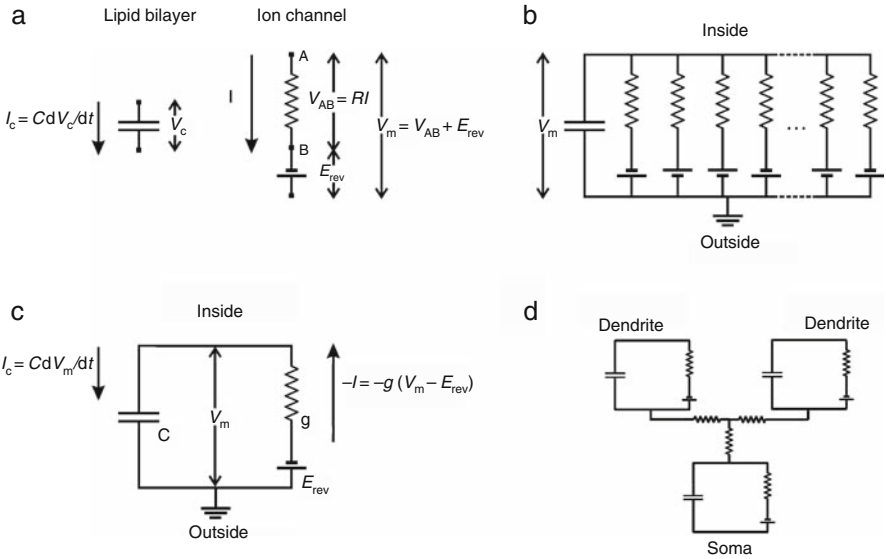

Fig. 1 Constructing the equivalent circuit of a cell. (**a**) The main circuit elements: a capacitor representing the electrical properties of the phospholipid bilayer (*left*), and a resistor in series with a battery, representing the electrical properties of an ion channel with reversal potential E_{rev} (*right*). (**b**) Many such elements can be combined in parallel to represent a patch of cellular membrane. (**c**) Such a parallel arrangement can be represented by an equivalent circuit, with one capacitor, one equivalent resistor and one equivalent battery. (**d**) The spatial organization of a cell (here, a neuron) can be represented using the same formalism, with additional resistors representing the cytoplasm connecting different compartments. See text for details

electrochemical equilibrium between the intracellular and extracellular side: in the case of specific ion channels through which only one or a few ionic species can flow, the equilibrium is not at 0 mV potential difference, but is also set by the difference of concentrations of these specific ions between the intracellular and extracellular media. The equilibrium is reached when the electrical force due to electrostatic repulsion exactly counterbalances the diffusion force due to difference in concentration: the difference in potential at this equilibrium point, where by definition total flow for the considered ion is zero, is called the *Nernst potential* or, more commonly, the *reversal potential* E_{rev} of a given ion.[2] This

[2] In most cases, the difference in ionic concentrations – and, consequently, the E_{rev} – is considered constant on the timescale of an electrophysiological experiment: it is continuously maintained by ATP-consuming pumps or ion co-transporters working against the concentration gradient. The instantaneous changes in ion numbers consecutive to ion flow through the channels are considered negligible compared to the total quantities of ions present inside or outside a cell, instantly flowing in to restore the ion concentration close to the membrane. This assumption does not hold in some cases, like intense firing activity modifying the equilibrium for $K+$ and Cl^- ions in the hippocampus (McCarren and Alger 1985; Thompson and Gähwiler 1989a, b). Moreover, these ionic concentrations evolve on longer timescales: for

notion of non-zero equilibrium can be represented in a circuit by a battery generating a difference of potential E_{rev} and placed in series with the resistor: in such a circuit, as represented in Fig. 1a, equilibrium is reached when the total difference of potential V_{m} across the resistor and the battery (i.e., the membrane potential) is equal to the difference of potential E_{rev} across the battery, so that the points A and B are at the same potential ($V_{\text{AB}} = 0$) and no current flows through the resistor. When V_{m} is not equal to E_{rev}, we have $V_{\text{m}} = E_{\text{rev}} + V_{\text{AB}}$, and $V_{\text{AB}} = RI$ by Ohm's law. It follows that:

$$I = \frac{1}{R}(V_{\text{m}} - E_{\text{rev}}) = g(V_{\text{m}} - E_{\text{rev}}) \tag{1}$$

with the convention that outward current (positive charges *leaving* the cell) is positive. $V_{\text{m}} - E_{\text{rev}}$ is called the *driving force* for this current, which flows so as to restore equilibrium. Channels associated with excitatory synapses have an E_{rev} around 0 mV, much more depolarized than the cell's resting V_m, so that their activation leads to inward current flow and depolarization of the membrane. Channels associated with inhibitory synapses have an E_{rev} close to the resting V_{m}, and often (although not always) more hyperpolarized, in which case their activation leads to outward current flow and hyperpolarization of the membrane.

The point that makes this circuit not immediately, intuitively obvious is the fact that we can somehow visualize the lipid bilayer as a capacitor and ion channels as resistors, but the battery in this representation has no clear visual counterpart. However, as explained above, it does have a physical counterpart when we think about how to represent the notion of non-zero equilibrium. The energy stored in the battery corresponds to the energy stored in the maintained difference of ionic concentrations between the two sides of the membrane. Thus, to be exact, an ion channel is actually represented in the circuit not as a resistor, but as a resistor in series with a battery.

The equivalent circuit of a patch of cellular membrane is, then, composed of a capacitor and of resistors-in-series-with-batteries representing ion channels, arranged in parallel (Fig. 1b): this parallel arrangement can be understood by considering that if all these membrane elements are sufficiently close to each other, and given the low resistivity of the cytoplasm (e.g., Destexhe and Paré 1999), the redistribution of charges in the patch is instantaneous, this piece of membrane (often, e.g., the whole soma of a neuron) is isopotential, and any additional charges flowing into it will distribute between all of the available circuit elements (the open channels and the capacitor).

---

example, during development in the mammalian central nervous system, the intracellular $[Cl^-]$ is progressively lowered due to the delayed expression of a chloride exporter, shifting the E_{rev} of gamma-amino butyric acid (GABA)ergic, Cl-permeable synaptic receptor channels toward more negative values and transforming the function of GABAergic synapses from excitatory to inhibitory (e.g., review by Ben-Ari 2002).

Multiple resistors-in-series-with-batteries in parallel can be represented by a single equivalent resistor in series with a single equivalent battery, in the following way: assuming n such elements in parallel, the current flowing through each element is (for $i = 1$ to n) $I_i = g_i(V_\mathrm{m} - E_i)$, and the total current, that has to be the same in an equivalent circuit, is

$$\begin{aligned} I &= \sum_n I_i = \sum_n \left(g_i(V_\mathrm{m} - E_i)\right) = V_\mathrm{m} \sum_n g_i - \sum_n \left(g_i E_i\right) \\ &= \sum_n g_i \times \left[V_\mathrm{m} - \frac{\sum_n \left(g_i E_i\right)}{\sum_n g_i}\right] \end{aligned} \tag{2}$$

The last expression is of the same form as the expression of I for a single element, with the equivalent conductance $g = \sum_n g_i$ and the equivalent reversal potential

$$E_\mathrm{rev} = \frac{\sum_n \left(g_i E_i\right)}{\sum_n g_i}$$

(average of the E_i's weighted by the associated conductances). This is routinely (and implicitly) used to represent a population of identical channels by only one circuit element (in this specific case, $E_\mathrm{rev} = E_i$). When a diversity of channels is considered, depending on the question at hand, they are either represented separately, each homogeneous population a resistor with its own battery, or they might also be lumped, forming, together with the capacitor in parallel, a single equivalent RC (resistor–capacitor) circuit (Fig. 1c). For a spatially extended cell, like a neuron with a complex dendritic tree, or a myocyte, the correct representation is an ensemble of such RC circuits, connected in series by resistors representing portions of the cytoplasm (Fig. 1d): this representation is at the basis of compartmental modelling, in which each parallel RC circuit is situated in one compartment and the compartments are connected in series to mimic, more or less precisely, the morphology of the cell.

Putting all those elements together in a simple equivalent RC circuit which can, as we have seen, represent a combination of various ion channels embedded in a lipid membrane, and knowing, by virtue of conservation of charge, that the total current flowing through the equivalent resistor charges the capacitor, we have the following relationship (Fig. 1c):

$$C\frac{\mathrm{d}V_\mathrm{m}}{\mathrm{d}t} = -I = -g \times (V_\mathrm{m} - E_\mathrm{rev}) \tag{3}$$

1.2 Back to the Dynamic Clamp

In current-clamp mode, the experimentalist can inject a chosen current into the cell, and in present-day amplifiers, this current is not affected by the recorded V_m in any uncontrolled way. The injected charges sum with all the other currents passing through the membrane to charge the capacitor, so that Eq. (3) becomes

$$C\frac{dV_m}{dt} = -g \times (V_m - E_{rev}) + I_{inj} \tag{4}$$

where I_{inj} is the injected current (the opposite sign used for I_{inj} is due to the fact that traditionally, the opposite convention is used for the injected current – positive charges injected *into* the cell are considered "positive current" – and for the currents flowing through the channels, for which *outward* is positive). It is easy to see, then, that if this injected current is made to depend, in a controlled way, on the recorded V_m of the cell, according to Eq. (1), it is strictly equivalent to adding an additional open ion channel to the membrane:

$$I_{inj} = -g_{add}(V_m - E_{add}) \tag{5}$$

$$C\frac{dV_m}{dt} = -g \times (V_m - E_{rev}) - g_{add}(V_m - E_{add}) \tag{6}$$

where g_{add} is the conductance of the channel and E_{add} is its reversal potential. This is exactly what happens in dynamic clamp: a loop between recorded V_m and injected current I_{inj} is implemented, I_{inj} being calculated according to Eq. (5) from pre-established g_{add} and E_{add}. This calculation can be done either with an analog device, the dependency between I_{inj} and V_m being really instantaneous in this case, or digitally using a computer, in which case the time step required for the calculation, that is, the delay between V_m measure and I_{inj} injection, has to be as small as possible.

In this way, any *conductance waveform* can be "inserted in the membrane," indeed, since g_{add} can be time dependent. g_{add} can also be negative, which provides a way for subtracting existing channels from the membrane, through the injection of a negative image of the current flowing through the biological channels (the two currents cancelling out).[3] In principle, any type of channel can be added (or subtracted) by the procedure: to insert a voltage-dependent channel, g_{add} itself has to be calculated in real time, using the recorded V_m and any necessary equations describing the voltage dependency; to insert a

[3] This application requires, however, a very precise model of the channels existing in the recorded cell, in order to ensure that the injected current really cancels the biological current. It might not be obvious to detect a mismatch between the two, so that interpretation of such experiments is more difficult that when channels are added.

virtual chemical synapse, the synaptic conductance change has to be triggered by some presynaptic signal. This signal can be set in advance, but it can also correspond to an action potential detected in a biological cell, in which case a virtual connection can be created between two previously unconnected cells. It can also originate from a model of a cell or network simulated in real time, that is, with the time step used to numerically integrate the model equations equal to the time step of the dynamic-clamp system. Moreover, such a model cell can also receive inputs triggered by action potentials detected in the recorded cell, which establishes a bidirectional connection between the biological cell and the model cell, creating a small *hybrid network* (Le Masson et al. 1995). Specific examples of these diverse applications, which we briefly introduce in Section 3 below, are the topics of this book.

From the analysis of the equations above, it is clear that the dynamic-clamp loop is indeed equivalent to the insertion of a chosen ion channel (or combination of ion channels, since an equivalent conductance and an equivalent E_{rev} can be used in the same manner) at the site of the recording. However, questions of the type "but is it really equivalent?" or "does it really shunt the membrane, how can it increase the effective conductance and reduce the time constant of the membrane?" are often asked, so that these points are further clarified below.

The equivalence, of course, concerns only electrical phenomena, since the ions carrying the electrical charge when current is injected through a microelectrode are in most cases different from the specific ions flowing through the corresponding biological channel. Whatever depends on the precise nature of these ions, and not only on their charge, is not reproduced – the main situation when this actually matters being the case of Ca^{2+} signaling. This could also be seen as an advantage in some cases, since it allows the dissociation between purely electrical effects and chemical effects. In addition, the chemical effects can in fact also be investigated to some extent, as described by Jaeger and Lin ("Unraveling the Dynamics of Deep Cerebellar Nucleus Neurons with the Application of Artificial Conductances") in this volume: adding in dynamic clamp a model of V_{m} -dependent Ca^{2+} influx and intracellular Ca^{2+} concentration, together with a model of Ca^{2+}-dependent K^+ conductance, allows the mimicking of this K^+ conductance's effects on the spiking patterns of cerebellar neurons recorded in vitro.

Does such a virtual channel "shunt the membrane"? In order to be convinced about this, it is important to understand how the equivalent electrical circuit works, in particular, how additional ion channels impact on the electrical properties of a cell. Experimentally, those properties are often probed, for example, by injection of a constant current I_{const} into the cell. Given the equivalent circuit described in detail above, and an initial condition V_0 for the V_{m}, we have

$$C\frac{\mathrm{d}V_{\text{m}}}{\mathrm{d}t} = -g \times (V_{\text{m}} - E_{\text{rev}}) + I_{\text{const}} \tag{7}$$

$$V_{\text{m}}(t = 0) = V_0$$

In the simple case when the injected current, as well as the circuit parameters g, C, and E_{rev} are constant, Eq. (7) can be integrated, which gives (see the Appendix for details of the calculation):

$$V_{\mathrm{m}}(t) = (V_0 - E_{\mathrm{rev}} - RI_{\mathrm{const}}) \exp\left[\frac{-t}{\tau}\right] + E_{\mathrm{rev}} + RI_{\mathrm{const}} \tag{8}$$

where $R = 1/g$ is called the input resistance of the circuit and $\tau = RC$ its time constant.

In a system initially at rest, without any current flow, $V_0 = E_{\mathrm{rev}}$ and when, at $t = 0$, I_{const} is applied, V_{m} goes exponentially, with a time constant $\tau = RC$, to $E_{\mathrm{rev}} + RI_{\mathrm{const}}$. R can then be computed from the steady-state V_{m} change divided by the applied current, and C from the time constant of an exponential fit to the V_{m} rise and R. Now, when additional ion channels open, R is decreased, so that for the same injected current I_{const}, the steady-state V_{m} change is reduced, and it is also achieved with a faster time constant: this effect is called "shunting." This is clear from Eq. (8), but to understand more intuitively the origin of this effect, it is perhaps better to turn back to the differential equation (7) recalled below:

$$C\frac{\mathrm{d}V_{\mathrm{m}}}{\mathrm{d}t} = -g \times (V_{\mathrm{m}} - E_{\mathrm{rev}}) + I_{\mathrm{const}}$$

When the system is at rest, $V_{\mathrm{m}} = E_{\mathrm{rev}}$ and no current flows across the membrane. When I_{const} is applied, it changes V_{m}, so that now a current starts to flow in the opposite direction through the conductance g, to restore equilibrium in the circuit. Progressively, this opposing current increases, until the two balance out when steady state is reached:

$$\frac{\mathrm{d}V_{\mathrm{m}}}{\mathrm{d}t} = 0 \text{ when } V_{\mathrm{m}} = E_{\mathrm{rev}} + \frac{I_{\mathrm{const}}}{g} = E_{\mathrm{rev}} + RI_{\mathrm{const}}$$

The bigger the conductance g, the bigger the opposing current at each infinitesimal time step, for a given driving force $V_{\mathrm{m}} - E_{\mathrm{rev}}$, and so the smaller the change of V_{m} achieved at steady state. In other words, each channel is "pulling" the V_{m} toward its E_{rev}, and the bigger the conductance g, the stronger the pull. When a channel is added with dynamic clamp, since the dynamic-clamp current depends on the instantaneous driving force, the same effect is obtained, according to the following equation:

$$C\frac{\mathrm{d}V_m}{\mathrm{d}t} = -g \times (V_{\mathrm{m}} - E_{\mathrm{rev}}) - g_{\mathrm{add}}(V_{\mathrm{m}} - E_{\mathrm{add}}) + I_{\mathrm{const}} \tag{9}$$

Now the sum of two currents is injected by the experimentalist: a constant, probing current I_{const} and a voltage-dependent current

$I_{add} = -g_{add}(V_m - E_{add})$. The I_{add} will oppose the effect of the I_{const} just as a corresponding, real ion channel would do, so that the steady-state V_m reached will be reduced compared to a situation where I_{const} is injected alone into the same cell.

The same shunting effect is observed, based on the same principle of an opposing "pull" toward the E_{rev}, for a time-varying current, and regardless of its origin – be it injected through the electrode, or originating from the opening of other synaptic or intrinsic channels in the membrane. Any open channel, biological or dynamic clamp inserted, is thus in competition with other open channels and current sources, and the notion of "shunt" refers exactly to this competition.

Note that if we recall Eq. (9), the response of the circuit to the sum of I_{add} and I_{const} is obviously determined solely by the remaining channels, that is, by g and E_{rev}. This is true whether I_{add} flows through a real channel, or through the pipette in a dynamic-clamp experiment. Obviously, the same is also true if an identical I_{add} is injected in a simple current-clamp mode (see the direct comparison of dynamic clamp and current clamp for the average injected current, in Dorval and White 2006). One might then ask what, then, is the use of dynamic clamp. The crucial word here is "identical." If the experimentalist knew in advance what the V_m response of the membrane was going to be, she could first precompute I_{add} and then inject it in current-clamp mode. But this would make the experiment useless (other than as a verification), since everything would be known from the start. In reality, the V_m response is, in many situations, precisely what we do not know and what we want to record and understand – in the case of dynamic clamp, by tinkering with the ion channels present in the membrane, with the hope of understanding the complex interactions they might produce at the output level.

One last point worth mentioning in this theoretical section is the similarity between dynamic clamp and voltage clamp (also cited above from Jaeger and Bower 1999, who refer to a "partial voltage-clamp"). As we have seen, an ion channel, be it biological or virtual, is basically a device for pulling the V_m toward its equilibrium potential E_{rev}. This is exactly what any voltage-clamp system is doing, only much more efficiently: it is pulling the V_m toward a chosen potential V_{clamp} by injecting a current that dynamically opposes the perturbations produced by other currents. The conductance of a channel corresponds to the gain of the voltage-clamp system, which should in the latter case be as high as possible. The conductance values used in dynamic clamp in most cases are too low, compared to the other conductances present in the membrane, to completely clamp the V_m (as are those of most biological channels; but consider, for example, the huge conductance of Na^+ channels underlying an action potential, and the way it dramatically changes the V_m), which justifies the term of *partial* voltage clamp, but the principle is the same.

2 A Few Words About Implementation

2.1 The Issue of the Time Step

When the practical implementation of the dynamic-clamp loop is considered, a first concern that has to be raised, already mentioned above, is the delay between measured V_m and I_{inj}. For analog and digital systems alike, this delay is related to the filtering of the input and output signals by the whole recording chain. In digital systems, however, the delay is also related to the time needed for the processor to perform the calculation of the injected current. This time depends of course on the model to be simulated. In the simplest, but often not very interesting case of a constant, voltage-independent conductance, or in the case of a precalculated conductance waveform, the system only has to perform a subtraction and a multiplication (see Eq. (5)). In many cases however, at least a few differential equations, describing the voltage-dependent gating of a channel or the activity of a simple cell or even network, have to be numerically integrated at each time step. For this reason, processor speed is an essential factor limiting the complexity of the models that can in practice be implemented for dynamic-clamp experiments. However, the constantly increasing performance of digital computers indicates that processor speed will become less and less of a limitation in the coming years.

Processor speed in itself, however, is unfortunately not the only issue. Another crucial point is the way the operating system (OS) assigns tasks to the processor. In a so-called real-time OS, the user has total control over this task management, and so she can ensure that no external task interferes with the integration of the model equations and the calculation of I_{inj}. Some Unix systems allow this (see Dorval et al. 2001 for a dynamic-clamp system running under real-time Linux). Windows OSs, on the other hand, are not real time, which means that independent of the user, the OS can sometimes assign a system-related task to the processor, interrupting for a time the on-going calculations related to the dynamic-clamp experiment and introducing a jitter in the dynamic-clamp loop. Jitter is especially deleterious when attempting to mimick fast channels such as Na^+ channels underlying action potentials (Bettencourt et al. 2008), as reviewed by White et al ("Using "Hard" Real-Time Dynamic Clamp to Study Cellular and Network Mechanisms of Synchronization in the Hippocampal Formation") in this volume.

One way to avoid this problem, which can also increase the available processor speed, is to run the calculations on a devoted chip, instead of the main processor of a computer, for example, on the processor directly integrated to a digital signal processing (DSP) board. This type of board acts like an acquisition board, performing analog-to-digital conversion at its inputs, and digital-to-analog conversion at its outputs, but also has its own processor, optimized for fast signal processing. One such dynamic-clamp implementation, specifically designed to mimic a fast voltage-dependent K^+ channel, achieved a rate

around 50 kHz (Lien and Jonas 2003). A scriptable DSP-based dynamic-clamp system allowing the flexible implementation of user-defined conductances was recently developed (Robinson 2008).

In the real-time NEURON dynamic-clamp system (Sadoc et al. "Re-Creating In Vivo-Like Activity and Investigating the Signal Transfer Capabilities of Neurons: Dynamic-Clamp Applications Using Real-Time NEURON" in this volume), which is fully digital and runs on a standard Windows PC, a DSP board and its clock are used in order to time the inputs to and outputs from the dynamic-clamp software at regular intervals (Le Franc et al. 2001; Le Masson et al. 2002; Wolfart et al. 2005), largely eliminating the jitter problem, with the calculations still being performed by the PC's processor. This approach has the advantage of offering all the flexibility and power of the NEURON simulation software (Hines and Carnevale 1997), as well as a good compatibility with models developed using NEURON.

Another approach is to use an analog system for all or part of the dynamic-clamp calculations. In such a system, the calculations are performed by dedicated circuits: instead of being digitized and then processed, bit by bit, by logic circuits in a computer processor, the recorded V_m, for example, directly influences an electric circuit that is specifically designed in order to produce the desired current at its output. In this case, the calculation is performed in real-time, without any processing delay. The drawback of fully analog systems is their relative lack of flexibility. A specific analog circuit is needed to implement each model, even though some of the model's parameters can be implemented with an external command to the chip (e.g., Sorensen et al. 2004). In addition, it is technically very challenging to obtain the same precision as in digital models due to transistor noise (S. Le Masson et al. 1999). A combination of analog and digital computations is one option for combining flexibility with speed (e.g., Harsch and Robinson 2000).

2.2 The Issue of Precise V_m Measurement

Not only has the $V_m - I_{inj}$ loop to be fast, it also has to rely on an accurate measure of the V_m. This means that if a single electrode is used for both current injection and V_m recording, the voltage drop U_e due to flow of current through the electrode's resistance has to be adequately compensated. The use of two electrodes solves this problem, but it is not possible in all preparations and it considerably complicates the experiment. In "Key Factors for Improving Dynamic-Clamp Performance" in this volume, Butera and Lin provide a detailed analysis of factors that limit dynamic-clamp performance and stability. In "Dynamic Clamp with High-Resistance Electrodes Using Active Electrode Compensation In Vitro and In Vivo" in this volume, Brette et al. present the limitations of traditional single-electrode compensation techniques, especially when used in dynamic-clamp protocols, and describe a new, improved technique for high-resolution V_m recording during simultaneous current injection.

3 Examples of Application

Recent reviews (Prinz et al. 2004; Prinz 2004; Goaillard and Marder 2006) list an impressive number of studies applying the dynamic-clamp technique to a variety of physiological questions at the level of single cells as well as tissues of interacting cells. Until now, the word "neuron" was avoided in this chapter, for the reason that electrophysiological tools in general, and dynamic clamp among them, are used in fields other than neuroscience, like cardiac physiology with the study of cardiomyocytes or endocrine physiology with the study of β-cells in the pancreas (as reviewed by Goaillard and Marder 2006). An early form of the dynamic-clamp technique, called the "Ersatz Nexus," has been described in cardiac physiology as early as 1979, in a PhD thesis studying the impact of electrical synapses (gap junctions) on the synchronization of clusters of cardiomyocytes in the chicken (Scott 1979). Later studies of cardiac tissue re-introduced a technique named "coupling clamp" (Tan and Joyner 1990) for bi-directionally connecting two isolated myocytes by a virtual gap junction of chosen conductance. The injected current flowing through the virtual gap junction is calculated according to a driving force determined in real time and equal to the difference of membrane potential between the two cells (see Verheijck et al. 1998 for an example of application exploring the synchronization between two spontaneously active rabbit cardiac cells). An extension of this technique, named the "model clamp" by the authors, consists in coupling, through such a virtual gap junction, a real myocyte and a model myocyte simulated in real time (Wilders et al. 1996). Both of these approaches are conceptually identical to the technique described in Section 1, their specificity lying in the precise type of membrane conductance they implement, the gap junction. The history and use in cardiac physiology of the technique now know as dynamic clamp is reviewed by Verkerk et al. ("Development of a Genetically Engineered Cardiac Pacemaker: Insights from Dynamic Action Potential Clamp Experiments") in this volume. The authors also present a new, related technique they have recently developed, "dynamic action potential clamp" (Berecki et al. 2005). In this approach, a cell recorded under current clamp is bi-directionally connected in real time with a voltage-clamped genetically modified cell expressing a large density of an ion channel of interest. The ion channel is thus electrically "inserted" in the current-clamped cell at the site of the recording, in a way similar to the insertion of a modeled channel in dynamic clamp. The innovation lies in the fact that no model of the channel needs to be built, so that channels that are only identified genetically (e.g., when a mutation in a channel gene has been linked to a disease) can be directly studied in a functional framework, via their effects on, for example, the spiking pattern of a given cell type.

In neuroscience, the dynamic-clamp technique in its general form, with the general purpose of inserting into the membrane of a neuron any conductance the experimentalist might be interested in, has been introduced independently by Hugh Robinson (Robinson and Kawai 1993) and by a team led by Eve

Marder and Larry Abbott, based on a collaboration with Gwendal Le Masson (Le Masson et al. 1992; Sharp et al. 1993; see also Le Masson et al. 1995). From the onset, based on the same principle of injecting a V_m -dependent current into a neuron, different implementations and applications were explored by the different groups: using digital systems, Robinson and Kawai injected synaptic inputs into cultured hippocampal neurons of the vertebrate central nervous system (CNS), while Sharp and colleagues studied various conductances and artificial networks in the stomatogastric ganglion (STG) of decapod crustaceans (lobsters and crabs) nervous system. Le Masson et al. (1995) developed an analog and a digital approach simultaneously for studies of the invertebrate preparation (and subsequently combined both approaches in a single study of mammalian thalamus networks, see Le Masson et al. 2002). Since this time, dynamic clamp has been widely used in both vertebrate (Jaeger and Lin "Unraveling the Dynamics of Deep Cerebellar Nucleus Neurons with the Application of Artificial Conductances," Hughes et al. "Using the Dynamic Clamp to Dissect the Properties and Mechanisms of Intrinsic Thalamic Oscillations," Piwkowska et al. "Testing Methods for Synaptic Conductance Analysis Using Controlled Conductance Injection with Dynamic Clamp," Sadoc et al. "Re-Creating In Vivo-Like Activity and Investigating the Signal Transfer Capabilities of Neurons: Dynamic-Clamp Applications Using Real-Time NEURON," Robinson "Synaptic Conductances and Spike Generation in Cortical Cells," Chance and Abbott "Simulating In Vivo Background Activity in a Slice with the Dynamic Clamp," Williams "Dendritic Dynamic Clamp – A Tool to Study Single Neuron Computation," Prescott and De Koninck "Impact of Background Synaptic Activity on Neuronal Response Properties Revealed by Stepwise Replication of In Vivo-Like Conditions In Vitro," Fellous et al. "Intrinsic and Network Contributions to Reverberatory Activity: Reactive Clamp and Modeling Studies," Graham and Schramm "In Vivo Dynamic-Clamp Manipulation of Extrinsic and Intrinsic Conductances: Functional Roles of Shunting Inhibition and I_{BK} in Rat and Cat Cortex," Verkerk et al. "Development of a Genetically Engineered Cardiac Pacemaker: Insights from Dynamic Action Potential Clamp Experiments," in this volume) and invertebrate preparations (Tobin et al. "Using the Dynamic Clamp to Explore the Relationship Between Intrinsic Activity and Network Dynamics," Canavier et al. "Dynamic-Clamp-Constructed Hybrid Circuits for the Study of Synchronization Phenomena in Networks of Bursting Neurons" in this volume).

3.1 Manipulations of Intrinsic Channels in Single Neurons

One branch of dynamic-clamp applications could be called "virtual pharmacology" (or "virtual knock-in" following Dorval and White 2005): it consists in adding or, more seldom, subtracting intrinsic (as opposed to synaptic) channels in a single cell recorded intracellularly, with the enormous advantage – compared

to the non-virtual equivalent – of being able to finely control all the properties of the channel and to scan the space of channel parameters in a single cell. Automated fitting of the channel model's parameters can also be performed during the recording so as to reproduce a chosen feature of the cell's control output, such as spike shape, after the real channel has been pharmacologically blocked (Milescu et al. 2008): this procedure is a recently proposed alternative to classical voltage-clamp characterization of ion channels.

Using dynamic clamp, Lien and Jonas (2003) showed that the Kv3 delayed rectifier K^+ channel is necessary, and perhaps even sufficient under some conditions, for the fast spiking (FS) phenotype of hippocampal inhibitory neurons. The systematic scanning of different parameters of the injected Kv3 conductance indicated that the observed "wild-type" parameters (especially deactivation kinetics) fall into a small region of parameter space producing the high-frequency, non-adapting firing pattern typical of FS neurons, and so appear to be finely tuned to this effect. These results could not have been obtained with classical pharmacological exploration nor theoretical simulation alone, the latter always facing the difficulty of properly adjusting all the parameters that are not under investigation.

In thalamocortical cells, Hughes et al. (1998, 1999) applied dynamic clamp to the manipulation of I_h, I_T, and leak currents: they showed how these channels can regulate the oscillatory properties of these cells, which are crucial for the generation of natural sleep as well as pathological thalamo-cortical rhythms. This work is presented in more detail by Hughes et al. ("Using the Dynamic Clamp to Dissect the Properties and Mechanisms of Intrinsic Thalamic Oscillations") in this volume. In prefrontal cortical cells, a slow potassium conductance was shown to regulate the input frequency at which maximal spike timing reliability can be achieved (Schreiber et al. 2004). In spinal cord motoneurons, dynamic clamp was used to investigate in vivo the impact of an after-hyperpolarizing conductance on firing rate gain and coefficient of variation (Manuel et al. 2006), as well as to demonstrate that depending on their time constant, persistent inward currents interact with I_h to set different modes of amplification of proprioceptive inputs (Manuel et al. 2007). The dynamic clamp was also used to inject conductances in cat visual cortical neurons in vivo using the active electrode compensation (AEC) technique (Brette et al. 2008; see Brette et al. "Dynamic Clamp with High-Resistance Electrodes Using Active Electrode Compensation In Vitro and In Vivo" in this volume). In these experiments, different stimulation protocols were compared in vitro and in vivo, including white noise injection and injection of fluctuating synaptic conductances. In another application of the dynamic clamp in vivo, Graham and Schramm ("In Vivo Dynamic-Clamp Manipulation of Extrinsic and Intrinsic Conductances: Functional Roles of Shunting Inhibition and I_{BK} in Rat and Cat Cortex" in this volume) investigated the role of the I_{BK} potassium channel in modulating the responsiveness of visual cortical neurons to simulated as well as to real visual inputs, and confirmed their prediction of increased spike frequency in the presence of the channel,

despite the hyperpolarizing nature of the potassium current. Such "virtual pharmacology" in vivo appears as a promising new research direction, as it combines the precise manipulation of chosen channels with the evaluation of functional responses of neurons, for example, to sensory stimuli, impossible to perform in slice preparations. AEC (Brette et al. 2008), presented in "Dynamic Clamp with High-Resistance Electrodes Using Active Electrode Compensation In Vitro and In Vivo" by Brette et al., improves the feasibility of such in vivo dynamic-clamp experiments, as shown in visual cortical neurons of anaesthetized cat using a variety of protocols (such as injection of synaptic fluctuating conductances).

Dynamic clamp also allows the selective manipulations of channels for which specific pharmacological agonists and antagonists are not known, as in a recent study on the persistent sodium current in CA1 hippocampal pyramidal neurons (Vervaeke et al. 2006), presented by Storm et al. in "Functions of the Persistent Na^+ Current In Cortical Neurons Revealed by Dynamic Clamp" in this volume. Specific pharmacological agents cannot be used for this current as it is probably due, at least in part, to the activation of the same population of channels that also give rise to the transient inactivating sodium current responsible for action potentials. Selectively manipulating the persistent current with dynamic clamp, while leaving the transient current intact, allowed the investigation of the persistent current's impact on the spiking of hippocampal neurons in vitro.

The study of Dorval and White (2005) is another example of the benefits of virtual pharmacology. By inserting, into enthorinal cortex stellate cells, either a deterministic or a stochastic model of the already mentioned persistent Na^+ channel, the authors show that channel noise, present in the latter case, restores perithreshold membrane oscillations and the level of spike time reliability observed before the block of the native channel, while the deterministic model fails to do so. This study, presented by White et al. ("Using "Hard" Real-Time Dynamic Clamp to Study Cellular and Network Mechanisms of Synchronization in the Hippocampal Formation") in this volume, could not have been performed by means other than dynamic clamp, since any manipulation influencing the stochasticity of the channel (like change in temperature) would also have affected its deterministic gating parameters, and the two effects would have been difficult to disambiguate.

In an invertebrate motor network controlling the contractions of the digestive system, the STG of the crab, dynamic clamp was used to complement modeling approaches systematically characterizing the influence of five intrinsic conductances on the spontaneous firing patterns of STG neurons (Goldman et al. 2001). In addition, in such a small network (about 30 neurons, some of which electrically coupled), the modulation of an intrinsic current in one or two cells only can have an impact on the oscillatory dynamics of the whole network: mimicking currents triggered by proctoline, a neuromodulator, specifically in some of the cells responsive to this substance allows the emergence of a motor

rhythm similar to the one elicited by bath application of proctoline (Swensen and Marder 2001).

In all the applications mentioned above, the virtual conductances are placed at the site of the current-injecting electrode, that is, at the soma of the recorded cell. This point location of the inserted conductances constitutes one of the limitations of the dynamic-clamp technique. However, as presented by Hughes and colleagues ("Using the Dynamic Clamp to Dissect the Properties and Mechanisms of Intrinsic Thalamic Oscillations") in this volume, with their recently developed dynamic-clamp system NeuReal, the authors could add artificial dendritic trees, modeled using more than a hundred compartments and containing various voltage-dependent conductances, onto the soma of thalamic relay cells recorded in vitro (Hugues et al. 2008): in this application, the biological, somatic V_m recorded at the soma is used to compute the current flowing from the soma into the modeled dendritic tree, which is combined with currents flowing through modeled dendritic channels to yield the V_m in each of the dendritic compartments. The dendritic V_m is in turn used to determine the current flowing from the dendrites to the soma at the next time step, which is then injected through the somatic electrode into the biological soma. Such an artificial dendritic tree can transform a thalamic cell that does not spontaneously oscillate into an oscillating one, demonstrating that non-trivial effects can be investigated using this new application of the dynamic-clamp technique.

3.2 Manipulations of Single Synaptic Inputs

The earliest publications introducing the dynamic-clamp technique in neuroscience (Robinson and Kawai 1993; Sharp et al. 1993; Le Masson et al. 1995) were all focused on the possibility of implementing artificial synapses in neurons. The dynamic clamp is especially adapted to the study of synaptic inhibition: since the V_m fluctuates close to the E_{rev} of inhibition, the driving force for inhibitory currents also fluctuates in an important way, so that approximating inhibition by a driving-force-independent current is bound to be incorrect in many cases. Dynamic clamp was thus used, for example, to investigate the impact of single GABA-A- and GABA-B-like synaptic inputs on the bursting of thalamic neurons (Ulrich and Huguenard 1996, 1997), as well as to assess how the heterogeneity between inhibitory synapses converging onto single hippocampal cells affects their responsiveness (Foldy et al. 2004; Aradi et al. 2004). In the first dendritic application of the dynamic-clamp technique, Williams and Stuart (2003) investigated how the attenuation of the somatic impact of apical dendritic IPSPs (inhibitory postsynaptic potentials) was modulated by voltage-dependent mechanisms, as reviewed by Williams ("Dendritic Dynamic Clamp – A Tool to Study Single Neuron Computation") in this volume.

Dynamic clamp has also been used in two recent studies (Gulledge and Stuart 2003; Vida et al. 2006) investigating the effect of depolarizing

inhibition,[4] that is, inhibition with a reversal potential between V_{rest} and spike threshold. Activation of such GABAergic conductances leads to depolarization from rest – a potentially excitatory effect – but, if strong enough, also effectively clamps the V_m below spike threshold, which, combined with the activation of excitatory, glutamatergic synapses, can actually inhibit spiking. This double effect of such depolarizing inhibition potentially makes it a polyvalent mechanism, with a context-dependent impact, and not straightforward to apprehend intuitively: this is where a systematic, quantitative approach using modeling and dynamic clamp can prove useful.

Gulledge and Stuart (2003) showed that if the depolarizing GABAergic-like conductance transient coincided with a glutamatergic excitatory postsynaptic potential (EPSP) evoked by extracellular stimulation within a small temporal window of duration similar to the half-width of the conductance change, it had an inhibitory effect, presumably due to clamping of the V_m at the E_{rev} of the artificial conductance; however, when the GABAergic-like conductance preceded the EPSP, so that the conductance decayed, but the depolarization persisted until the time the EPSP arrived, its effect was excitatory. A similar issue was investigated by Vida et al. (2006) in hippocampal interneurons. Tonic excitation was provided by constant depolarizing current injection, and depolarizing GABAergic-like conductance transients were injected in dynamic clamp following each spike – mimicking a case in which GABAergic inputs are triggered by the synchronous firing of a network of inhibitory neurons that also includes the recorded neuron. Provided the GABAergic conductance was strong enough, it increased firing frequency for weak excitatory drive, but decreased it for strong excitatory drive, effectively homogenizing the firing rate in response to a diversity of excitatory inputs.

These two studies are reported here in some detail to illustrate that far from being a gadget, the specificity of the dynamic clamp, consisting in injecting driving-force-dependent-currents in intracellularly recorded neurons, allows the investigation of neuronal integration mechanisms that depend in a crucial way on the precise reversal potentials of membrane conductances. Dynamic-clamp experiments could thus possibly help elucidating how developmental (e.g., Tyzio et al. 2006; see also Ben-Ari 2002 and Stein and Nicoll 2003 for reviews) or pathological (Cohen et al. 2002) changes in E_{GABA} influence network dynamics, by manipulating single synaptic inputs or perhaps by constructing *hybrid networks*.

---

[4] Such inhibition is sometimes called *shunting* (e.g., Vida et al. 2006): the term *shunting* is used in this specific case because the main source of inhibition of spikes is the clamp at E_{rev} below spike threshold – as opposed to *hyperpolarizing* inhibition, which has the effect of actively pulling the V_m below rest. However, as we have seen, all membrane conductances are shunting in the sense that they are tending to clamp the V_m at their reversal potentials. The term is thus a little bit misleading at first because it seems to falsely imply that only shunting inhibition shunts, by virtue of some special property other conductances would not have.

3.3 Hybrid Networks

The possibility of inserting single synaptic inputs into living neurons with dynamic clamp has been extended in many creative ways to build *hybrid networks* composed of biological neurons connected by virtual synapses, or biological neurons connected to model neurons by virtual synapses (see Prinz 2004, for a short review). Prior to the introduction of the dynamic-clamp technique, some studies were performed in which biological neurons were connected by virtual synapses using current, rather than conductance, injection, in both mollusc (Zosimovskii 1980; Zosimovskii et al. 1980) and mammalian preparations (Yarom 1991).

The hybrid networks approach has been widely used in the small, well-identified neuronal networks of invertebrate nervous systems, especially in the pyloric motor network of the STG of decapod crustaceans (see Tobin et al. "Using the Dynamic Clamp to Explore the Relationship Between Intrinsic Activity and Network Dynamics" and Canavier et al. "Dynamic-Clamp-Constructed Hybrid Circuits for the Study of Synchronization Phenomena in Networks of Bursting Neurons" in this volume). In this model system, a small number of neurons connected by electrical and chemical inhibitory synapses generate oscillatory patterns of activity, constituting a central pattern generator (CPG). Using dynamic clamp, Le Masson et al. (1995) showed how the pattern could be modulated by varying the conductance of intrinsic channels in a model neuron replacing a biological neuron in the network, or by varying the strength of an inhibitory synapse. The impact of the instrinsic current I_h as well as that of maximal synaptic conductance, synaptic time constant and threshold were further studied in similar systems by Sharp et al. (1996) and Elson et al. (2002). I_h was also shown to modulate burst duration and the period of oscillation in a hybrid network reconstruction of the CPG pacing the heartbeat of the medicinal leech (Sorensen et al. 2004). Phase response curves (PRCs) were used by other authors to characterize how a synaptic input perturbs the period of a spontaneously oscillating STG cell, depending on the phase of the oscillation on which it is applied. With dynamic-clamp synaptic inputs, the impact of synaptic conductance and duration on the PRC could be established, indicating how the modulation of synaptic properties could control the period of a network (Prinz et al. 2003). Furthermore, it was explicitly shown that PRCs, which are an open-loop measure, could be used to predict the oscillatory behavior in a closed-loop hybrid network composed of a biological STG bursting neuron and a model bursting neuron connected by virtual synapses (Oprisan et al. 2004), as reviewed by Canavier et al. ("Dynamic-Clamp-Constructed Hybrid Circuits for the Study of Synchronization Phenomena in Networks of Bursting Neurons") in this volume. The impact of synaptic plasticity on the oscillatory behavior of small networks could also be assessed using the hybrid network approach (Manor and Nadim 2001; Nowotny et al. 2003). Finally, Tobin et al. ("Using the Dynamic Clamp to Explore the Relationship Between Intrinsic Activity and Network Dynamics" in this volume) propose that including different biological STG neurons into hybrid networks with

defined model cells, and comparing network outputs, provides a new method for comparing biological cells, in a way that might be more meaningful for network function than comparing intrinsic properties of cells such as input resistance.

In vertebrate CNSs, neuronal networks are several orders of magnitude larger; however, it is still possible to build hybrid networks in order to investigate the functioning of small, elementary network modules composed of a few cells (the next section presents approaches for including larger numbers of cells). In the hippocampal formation, the oscillatory properties of two reciprocally connected entorhinal neurons were explored on the basis of spike time response curves (STRCs), in a manner similar to the PRC approach applied to the decapod pyloric network (Netoff et al. 2005; see White et al. "Using "Hard" Real-Time Dynamic Clamp to Study Cellular and Network Mechanisms of Synchronization in the Hippocampal Formation" in this volume for a review of this and more recent hybrid network investigations in entorhinal cortex): these functions indicate by how much a single synaptic input, applied at a given time after a spike, perturbs (advances or delays, relative to the unperturbed condition) the timing of the next spike. The authors compared behavior theoretically predicted from such measured STRCs with oscillations observed in hybrid networks composed of two biological cells connected with a virtual synapse, or of a biological cell connected to a cell modeled with a given STRC, and found a close agreement between all these cases.

Le Masson et al. (2002) studied the transmission of information from the retina (implemented by an analog retinal model neuron) to the cortex through a hybrid thalamic network composed of a biological thalamic relay cell recorded in vitro and a model reticular cell providing feedback inhibition onto the biological neuron. Progressively decreasing the strength of the inhibitory feedback onto the relay cell allowed the switching of the network from a mode of spontaneous oscillations during which the output of the thalamic relay cell is uncorrelated to the ongoing retinal input, and similar to the thalamic spindles observed in vivo during sleep or anesthesia, to a mode of effective information transmission, during which the output spike train of the thalamic relay cell (which constitutes the input to primary visual cortex) is correlated to the retinal input, possibly similar to the awake state. A conceptually similar study by Derjean et al. (2003), in spinal deep dorsal horn neurons relaying sensory inputs from nociceptive afferents, used a detailed model afferent fiber connected to the investigated neuron through a dynamic-clamp synapse in order to probe the effectiveness of information transmission by these neurons during their different intrinsic firing modes (tonic, plateau potentials or endogenous bursting). It showed quantitatively that each firing mode corresponded to a different capability for information transfer and could contribute to a specific functional state of sensitivity to pain. These studies are evoked in more detail by Sadoc et al. ("Re-Creating In Vivo-Like Activity and Investigating the Signal Transfer Capabilities of Neurons: Dynamic-Clamp Applications Using Real-Time NEURON") in this volume.

3.4 Manipulations of Multiple Synaptic Inputs

Another approach for studying large vertebrate networks consists in inserting into a neuron in vitro time-varying conductance waveforms mimicking the thousands of synaptic inputs which are known to converge in vivo onto single neurons in structures such as the cortex, the thalamus, the hippocampus, the cerebellum or the basal ganglia. The conductance waveforms are generated either by the convolution of presynaptic spike trains with unitary synaptic conductances (Reyes et al. 1996; Jaeger and Bower 1999; Harsch and Robinson 2000; Gauck and Jaeger 2000; Chance et al. 2002; Hanson and Jaeger 2002; Gauck and Jaeger 2003; Kreiner and Jaeger 2004; Suter and Jaeger 2004; de Polavieja et al. 2005; Zsiros and Hestrin 2005; Dorval and White 2006; Tateno and Robinson 2006; Morita et al. 2008), or by effective stochastic models of "synaptic bombardment" or "synaptic noise," without explicit representation of the presynaptic spike trains (Destexhe et al. 2001; Shu et al. 2003; McCormick et al. 2003; Fellous et al. 2003; Wolfart et al. 2005; Hasenstaub et al. 2005; Shu et al. 2006; Desai and Walcott 2006; Piwkowska et al. 2008). In most studies, two independent (uncorrelated) conductance waveforms are used, one excitatory (AMPA, α-amino-3-hydroxy-5-methyl-4-isoazoleprionic acid) and one inhibitory (GABA-A), but some authors also explore the impact of a voltage-dependent NMDA (*N*-methyl-D-aspartate) conductance (Harsch and Robinson 2000; Gauck and Jaeger 2003) or start addressing the issue of correlation between the excitatory and inhibitory waveforms (Tateno and Robinson 2006) or more generally the issue of temporal structure like gamma oscillations within the input (Morita et al. 2008). Studies of this type are presented in this volume by Jaeger and Lin ("Unraveling the Dynamics of Deep Cerebellar Nucleus Neurons with the Application of Artificial Conductances" in this volume), Robinson ("Synaptic Conductances and Spike Generation in Cortical Cells" in this volume), Sadoc et al. ("Re-Creating In Vivo-Like Activity and Investigating the Signal Transfer Capabilities of Neurons: Dynamic-Clamp Applications Using Real-Time NEURON" in this volume), Fellous et al. ("Intrinsic and Network Contributions to Reverberatory Activity: Reactive Clamp and Modeling Studies" in this volume), White et al. ("Using "Hard" Real-Time Dynamic Clamp to Study Cellular and Network Mechanisms of Synchronization in the Hippocampal Formation"), Chance and Abott ("Simulating In Vivo Background Activity in a Slice with the Dynamic Clamp" in this volume). Prescott and De Koninck ("Impact of Background Synaptic Activity on Neuronal Response Properties Revealed by Stepwise Replication of In Vivo-Like Conditions In Vitro" in this volume) propose a related approach, in which the different components of a massive in vivo-like synaptic input to cortical and hippocampal neurons – increased conductance (shunting), depolarization, and fluctuations – are controlled separately, in order to better understand their respective impact and that of their interactions on neuronal integration.

The results obtained by manipulating massive synaptic input to a neuron with dynamic clamp can be tentatively classified within a few different neuronal coding frameworks. Some studies consider that the relevant output of a neuron is its firing rate over some integration window (rate coding framework), and investigate how such an output is modulated by different aspects of the virtual synaptic input (Reyes et al. 1996; Jaeger and Bower 1999; Gauck and Jaeger 2000; Harsch and Robinson 2000; Hanson and Jaeger 2002; Chance, Abbott and Reyes 2002; Fellous et al. 2003; Suter and Jaeger 2004; Tateno and Robinson 2006). In the related population coding framework, neuronal output is integrated over space, not time, so that for a single neuron the probability of firing in response to an input can be considered as the relevant output (Shu et al. 2003; Wolfart et al. 2005). Within both these frameworks, the slope of input–output functions, also called gain, is a matter of particular interest, and has been shown, for example, to either increase (Fellous et al. 2003; see also Fellous et al. "Intrinsic and Network Contributions to Reverberatory Activity: Reactive Clamp and Modeling Studies" in this volume), decrease (Chance et al. 2002; Shu et al. 2003; see also Chance and Abbott "Simulating In Vivo Background Activity in a Slice with the Dynamic Clamp" in this volume), or remain unchanged (Tateno and Robinson 2006; see also Robinson "Synaptic Conductances and Spike Generation in Cortical Cells" in this volume) with increased synaptic conductance fluctuations, depending on neuron type and on the precise structure of the input. In thalamic relay neurons, in vivo-like fluctuating synaptic input was shown to interact with intrinsic properties such as the T current to shape the input–output function, with increased synaptic noise acting to reduce the classically described voltage dependency of these neurons' integrative properties (Wolfart et al. 2005; see also Sadoc et al. "Re-Creating In Vivo-Like Activity and Investigating the Signal Transfer Capabilities of Neurons: Dynamic-Clamp Applications Using Real-Time NEURON" in this volume). The specific role of inhibitory shunting on neuronal responsiveness could also be addressed quantitatively (Mitchell and Silver 2003). Prescott and De Koninck ("Impact of Background Synaptic Activity on Neuronal Response Properties Revealed by Stepwise Replication of In Vivo-Like Conditions In Vitro" in this volume; Prescott and De Koninck 2003; Prescott et al. 2006) explored in detail how shunting and fluctuations interact in modifying input–output functions in a divisive (gain modulation) or subtractive manner, and how they can switch hippocampal neurons from integrators to coincidence detectors via modulation of spike frequency adaptation. In vivo-like massive synaptic inputs were also found to abolish intrinsic theta oscillations at both subthreshold and spiking level in single entorhinal cells, indicating that mechanisms of theta oscillations at the population level in vivo might be different than previously thought (Fernandez and White 2008), as presented by White et al. ("Using "Hard" Real-Time Dynamic Clamp to Study Cellular and Network Mechanisms of Synchronization in the Hippocampal Formation") in this volume. Finally, Graham and Schramm ("In Vivo Dynamic-Clamp Manipulation of Extrinsic and Intrinsic Conductances: Functional Roles of Shunting

Inhibition and I_{BK} in Rat and Cat Cortex" in this volume) for the first time directly studied the effect of shunting in vivo via constant dynamic-clamp inhibition in cortical neurons responding to both artificial and visual stimuli.

Another line of investigation revolves around the idea that the precise timing of single spikes is relevant for neuronal computations (time code), and dynamic clamp was used to investigate which parameters of the input are crucial for spike timing precision and reliability (Jaeger and Bower 1999; Harsch and Robinson 2000; Gauck and Jaeger 2000, 2003; Suter and Jaeger 2004; Kreiner and Jaeger 2004; Zsiros and Hestrin 2005; Tateno and Robinson 2006; Dorval and White 2006). In deep cerebellar nucleus neurons, dynamic-clamp experiments, reviewed by Jaeger and Lin ("Unraveling the Dynamics of Deep Cerebellar Nucleus Neurons with the Application of Artificial Conductances") in this volume, revealed the possible importance of synchronous drops in inhibitory inputs from Purkinje cell for reliably triggering spikes. In both RS and FS cortical neurons, the control of spike time precision and reliability by both stationary and transient properties of realistic synaptic inputs is described by Robinson ("Synaptic Conductances and Spike Generation in Cortical Cells" in this volume). Finally, a new "analog" coding scheme, exploiting spike shape in addition to spike timing, was recently proposed for cortical neurons on the basis of dynamic-clamp experiments (de Polavieja et al. 2005) and is also presented by Robinson ("Synaptic Conductances and Spike Generation in Cortical Cells") in this volume. In all these studies, the ability to precisely and independently manipulate different parameters of the synaptic input, specific to the dynamic-clamp technique, opened the way to new quantitative assessments of the integrative properties of single neurons embedded in large active networks.

The injection of a known, precisely controlled synaptic input, resembling the total input received by neurons in vivo, can also be used to test analysis methods for extracting underlying synaptic conductances from recorded V_m traces (Rudolph et al. 2004, Pospischil et al. 2007, Piwkowska et al. 2008), as presented by Piwkowska et al. ("Testing Methods for Synaptic Conductance Analysis Using Controlled Conductance Injection with Dynamic Clamp") in this volume. In a conceptually similar approach, Williams and Mitchell (2008; see also Williams "Dendritic Dynamic Clamp – A Tool to Study Single Neuron Computation" in this volume) recently showed the severity of space-clamp problems in cortical neurons, by injecting dynamic-clamp synaptic inputs at different dendritic sites and attempting to measure the resulting synaptic currents with voltage clamp at the soma. It is the most recent of a series of studies, presented by Williams ("Dendritic Dynamic Clamp – A Tool to Study Single Neuron Computation") in this volume, in which dynamic-clamp injection of synaptic conductances in both the apical dendrites and the soma of pyramidal cells was used to investigate local, compartmentalized synaptic integration in the dendrites, its impact on somatic firing and its modulation by in vivo-like excitatory and inhibitory synaptic bombardment (Williams 2004, 2005).

In all the studies mentioned above, the network is considered as a source of input only: the fact that the investigated neuron itself belongs to the network, and so can provide feedback to some of its input neurons, or participate in the activation of successive network layers in a feedforward manner, was not taken into account. One of the mentioned studies (Morita et al. 2008), however, reviewed by Robinson ("Synaptic Conductances and Spike Generation in Cortical Cells") in this volume, investigated which properties of the synaptic inputs allow the self-consistent matching of a cortical neuron's spiking output with a gamma-modulated input spike train. In other studies, the recorded neuron was replaced within a network by using its output to influence the dynamic-clamp input, in a feedforward (Reyes 2003; Sohal and Huguenard 2005) or feedback manner (Fellous and Sejnowski 2003; see also Arsiero et al. 2005 for a related, current-clamp-based approach), as presented in more detail by Fellous et al. ("Intrinsic and Network Contributions to Reverberatory Activity: Reactive Clamp and Modeling Studies") in this volume. In prefrontal cortical neurons, the authors combined a background of synaptic excitatory and inhibitory inputs with feedback inputs triggered by the spikes of the recorded cell in a "reactive clamp" protocol, and succeeded in reproducing characteristic features of cortical recurrent network activity such as periodic up-states and persistent delay activity following a brief stimulus.

Finally, the recently proposed dynamic-clamp system NeuReal, already mentioned in the context of artificial dendritic trees, allows the real-time simulation of around a thousand intrinsic and synaptic conductances: the authors illustrate its performance by constructing a hybrid thalamic network composed of 49 single-compartment model neurons containing five conductances each, sparsely coupled by electrical synapses, and of one real thalamocortical relay cell recorded in vitro (Hughes et al. 2008; see Hughes et al. "Using the Dynamic Clamp to Dissect the Properties and Mechanisms of Intrinsic Thalamic Oscillations" in this volume). Thus, it also appears possible to study neuronal integration in large mammalian networks by embedding a biological neuron within a sizeable hybrid network of individually simulated model cells.

3.5 On the Many Possibilities of Dynamic-Clamp Applications, and Beyond

The examples briefly mentioned above and presented in this book illustrate, on the one hand, the complexity of the phenomena electrophysiologists are confronted with, from the level of single channels to the network level, and on the other hand, the many possibilities offered by dynamic clamp to deal with this complexity. The dynamic-clamp technique and its extensions, like the hybrid networks approach, allow a combination of the best aspects of modelling with the advantages of an experimental approach, through simulations performed

within the biological system itself. In this way, a systematic exploration of the parameter space of the modelled element (channel, synapse, neuron, effective network activity, etc.) can be performed, while ensuring that the remaining parameters of the investigated system are correct and do not need to be adjusted to any external experimental data.

However, it is striking to note that almost all of the dynamic-clamp applications have been restricted until now to one (admittedly, major) branch of single cell electrophysiology, namely, in vitro preparations and somatic recordings, while the important domains of in vivo electrophysiology, as well as dendritic recordings in vitro, have almost not benefited from the many possibilities offered by the technique – the few notable exceptions being the studies by Williams and colleagues (Williams and Stuart 2003; Williams 2004, 2005; Williams and Mitchell 2008), presented by Williams in "Dendritic Dynamic Clamp – A Tool to Study Single Neuron Computation" in this volume and dealing with dendritic mechanisms of synaptic integration; and, in vivo, a few recent studies: Brizzi et al. (2004) and Manuel et al. (2005, 2006, 2007) in cat spinal motoneurons, and Graham and Schramm ("In Vivo Dynamic-Clamp Manipulation of Extrinsic and Intrinsic Conductances: Functional Roles of Shunting Inhibition and I_{BK} in Rat and Cat Cortex" in this volume) as well as Haider et al. (2007) in visual cortical neurons.

This situation is in part due to important limitations imposed on high-resolution dynamic clamp by the properties of the recording microelectrodes (see Brette et al. "Dynamic Clamp with High-Resistance Electrodes Using Active Electrode Compensation In Vitro and In Vivo", Butera and Lin "Key Factors for Improving Dynamic-Clamp Performance", and Williams "Dendritic Dynamic Clamp – A Tool to Study Single Neuron Computation" in this volume). AEC (Brette et al. 2008), presented by Brette et al. ("Dynamic Clamp with High-Resistance Electrodes Using Active Electrode Compensation In Vitro and In Vivo") in this volume, provides a new digital technique for overcoming these limitations. AEC is another example of application for computing devices interfaced in real time with an electrophysiological recording setup: a dynamic-clamp system is used to implement a computational model of the recording electrode, calibrate the model to a particular recording, and then operate in real time a correction of the recorded membrane potential, as a function of the injected current, with unprecedented accuracy. This technique is particularly useful for conditions where the stimulus contains fast transients, for example, when injecting noise in neurons. A similar approach can also be used in the other direction, by correcting the current as a function of the imposed voltage, leading to a method to obtain high-precision voltage-clamp recordings (work in progress). AEC was used to perform, for the first time, injections of synaptic conductance noise in cortical neurons in vivo, and it should contribute to extend the field of application of the dynamic-clamp technique to a variety of new, promising experimental situations that could benefit from approaches similar to the ones that are presented in this book.

4 Appendix

Integration of the membrane equation describing the evolution of the membrane potential V, in the case of a constant injected current I and constant parameters g, C, and E of the equivalent circuit

$$C\frac{\mathrm{d}V}{\mathrm{d}t} = -g \times (V - E) + I$$

$$V(t = 0) = V_0$$

By making the change of variable

$$W = \frac{-g \times (V - E) + I}{C}$$

$$\frac{\mathrm{d}W}{\mathrm{d}t} = \frac{-g}{C} \times \frac{\mathrm{d}V}{\mathrm{d}t}$$

we obtain

$$\frac{\mathrm{d}W}{\mathrm{d}t} = \frac{-g}{C} \times W$$

This type of differential equation has a known solution, which is

$$W = K_1 \exp\left[\frac{-g}{C}t\right]$$

or, defining $\tau = C/g = RC$,

$$W = K_1 \exp\left[\frac{-t}{\tau}\right]$$

Replacing V in this equation gives

$$V = K_2 \exp\left[\frac{-t}{\tau}\right] + E + \frac{\tau}{C}I = K_2 \exp\left[\frac{-t}{\tau}\right] + E + RI$$

(K_1 and K_2 are arbitrary constants) and by introducing the initial condition V_0, we have $V_0 = K_2 + E + RI$, so that, finally

$$V = (V_0 - E - RI) \exp\left[\frac{-t}{\tau}\right] + E + RI$$

Acknowledgments We thank Jose Gomez and Charlotte Deleuze for comments on an earlier version of this chapter. Research supported by CNRS, ANR, ACI, HFSP, and the European Community (FACETS grant FP6 15879). Z.P. gratefully acknowledges the support of the FRM.

References

Aradi I, Santhakumar V, Soltesz I (2004) Impact of heterogeneous perisomatic IPSC populations on pyramidal cell firing rates. J Neurophysiol 91:2849–2858.

Arsiero M, Luescher HR, Giugliano M (2005) The mean-field dynamic-clamp: linking single-neuron properties to network activity in in vitro preparations. In: Society for Neuroscience Meeting. 823.1.

Bedard C, Destexhe A (2008) A modified cable formalism for modeling neuronal membranes at high frequencies. Biophys J 94:1133–1143.

Ben-Ari Y (2002) Excitatory actions of gaba during development: the nature of the nurture. Nat Rev Neurosci 3:728–739.

Berecki G, Zegers JG, Verkerk AO, Bhuiyan ZA, de Jonge B, Veldkamp MW, Wilders R, van Ginneken ACG (2005) HERG channel (dys)function revealed by dynamic action potential clamp technique. Biophys J 88:566–578.

Bettencourt JC, Lillis KP, Stupin LR, White JA (2008) Effects of imperfect dynamic clamp: Computational and experimental results. J Neurosci Methods 169:282–289.

Brette R, Piwkowska Z, Monier C, Rudolph-Lilith M, Fournier J, Levy M, Fregnac Y, Bal T, Destexhe A (2008) High-resolution intracellular recordings using a real-time computational model of the electrode. Neuron 59:379–391.

Brizzi L, Meunier C, Zytnicki D, Donnet M, Hansel D, LaMotte D'Incamps B, Van Vreeswikj C (2004) How shunting inhibition affects the discharge of lumbar motoneurones. A dynamic clamp study in anaesthetised cats. J Physiol 558:671–683.

Chance FS, Abbott LF, Reyes AD (2002) Gain modulation from background synaptic input. Neuron 35:773–782.

Cohen I, Navarro V, Clemenceau S, Baulac M, Miles R (2002) On the origin of interictal activity in human temporal lobe epilepsy in vitro. Science 298:1418–1421.

de Polavieja GG, Harsch A, Kleppe I, Robinson HP, Juusola M (2005) Stimulus history reliably shapes action potential waveforms of cortical neurons. J Neurosci 25:5657–5665.

Derjean D, Bertrand S, Le Masson G, Landry M, Morisset V, Nagy F (2003) Dynamic balance of metabotropic inputs causes dorsal horn neurons to switch functional states. Nat Neurosci 6:274–281.

Desai NS, Walcott EC (2006) Synaptic bombardment modulates muscarinic effects in forelimb motor cortex. J Neurosci 26:2215–2226.

Destexhe A, Pare D (1999) Impact of network activity on the integrative properties of neocortical pyramidal neurons in vivo. J Neurophysiol 81:1531–1547.

Destexhe A, Rudolph M, Fellous JM, Sejnowski TJ (2001) Fluctuating synaptic conductances recreate in vivo-like activity in neocortical neurons. Neuroscience 107:13–24.

Dorval AD, Christini DJ, White JA (2001) Real-Time linux dynamic clamp: a fast and flexible way to construct virtual ion channels in living cells. Ann Biomed Eng 29:897–907.

Dorval AD, Jr., White JA (2005) Channel noise is essential for perithreshold oscillations in entorhinal stellate neurons. J Neurosci 25:10025–10028.

Dorval AD, White JA (2006) Synaptic input statistics tune the variability and reproducibility of neuronal responses. Chaos 16:026105.

Elson RC, Selverston Al, Abarbanel HD, Rabinovich MI (2002) Inhibitory synchronization of bursting in biological neurons: dependence on synaptic time constant. J Neurophysiol 88:1166–1176.

Fellous JM, Rudolph M, Destexhe A, Sejnowski TJ (2003) Synaptic background noise controls the input/output characteristics of single cells in an in vitro model of in vivo activity. Neuroscience 122:811–829.

Fellous JM, Sejnowski TJ (2003) Regulation of persistent activity by background inhibition in an in vitro model of a cortical microcircuit. Cereb Cortex 13:1232–1241.

Fernandez FR, White JA (2008) Artificial synaptic conductances reduce subthreshold oscillations and periodic firing in stellate cells of the entorhinal cortex. J Neurosci 28:3790–3803.

Foldy C, Aradi I, Howard A, Soltesz I (2004) Diversity beyond variance: modulation of firing rates and network coherence by GABAergic subpopulations. Eur J Neurosci 19:119–130.
Gauck V, Jaeger D (2000) The control of rate and timing of spikes in the deep cerebellar nuclei by inhibition. J Neurosci 20:3006–3016.
Gauck V, Jaeger D (2003) The contribution of NMDA and AMPA conductances to the control of spiking in neurons of the deep cerebellar nuclei. J Neurosci 23:8109–8118.
Goaillard JM, Marder E (2006) Dynamic clamp analyses of cardiac, endocrine, and neural function. Physiology (Bethesda) 21:197–207.
Goldman MS, Golowasch J, Marder E, Abbott LF (2001) Global structure, robustness, and modulation of neuronal models. J Neurosci 21:5229–5238.
Gulledge AT, Stuart GJ (2003) Excitatory actions of GABA in the cortex. Neuron 37:299–309.
Haider B, Duque A, Hasenstaub AR, Yu Y, McCormick DA (2007) Enhancement of visual responsiveness by spontaneous local network activity in vivo. J Neurophysiol 97:4186–4202.
Hanson JE, Jaeger D (2002) Short-term plasticity shapes the response to simulated normal and parkinsonian input patterns in the globus pallidus. J Neurosci 22:5164–5172.
Harsch A, Robinson HP (2000) Postsynaptic variability of firing in rat cortical neurons: the roles of input synchronization and synaptic NMDA receptor conductance. J Neurosci 20:6181–6192.
Hasenstaub A, Shu Y, Haider B, Kraushaar U, Duque A, McCormick DA (2005) Inhibitory postsynaptic potentials carry synchronized frequency information in active cortical networks. Neuron 47:423–435.
Hines ML, Carnevale NT (1997) The NEURON simulation environment. Neural Comput 9:1179–1209.
Hughes SW, Cope DW, Crunelli V (1998) Dynamic clamp study of Ih modulation of burst firing and delta oscillations in thalamocortical neurons in vitro. Neuroscience 87:541–550.
Hughes SW, Cope DW, Toth TI, Williams SR, Crunelli V (1999) All thalamocortical neurones possess a T-type Ca2+ 'window' current that enables the expression of bistability-mediated activities. J Physiol 517:805–815.
Hughes SW, Lorincz M, Cope DW, Crunelli V (2008) NeuReal: An interactive simulation system for implementing artificial dendrites and large hybrid networks. J Neurosci Methods 169:290–301.
Jaeger D, Bower JM (1999) Synaptic control of spiking in cerebellar Purkinje cells: dynamic current clamp based on model conductances. J Neurosci 19:6090–6101.
Kreiner L, Jaeger D (2004) Synaptic shunting by a baseline of synaptic conductances modulates responses to inhibitory input volleys in cerebellar Purkinje cells. Cerebellum 3:112–125.
Le Franc Y, Foutry B, Nagy F, Le Masson G (2001) Nociceptive signal transfer through the dorsal horn network: hybrid and dynamic clamp approaches using a real-time implementation of the Neuron simulation environment. In: Society for Neuroscience Meeting. 927.18
Le Masson G, Renaud-Le Masson S, Sharp AA, Marder E, Abbott LF (1992) Real-time interaction between a model neuron and the crustacean stomatogastric nervous system In: Society for Neuroscience Meeting. 18, 1055.
Le Masson G, Le Masson S, Moulins M (1995) From conductances to neural network properties: analysis of simple circuits using the hybrid network method. Prog Biophys Mol Biol 64:201–220.
Le Masson S, Laflaquiere A, Bal T, Le Masson G (1999) Analog circuits for modeling biological neural networks: design and applications. IEEE Trans Biomed Eng 46:638–645.
Le Masson G, Renaud-Le Masson S, Debay D, Bal T (2002) Feedback inhibition controls spike transfer in hybrid thalamic circuits. Nature 417:854–858.
Lien CC, Jonas P (2003) Kv3 potassium conductance is necessary and kinetically optimized for high-frequency action potential generation in hippocampal interneurons. J Neurosci 23:2058–2068.

Manor Y, Nadim F (2001) Synaptic depression mediates bistability in neuronal networks with recurrent inhibitory connectivity. J Neurosci 21:9460–9470.
Manuel M, Meunier C, Donnet M, Zytnicki D (2005) How much afterhyperpolarization conductance is recruited by an action potential? A dynamic-clamp study in cat lumbar motoneurons. J Neurosci 25:8917–8923.
Manuel M, Meunier C, Donnet M, Zytnicki D (2006) The afterhyperpolarization conductance exerts the same control over the gain and variability of motoneurone firing in anaesthetized cats. J Physiol 576:873–886.
Manuel M, Meunier C, Donnet M, Zytnicki D (2007) Resonant or not, two amplification modes of proprioceptive inputs by persistent inward currents in spinal motoneurons. J Neurosci 27:12977–12988.
McCarren M, Alger BE (1985) Use-dependent depression of IPSPs in rat hippocampal pyramidal cells in vitro. J Neurophysiol 53:557–571.
McCormick DA, Shu Y, Hasenstaub A, Sanchez-Vives M, Badoual M, Bal T (2003) Persistent cortical activity: mechanisms of generation and effects on neuronal excitability. Cereb Cortex 13:1219–1231.
Milescu LS, Yamanishi T, Ptak K, Mogri MZ, Smith JC (2008) Real-time kinetic modeling of voltage-gated ion channels using dynamic clamp. Biophys J 95:66–87.
Mitchell SJ, Silver RA (2003) Shunting inhibition modulates neuronal gain during synaptic excitation. Neuron 38:433–445.
Morita K, Kalra R, Aihara K, Robinson HP (2008) Recurrent synaptic input and the timing of gamma-frequency-modulated firing of pyramidal cells during neocortical "UP" states. J Neurosci 28:1871–1881.
Netoff TI, Banks MI, Dorval AD, Acker CD, Haas JS, Kopell N, White JA (2005) Synchronization in hybrid neuronal networks of the hippocampal formation. J Neurophysiol 93:1197–1208.
Nowotny T, Zhigulin VP, Selverston AI, Abarbanel HD, Rabinovich MI (2003) Enhancement of synchronization in a hybrid neural circuit by spike-timing dependent plasticity. J Neurosci 23:9776–9785.
Oprisan SA, Prinz AA, Canavier CC (2004) Phase resetting and phase locking in hybrid circuits of one model and one biological neuron. Biophys J 87:2283–2298.
Piwkowska Z, Pospischil M, Brette R, Sliwa J, Rudolph-Lilith M, Bal T, Destexhe A (2008) Characterizing synaptic conductance fluctuations in cortical neurons and their influence on spike generation. J Neurosci Methods 169:302–322.
Pospischil M, Piwkowska Z, Rudolph M, Bal T, Destexhe A (2007) Calculating event-triggered average synaptic conductances from the membrane potential. J Neurophysiol 97:2544–2552.
Prescott SA, De Koninck Y (2003) Gain control of firing rate by shunting inhibition: roles of synaptic noise and dendritic saturation. Proc Natl Acad Sci USA 100:2076–2081.
Prescott SA, Ratté S, De Koninck Y, Sejnowski TJ (2006) Nonlinear interaction between shunting and adaptation controls a switch between integration and coincidence detection in pyramidal neurons. J Neurosci 26: 9084–9097.
Prinz AA, Thirumalai V, Marder E (2003) The functional consequences of changes in the strength and duration of synaptic inputs to oscillatory neurons. J Neurosci 23:943–954.
Prinz AA, Abbott LF, Marder E (2004) The dynamic clamp comes of age. Trends Neurosci 27:218–224.
Prinz AA (2004) Neural networks: models and neurons show hybrid vigor in real time. Curr Biol 14:R661–662.
Reyes AD, Rubel EW, Spain WJ (1996) In vitro analysis of optimal stimuli for phase-locking and time-delayed modulation of firing in avian nucleus laminaris neurons. J Neurosci 16:993–1007.
Reyes AD (2003) Synchrony-dependent propagation of firing rate in iteratively constructed networks in vitro. Nat Neurosci 6:593–599.

Robinson HP, Kawai N (1993) Injection of digitally synthesized synaptic conductance transients to measure the integrative properties of neurons. J Neurosci Methods 49:157–165.
Robinson HP (2008) A scriptable DSP-based system for dynamic conductance injection. J Neurosci Methods 169:271–281.
Rudolph M, Piwkowska Z, Badoual M, Bal T, Destexhe A (2004) A method to estimate synaptic conductances from membrane potential fluctuations. J Neurophysiol 91:2884–2896.
Schreiber S, Fellous JM, Tiesinga P, Sejnowski TJ (2004) Influence of ionic conductances on spike timing reliability of cortical neurons for suprathreshold rhythmic inputs. J Neurophysiol 91:194–205.
Scott S (1979) Stimulation Simulations of Young Yet Cultured Beating Hearts. In: Buffalo, NY: State University of New York.
Sharp AA, O'Neil MB, Abbott LF, Marder E (1993) Dynamic clamp: computer-generated conductances in real neurons. J Neurophysiol 69:992–995.
Sharp AA, Skinner FK, Marder E (1996) Mechanisms of oscillation in dynamic clamp constructed two-cell half-center circuits. J Neurophysiol 76:867–883.
Shu Y, Hasenstaub A, Badoual M, Bal T, McCormick DA (2003) Barrages of synaptic activity control the gain and sensitivity of cortical neurons. J Neurosci 23:10388–10401.
Shu Y, Hasenstaub A, Duque A, Yu Y, McCormick DA (2006) Modulation of intracortical synaptic potentials by presynaptic somatic membrane potential. Nature 441:761–765.
Siegelbaum SA, Koester J (2000) Ion channels. In: Principles of neural science, 4th Edition (Kandel ER, Schwartz JH, Jessell TM, eds). New York, NY: McGraw-Hill.
Sohal VS, Huguenard JR (2005) Inhibitory coupling specifically generates emergent gamma oscillations in diverse cell types. Proc Natl Acad Sci USA 102:18638–18643.
Sorensen M, DeWeerth S, Cymbalyuk G, Calabrese RL (2004) Using a hybrid neural system to reveal regulation of neuronal network activity by an intrinsic current. J Neurosci 24:5427–5438.
Stein V, Nicoll RA (2003) GABA generates excitement. Neuron 37:375–378.
Suter KJ, Jaeger D (2004) Reliable control of spike rate and spike timing by rapid input transients in cerebellar stellate cells. Neuroscience 124:305–317.
Swensen AM, Marder E (2001) Modulators with convergent cellular actions elicit distinct circuit outputs. J Neurosci 21:4050–4058.
Tan RC, Joyner RW (1990) Electrotonic influences on action potentials from isolated ventricular cells. Circ Res 67:1071–1081.
Tateno T, Robinson HP (2006) Rate coding and spike-time variability in cortical neurons with two types of threshold dynamics. J Neurophysiol 95:2650–2663.
Thompson SM, Gahwiler BH (1989a) Activity-dependent disinhibition. I. Repetitive stimulation reduces IPSP driving force and conductance in the hippocampus in vitro. J Neurophysiol 61:501–511.
Thompson SM, Gahwiler BH (1989b) Activity-dependent disinhibition. II. Effects of extracellular potassium, furosemide, and membrane potential on ECl- in hippocampal CA3 neurons. J Neurophysiol 61:512–523.
Tyzio R, Cossart R, Khalilov I, Minlebaev M, Hubner CA, Represa A, Ben-Ari Y, Khazipov R (2006) Maternal oxytocin triggers a transient inhibitory switch in GABA signaling in the fetal brain during delivery. Science 314:1788–1792.
Ulrich D, Huguenard JR (1996) Gamma-aminobutyric acid type B receptor-dependent burst-firing in thalamic neurons: a dynamic clamp study. Proc Natl Acad Sci USA 93:13245–13249.
Ulrich D, Huguenard JR (1997) GABA(A)-receptor-mediated rebound burst firing and burst shunting in thalamus. J Neurophysiol 78:1748–1751.
Verheijck EE, Wilders R, Joyner RW, Golod DA, Kumar R, Jongsma HJ, Bouman LN, van Ginneken AC (1998) Pacemaker synchronization of electrically coupled rabbit sinoatrial node cells. J Gen Physiol 111:95–112.

Vervaeke K, Hu H, Graham LJ, Storm JF (2006) Contrasting effects of the persistent Na + current on neuronal excitability and spike timing. Neuron 49:257–270.
Vida I, Bartos M, Jonas P (2006) Shunting inhibition improves robustness of gamma oscillations in hippocampal interneuron networks by homogenizing firing rates. Neuron 49:107–117.
Wilders R, Verheijck EE, Kumar R, Goolsby WN, van Ginneken AC, Joyner RW, Jongsma HJ (1996) Model clamp and its application to synchronization of rabbit sinoatrial node cells. Am J Physiol 271:H2168–2182.
Williams SR and Stuart GJ (2003) Voltage- and site-dependent control of the somatic impact of dendritic IPSPs. J Neurosci 23, 7358–7367.
Williams SR (2004) Spatial compartmentalization and functional impact of conductance in pyramidal neurons. Nat Neurosci 7:961–967.
Williams SR (2005) Encoding and decoding of dendritic excitation during active states in pyramidal neurons. J Neurosci 25:5894–5902.
Williams SR and Mitchell SJ (2008) Direct measurement of somatic voltage clamp errors in central neurons. Nature Neurosci 11:790–798.
Wolfart J, Debay D, Le Masson G, Destexhe A, Bal T (2005) Synaptic background activity controls spike transfer from thalamus to cortex. Nat Neurosci 8:1760–1767.
Yarom Y (1991) Rhythmogenesis in a hybrid system – interconnecting an olivary neuron to an analog network of coupled oscillators. Neuroscience 44:263–275.
Zosimovskii VA, Balaban PM, Zakharov IS, Sokolov EN (1980) [Study of monosynaptic excitatory connections using a biomathematical model of neuronal interaction] Neirofiziologiia 12(4):413–420. Russian.
Zosimovskii VA (1980) [Use of EC-1020 computers for experimental studies of synaptic interaction of mollusk neurons] Zh Vyssh Nerv Deiat Im I P Pavlova. 30(6):1306–1311. Russian.
Zsiros V, Hestrin S (2005) Background synaptic conductance and precision of EPSP-spike coupling at pyramidal cells. J Neurophysiol 93:3248–3256.

Dendritic Dynamic Clamp – A Tool to Study Single Neuron Computation

Stephen R. Williams

Abstract Central neurons receive the majority of synaptic input at dendritic sites. Classical models of neuronal function suggest that dendrites simply funnel synaptic input to the site of action potential initiation in the axon. Direct dendritic whole-cell recording techniques have however demonstrated that dendrites are electrically excitable. Recently, the dynamic clamp has been used to simulate synaptic activity at determined dendritic sites in neurons, to explore the constraints of the dendrosomatic spread of synaptic potentials and to examine the properties of local dendritic synaptic integration. Here, I describe the implementation of the dendritic dynamic-clamp technique and review the results of recent experiments using the dendritic dynamic clamp to explore the properties of synaptic integration in the dendrites of cortical pyramidal neurons.

1 Introduction

Neurons of the central nervous system have a complex morphology. Typically, central neurons possess an elaborate dendritic tree, where the majority of synaptic input is received (Hausser et al. 2000). Yet, action potential output is generated within the proximal axon (Clark et al. 2005, Khaliq and Raman 2006, Palmer and Stuart 2006, Kole et al. 2008). This anatomical arrangement poses a problem, as pioneering modelling studies have shown that the amplitude of synaptic potentials decrease as they spread through the dendritic tree (Rall 1977). Synapses targeted to distal dendritic sites that can be millimetres from the axon may therefore have little impact on neuronal output. Why then do central neurons have such a complex and electrically distributed morphology? One reason could be that synaptic integration is not restricted to the site of

S.R. Williams (✉)
Neurobiology Division, Medical Research Council Laboratory of Molecular Biology, Hills Road, Cambridge CB2 0QH, UK
e-mail: srw@mrc-lmb.cam.ac.uk

A. Destexhe, T. Bal (eds.), *Dynamic-Clamp*, Springer Series in Computational Neuroscience 1, DOI 10.1007/978-0-387-89279-5_2,

axonal action potential initiation, but is operational within the dendritic tree, where synaptic potentials are amplified and/or locally integrated following the recruitment of dendritic voltage-activated ion channels (London and Hausser 2005). Synaptic integration in central neurons may therefore operate independently at many sites within the dendritic tree, potentially expanding the computational repertoire of single neurons (Archie and Mel 2000, Poirazi and Mel 2001, Hausser and Mel 2003, London and Hausser 2005). In order to test this hypothesis, direct recording from the fine calibre dendrites of central neurons is required, coupled with an ability to evoke or simulate synaptic activity at determined sites. The dynamic clamp provides a useful tool to address this problem. Here I review results of recent experiments that have used the dynamic clamp to study dendritic synaptic integration in cortical pyramidal neurons.

2 Implementation and Methodological Considerations

The dynamic clamp can be used to simulate the operation of synapses (Prinz et al. 2004). Fast synaptic activity is mediated by the opening of postsynaptic ionotropic neurotransmitter receptors. The gating of these receptors leads to the permeation of ions along electrochemical gradients. For example, α-amino-3-hydroxy-5-methyl-4-isoazoleprionic acid (AMPA)-type glutamate receptors, predominately, gate sodium and potassium ions leading to postsynaptic depolarization. The postsynaptic consequence of synaptic activation can therefore be modelled simply as a voltage-dependent current source. Thus, the dynamic clamp can be used to simulate synaptic activity, and key parameters such as the magnitude and time course of the conductance change and the reversal potential controlled. This allows the generation of simulated excitatory and inhibitory postsynaptic potentials (referred to as dEPSPs and dIPSPs, where d refers to events simulated with the dynamic clamp) in a manner comparable to the activation of real synaptic inputs. Synapses are however predominately targeted to dendritic sites; to explore the impact of simulated synapses on neuronal output dEPSPs and dIPSPs should be generated dendritically. Improvements in the visualization of neurons using infrared differential interference contrast and two-photon microscopy have allowed high-quality recordings to be made from the dendrites of many classes of central neurons maintained in brain-slice preparations (Stuart et al. 1993) and recently in vivo (Kitamura et al. 2008) under visual guidance. Despite the benefits of low-access resistance whole-cell dendritic recordings, problems of bridge balancing and capacitance neutralization are manifest. First, the apparent membrane time constant at dendritic sites of pyramidal neurons is fast relative to the soma, and can be less than 2 ms at distal apical dendritic trunk sites (Williams and Stuart 2003a). The fast local time constant makes accurate bridge balancing difficult. Second, relatively high resistance (10–50 MΩ) electrodes are used for dendritic recordings, and so the capacitance neutralization circuitry of the amplifier requires careful adjustment

(Nevian et al. 2007). Under these conditions, and for all current clamp recordings, a capacitive artifact is generated when current is injected through the recording electrode. Thus, the time course of recorded membrane potential changes contain significant artifacts that preclude the use of single electrode recording techniques to accurately simulate EPSPs and IPSPs with the dynamic clamp. To overcome these problems, Stuart and colleagues developed a dual somatic recording approach to generate and record simulated synaptic potentials (Stuart and Sakmann 1995, Stuart 1999, Williams and Stuart 1999). The use of a separate electrode and amplifier to inject current and to record membrane potential allowed the recording of the undistorted voltage waveform of simulated synaptic potentials. Recently this technique has been adapted for the generation and recording of dEPSPs and dIPSPs from dendritic sites, using dual dendritic whole-cell recordings from closely separated (<10 μm) apical dendritic sites in cortical pyramidal neurons (Fig. 1) (Williams and Stuart 2002, 2003b, Williams 2004, 2005, Williams and Mitchell 2008). Under these conditions, simulated dendritic synaptic activity can be accurately generated with the dynamic clamp, and when coupled with simultaneous recording from other dendritic and somatic sites, the spread of synaptic potentials through a neuron can be unequivocally measured (Fig. 1).

2.1 Why Not Voltage-Clamp Dendritic Neurons?

The somatic voltage clamp is the prevalent technique used to the study synaptic physiology in central neurons. Why then use dendritic recording techniques to study the impact of dendritic synapses at the soma, when simply recording synaptic currents from the soma could yield information about the properties and efficacy of dendritic synapses? To answer this question, the limitations of the somatic voltage clamp have recently been investigated in dendritic neurons (Williams and Mitchell 2008). Using the dynamic-clamp, excitatory and inhibitory postsynaptic conductances (dEPSCs and dIPSCs) were generated from apical dendritic sites in cortical pyramidal neurons and an independent low-access resistance whole-cell voltage-clamp recording made from the soma (Williams and Mitchell 2008). This configuration allowed a direct comparison of the synaptic current injected at the dendritic site of generation and that recorded under voltage clamp from the soma (Fig. 2). Moreover, the use of dual dendritic recording allowed the precise measurement of voltage escape at the site of dEPSC or dIPSC generation. Results indicated that the somatic voltage clamp underestimated the peak synaptic current generated at dendritic sites, reporting only a small fraction of the synaptic current generated from distal apical dendritic sites (Fig. 2) (Williams and Mitchell 2008). Indeed, when dEPSCs with kinetics that replicate those of fast spontaneous and stimulus evoked excitatory synaptic inputs to cortical pyramidal neurons were generated from dendritic sites, the somatic voltage clamp reported only half the injected

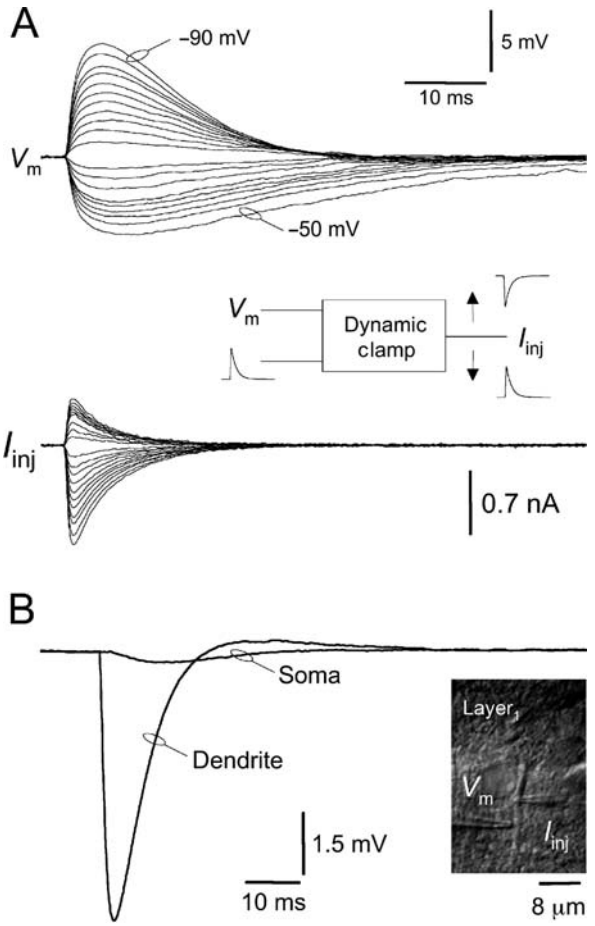

Fig. 1 Dendritic dynamic clamp. A. Simulation of IPSPs using the dynamic clamp. A separate electrode was used to inject current (I_{inj}) and record membrane potential (V_m). The membrane potential was controlled by current injection, and set over a range of potentials (−50 to −90 mV). At each holding potential a dIPSP was generated. Dynamic IPSPs generated across this membrane potential range have been overlain. The reversal potential of the inhibitory conductance (E_{IPSP}) was −65 mV. A schematic of the dynamic clamp is shown in the inset, indicating the input – the recorded membrane potential (V_m) and the conductance waveform and the output – current injection (I_{inj}). The value of I_{inj} was calculated according to the formulae: $I_{inj} = g_{IPSP}.(V_m - E_{IPSP})$. **B**. Dendrosomatic spread of dIPSPs during triple whole-cell recording. Voltage records were recorded from the soma and a dendritic site (680 μm). The inset shows the placement of dendritic recording pipettes used to record membrane potential and inject current. Modified from Williams and Stuart (2003b)

synaptic current when dEPSCs were generated just 90 μm from the soma. Similarly, voltage control at the dendritic site of dEPSC generation deteriorated in a distance-dependent manner, resulting in the generation of escape EPSPs

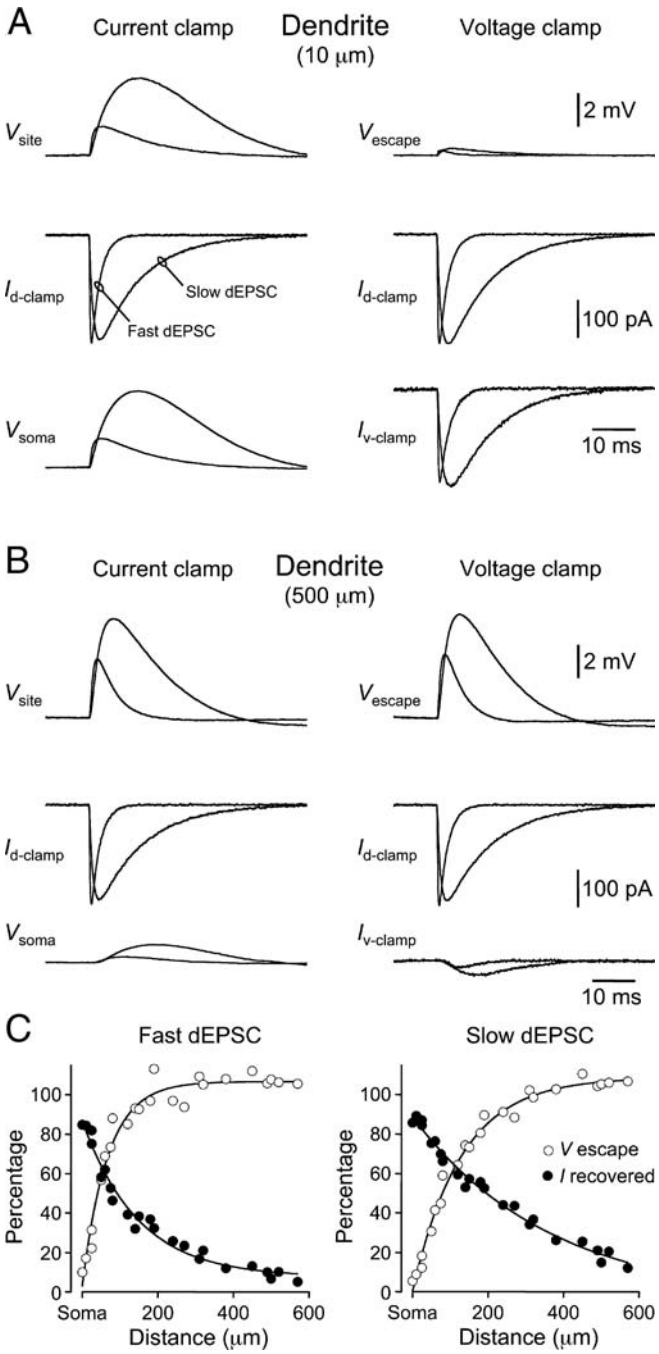

Fig. 2 Somatic voltage clamp errors. A. The somatic voltage clamp adequately controls perisomatically generated simulated excitatory postsynaptic conductance (dEPSCs) (I_{dclamp}),

(Fig. 2). Voltage control was completely lost at dendritic sites more than 180 μm from the soma (Fig. 2). Throughout the majority of the dendritic tree, therefore, the somatic voltage clamp did not control the membrane potential during synaptic events, so that EPSPs at their site of generation were of the same amplitude when the somatic recording amplifier was configured in voltage and current clamp mode (Fig. 2) (Williams and Mitchell 2008). Further experiments demonstrated that the somatic voltage clamp inaccurately reported the kinetics and reversal potential of dendritic synapses. Together these data illustrate the use of the dynamic clamp to simulate dendritic synaptic inputs and indicate that the somatic voltage clamp cannot be used to measure the properties of post-synaptic currents in dendritic neurons.

3 Dendrosomatic Attenuation of Synaptic Potentials

The dynamic clamp has been used to accurately measure the spread of simulated synaptic potentials from dendritic site of generation to the soma. This technique has allowed for the first time direct measurement of the distance-dependent attenuation of dendritic synaptic inputs. In confirmation of classical modelling studies (Rall 1977), direct observation revealed that the amplitude of simulated and spontaneously occurring EPSPs and IPSPs dramatically attenuate as they spread from dendritic site of generation to the soma (Berger et al. 2001, Williams and Stuart 2002, 2003b, Williams 2005). For example, the peak amplitude of simulated EPSPs generated 750 μm from the soma are attenuated by 40-fold as they spread to the soma of neocortical pyramidal neurons (Williams and Stuart 2002). The dendrosomatic spread of synaptic potentials are however not solely governed by the passive electrical properties of neurons, but are also shaped by the recruitment of voltage-activated ion channels (London and Hausser 2005). The use of the dynamic clamp has

Fig. 2 (continued) recovering a large fraction of the injected synaptic current (I_{vclamp}), and maintaining good voltage control, shown by the minimal recorded escape voltage (V_{escape}). **B**. The somatic voltage clamp recovers only a small fraction of dendritic synaptic current and does not control the membrane potential, as shown by the similarity between EPSPs recorded at the dendritic site of generation under current clamp (V_{site}) and the dendritic escape voltage under voltage clamp. **C**. Quantification of the distance-dependent loss of recovered synaptic current and dendritic voltage control when synaptic inputs were generated from apical dendritic sites. Recovered current represents percentage of injected current, and dendritic voltage escape as a percentage of the amplitude of EPSPs recorded under current clamp at the dendritic site of generation. Data are shown for dEPSCs with fast and slow kinetics (fast: $\tau_{rise} = 0.2$ ms. $\tau_{decay} = 2$ ms; slow: $\tau_{rise} = 1$ ms, $\tau_{decay} = 10$ ms) and have been fit with single exponential functions (*lines*). All recordings were made at near physiological temperatures (35–37°C). Voltage clamp recordings used >90% series resistance compensation. Modified from Williams and Mitchell (2008)

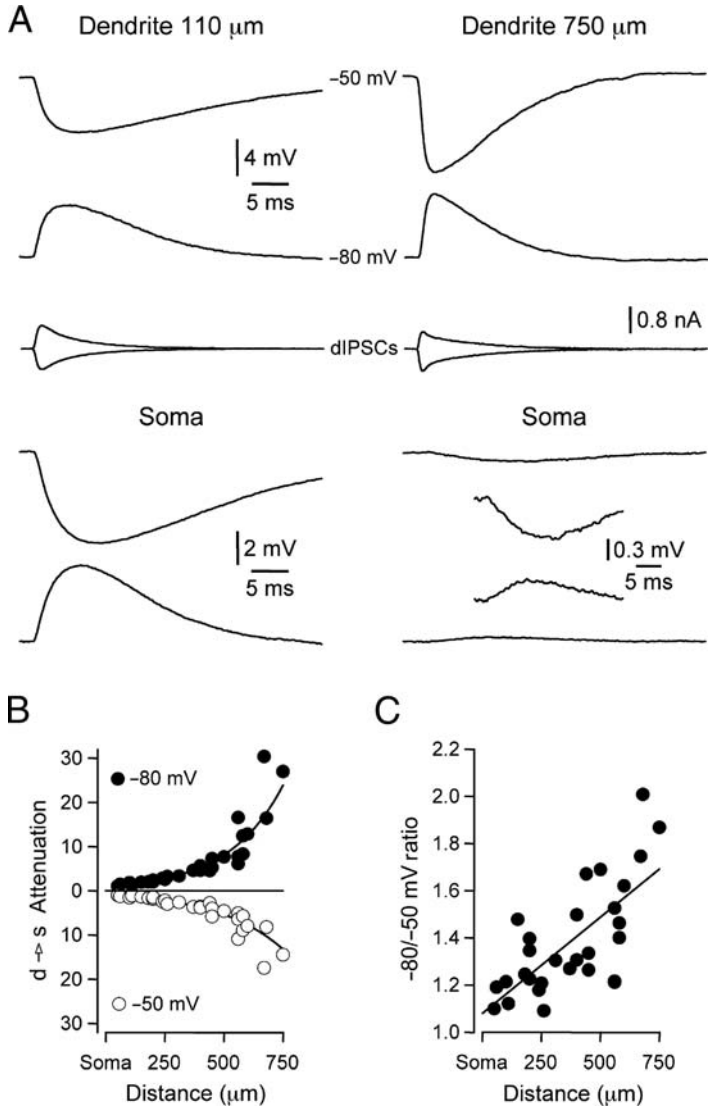

Fig. 3 Voltage dependence of dendritic dIPSPs. A. Simultaneous recording of local dendritic (*upper traces*) and somatic (*lower traces*) dynamic IPSPs generated at the indicated sites from dendritic membrane potentials of −50 and −80 mV. The middle traces show the injected inhibitory postsynaptic current (dIPSC). Note the different voltage calibration for somatic and dendritic recordings. The inset shows the somatic recording of dIPSPs generated at 750 μm from the soma at higher magnification. **B**. Pooled data describing the voltage dependence of the dendrosomatic attenuation dIPSPs. **C**. Ratio of the dendrosomatic attenuation of dIPSPs generated from membrane potentials of −50 and −80 mV. Note the 1.7-fold increase in the dendrosomatic attenuation of dIPSPs generated from hyperpolarized membrane potentials. Data were fit with single exponential relationship (B) or a linear regression (C). Modified from Williams and Stuart (2003b)

illustrated the voltage-dependent nature of the dendrosomatic attenuation of synaptic potentials (Williams and Stuart 2003b). In particular, the dynamic clamp has allowed investigation of the factors that shape the dendrosomatic spread of IPSPs. In cortical pyramidal neurons, dendrosomatic attenuation of dIPSPs was found to be highly voltage-dependent (Fig. 3). The dendrosomatic attenuation of dIPSPs was greatest when generated from hyperpolarized dendritic membrane potentials and decreased as the membrane potential was depolarized (Fig. 3) (Williams and Stuart 2003b). Similarly, changing the dendritic membrane potential transformed the somatic time-course of dendritic IPSPs (Fig. 4) (Williams and Stuart 2003b). When generated from a depolarized membrane potential, the somatically recorded time course of dendritic dIPSPs decreased as events were generated from progressively distal apical dendritic sites (Williams and Stuart 2003b), in violation of the rules predicted by cable theory (Rall 1977). In contrast, when dIPSPs were generated from a hyperpolarized dendritic membrane potential, the somatic time course was independent of the dendritic site of generation, again in contrast to the predications of cable theory; which indicates that the somatically recorded time course of dendritic synaptic potentials should increase as events are generated more remotely in the dendritic tree (Rall 1977). These behaviours were found to result from the non-uniform distribution of two classes of voltage-activated ion channels, the persistent sodium current, I_{NaP}, and the hyperpolarization-activated mixed cation current,

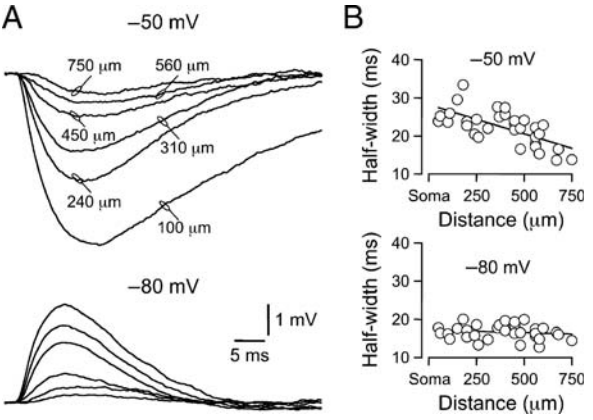

Fig. 4 Somatic time course of dendritic dIPSPs. A. Somatic recording of dIPSPs generated from the indicated dendritic sites at local dendritic membrane potentials of −50 and −80 mV. Note the somatic time course of dynamic IPSPs generated from proximal dendritic sites is prolonged at depolarized membrane potentials. **B**. Site dependence of the somatic time course (measured at half-amplitude) of dendritic dIPSPs generated from the indicated membrane potentials. Note from local dendritic membrane potentials of −50 mV (*upper graph*), the somatic timecourse of dIPSPs decreases in a distance-dependent manner, while from local dendritic membrane potentials of −80 mV the somatic time course is site-independent. Lines represent linear regression. Modified from Williams and Stuart (2003b)

I_H (Williams and Stuart 2003b). The persistent sodium current is activated from membrane potentials just subthreshold for the generation of actions potentials and has been suggested to be, predominantly, generated by the high density of sodium channels at the axon initial segment (Stuart and Sakmann 1995, Williams and Stuart 2003b, Astman et al. 2006). The activation or deactivation of I_{NaP} has been shown to extend the time course and enhance the amplitude of somatically generated simulated EPSPs and IPSPs (Stuart and Sakmann 1995, Stuart 1999, Williams and Stuart 1999, Zsiros and Hestrin 2005). Therefore, the enhancement of the time course of relatively proximal dendritic dIPSPs can be accounted for by the larger voltage deviation produced at the level of the axon initial segment (Williams and Stuart 2003b). In contrast, the normalization of the time course of dendritic dIPSPs generated from hyperpolarized potentials was found to be mediated by I_H (Williams and Stuart 2003b). The channels that underlie I_H are distributed at high and increasing density in the apical dendritic tree of cortical pyramidal neurons (Magee 1998, Williams and Stuart 2000, Berger et al. 2001, Lorincz et al. 2002, Kole et al. 2006). The activation or deactivation of the inward current I_H accelerates the time course of dendritic-simulated IPSPs and EPSPs at the site of generation (Magee 1998, 1999, Williams and Stuart 2000, 2003b). I_H therefore acts to counteract the filtering effects of the dendritic membrane on the time course of synaptic potentials, to render the somatically recorded time course independent of the dendritic site of generation (Magee 1999, Williams and Stuart 2000, 2003b). The voltage-dependent dendrosomatic attenuation of dIPSPs can be explained by the amplification of dIPSPs at depolarized membrane potential by I_{NaP}, while the shunting effect of I_H at hyperpolarized membrane potentials exaggerates the effects of cable filtering (Williams and Stuart 2003). Taken together, these data reveal that the dynamic clamp can provide important insight into the mechanisms that shape the spread of synaptic potentials through the dendritic tree to the site of action potential generation

4 Conductance Compartmentalization

The voltage-dependent properties of dIPSPs suggest that the control of action potential output by dendritic inhibition will be highly voltage dependent. This issue has been directly addressed in cortical pyramidal neurons (Williams and Stuart 2003b). Action potential firing was evoked by the passage of a short current step through a somatic recording electrode, while dIPSPs were generated from dendritic sites (Fig. 5). From a membrane potential set close to action potential firing threshold, dIPSPs generated widely across the apical dendritic arbor were capable of silencing action potential firing (Fig. 5). In contrast, when the membrane potential was set close to the dIPSC reversal potential (−65 mV), only inhibition generated from relatively proximal apical dendritic sites silenced action potential output. This data demonstrates that the spatial reach of

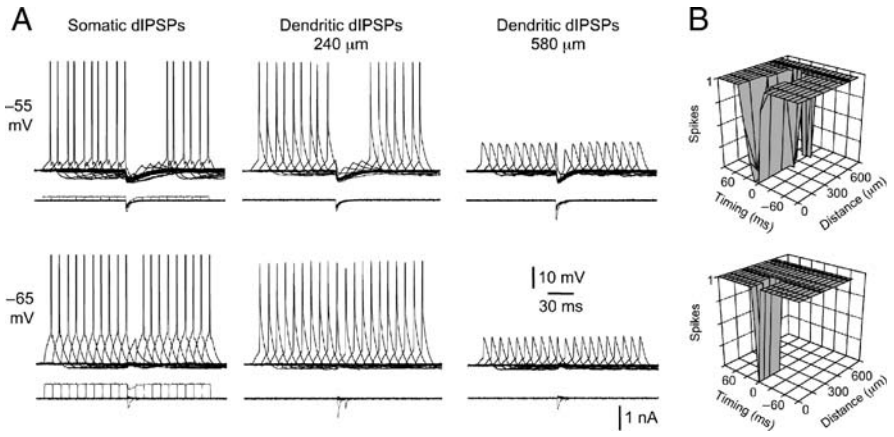

Fig. 5 Impact of dendritic dIPSPs on action potential output. A. Overlain records of single action potential firing evoked by short somatic current steps, offset in time by 10 ms, recorded at somatic (*left*), proximal (*middle*) and distal (*right*) dendritic sites. Dynamic IPSPs, generated at the indicated sites, suppress axonal action potential initiation over a time window defined by the site of dynamic IPSP generation (compare panels horizontally) and membrane potential (compare panels vertically). **B**. Summary plots describing the relationship between the spatial reach of dendritic inhibition on action potential firing when generated from a membrane potential of −55 mV (*upper graph*) or −65 mV. Timing = 0 represents coincidence of somatic current step and dynamic IPSC onset. Note from the most hyperpolarized membrane potential dendritic inhibition is relatively ineffective. Modified from Williams and Stuart (2003b)

dendritic inhibition is voltage dependent (Williams and Stuart 2003b). Moreover, from membrane potentials close to the reversal potential where little voltage change occurs, inhibition is considered to act as a shunt conductance (Fregnac et al. 2003). The spatially restricted impact of shunting inhibition suggests a dissociation between the spatial 'visibility' of voltage and conductance.

This comparison prompted investigation of the spatial compartmentalization of conductance, an overlooked parameter in neurons. All synaptic activity is mediated by a change in conductance. If areas of a neuron are to operate as independent integrators, the conductance load imparted by synaptic activity in one region should not interfere with synaptic integration in another. Indeed, the compartmentalization of conductance may define the number of possible integration compartments (London and Segev 2004). To test the spatial compartmentalization of conductance in dendritic neurons, the dynamic clamp has been used to evoke a large conductance change at dendritic sites. This can be implemented simply by generating a conductance change with a reversal potential set to the dendritically recorded membrane potential (Fig. 6) (Williams 2004). The impact of a dendritic conductance can then be measured independently from a remote site, such as the soma. The spatial impact of dendritic

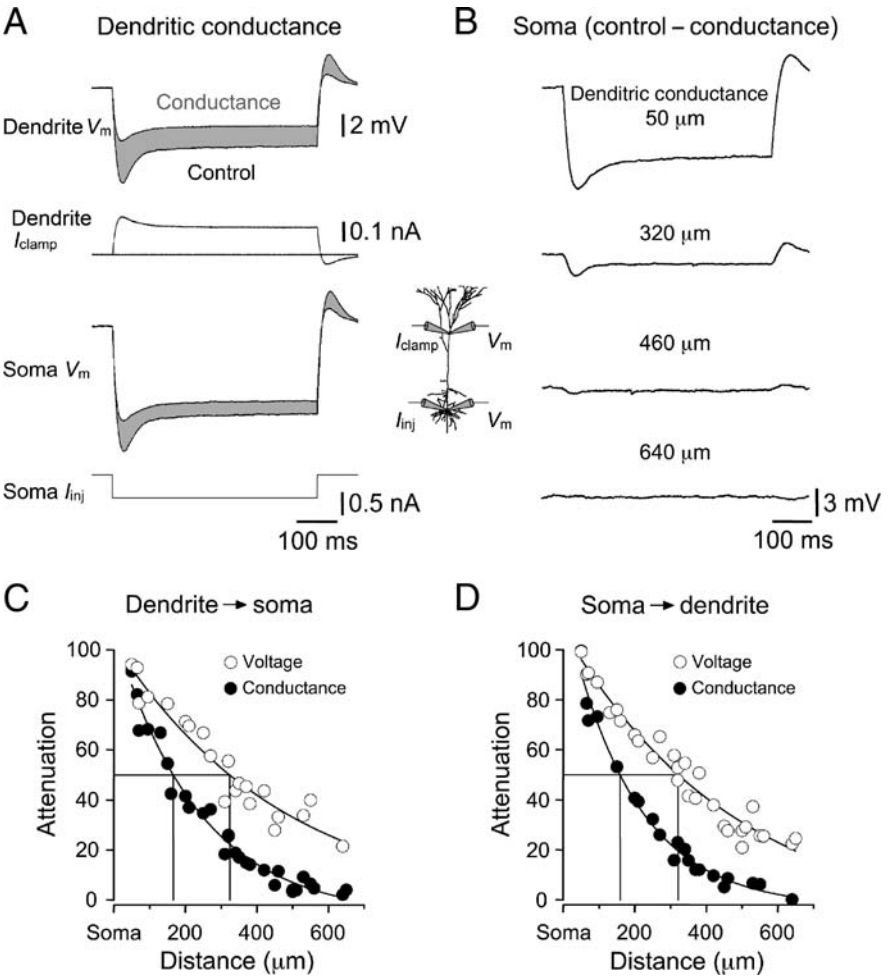

Fig. 6 Conductance compartmentalization. A. Simultaneous somatodendritic recording of voltage responses evoked by a somatic current step (*lower trace*) under control and in the presence of a dendritic conductance source (50 nS; dendritic recording 150 μm from soma). The grey shading delineates the reduction of voltage responses produced by the conductance source at somatic and dendritic sites. The current injected by the dynamic clamp system is shown (dend I_{clamp}). The experimental arrangement is shown in the inset. **B**. Spatial 'visibility' of conductance. Digitally subtracted somatic voltage traces (control – conductance) evoked by negative current steps (−0.5 nA). A conductance change (50 nS) was injected at the indicated apical dendritic sites. **C**. Dendrosomatic distance-dependent attenuation of conductance (*filled symbols*) and voltage (*open symbols*). Attenuation of conductance was calculated as the relative reduction of R_{in} produced by identical conductance changes delivered at the recording and a remote site. Voltage attenuation represents the attenuation of voltage between recording loci under control. Continuous lines represent single exponential fits and drop lines show 50% attenuation points. **D**. Somatodendritic attenuation of conductance and voltage. Note the attenuation profiles are in close agreement with the dendrosomatic case. Modified from Williams (2004)

conductance can be assayed by probing for the change in apparent input resistance produced at the soma. This can be quantified by calculating the change in somatic input resistance imparted by a dendritic conductance, relative to that produced by an identical somatically generated conductance change (Fig. 6). Experiments revealed that dendritic conductance is 'visible' at the soma only when generated from relatively proximal apical dendritic sites (Fig. 6) (Williams 2004). Indeed, the conductance length constant was found to be on the order of half of the voltage length constant (Fig. 6) (Williams 2004), as predicted by passive cable models (Rall 1967, Koch et al. 1990). Interestingly, the visibility of a conductance change produced at the soma was also spatially restricted, and had little influence at distal apical dendritic sites (Fig. 6). These data suggest that a conductance load imposed by synaptic activity generated in the distal apical dendritic tree should not interfere with synaptic integration at the soma; inversely activity in the basal dendritic tree should not interfere with apical dendritic synaptic integration (Williams 2004).

5 Compartmentalized Synaptic Integration

Local dendritic synaptic integration has been studied in detail in cortical pyramidal neurons. Local dendritic spikes can be generated at basal, apical trunk and apical oblique sites (Kim and Connors 1993, Schiller et al. 1997, Larkum et al. 2001, Larkum and Zhu 2002, Williams and Stuart 2002, Losonczy and Magee 2006, Larkum et al. 2007, Nevian et al. 2007, Losonczy et al. 2008). One of the clearest examples of dendritic synaptic integration has been described in the apical dendrite of layer 5 pyramidal neurons (Schiller et al. 1997, Larkum et al. 2001, Williams and Stuart 2002). When currents steps or EPSPs are generated from distal apical dendritic sites the threshold response is not the firing of axonal action potentials, but rather the generation of an all-or-none dendritic spike (Schiller et al. 1997, Larkum et al. 2001, Williams and Stuart 2002). Multi-site recordings have shown that apical dendritic spikes robustly forward propagate through the apical dendritic tree, leading to an ordered sequence of regenerative activity that finally results in the generation of axonal action potential output (Fig. 7). Indeed, the action potential output evoked by the delivery of identical simulated EPSPs at the soma or distal apical dendritic sites are similar (Fig. 7). The mechanisms underlying action potential firing are however distinct. When EPSPs are generated from the soma, the threshold for axonal action potential initiation is directly reached. In contrast, when EPSPs are generated from distal apical dendritic sites, a forward propagating dendritic spike is evoked, that in turn leads to the generation of axonal action potential firing (Fig. 7). Pyramidal neurons therefore exhibit multiple sites for synaptic integration, where each compartment is capable of evoking a dendritic spike as an output. Interestingly, the properties of synaptic integration in dendritic compartments are different from those of the axon and soma. For

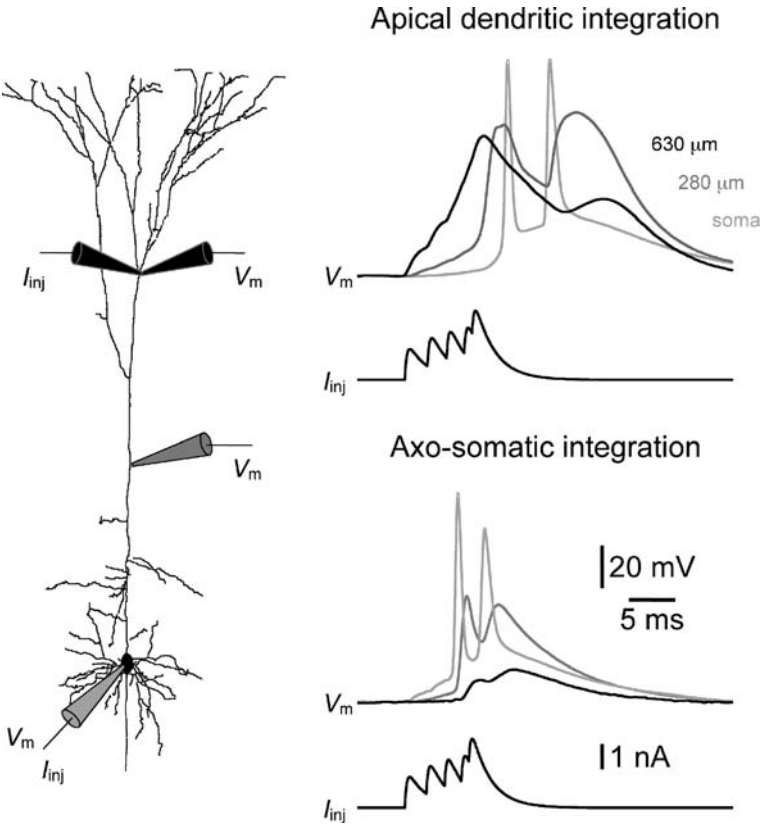

Fig. 7 Forward propagation of dendritic spikes. Simultaneous quadruple whole-cell recording demonstrates the forward propagation of a dendritic spike in a layer 5 neocortical pyramidal neuron. When a brief burst of simulated EPSCs (I_{inj}) are injected at a distal apical dendritic site, a dendritic spike is evoked that forward propagates to the axon to initiate action potential output. In contrast, when the same input is generated at the soma, action potential firing threshold is directly reached, and action potentials decrementally backpropagate into the dendritic tree. The inset shows the placement of recording pipettes cartooned onto the morphology of a layer 5 pyramidal neuron, the distances from the soma are indicated. S.R. Williams, unpublished observations

example, the time-window for synaptic integration has been shown to be narrow at apical dendritic sites, relative to the soma, primarily due to the fast nature of local dendritic EPSPs that are sped by the vanishingly fast local time constant (Williams and Stuart 2002). Such findings are inconsistent with classical models of neuronal function, proposing that synaptic inputs targeted to distal dendrites provide a substrate for long lasting temporal integration (Rall 1977), but rather suggest that synaptic integration at distal dendritic sites operates in a manner consistent with coincidence detection (Williams and Stuart 2002).

In order to be of functional relevance however, dendritic spikes must have an impact on action potential firing under realistic conditions. In vivo recordings have shown that dendritic spikes can be evoked in the intact anaesthetized animal (Larkum and Zhu 2002). However, under active network conditions, cortical pyramidal neurons are bombarded with ongoing synaptic activity (Destexhe et al. 2003). Do dendritic spikes have a salient signalling role under such a high conductance state? This question was directly answered by the use of the dynamic clamp to simulate the impact of a bombardment of excitatory and inhibitory synaptic activity at the soma of cortical pyramidal neurons (Williams 2004). Under these conditions, apical dendritic spikes could forward propagate to the soma and trigger action potential output (Fig. 8). Interestingly, under this emulated high conductance state, input generated at proximal dendritic sites was incapable of driving neuronal output. These data

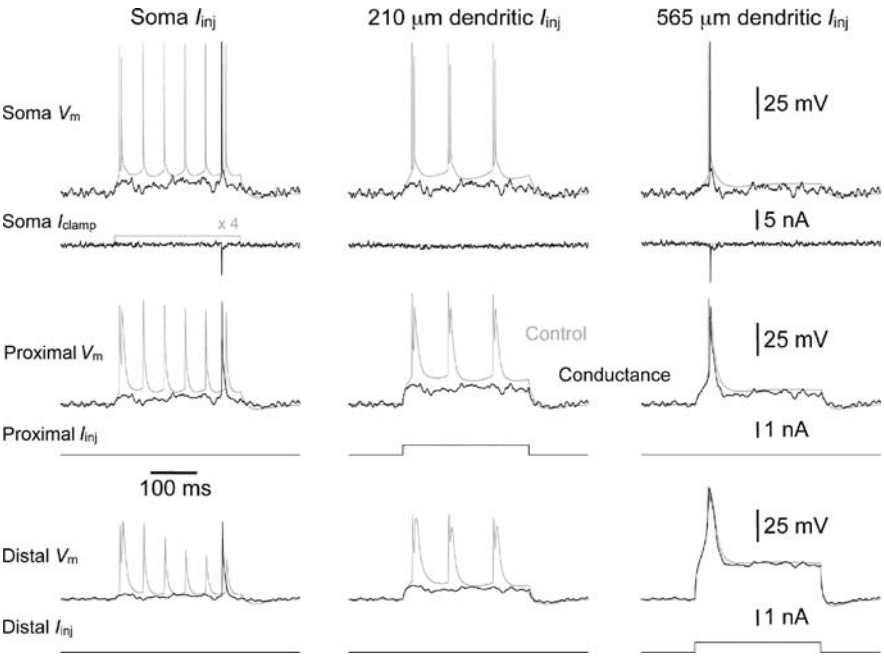

Fig. 8 Background activity controls synaptic integration. Simultaneous somatodendritic recording of action potential output evoked by the delivery of positive current steps at somatic (*left traces*), proximal apical (*middle traces*) and distal apical dendritic (*right traces*) sites, under control (*grey traces*) and in the presence of simulated somatic synaptic conductance (simulated AMPA-type and gamma-amino butyric acid $(GABA)_A$-type conductance delivered at 2000 Hz, black traces). Somatic synaptic activity strongly reduced or prevented action potential firing generated by somatic or proximal apical dendritic excitation, respectively. Somatic synaptic activity however did not prevent the initiation, forward propagation and generation of action potential output following distal apical dendritic excitation. Modified from Williams (2004)

demonstrate the functional impact of conductance compartmentalization in neurons and suggest that distal apical dendritic synaptic integration is operational under active network conditions (Williams 2004).

It remains a challenge for future investigation to study how many sites for synaptic integration exist in the dendrites of cortical pyramidal neurons. The necessity to make whole-cell recording to simulate synaptic activity with the dynamic clamp makes direct investigation of thin calibre dendrites, such as basal dendrites, problematic. Recently however, Nevian et al. (2007) have successfully made direct recordings from basal dendrites of cortical pyramidal neurons, providing an opportunity to study synaptic integration in the basal dendritic tree that receives the majority of synaptic input. Alternative approaches may however prove more practicable. For example, multi-site two-photon un-caging of glutamate has recently been used to study synaptic integration in fine calibre dendrites (Losonczy and Magee 2006, Losonczy et al. 2008). The functional role of multiple integration sites in cortical pyramidal neurons remains a fascinating question. Modelling studies have demonstrated that dendritic synaptic integration acts to increase the computational power of single neurons (Archie and Mel 2000, Poirazi and Mel 2001, Hausser and Mel 2003, London and Hausser 2005). How compartmentalized dendritic integration is engaged in the working brain to shape the output of single neurons however remains the goal for future work.

Acknowledgments I am very grateful to Greg Stuart for introducing me to the field of dendritic physiology. The author's work is supported by the Medical Research Council (UK).

References

Archie KA and Mel BW (2000) A model for intradendritic computation of binocular disparity. Nat Neurosci 3, 54–63.

Astman N Gutnick MJ and Fleidervish IA (2006) Persistent sodium current in layer 5 neocortical neurons is primarily generated in the proximal axon. J Neurosci 26, 3465–73.

Berger T Larkum ME and Luscher HR (2001) High I(h) channel density in the distal apical dendrite of layer V pyramidal cells increases bidirectional attenuation of EPSPs. J Neurophysiol 85, 855–68.

Clark BA Monsivais P Branco T London M and Hausser M (2005) The site of action potential initiation in cerebellar Purkinje neurons. Nat Neurosci 8, 137–9.

Destexhe A Rudolph M and Pare D (2003) The high-conductance state of neocortical neurons in vivo. Nat Rev Neurosci 4, 739–51.

Fregnac Y Monier C Chavane F Baudot P and Graham L (2003) Shunting inhibition, a silent step in visual cortical computation. J Physiol (Paris) 97, 441–51.

Hausser M Spruston N and Stuart GJ (2000) Diversity and dynamics of dendritic signaling. Science 290, 739–44.

Hausser M and Mel B (2003) Dendrites: bug or feature? Curr Opin Neurobiol 13, 372–83.

Khaliq ZM and Raman IM (2006) Relative contributions of axonal and somatic Na channels to action potential initiation in cerebellar Purkinje neurons. J Neurosci 26, 1935–44.

Kim HG and Connors BW (1993) Apical dendrites of the neocortex: correlation between sodium- and calcium-dependent spiking and pyramidal cell morphology. J Neurosci 13, 5301–11.

Kitamura K Judkewitz B Kano M Denk W and Hausser M (2008) Targeted patch-clamp recordings and single-cell electroporation of unlabeled neurons in vivo. Nat Methods 5, 61–7.

Koch C Douglas R and Wehmeier U (1990) Visibility of synaptically induced conductance changes: theory and simulations of anatomically characterized cortical pyramidal cells. J Neurosci 10, 1728–44.

Kole MH Hallermann S and Stuart GJ (2006) Single Ih channels in pyramidal neuron dendrites: properties, distribution, and impact on action potential output. J Neurosci 26, 1677–87.

Kole MH Ilschner SU Kampa BM Williams SR Ruben PC and Stuart GJ (2008) Action potential generation requires a high sodium channel density in the axon initial segment. Nat Neurosci 11, 178–86.

Larkum ME Zhu JJ and Sakmann B (2001) Dendritic mechanisms underlying the coupling of the dendritic with the axonal action potential initiation zone of adult rat layer 5 pyramidal neurons. J Physiol (Lond) 533, 447–66.

Larkum ME and Zhu JJ (2002) Signaling of layer 1 and whisker-evoked Ca2+ and Na+ action potentials in distal and terminal dendrites of rat neocortical pyramidal neurons in vitro and in vivo. J Neurosci 22, 6991–7005.

Larkum ME Waters J Sakmann B and Helmchen F (2007) Dendritic spikes in apical dendrites of neocortical layer 2/3 pyramidal neurons. J Neurosci 27, 8999–9008.

London M and Segev I (2004) Conducting synaptic music in dendrites. Nat Neurosci 7, 904–5.

London M and Hausser M (2005) Dendritic computation. Annu Rev Neurosci 28, 503–532.

Lorincz A Notomi T Tamas G Shigemoto R and Nusser Z (2002) Polarized and compartment-dependent distribution of HCN1 in pyramidal cell dendrites. Nat Neurosci 5, 1185–93.

Losonczy A and Magee JC (2006) Integrative properties of radial oblique dendrites in hippocampal CA1 pyramidal neurons. Neuron 50, 291–307.

Losonczy A Makara JK and Magee JC (2008) Compartmentalized dendritic plasticity and input feature storage in neurons. Nature 452, 436–41.

Magee JC (1998) Dendritic hyperpolarization-activated currents modify the integrative properties of hippocampal CA1 pyramidal neurons. J Neurosci 18, 7613–24.

Magee JC (1999) Dendritic Ih normalizes temporal summation in hippocampal CA1 neurons. Nat Neurosci 2, 848.

Nevian T Larkum ME Polsky A and Schiller J (2007) Properties of basal dendrites of layer 5 pyramidal neurons: a direct patch-clamp recording study. Nat Neurosci 10, 206–214.

Palmer LM and Stuart GJ (2006) Site of action potential initiation in layer 5 pyramidal neurons. J Neurosci 26, 1854–63.

Poirazi P and Mel BW (2001) Impact of active dendrites and structural plasticity on the memory capacity of neural tissue. Neuron 29, 779–96.

Prinz AA Abbott LF and Marder E (2004) The dynamic clamp comes of age. Trends Neurosci 27, 218–24.

Rall W (1967) Distinguishing theoretical synaptic potentials computed for different soma-dendritic distributions of synaptic input. J Neurophysiol 30, 1138–68.

Rall W (1977) Core conductor theory and cable properties of neurons. In Handbook of Physiology – The Nervous System 1, ed. E. R. Kandel, pp. 39–97. American Physiological Society, Bethesda, Maryland.

Schiller J Schiller Y Stuart G and Sakmann B (1997) Calcium action potentials restricted to distal apical dendrites of rat neocortical pyramidal neurons. J Physiol (Lond) 505, 605–16.

Stuart GJ Dodt HU and Sakmann B (1993) Patch-clamp recordings from the soma and dendrites of neurons in brain slices using infrared video microscopy. Pflugers Arch 423, 511–8.
Stuart G and Sakmann B (1995) Amplification of EPSPs by axosomatic sodium channels in neocortical pyramidal neurons. Neuron 15, 1065–76.
Stuart G (1999) Voltage-activated sodium channels amplify inhibition in neocortical pyramidal neurons. Nat Neurosci 2, 144–50.
Williams SR and Stuart GJ (1999) Mechanisms and consequences of action potential burst firing in rat neocortical pyramidal neurons. J Physiol (Lond) 521, 467–82.
Williams SR and Stuart GJ (2000) Site independence of EPSP time course is mediated by dendritic Ih in neocortical pyramidal neurons. J Neurophysiol 83, 3177–82.
Williams SR and Stuart GJ (2002) Dependence of EPSP efficacy on synapse location in neocortical pyramidal neurons. Science 295, 1907–10.
Williams SR and Stuart GJ (2003a) Role of dendritic synapse location in the control of action potential output. Trends Neurosci 26, 147–54.
Williams SR and Stuart GJ (2003b) Voltage- and site-dependent control of the somatic impact of dendritic IPSPs. J Neurosci 23, 7358–67.
Williams SR (2004) Spatial compartmentalization and functional impact of conductance in pyramidal neurons. Nat Neurosci 7, 961–7.
Williams SR (2005) Encoding and decoding of dendritic excitation during active states in pyramidal neurons. J Neurosci 25, 5894–902.
Williams SR and Mitchell SJ (2008) Direct measurement of somatic voltage clamp errors in central neurons. Nat Neurosci 11, 790–8.
Zsiros V and Hestrin S (2005) Background synaptic conductance and precision of EPSP-spike coupling at pyramidal cells. J Neurophysiol 93, 3248–56.

Synaptic Conductances and Spike Generation in Cortical Cells

Hugh P.C. Robinson

Abstract Investigating how cortical neurons integrate their electrical inputs has commonly involved injecting fixed patterns of current and observing the resulting membrane potential and spike responses. However, we now have accurate biophysical models of the ionic conductances at the postsynaptic sites of cortical synapses and of the conductances which generate action potentials (APs). Using conductance injection or dynamic clamp, it is possible to inject point conductances which closely capture the electrical properties of synaptic inputs, including the shunting, reversible nature of inhibitory gamma-amino butyric acid $(GABA)_A$ receptor input, the saturating or "choking" behaviour of α-amino-3-hydroxy-5-methyl-4-isoazoleprionic acid (AMPA) receptor input and the voltage-dependent block of *N*-methyl-D-aspartate (NMDA) receptor input. Complex conductance signals which reproduce the effects of stochastic and oscillatory network activity can be applied repeatedly and precisely to neurons. In this chapter, I review our work using this approach, addressing the nature of the threshold and of the reliability of spike generation in cortical neurons, how synaptic conductance input patterns are encoded into variations in AP shape and how neurons integrate network burst and gamma oscillatory activity.

1 Introduction

The dynamics of synaptic integration – the transformation of patterns of synaptic inputs of a neuron into changes in membrane potential, and ultimately axonal spike firing – underlie the neuron's role in rapid signalling and information processing. Unravelling the mechanisms of synaptic integration is the key to understanding how local cortical networks operate. Our current understanding of synaptic integration began with the characterization of synaptic

H.P.C. Robinson (✉)
Department of Physiology, Development and Neuroscience, University of Cambridge, Cambridge CB2 3EG, UK
e-mail: hpcr@cam.ac.uk

A. Destexhe, T. Bal (eds.), *Dynamic-Clamp*, Springer Series in Computational Neuroscience 1, DOI 10.1007/978-0-387-89279-5_3,

conductances (Coombs, Eccles et al. 1955; Eccles 1963) and of the voltage-dependent conductances involved in spike generation (Hodgkin and Huxley 1952). Theoretical investigations based on passive cable theory (Rall 1962) opened up the possibility of a rich complexity of spatial processing in neurons, and it was shown that even linear *conductance* inputs in spatially extended dendritic trees can carry out significant nonlinear computations (Koch, Poggio et al. 1983). With increasing knowledge of the biophysical components involved, especially through the use of the patch-clamp technique (Sakmann and Neher 1995), work began on quantifying and understanding the integrative responses of cortical neurons. Patterns of spiking produced by current injection in intracellular recording into the soma were described and classified (Connors, Gutnick et al. 1982), and the advent of dendritic whole-cell patch clamp started to yield insights into dendritic spike generation (Stuart and Sakmann 1994).

A new paradigm for studying synaptic integration was introduced with the conductance injection or dynamic-clamp technique (Robinson 1991; Robinson and Kawai 1993; Sharp, O'Neil et al. 1993), which involves dynamically updating the stimulating current according to the membrane potential, using a real-time computer, to inject current sources which mimic the behaviour of biological ionic conductances. Thus, defined patterns of synaptic-like conductance inputs can be applied, and the responses of cells to these realistic electrical inputs measured directly. This differs fundamentally from applying a fixed, predetermined pattern of current: conductance injection stimulates changes in the membrane potential by adding dynamical components which are equivalent to the natural components of the membrane, capturing the rapid interplay between the current flowing through ionic channels and the membrane potential. It is thus, potentially, a much more powerful way of investigating the integrative properties of neurons. It is important, though, to recognize its current limitations – for example, it does not duplicate the calcium influx that can occur through synaptic conductances, although the electrical effects of such influx, accumulation and buffering and activation of downstream conductances such as calcium-dependent potassium channels can indeed be reproduced (see Jaeger and Lin "Unraveling the Dynamics of Deep Cerebellar Nucleus Neurons with the Application of Artificial Conductances" in this volume).

We still have a long way to go before understanding adequately how cortical neurons work, even the most thoroughly studied pyramidal subtype (Spruston 2008). Advances in characterizing the functional dynamics of cortical neurons will still largely be experiment-led, since models with an adequate level of biophysical detail still depend upon far too many assumptions about channel properties and distributions throughout the dendritic and axonal arbors. The ability to insert dynamic, electrically realistic point conductances into neurons will play an increasing part in the experimental unravelling of synaptic integration.

In this chapter I review our recent work using conductance injection to study several aspects of synaptic integration in cortical neurons: the nature of the threshold for spike initiation and of the reliability of spike generation in cortical

neurons, how synaptic conductance input patterns are encoded into variations in action potential (AP) shape and how neurons integrate network burst and gamma oscillatory activity.

2 The Electrical Nature of Synaptic Conductance Inputs

Synaptic input to a neuron typically consists of a stereotypical transient of permeability to ions or conductance transient. Ignoring Nernst–Planck electrodiffusion (though this may be significant in small postsynaptic structures like dendrites and spines, see Qian and Sejnowski 1990), this electrical behaviour is accurately modelled as a time- and voltage-dependent resistor and an ionic battery in series (see Fig. 1, top inset). A unitary synaptic input to a cortical neuron most commonly follows one of the three patterns shown in Fig. 1B: (a) a relatively fast α-amino-3-hydroxy-5-methyl-4-isoazoleprionic acid (AMPA) receptor-mediated transient decaying usually in 1–2 ms and with a reversal potential near zero (b) a slower rising, slower-decaying *N*-methyl-D-aspartate (NMDA) receptor-mediated transient, also reversing near zero, with a multicomponent decay mostly over tens of milliseconds. This is usually initiated coincidentally with a colocalized AMPA receptor transient (Forsythe and

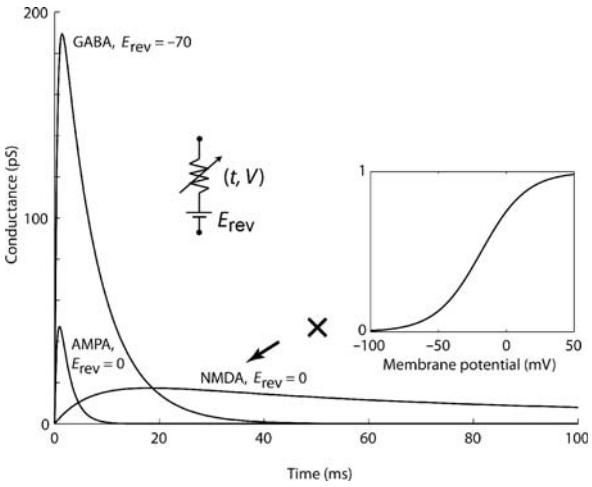

Fig. 1 Typical time courses of unitary synaptic conductance transients in cortical neurons. Each conductance behaves as a time-dependent and possibly voltage-dependent resistor, in series with a battery representing the offset of reversal potential. AMPA receptor fraction of glutamatergic excitatory input is fast. $GABA_A$ receptor-mediated inhibitory conductance is a little slower, and reverses near the resting potential. NMDA receptor-mediated fraction of glutamatergic excitatory input, is much slower and further subject to a voltage-dependent block (inset) by extracellular magnesium which reduces the conductance in a voltage-dependent manner. Unblock and block are not in fact instantaneous (see Fig. 11)

Westbrook 1988), except at "silent" synapses. As indicated in the figure, though, this conductance transient is subject to a highly voltage-dependent block due to extracellular magnesium ions – the commanded conductance waveform of Fig. 1 would be achieved only at very high depolarizations, above +40 mV (Mayer, Westbrook et al. 1984; Nowak, Bregestovski et al. 1984). Indeed at a typical "resting" potential of –70 mV, virtually no NMDA-R conductance is injected – the "silent" behaviour of this type of synaptic receptor. Finally, fast inhibition is mediated by γ-amino butyric acid $(GABA)_A$ receptors, typically giving rise to a transient as in Fig. 1 (though it can be slower), with a reversal potential near to the resting potential (though it can be significantly depolarized, and may change with locality in the cell and with development). Reversal potentials may to some extent be dynamic quantities according to accumulation and depletion of ions in a cell.

Thus the current flowing through these natural synaptic conductances is sensitive, reactive to the membrane potential, either linearly or nonlinearly. Another important difference from a current input lies in how these conductance inputs interact with other inputs and with charge flow from other points in the cell. Adding conductance to a location in the membrane changes its passive properties, the membrane time constant and the input resistance – fundamental parameters for electrical activity. It has been shown that during activity in vivo, synaptic input to cortical neurons may contribute up to 80% of the total conductance of the membrane, and that injecting stochastic excitatory and inhibitory conductances reproduces in vivo-like membrane potential distributions (Destexhe, Rudolph et al. 2001). In cortical slice studies of synaptic integration, therefore, it is extremely important to stimulate with conductance, in order to force the neuron's spike generation mechanisms into an in vivo-like electrical state. For example, a layer 2/3 pyramidal cell in a quiescent slice might have an input conductance at rest of 2 nS (500 MΩ input resistance). When driven to fire at a medium fast frequency of 10 Hz by 18 nS of conductance, there is a *tenfold* increase in the passive conductance of the membrane, and a consequent drop in the time constant from 40 to 4 ms. Such changes are even more significant when excitation and inhibition oppose each other, as is always the case to some extent in vivo, possibly in a fixed ratio despite variations in each (a "balance").

As an illustrative example of the complexity of synaptic integration of natural inputs, consider the segment of firing shown in Fig. 2 – a simulation of a fast-spiking (FS) inhibitory cortical neuron driven by fluctuating AMPA-R excitation and $GABA_A$-R inhibition. What actually drives APs to occur at specific times? The first AP is associated with a preceding surge in g_{AMPA}, the second with a drop in g_{GABA}. Trying to predict when APs should occur is a difficult problem, even in this simplified case: the current shunted through GABA receptors during spikes is seen to be a sensitive function of the membrane potential, reversing in sign during the integration up to individual spikes, vanishing when g_{GABA} drops, while the current through AMPA-Rs also becomes highly voltage dependent near to its reversal potential, "choking" off

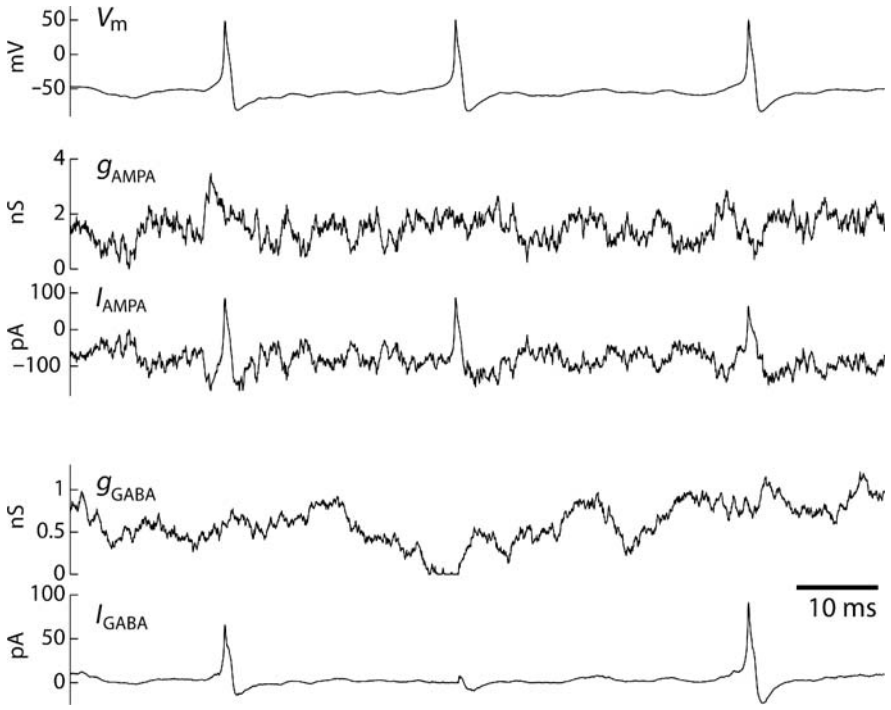

Fig. 2 The complexity of the decision to spike. A biophysical model (Erisir, Lau et al. 1999) of a cortical FS cell driven by independently fluctuating AMPA receptor-like conductance (reversing at 0 mV) and GABA receptor-like conductance (reversing at –65 mV). See text for details

the inward current, indeed reversing transiently during each spike. Note, though, that in small, parvalbumin-expressing inhibitory neurons, AMPA-Rs lacking GluRB subunits give rise to complete inwardly rectification (and calcium permeability) of AMPA receptors (Itazawa, Isa et al. 1997), due to block by intracellular spermine. Conductance injection shows that this rectification boosts the excitation (A. Harsch and H.P.C. Robinson, *unpublished observations*) that a given amount of conductance can achieve, by reducing the shunting of the AP and so conserving energy, which may be important in small cells.

In the next two sections, I will consider excitatory and inhibitory influences on spike generation and its reliability.

3 Excitatory Conductance Drive During Stochastic Synaptic Input

Spike-triggered averaging or "reverse correlation" of a noisy fluctuating conductance signal is a way of picking out the most representative trajectory of conductance leading up to spikes, and gives considerable insight into how

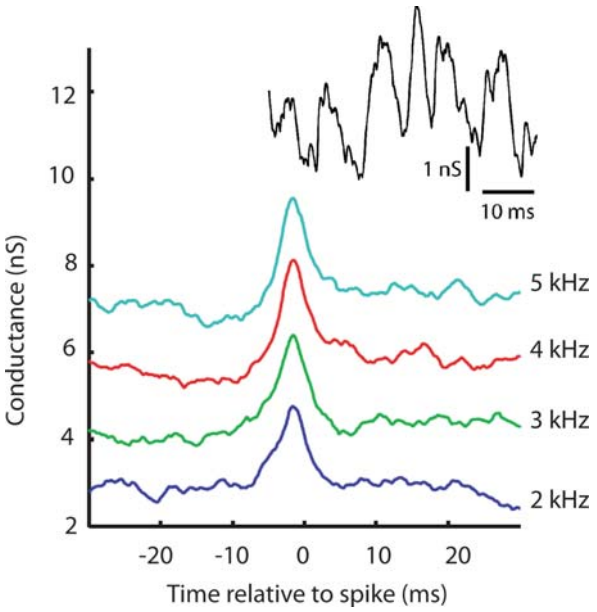

Fig. 3 Spike-triggered average AMPA conductance during stimulation with a Poisson train of AMPA transients. Inset: example fragment of the stimulus signal. Modified from Tateno and Robinson (2006) (Fig. 3Ba). Conductance injection in the work described in this chapter is carried out with SM-1 or SM-2 systems from Cambridge Conductance (Robinson 2008, www.cambridgeconductance.com). The SM-1 uses custom analogue computational circuits with an extremely fast settling time (nanoseconds). The SM-2 is a "hard" real-time system (see discussion by White et al. "Using "Hard" Real-Time Dynamic Clamp to Study Cellular and Network Mechanisms of Synchronization in the Hippocampal Formation" in this volume), which employs Euler integration for updating kinetic variables (see discussion by Butera and Lin "Key Factors for Improving Dynamic Clamp Performance" in this volume)

spikes are generated. Of course, because the dynamics of spike generation are highly nonlinear, the *average* trajectory does not in general have to lead to a spike at time zero – but since some of the nonlinearity will be averaged away, the spike-triggered average is at least a well-specified "kernel" whose trajectory is close to the most typical one for eliciting a spike. Figure 3 shows the average AMPA conductance as a function of time relative to spikes, when a regular-spiking (RS) pyramidal neuron is being stimulated with a random (Poisson process) train of unitary AMPA conductance transients, at rates between 2 and 5 kHz (Harsch and Robinson 2000; Tateno and Robinson 2006). In this average sense, spikes are triggered by sharp, fairly symmetrical surges in conductance lasting some 10 ms over the background level (the decay time constant of the unitary events is only 2 ms) and peaking about 2 ms before the spike. This illustrates that, typically, multiple unitary AMPA events summate within a narrow time window just before the spike. There is little change in the shape or amplitude of this surge, as the rate of unitary events increases up to

5 kHz – however at high-input rates (4 and 5 kHz), it is clear that AMPA conductance becomes depressed before the rise, an asymmetry which gives a larger transient in the conductance, and allows time for some removal of sodium channel inactivation prior to the surge in excitatory conductance.

In vivo, however, the arrival times of excitatory events are not completely random (exponentially distributed), but correlated – arriving in clusters or bursts. Correlated input events could range simply from a pair of presynaptic spikes arriving within a few milliseconds, to phenomena such as slow oscillations or "UP-" and "DOWN"-state transitions (Steriade, Nunez et al. 1993), involving thousands of presynaptic spikes arriving in surges lasting up to a second. In Harsch and Robinson (2000), we examined the consequences of this using conductance inputs. We found that a high degree of correlation of conductance inputs is required to explain in vivo spike irregularity. We also discovered that spike-time *reliability* is divided into epochs defined by the input bursts. An intense burst of inputs, by forcing the neuron to spike in a very confined period of time, *resets* the variability or reliability of spike timing, which then decays with time. It is interesting, therefore, not only to address the overall statistics of spike generation and reliability over time, but also to focus on the time-resolved trajectory of variability during individual bursts of inputs.

Figure 4A illustrates a fundamental property of an excitatory input conductance burst, which is apparent even with a period train of excitatory inputs: owing to the slow activation of NMDA receptors, initial input is exclusively AMPA receptor driven, with fast and large transients of linear conductance, but there is a progressive shift towards a smooth, but highly voltage-dependent NMDA-R input, which lingers long after the AMPA-R component subsides. As already mentioned, the NMDA-R conductance signal is the maximum conductance achievable *if* the membrane potential becomes highly depolarized – in general the actual instantaneous conductance is much less than this. It turns out that, with typically sized unitary events, the overall contribution of charge flux through NMDA receptors, averaged over time, is usually roughly equal to that through AMPA receptors. In any transient burst of input, then, the elementary properties of the two conductances dictate that there is a progressive shift from sharply-fluctuating to smooth excitatory input, from high frequencies to low, from current through AMPA-Rs to current through NMDA-Rs. It is also worth remarking that short-term plasticity will typically accentuate this transition. Following any initial facilitation during a burst of inputs, short-term depression and desensitization should ultimately diminish the AMPA-R transients, further enhancing the relative contribution of the NMDA-R activation.

This has consequences for the reliability of spiking during input bursts. One of the great advantages of the technique of conduction injection, in contrast to stimulating the actual synaptic inputs of the neuron, is that exactly the same complex, electrically realistic input pattern can be applied again and again, allowing one to estimate the reproducibility or reliability of postsynaptic responses. Figure 4B (from Harsch and Robinson 2000) shows responses to a

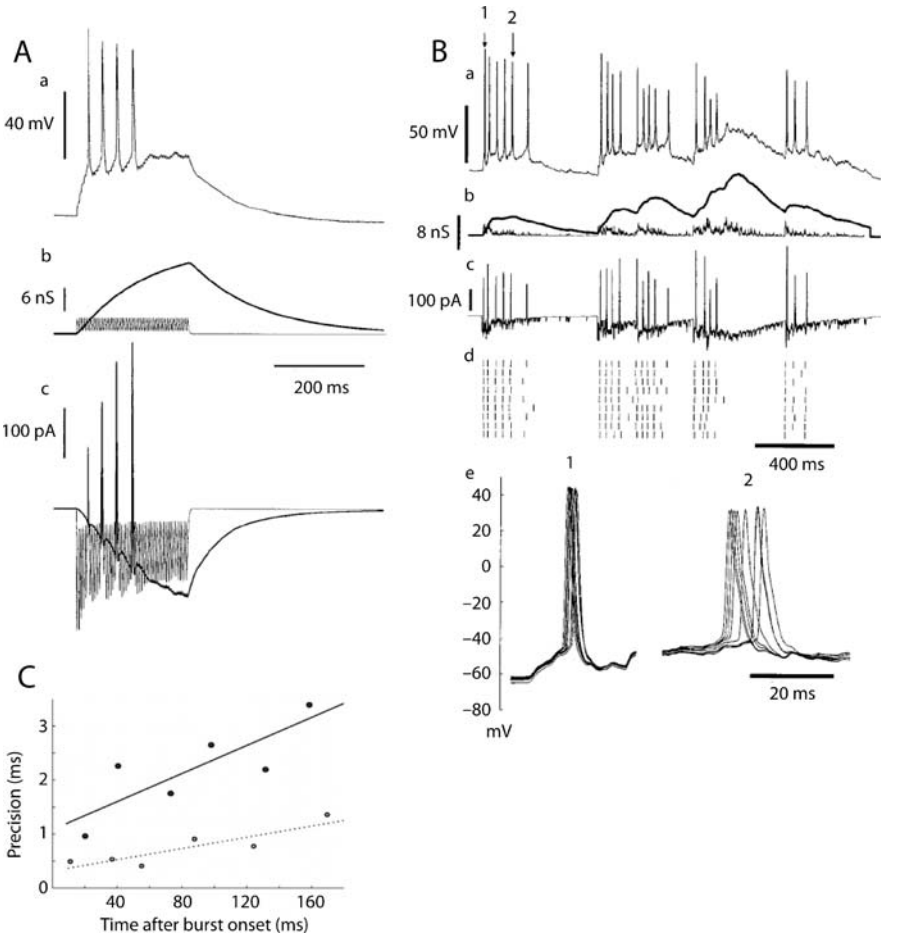

Fig. 4 **A**) The transition from AMPA-R-dominated conductance fluctuations towards smooth NMDA-R-dominated conductance with time during a burst of compound excitatory input. **A,a**) membrane potential response of an RS neuron; **b**) conductance command signals, split into AMPA-R (fast transients) and NMDA-R (smoothly integrating) components; **c**) resulting current injected. Note that the NMDA-R component is subject to a strong voltage-dependent block – in general much less conductance is injected than commanded. Current becomes outward during the peaks of action potentials. **B**) Time-resolved spike-time variability during bursts of excitatory input: **a**) an example spike response, in response to **b**) complex burst, slow-wave-like excitatory inputs; **c**) resulting current injected; **d**) raster plot of spike times in successive trials of the same stimulus, showing the degradation in reliability of generation and timing of spikes with time during each burst; **e**) comparison of timing of an early-burst (1) and late-burst spike in the ensemble (indicated in a), showing the typical explosion of spike-time variability. **C**) growth in spike-time reliability is amplified by NMDA-R conductance input (*solid circles* and *solid line*: AMPA+NMDA; *open circles* and *dotted line*: AMPA only). Modified from Harsch and Robinson (2000)

more naturally structured excitation, composed of clusters of unitary compound AMPA–NMDA inputs resembling slow-wave or UP-state bursts, which give rise to spike statistics (mean rate and CV) similar to those observed in vivo. From the spike raster plots (Fig. 4Bd) and superpositions of particular APs within the ensemble of trials (Fig. 4Be), it can be seen that spikes at the beginning of bursts are precisely timed while those towards the end of bursts are imprecise.

We modelled this behaviour to understand its dynamical basis (Robinson and Harsch 2002). The intrinsic kinetics of AMPA-R and NMDA-R unitary conductance transients mean that each burst of excitation makes a transition from sharper, more transient fluctuations above threshold towards smoother, albeit nonlinear, conductance below the threshold for firing. For any periodically firing system with inherent noise, spiking will switch from nearly periodic to a completely random Poisson process before being silenced, as an exciting stimulus decays smoothly from above the threshold to below the threshold. The coefficient of variation of spike intervals thus passes from near zero to the expected Poisson limit of 1 in the latest phase of the response. In simple dynamical models of spike generation, this essentially happens because there is a shift from fast motion in the dynamics which is relatively insensitive to noise, to a capture in a basin of a resting fixed point, with only occasional random-walk escapes to spike (noise-dominated spike timing, Robinson and Harsch 2002).

The contribution of NMDA-R input is extremely important in the growth of spike-timing variance during a transient neuronal response (Fig. 4C). The rate of growth in variance during a burst is some three times faster for a compound AMPA-R/NMDA-R input, throughout the burst, than for an AMPA-R only input (when the input amplitude is scaled to give the same output spike rate). The smooth NMDA-R phase dominates during the later decay from an input burst, prolonging the late phase of high spike-time variance, in the absence of sharp synchronizing AMPA transients. Furthermore, the voltage-dependent, negative conductance behaviour of NMDA-Rs appears to amplify noise and thus destabilize the membrane potential around threshold, leading to additional variance of spike timing. Thus, the structure of input conductance bursts effectively leads to a transition from initial spike-*time* coding towards spike-*rate* coding We found that the nature of this transition is fundamentally different for (periodically firing) neurons with type 1 and those with type 2 thresholds (see Section 5).

4 Inhibitory Conductance Drive During Stochastic Synaptic Input

Of course, cortical neurons experience excitatory input not in isolation, but together with inhibition, whose relative strength may vary or remain steady over time (balanced), and which may be uncorrelated or correlated to different

degrees with the excitation. Increasing the rate of *independent* random inhibition leads to greater reliability and precision of excitation-driven firing (Harsch and Robinson 2000) in RS neurons, while there is a *resonance* or optimum level for precision in FS neurons (Tateno and Robinson 2006). When inhibition is correlated in time with excitation, we found that there is an optimal excitation-to-inhibition lag of about 2–3 ms, which yields the maximum precision and reliability of output spiking, in both RS and FS cells. Clearly, however, this increased precision comes at the expense of higher energy usage, with more of the AMPA-R current shunted through the $GABA_A$-R conductance.

Spike-triggered averaging of independent random excitation and inhibition conductance inputs in RS neurons (Fig. 5) shows that inhibition modifies the shape of the average excitatory drive for spikes, causing a pronounced dip in the average prespike excitatory conductance preceding the peak at strong levels of excitation (Fig. 5A). Thus, as inhibition increases, an even more emphatic excitatory transient becomes necessary to remove more inactivation from Na channels in conjunction with the rise. Spike-triggered averaging of the *inhibitory* signal shows a small disinhibition preceding spikes, which becomes more pronounced and extends further back in time as the rate of inhibition becomes comparable to that of the excitation (traces labelled 2 and 3 kHz in Fig. 5B). Spike generation and timing in RS cells, then, can be determined by both inhibition and excitation, in different ways.

How do excitatory and inhibitory input conductance control *rate* coding in cortical neurons? One way to characterise this is to examine gain functions of

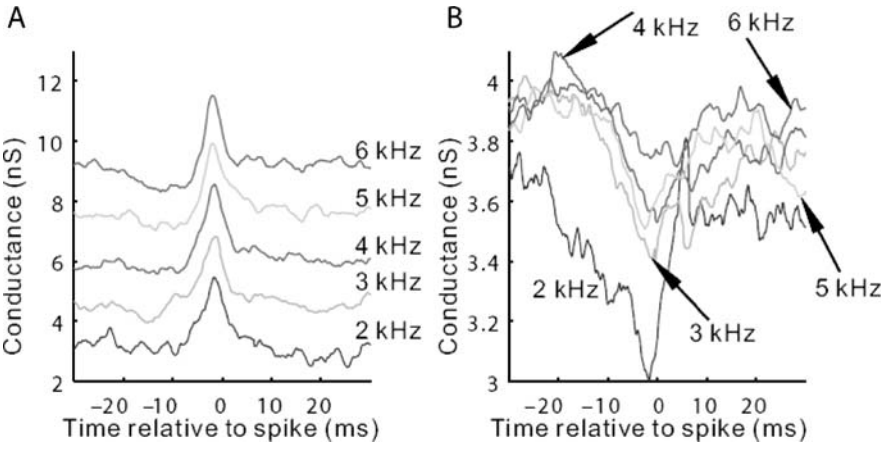

Fig. 5 Spike-triggered averages of conductance input signals during simultaneous AMPA-R excitation and $GABA_A$-R inhibition in an RS neuron. **A**) AMPA-R conductance at six different rates of Poisson AMPA-R unitary conductances, as indicated. **B**) $GABA_A$-R conductance, at an inhibitory rate of 2 kHz, and six different levels of excitatory conductance, as in (A). From Tateno and Robinson (2006) (Fig. 3Bc, 3Cc)

cortical neurons, plots of the output firing rate versus the rate of stochastic (Poisson) excitatory inputs (Harsch and Robinson 2000). Such curves are always continuous at zero output firing rate, because of the linearizing effect of the random input, and rise with increasing rate of excitation. There are two distinct (possibly simultaneous) effects that inhibitory conductance inputs can have on these gain functions: a shift to the right, i.e. inhibition effectively *subtracts* from the level of excitation (dotted lines in Fig. 6A) or a reduction in slope, or gain, i.e. inhibition *divides* the level of excitation (grey lines in Fig. 6A). In practice, we found that in RS and FS cortical neurons, the effect is almost completely subtractive, for these unitary conductance parameters. However, other studies in cerebellar granule cells (Mitchell and Silver 2003) and cortical neurons (see Chance and Abbott "Simulating In Vivo Background Activity in a Slice with the Dynamic Clamp" in this volume and Chance et al. 2002) have shown gain modulation under certain conditions: Chance et al. (2002) showed that if excitation and inhibition remain precisely balanced, i.e. if inhibition is scaled with the level of excitation, then a gain modulation could occur in RS cortical neurons by adjusting the fixed ratio between excitation and inhibition. Mitchell and Silver (2003) showed that gain modulation occurred when unitary inhibitory events had especially long time constants and when excitation was highly variable. Clearly, the details depend on the particular integrative properties of the neuron, and on the precise timing and location of inhibition and excitation, to determine to what extent the inhibition can shunt the excitation divisively.

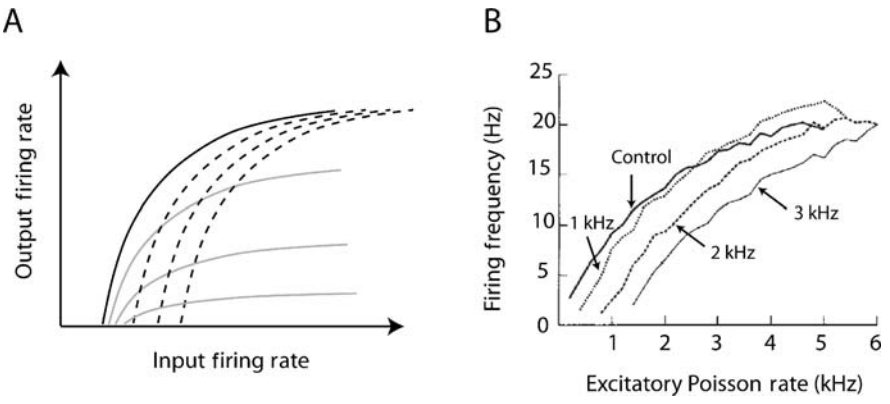

Fig. 6 A) Diagrammatic representation of the effect of inhibition on rate coding of excitatory input. Increasing inhibition can effectively subtract from the excitation, shifting the gain curve to the right (*dashed curves*), or divide the effect of excitation, reducing the slope of the gain curve (gain modulation, *grey curves*). **B**) Measured changes in the rate coding curve of an RS cell, as the rate of independent Poisson inhibition is increased. The predominant effect is a shift. From Tateno and Robinson (2006), Fig. 2A

5 Oscillatory Firing

Periodically spiking neurons can be classified into two fundamental types: those with type 1 thresholds (a continuous firing frequency vs. input curve) and those with type 2 thresholds (a discontinuous firing frequency vs. input curve) (Hodgkin 1948). Dynamical models which reproduce these behaviours have saddle-node (on invariant circle) bifurcations (type 1) or subcritical Andronov–Hopf bifurcations (type 2) at the threshold for firing (Izhikevich 2007). In the context of time-resolved spike reliability during correlated input bursts, type 1 neurons show a much faster accumulation of spike-time variance through a burst than type 2 neurons do, a consequence of the much slower noise-sensitive subthreshold dynamics of type 1 as opposed to the subthreshold oscillatory behaviour of the type 2 dynamics (Robinson and Harsch 2002). These distinctions are not merely of mathematical interest. The most common electrophysiological cell type in the cortex, the RS (usually pyramidal, excitatory) neuron is type 1 for *conductance* (as well as current) input, while the most common inhibitory firing type, the FS (usually basket morphology) cell is type 2 (Tateno, Harsch et al. 2004). Figure 7 shows the firing frequency versus excitatory conductance curves for an FS cell, showing how they are *discontinuous* at a critical, lowest possible stable firing frequency, in the range 20–30 Hz. Moreover this critical firing frequency can be shifted towards a higher value by the level of coincident inhibitory conductance.

The type 2 behaviour means that around threshold, firing stutters between bursts of spiking at the critical frequency and in-phase subthreshold oscillations at the same frequency. FS neurons are highly and specifically interconnected in a gap-junctional network, as well as exerting strong mutual $GABA_A$-R

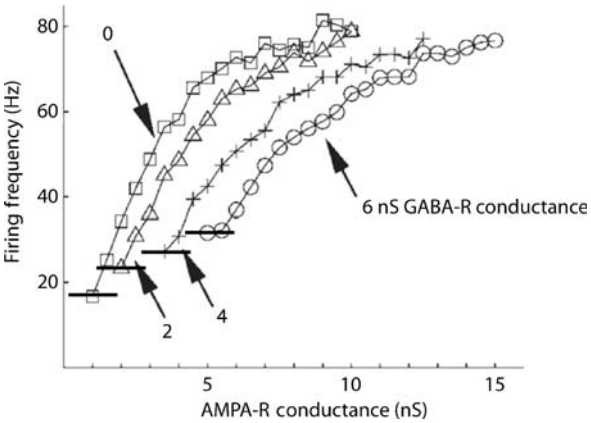

Fig. 7 FS neurons have a hard type 2 threshold for AMPA-R conductance stimulation, at a frequency in the gamma range, which is modulated by the level of shunting inhibitory conductance. Plots of firing rate versus AMPA-R conductance stimulus level, at four different levels of GABA-R conductance. Threshold (critical) frequency for periodic spiking is indicated by thick black lines

inhibition (Beierlein, Gibson et al. 2003), and they can fire in tight synchrony with their connected FS neighbours. It is evident therefore that with random, distributed excitation of the network, synchronous firing at the critical frequency should be an attracting state over a wide range of activation levels: the critical threshold firing frequency of the type 2 FS cells is probably a major factor determining the frequency of network gamma oscillations (30–80 Hz), the most salient form of synchronized activity in the cortex during sensory processing and cognition (Singer and Gray 1995).

In Robinson, Tsumoto et al. (2004), we used conductance injection to examine the different roles of gap junctional and $GABA_A$-R conductance in synchronizing FS neurons, by examining the entrainment of FS cell firing to artificial conductances mimicking this complex connection (Fig. 8). When a connected presynaptic FS cell fires, the postsynaptic cell simultaneously experiences an IPSP, or $GABA_A$-R conductance transient, as well as current flow through the connecting gap-junctional conductance during the transient of presynaptic membrane potential (Fig. 8A). Applying this compound conductance perturbation at many points in the firing cycle of an excited, periodically firing FS neuron, we measured the resulting phase shift in spiking as a function of the point in the cycle at which it is applied – termed the "synaptic interaction function" (SIF), the physiological analogue of a phase-response curve (which refers to the function describing phase shifts resulting from extremely small, brief *current* perturbations at different points in the cycle). We found that SIFs were characterized by almost linear regions of phase delay and phase advance, separated by a sharp, midcycle discontinuity. The slope of the phase delay region was determined by the strength of the inhibitory conductance, while the slope of the phase advance region, as well as the position of the discontinuity, was controlled by the strength of the gap-junctional conductance. Moreover the SIF, applied as a sequential map, is sufficient to predict the time course and extent of entrainment of firing by a train of synaptic perturbations (Fig. 8C). Analysis of a piecewise linear SIF model showed that conductances amongst FS cells are tuned to produce very rapid entrainment over a broad range of frequencies both above and below the preferred (unperturbed) firing frequency of the postsynaptic cell, providing a functional rationale for the seemingly opposed mixture of gap-junctional excitation and chemical inhibition.

If tight synchronization of the local network of FS cells, with their critical, gamma threshold frequencies is a major influence in the generation of gamma synchronized firing in the principal RS neurons, what about the role of the strong recurrent excitation from RS cells? How do inhibition and excitation work together to determine spike timing during gamma oscillations? We took advantage of measurements by Hasenstaub, Shu et al. (2005) of the spike-timing preference of RS and FS neurons through the gamma cycle, to attempt to reconstruct gamma oscillations in individual RS neurons using conductance injection (Morita, Kalra et al. 2008), by generating the conductance signals which are expected to converge on individual RS neurons from the local network activity (Fig. 9A). Hasenstaub, Shu et al. (2005) showed that there is a surge in RS cell firing early in the cycle, leading to a rise in FS cell firing, which

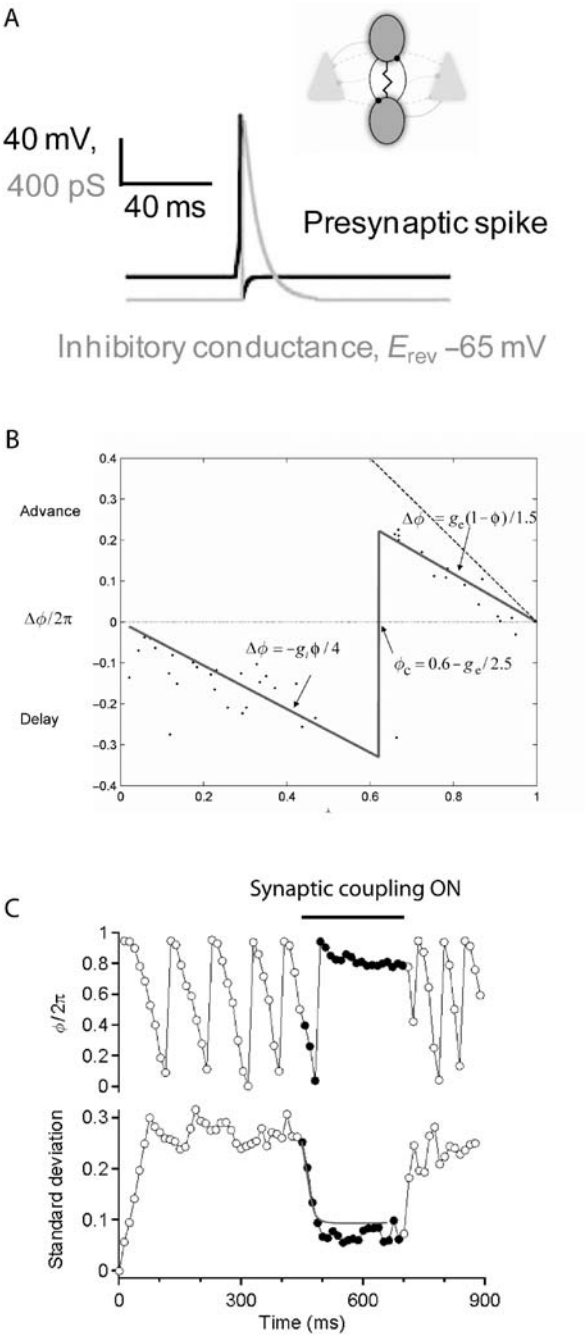

Fig. 8 Entrainment of FS cell firing by compound gap-junctional/$GABA_A$-R conductance inputs mimicking the firing of a connected presynaptic FS neuron (inset, A). **A**) Compound conductance event consisting of a synaptic $GABA_A$-R transient of shunting conductance, together with a static gap-junctional conductance connecting the recorded neuron to a stereotyped presynaptic action potential waveform. **B**) Synaptic interaction function (SIF) showing the change in phase of firing due to compound inputs applied at different phases in the firing cycle, fitted with a piecewise linear model. **C**) Entrainment and detuning of spiking as the coupling to a train of periodic inputs is turned on and off. From experimental data recorded by Nathan Gouwens. Superimposed curve shows time course predicted by the SIF in B

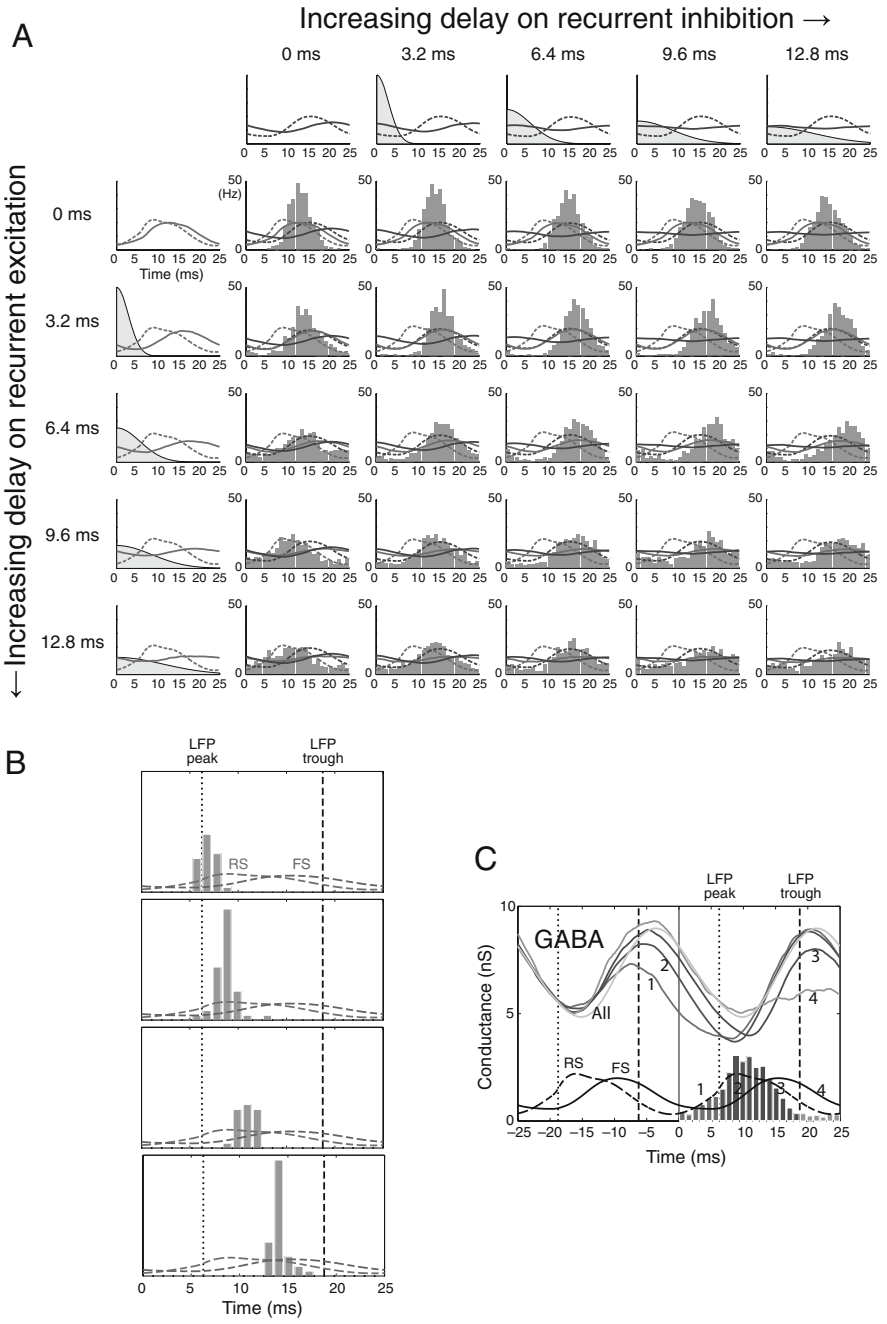

Fig. 9 Re-creating gamma oscillations in RS pyramidal neurons with conductance injection. **A**, Effects of distributed delay in recurrent inputs on the postsynaptic RS spike phase

in turn chokes off the RS cell firing. The subsequent fall in FS cell firing then frees the RS cell firing to rise again. We treated RS and FS firing as separate nonstationary Poisson processes generating unitary excitatory and inhibitory synaptic inputs, respectively, and introduced a variety of stochastic delays in each pathway. We found that in order to reproduce correctly-distributed gamma-modulated firing, RS cells require strongly gamma-modulated, low-latency *inhibitory* inputs from FS cells, but *little or no* gamma-modulation in recurrent RS → RS *excitatory* connections. This selective demodulation of the recurrent excitatory signal probably reflects several characteristics of recurrent excitation including distributed propagation delays and widespread divergence of local excitatory projections, but can not be accounted for by dendritic filtering and integration delays in detailed compartmental models. With this scenario for the structure of synaptic input, encoding of particular input patterns into the *phase* of gamma-synchronized postsynaptic firing can be very precise, as shown by measuring ensembles of responses to exactly the same stochastic realization of input (Fig. 9B). Computing the spike-triggered conductance input shows that the phase of firing is almost completely determined by the timing of the inhibition (Fig. 9C), not the excitation (not shown, but see Fig. 7C of Morita, Kalra et al. 2008).

Our results indicate that RS cells are likely to receive strongly gamma-modulated, low-latency inhibition from FS cells and excitation with little or no gamma-modulation from other RS cells, as a result of comparatively long distributed delays in recurrent excitation. This indicates a clear separation of function in the network between excitatory and inhibitory connections. Inhibitory inputs from FS cells are responsible for setting a reliable rhythm, while recurrent excitation between RS cells has no overall effect on the gamma rhythm, but still contributes a strong local reinforcement to the maintenance of the oscillation. The lack of overall phase modulation in RS–RS cell recurrent excitation would allow a large capacity for encoding information with reference to a gamma clock signal, since the uniform distribution of recurrent excitatory inputs through the gamma period permits a great number of different arrangements of recurrent input timing, without impacting on the timing of the "clock" itself.

Fig. 9 (continued) distribution. Panels in the leftmost column show how a half-Gaussian distribution of delays (shaded distribution) of recurrent excitation affects the shape of the gamma-modulated AMPA conductance (*solid grey lines*), injected into RS cells. Panels in the top row show how delays in recurrent inhibition affect the shape of the total inhibitory conductance (*solid dark grey lines*). Numbers in milliseconds indicate the means of the delay distributions, which are the positive parts of Gaussians with SDs of 4, 8, 12 and 16 (ms). Histograms show the spike phase distributions of RS cells with the corresponding distribution of delays in excitation and inhibition. Dashed lines indicate the presynaptic RS and FS spike phase distributions. **B**, Gamma phase encoding of synaptic input. Four different examples of precise spike-time distributions in response to repeated trials using identical stochastic instances of gamma-modulated GABA conductance and Poisson glutamatergic conductances (data not shown). **C**, Reverse correlation of the GABA input. LFP= local field potential. Strong decreases in GABA input are linked to subsequent spiking. Modified from Morita, Kalra et al. (2008)

6 Spike Shape Encoding of Synaptic Conductance Input

In cortical neurons, it has often been assumed that analogue dendritic potentials are encoded into patterns of stereotyped, effectively *digital* AP events in the soma and axon. According to this view, the outputs of cortical neurons are completely encapsulated by the temporal patterns of spikes. Although it has long been appreciated that spike broadening occurs with spike frequency adaptation and depolarization block, during responses to maintained currents, it is now clear that the RS neuron excitatory postsynaptic potential (EPSP) (Zsiros and Hestrin 2005) and spike *shape* are sensitively controlled by the level of conductance input.

Recently, we demonstrated an "AP waveform" coding in cortical pyramidal neurons, showing that the spike shape carries information about the synaptic conductance input (de Polavieja, Harsch et al. 2005; Juusola, Robinson et al. 2007). Wider and lower-amplitude somatic APs are reliably produced in response to a higher preceding level of conductance (Fig. 10A), during fluctuating naturalistic input – a correlation which is much lower for a fluctuating current input producing similar output frequencies and membrane potential variation (see de Polavieja, Harsch et al. 2005, Supplementary Material). Why is this? Unlike spikes driven by a predetermined *current* fluctuation, the peak of a conductance-driven AP is subject to a shunting effect, pulling it down towards E_{AMPA}/E_{NMDA}. Also, E_{GABA} attracts the membrane potential to an extent determined by the momentary level of inhibitory input, a particularly nonlinear, even reversible effect near to the resting potential (Fig. 10B). This directly shapes the spike width as well as the interspike trajectory of the membrane potential – in particular the rate at which it traverses the threshold region, and therefore the availability of sodium channels, which in turn has major effects on spike shape. The feedback between the membrane potential and the synaptic current arising from the voltage sensitivity of the synaptic conductances, creates a consistent mapping from input (conductance) to output (spike width). This is seen in Fig. 10C, where by repeatedly applying the same conductance input and measuring the variability of the result, we were able to calculate the rates of information transfer from the fluctuating conductance waveform: (1) to the membrane potential trajectory, (2) to spikes including their variations in shape or (3) to spike times alone. As seen in Fig. 10C, spike shape variations carry some five times more information than spike times alone (while the full membrane potential trajectory carries much more still) – and both spike time and spike shape encoding increase their information rate with the rate of spiking.

It has recently been shown that such modulations of AP shape do actually reach local presynaptic terminals and lead to large variations in synaptic transmission (Alle and Geiger 2006; Shu, Hasenstaub et al. 2006). Individual spikes carry much more information than just their time of occurrence. In addition, different shapes of backpropagating APs will also interact differentially with coincident synaptic input, determining the pattern of invasion of the

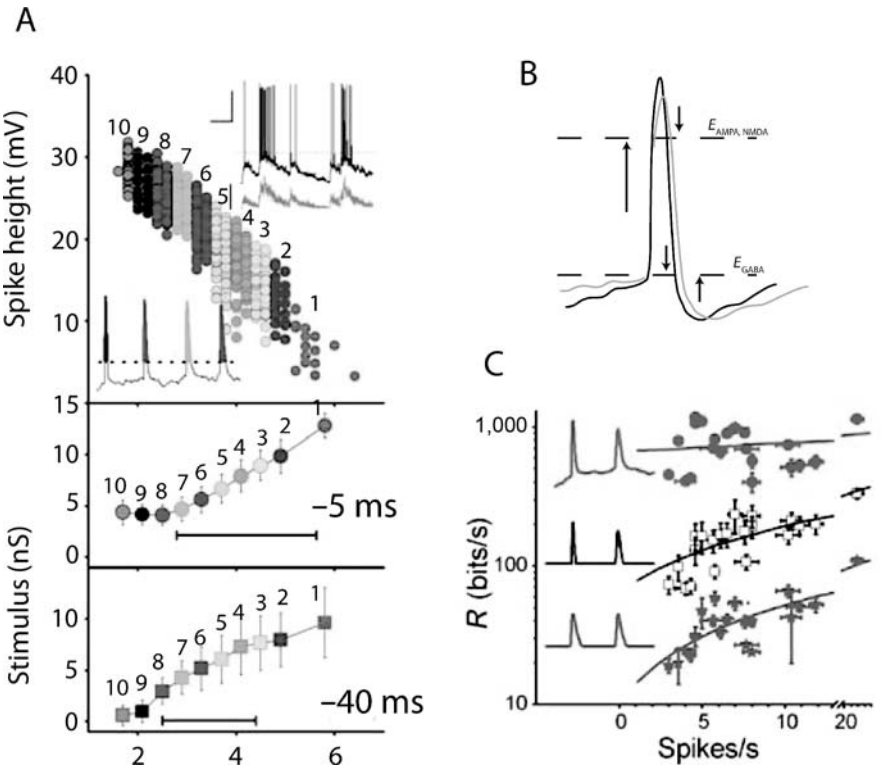

Fig. 10 Spike shape encoding of conductance input. Action potential waveforms of pyramidal neurons encode information about the stimulus history. (**A**) The heights and widths of action potentials (filled circles; $n = 4{,}137$) occupy a large linear range during naturalistic conductance stimulation; here: height = 37.4 – 4.8 × width. This recording is from a layer 2/3 pyramidal cell. Action potential waveforms (top inset; black trace) vary with synaptic input patterns of a sum of AMPA unitary events (top inset; grey trace). Scale bars: 30 mV and 0.5 s; scale bar for conductance: 10 nS. The thin dotted line indicates the voltage (–30 mV) where the action potential widths were measured. The widths are divided into ten groups (lower inset, nine equally spaced with the tenth including the remainder), from narrow to wide as 1–10. Lower panels: Average stimulus (conductance) history preceding the peak of the action potentials for each group (same labelling). The circles and squares indicate the conductance values at 5 and 40 ms before the spiking time, respectively. (**B**) Diagrammatic representation of shape modulations by different membrane potential histories and levels of synaptic conductance during a spike. (**C**) Information transfer rate of pyramidal neurons ($n = 21$) for different conductance patterns (both stationary and non-stationary) plotted against the mean firing rate of each experiment. The information transfer rate was calculated for the full voltage responses (*filled circles*), the action potential waveforms (*open squares*) and stereotyped action potentials (*stars*), each sampled at 2 kHz. The inset shows a short sample of the three waveforms containing two action potentials. Information transfer rate, R, for each signal type increases with the mean firing rate, f (full voltage responses: $R = 10.4 \times f + 660.6$, top; action potential waveforms: $R = 12.9 \times f + 64.7$, middle; stereotyped spikes: $R = 4.2 \times f + 9.8$, bottom). Modified from de Polavieja, Harsch et al. (2005)

dendritic tree by the AP (Hausser, Major et al. 2001). Thus, spike shape encoding is able to transmit the dynamical state of neurons in the local cortical circuit more rapidly, and more reliably, than rate or spike-time coding alone, and enriches the computational possibilities in local cortical networks (Juusola, Robinson et al. 2007). Interestingly, RS cells appear to be specifically adapted for signalling spike shape modifications – FS cells show almost no shape modulation at all for a variety of naturalistic conductance inputs (Tateno and Robinson 2006).

7 Voltage-Dependent NMDA Receptor Gating Revisited – A Special Role in Spike Shape Coding

NMDA receptors mediate a very large component of the excitatory drive of pyramidal neurons. However, their block by extracellular magnesium means that this is highly voltage-dependent: masked or "silent" near the resting potential, providing a regenerative or positive-feedback inward current with depolarization. Intriguingly, though it is a synaptic receptor, it is also a powerful active mechanism, capable of driving full-blown NMDA-R spikes in basal dendrites (Nevian, Larkum et al. 2007). In order to assess quantitatively the role of NMDA receptors in spike generation, we recently re-examined the fast dynamics of the voltage dependence of the NMDA receptor under conditions of high-quality voltage clamp, by applying voltage steps to nucleated patches containing receptors activated by fast perfusion (Vargas-Caballero and Robinson 2003, 2004, also see Kampa, Clements et al. 2004). Surprisingly, we found that *unblock* is much slower than predicted by previous kinetic models of the receptor, with two distinct phases – one lasting on the order of a millisecond and the other lasting tens of milliseconds, a phenomenon whose NR2 subunit-dependence has since been studied in an expression system by Clarke and Johnson (2006). Figure 11A shows a family of NMDA receptor currents recorded from a nucleated patch taken from a rat layer 2/3 cortical pyramidal neuron. Depolarizing steps from a potential of –70 to +40 mV relieve the magnesium block of receptors, which open in two phases – fast and slow. Brief repolarizations after full unblock show how the slow phase of unblock is reinstated at hyperpolarized potentials, with a time constant of 4.5 ms (Fig. 11B, C). This time and voltage dependence of NMDA receptor block and unblock is accurately described by an "asymmetric trapping block" (ATB) model, in which only one rate constant (for channel closure) has to be higher in the Mg-blocked side of the "trapping block" kinetic scheme (Fig. 11D). We have recently begun to inject this voltage-dependent, kinetically accurate model of NMDA-Rs into RS cortical neurons (Fig. 11D, E, F, G). We found that slow unblock is particularly suited to a role in spike shape encoding according to the level of NMDA–R activation. The unblock kinetics mean that NMDA receptors hardly participate in the upstroke of APs, but kick in strongly by the

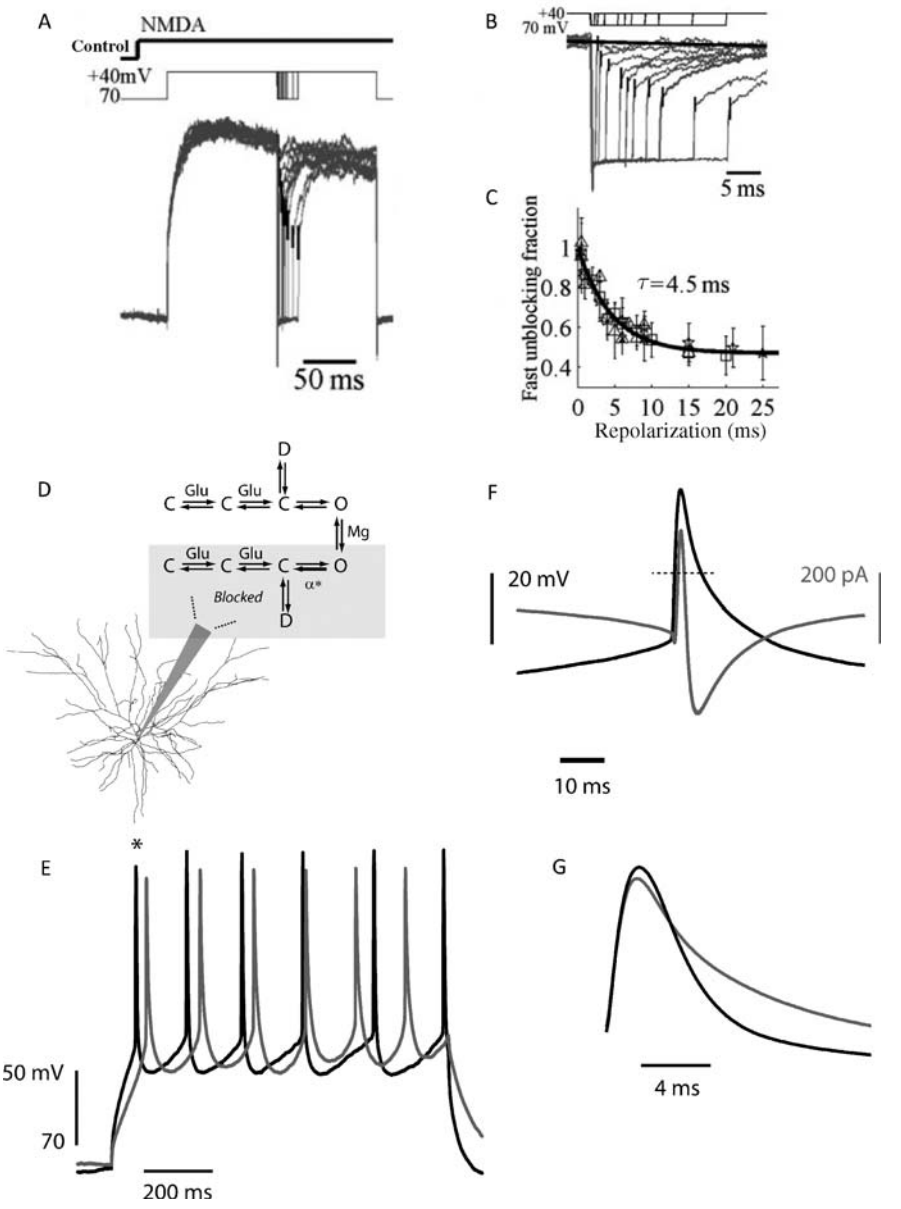

Fig. 11 A, B, C) NMDA-R conductance shows a complex time dependence of voltage-dependent unblock, with components lasting tens of milliseconds. Block with hyperpolarization is rapid, while slow unblock takes about 10 ms to be reinstated by brief hyperpolarizations. This behaviour is precisely accounted for by the asymmetric trapping block model of NMDA receptor gating (Vargas-Caballero and Robinson 2004). (**D**) Schematic diagram showing the somatic injection of the kinetic model, specified as a Markov process using the SM-2 conductance injection system, in a layer 2/3 pyramidal neuron. (**E**) Current injection with (*black*)

repolarization phase of the AP, resulting in a highly asymmetric peak inward current (Fig. 11E) during depolarization and repolarization. Thus, in response to a transient (e.g. AMPA-R) input to a cell, NMDA receptors can have less effect on spike initiation time, while strongly modulating spike width.

8 Conclusions

In this chapter, I have demonstrated how artificial conductance injection is used to reproduce the natural dynamics of fast synaptic integration, allowing controlled measurement of the computational function of cortical neurons. The shift between AMPA-R and NMDA-R excitation is an important feature of the integration of any correlated burst of excitation, effectively implementing a switch from spike-time to spike-rate coding of the input. Shunting inhibition emerges as a powerful determinant of spike timing. In conductance-driven FS inhibitory cells, the sharp threshold frequency is an obvious intrinsic source of the gamma rhythm, and is tuned by the level of inhibitory conductance, while the complex conductance connections between FS cells ensure their synchrony over the broad gamma frequency range. During gamma oscillations, RS neurons appear to receive recurrent excitation which is, on average, *de*modulated – thus oscillatory spike timing, which can be very precise, is determined almost completely by the timing of phasic inhibition from FS cells. A new facet of synaptic integration is the modulation of spike shape according to the conductance input. The work described in this chapter is based upon somatic injection of conductance, and may give a broadly valid picture of in vivo activity when considering the overall integration of population input, and for proximal inhibitory input. Clearly, however, it is now important to begin to use this technique to address the complexity of the spatial integration of conductance inputs in the dendritic tree (e.g. see Williams "Dendritic Dynamic Clamp – A Tool to Study Single Neuron Computation" in this volume and Williams 2004), in conjunction with new optical recording and stimulation techniques.

Acknowledgments I am deeply grateful to all my collaborators in this work: Kazuyuki Aihara, Gonzalo de Polavieja, Nathan Gouwens, Annette Harsch, Mikko Juusola, Rita Kalra, Nobufumi Kawai, Ingo Kleppe, Kenji Morita, Takashi Tateno, Kunichika Tsumoto, Mariana Vargas-Caballero and Hugo Zeberg. Supported by grants from the EC, BBSRC and the Daiwa Foundation.

Fig. 11 (continued) or without (*grey*) injection of the conductance. Amplitude of current step is reduced for NMDA receptor injection, to allow comparison at the same spike frequency. (**F**) NMDA receptor current reaches a much higher inward peak during repolarization than during depolarization of the spike. (**G**) Comparison of the width of the fourth spike, showing how NMDA receptor conductance prolongs the action potential. D, E, F, G modified from Robinson (2008)

References

Alle, H. and J. R. Geiger (2006). "Combined analog and action potential coding in hippocampal mossy fibers." *Science* **311**(5765): 1290–3.

Beierlein, M., J. R. Gibson, et al. (2003). "Two dynamically distinct inhibitory networks in layer 4 of the neocortex." *J Neurophysiol* **90**: 2987–3000.

Chance, F., L. Abbott, and A. Reyes (2002). "Gain modulation from background synaptic input." *Neuron* **35**: 773–82.

Clarke, R. J. and J. W. Johnson (2006). "NMDA receptor NR2 subunit dependence of the slow component of magnesium unblock." *J Neurosci* **26**(21): 5825–34.

Connors, B. W., M. J. Gutnick, et al. (1982). "Electrophysiological properties of neocortical neurons in vitro." *J Neurophysiol* **48**(6): 1302–20.

Coombs, J. S., J. C. Eccles, et al. (1955). "Excitatory synaptic action in motoneurones." *J Physiol* **130**: 374–95.

de Polavieja, G. G., A. Harsch, et al. (2005). "Stimulus history reliably shapes action potential waveforms of cortical neurons." *J Neurosci* **25**(23): 5657–65.

Destexhe, A., M. Rudolph, et al. (2001). "Fluctuating synaptic conductances recreate in vivo-like activity in neocortical neurons." *Neuroscience* **107**(1): 13–24.

Eccles, J. (1963). "The ionic mechanism of postsynaptic inhibition." *Nobel Prize Lecture*.

Erisir, A., D. Lau, et al. (1999). "Function of specific K(+) channels in sustained high-frequency firing of fast-spiking neocortical interneurons." *J Neurophysiol* **82**(5): 2476–89.

Forsythe, I. D. and G. L. Westbrook (1988). "Slow excitatory postsynaptic currents mediated by N-methyl-D-aspartate receptors on cultured mouse central neurones." *J Physiol* **396**: 515–33.

Harsch, A. and H. P. C. Robinson (2000). "Postsynaptic variability of firing in rat cortical neurons: the roles of input synchronization and synaptic NMDA receptor conductance." *J Neurosci* **20**(16): 6181–92.

Hasenstaub, A., Y. Shu, et al. (2005). "Inhibitory postsynaptic potentials carry synchronized frequency information in active cortical networks." *Neuron* **47**(3): 423–35.

Hausser, M., G. Major, et al. (2001). "Differential shunting of EPSPs by action potentials." *Science* **291**(5501): 138–41.

Hodgkin, A. L. (1948). The local electric changes associated with repetitive action in a non-medullated axon. *J Physiol* **107**: 165–81.

Hodgkin, A. L. and A. F. Huxley (1952). "A quantitative descrption of membrane current and its application to conduction and excitation in nerve." *J Physiol* **117**: 500–44.

Itazawa, S.-I., T. Isa, et al. (1997). "Inwardly rectifying and Ca2+-permeable AMPA-type glutamate receptor channels in rat neocortical neurons." *J Neurophysiol* **78**: 2592–601.

Izhikevich, E. M. (2007). *Dynamical Systems in Neuroscience: The Geometry of Excitability and Bursting*, MIT Press, Cambridge.

Juusola, M., H. P. Robinson, et al. (2007). "Coding with spike shapes and graded potentials in cortical networks." *Bioessays* **29**(2): 178–87.

Kampa, B. M., J. Clements, et al. (2004). "Kinetics of Mg2+ unblock of NMDA receptors: implications for spike-timing dependent synaptic plasticity." *J Physiol* **556**: 337–45.

Koch, C., T. Poggio, et al. (1983). "Nonlinear interactions in a dendritic tree: localization, timing and role in information processing." *Proc Natl Acad Sci USA* **80**: 2799–2802.

Mayer, M. L., G. L. Westbrook, et al. (1984). "Voltage-dependent block by Mg2+ of NMDA responses in spinal cord neurones. " *Nature* **309**: 261–3.

Mitchell, S. J. and R. A. Silver (2003). "Shunting inhibition modulates neuronal gain during synaptic excitation." *Neuron* **38**: 433–45.

Morita, K., R. Kalra, et al. (2008). "Recurrent synaptic input and the timing of gamma-frequency-modulated firing of pyramidal cells during neocortical "UP" states." *J Neurosci* **28**: 1871–81.

Nevian, T., M. E. Larkum, et al. (2007). "Properties of basal dendrites of layer 5 pyramidal neurons: a direct patch-clamp recording study." *Nature Neurosci* **10**: 206–14.

Nowak, L., P. Bregestovski, et al. (1984). "Magnesium gates glutamate-activated channels in mouse central neurones." *Nature* **307**: 462–5.

Qian, N. and T. J. Sejnowski (1990). "When is an inhibitory synapse effective?" *Proc Natl Acad Sci USA* **87**: 8145–9.

Rall, W. (1962). "Electrophysiology of a dendrite neuron model." *Biophys J* **2**: 145–67.

Robinson, H. P. C. (1991). "Kinetics of synaptic conductances in mammalian central neurons." *Neurosci Res* **16**: VI.

Robinson, H. P. C. (2008). "A scriptable DSP-based system for dynamic conductance injection." *J Neurosci Methods* **169**: 271–81.

Robinson, H. P. and A. Harsch (2002). "Stages of spike time variability during neuronal responses to transient inputs." *Phys Rev E Stat Nonlin Soft Matter Phys* **66**(6 Pt 1): 061902.

Robinson, H. P. C. and N. Kawai (1993). "Injection of digitally synthesized synaptic conductance transients to measure the integrative properties of neurons." *J Neurosci Methods* **49**(3): 157–65.

Robinson, H. P. C., K. Tsumoto, et al. (2004). *Modelling phase-locking in electrically-coupled networks of inhibitory cortical interneurons*. Proceedings of Nonlinear Theory and its Applications, Fukuoka, Japan.

Sakmann, B. and E. Neher (1995). *Single Channel Recording*. New York and London, Plenum.

Sharp, A. A., M. B. O'Neil, et al. (1993). "Dynamic clamp: computer-generated conductances in real neurons." *J Neurophysiol* **69**(3): 992–5.

Shu, Y., A. Hasenstaub, et al. (2006). "Modulation of intracortical synaptic potentials by presynaptic somatic membrane potential." *Nature* **441**(7094): 761–5.

Singer, W. and C. M. Gray (1995). "Visual feature integration and the temporal hypothesis." *Annual Rev Neurosci* **18**: 555–86.

Spruston, N. (2008). "Pyramidal neurons: dendritic structure and synaptic integration." *Nat Rev Neurosci* **9**(3): 206–21.

Steriade, M., A. Nunez, et al. (1993). "A novel slow (< 1 Hz) oscillation of neocortical neurons in vivo: depolarizing and hyperpolarizing components." *J Neurosci* **13**(8): 3252–65.

Stuart, G. J. and B. Sakmann (1994). "Active propagation of somatic action potentials into neocortical pyramidal cell dendrites." *Nature* **367**(6458): 69–72.

Tateno, T., A. Harsch, et al. (2004). "Threshold firing frequency-current relationships of neurons in rat somatosensory cortex: type 1 and type 2 dynamics." *J Neurophysiol* **92**(4): 2283–94.

Tateno, T. and H. P. Robinson (2006). "Rate coding and spike-time variability in cortical neurons with two types of threshold dynamics." *J Neurophysiol* **95**(4): 2650–63.

Vargas-Caballero, M. and H. P. Robinson (2003). "A slow fraction of Mg2+ unblock of NMDA receptors limits their contribution to spike generation in cortical pyramidal neurons." *J Neurophysiol* **89**(5): 2778–83.

Vargas-Caballero, M. and H. P. Robinson (2004). "Fast and slow voltage-dependent dynamics of magnesium block in the NMDA receptor: the asymmetric trapping block model." *J Neurosci* **24**(27): 6171–80.

Williams, S. R. (2004). "Spatial compartmentalization and functional impact of conductance in pyramidal neurons." *Nature Neurosci* **7**: 961–7.

Simulating In Vivo Background Activity in a Slice with the Dynamic Clamp

Frances Chance and Larry F. Abbott

Abstract Neurons in vivo receive a large amount of internally generated "background" activity in addition to synaptic input directly driven by an external stimulus. Stimulus-driven and background synaptic inputs interact, through the nonlinearities of neuronal integration, in interesting ways. The dynamic clamp can be used in vitro to duplicate background input, allowing the experimenter to take advantage of the accessibility of neurons in vitro while still studying them under in vivo conditions. In this chapter we discuss some results from experiments in which a neuron is driven by current injection that simulates a stimulus-driven input as well as dynamic-clamp-generated background activity. One of the effects uncovered in this way is multiplicative gain modulation, achieved by varying the level of background synaptic input. We discuss how the dynamic clamp was used to discover this effect and also how to choose parameters to simulate in vivo background synaptic input in slice neurons.

1 Introduction

Much of what we know about the response properties of neurons comes from studies done in fairly inactive slices or in cell cultures. These preparations are ideal for exploring basic electrophysiological characteristics, but they do not duplicate in vivo conditions. Neurons in a living brain are subject to a continual barrage of activity arising from both nearby and distal sources. The synaptic input from this background barrage is highly irregular (Softky and Koch, 1993; Shadlen and Newsome, 1994; Troyer and Miller, 1997; Stevens and Zador, 1998; Jaeger and Bower, 1999; Santamaria et al., 2002; Wolfart et al., 2005; Desai and Walcott, 2006), so it acts as a source of noise that introduces variability into the stimulus-evoked responses of neurons (Schiller et al., 1976; Heggelund and Albus, 1978; Vogels et al., 1989; Holt et al., 1996). As would be

F. Chance (✉)
Department of Neurobiology and Behavior, University of California Irvine, Irvine, CA 92697, USA
e-mail: frances.chance@uci.edu

A. Destexhe, T. Bal (eds.), *Dynamic-Clamp*, Springer Series in Computational Neuroscience 1, DOI 10.1007/978-0-387-89279-5_4,

expected, noise from background input limits the sensitivity and precision of stimulus-driven responses, but in some cases it can actually have an enhancing effect (Troyer and Miller, 1997; Hô and Destexhe, 2000; Anderson et al., 2000; Shu et al., 2003; Wenning et al., 2005) . In addition, background synaptic input is thought to significantly increase the membrane conductance of neurons (Borg-Graham et al., 1998; Hirsch et al., 1998; Destexhe and Paré, 1999, but see Waters and Helmchen, 2006), which affects their input integration properties (Destexhe and Paré, 1999; Azouz, 2005; Zsiros and Hestrin, 2005). The "noise" effects of background input can be mimicked in vitro by injecting a fluctuating current into the neuron being recorded, but this does not replicate conductance changes. Fortunately, the dynamic clamp can be used to simulate both the noise and conductance effects of background synaptic input, allowing us to bridge the gap between typically silent slice preparations and active, functioning neural circuits.

Although the summed background input to a neuron in vivo can be quite large, it does not, in the absence of stimulus-dependent or other drive, cause neurons to fire at high rates, nor does it hyperpolarize the neuron far below threshold. Reconciling this high level of synaptic input with a relatively small change in mean membrane potential requires the excitatory effects of background input to consist of a well-balanced combination of excitation and inhibition (Shadlen and Newsome, 1994; Shu et al., 2003; Haider et al., 2006; Baca et al., 2008; Okun and Lampl, 2008). Thus, background input to a neuron consists of large amounts of excitation and inhibition that, to a large extent, cancel each other. Cancellation between two large, random sources of opposite sign generates input currents with small means and large variances. However, in spite of the large variance of the fluctuating conductances, the membrane potential fluctuations are limited by the reversal potentials of the synaptic input currents. Attempting to mimic background synaptic input by current injection can result in unrealistically and even excessively large hyperpolarizations of the neuron, a problem that is eliminated by using the dynamic clamp.

It is convenient to divide the total synaptic input to a neuron into a component that controls the total synaptic current, which we call the driving input, and a balanced component that affects both the total synaptic conductance and the variance arising from the synaptic input but makes little contribution to the total synaptic current. The total synaptic current to the neuron is essentially equal to the driving component because, by definition, synaptic currents generated by the balanced component are small. On the other hand, because the total synaptic drive consists of two large, essentially canceling terms, the total synaptic conductance and the variability of the synaptic current are dominated by the balanced component. These two components of the synaptic input can act as two independent signal-carrying channels. The driving component can be modulated by changing excitatory and inhibitory drive in opposite directions, increasing excitation and decreasing inhibition, for example. The balanced component can be modified by changing excitation and inhibition in parallel, such as increasing both excitatory and inhibitory inputs. Often the synaptic

input to a neuron is modeled as consisting of a variable stimulus-dependent driving component and a fixed, though large, balanced component. Some studies, however, have considered the impact of modulating the balanced component of synaptic input, with interesting results. Changes in balanced input provide an alternative way of modulating neural responses (Silberberg et al., 2004; Fourcaud-Trocmé and Brunel, 2005; Khorsand and Chance, 2008) or of modifying neuronal gain, defined by the relationship between firing rate and input current (Doiron et al., 2001; Chance et al., 2002; Fellous et al., 2003; Prescott and De Koninck, 2003) or EPSP (excitatory postsynaptic potential) rate (Mitchell and Silver, 2003), or spiking probability and EPSC (excitatory postsynaptic current) size (Hô and Destexhe, 2000; Shu et al., 2003; Chance, 2007). The gain modulation effect relies, in particular, on the impact of the conductance introduced by background synaptic input. Reproducing this effect in slice experiments therefore requires the dynamic clamp. We focus on this effect in this chapter.

In addition to demonstrating the gain modulation effect that arises from simulated background activity, we discuss in this chapter how the dynamic clamp can be used, in general, to simulate the input that a neuron might receive in vivo (Destexhe et al., 2001; Chance et al., 2002). In the latter part of this chapter, we focus on calculations needed to adjust the parameters of the dynamic-clamp input to reproduce desired values for the mean and variance of the conductance and membrane potential.

2 Gain Modulation from Dynamic-Clamp Input

The dynamic clamp allows any combination of conductance changes and current injections to be introduced into a recorded neuron. In this section, we discuss the effects of introducing a fluctuating conductance and current, similar to what would be generated by spontaneous activity in vivo, into a cortical neuron recorded in a slice preparation. We also analyze separate conductance and current effects by considering them independently.

2.1 Generating the Dynamic-Clamp Input

The essential feature that allows conductances to be mimicked by the dynamic clamp is that the current it injects into a neuron depends on the membrane potential of the neuron. To duplicate the effects of time-dependent excitatory and inhibitory synaptic conductances $G_{\mathrm{ex}}(t)$ and $G_{\mathrm{in}}(t)$ with reversal potentials E_{ex} and E_{in}, respectively, the current injected by the dynamic clamp should be

$$I = G_{\mathrm{ex}}(t)(E_{\mathrm{ex}} - V) + G_{\mathrm{in}}(t)(E_{\mathrm{in}} - V) \ ,$$

where V is the membrane potential of the neuron. Given computer generated values of $G_{ex}(t)$ and $G_{in}(t)$ and preset values of E_{ex} and E_{in}, this is exactly what the dynamic clamp does. We have a good idea of the values of the reversal potentials of excitatory and inhibitory synaptic conductances, so the problem of duplicating in vivo synaptic input lies in mimicking the time-dependent conductances that real synaptic input generates.

One way to generate a time-dependent synaptic conductance mimicking the total conductance produced by a set of afferents to a neuron is to model the spike trains carried by those afferents. Typically, these are assumed to have Poisson statistics. The dynamic-clamp attempts to reproduce the effects of synapses distributed across the dendritic arbor by simulating a conductance located at the site of an electrode. Within this unavoidable approximation, the effects of all the afferents on a given conductance (excitatory or inhibitory) add linearly and the Poisson model is similarly additive, so we can simply generate spikes at a rate obtained by adding together the rates on all of the afferents. This is done, for a desired total firing rate R, by generating an action potential at each small time step Δt with a probability $R\Delta t$. These Poisson-generated action potentials are then fed into a model of the synaptic conductance. A simple model, for example, increments the total conductance by an amount that represents the unitary maximal synaptic conductance every time a spike is generated, and allows it to decay exponentially back toward zero between spikes. In mathematical terms, we compute G_{ex} and G_{in} by integrating the differential equations

$$\tau_{ex}\frac{dG_{ex}}{dt} = -G_{ex} \quad \text{and} \quad \tau_{in}\frac{dG_{in}}{dt} = -G_{in} \ ,$$

where τ_{ex} and τ_{in} are the decay time constants for the excitatory and inhibitory synaptic conductances, and we increment these conductances by

$$G_{ex} \rightarrow G_{ex} + g_{ex} \quad \text{and} \quad G_{in} \rightarrow G_{in} + g_{in}$$

every time an excitatory (left equation) or inhibitory (right equation) action potential is generated by the Poisson model. This model works well (with a small but inessential rise time included, see Chance et al., 2002), but later in this chapter we discuss another procedure that has the virtue of being convenient for mathematical analysis.

It is a good idea to use two recording electrodes when duplicating synaptic input with the dynamic clamp in this way: one electrode to record the membrane potential and a second to inject the computed dynamic-clamp current. Using two electrodes eliminates artifacts that can be introduced into the membrane potential measurements by the injection of rapidly fluctuating current. Figure 1A shows the membrane potential of a neuron recorded from a slice of somatosensory cortex driven to fire by a constant injected current without any additional dynamic-clamp input. The firing pattern is regular and the membrane potential shows no significant fluctuations due to the relative silence of

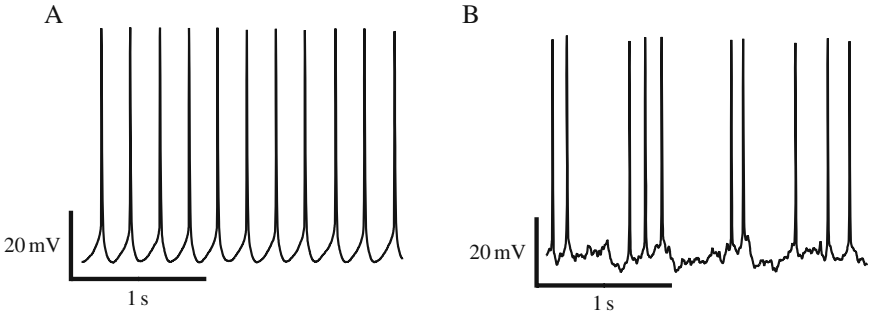

Fig. 1 Intracellular recordings from a layer 5 pyramidal neuron in a slice of rat somatosensory cortex with and without simulated background activity. In both cases, constant current was injected to drive the neuron at approximately 5 Hz. **A**) The membrane potential of the spiking neuron in the absence of simulated background activity. **B**) The dynamic clamp was used to simulate 1X background activity. (Adapted from Chance et al., 2002.)

this slice preparation. For Fig. 1B, excitatory inputs were simulated at a total rate of 7,000 Hz and inhibitory inputs at a total rate of 3,000 Hz, representing the summed effects of many simulated afferents. The arrival times of these synaptic inputs were randomly generated with Poisson statistics. The unitary synaptic conductance for each synaptic input was set to 2% of the measured resting membrane conductance for excitatory input and 6% of the resting conductance for inhibitory input. The synaptic time constants were $\tau_{ex} = 5\,ms$ and $\tau_{in} = 10\,ms$. In the following discussion, we refer to this as the 1X condition (see filled circles in Fig. 2), and we will consider 2X and 3X conditions produced by doubling or tripling the rates of both the excitatory and inhibitory synaptic inputs. These parameters were chosen to achieve realistic conductance changes and levels of noise, and to put the synaptic inputs into a configuration in which excitation approximately balanced inhibition. Because of the balance between excitation and inhibition, the background synaptic activity by itself was not very effective at driving the recorded neuron. Instead, the dominant effect of this background activity was to increase the effective membrane conductance and also to introduce noise into the neuronal response, as illustrated in Fig. 1B.

2.2 Multiplicative Gain Modulation in a Slice

Varying the level of dynamic-clamp background activity, by multiplying excitatory and inhibitory input rates by factors of 0, 1, 2, or 3, for example, has an interesting effect on the firing properties of a neuron. We characterize firing by plotting firing rates as a function of constant injected current. Multiple firing-rate curves are obtained by measuring the firing rate as a function of driving current for different levels of background activity. Gain is defined as the slope of the nonzero portion of the firing-rate curve. Fig. 2A shows firing-rate curves of the same neuron under four different levels of background activity.

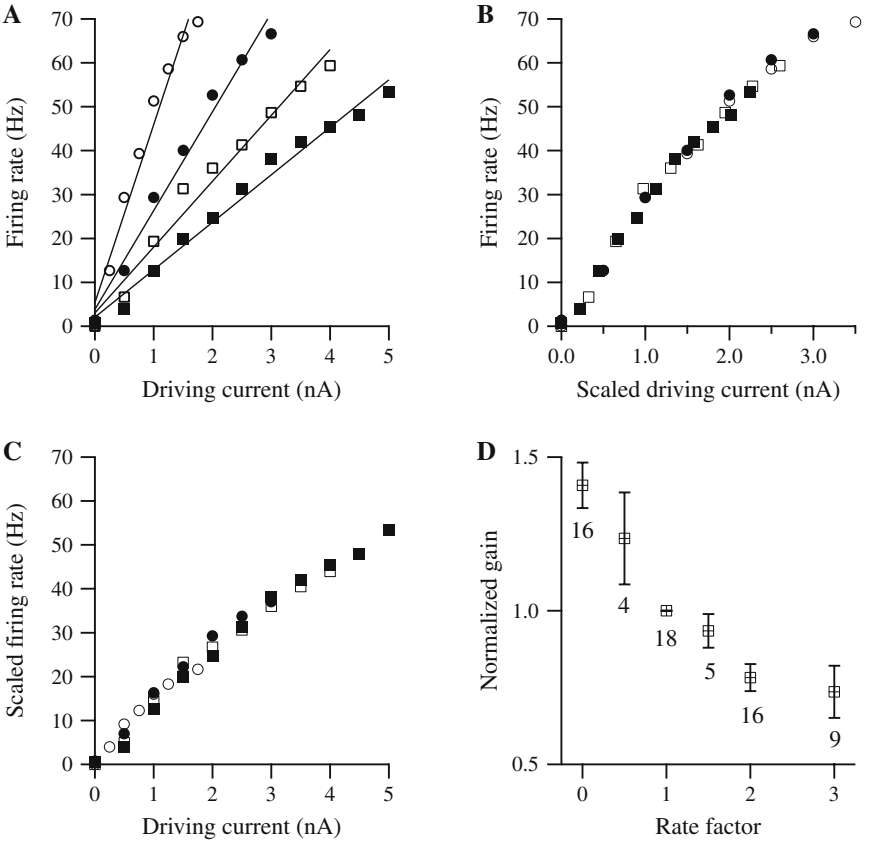

Fig. 2 Effects of background activity on the firing-rate curves of neurons. **A**) Firing rate-curves under 0X (no background activity, *open circles*), 1X (*filled circles*), 2X (*open squares*), and 3X (*filled squares*) conditions. Lines are linear fits. **B**) The firing-rate curves from (A) except that the driving currents of the 1X, 2X, and 3X firing-rate curves were scaled so that the firing-rate curves overlay the firing-rate curve in the 0X condition. **C**) The firing-rate curves from (A) with the firing rates of the 0X, 1X, and 2X curves divisively scaled to overlay the 3X firing-rate curve. **D**) Slope of the firing-rate curves, normalized to the slope of the 1X firing-rate curve, plotted as a function of rate factor. (Adapted from Chance et al., 2002.)

For the open circles, no background activity was present. The filled circles, open squares, and filled squares are firing-rate curves recorded under 1X, 2X, and 3X conditions, respectively. The solid lines are the best linear fits to these data. The curves show that increasing background input led to a reduction of the firing rate, but did not significantly change the minimum threshold current required to fire the neuron. The dominant effect of changing the level of background activity was to divisively scale the curve of firing-rate versus input current for the neuron. This indicates a change of gain.

To create Fig. 2B, the constant current input for the 1X, 2X, and 3X cases were divisively scaled by appropriate factors to make the corresponding firing-rate curves overlay the control (0X or no background activity) curve (open circles). The good match between the resulting curves indicates that the gain modulation effect is, indeed, divisive (or equivalently multiplicative if we invert the scaling factors). Two different possibilities exist, however, for how the divisive effect can be realized. A firing rate function of input current, $r = f(I)$ can be scaled, as in Fig. 2B, by dividing the input current by a factor c, so that $r = f(I/c)$. Alternatively, the rate itself can be scaled by a factor, $r = f(I)/c$. In either case, c takes different values for each condition. In Fig. 2C, the firing rates of the control, 1X and 2X firing-rate curves were divisively scaled to overlay the 3X firing-rate curve (filled squares). This shows that the results are accounted for equally well by a scaling of the rate. In fact, it is impossible to determine whether the gain modulation effect illustrated here represents input gain control (where the input is divisively scaled) or response gain control (where the firing rates are divisively scaled). This ambiguity arises because of the linearity of the neuron firing-rate curves, but further analysis of the effect suggests that raising the level of background activity results in changes in both response gain and input gain (Chance et al., 2002).

We summarize the effect of background activity on 18 different neurons in Fig. 2D. For each neuron, the slope of the firing-rate curve for each level of background input was measured and then normalized by the gain in the 1X condition. Mean gain (averaged across all neurons recorded in each condition) is plotted as a function of rate factor (the factor multiplying the excitatory and inhibitory firing rates, i.e., the 1, 2, or 3 in the 1X, 2X, or 3X conditions) in Fig. 2D. The numbers under each data point describe the number of cells that were recorded in each condition.

Although gain modulation arises through this mechanism in part because of increased variance in the neuronal input, gain modulation occurs without a corresponding change in response variability. This is illustrated in Fig. 3A, where variability is measured either as the coefficient of variation of the inter-spike intervals (filled triangles) or the standard deviation of the membrane potential (open triangles) under different levels of background activity. This relative constancy of variability occurs because the effect of the increased variance of the synaptic current is cancelled by the increased conductance of the neuron (see Chance et al., 2002 for a more detailed explanation). This is an example of an effect for which the ability of the dynamic clamp to mimic conductances is essential.

By Ohm's law, increases in membrane conductance will have a divisive effect on the subthreshold membrane potential fluctuations arising from fluctuating input current. However, the multiplicative effect on firing rate illustrated here is not simply a result of the increased conductance induced by the dynamic-clamp-simulated input (see Chance et al., 2002 for a full explanation). Two fundamental components of synaptic input increase when background synaptic

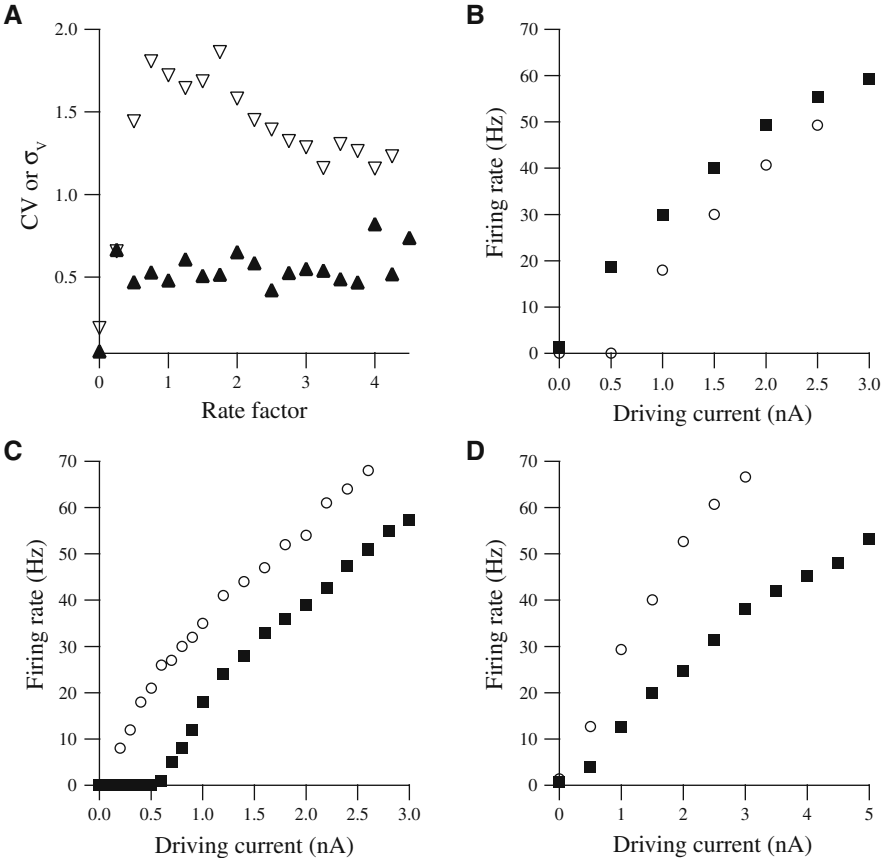

Fig. 3 Effects of background activity on the firing of neurons. **A**) Standard deviation of subthreshold membrane potential fluctuations (*open triangles*) or coefficient of variation of interspike intervals (*filled triangles*) as a function of rate factor. For the filled triangles, constant current was injected to drive the neuron at 20 Hz. **B**) Firing-rate curves in the 1X condition (*open circles*) and with 3X current variance but 1X conductance changes (*filled squares*). **C**) Firing-rate curves in the absence of background activity (*open circles*) and with 32 nS of additional conductance (*filled squares*). **D**) Firing-rate curves of a neuron in the 1X (*open circles*) or the 3X (*filled squares*) condition. (Adapted from Chance et al., 2002.)

activity is increased: the variance of the synaptic current entering the neuron and the overall membrane conductance of the neuron.

Increasing the variance of the input current leads to an increase in neuronal firing rate. Of particular relevance is that the elevation in firing rate is also associated with a decrease in gain. The firing-rate curve of a neuron in the 1X condition is plotted in Fig. 3B with open circles. To produce the filled squares, the size of the unitary synaptic conductance change associated with a particular synaptic input was tripled while the input rates were divided by three. This

increased the variance of the synaptic input current without changing the average synaptic conductance. Thus, the variance of the input current was equivalent to the variance of the input current in the 3X condition, but the average conductance was unchanged from the 1X case. The effect of the increased current variance alone is a decrease in gain combined with an additive (leftward) shift in firing rate. This is equivalent to what would be obtained simply by adding fluctuating current to the input.

In Fig. 3C, the open circles are the firing-rate curve of a neuron with no simulated background activity. To produce the filled squares, an additional constant conductance of 32 nS was added (the reversal potential of the resulting current was set to -57 mV, the effective reversal potential of the simulated background inputs). The effect of this additional conductance was subtractive, so it shifted the firing-rate curve along the driving current axis. This result is consistent with previous studies examining the effects of increased conductance on the firing-rate curves of neurons (Gabbiani et al., 1994; Holt and Koch, 1997, Chance et al., 2002).

When the rate of background synaptic input is increased, the effect of the increased input current variance illustrated in Fig. 3B is combined with the effect of the increased membrane conductance illustrated in Fig. 3C. For a certain parameter range, the subtractive effect of the conductance increase cancels the additive effect of the current variance increase, leaving a divisive gain change. The effect of increasing background input from 1X to 3X is illustrated in Fig. 3D.

If excitation and inhibition arising from the background input are not appropriately balanced, mixed multiplicative/divisive and additive/subtractive effects occur. For example, if inhibition is slightly stronger than excitation, a subtractive shift (shifting the curve to the right along the input axis) will accompany the divisive modulation. Therefore, mixed multiplicative and additive effects can arise from this mechanism through nonbalanced background activity. This implies that we should not think of firing-rate curves plotted as a function of a single variable (the mean input current or, equivalently, the driving input), but as firing-rate surfaces in a two-dimensional plot with the two variables being driving input and balanced input (Abbott and Chance, 2005).

3 Computing the Dynamic-Clamp Input

In this section, we present another model for generating dynamic-clamp input that is very similar to the input discussed in the previous section, but the model is more analytically tractable, allowing us to discuss how the appropriate parameters of the dynamic-clamp model are determined for a given application (see also Rudolph and Destexhe, 2003). To begin our discussion, we consider a single, generic conductance and only later discuss the effects of both excitation

and inhibition. Thus, in the initial discussion that follows, the conductance G_s can represent either an excitatory (G_{ex}) or an inhibitory (G_{in}) conductance.

3.1 Driving the Synaptic Conductance with White-Noise Input

The alternative approach we now consider is to approximate the Poisson spike train used in the previous section with white noise. This approximation has been used in a number of studies (Destexhe et al., 2001; Fellous et al., 2003; Wolfart et al., 2005; Desai and Walcott, 2006; Piwkowska et al., 2008). According to this method, we determine the total synaptic conductance from the stochastic differential equation

$$\tau_s \frac{dG_s(t)}{dt} = -G_s(t) + \overline{G}_s + \sqrt{2D_s}\eta(t)\,,$$

where $\overline{G}_s$ and D_s are parameters, and $\eta(t)$ is a stochastic term satisfying

$$\langle \eta(t) \rangle = 0 \quad \text{and} \quad \langle \eta(t)\eta(t') \rangle = \delta(t - t')\,,$$

where the angle brackets denote time averages. In practice, $\eta(t)$ is generated randomly at discrete times that are integer multiples of a minimum time interval Δt from a Gaussian distribution with zero mean and variance equal to $1/\Delta t$. The parameters $\overline{G}_s$, which is the time average of $G_s(t)$, and D_s are related to the unitary synaptic conductance g_s and the total afferent firing rate R of the Poisson model discussed in the previous section by

$$\overline{G}_s = g_s \tau_s R \quad \text{and} \quad D_s = \frac{1}{2} g_s^2 \tau_s^2 R\,.$$

Note that $\overline{G}_s$ and D_s can be varied independently by adjusting g_s and R. The white-noise-driven model therefore defines a two-parameter model of a synaptic conductance. When we include both excitation and inhibition, this will become a four-parameter model described by $\overline{G}_{ex}$, $\overline{G}_{in}$, D_{ex}, and D_{in}. The problem we discuss is how to constrain these four parameters.

3.2 Determining the White-Noise Parameters

The autocorrelation function of the conductance determined by the equation above is

$$\left\langle \left(G_s(t) - \overline{G}_s\right)\left(G_s(t') - \overline{G}_s\right) \right\rangle = \frac{D_s}{\tau_s} \exp(-|t - t'|/\tau_s)\,.$$

The variance of the conductance is just this correlation function evaluated at zero, which is

$$\sigma_G^2 = \frac{D_s}{\tau_s} .$$

To determine the effects of this conductance on the membrane potential, we use a passive RC model with membrane capacitance C_m, resting conductance (in the absence of synaptic input) G_{rest}, and resting potential V_{rest}. The resulting mean membrane potential is

$$\overline{V} = \frac{1}{G_{tot}} \left(G_{rest} V_{rest} + \overline{G}_s E_s \right) ,$$

where

$$G_{tot} = G_{rest} + \overline{G}_s$$

is the average total conductance of the neuron. We can also compute the autocorrelation function for the voltage and, from this, the variance of the membrane potential,

$$\sigma_V^2 = \frac{D_s (\overline{V} - E_s)^2}{G_{tot}(C_m + G_{tot}\tau_s)} .$$

In performing this calculation, we have used the approximation that V stays close to the value $\overline{V}$. If there are excitatory and inhibitory synapses, their variances simply add together to give the total variance.

3.3 Determining the Dynamic-Clamp Parameters

We now show how to determine the parameters of the underlying model that drives the dynamic clamp from the simulated electrophysiological properties. When we have both excitatory and inhibitory conductances, the parameters $\overline{G}_{ex}$, $\overline{G}_{in}$, D_{ex}, and D_{in} can be determined in terms of more biophysically relevant variables using the equations and approximations discussed above. $\overline{G}_{ex}$ and $\overline{G}_{in}$ determine the average total conductance of the neuron,

$$G_{tot} = G_{rest} + \overline{G}_{ex} + \overline{G}_{in} ,$$

and the average potential is given by

$$\overline{V} = \frac{1}{G_{\text{tot}}} \left(G_{\text{rest}} V_{\text{rest}} + \overline{G}_{\text{ex}} E_{\text{ex}} + \overline{G}_{\text{in}} E_{\text{in}} \right) .$$

If we know the values of G_{tot} and $\overline{V}$ that we want to simulate, we can determine the parameters we need,

$$\overline{G}_{\text{ex}} = \frac{G_{\text{tot}}(\overline{V} - E_{\text{in}}) - G_{\text{rest}}(V_{\text{rest}} - E_{\text{in}})}{E_{\text{ex}} - E_{\text{in}}} \text{ and } \overline{G}_{\text{in}} = \frac{G_{\text{tot}}(\overline{V} - E_{\text{ex}}) - G_{\text{rest}}(V_{\text{rest}} - E_{\text{ex}})}{E_{\text{in}} - E_{\text{ex}}}.$$

To determine D_{ex} and D_{in}, we relate them to the variances of the synaptic conductance and the membrane potential. From the above equations, the variance of the conductance is

$$\sigma_G^2 = \frac{D_{\text{ex}}}{\tau_{\text{ex}}} + \frac{D_{\text{in}}}{\tau_{\text{in}}}$$

and the variance of the membrane potential is

$$\sigma_V^2 = \frac{D_{\text{ex}}(\overline{V} - E_{\text{ex}})^2}{G_{\text{tot}}(C_{\text{m}} + G_{\text{tot}}\tau_{\text{ex}})} + \frac{D_{\text{in}}(\overline{V} - E_{\text{in}})^2}{G_{\text{tot}}(C_{\text{m}} + G_{\text{tot}}\tau_{\text{in}})} .$$

These equations are sufficient to determine both parameters. If we define

$$\alpha_{\text{ex}} = \frac{G_{\text{tot}}(C_{\text{m}} + G_{\text{tot}}\tau_{\text{ex}})}{(\overline{V} - E_{\text{ex}})^2} \quad \text{and} \quad \alpha_{\text{in}} = \frac{G_{\text{tot}}(C_{\text{m}} + G_{\text{tot}}\tau_{\text{in}})}{(\overline{V} - E_{\text{in}})^2} ,$$

the variance parameters of the white-noise-driven model are given by

$$D_{\text{ex}} = \frac{\alpha_{\text{ex}}\tau_{\text{ex}}(\alpha_{\text{in}}\sigma_V^2 - \tau_{\text{in}}\sigma_G^2)}{\alpha_{\text{in}}\tau_{\text{ex}} - \alpha_{\text{ex}}\tau_{\text{in}}} \quad \text{and} \quad D_{\text{in}} = \frac{\alpha_{\text{in}}\tau_{\text{in}}(\alpha_{\text{ex}}\sigma_V^2 - \tau_{\text{ex}}\sigma_G^2)}{\alpha_{\text{ex}}\tau_{\text{in}} - \alpha_{\text{in}}\tau_{\text{ex}}} .$$

Using the above equations, all of the parameters of the dynamic clamp can be determined on the basis of the total synaptic conductance, mean membrane potential, and variances of the synaptic conductance and membrane potential that are desired. If all of these are not known, other assumptions, such as fixing g_{ex} or g_{in} to experimentally constrained values, can by used to reduce the number of free parameters. If the Poisson model is used instead, the unitary conductances and firing rates can be obtained from the conversion formulas between these parameters and G_{ex}, D_{ex}, G_{in}, and D_{in}.

4 Conclusions

The dynamic clamp is an effective means of mimicking in vivo conditions in vitro. This allows us to take advantage of the accessibility of neurons in the slice for recording without losing the background synaptic input that strongly affects their response properties in an intact animal. We have discussed the impact of background activity on neuronal gain, but it would be extremely interesting to examine a number of other phenomena, including dendritic integration, dendritic spiking, and synaptic plasticity, in the presence of dynamic-clamp-simulated background synaptic input.

Acknowledgments Research supported by the National Institute of Mental Health (MH-58754) an NIH Director's Pioneer Award, part of the NIH Roadmap for Medical Research, through grant number 5-DP1-OD114-02 to LFA and by NSF-IOB-0446129, funds provided by the University of California and an Alfred P. Sloan Foundation Research Fellowship to FSC.

References

Abbott LF and Chance FS (2005) Drivers and modulators from push-pull and balanced synaptic input. Prog Brain Res 149:147–155.

Azouz R (2005) Dynamic spatiotemporal synaptic integration in cortical neurons: neuronal gain, revisited. J Neurophysiol 94:2785–2796.

Anderson JS, Lampl I, Gillespie DC and Ferster D (2000) The contribution of noise to contrast invariance of orientation tuning in cat visual cortex. Science 290:1968–1972.

Baca SM, Marin-Burgin A, Wagenaar DA and Kristan WB (2008) Widespread inhibition proportional to excitation controls the gain of a leech behavioral circuit. Neuron 57:276–289.

Borg-Graham LJ, Monier, C, and Frgnac Y. (1998) Visual input evokes transient and strong shunting inhibition in visual cortical neurons. Nature 393:369–372.

Chance FS (2007) Receiver operating characteristic (ROC) analysis for characterizing synaptic efficacy. J Neurophysiol 97:1799–1808.

Chance FS, Abbott LF and Reyes AD (2002) Gain modulation through background synaptic input. Neuron 35:773–782.

Desai NS and Walcott EC (2006) Synaptic bombardment modulates muscarinic effects in forelimb motor cortex. J Neurosci 26:2215–226.

Destexhe A and Paré D (1999) Impact of network activity on the integrative properties of neocortical pyramidal neurons in vivo. J Neurophysiol 81:1531–1547.

Destexhe A, Rudolph M, Fellous J-M and Sejnowski TJ (2001) Fluctuating synaptic conductances recreate in vivo-like activity in neocortical neurons. Neuroscience 107:13–24.

Doiron B, Longtin A, Berman N and Maler L (2001) Subtractive and divisive inhibition: effects of voltage-dependent inhibitory conductances and noise. Neural Comput. 13:227–248.

Fellous J-M, Rudolph M, Destexhe A, and Sejnowski TJ (2003) Synaptic background noise controls the input/output characteristics of single cells in an in vitro model of in vivo activity. Neuroscience 122:811–829.

Fourcaud-Trocmé N and Brunel N (2005) Dynamics of the instantaneous firing rate in response to changes in input statistics. J Comput Neurosci 18:311–321.

Gabbiani F, Midtgaard J and Knopfel T (1994) Synaptic integration in a model of cerebellar granule cells. J Neurophysiol 72:999–1009.

Haider B, Duque A, Hasenstaub AR and McCormick DA (2006) Neocortical network activity in vivo is generated through a dynamic balance of excitation and inhibition. J Neurosci 26:4535–4545.
Heggelund P and Albus K (1978) Response variability and orientation discrimination of single cells in striate cortex of cat. Exp Brain Res 32:197–211.
Hirsch JA, Alonso J-M, Reid RC and Martinez LM (1998) Synaptic integration in striate cortical simple cells. J Neurosci 18:9517–9528.
Hô N and Destexhe A (2000) Synaptic background activity enhances the responsiveness of neocortical pyramidal neurons. J Neurophysiol 84:1488–1496.
Holt GR and Koch C (1997) Shunting inhibition does not have a divisive effect on firing rates. Neural Comput 9:1001–1013.
Holt GR, Softky GW, Koch C and Douglas RJ (1996) Comparison of discharge variability in vitro and in cat visual cortex neurons. J Neurophysiol 75:1806–1814.
Jaeger D and Bower JM (1999) Synaptic control of spiking in cerebellar Purkinje cells: dynamic current clamp based on model conductances. J Neurosci 19:6090–6101.
Khorsand P and Chance FS (2008) Transient responses to rapid changes in mean and variance in spiking models. PLoS One 3:e3786.
Mitchell SJ and Silver RA (2003) Shunting inhibition modulates neuronal gain during synaptic excitation. Neuron 38:433–445.
Okun M and Lampl I (2008) Instantaneous correlation of excitation and inhibition during ongoing and sensory-evoked activities. Nat Neurosci 11:535–537.
Piwkowska Z, Pospischil M, Brette R, Sliwa J, Rudolph-Lilith M, Bal T and Destexhe A (2008) Characterizing synaptic conductance fluctuations in cortical neurons and their influence on spike generation. J Neurosci Methods 169:302–322.
Prescott SA and De Koninck Y (2003) Gain control of firing rate by shunting inhibition: roles of synaptic noise and dendritic saturation. Proc Natl Acad Sci USA 100:2076–2081.
Rudolph M and Destexhe A (2003) Characterization of subthreshold voltage fluctuations in neuronal membranes. Neural Comput 15:2577–2618.
Santamaria F, Jaeger D, De Schutter E and Bower JM (2002) Modulatory effects of parallel fiber and molecular layer interneuron synaptic activity on purkinje cell responses to ascending segment input: a modeling study. J Comput Neurosci 13:217–235.
Schiller PH, Finlay BL, and Volman SF (1976) Short-term response variability of monkey striate neurons. Brain Res 105:347–349.
Shadlen MN and Newsome WT (1994). Noise, neural codes and cortical organization. Curr Opin Neurobiol 4:569–579.
Schiller PH, Finlay BL, and Volman SF (1976) Short-term response variability of monkey striate neurons. Brain Res 105:347–349.
Shadlen MN and Newsome WT (1994). Noise, neural codes and cortical organization. Curr Opin Neurobiol 4:569–579.
Shu Y, Hasenstaub A, Badoual M, Bal T, and McCormick DA (2003) Barrages of synaptic activity control the gain and sensitivity of cortical neurons. J Neurosci 23:10388–10401.
Silberberg G, Bethge M, Markram H, Pawelzik K and Tsodyks M (2004) Dynamics of population rate codes in ensembles of neocortical neurons. J Neurophysiol 91 :704–709.
Softky WR and Koch C (1993) The highly irregular firing of cortical cells is inconsistent with temporal integration of random EPSPs. J Neurosci 13:334–350.
Stevens CF and Zador AM (1998) Input synchrony and the irregular firing of cortical neurons. Nature Neurosci 3:210–217.
Troyer TW and Miller KD (1997) Physiological gain leads to high ISI variability in a simple model of a cortical regular spiking cell. Neural Comput 9:971–983.
Vogels R, Spileers W, and Orban GA (1989) The response variability of striate cortical neurons in the behaving monkey. Exp Brain Res 77:432–436.
Waters J and Helmchen F (2006) Background synaptic activity is sparse in neocortex. J Neurosci 26:8267–8277.

Wenning G, Hoch T, and Obermayer K (2005) Detection of pulses in a colored noise setting. Phys Rev E 71:e021902.
Wolfart J, Debay D, Le Masson G, Destexhe A and Bal T (2005) Synaptic background activity controls spike transfer from thalamus to cortex. Nat Neurosci 8:1760–1767.
Zsiros V and Hestrin S (2005) Background synaptic conductance and precision of EPSP-spike coupling at pyramidal cells. J Neurophysiol 93:3248–3256.

Impact of Background Synaptic Activity on Neuronal Response Properties Revealed by Stepwise Replication of In Vivo-Like Conditions In Vitro

Steven A. Prescott and Yves De Koninck

Abstract Neurons in the intact brain are bombarded by spontaneous synaptic input that causes increased membrane conductance (i.e. shunting), tonic depolarization, and noisy fluctuations in membrane potential. By comparison, neurons in acute brain slices experience little spontaneous synaptic input and are therefore less leaky, more hyperpolarized, and less noisy. Such differences can compromise the extrapolation of in vitro data to explain neuronal operation in vivo. Here, we replicated three effects of synaptic background activity in acute brain slices, using dynamic clamp to artificially increase membrane conductance, constant current injection to cause tonic depolarization, and time-varying current injection to introduce noise. These manipulations were applied separately and in different combinations in order to resolve their specific influence on neuronal activity. In addition to straightforward effects on passive membrane properties, shunting caused nonlinear effects on spiking. As a result, shunted neurons behaved more like coincidence detectors and less like integrators. Furthermore, shunting caused either divisive or subtractive modulation of firing rate depending on the presence or absence of background noise. These results demonstrate that even simplistic applications of dynamic clamp can reveal interesting phenomena and expand our ability to use in vitro experiments to help understand neuronal operation in vivo.

1 Introduction

Neurons within the intact brain are bombarded by high levels of spontaneous synaptic input. Destexhe and Paré (1999) reported that, on average, the background synaptic activity experienced by neocortical pyramidal neurons reduced input resistance by 80%, depolarized membrane potential by 20 mV, and

S.A. Prescott (✉)
Department of Neurobiology, University of Pittsburgh, Biomedical Science Tower, W1455, 200 Lothrop Street, Pittsburgh, PA 15213, USA
e-mail: prescott@neurobio.pitt.edu

A. Destexhe, T. Bal (eds.), *Dynamic-Clamp*, Springer Series in Computational Neuroscience 1, DOI 10.1007/978-0-387-89279-5_5,

increased the standard deviation of voltage noise tenfold (for review, see Destexhe et al., 2003). As a result, synaptic background has a profound influence on the integrative properties of those neurons (Bernander et al., 1991; Destexhe and Paré, 1999; Paré et al., 1998). Increased membrane conductance or shunting reduces input resistance, causing concomitant shortening of the membrane time and length constants, which in turn causes the cell to behave more like a coincidence detector and less like an integrator insofar as the neuron responds more selectively to synchronized inputs (Bernander et al., 1991; König et al., 1996; Rudolph and Destexhe, 2003).

This alone should be cause for alarm in terms of our ability to extrapolate from in vitro experiments to explain neuronal operation in vivo, since neurons in acute brain slices experience only a small fraction of the synaptic background activity experienced in vivo. As a result, neurons recorded from acute brain slices are typically less leaky, more hyperpolarized, and less noisy than comparable neurons recorded in vivo and, therefore, are more likely to behave like integrators. Neurons in vitro also appear to have qualitatively different synchronization properties than those in vivo (Prescott et al., 2008b), which is liable to have important implications for generating and/or responding to network oscillations.

Nonetheless, by recognizing what differences exist between conditions in the intact brain and conditions in the acute slice, steps can be taken to try to replicate in vivo conditions in vitro. One approach would be to replicate synaptic activity as realistically as possible (notwithstanding technical limitations; see below) using time-varying conductances associated with distinct reversal potentials for excitatory and inhibitory synaptic inputs (e.g. Destexhe et al., 2001). A different approach, which we have used here, is to replicate each of the effects of synaptic input separately. In other words, we used dynamic clamp to artificially increase membrane conductance, constant current injection to cause tonic depolarization, and time-varying current injection to introduce noise. In reality, conductance change, average depolarization, and membrane potential variance are related (Destexhe and Paré, 1999), but there are benefits of deliberately dissociating the effects and replicating them separately or in combination to identify their specific influence on neuronal response properties. Other chapters in this volume (Chance and Abbott "Simulating In Vivo Background Activity in a Slice with the Dynamic Clamp," Jaeger and Lin "Unraveling the Dynamics of Deep Cerebellar Nucleus Neurons with the Application of Artificial Conductances," Piwkowska et al. "Testing Methods for Synaptic Conductance Analysis Using Controlled Conductance Injection with Dynamic Clamp," White et al. "Using "Hard" Real-Time Dynamic Clamp to Study Cellular and Network Mechanisms of Synchronization in the Hippocampal Formation," and Fellous et al. "Intrinsic and Network Contributions to Reverberatory Activity: Reactive Clamp and Modeling Studies") also discuss the use of dynamic clamp to simulate in vivo-like synaptic activity.

We begin with a short overview of our methodology. The rest of this chapter is divided into four thematically distinct sections. In Section 3.1,

we demonstrate how shunting affects passive membrane properties. In Section 3.2, we discuss effects of shunting on active membrane properties and explain how shunting can enhance adaptation in hippocampal CA1 pyramidal cells so that those cells stop spiking repetitively in response to constant depolarizing stimulation. In Section 3.3, we explain how repetitive spiking in the high-conductance state is recovered when conditions are noisy. Results from these first three sections suggest that CA1 pyramidal neurons switch from integrators in the low-conductance state to coincidence detectors in the high-conductance, in vivo-like state. In Section 3.4, we demonstrate how noise influences the modulation of firing rate by shunting, showing that shunting causes divisive modulation under noisy conditions whereas it otherwise causes subtractive modulation. Although we emphasize experimental data, this chapter also presents results from computational modeling. A brief description of our model together with an overview of analysis methods are therefore provided in the Appendix.

2 Experimental Methods

Following standard procedures, brains of adult male Sprague–Dawley rats were sectioned coronally to produce 400-μm-thick slices. Neurons in the CA1 region of hippocampus or in layer 5 of somatosensory cortex were recorded in the whole-cell configuration at 30–31°C. Pyramidal morphology was confirmed with epifluorescence after recording based on intracellular labeling with Lucifer yellow. Only data from regular spiking pyramidal cells judged healthy on the basis of three criteria (resting membrane potential <-50 mV, spikes overshooting 0 mV, and input resistance > 100 MΩ) were included in analysis presented here. Variations in resting voltage were eliminated by adjusting membrane potential to –70 mV through tonic current injection. All experiments were performed in 10 μM bicuculline, 10 μM CNQX, and 40 μM D-AP-5 to block $GABA_A$, AMPA, and NMDA receptors, respectively, thus preventing any residual fast synaptic input and allowing full experimental control over noise level. See Prescott et al. (2006a) for additional details on slicing and recording methods.

As described in Section 1, background synaptic activity has three notable effects: shunting, depolarization, and noise. These effects were deliberately isolated from each other (see below) and were replicated alone or in different combinations. To recreate increased membrane conductance (i.e. shunting), an artificial conductance was applied via dynamic clamp (Robinson and Kawai, 1993; Sharp et al., 1993a, b) implemented with a Digidata 1200A ADC/DAC board and DYNCLAMP2 software (Pinto et al., 2001) running on a dedicated processor; update rate was 10 kHz. The conductance was constant at the magnitude reported in the text and had a reversal potential of –70 mV. To

recreate tonic depolarization, long depolarizing current steps were injected into the cell via the recording pipette. DC offset is reported as I_{DC}. To introduce noise, noisy stimulus waveforms were generated according to an Ornstein–Uhlenbeck process (Uhlenbeck and Ornstein, 1930) in which $dI_{noise}/dt = -I_{noise}/\tau_{noise} + \sigma_{noise}N(0, 1)$, and were injected into the neuron through the recording pipette. According to this process, I_{noise} follows a random walk but constantly decays, with a specified time constant (τ_{noise}), toward an average (in this case 0, since I_{DC} was specified separately). N is a random number with 0 mean and unit variance, σ_{noise} controls noise amplitude and is reported in the text, and $\tau_{noise} = 5$ ms.

For technical reasons, all currents (I_{DC}, I_{noise}, and I_{shunt}) were applied through the recording pipette to the soma. This represents an oversimplification, since real synaptic inputs occur throughout the dendrites and soma. Dynamic clamp can be applied to a dendritic location (e.g. White et al. "Using "Hard" Real-Time Dynamic Clamp to Study Cellular and Network Mechanisms of Synchronization in the Hippocampal Formation" in this volume and Williams "Dendritic Dynamic Clamp – A Tool to Study Single Neuron Computation" in this volume), but this still fails to account for the spatial distribution of true synapses. In any case, effects of electrotonic filtering, dendritic nonlinearities, and spatiotemporal relationships were overlooked in our experiments (see Piwkowska et al. "Testing Methods for Synaptic Conductance Analysis Using Controlled Conductance Injection with Dynamic Clamp" in this volume for additional discussion of these points). Simulations in a multicompartmental model have identified how the location of inputs may affect firing rate modulation by shunting (see Section 3.4). But other phenomena, like the prohibition of repetitive spiking by shunting described in Section 3.2, can be replicated in a single compartment model, which suggests that the stimulus location is not critical for that phenomenon. Discussion of these issues is expanded in each of the relevant sections.

Other aspects of the stimulation were "unphysiological" by design. As already explained, our goal was not to reproduce synaptic input as realistically as possible, but, rather, it was to isolate the various effects of synaptic background activity and to replicate those effects separately and in different, controlled combinations. This imposes some limitations. For example, although the net reversal potential for mixed excitatory/inhibitory input is less negative than −70 mV, E_{shunt} was set to −70 mV in order to prevent g_{shunt} from causing depolarization, thus preventing the effects of shunting from being confounded with the effects of depolarization. Similarly, by generating noise through an Ornstein–Uhlenbeck process, the confound between depolarization and noise is avoided because stimulus mean and variance are specified separately, unlike, for instance, when noise is generated through a Poisson process (e.g. Chance et al., 2002). Thus, our approach comes with a certain cost to biological reality but offers some significant benefits for interpretability.

3 Results

3.1 Impact of Shunting on Passive Membrane Properties

To investigate quantitatively the effects of membrane conductance on neuronal response properties, one must be able to systematically alter membrane conductance in real neurons. This was achieved using dynamic clamp, in which recorded membrane potential V was used to calculate a current I_{shunt} that was injected back into the neuron, where $I_{shunt} = g_{shunt}(V - E_{shunt})$, $g_{shunt} = 10$ nS, and $E_{shunt} = -70$ mV unless otherwise stated. Effects of this artificial increase in membrane conductance on passive membrane properties are reasonably straightforward, and thus serve as a good opportunity to confirm that the artificial current has the same effects as a true transmembrane current.

Figure 1A shows responses from a hippocampal pyramidal cell to brief hyperpolarizing stimuli with and without a 10 nS shunt. The voltage change

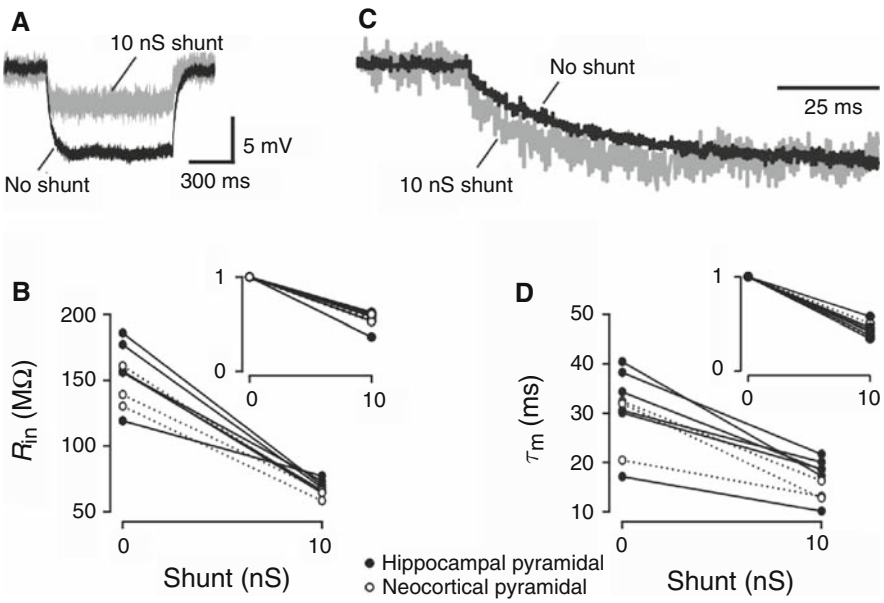

Fig. 1 Effects of shunting on input resistance (R_{in}) and the membrane time constant (τ_m). (**A**) Responses to 60 pA hyperpolarizing current steps with no shunt (*black*) vs. with a 10 nS shunt implemented by dynamic clamp (*gray*). R_{in} was reduced from 158 to 56 MΩ for the hippocampal CA1 pyramidal neuron shown. (**B**) Effect of 10 nS shunt on R_{in} summarized for all CA1 hippocampal and layer 5 neocortical pyramidal neurons upon which subsequent analyses are based ($n = 6$ and 3, respectively). Inset shows the relative change. Average reduction of 55.4 ± 2.6% (mean ± SEM) was highly significant ($p < 0.001$, paired t-test). (**C**) Responses from A with amplitude normalized to show shortening of τ_m from 40 to 17 ms. (**D**) Effect of 10 nS shunt on τ_m summarized for all cells. Average reduction was 45.2 ± 3.0% ($p < 0.001$, paired t-test)

was clearly reduced when the neuron was shunted, as expected from the reduction in input resistance, R_{in}. Neocortical pyramidal cells behaved in exactly the same way. Based on six pyramidal neurons from the CA1 region of hippocampus and three from layer 5 of the somatosensory cortex, a 10 nS shunt reduced R_{in} by $55.4 \pm 2.6\%$ (Fig. 1B), which is modest compared to changes reported in vivo (Destexhe and Paré, 1999). Reduction in R_{in} was accompanied by an appropriate reduction in τ_m (Fig. 1C, D), given $\tau_m = R_{in} C_m$, where τ_m is the membrane time constant and C_m is membrane capacitance.

These changes in passive membrane properties are liable to influence how neurons respond to inputs with different frequencies, which is important under noisy conditions where inputs comprise a broad range of frequencies. To investigate this, we looked at the power spectra of voltage responses to noisy stimulation in the low- and high-conductance state. For the neocortical pyramidal cell illustrated in Fig. 2A, R_{in} was reduced from 161 to 64 MΩ and τ_m was reduced from 31.9 to 12.7 ms by a 10 nS shunt; both changes constitute 60% reductions. The change in R_{in} reduced depolarization caused by DC stimulation (data not shown), but it also reduced the standard deviation of membrane potential fluctuations elicited by noisy input (Fig. 2A). Voltage fluctuations were not only attenuated by shunting, but were also sped up by it; the latter effect is explained by shortening of τ_m. Power spectral analysis showed that shunting reduced voltage power preferentially at low frequencies (Fig. 2B), unlike reducing the amplitude of stimulus noise, which reduced voltage power across all frequencies (Fig. 2C). If we compare voltage fluctuations with nearly equivalent standard deviation generated by different combinations of noise and shunting, one sees that responses generated in the high-conductance state (i.e. strong noise plus shunt) exhibited lower power at low frequencies and higher power at high frequencies than responses generated in the low-conductance state (i.e. weak noise without shunt) (Fig. 2D); the crossover occurred near 10 Hz. The same trends were observed in hippocampal pyramidal cells using power spectral analysis of responses to noisy stimulation (Fig. 2E) as well as impedance measurements from responses to sine wave stimulation at different frequencies (Fig. 2F). We have observed similar results in multicompartmental spinal lamina I neuron models bombarded by synaptic input distributed throughout the dendritic tree (Prescott et al., 2006b) and in comparable pyramidal neuron models (unpublished data), which indicates that this shunting-induced change in filtering occurs regardless of the spatial distribution of inputs, although this is not to say that dendritic excitation would not produce a differently shaped power spectrum (see Piwkowska et al. "Testing Methods for Synaptic Conductance Analysis Using Controlled Conductance Injection with Dynamic Clamp" in this volume).

These results suggest that in the high-conductance conditions that exist in vivo, neurons are less responsive to low-frequency inputs, but may be more responsive to high-frequency inputs. This is consistent with the suggestion that pyramidal neurons behave more like coincidence detectors under in vivo conditions (Bernander et al., 1991; Kuhn et al., 2004; Rudolph and Destexhe,

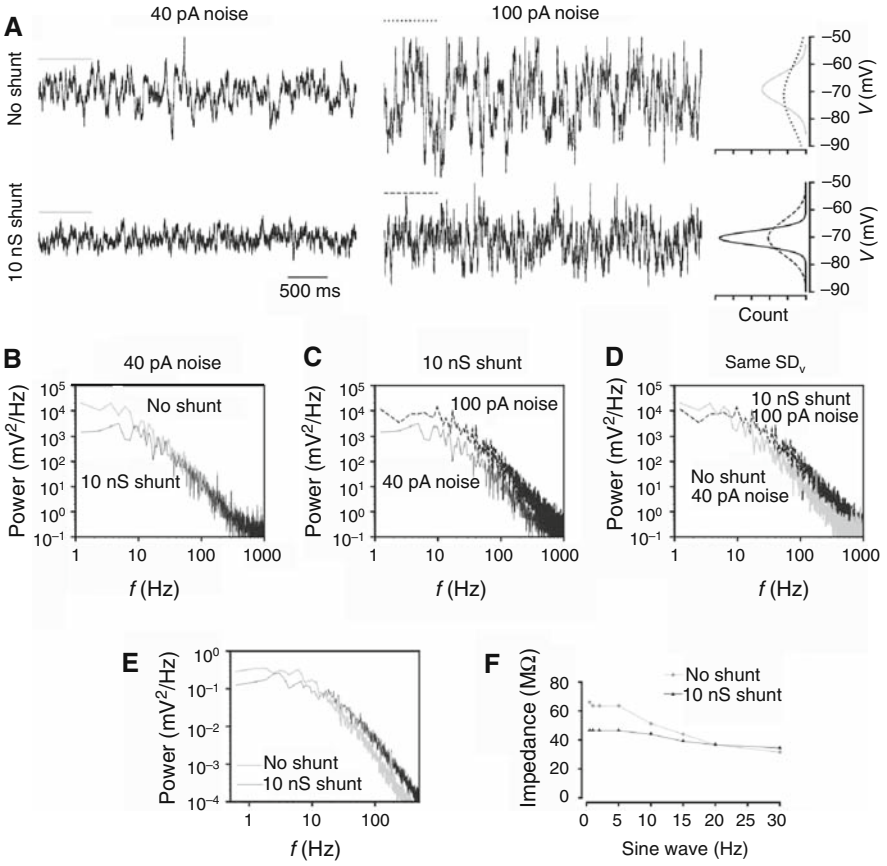

Fig. 2 Effects of shunting on subthreshold responses to noisy stimulation. I_{DC} was 0 pA for all experiments shown here. (**A**) Traces show sample responses from a layer 5 neocortical pyramidal neuron stimulated with low and high amplitude noise (*left and right*) in the low- and high-conductance state (*top and bottom*). Histograms on right show voltage distributions fitted with Gaussian curves; line types here and in B–D correspond to lines types shown beside each sample trace. With weak noise, a 10 nS shunt reduced the standard deviation of voltage fluctuations (SD_V) from 5.1 to 2.6 mV. With strong noise stimulation, the same shunt reduced SD_V from 9.7 to 5.9 mV. Graphs in B–D show power spectra of voltage responses (same as those in A) to different combinations of noise and shunting. (**B**) Shunting selectively reduced voltage power at low frequencies. (**C**) Reducing noise amplitude, on the other hand, reduced voltage power across all frequencies, consistent with the reduction in stimulus power. (**D**) Comparing responses with nearly equivalent SD_V generated with different combinations of stimulus noise and shunting produced power spectra that crossed near 10 Hz, with the shunted response showing relatively higher power at high frequencies, consistent with the shunting-induced shortening of τ_m. (**E**) Shunting had the same effects on the voltage power spectrum in CA1 pyramidal cells, as shown here for a typical cell. (**F**) Impedance measurements from responses to sine wave stimulation with different frequencies confirmed the effects of shunting seen with power spectral analysis. Data here are from another CA1 pyramidal neuron

2003). Moreover, as explained in the next section, these changes in passive membrane properties combine with changes in active membrane properties that further encourage coincidence detection.

3.2 Impact of Shunting on Repetitive Spiking Driven by Constant Input

In the process of investigating the effects described above, we observed that shunting modulated spiking in ways that could not be readily explained by simple changes in passive membrane properties. Because of spike frequency adaptation, the spike rate in CA1 pyramidal cells gradually slows down over the course of prolonged stimulation, but whereas low-frequency spiking persisted in the low-conductance state, it was completely abolished in the high-conductance state and could not be recovered by increasing I_{DC} (Fig. 3A). On closer analysis, shunting was seen to have different effects on the different phases of firing. For initial firing rate ($f_{initial}$ = reciprocal of first interspike interval [ISI]), shunting had a subtractive effect on the $f_{initial}$–I_{DC} curve, shifting the curve to the right with virtually no effect on its slope (Fig. 3B); this equates with a decrease in excitability that is manifested as an increase in rheobase (i.e. the minimum I_{DC} capable of eliciting spikes). On the other hand, the number of spikes within the initial burst was divisively reduced by shunting (Fig. 3C) because shunting truncates the phase of high-frequency firing that occurs at the start of the response. And as already mentioned, shunting completely abolished spiking after the onset of adaptation (Fig. 3D).

The fact that shunted neurons could not maintain repetitive spiking in the high-conductance state, even when I_{DC} was increased substantially, indicated that shunting had caused a nonlinear phenomenon. We hypothesized that shunting enhanced the strength of spike frequency adaptation. To test this, we plotted $f_{initial}$ against either spikes per burst (Fig. 3E) or $f_{adapted}$ (Fig. 3F) in order to remove the direct effect of shunting on excitability and isolate how shunting interacts with adaptation. After accounting for variation in $f_{initial}$, there were significantly fewer spikes in the initial burst ($p < 0.001$, ANOVA) and $f_{adapted}$ was significantly less ($p < 0.001$, Kruskal–Wallis test) when the neuron was shunted. From this, we conclude that shunting caused a significant enhancement in the strength of adaptation.

To decipher how shunting enhances adaptation, we turned to computational modeling. The first step involved replicating the dynamic-clamp data (Fig. 3) in a computational model. Sample responses from the model are shown in Fig. 4A; a more thorough comparison of simulation data with experimental data is provided in Prescott et al. (2006a). The Morris–Lecar model that we used is a single compartment, low-dimensional model (see the Appendix). The benefit of such a model is that it is well suited to quantitative analysis methods such as bifurcation analysis, in which a parameter of interest is varied continuously in

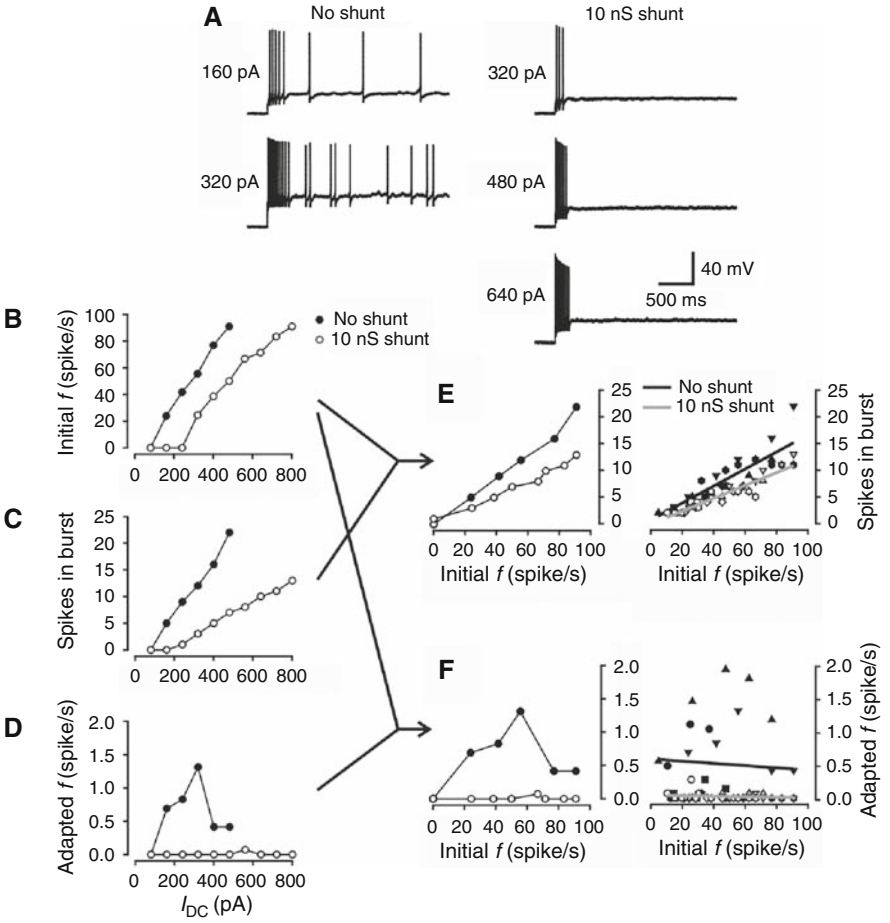

Fig. 3 Shunting interacts nonlinearly with adaptation to control repetitive spiking. (**A**) Sample responses from a typical CA1 pyramidal cell to constant stimulation (I_{DC}) with and without shunting. Horizontally aligned traces show responses with equivalent initial firing rate ($f_{initial}$ = reciprocal of first interspike interval). Shunting shifted the $f_{initial}$–I_{DC} curve to the right (**B**), reduced the number of spikes in the burst (**C**), and completely abolished spiking once adaptation developed (**D**). To remove the direct effects of shunting on excitability and isolate how shunting interacts with adaptation, we plotted $f_{initial}$ against either spikes per burst (**E**) or adapted firing rate ($f_{adapted}$) (**F**). Graphs on the left show data for cell illustrated in A and those on the right show cumulative data ($n = 6$ CA1 pyramidal cells, with four to five measurements per neuron for each condition; thick lines show linear regressions). After accounting for variation in $f_{initial}$, there were significantly fewer spikes within the initial burst in the high-conductance state compared with the low-conductance state ($p < 0.001$, ANOVA) and $f_{adapted}$ was also significantly lower in the high-conductance state ($p < 0.001$, Kruskal–Wallis test). Modified from Prescott et al. (2006a)

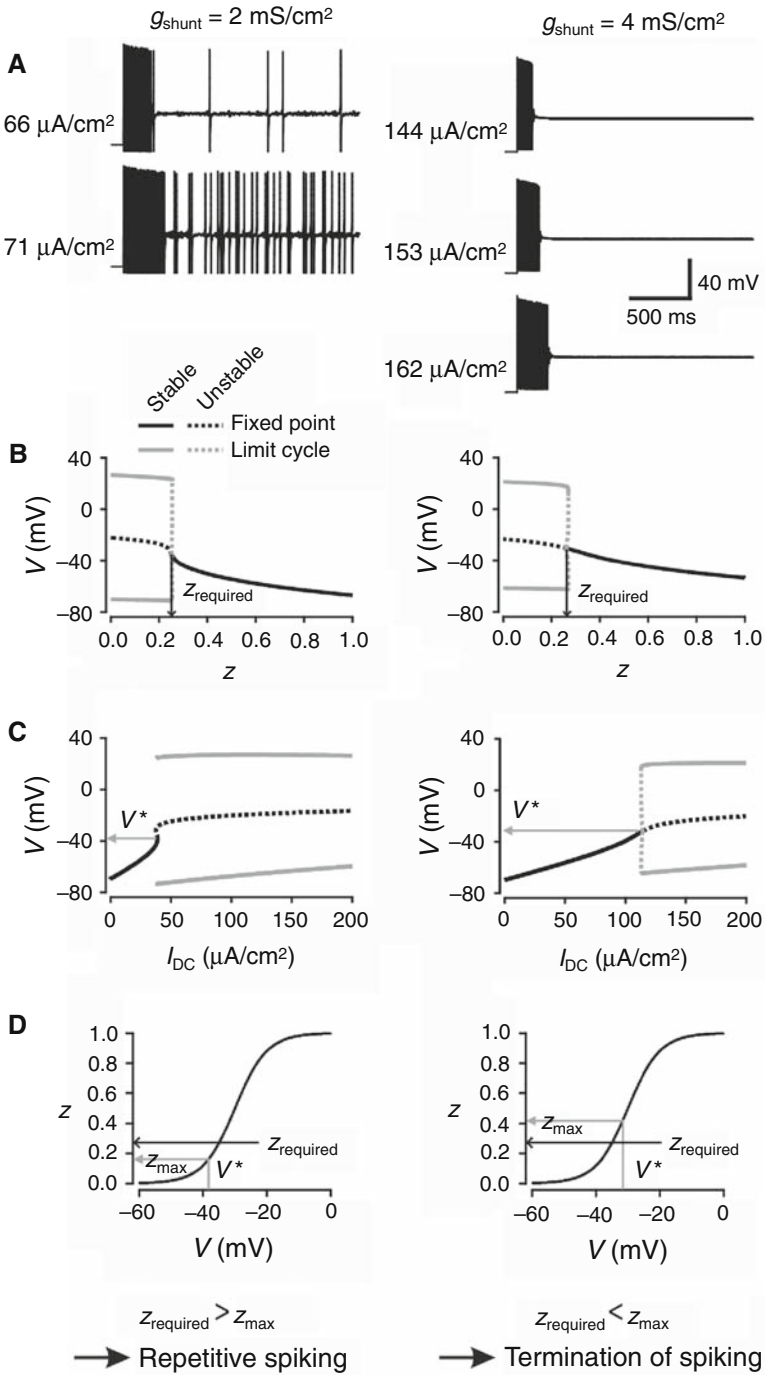

Fig. 4 Nonlinear interaction between shunting and adaptation explained by modeling. (**A**) Sample responses from Morris–Lecar model in the low- and high-conductance states.

order to identify when a discontinuous, qualitative change in behavior (i.e. bifurcation) occurs. In our case, the bifurcation of interest is the transition from quiescence to repetitive spiking, or vice versa.

By applying bifurcation analysis to our model, we were able to address two questions. First, we asked how strong adaptation must be in order to terminate spiking. To answer this, we systematically increased the strength of adaptation (z) until the model switched from repetitive spiking to quiescence; the adaptation required to cause this bifurcation was labeled z_{required} (Fig. 4B). This analysis was repeated in the low- and high-conductance states. Second, we asked how strongly adaptation can be activated at or below spike threshold. To answer this, we systematically increased I_{DC} until a bifurcation occurred; the voltage at the bifurcation corresponds to spike threshold and was labeled V^* (Fig. 4C). By looking at the voltage-dependent activation curve for the M-type potassium current (I_{M}) responsible for adaptation, we found z at V^* and labeled it z_{max} since it represents the maximal adaptation possible at threshold (Fig. 4D). This analysis was also repeated in the low- and high-conductance states. Notice that shunting caused a small change in V^* that translated into a large change in z_{max} because V^* occurred in a steep region of the activation curve (Fig. 4D). Consequently, although z_{max} was less than z_{required} in the low-conductance state, meaning adaptation was not sufficient to terminate spiking under those conditions, z_{max} became greater than z_{required} in the high-

Fig. 4 (continued) Horizontally aligned traces show responses with equivalent f_{initial}, like in Fig. 3A. As in real CA1 neurons, the initial burst was shorter and repetitive spiking was absent in the high-conductance state. (**B**) To determine how much adaptation was necessary to stop the neuron from spiking, proportional activation of I_{M} (which is controlled by z; $0 \leq z \leq 1$) was treated as a bifurcation parameter (see Section 3.2) and systematically varied in order to determine the minimum z required to stop the model from spiking (z_{required}); $z_{\text{required}} = 0.25$ and 0.27 for the low- and high-conductance states (for $I_{\text{DC}} = 71$ and 153 $\mu A/cm^2$), respectively. In B and C, limit cycles are represented by plotting the maximum and minimum V during the spike, which explains why these curves each have two branches; fixed points correspond to subthreshold voltages and are represented by a single value of V. Having identified z_{required}, the next step was to identify the maximal activation of adaptation (z_{max}) that is possible at voltage threshold (V^*). (**C**) V^* was identified by repeating the bifurcation analysis, but this time varying I_{DC} instead of z and measuring V at the bifurcation. V^* was -38.3 and -31.7 mV in the low- and high-conductance states, respectively. Adaptation was removed from the model for this analysis. (**D**) z_{max} corresponds to z at V^* and was determined from the voltage-dependent activation curve for I_{M}. z_{max} was only 0.16 in the low-conductance state but rose to 0.42 in the high-conductance state; in other words, a small shunting-induced increase in V^* caused a large increase in subthreshold activation of I_{M} because of the nonlinear shape of I_{M}'s activation curve. Repetitive spiking continues despite adaptation when $z_{\text{required}} > z_{\text{max}}$, but stops when $z_{\text{required}} < z_{\text{max}}$. Modified from Prescott et al. (2006a). As an aside, note that bifurcation diagrams in C are qualitatively different between the low- and high-conductance states. The switch in bifurcation mechanism suggests that shunting and its enhancement of I_{M} cause a switch in excitability from class 1 to class 2 according to Hodgkin's classification scheme (Hodgkin, 1948). The full implications of this are beyond the scope of this chapter; see Prescott et al. (2008b) for additional information on this topic

conductance state, meaning adaptation was sufficient to terminate spiking. In other words, a small increase in voltage threshold allowed nonlinearly increased activation of I_M so that adaptation became strong enough to completely abolish repetitive spiking driven by constant (i.e. non-noisy) stimulation.

A depolarizing shift in voltage threshold was thus identified as a key component in the mechanism whereby increased membrane conductance prohibits repetitive spiking. The biophysical basis for this shift is explained in Fig. 5A. Shunting increased the slope of the *I–V* curve (which reflects the reduction in R_{in}) and increased the height of the local maximum of the *I–V* curve (which reflects the outward current contributed by I_{shunt} at perithreshold potentials). To counterbalance the increase in outward current, the fast sodium current must activate more strongly (compare lengths of arrows on Fig. 5A); stronger activation of the sodium current requires greater depolarization, hence the

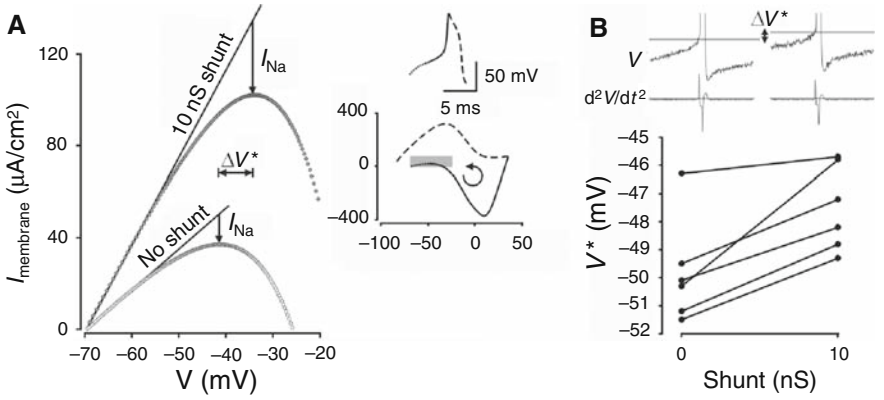

Fig. 5 Shunting causes a depolarizing shift in voltage threshold. (**A**) $I_{membrane}$ represents the sum of all transmembrane currents in our model, and was plotted against voltage based on the first spike elicited by $I_{DC} = 71$ and 153 μA/cm^2 in the low- and high-conductance states, respectively. Inset shows a single, complete spike plotted against time (*top*) and against $I_{membrane}$ (*bottom*) with each phase of the spike represented by a different line-type in order to help relate the two representations; main graph (*left*) only shows region highlighted in gray. The difference in R_{in} is evident from the initial slope of the *I–V* curve (*lines*). To counterbalance increased I_{shunt} and reverse the direction of change in $I_{membrane}$ as voltage increases, sodium current (I_{Na}) must be more strongly activated in the high-conductance state than in the low-conductance state (compare lengths of *vertical arrows*); greater activation of I_{Na} requires greater depolarization, thus explaining the depolarizing shift in voltage threshold (V^*) that results from shunting (*horizontal arrow*). (**B**) For experimental data, V^* was estimated from the voltage at which d^2V/dt^2 (which reflects the first derivative or rate of activation of $I_{membrane}$) exceeded a cutoff value defined as 5 × the root-mean-square noise in the baseline d^2V/dt^2 trace. Using responses to an arbitrarily chosen I_{DC} of 40 pA greater than rheobase, we analyzed the second spike within each spike train since the second spike occurs before adaptation develops and its analysis is not confounded by initial membrane charging, as can occur with the first spike. The 10 nS shunt significantly increased V^* ($p < 0.01$, paired *t*-test, $n = 6$ CA1 pyramidal cells) that averaged 2.3 ± 0.5 mV (mean ± SEM). Modified from Prescott et al. (2006a)

horizontal shift in the peak of the *I–V* curve, which corresponds to the depolarizing shift in voltage threshold.

We then checked if shunting caused a shift in the voltage threshold of CA1 pyramidal neurons. Indeed, shunting did cause a small but statistically significant depolarizing shift in threshold (Fig. 5B). Given the voltage-dependency of I_M (i.e. its activation curve extends below voltage threshold; Wang and McKinnon, 1995), the observed shift in threshold should cause nonlinearly increased activation of I_M, consistent with our simulations. In future experiments, it would be interesting to pharmacologically block I_M and then re-introduce an artificial I_M using dynamic clamp. In those experiments, the voltage dependency of I_M would be controlled by user-defined parameters and could be systematically varied in order to investigate how nonlinear activation properties interact with voltage threshold.

Thus, according to these data, shunting directly contributes an outward current and can indirectly modify the activation of other currents. The latter effect can produce dramatic changes in spiking because of the nonlinear shape of voltage-dependent activation curves of currents like I_M. Shunting produces an outward (hyperpolarizing) current at perithreshold potentials because E_{shunt} is more negative than spike threshold. E_{shunt} was -70 mV for all simulations and experiments reported here, but results were qualitatively unchanged (data not shown) when E_{shunt} was shifted to less negative values (although still more negative than threshold) that more accurately reflects the net reversal potential for a combination of excitatory and inhibitory input (see above). Also, simulation of shunting in our single compartment model accurately replicated our dynamic-clamp experiments, even if applying the shunt exclusively to the soma does not accurately replicate spatially distributed synaptic input (see above). With that said, the perisomatic region is targeted by large numbers of inhibitory synapses (Buhl et al., 1994) that can produce a significant shunt that is likely to have a strong effect on spike initiation since spike initiation occurs in relatively close proximity to the soma (Mainen et al., 1995; Shu et al., 2007; Stuart et al., 1997); by comparison, effects of dendritic shunting are spatially restricted (Jean-Xavier et al., 2007) and should have relatively less influence on spike initiation. Moreover, the KCNQ channels responsible for I_M are located perisomatically (Hu et al., 2007). Thus, our experiments arguably provide quite accurate information about how CA1 pyramidal neurons transduce somatic voltage fluctuations into spike trains, including how this differs between the low- and high-conductance states.

3.3 Impact of Noise on Repetitive Spiking

Despite not spiking repetitively in the high-conductance state when conditions were quiet, CA1 pyramidal neurons in the high-conductance state spiked vigorously when stimulated with noisy input (Fig. 6A). Why does adaptation that

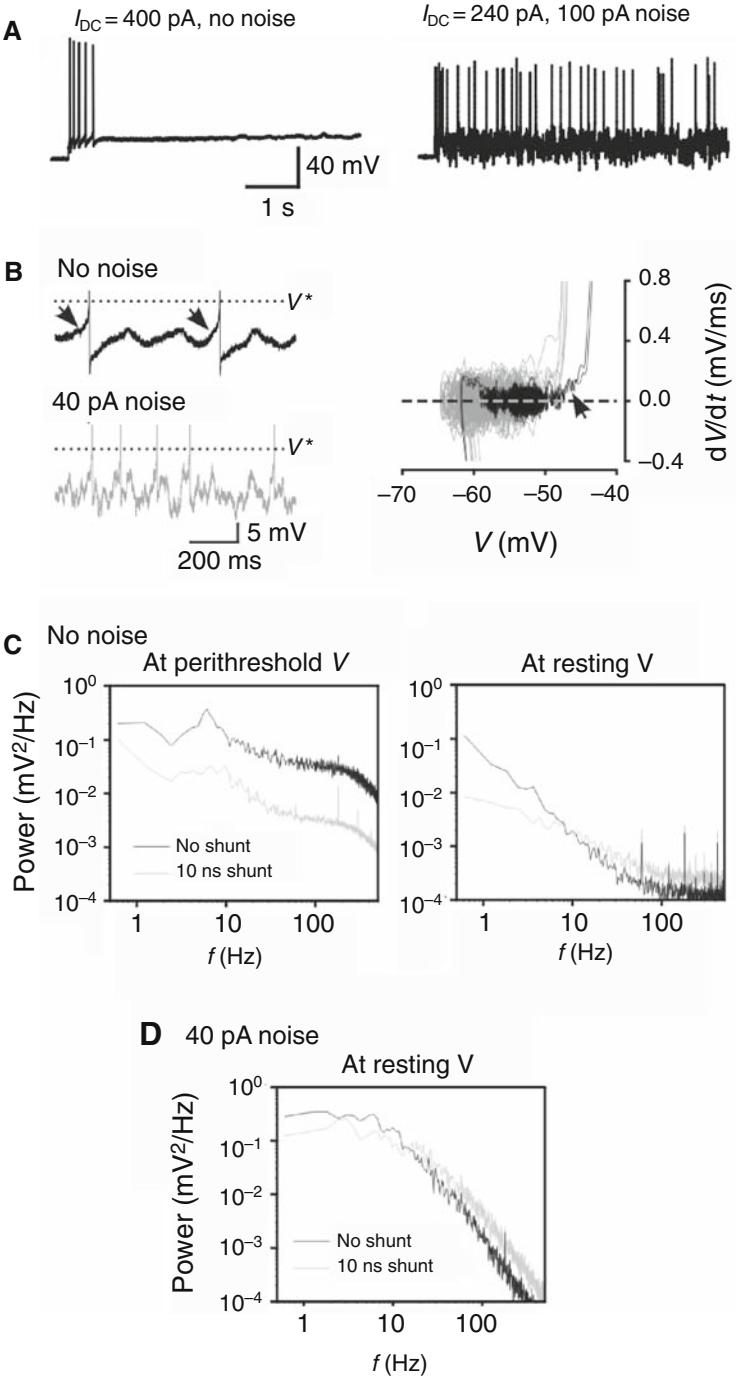

Fig. 6 Effects of shunting on repetitive spiking in quiet vs. noisy conditions. All data here are from CA1 pyramidal neurons. (**A**) Even extremely strong I_{DC} failed to elicit repetitive spiking

is able to prohibit spiking driven by constant input fail to prohibit spiking driven by noisy input? The answer depends on the kinetics of voltage changes relative to the activation kinetics of I_M. Subthreshold activation of I_M produces an outward current that should counteract depolarization toward threshold; however, because the activation kinetics of I_M are slow, I_M is likely to prevent slow depolarizations from reaching threshold, but rapid depolarizations may reach threshold and elicit spikes before I_M has time to activate. We therefore investigated the voltage trajectories associated with constant vs. noisy stimulation.

The voltage trajectory immediately preceding each spike was clearly much faster when elicited by noisy stimulation than when elicited by constant stimulation (Fig. 6B); these data are from the low-conductance state. Without noise, spikes resulted from slow membrane potential oscillations in the theta frequency range (3–10 Hz) that occasionally reached threshold when the neuron was in the low-conductance state; however, the amplitude of those oscillations was dramatically reduced in the high-conductance state (Fig. 6C), so much so that they were unable to reach threshold. This phenomenon is evident on the sample traces in Fig. 3A and is consistent with a recent study on the effects of shunting on oscillations in entorhinal stellate cells (Fernandez and White, 2008; see also White et al. "Using "Hard" Real-Time Dynamic Clamp to Study Cellular and Network Mechanisms of Synchronization in the Hippocampal Formation" in this volume). The reduction in oscillation amplitude is attributable to the reduction in input resistance and to the enhancement of I_M. When conditions were noisy, however, spike generation did not rely on slow intrinsic voltage oscillations and instead resulted from rapid voltage fluctuations driven by stimulus transients (Fig. 6D). Unlike intrinsic voltage oscillations, stimulus-driven voltage fluctuations were fast enough that I_M was not given sufficient time to activate and counteract depolarization. Furthermore, unlike the amplitude of intrinsic voltage oscillations, the amplitude of stimulus-driven voltage fluctuations was not dramatically reduced by shunting (compare Fig. 6C, D).

Fig. 6 (continued) in the high-conductance state (10 nS shunt), whereas the same neuron spiked vigorously when noise ($\sigma_{noise} = 100$ pA) was superimposed on a much weaker DC stimulus. (**B**) Voltage trajectories to threshold were much slower without noise (*arrows*) than they were with noise. This is highlighted on the graph showing rate of change of voltage plotted against voltage. Notice that slow trajectories were associated with a higher threshold than fast trajectories, consistent with previous work (Azouz and Gray, 2000). Data here are from a neuron without dynamic-clamp-applied shunting. (**C**) Slow trajectories shown in B resulted from intrinsic voltage oscillations that occurred when membrane potential was near threshold, as occurred following adaptation to suprathreshold DC stimulation (*left*); oscillations were not seen at resting membrane potential (*right*). Oscillation amplitude was significantly attenuated by shunting, even though I_{DC} was increased to ensure that membrane potential remained near threshold. (**D**) Noisy stimulation caused fast voltage fluctuations whose amplitude, unlike that of the intrinsic oscillations in C, was not substantially reduced by shunting

To summarize, subthreshold activation of I_M actively deters membrane potential from approaching threshold, but although this is very effective for reducing spiking driven by slow oscillations, it is relatively ineffective for spiking driven by rapid fluctuations.

Work described by us in detail elsewhere (Prescott et al., 2006a) has shown that the prohibition of repetitive spiking caused by shunting (via enhancement of adaptation) impairs rate coding of slow signals but improves temporal coding of fast signals. In other words, enhanced activation of I_M (as occurs in the high-conductance state) implements a high-pass filter that causes the neuron to operate more like a coincidence detector (or differentiator) and less like an integrator insofar as spikes are elicited preferentially, if not exclusively, by fast voltage fluctuations driven by coincident synaptic inputs. Fast voltage fluctuations are known to elicit spikes more reliably and with less jitter than slow fluctuations (Mainen and Sejnowski, 1995). Interestingly, shunting-induced changes in passive membrane properties produce the same shift in coding strategy by shortening the membrane time constant, which encourages fast voltage fluctuations (see Section 3.1). In other words, changes in passive and active membrane properties synergize insofar as reduced filtering of high-frequency signals encourages rapid voltage fluctuations and the high-pass filter implemented by I_M allows only those rapid voltage fluctuations to reach threshold, thus ensuring precisely timed spikes.

3.4 Impact of Noise on Firing Rate Modulation by Shunting

In this section, we continue considering the effects of noise, focusing specifically on how noise influences firing rate modulation. This line of enquiry was prompted by modeling work that concluded that shunting caused subtractive modulation of firing rate (Holt and Koch, 1997) despite the long-standing assumption that shunting mediated gain control or divisive modulation of firing rate (Eccles, 1964; Blomfield, 1974) (see Fig. 7A). Data from in vitro experiments were consistent with subtractive modulation (Connors et al., 1988; Berman et al., 1992) but were inconsistent with data from in vivo experiments, which showed divisive modulation (Rose, 1977; Bruckner and Hyson, 1998). More recent modeling and experimental work has shown that shunting can have divisive or subtractive effects on firing rate depending on whether or not conditions are noisy (Chance et al., 2002; Prescott and De Koninck, 2003; Mitchell and Silver, 2003; Longtin et al., 2002; see also Chance and Abbott "Simulating In Vivo Background Activity in a Slice with the Dynamic Clamp" in this volume). This qualitative change in firing rate modulation results from the dithering effect of noise (i.e. noise-induced smoothing of the threshold nonlinearity), which allows firing rate to more closely parallel average depolarization, meaning divisive modulation of depolarization translates into divisive modulation of firing rate (Fig. 7B). However, other studies have subsequently

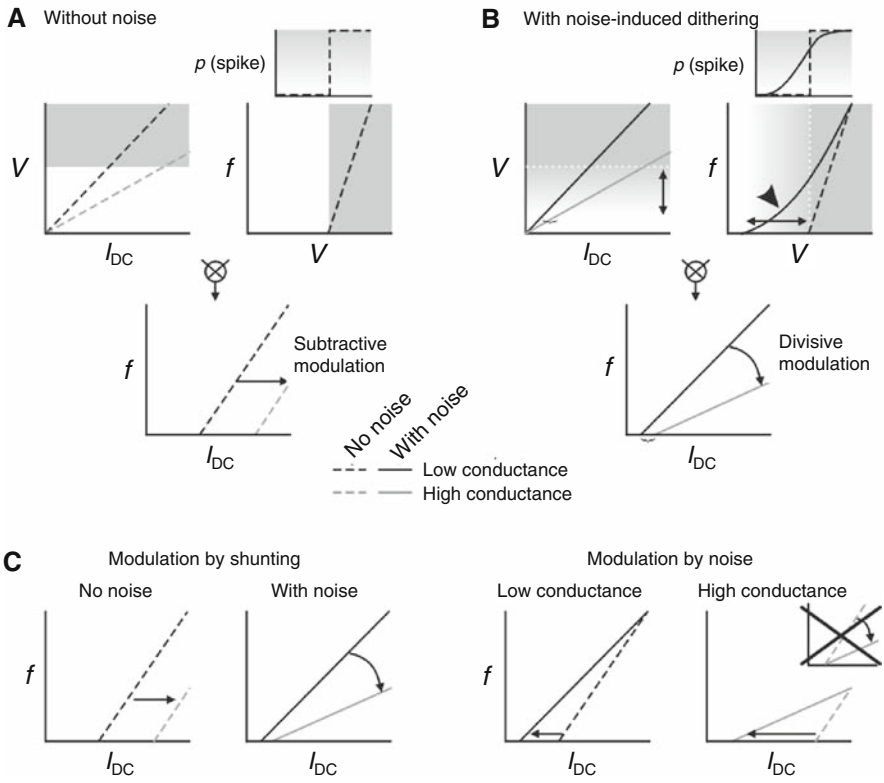

Fig. 7 Subtractive vs. divisive modulation of firing rate. (**A**) Shunting changes the slope of the *I–V* curve, which constitutes a divisive effect (*top left panel*). However, when the *I–V* curve is convolved with a steep *f–V* curve (*top right panel*), the effect of shunting on the *f–I* curve is purely subtractive insofar as the curve is shifted but does not change slope (*bottom panel*). (**B**) Noise smoothes out the *f–V* curve (*arrowhead*), an effect known as threshold-smoothing or dithering. The basis for dithering is explained in the inset above the top right panel: When conditions are noisy, probability of spiking ($0 \leq p$ (spike) ≤ 1, represented as white → gray shading) increases gradually as average voltage approaches threshold because voltage fluctuations may cross threshold even while average voltage remains below threshold (*solid line*); without noise, p (spike) jumps abruptly from 0 to 1 at threshold, i.e. not spiking or spiking (*dashed line*). In the latter case, firing rate is determined solely by intrinsic neuronal properties rather than by the probability of threshold crossings. Double-headed arrows highlight the voltage range associated with fluctuation-driven spiking; firing rate does not rise above 0 spike/s until voltage enters this zone. The difference in entry point (bracket) is relevant for appreciating the relative contribution of subtractive and divisive modulation of the *f–I* curve (see Fig. 9). (**C**) Left panels summarize modulation attributable to shunting. Right panels summarize modulation attributable to noise. Although noise could be said to modulate the gain of the *f–I* curve, the most significant effect is the increased sensitivity (*arrows*); indeed, to say that noise mediates gain control would imply changes shown in the inset, which is not what occurs. Modified from Prescott and De Koninck (2003)

suggested that noise itself mediates gain control (Higgs et al., 2006; Shu et al., 2003; Fellous et al., 2003) rather than being a factor that enables shunting to mediate gain control. This may simply reflect variations in the use of the term "gain control" (see Fig. 7C), but our approach of dissociating membrane conductance and stimulus noise is ideal for resolving precisely these sorts of issues. Unless otherwise stated, all data shown in this section are from CA1 pyramidal cells.

We began by confirming the modulatory effects of shunting. Shunting had a purely divisive effect on the neuron's voltage response (Fig. 8A), whereas it had a purely subtractive effect on initial firing rate (Fig. 3B). Effects of shunting on adapted firing rate are complicated by the nonlinear interaction between shunting and adaptation, which prevents constant or slow inputs from eliciting spikes (see Section 3.2) but, as shown in Section 3.3, CA1 pyramidal neurons continue spiking if moderate amplitude noise is superimposed on the DC step. Under noisy conditions, spiking was reduced but not terminated by increases in membrane conductance (Fig. 8B; compare with Fig. 3A). Moreover, f–I_{DC} curves confirmed that shunting had a divisive effect on spiking elicited by noisy input, both before and after the onset of adaptation (Fig. 8C, top and bottom panels, respectively). Effects of shunting on the relative slope of the $f_{adapted}$–I_{DC} curve are summarized in Fig. 8D. The reduction in slope caused by a 10 nS shunt was significant with 40 pA noise ($p < 0.05$, $n = 3$ hippocampal + 2 neocortical cells, paired t-test) and with 100 pA noise ($p < 0.01$, $n = 6$ hippocampal + 3 neocortical cells, paired t-test).

This indicates that dithering allows shunting's divisive modulation of average membrane potential to translate into divisive modulation of firing rate (as predicted in Fig. 7B), but other effects of shunting may also affect firing rate and must be considered. Indeed, shunting not only reduces the average depolarization caused by I_{DC}, but also reduces the voltage fluctuations driven by I_{noise} (Fig. 9A; see also Fig. 2A). To isolate the effects of membrane potential variance on firing rate from the effects of average membrane potential, we plotted f against average V while changing the variance of V by varying σ_{noise} (rather than by varying the shunt). Reducing σ_{noise} caused a purely subtractive shift in the f–V curve (Fig. 9B), although removing noise altogether caused near-cessation of spiking, for reasons explained in Section 3.3. These results are consistent with our previous simulations (Prescott and De Koninck, 2003) and with results reported by Fellous et al. (2003), although we only tested moderate to large amplitude noise based on the amplitude of voltage fluctuations reported in vivo (Destexhe and Paré, 1999); smaller amplitude noise might give a shallower f–V curve, like Fellous et al. observed.

Results in Fig. 9B tell us that average membrane potential must get closer to threshold before smaller amplitude voltage fluctuations start crossing threshold. This interpretation is perhaps obvious, but it has important implications: Because voltage noise is responsible for dithering (see Fig. 7), reducing voltage noise leads to reduced dithering and may compromise the ability of shunting to divisively modulate firing rate (Fig. 9C). This predicts, under noisy conditions,

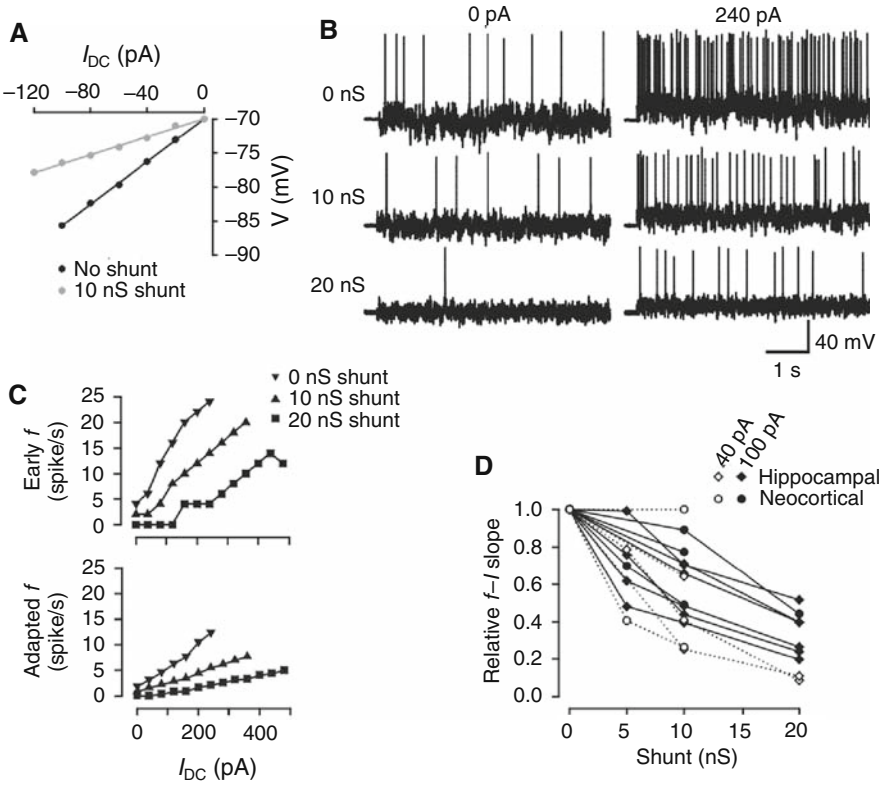

Fig. 8 Noise allows shunting to mediate firing rate gain control. (**A**) Shunting has a purely divisive effect on the voltage response, i.e. it changes the slope of the *I–V* curve, which corresponds to changing input resistance, but that does not necessarily translate into divisive modulation of firing rate (see Figs. 3 and 7). (**B**) Traces show samples responses from typical CA1 pyramidal neuron to noisy stimulation ($\sigma_{noise} = 100$ pA) at two different I_{DC} and three levels of shunting. Under these conditions, increasing membrane conductance reduced but did not terminate repetitive spiking. (**C**) *f–I* curves from responses in B exhibited a reduction in slope as shunting was increased. *Early f* was calculated from the number of spikes in the first 500 ms of the response and *adapted f* was calculated from the subsequent 14.5 s; those values represent responsiveness before and after the onset of adaptation, respectively. (**D**) Summary of reduction in *f–I* slope relative to slope without shunting for 40 and 100 pA noise for all cells analyzed. Reduction in slope caused by a 10 nS shunt was significant for 40 pA noise ($p < 0.05$, $n = 3$ hippocampal + 2 neocortical cells, paired *t*-test) and for 100 pA noise ($p < 0.005$, $n = 6$ hippocampal + 3 neocortical cells , paired *t*-test)

that shunting will cause mixed divisive/subtractive modulation of firing rate, where the subtractive component is attributable to shunting-induced reduction of membrane potential variance while the divisive component reflects divisive reduction of average depolarization. The average $f_{adapted}$–I_{DC} curve exhibited this pattern of mixed modulation (Fig. 9D).

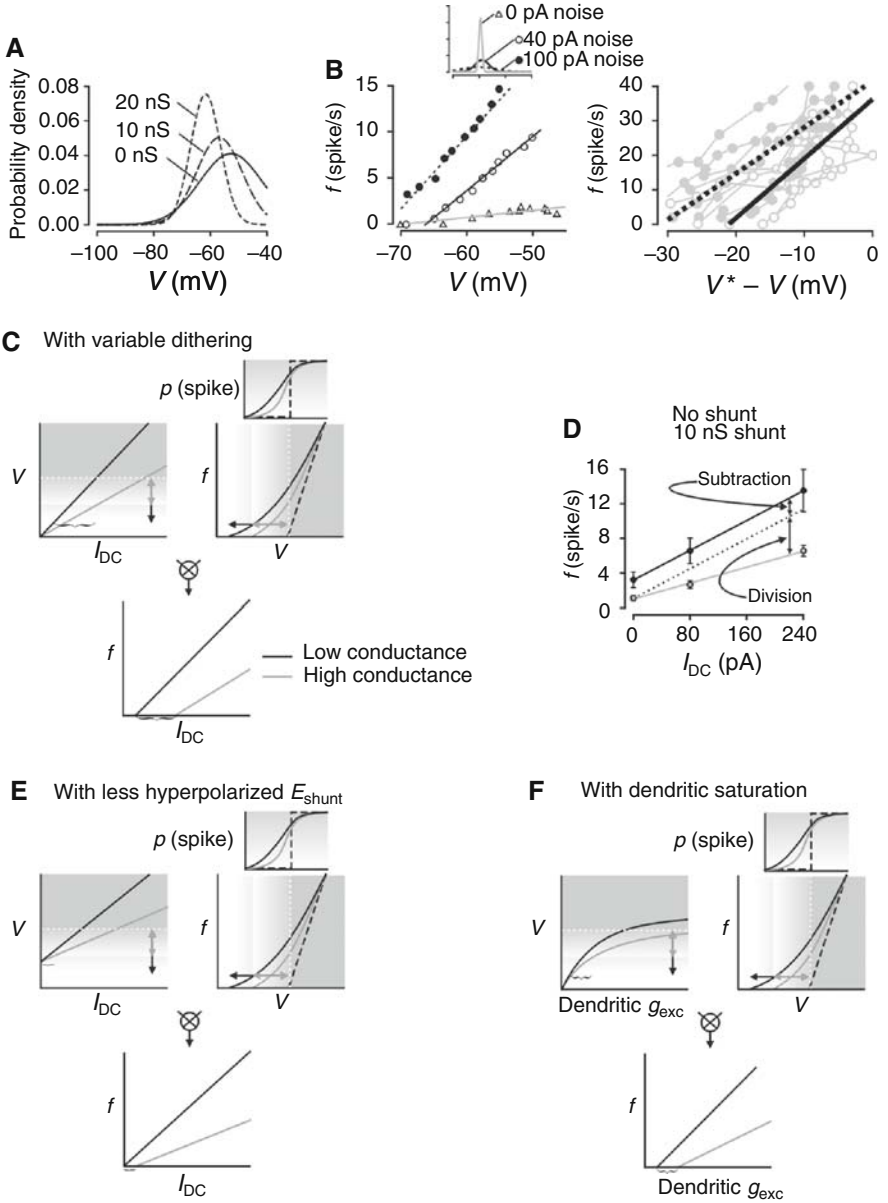

Fig. 9 Other factors affecting the modulation of firing rate. (**A**) Probability distributions of V for stimulation with $I_{DC} = 240$ pA and $\sigma_{noise} = 100$ pA (same cell as in Fig. 8B) are shown fitted with Gaussian curves. Increasing the shunt from 0 to 10 to 20 nS reduced average V from −55.5 to −57.5 to −62.2 mV and reduced the standard deviation of V (SD_V) from 9.0 to 7.7 to 5.3 mV. (**B**) To demonstrate how amplitude of voltage noise affects firing rate independent of changes in average depolarization, we varied σ_{noise} and plotted f against average V based on responses to different I_{DC}. In a typical CA1 pyramidal cell (left panel), SD_V increased from 0.5

The relative contribution of divisive and subtractive modulation therefore depends on the amplitude of the voltage fluctuations inasmuch as those fluctuations control the degree of dithering. However, the likelihood of a voltage fluctuation crossing threshold depends not only on the amplitude of the fluctuation, but also on how close the average membrane potential is to threshold. From this, one can appreciate why shunting with a conductance whose reversal potential lies within the voltage range associated with fluctuation-driven spiking has a purely divisive effect (Fig. 9E); consider that $E_{\text{shunt}} = -57$ mV in Chance and Abbott "Simulating In Vivo Background Activity in a Slice with the Dynamic Clamp" in this volume. Similarly, we have shown through simulations in a multicompartmental model that synaptic excitation in the dendrites leads to dendritic saturation (i.e. reduced depolarization as dendritic membrane potential approaches the reversal potential for glutamatergic input); this causes the relationship between somatic depolarization and synaptic excitation to become nonlinear (Prescott and De Koninck, 2003), which flattens the trajectory of the g_{exc}–V curve through the voltage range associated with fluctuation-driven spiking and, in turn, mitigates shunting's subtractive modulation of firing rate (Fig. 9F).

This last observation regarding the effects of dendritic saturation illustrates one of the shortcomings of applying all stimuli to the soma. Simulations in a multicompartmental model suggest there may be other, similar problems with somatic stimulation. For instance, when synaptic input is modeled as a Poisson

Fig. 9 (continued) to 2.6 to 6.6 mV as σ_{noise} was increased from 0 to 40 to 100 pA (inset). Although spiking was abolished when noise was removed, changing from 100 to 40 pA noise caused a purely subtractive shift in the f–V curve. Right panel shows data from all cells tested ($n = 6$ hippocampal + 3 neocortical cells) with voltage shown relative to threshold (V^*), which was determined according to the methodology in Fig. 5B. Regression lines based on cumulative data indicated that reducing voltage noise caused a predominantly subtractive shift in the f–V curve. This shift is indicative of reduced dithering. (**C**) If dithering is responsible for allowing shunting to divisively modulate firing rate, then reduced dithering (see B) should compromise the divisive process. A reduction in dithering compresses the voltage range associated with fluctuation-driven spiking (double-headed arrows). See Fig. 7B for explanation of bracket. Therefore, we predicted that shunting should have a mixed divisive/subtractive effect on firing rate, the former being attributable to modulation of average V and the latter being attributable to reduction of SD_V. (**D**) Average f_{adapted}–I_{DC} curve ($n = 9$ cells) based on 100 pA noise with and without a 10 nS shunt was consistent with that prediction. Error bars show SEM. (**E**) Shunting with a conductance whose reversal potential is closer to threshold shifts the I–V curves upward. As a result, those curves can start inside the voltage range associated with fluctuation-driven spiking. This causes modulation of firing rate to become more divisive and less subtractive. (**F**) Dendritic saturation renders synaptic excitation (g_{exc}) in the dendrites less effective at depolarizing the soma as the strength of excitation increases. The g_{exc}–V curve is thereby flattened in the voltage range associated with fluctuation-driven spiking, which causes the modulation of firing rate to become more divisive and less subtractive, as in E

process, stimulus variance increases as the rate of synaptic input to the soma increases (see Chance and Abbott "Simulating In Vivo Background Activity in a Slice with the Dynamic Clamp" in this volume), but, according to our simulations, the amplitude of somatic voltage fluctuations remained constant when the rate of excitatory synaptic input to the *dendrites* was increased (Prescott and De Koninck, 2003). This is caused (1) by the enhanced attenuation of signal transmission from the dendrites to the soma as the length constant becomes shorter because of increased membrane conductance and (2) by the reduction in stimulus variance caused by driving force decreasing as dendritic saturation develops (unpublished observations) (see also Holmes and Woody, 1989). These discrepancies between somatic and dendritic excitation highlight the benefits of combining experiments and simulations in order to exploit the strengths of each approach and to identify inconsistencies that can be resolved with additional, targeted investigations.

Nonetheless, the experimental data shown here demonstrate that moderate-to-large amplitude noise causes dithering that allows shunting to divisively modulate firing rate. We believe it is helpful to distinguish the effects of noise amplitude on dithering from the effects of dithering on firing rate modulation of the traditional *f–I* curve. Indeed, these effects can be distinguished by separately replicating different aspects of background synaptic input.

4 Conclusions

Neuronal response properties have been characterized largely by experiments performed in acute slices because of technical benefits (stability of recording, ease of pharmacological manipulation, etc.) compared with working in the intact brain. But although individual neuron structure may remain largely intact, neural networks are usually disrupted. Steps should be taken to minimize those disruptions, but it is also feasible to replicate at least some effects of network activity in acute slices using techniques like dynamic clamp. When we replicated the shunting, tonic depolarization, and membrane potential noise caused by synaptic background activity, we observed clear changes in the so-called intrinsic response properties, which included both passive membrane properties as well as spiking pattern. Overall, pyramidal neurons that behaved like integrators under typical in vitro conditions behaved more like coincidence detectors under simulated in vivo conditions. Furthermore, the biophysical implementation of firing rate gain control, which plays an important computational role (Carandini and Heeger, 1994; Salinas and Thier, 2000) depends on the effects of background synaptic input. In short, neural coding and computational processes such as gain control can be profoundly altered by the effects of background synaptic input. Those effects have been largely overlooked in slice experiments, but the dynamic-clamp technique together with other manipulations allow in vivo-like conditions to be replicated in vitro, thus enhancing our

capacity to use slice experiments to explore how neurons operate under realistic conditions.

Appendix – Simulation and Dynamical Analysis Methods

Simulations were based on a modified Morris–Lecar model (Morris and Lecar, 1981; Prescott et al., 2008a; Rinzel and Ermentrout, 1998). This single compartment model is described by the following equations:

$$C\frac{dV}{dt} = \begin{array}{l} I_{DC} + I_{noise} - \bar{g}_{Na}\, m_\infty(V)(V - E_{Na}) - \bar{g}_{K,dr} w(V - E_K) \\ -g_{shunt}(V - E_{shunt}) - \bar{g}_{adapt} z(V - E_K) \end{array} \quad (1)$$

$$\frac{dw}{dt} = \phi_w \frac{w_\infty(V) - w}{\tau_w(V)} \quad (2)$$

$$\frac{dz}{dt} = \phi_z \left[\frac{1}{1 + e^{(\beta_z - V)/\gamma_z}} - z \right] \quad (3)$$

$$m_\infty(V) = 0.5\left[1 + \tanh\left(\frac{V - \beta_m}{\gamma_m}\right)\right] \quad (4)$$

$$w_\infty(V) = 0.5\left[1 + \tanh\left(\frac{V - \beta_w}{\gamma_w}\right)\right] \quad (5)$$

$$\tau_w(V) = \frac{1}{\cosh\left(\frac{V - \beta_w}{2\gamma_w}\right)} \quad (6)$$

where $E_{Na} = 50$ mV, $E_K = -100$ mV, $E_{shunt} = -70$ mV, $\bar{g}_{Na} = 20\,mS/cm^2$, $\bar{g}_{K,dr} = 20\,mS/cm^2$, $\phi_w = 0.25$, $C = 2\,\mu F/cm^2$, $\beta_m = -1.2$ mV, $\gamma_m = 18$ mV, $\beta_w = -9$ mV, and $\gamma_w = 10$ mV. Parameters were set to the indicated values in order to reproduce experimentally recorded response patterns. Low- and high-conductance states were simulated by setting g_{shunt} to 2 or 4 mS/cm^2, respectively. Adaptation comprised two currents: M-type K^+ current with $\bar{g}_M = 2\,mS/cm^2$, $\phi_z = 0.005$ m/s, $\beta_z = -30$ mV, and $\gamma_z = 5$ mV and calcium-activated K^+ current with $\bar{g}_{AHP} = 1\,mS/cm^2$, $\phi_z = 0.005$ m/s, $\beta_z = 0$ mV, and $\gamma_z = 5$ mV. Activation of I_M and I_{AHP} were controlled separately by z_M and z_{AHP}. In some simulations (specified in text), z was treated as a parameter rather than as variable, which has the benefit of reducing the dimensionality of the model (see below). Constant and noisy current (I_{DC} and I_{noise}) were simulated in the same way that they were applied in electrophysiological experiments. Equations were integrated numerically in XPP (Ermentrout, 2002) using the Euler method and a 0.1–0.01 ms time step.

The benefits of such a simple model is that it is amenable to dynamical analysis techniques like phase plane and bifurcation analysis. For instance, without adaptation, the model is 2D, which means its behavior can be explained entirely by the interaction between two variables: a fast activation variable V and a slower recovery variable w. This interaction can be visualized by plotting V against w to create a phase portrait. Nullclines represent areas in phase space where a given variable remains constant. How the nullclines intersect (i.e. whether the intersection is stable or unstable) determines whether the system evolves toward a fixed point or toward a limit cycle (i.e. subthreshold membrane potential or repetitive spiking, respectively). This constitutes phase plane analysis. In order to determine the effects of certain parameters, the parameter of interest (e.g. z or I_{DC}) can be continuously varied to determine its effects on the system's behavior, which will be reflected in the nullcline intersection. Of particular interest are bifurcations or abrupt transitions in the system's behavior, such as the transition between quiescence and repetitive spiking. Characterizing those transitions constitutes bifurcation analysis. See Rinzel and Ermentrout (1998) for a more detailed discussion of these methods in the context of neuronal excitability or Strogatz (1998) for an in-depth explanation.

The multicompartmental, conductance-based model discussed in Section 3.4 was based on a reconstructed n layer 5 neocortical pyramidal neuron and was simulated in NEURON. Further details are available in the original publication (Prescott and De Koninck, 2003).

References

Azouz R, Gray CM (2000) Dynamic spike threshold reveals a mechanism for synaptic coincidence detection in cortical neurons in vivo. Proc Natl Acad Sci USA 97: 8110–8115.

Berman NJ, Douglas RJ, Martin KA (1992) GABA-mediated inhibition in the neural networks of visual cortex. Prog Brain Res 90: 443–476.

Bernander Ö, Douglas RJ, Martin KA, Koch C (1991) Synaptic background activity influences spatiotemporal integration in single pyramidal cells. Proc Natl Acad Sci USA 88: 11569–11573.

Blomfield S (1974) Arithmetical operations performed by nerve cells. Brain Res 69: 115–124.

Bruckner S, Hyson RL (1998) Effect of GABA on the processing of interaural time differences in nucleus laminaris neurons in the chick. Eur J Neurosci 10: 3438–3450.

Buhl EH, Halasy K, Somogyi P (1994) Diverse sources of hippocampal unitary inhibitory postsynaptic potentials and the number of synaptic release sites. Nature 368: 823–828.

Carandini M, Heeger DJ (1994) Summation and division by neurons in primate visual cortex. Science 264: 1333–1336.

Chance FS, Abbott LF, Reyes AD (2002) Gain modulation from background synaptic input. Neuron 35: 773–782.

Connors BW, Malenka RC, Silva LR (1988) Two inhibitory postsynaptic potentials, and GABAA and GABAB receptor-mediated responses in neocortex of rat and cat. J Physiol 406: 443–468.

Destexhe A, Paré D (1999) Impact of network activity on the integrative properties of neocortical pyramidal neurons in vivo. J Neurophysiol 81: 1531–1547.

Destexhe A, Rudolph M, Fellous JM, Sejnowski TJ (2001) Fluctuating synaptic conductances recreate in vivo-like activity in neocortical neurons. Neuroscience 107: 13–24.
Destexhe A, Rudolph M, Pare D (2003) The high-conductance state of neocortical neurons in vivo. Nat Rev Neurosci 4: 739–751.
Eccles JC (1964) The Physiology of Synapses. Berlin: Springer-Verlag.
Ermentrout B (2002) Simulating, Analyzing, and Animating Dynamical Systems: A Guide to XPPAUT for Researchers and Students. Philadelphia, PA: SIAM.
Fellous JM, Rudolph M, Destexhe A, Sejnowski TJ (2003) Synaptic background noise controls the input/output characteristics of single cells in an in vitro model of in vivo activity. Neuroscience 122: 811–829.
Fernandez FR, White JA (2008) Artificial synaptic conductances reduce subthreshold oscillations and periodic firing in stellate cells of the entorhinal cortex. J Neurosci 28: 3790–3803.
Higgs MH, Slee SJ, Spain WJ (2006) Diversity of gain modulation by noise in neocortical neurons: regulation by the slow afterhyperpolarization conductance. J Neurosci 26: 8787–8799.
Hodgkin AL (1948) The local electric changes associated with repetitive action in a non-medullated axon. J Physiol 165–181.
Holmes WR, Woody CD (1989) Effects of uniform and non-uniform synaptic 'activation-distributions' on the cable properties of modeled cortical pyramidal neurons. Brain Res 505: 12–22.
Holt GR, Koch C (1997) Shunting inhibition does not have a divisive effect on firing rates. Neural Comput 9: 1001–1013.
Hu H, Vervaeke K, Storm JF (2007) M-channels (Kv7/KCNQ channels) that regulate synaptic integration, excitability, and spike pattern of CA1 pyramidal cells are located in the perisomatic region. J Neurosci 27: 1853–1867.
Jean-Xavier C, Mentis GZ, O'Donovan MJ, Cattaert D, Vinay L (2007) Dual personality of GABA/glycine-mediated depolarizations in immature spinal cord. Proc Natl Acad Sci USA 104: 11477–11482.
König P, Engel AK, Singer W (1996) Integrator or coincidence detector? The role of the cortical neuron revisited. Trends Neurosci 19: 130–137.
Kuhn A, Aertsen A, Rotter S (2004) Neuronal integration of synaptic input in the fluctuation-driven regime. J Neurosci 24: 2345–2356.
Longtin A, Doiron B, Bulsara AR (2002) Noise-induced divisive gain control in neuron models. Biosystems 67: 147–156.
Mainen ZF, Joerges J, Huguenard JR, Sejnowski TJ (1995) A model of spike initiation in neocortical pyramidal neurons. Neuron 15: 1427–1439.
Mainen ZF, Sejnowski TJ (1995) Reliability of spike timing in neocortical neurons. Science 268: 1503–1506.
Mitchell SJ, Silver RA (2003) Shunting inhibition modulates neuronal gain during synaptic excitation. Neuron 38: 433–445.
Morris C, Lecar H (1981) Voltage oscillations in the barnacle giant muscle fiber. Biophys J 35: 193–213.
Paré D, Shink E, Gaudreau H, Destexhe A, Lang EJ (1998) Impact of spontaneous synaptic activity on the resting properties of cat neocortical pyramidal neurons in vivo. J Neurophysiol 79: 1450–1460.
Pinto RD, Elson RC, Szucs A, Rabinovich MI, Selverston AI, Abarbanel HD (2001) Extended dynamic clamp: controlling up to four neurons using a single desktop computer and interface. J Neurosci Methods 108: 39–48.
Prescott SA, De Koninck Y (2003) Gain control of firing rate by shunting inhibition: roles of synaptic noise and dendritic saturation. Proc Natl Acad Sci USA 100: 2076–2081.
Prescott SA, De Koninck Y, Sejnowski TJ (2008a) Biophysical basis for three distinct dynamical mechanisms of action potential initiation. PLoS Comput Biol 4: e1000198.

Prescott SA, Ratté S, De Koninck Y, Sejnowski TJ (2006a) Nonlinear interaction between shunting and adaptation controls a switch between integration and coincidence detection in pyramidal neurons. J Neurosci 26: 9084–9097.

Prescott SA, Ratté S, De Koninck Y, Sejnowski TJ (2008b) Pyramidal neurons switch from integrators in vitro to resonators under in vivo-like conditions. J Neurophysiol 100: 3030–3042.

Prescott SA, Sejnowski TJ, De Koninck Y (2006b) Reduction of anion reversal potential subverts the inhibitory control of firing rate in spinal lamina I neurons: towards a biophysical basis for neuropathic pain. Mol Pain 2(32).

Rinzel J, Ermentrout GB (1998) Analysis of neural excitability and oscillations. In: Methods in Neuronal Modeling: From Ions to Networks (Koch C, Segev I, eds), pp 251–291. Cambridge, MA: The MIT Press.

Robinson HP, Kawai N (1993) Injection of digitally synthesized synaptic conductance transients to measure the integrative properties of neurons. J Neurosci Methods 49: 157–165.

Rose D (1977) On the arithmetical operation performed by inhibitory synapses onto the neuronal soma. Exp Brain Res 28: 221–223.

Rudolph M, Destexhe A (2003) Tuning neocortical pyramidal neurons between integrators and coincidence detectors. J Comput Neurosci 14: 239–251.

Salinas E, Thier P (2000) Gain modulation: a major computational principle of the central nervous system. Neuron 27: 15–21.

Sharp AA, O'Neil MB, Abbott LF, Marder E (1993a) Dynamic clamp: computer-generated conductances in real neurons. J Neurophysiol 69: 992–995.

Sharp AA, O'Neil MB, Abbott LF, Marder E (1993b) The dynamic clamp: artificial conductances in biological neurons. Trends Neurosci 16: 389–394.

Shu Y, Duque A, Yu Y, Haider B, McCormick DA (2007) Properties of action-potential initiation in neocortical pyramidal cells: evidence from whole cell axon recordings. J Neurophysiol 97: 746–760.

Shu Y, Hasenstaub A, Badoual M, Bal T, McCormick DA (2003) Barrages of synaptic activity control the gain and sensitivity of cortical neurons. J Neurosci 23: 10388–10401.

Strogatz SH (1998) Nonlinear Dynamics and Chaos: With Applications to Physics, Biology, Chemistry, and Engineering. Don Mills, ON: Addison-Wesley.

Stuart G, Spruston N, Sakmann B, Hausser M (1997) Action potential initiation and back-propagation in neurons of the mammalian CNS. Trends Neurosci 20: 125–131.

Uhlenbeck GE, Ornstein LS (1930) On the theory of Brownian motion. Phys Rev 36: 823–841.

Wang HS, McKinnon D (1995) Potassium currents in rat prevertebral and paravertebral sympathetic neurones: control of firing properties. J Physiol 485: 319–335.

Testing Methods for Synaptic Conductance Analysis Using Controlled Conductance Injection with Dynamic Clamp

Zuzanna Piwkowska, Martin Pospischil, Michelle Rudolph-Lilith, Thierry Bal, and Alain Destexhe

Abstract In this chapter, we present different methods to analyze intracellular recordings and the testing of these methods using dynamic-clamp techniques. The methods are derived from a model of synaptic background activity where the synaptic membrane conductances are considered as stochastic processes. Because this *fluctuating point-conductance* model can be treated analytically, different methods can be outlined to estimate different characteristics of synaptic noise from the membrane potential (V_m) activity, such as the mean and variance of the excitatory and inhibitory conductance distributions (the *VmD method*) or spike-triggered averages of conductances. These analysis methods can be validated in controlled conditions using dynamic-clamp injection of known synaptic conductance patterns, as we illustrate here. Our approach constitutes a novel application of the dynamic clamp, which could be extended to the testing of other methods for extracting conductance information from the recorded V_m activity of neurons.

1 Introduction

To understand the functioning of neural networks, an important step is to characterize the synaptic inputs impinging on individual neurons, and originating both from other neurons in the network and from external sources. In this chapter, we provide an overview of methods that we have developed for extracting characteristics of excitatory and inhibitory synaptic conductances from membrane potential (V_m) recordings of cortical neurons, and we present how such methods can be tested by taking advantage of controlled conductance injection with dynamic clamp (Rudolph et al. 2004; Pospischil et al. 2007; Piwkowska et al. 2005, 2008).

Z. Piwkowska (✉)
Unité de Neurosciences Intégratives et Computationnelles (UNIC), CNRS, 91 198 Gif-sur-Yvette, France
e-mail: piwkowska@unic.cnrs-gif.fr

A. Destexhe, T. Bal (eds.), *Dynamic-Clamp*, Springer Series in Computational Neuroscience 1, DOI 10.1007/978-0-387-89279-5_6,

Numerous studies report that cortical neurons in vivo in the awake state display a depolarized, fluctuating V_m, rather low input resistance, and sustained irregular firing (Woody and Gruen 1978; Matsumura et al. 1988; Baranyi et al. 1993; Steriade et al. 2001; Timofeev et al. 2001; Rudolph et al. 2007; but see Margrie et al. 2002, Crochet and Petersen 2006 and Lee et al. 2006 for reports of much sparser firing of cortical neurons in vivo in the awake state). During slow-wave sleep or under anesthetics such as urethane or ketamine–xylazine, the V_m displays an alternation of "up-" and "down-" states (Metherate and Ashe 1993; Steriade et al. 1993, 2001; Timofeev et al. 2001): during the up-state, the V_m of cortical neurons is depolarized compared to the down-state and highly fluctuating, similar to the sustained activity found in awake animals (Destexhe et al. 2007). Up- and down-states have also been found in some in vitro cortical preparations (Sanchez-Vives and McCormick 2000; Silberberg et al 2004; Cunningham et al. 2006), indicating that isolated intracortical circuits are able to generate such states, presumably through recurrent synaptic excitation and inhibition. The synaptic origin of the depolarized, fluctuating states has been confirmed by pharmacological experiments: these states are abolished when action potentials are blocked in vivo (Paré et al. 1998) and when excitatory synaptic transmission is blocked in vitro (McCormick et al. 2003; Cunningham et al. 2006). Characterizing the synaptic conductances underlying such states is the goal of the different analysis methods discussed in this chapter.

The starting point for our analysis methods is the simplified *fluctuating point-conductance model* of recurrent cortical activity. In this model, the effective synaptic conductances seen at the soma of a cortical neuron, resulting from the Poisson-like activation of thousands of synapses distributed over the dendritic tree, are represented by only two stochastic, Gaussian-distributed variables: $g_e(t)$ for total excitation and $g_i(t)$ for total inhibition, with respective reversal potentials E_e and E_i (Destexhe et al. 2001). Each of these variables follows a random walk that decays with some time constant τ toward an average. To study theoretically how such a synaptic input influences the V_m dynamics, these two stochastic variables were inserted into a passive single-compartment model neuron (see Appendix 1 for equations).

The relative simplicity of such a model allows the derivation of various expressions relating the synaptic excitatory and inhibitory conductances to the V_m: an invertible expression for the steady-state distribution of V_m fluctuations (Rudolph and Destexhe 2003, 2005), an expression for the power spectral density (PSD) of V_m fluctuations (Destexhe and Rudolph 2004), and a probabilistic method for calculating the most likely conductance time course preceding spikes given an average V_m time course (Pospischil et al. 2007). Based on these expressions, various parameters of the synaptic input can in principle be obtained from V_m recordings.

This approach for analyzing synaptic conductances relies on two sets of assumptions: first, that the synaptic conductances seen at the soma can effectively be described with the two independent stochastic processes proposed in the model; and second, that the approximation of V_m dynamics at the

soma by a passive equation in a single compartment is reasonably valid. By injecting controlled synaptic inputs into the soma of cortical neurons with the dynamic-clamp technique, we could start to assess the validity of these assumptions and of the synaptic conductance analysis methods derived from them.

2 The VmD Method for Extracting Synaptic Conductance Parameters

2.1 Outline of the VmD Method

The *VmD method* (Rudolph et al. 2004) is based on an analytic approximation describing the steady-state distribution of the V_m fluctuations of a neuron subject to fluctuating conductances g_e and g_i (Rudolph and Destexhe 2003, 2005). More specifically, the steady-state V_m distribution is approximated by a Gaussian of average $<V>$ and standard deviation σ_V (for other approaches, see Richardson 2004 and Lindner and Longtin 2006; for a comparative study, see Rudolph and Destexhe 2006). As the V_m distributions obtained experimentally during up-states and activated states show little asymmetry, the Gaussian approximation is a reasonable choice (for specific examples, see Figs. 2 and 3, and Rudolph et al. 2004, 2005, 2007). It has the advantage of allowing the inversion of equations relating the synaptic conductance parameters to the V_m distribution parameters, leading to expressions of the synaptic conductance parameters as a function of the V_m measurements, $<V>$ and σ_V.

Each of the two stochastic conductance variables is characterized by three parameters: the mean g_0 and the standard deviation σ of its Gaussian distribution, as well as by an autocorrelation time constant τ (see Appendix 1 for equations). By fixing the values of τ_e and τ_i, which are related to the decay time of synaptic currents and can be estimated from voltage-clamp data and validated to some extent from current-clamp data (see Section 3) by using power spectral analysis, four parameters remain to be estimated: the means (g_{e0}, g_{i0}) and standard deviations (σ_e, σ_i) of excitatory and inhibitory synaptic conductances. In order to obtain a system of four equations relating V_m parameters with conductance parameters, one possibility is to consider two V_m distributions obtained at two different constant levels of injected current I_{ext1} and I_{ext2}. In this case, the Gaussian approximation of the two distributions gives two mean V_m values, $<V1>$ and $<V2>$, and two standard deviation values, σ_{V1} and σ_{V2} . Solving the system of four equations yields estimates for g_{e0} and g_{i0} as well as for σ_e and σ_i (see equations in Appendix 2), as a function of $<V1>$, $<V2>$, σ_{V1} and σ_{V2}, τ_e and τ_i, the synaptic reversal potentials E_e and E_i, and the passive parameters of the cell (leak conductance G_L and associated reversal potential E_L, membrane capacitance C).

2.2 Testing the VmD Method with Dynamic Clamp

We took advantage of the possibility, given by the dynamic-clamp technique, to inject the fluctuating conductances g_e and g_i in biological neurons, and performed in vitro tests of the VmD method (Rudolph et al. 2004; Piwkowska et al. 2005, 2008). All the experiments described in this chapter were performed on acute slices of the occipital cortex of adult guinea pigs and ferrets, using sharp intracellular electrodes and the real-time Neuron dynamic-clamp system (presented in "Re-Creating In Vivo-Like Activity and Investigating the Signal Transfer Capabilities of Neurons: Dynamic-Clamp Applications Using Real-Time NEURON" in this volume by Sadoc et al.). We used standard procedures, described in more detail in Rudolph et al. 2004, Pospischil et al. 2007 and Piwkowska et al. 2008. The contamination of measured membrane voltage by electrode artifacts was avoided either through the use of the discontinuous current-clamp mode (in which current injection and voltage recording alternate at frequencies of 2–3 kHz with our electrodes) or with active electrode compensation (AEC), a novel, high-resolution digital online compensation technique we have recently developed (Brette et al. 2008; see also Brette et al. "Dynamic Clamp with High-Resistance Electrodes Using Active Electrode Compensation In Vitro and In Vivo" in this volume).

In two neurons, we injected fluctuating conductance noise (with one set of parameters) at two levels of constant injected current, and then attempted to recover the means and standard deviations of the conductances, using the VmD method, from the parameters of the resulting V_m fluctuations, as well as from the passive parameters of the cell obtained from responses to current pulse injection. The reversal potentials E_e and E_i as well as τ_e and τ_i were assumed to be known. Figure 1A illustrates schematically the procedure, and Fig. 1B shows the results. Parameters overall similar to the known parameters of the injected conductances were found, with however less accuracy for the parameters of inhibition: this can be explained by the fact that the reversal potential of inhibition (–75 mV) is close to the reversal potential of the leak (taken as the resting potential of the recorded neurons), so that any error in the estimation of the leak conductance is mainly reflected in errors in the subsequent estimation of inhibition parameters.

From these tests, we can conclude that in the studied cases, the passive membrane equation of a single-compartment model neuron is a reasonable approximation for the V_m dynamics of a real cortical neuron subjected to a point-conductance input at the soma. It would be interesting to perform this test in a larger number of cells and for a diversity of parameters of excitation and inhibition, to identify the situations for which the VmD method might give the most reliable results.

In five neurons, we performed another test, in which we applied the VmD method to V_m fluctuations recorded in cortical neurons during up-states occurring in "active" cortical slices (adult ferret cortical slices, placed in

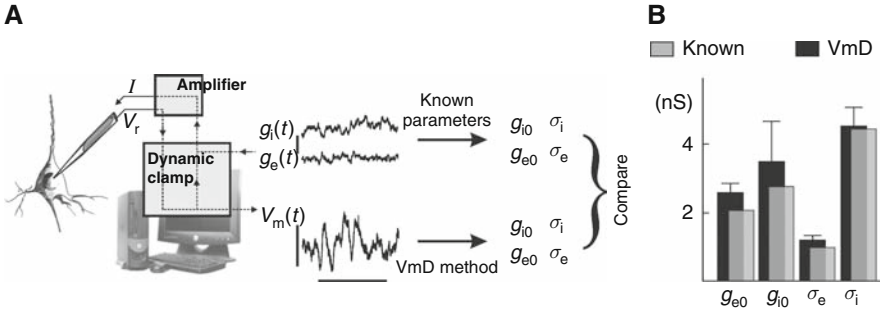

Fig. 1 **A**. Schematic representation of a first procedure to test the VmD analysis method in real cortical neurons using dynamic clamp. Synaptic conductances, generated with the fluctuating point-conductance model with parameters chosen by the experimentalist, are injected in a cortical cell in vitro. The resulting V_m fluctuations (at two levels of constant injected current) are collected and the VmD method is applied to the V_m distributions to yield estimates of synaptic conductance parameters. These parameters can then be compared to the know parameters used to generate the injected conductances. Calibration bars, 100 ms, 5 mV, and 20 nS. **B**. Comparison of known and estimated synaptic conductance parameters ($n = 2$: mean $\pm$ standard deviation)

artificial cerebrospinal fluid [ACSF] with lowered magnesium and calcium, but increased potassium concentrations compared to traditional ACSF, and possibly closer to the concentrations of physiological CSF; Sanchez-Vives and McCormick 2000). We computed V_m distributions selectively from periods of subthreshold activity collected within up-states, recorded at two levels of constant current injection. We subsequently extracted synaptic conductance parameters from Gaussian fits to these distributions, using the VmD method (Fig. 2A). Using dynamic clamp, in the same cell but during down-states, we then injected synaptic fluctuating conductances generated from distributions with these same parameters (Fig. 2B). Finally, we compared the biological up-states with these dynamic-clamp injections: Fig. 2C shows a typical example of a real up-state and, shortly after, an up-state re-created in dynamic clamp.

In three of these cells, the actual analysis procedure was the following: synaptic conductance parameters were computed for a few different, realistic values of leak conductance and cell capacitance, and were then tested by comparing the resulting V_m fluctuations with real up-states. The best matches in terms of V_m distributions are shown on Figs. 2B and 3A.

In two cells, in a more demanding test, leak conductance and cell capacitance were estimated using standard procedures from the cell's response to short current pulses, and those values were then used for estimating the synaptic conductance parameters: the good match obtained between the V_m distributions resulting from dynamic-clamp injection and the V_m distributions obtained from real up-states is apparent on Fig. 3B. Moreover, in these two

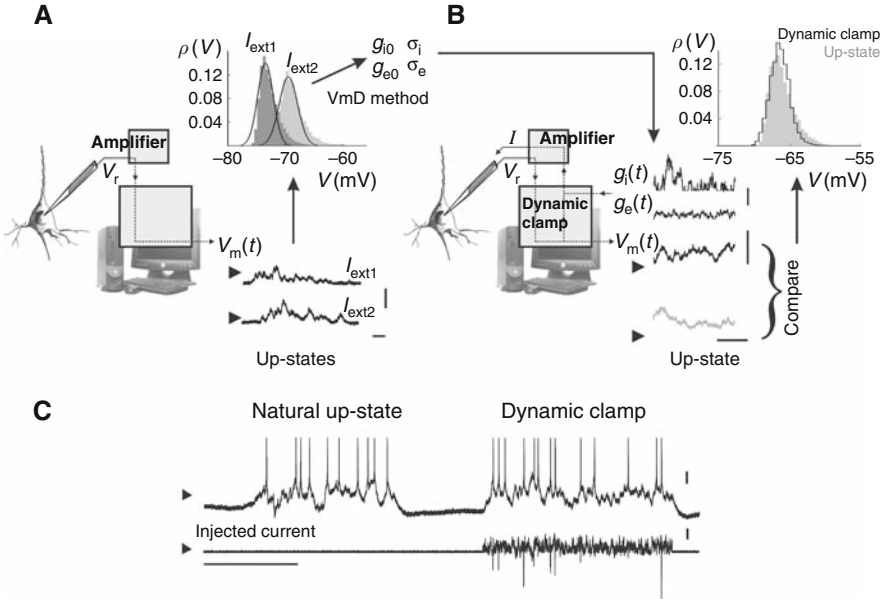

Fig. 2 **A**. Schematic representation of a second procedure to test the VmD analysis method in real cortical neurons using dynamic clamp. In cortical neurons in vitro, V_m fluctuations are recorded during real up-states at two constant current levels. The VmD method is applied to yield estimates of the underlying synaptic conductance parameters, assuming that the real synaptic input to the soma follows the fluctuating point-conductance model. **B**. These estimated parameters are then used to generate fluctuating synaptic conductances (using the point-conductance model) and inject them into the same cell using dynamic clamp, during down-states (i.e., in between real up-states). The V_m fluctuations obtained during dynamic-clamp injection are then compared, in terms of distributions, to the V_m fluctuations from real up-states. **C**. An example of a real up-state followed, in the same cell, by an artifical up-state re-created through dynamic-clamp injection of synaptic conductances, generated using the fluctuating point-conductance model with parameters estimated from real up-states by the VmD method. Calibration bars: 100 ms, 10 mV (A); 50 ms, 10 mV, 10 nS(B); and 500 ms, 0.2 nA, 10 mV (C)

cells, the comparison could be performed for two levels of constant injected current: two distributions are thus shown for each cell (in the bottom panel, the two distributions are largely overlapping).

Taken together, these experimental results show that the VmD analysis method can yield effective synaptic conductance parameters which can indeed account for the statistics of V_m fluctuations observed during real synaptic activity in cortical neurons.

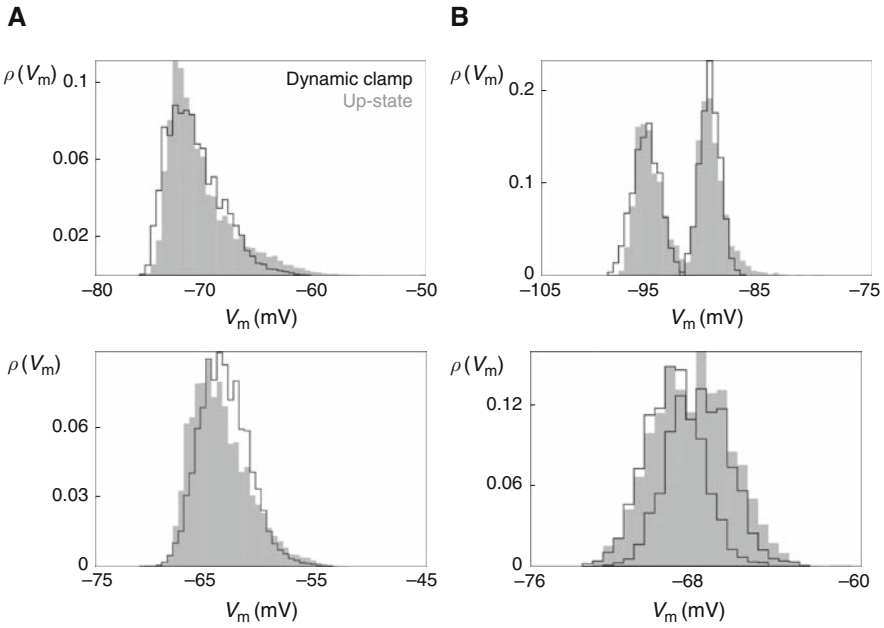

Fig. 3 Comparison between V_m distributions obtained from real up-states (*gray*) and V_m distributions obtained from dynamic-clamp injections of synaptic conductances with parameters obtained with the VmD method (*black*), for four different cortical cells. **A**. Synaptic conductance parameters were estimated for a few different sets of realistic leak parameters and the best-matching distributions are shown here. **B**. Leak parameters were obtained from responses to the injection of brief current pulses (see text for details). Note that in each of the panels in B, two distributions are shown (for two different constant current levels)

3 Validating Conductance Time Constants Using the Power Spectral Density of the V_m

3.1 Outline of the Method

As mentioned in the previous section, in order to fully characterize the synaptic conductances according to the fluctuating point-conductance model, in addition to the mean and standard deviations of the conductance distributions, we also need the autocorrelation time constants τ_e and τ_i, which describe how fast each of the conductances decays toward its average value after a random perturbation. τ_e and τ_i appear in an expression approximating the PSD of the V_m as a function of the conductance parameters (Destexhe and Rudolph 2004; see Appendix 3 for equations). One way to evaluate these two parameters would thus be to fit this analytical template to the PSD obtained from V_m recordings:

in this procedure, assuming that the effective time constant of the membrane has been measured, four parameters have to be adjusted by the fitting procedure, two of which correspond to τ_e and τ_i.

Fitting all four parameters is problematic, but the procedure can nonetheless be used to check if values of τ_e and τ_i approximated from other data (like voltage clamp) are accurate. By fixing τ_e and τ_i at their independently approximated values and fitting the other two parameters, one can check to see if a satisfactory fit of the experimental V_m PSD is obtained. Failure to obtain a satisfactory fit would suggest that τ_e and τ_i had been estimated inaccurately.

3.2 Testing the Analytic Expression of the PSD with Dynamic Clamp

We verified this procedure by setting τ_e and τ_i to 3 and 10 ms, respectively, and then fitting the analytical template to the PSD of V_m fluctuations recorded in vitro from cortical neurons injected with fluctuating conductances with these same autocorrelation time constants (Fig. 4A; we used a new, high-resolution electrode compensation technique allowing accurate recording of high frequencies in the V_m, see Brette et al. 2008 and also Brette et al. "Dynamic Clamp with High-Resistance Electrodes Using Active Electrode Compensation In Vitro and In Vivo" in this volume). In this case (Fig. 4B), the theoretical template can provide a very good fit of the experimentally obtained PSD, up to around 400 Hz, where recording noise becomes important. This shows that the analytic expression for the PSD is consistent not only with models, but also with conductance injection in real neurons in vitro.

3.3 PSD Analysis of V_m Fluctuations In Vitro

However, we have not developed this approach further, beyond the checking of assumed τ_e and τ_i parameters, as we found that for V_m fluctuations resulting from real synaptic activity, the experimental PSDs cannot be fitted with the theoretical template as nicely as the dynamic-clamp data (see Fig. 4C for the fitting of V_m fluctuations obtained from up-states recorded in cortical neurons in vitro, and Piwkowska et al. 2008 for a similar result based on in vivo data): the PSD presents a frequency scaling region at high frequencies, and scales as $1/f^{\alpha}$ with a different exponent α as predicted by the theory. The analytic expression (see Appendix 3) predicts that the PSD should scale as $1/f^4$ at high frequencies, but the experiments show that the exponent α is obviously lower than that value.

Including the values of $\tau_e = 3$ ms and $\tau_i = 10$ ms provided acceptable fits to the low-frequency ($<$100 Hz) part of the spectrum (Fig. 4C). For higher

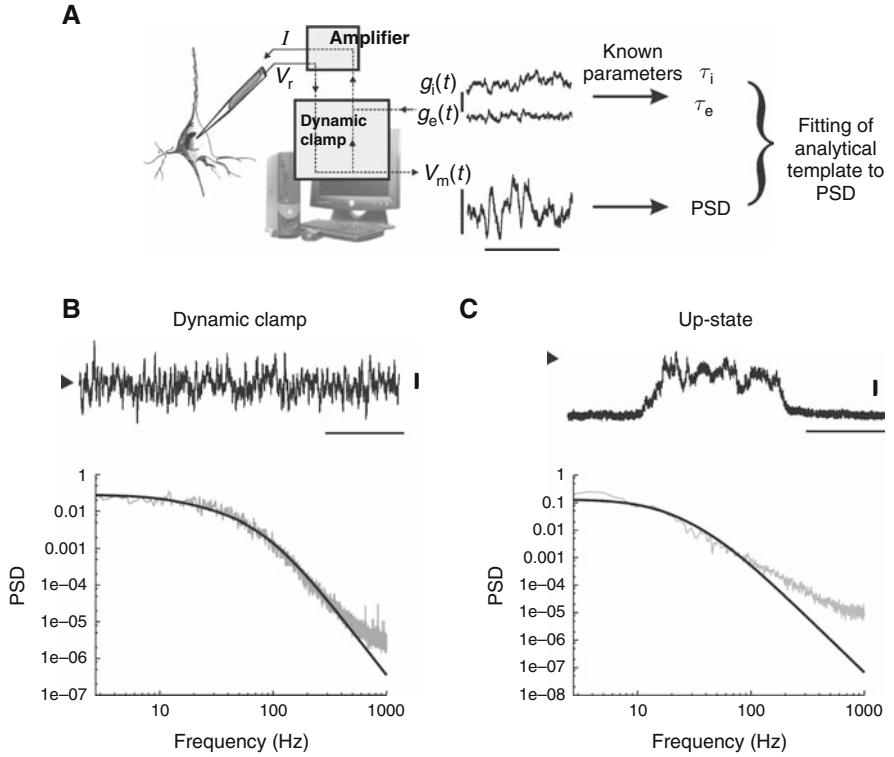

Fig. 4 **A**. Schematic representation of the procedure for evaluating the analytic expression of the PSD of V_m fluctuations resulting from a point synaptic input at the soma. Synaptic conductances, generated with the fluctuating point-conductance model with parameters chosen by the experimentalist, are injected in a cortical cell in vitro using dynamic clamp. The PSD of the resulting V_m fluctuations is calculated, and an analytical template is fit to this experimental PSD, while fixing the values of τ_e and τ_i to the values actually used during the dynamic-clamp injection. **B**. The resulting fit of dynamic-clamp data (*top*: example of V_m trace; *bottom*, grey: corresponding PSD, in log–log coordinates) with the analytical template (*black*) is excellent. **C**. The PSD (*bottom*, gray, in log–log coordinates) obtained from a recording of V_m fluctuations during spontaneous up-states (*top trace*) cannot be satisfactorily fitted with the analytical template at high frequencies; the slope at high frequencies is shallower (around –2.5) than the one predicted by the theory (–4). Calibration bars: 100 ms, 5 mV, 20 nS (A); 500 ms, 5 mV, arrow –65 mV (B, C)

frequencies, it can be seen that the experimental spectrum diverges from the analytical template and does not present the same slope. Small variations (around 20–30%) around these values of τ_e and τ_i yielded equally good fits (not shown; see also Rudolph et al. 2005). Thus, the method in its present form can at best be used to broadly estimate τ_e and τ_i with an error of the order of 30%.

It has recently been shown (Bedard and Destexhe 2008) that the frequency scaling of the V_m PSDs observed experimentally in vivo can be reproduced by models in which the synaptic inputs are distributed on the dendritic tree, as during real synaptic activity, but only if the standard cable theory is modified to incorporate non-ideal capacitors. These modified models also confirm that if the synaptic inputs impinge on the soma, the exponent α still equals 4, which is in keeping with our results of dynamic-clamp injections at the soma. However, the difference in PSD scaling between distributed dendritic and point somatic inputs shows the limits of the dynamic-clamp approach, which can only reproduce the latter situation.

4 Estimating Spike-Triggered Averages of Synaptic Conductances from the V_m

4.1 Outline of the Method

In order to investigate not only the global statistics of synaptic conductances underlying V_m fluctuations in cortical neurons, but also the patterns of synaptic conductances underlying the specific V_m fluctuations which trigger spikes, we recently developed a procedure to extract the spike-triggered averages (STAs) of conductances from recordings of the V_m (Pospischil et al. 2007; Piwkowska et al. 2008). The STA of the V_m is calculated first, and this probabilistic method searches (see Appendix 4 for equations) for the most likely spike-related conductance time courses ($g_e(t)$, $g_i(t)$) that are compatible with the observed voltage STA – assuming that the system is well decribed by the point-conductance model and given the statistical parameters of the conductances (mean, standard deviation, and autocorrelation time constant) and the leak parameters of the cell.

4.2 Testing STA Estimation with Dynamic Clamp

To evaluate the accuracy of the conductance STA estimation method, we performed dynamic-clamp injections of fluctuating synaptic conductances in cortical neurons, choosing conductance parameters that triggered spiking at moderate frequencies (below 30 Hz). The conductance STAs estimated from the V_m STAs were compared to conductance STAs obtained directly by averaging conductance traces, again making use of the fact that in dynamic clamp the injected conductances are perfectly controlled by the experimentalist (Fig. 5A).We intended to evaluate the STA method specifically, so that we assumed that conductance distribution parameters were known. In addition, we estimated the cell's leak parameters in the following way: the leak conductance was obtained by dividing the average injected current by the average voltage

during conductance injection, relative to rest (which yields an effective leak conductance possibly comprising different types of voltage-dependent conductances); responses to depolarizing current pulses were used to estimate the membrane capacitance from the time constant of exponential fits to the decay of the V_m; the resting potential of the cell was taken as the reversal potential of the leak conductance. Figure 5B shows an example of a comparison between conductance STAs estimated by the method and conductance STAs obtained by directly averaging conductance traces.

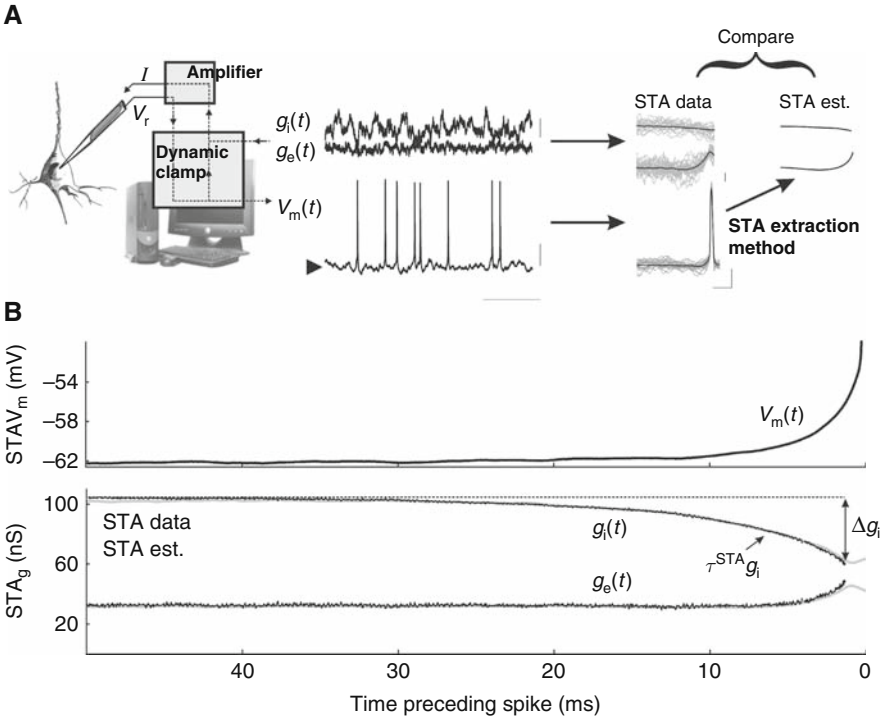

Fig. 5 **A**. Schematic representation of the procedure for evaluating the probabilistic method for extracting STAs of synaptic conductances from the STA of the recorded V_m. Synaptic conductances, generated with the fluctuating point-conductance model with parameters chosen so that the neuron spikes at a moderate rate, are injected in a cortical cell in vitro using dynamic clamp. 50-ms-long fragments of the resulting V_m preceding spikes are collected and averaged, yielding the STA of the V_m. The probabilistic method is used to extract the conductance STAs (STA est.). The 50-ms-long fragments of the injected conductance traces preceding spikes are also collected and averaged to yield the "measured" conductance STAs (STA data). These can then be compared to the extracted STAs. Calibration bars: 200 ms, 20 mV, 20 nS, arrow –60 mV (*left*); 10 ms, 20 mV, 10 nS (*right*). **B**. An example of measured conductance STAs (*gray*) and estimated conductance STAs (*black*), which are in close correspondence up to around a millisecond before the spike. Measures compared at the population level (Δg and $\tau^{STA}g$), which are extracted from exponential fits to both the measured and the extracted STAs, are schematically represented (see text for details)

We further analyzed 36 different conductance injections (in eight regular spiking cortical neurons in vitro), generally observing a good match between estimated and measured STAs. We quantifed the comparison on a population basis as follows: exponential functions were fitted to each conductance STA (estimated and directly measured) starting at 1 ms before the spike and decaying to baseline backwards in time. We then compared the asymptotic values (i.e., the average baseline conductances) and the time constants ($\tau^{STA}g$) of these fits, as well as the amplitude of conductance change from the start of the fit to the asymptote (i.e., the amplitude of conductance change preceding the spike; Δg), as illustrated in the example in Fig. 5B. Note that for inhibition, as the exponential template used for fitting the STAs differs by one sign from the template used for excitation, a positive Δg corresponds to a drop in inhibitory conductance (see Piwkowska et al. 2008 for details). In all cases but one, the exponential functions provided excellent fits to the conductance STAs. It was necessary to exclude the 1 ms time window preceding the spike to avoid severe contamination of the analyses by intrinsic conductances. Excluding a broader time window did not improve the analyses for these neurons. For all analyses, we selected spikes which were not preceded by another spike in a 100 ms time window (using the recorded conductance traces, we checked that excluding spikes following interspike intervals [ISIs] shorter than 100 ms did not affect the measured STAs in an important way; see Piwkowska et al. 2008 for details).

There was an excellent match of the average baseline conductances, between the estimated and measured STAs (error of -0.1 ± 0.25 nS, or -0.8 ± 2.6 %, for excitation; 0.8 ± 1.5 nS, or 0.6 ± 4.5%, for inhibition; not shown). More importantly, the estimates of the average conductance patterns leading to spikes were also in good correspondence with the measured patterns, in terms of both the amplitude of conductance change (Fig. 6A, top; error of -1.2 ± 3 nS, or -26 ± 28.8 %, for excitatory amplitude change, and -2.0 ± 2.5 nS, or -10.7 ± 47%, for inhibitory amplitude change) and the time constant (Fig. 6A, bottom; error of 0.39 ± 0.48 ms, or 11.2 ± 21.1% for excitatory time constant, and 0.36 ± 1.71, or 2.6 ± 18.8%, for inhibitory time constant). For excitation, the error on the estimate of the amplitude is correlated with the error on the estimate of the time constant (not shown): this suggests that, in most cases, a slight overestimate of the excitatory conductance rate of change results in a slight overestimate of the total change in conductance. The lack of correlation between the two error measures in the case of the inhibitory conductance points to a more complex origin for the observed errors. Moreover, the errors on the amplitude of the two conductance changes are positively correlated (Fig. 6B, top). This dependency actually ensures that the error on the estimated total conductance change (excitation–inhibition) remains small (-0.8 ± 2.4 nS; Fig. 6B, bottom).

These results show again that approximating the V_m dynamics in response to a fluctuating point-conductance input by a passive membrane equation is a reasonably valid assumption, provided the right passive parameters are chosen. We have to stress here that the conductance STA extraction method

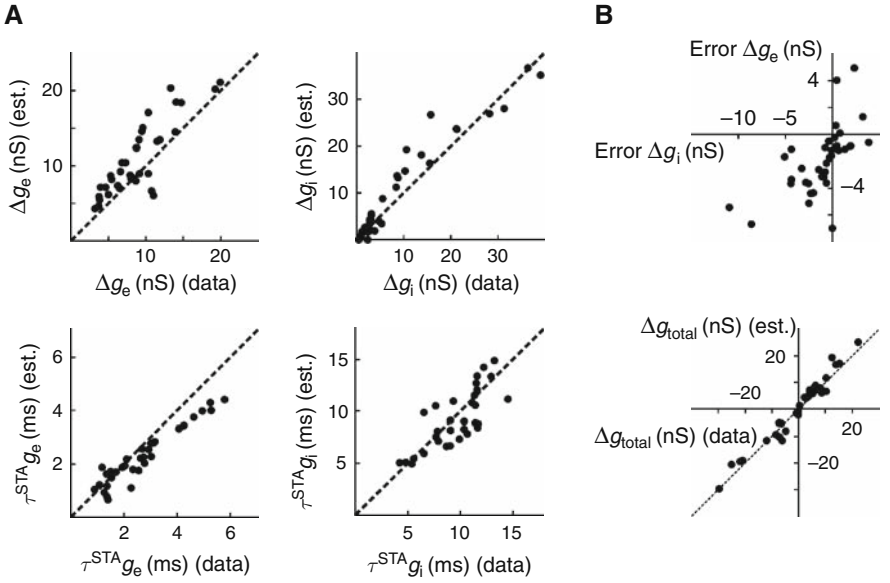

Fig. 6 **A**. Population analysis comparing measured and extracted STAs. *Top*: Δg for both excitation (*left*) and inhibition (*right*; note that a positive Δg_i corresponds to a drop of inhibition before the spike). Bottom: $\tau^{STA} g$ for both excitation (*left*) and inhibition (*right*). **B**. Correlation between errors on Δg for excitation and inhibition. As a result of this correlation, the total conductance change before the spike ($\Delta g_e - \Delta g_i$) remains small, the experimental points lie closely to the first diagonal

allows the extraction of average conductances from recordings obtained at a single level of injected current (on the contrary of previously used conductance analysis methods, see Section 5), which minimizes the variations in the activation of various voltage-dependent intrinsic conductances during a single protocol.

5 Discussion

5.1 A Novel Use for the Dynamic-Clamp Technique

In this chapter, we specifically reviewed how we have been applying the dynamic-clamp technique to the evaluation of synaptic conductance analysis methods (Rudolph et al. 2004; Piwkowska et al. 2005; Pospischil et al. 2007; Piwkowska et al. 2008). To our knowledge, the approach we developed in our studies constitutes a novel, original application of this electrophysiological technique.

The synaptic analysis techniques we developed are based on current-clamp data, which are technically easier to obtain (especially in vivo) than voltage-clamp data. In other terms, we are attempting to retrieve some information

about the underlying synaptic conductances from recordings of the V_m of cortical neurons, during naturally occurring synaptic inputs. We have used dynamic clamp to directly manipulate the V_m of intracellularly recorded cells as if additional, user-defined conductances were inserted at the site of the recording electrode (Le Masson et al. 1992; Sharp et al. 1993; Robinson and Kawai 1993). We could therefore check how synaptic conductance parameters extracted from V_m recordings obtained during such dynamic-clamp manipulations compare to the actual synaptic conductance parameters, which in this case are precisely known (see procedures shown on Figs. 1 and 5).

In all our dynamic-clamp experiments, we generated the injected excitatory and inhibitory synaptic conductances according to the fluctuating point-conductance model (detailed in Appendix 1) – that is, the same model which was used in theoretical studies to derive the different expressions relating V_m fluctuations to conductance fluctuations, and on which the analysis techniques are based. This means that from the two assumptions mentioned in the Introduction, we have mainly been testing the second one: whether the observed V_m dynamics at the site of conductance injection could be described in a satisfactory way by a single-compartment model governed by a passive membrane equation. This assumption appeared to hold in the studied cases, however the non-trivial issue is how to obtain the appropriate "leak" parameters for the passive membrane equation. These "leak" parameters can in fact take into account voltage-dependent intrinsic conductances and are thus, in this sense, "effective leak parameters."

We used a variety of approaches to address this issue. In some initial tests of the VmD method, we scanned a variety of realistic effective leak and capacitance parameters and kept those that yielded the best match in our test, when comparing dynamic clamp to real up-states (Fig. 3A): this is of course not feasible when simply applying the VmD method to V_m fluctuations recorded in vivo. However, we could imagine repeating in vivo the type of experiment we did here in vitro, that is, attempting to re-create real up-states with dynamic clamp (during down-states) and then checking a posteriori which of the estimated conductance parameters allow the best matching of the V_m distributions (see Brette et al. 2008 and Brette et al. "Dynamic Clamp with High-Resistance Electrodes Using Active Electrode Compensation In Vitro and In Vivo" in this volume on AEC for our new electrode compensation technique which improves the feasibility of dynamic clamp experiments in vivo). In other tests (Figs. 1 and 3B), we extracted passive parameters, using standard procedures, from V_m responses to square current pulses applied during down-states. This is the approach that might seem the most straightforward to use in vivo in cases were up- and down-states are also present; however, it suffers from the major drawback that especially in vivo, activation of intrinsic voltage-dependent conductances can be expected to vary in an important manner during up- and down-states (see, e.g., Sanchez-Vives et al. 2000 for the importance of adaptation currents following the up-states in vivo). In tests of the STA extraction method, finally, we obtained the effective "leak" conductance by dividing the

average injected current by the average resulting change in V_m (relative to rest): the good matching of the subsequently estimated STAs with the directly measured STAs (Figs. 5 and 6) shows that this approach gives an effective leak conductance which allows the accurate description of V_m dynamics by a passive membrane equation, in the studied case. Again, this effective leak might include some voltage-dependent conductances, but these appear to evolve on a timescale which is sufficiently slow, so that the total intrinsic membrane conductance can be approximated by a fixed, voltage-independent conductance in these experiments (up to 1 ms before the spike, when fast voltage-dependent conductances activate and preclude the use of our method; see Pospischil et al. 2007 for details). However, this precise approach for obtaining the effective leak parameters clearly cannot be used to analyze V_m fluctuations recorded in vivo.

In summary, our various dynamic-clamp tests show that the subthreshold V_m dynamics of real cortical neurons, subjected to synaptic inputs following our fluctuating point-conductance model, and also subjected to real synaptic inputs during up-states in "active" slices, can be modelled using a simple one-compartment passive model, at least as far as V_m distributions and STAs of conductances are considered (but in the case of real up-states, this does not hold for the PSDs of the fluctuations, see below). However, these tests do not tell us how such a passive model should be parametrized in vivo to yield the best possible estimates of synaptic conductance parameters. The approaches that were actually used to analyze in vivo data (Rudolph et al. 2005, 2007) are reviewed and commented in detail in Piwkowska et al. 2008, and clearly demand further work in order to establish the optimal solution to this issue of effective leak parameters.

As to the first of the two assumptions mentioned in the Introduction – that the effective inhibitory and excitatory synaptic conductances seen at the soma are accurately described by the two independent stochastic processes postulated in the fluctuating point-conductance model – it has also been evaluated, to a limited extent, by some of our tests. Indeed, our experiments show that V_m distributions obtained during real up-states in active slices can be accurately reproduced by somatic injection of fluctuating synaptic conductances following this model (Figs. 2 and 3). It can be noted, interestingly, that one of the distributions reconstructed in this way (Fig. 3A, top panel) displays a marked asymmetry, and that this asymmetry is reproduced by our dynamic-clamp injection, even though the VmD method is based on a Gaussian (i.e., symmetric) approximation to the recorded V_m distributions – in other terms, the asymmetry was not considered by the synaptic parameter extraction method, yet it is reproduced by the model. This result indicates that the asymmetry might arise from interactions between the synaptic conductances and intrinsic voltage-dependent conductances, and that this interaction occurs during dynamic-clamp injection similarly to what happens during real up-states. It is also possible that the asymmetry is simply due to the non-linearity of the membrane equation subjected to conductance-based synaptic inputs, which is initially neglected by the Gaussian approximation of the V_m distribution, but reappears

when conductance-based synaptic fluctuations are injected into the cell using the correct parameters.

However, although this similarity between distributions speaks in favor of the chosen model of synaptic inputs, we have not evaluated alternative models in our experiments (e.g., models including a correlation between excitation and inhibition, or models including larger numbers of distinct synaptic conductances; see below). In conclusion, we do not know whether such models could similarly account for the observed distributions. Injecting synaptic conductances generated by different models, but analyzing the resulting V_m fluctuations with the same methods as used here (i.e., based on the point-conductance model), would help reveal if functionally important differences exist between the models and would, therefore, be an interesting extension of the studies presented in this chapter.

In addition, we have seen that when we analyze the PSDs of the V_m fluctuations recorded during real up-states in vitro (or in vivo, see Piwkowska et al. 2008), we find a discrepancy between the data and the predictions of the fluctuating point-conductance model (Fig. 4C). As mentioned before, a more complex model accounting for the scaling of the experimental PSDs has been proposed recently (Bedard and Destexhe 2008): this model includes distributed dendritic inputs and a modified cable equation. Whether this extended model could be used for analyzing synaptic conductance parameters is currently not known and should be investigated by future work.

5.2 Current Limitations of Dynamic Clamp in the Testing of Conductance Analysis Techniques

The example of the PSD scaling points to the main limitation of our approach for testing conductance analysis methods with dynamic clamp: the localized, point injection of conductance with the dynamic-clamp technique does not correspond to the distributed nature of synaptic input to cortical neurons.

Dynamic-clamp experiments in dendritic patch recordings (see Williams 2004, 2005 and Williams et al. "Dendritic Dynamic Clamp – A Tool to Study Single Neuron Computation" in this volume) could partly solve this problem, however in such experiments the conductance injection remains localized to a few discrete points, and the number of such points is severely limited by the number of stable dendritic recordings that can be established simultaneously in a single cell. This number is even more limited by the fact that until now, for accurate dynamic clamp in dendrites, two different electrodes have been used at each site, one for recording the V_m and another for current injection. This is due to the increased electrode resistance needed for the recording of fine structures like dendrites, compared to somatic patch recordings in vitro. In the near future, our new AEC technique (Brette et al. 2008 and Brette et al. "Dynamic Clamp with High-Resistance Electrodes Using Active Electrode Compensation

In Vitro and In Vivo" in this volume) might allow accurate dendritic dynamic-clamp recordings using a single electrode, which should increase the number of sites that can be stimulated at the same time in one cell.

However, this number will certainly remain restricted to a few sites, which is extremely limited when compared to the actual numbers of synapses (thousands to tens of thousands) impinging on cortical cells in vivo. An alternative approach for extending the experiments we presented here would be to graft whole virtual dendritic trees onto biological neurons, using dynamic clamp in combination with detailed multicompartmental models of dendritic trees and of the distributed synaptic input. Parameters of the synaptic input as well as of the dendritic structure could be systematically varied and the impact of such manipulations on V_m fluctuations seen at the soma, as well as on the results of synaptic conductance analysis techniques, could be investigated. Hughes et al. ("Using the Dynamic Clamp to Dissect the Properties and Mechanisms of Intrinsic Thalamic Oscillations") in this volume actually demonstrate the feasibility of such grafting of virtual dendritic trees onto real cells using dynamic clamp (Hughes et al. 2008).

5.3 Advantages and Limitations of the Conductance Analysis Techniques

As we have already discussed in detail in this chapter, the fluctuating point-conductance model, and the analysis methods derived from it, make simplifying assumptions about the nature of the synaptic inputs and the membrane dynamics, which might invalidate their use in some situations.

Thus, the assumption of independent excitation and inhibition appears to be wrong in the case of synaptic inputs onto cortical neurons evoked by sensory input, as many studies in recent years have shown that the two are correlated, with inhibitory input closely following excitatory input (Monier et al. 2003; Wehr and Zador 2003; Wilent and Contreras 2005). Until very recently, there were no estimations for the correlation between excitation and inhibition during spontaneous activity in vivo. However, such correlation has now been described in one ingenious recent study (Okun and Lampl 2008) where paired recordings of closely situated cortical cells sharing many of their synaptic inputs could be recorded in vivo: this protocol revealed a pattern similar to the situation when inputs are evoked by sensory stimulation, with inhibition (measured in one cell) closely following excitation (measured simultaneously in the second cell). In the view of these results, extending the fluctuating point-conductance model to include correlations between excitation and inhibition might be necessary (see Piwkowska et al. 2008 for a proposition of one way for including such correlations in the model and in the STA extraction method).

Another limitation of the fluctuating point-conductance model is the use of only two conductances, one for excitation and another one for inhibition, with

only one type of kinetics (given by τ_e and τ_i) and one reversal potential for each of these two input channels. This means that in practice, only fast AMPA-like inputs are considered for excitation, and fast GABA-A-like inputs are considered for inhibition. It can be argued that slower synaptic components – NMDA excitatory inputs and GABA-B inhibitory inputs – mainly change the average level of synaptic conductance at the soma (see, e.g., Harsch and Robinson 2000), due precisely to their slow dynamics, so that the analysis methods actually include these components in the estimation of g_{e0} and g_{i0}. This hypothesis has not been tested, however, and could be addressed in future modeling and dynamic-clamp studies.

On the other hand, the simplicity of the fluctuating point-conductance model is its main advantage. Until recently, it was an important advantage for dynamic-clamp experiments, with the limited number of required computations to be performed in real-time, however with the development of faster and faster real-time systems this advantage becomes less crucial. But in terms of analysis methods, this advantage is still present. The limited numbers of parameters used to characterize synaptic inputs allows the extraction of many of these parameters from recordings, and we can see that even with this limited numbers, some issues remain unresolved (the precise estimation of τ_e and τ_i from current-clamp data, or the optimal estimation of the effective leak parameters in vivo, mentioned at the beginning of this discussion). Assuming an underlying stochastic model allows the estimation of conductances in situations where traditional approaches, based on I–V curves established in time from repeated trials in voltage-clamp or current-clamp mode, are impossible (for examples of such approaches in the analysis of evoked sensory inputs, see Borg-Graham et al. 1998; Anderson et al. 2000; Monier et al. 2003; Wehr and Zador 2003; Wilent and Contreras 2005; see also Monier et al. 2008 for a review) – that is, in situations where one cannot assume exact repetitions of an input, like during spontaneous activity. In particular, the method for estimating synaptic conductance STAs from the STA of the V_m illustrates this advantage, since it requires recordings obtained at only one constant current level (see Pospischil et al. 2007 for details). In addition, the fact that the described methods rely on current-clamp data makes the recordings less demanding technically, and also makes possible the analysis of issues like the generation of spikes, whereas in voltage clamp, spikes are obviously not recorded.

5.4 Future Developments

All of the points above bring us to the following conclusions: on the one hand, the approaches we propose for analyzing V_m fluctuations to characterize the underlying inputs, based on a simple model of synaptic activity, appear as a powerful approach and can give us new information about cortical networks that cannot be obtained with previously used methods (like extracting the STAs

of conductances from recordings of spontaneous activity). On the other hand, the fluctuating point-conductance model does not yet include some potentially crucial facts concerning cortical activity in vivo, like the correlation between excitation and inhibition, which might be a general rule of functioning in cortical networks. Taken together, these two conclusions merge into one: new, more complete models should be developed (see, e.g., Piwkowska et al. 2008 for a proposed extension including correlations between excitation and inhibition) but these new models should be kept as simple and as general as possible, so that new analysis methods inspired from the ones reviewed here can be proposed.

Dynamic-clamp injection of various models of synaptic input to a cell could in the future be used to test these new analysis methods in ways similar to what we presented in this chapter. Generally speaking, two complementary types of dynamic-clamp tests emerge from our experiments. The first family of tests consists in checking whether known parameters of the injected model can indeed be recovered from V_m recordings, as proposed in theory. Such tests serve to verify assumptions regarding the V_m dynamics of the cell (e.g., a passive membrane equation). The second family of tests consists in comparing the V_m fluctuations generated by dynamic-clamp injection of the model with V_m fluctuations recorded during real network activity in vitro or in vivo. Such tests give indications as to the adequacy of the proposed model of synaptic inputs. A third type of test, which we did not attempt yet, would consist in injecting dynamic-clamp inputs generated according to a complex model (e.g., presynaptic spikes trains convolved with a variety of unitary synaptic conductance types; see, e.g., Harsch and Robinson 2000), and then in analyzing the resulting V_m fluctuations according to a simpler model (e.g., with the VmD method). In such a configuration, which reflects more closely the in vivo situation (inputs are complex, while analysis methods are simple), it would be interesting to investigate whether and how the estimated, effective conductance parameters (e.g., mean synaptic conductance level) can be related to the parameters of the actual, complex input (e.g., presynaptic firing rate).

Finally, dynamic clamp could also be used to characterize synaptic inputs to a cell in a more direct, "brute force" manner, in the case of the more complicated models of synaptic input (e.g., models including a virtual dendritic tree). In complex cases where an analytical solution for extracting synaptic conductances from V_m traces is not possible to establish, due to the complexity of the model, dynamic-clamp instances of the model with different parameters could be used in the considered cells (in the absence of real synaptic activity) to scan the parameter space and find the parameters which produce V_m dynamics most closely resembling the V_m recorded during real synaptic activity (as we also did in our initial tests of the VmD method). This approach has the advantage over conventional modeling of effortlessly assuring the correctness of many of the intrinsic properties of the cell, with the need to scan parameters of the input only (and, possibly, the parameters of the dendrite). Performing this type of experiments in vivo should, again, become more feasible with the use of the AEC

technique (Brette et al. 2008 and Brette et al. "Dynamic Clamp with High-Resistance Electrodes Using Active Electrode Compensation In Vitro and In Vivo" in this volume).

Acknowledgments Research supported by CNRS, ANR, ACI, HFSP, and the European Community (FACETS grant FP6 15879). Z.P. gratefully acknowledges the support of the FRM.

Appendix 1: The Fluctuating Point Conductance Model of Cortical Network Activity

The point-conductance model (Destexhe et al. 2001) of recurrent cortical activity describes the evolution of the subthreshold V_m of a point neuron based on two effective fluctuating conductances g_e and g_i, which are Gaussian-distributed stochastic variables, and with respective reversal potentials E_e and E_i. It was shown that the well-known Ornstein–Uhlenbeck model of Brownian noise (Uhlenbeck and Ornstein 1930) approximates very well the total synaptic conductances resulting from a large number of simulated conductance-based synaptic inputs (Destexhe et al. 2001; Destexhe and Rudolph 2004):

$$\frac{dg_e(t)}{dt} = -\frac{1}{\tau_e}\left[g_e(t) - g_{e0}\right] + \sqrt{\frac{2\sigma_e^2}{\tau_e}}\,\xi_e(t) \tag{1}$$

$$\frac{dg_i(t)}{dt} = -\frac{1}{\tau_i}\left[g_i(t) - g_{i0}\right] + \sqrt{\frac{2\sigma_i^2}{\tau_i}}\,\xi_i(t), \tag{2}$$

where g_{e0} and σ_e^2 are, respectively, the mean value and variance of the excitatory conductance, τ_e is the excitatory time constant, and $\xi_e(t)$ is a Gaussian white noise source with zero mean and unit standard deviation. The inhibitory conductance $g_i(t)$ is described by an equivalent equation (Eq. 2) with parameters g_{i0}, σ_i^2, τ_i and noise source $\xi_i(t)$.

In the simplest formulation for describing the subthreshold V_m dynamics of cortical neurons, these stochastic conductances are inserted into a single-compartment neuron model described by the following membrane equation:

$$C\,\frac{dV}{dt} = -G_L\,(V - E_L) - g_e\,(V - E_e) - g_i\,(V - E_i) + I_{ext}, \tag{3}$$

where C denotes the membrane capacitance, I_{ext} a stimulation current, G_L the leak conductance and E_L the leak reversal potential.

The fitting of a Gaussian model to the total synaptic conductances seen at the soma, in simulations performed using realistic cortical neuron morphologies and distributed synaptic inputs, indicates the following correspondences

between variables: the time constants (τ_e, τ_i) are identical to the decay time constants of synaptic currents. The average conductance (g_{e0}, g_{i0}) is related to the overall (integrated) conductance, which depends on the release frequency of the corresponding Poisson inputs, the quantal conductance and the decay time of synaptic currents. The variance of the conductances (σ_e^2, σ_i^2) is related to the same parameters, as well as to the amount of correlation between inputs of the same type (Destexhe et al. 2001). Correlations between presynaptic spike trains seem necessary in order to account for the high amplitude of V_m fluctuations observed in vivo (e.g., Destexhe and Paré 1999; Léger et al. 2005).

Appendix 2: The VmD Method

We consider a Gaussian approximation of the steady-state V_m distribution:

$$\rho(V) \sim \exp\left[-\frac{(V-\bar{V})^2}{2\sigma_V^2}\right], \tag{4}$$

where $\bar{V}$ is the average V_m and σ_V its standard deviation.

When this expression is fit to two V_m distributions, obtained at two different constant levels of injected current $I_{ext\,1}$ and $I_{ext\,2}$, we obtain two mean V_m values, $\bar{V}_1$ and $\bar{V}_2$, and two standard deviation values, σ_{V1} and σ_{V2}. The resulting system of four equations relating V_m parameters with conductance parameters can now be solved for four unknowns:

$$g_{\{e,i\}0} = \frac{(I_{ext\,1}-I_{ext\,2})\left[\sigma_{V2}^2\left(E_{\{i,e\}}-\bar{V}_1\right)^2-\sigma_{V1}^2\left(E_{\{i,e\}}-\bar{V}_2\right)^2\right]}{\left[(E_e-\bar{V}_1)(E_i-\bar{V}_2)+(E_e-\bar{V}_2)(E_i-\bar{V}_1)\right](E_{\{e,i\}}-E_{\{i,e\}})(\bar{V}_1-\bar{V}_2)^2} - \frac{(I_{ext\,1}-I_{ext\,2})(E_{\{i,e\}}-\bar{V}_2)+\left[I_{ext\,2}-G_L(E_{\{i,e\}}-E_L)\right](\bar{V}_1-\bar{V}_2)}{(E_{\{e,i\}}-E_{\{i,e\}})(\bar{V}_1-\bar{V}_2)}, \tag{5}$$

$$\sigma_{\{e,i\}}^2 = \frac{2C(I_{ext1}-I_{ext2})\left[\sigma_{V1}^2\left(E_{\{i,e\}}-\bar{V}_2\right)^2-\sigma_{V2}^2\left(E_{\{i,e\}}-\bar{V}_1\right)^2\right]}{\tilde{\tau}_{\{e,i\}}\left[(E_e-\bar{V}_1)(E_i-\bar{V}_2)+(E_e-\bar{V}_2)(E_i-\bar{V}_1)\right](E_{\{e,i\}}-E_{\{i,e\}})(\bar{V}_1-\bar{V}_2)^2}. \tag{6}$$

Here, $\tilde{\tau}_{\{e,i\}}$ are effective time constants given by (Rudolph and Destexhe 2005):

$$\tilde{\tau}_{\{e,i\}} = \frac{2\tau_{\{e,i\}}\tilde{\tau}_m}{\tau_{\{e,i\}}+\tilde{\tau}_m}, \tag{7}$$

where $\tilde{\tau}_m = C/(G_L + g_{e0} + g_{i0})$ is the effective membrane time constant.

Appendix 3: Power Spectral Density of the V_m for the Fluctuating Point-Conductance Model

The power spectral density (PSD) of the V_m fluctuations described by the point-conductance model (Eqs. (1,2,3)) can be well approximated by the following expression (Destexhe and Rudolph 2004):

$$S_V(\omega) = \frac{4}{G_T^2} \frac{1}{1+\omega^2\ \tilde{\tau}_m^2} \left[\frac{\sigma_e^2 \tau_e\ (E_e - \bar{V})^2}{1+\omega^2 tau_e^2} + \frac{\sigma_i^2 \tau_i\ (E_i - \bar{V})^2}{1+\omega^2 \tau_i^2} \right], \tag{8}$$

where $\omega = 2\pi f$, f is the frequency, $G_T = G_L + g_{e0} + g_{i0}$ is the total membrane conductance, $\tilde{\tau}_m = C/G_T$ is the effective time constant, and $\bar{V} = (G_L E_L + g_{e0} E_e + g_{i0} E_i)/G_T$ is the average membrane potential.

To evaluate the synaptic time constant parameters, τ_e and τ_i, the following simplified expression can be fitted:

$$S_V(\omega) = \frac{1}{1+\omega^2 \tilde{\tau}_m^2} \left[\frac{A_e \tau_e}{1+\omega^2 \tau_e^2} + \frac{A_i\ \tau_i}{1+\omega^2 \tau_i^2} \right], \tag{9}$$

where A_e and A_i are amplitude parameters. This five parameter template is used to provide estimates of the parameters τ_e and τ_i (supposing that $\tilde{\tau}_m$ has been measured). In practice, it is more feasible to assume reasonable values for τ_e and τ_i, and verify whether by fitting A_e and A_i, the observed V_m PSD can be well predicted by the analytical expression.

Appendix 4: Extracting Spike-Triggered Averages of Conductances from the V_m

The procedure for extracting conductance spike-triggered averages (STAs) from the V_m STA (Pospischil et al. 2007) is based on a discretization of the time axis in the point-conductance model (Eqs. (1,2,3)), which, rearranged, leads to the following relations:

$$g_i^k = -\frac{C}{V^k - E_i} \left\{ \frac{V^k - E_L}{\tau_L} + \frac{g_e^k (V^k - E_e)}{C} + \frac{V^{k+1} - V^k}{\Delta t} - \frac{I_{ext}}{C} \right\}, \tag{10}$$

$$\xi_e^k = \frac{1}{\sigma_e} \sqrt{\frac{\tau_e}{2\Delta t}} \left(g_e^{k+1} - g_e^k \left(1 - \frac{\Delta t}{\tau_e} \right) - \frac{\Delta t}{\tau_e} g_{e0} \right), \tag{11}$$

$$\xi_{\mathrm{i}}^{k} = \frac{1}{\sigma_{\mathrm{i}}}\sqrt{\frac{\tau_{\mathrm{i}}}{2\Delta t}}\left(g_{\mathrm{i}}^{k+1} - g_{\mathrm{i}}^{k}\left(1 - \frac{\Delta t}{\tau_{\mathrm{i}}}\right) - \frac{\Delta t}{\tau_{i}} g_{\mathrm{i}0}\right), \tag{12}$$

where $\tau_{\mathrm{L}} = C/G_{\mathrm{L}}$ is the resting membrane time constant. Note that $\xi_{\mathrm{e}}(t)$ and $\xi_{\mathrm{i}}(t)$ have become Gaussian–distributed random numbers ξ_{e}^{k} and ξ_{i}^{k}.

There is a continuum of combinations $\{g_{\mathrm{e}}^{k+1}, g_{\mathrm{i}}^{k+1}\}$ that can advance the membrane potential from V^{k+1} to V^{k+2}, each pair occurring with a probability

$$p^{k} := p(g_{\mathrm{e}}^{k+1}, g_{\mathrm{i}}^{k+1} | g_{\mathrm{e}}^{k}, g_{\mathrm{i}}^{k}) = \frac{1}{2\pi} \mathrm{e}^{-\frac{1}{2}\left(\xi_{\mathrm{e}}^{k2} + \xi_{\mathrm{i}}^{k2}\right)} = \frac{1}{2\pi} \mathrm{e}^{-\frac{1}{4\Delta t} X^{k}}, \tag{13}$$

$$\begin{aligned} X^{k} = {} & \frac{\tau_{\mathrm{e}}}{\sigma_{\mathrm{e}}^{2}}\left(g_{\mathrm{e}}^{k+1} - g_{\mathrm{e}}^{k}\left(1 - \frac{\Delta t}{\tau_{\mathrm{e}}}\right) - \frac{\Delta t}{\tau_{\mathrm{e}}} g_{\mathrm{e}0}\right)^{2} \\ & + \frac{\tau_{\mathrm{i}}}{\sigma_{\mathrm{i}}^{2}}\left(g_{\mathrm{i}}^{k+1} - g_{\mathrm{i}}^{k}\left(1 - \frac{\Delta t}{\tau_{\mathrm{i}}}\right) - \frac{\Delta t}{\tau_{\mathrm{i}}} g_{\mathrm{i}0}\right)^{2}. \end{aligned} \tag{14}$$

Because of Eq. (10), g_{e}^{k} and g_{i}^{k} are not independent and p^{k} is, thus, a unidimensional distribution only.

Given initial conductances $\{g_{\mathrm{e}}^{0}, g_{\mathrm{i}}^{0}\}$, one can write down the probability p for certain series of conductances $\{g_{\mathrm{e}}^{j}, g_{\mathrm{i}}^{j}\}_{j=0,\ldots,n}$ to occur that reproduce a given voltage trace $\{V^{l}\}_{l=1,\ldots,n+1}$:

$$p = \prod_{k=0}^{n-1} p^{k}. \tag{15}$$

Due to the symmetry of the distribution p, the average paths of the conductances coincide with the most likely ones. It is thus sufficient to determine the conductance series with extremal likelihood by solving the n-dimensional system of linear equations

$$\left\{\frac{\partial X}{\partial g_{\mathrm{e}}^{k}} = 0\right\}_{k=1,\ldots,n}, \tag{16}$$

where $X = \sum_{k=0}^{n-1} X^{k}$, for the vector $\{g_{\mathrm{e}}^{k}\}$. This is equivalent to solving $\left\{\frac{\partial p}{\partial g_{\mathrm{e}}^{k}} = 0\right\}_{k=1,\ldots,n}$ and involves the numerical inversion of an $n \times n$-matrix, which can be done using standard numeric methods (Press et al. 1986). The series $\{g_{\mathrm{i}}^{k}\}$ is subsequently obtained from Eq. (10). Details of this procedure can be found in Pospischil et al. (2007).

References

Anderson JS, Carandini M, Ferster D (2000) Orientation tuning of input conductance, excitation, and inhibition in cat primary visual cortex. J Neurophysiol 84:909–926.

Baranyi A, Szente MB, Woody CD (1993) Electrophysiological characterization of different types of neurons recorded in vivo in the motor cortex of the cat. II. Membrane parameters, action potentials, current-induced voltage responses and electrotonic structures. J Neurophysiol 69:1865–1879.

Bedard C, Destexhe A (2008) A modified cable formalism for modeling neuronal membranes at high frequencies. Biophys J 94:1133–1143.

Borg-Graham LJ, Monier C, Frégnac Y (1998) Visual input evokes transient and strong shunting inhibition in visual cortical neurons. Nature 393:369–373.

Brette R, Piwkowska Z, Monier C, Rudolph-Lilith M, Fournier J, Levy M, Fregnac Y, Bal T, Destexhe A (2008) High-resolution intracellular recordings using a real-time computational model of the electrode. Neuron, 59:379–391.

Crochet S, Petersen CC (2006) Correlating whisker behavior with membrane potential in barrel cortex of awake mice. Nat Neurosci 9:608–610.

Cunningham MO, Pervouchine DD, Racca C, Kopell NJ, Davies CH, Jones RS, Traub RD, Whittington M (2006) Neuronal metabolism governs cortical network response state. Proc Natl Acad Sci USA 103:5597–5601.

Destexhe A, Paré D (1999) Impact of network activity on the integrative properties of neocortical pyramidal neurons in vivo. J Neurophysiol 81:1531–1547.

Destexhe A, Rudolph M, Fellous J-M, Sejnowski TJ (2001) Fluctuating synaptic conductances recreate in vivo-like activity in neocortical neurons. Neuroscience 107:13–24.

Destexhe A, Rudolph M (2004) Extracting information from the power spectrum of synaptic noise. J Comput Neurosci 17:327–345.

Destexhe A, Hughes SW, Rudolph M, Crunelli V (2007) Are corticothalamic "up" states fragments of wakefulness? Trends Neurosci 30:334–342.

Harsch A, Robinson HP (2000) Postsynaptic variability of firing in rat cortical neurons: the roles of input synchronization and synaptic NMDA receptor conductance. J Neurosci 20:6181–6192.

Hughes SW, Lorincz M, Cope DW, Crunelli V (2008) NeuReal: An interactive simulation system for implementing artificial dendrites and large hybrid networks. J Neurosci Methods 169:290–301.

Le Masson G, Renaud-Le Masson S, Sharp AA, Marder E, Abbott LF (1992) Real-time interaction between a model neuron and the crustacean stomatogastric nervous system In: Society for Neuroscience Meeting. 18, 1055.

Lee AK, Manns ID, Sakmann B, Brecht M (2006) Whole-cell recordings in freely moving rats. Neuron 51:399–407.

Leger J-F, Stern EA, Aertsen A, Heck D (2005) Synaptic integration in rat frontal cortex shaped by network activity. J Neurophysiol 93:281–293.

Lindner B, Longtin A (2006) Comment on "Characterization of subthreshold voltage fluctuations in neuronal membranes", by M. Rudolph and A. Destexhe. Neural Comput 18:1896–1931.

Margrie TW, Brecht M, Sakmann B (2002) In vivo, low-resistance, whole-cell recordings from neurons in the anaesthetized and awake mammalian brain. Pflugers Arch 444:491–498.

Matsumura M, Cope T, Fetz EE (1988) Sustained excitatory synaptic input to motor cortex neurons in awake animals revealed by intracellular recording of membrane potentials. Exp Brain Res 70:463–469.

McCormick DA, Shu Y, Hasenstaub A, Sanchez-Vives M, Badoual M, Bal T (2003) Persistent cortical activity: mechanisms of generation and effects on neuronal excitability. Cereb Cortex 13:1219–1231.

Metherate R, Ashe JH (1993) Ionic flux contributions to neocortical slow waves and nucleus basalis-mediated activation:whole-cell recordings in vivo. J Neurosci 13:5312–5323.
Monier C, Chavane F, Baudot P, Graham LJ, Frégnac Y (2003) Orientation and direction selectivity of synaptic inputs in visual cortical neurons: a diversity of combinations produces spike tuning. Neuron 37:663–680.
Monier C, Fournier J, Frégnac Y (2008) In vitro and in vivo measures of evoked excitatory and inhibitory conductance dynamics in sensory cortices. J Neurosci Meth 169:323–365.
Okun M, Lampl I (2008) Instantaneous correlation of excitation and inhibition during ongoing and sensory-evoked activities. Nat Neurosci 11:535–537.
Paré D, Shink E, Gaudreau H, Destexhe A, Lang EJ (1998) Impact of spontaneous synaptic activity on the resting properties of cat neocortical neurons in vivo. J Neurophysiol 79:1450–1460.
Piwkowska Z, Rudolph M, Badoual M, Destexhe A, Bal T (2005) Re-creating active states in vitro with a dynamic-clamp protocol. Neurocomputing 65–66:55–60.
Piwkowska Z, Pospischil M, Brette R, Sliwa J, Rudolph-Lilith M, Bal T, Destexhe A. (2008) Characterizing synaptic conductance fluctuations in cortical neurons and their influence on spike generation. J Neurosci Meth 169:302–322.
Pospischil M, Piwkowska Z, Rudolph M, Bal T, Destexhe A (2007) Calculating event-triggered average synaptic conductances from the membrane potential. J Neurophysiol 97:2544–2552.
Press WH, Flannery BP, Teukolsky SA, Vetterling WT (1986) Numerical Recipes. The Art of Scientific Computing. Cambridge, MA: Cambridge University Press.
Richardson MJ (2004) Effects of synaptic conductance on the voltage distribution and firing rate of spiking neurons. Phys Rev E Stat Nonlin Soft Matter Phys 69:051918.
Robinson HP, Kawai N (1993) Injection of digitally synthesized synaptic conductance transients to measure the integrative properties of neurons. J Neurosci Methods 49:157–165.
Rudolph M, Destexhe A (2003) Characterization of subthreshold voltage fluctuations in neuronal membranes. Neural Comput 15:2577–2618.
Rudolph M, Piwkowska Z, Badoual M, Bal T, Destexhe A (2004) A method to estimate synaptic conductances from membrane potential fluctuations. J Neurophysiol 91:2884–2896.
Rudolph M, Destexhe (2005). An extended analytic expression for the membrane potential distribution of conductancebased synaptic noise. Neural Comput 17:2301–2315.
Rudolph M, Pelletier J-G, Paré D, Destexhe A (2005) Characterization of synaptic conductances and integrative properties during electrically-induced EEG-activated states in neocortical neurons in vivo. J Neurophysiol 94:2805–2821.
Rudolph M, Destexhe A (2006) On the use of analytic expressions for the voltage distribution to analyze intracellular recordings. Neural Comput 18: 2917–2922.
Rudolph M, Pospischil M, Timofeev I, Destexhe A (2007) Inhibition determines membrane potential dynamics and controls action potential generation in awake and sleeping cat cortex. J Neurosci 27:5280–5290.
Sanchez-Vives MV, McCormick DA (2000) Cellular and network mechanisms of rhythmic recurrent activity in neocortex. Nat Neurosci 3:1027–1034.
Sanchez-Vives MV, Nowak LG, McCormick DA (2000) Cellular mechanisms of long-lasting adaptation in visual cortical neurons in vitro. J Neurosci 20:4286–4299.
Silberberg G, Wu C, Markram H (2004) Synaptic dynamics control the timing of neuronal excitation in the activated neocortical microcircuit. J Physiol 556:19–27.
Sharp AA, O'Neil MB, Abbott LF, Marder E (1993) Dynamic clamp: computer-generated conductances in real neurons. J Neurophysiol 69:992–995.
Shu Y, Hasenstaub A, Badoual M, Bal T, McCormick DA (2003) Barrages of synaptic activity control the gain and sensitivity of cortical neurons. J Neurosci 23:10388–10401.
Steriade M, Nunez A, Amzica F (1993) A novel slow (< 1 Hz) oscillation of neocortical neurons in vivo: depolarizing and hyperpolarizing components. J Neurosci 13:3252–3265.

Steriade M, Timofeev I, Grenier F (2001) Natural waking and sleep states: a view from inside neocortical neurons. J Neurophysiol 85:1969–1985.
Timofeev I, Grenier F, Steriade M (2001) Disfacilitation and active inhibition in the neocortex during the natural sleepwake cycle: an intracellular study. Proc Natl Acad Sci USA 98:1924–1929.
Uhlenbeck GE and Ornstein LS (1930) On the theory of the Brownian motion. Phys Rev 36:823–841.
Wehr M, Zador AM (2003) Balanced inhibition underlies tuning and sharpens spike timing in auditory cortex. Nature 426:442–446.
Wilent W, Contreras D (2005) Dynamics of excitation and inhibition underlying stimulus selectivity in rat somatosensory cortex. Nature Neurosci 8:1364–1370.
Williams SR (2004) Spatial compartmentalization and functional impact of conductance in pyramidal neurons. Nat Neurosci 7:961–967.
Williams SR (2005) Encoding and decoding of dendritic excitation during active states in pyramidal neurons. J Neurosci 25:5894–5902.
Woody CD, Gruen E (1978) Characterization of electrophysiological properties of intracellularly recorded neurons in the neocortex of awake cats: a comparison of the response to injected current in spike overshoot and undershoot neurons. Brain Res 158:343–357.

In Vivo Dynamic-Clamp Manipulation of Extrinsic and Intrinsic Conductances: Functional Roles of Shunting Inhibition and I_{BK} in Rat and Cat Cortex

Lyle J. Graham and Adrien Schramm

Abstract We present in vivo dynamic-clamp electrophysiological recordings to characterize the influences of shunting inhibition and the potassium current I_{BK} on the input–output (I/O) transfer function of cortical neurons, in response to both artificial (injected current or conductance) and functional visual stimuli. In comparison to previous experimental and theoretical studies, we find that realistic levels of shunting inhibition have a significant divisive effect on the firing gain. We also quantitatively characterize the effect of shunting inhibition on threshold and saturation. Shunting inhibition applied by dynamic-clamp also has a non-linear effect on visual responses, not only reducing the response but also significantly changing the timing of the response. We confirm predictions that I_{BK} facilitates spike firing, despite this being a hyperpolarizing current. This effect is demonstrated by an increase in both the gain of the I/O transfer function, e.g. the f/I curve, and visual responses.

1 Introduction

A myriad of biophysical mechanisms underly the dynamics of the single neuron, including those governed by intrinsic signals, such as voltage or the concentration of second messenger systems, and by extrinsic signals, notably neurotransmitters. These properties have been studied for decades with remarkable quantitative precision primarily in reduced in vitro preparations. As well illustrated in the chapters of this volume, dynamic-clamp protocols are proving to be valuable tools in the study of these mechanisms in vitro, alongside classical methods such as current- and voltage-clamp electrophysiology and pharmacological protocols.

L.J. Graham (✉)
Neurophysiology of Visual Computation Laboratory, Laboratory of Neurophysics and Physiology, CNRS UMR 8119, Université Paris Descartes, 45 rue des Saint-Pères, 75006 Paris, France
e-mail: lyle@biomedicale.univ-paris5.fr

A. Destexhe, T. Bal (eds.), *Dynamic-Clamp*, Springer Series in Computational Neuroscience 1, DOI 10.1007/978-0-387-89279-5_7,

Certainly a fundamental assumption of cellular neurobiology is that the complex dynamics measured in vitro are relevant for the qualitative and quantitative establishment of functional properties – thus how the neuron operates in its natural environment – with respect to its own particular processing and in the emergent behavior of the intact neural network. Nevertheless, firmly establishing the relationship between specific biophysical mechanisms and functional properties requires in vivo studies, and like the in vitro case dynamic-clamp promises to be a powerful method. This application is still new, with dynamic clamp only rarely used in in vivo protocols (Brizzi et al., 2004; Manuel et al., 2005 in cat spinal cord, Haider et al., 2007 in cat visual cortex) and, to our knowledge, never associated directly with the measurement of functional responses.

In this chapter we will present work in progress on applying dynamic-clamp methods in rat and cat cortex in vivo to study synaptic and cellular mechanisms participating in functional responses to visual input. Specifically, we examined the roles of two mechanisms, first, synaptic inhibition mediated by gamma-amino butyric acid ($GABA_A$) receptors, or "shunting" inhibition, and second, the calcium- and voltage-dependent potassium "BK" current that is implicated in shaping the spiking response of, mainly, excitatory cortical neurons. We studied how both mechanisms contribute to the basic input/output (I/O) characteristics of cortical neurons, and to the expression of visual receptive fields. While of course basic I/O characteristics are studied in the in vitro preparation, specifically the response to artificial electrophysiological inputs, the in vivo preparation allows the study of these properties under more physiological conditions, as well as making for a more direct link to the study of functional responses to sensory input, which in turn necessitates the intact preparation.

2 Shunting Inhibition and the Neuronal Response

The interaction between synaptic inhibition and excitation can be classified into two modes – subtractive (linear) or divisive (non-linear) – depending whether the inhibition can be approximated as a current source or a conductance change, respectively. In particular, since its reversal potential is relatively near the operating point of the neuron, the impact of inhibition mediated by $GABA_A$ receptors would be expected to result mainly by an increase in conductance, or shunt. Our work and others (visual cortex: Borg-Graham et al., 1998; Monier et al., 2003; Anderson et al., 2000; 2001; Hirsch et al., 1998; Marino et al., 2005; Priebe and Ferster, 2005, 2006; auditory cortex: Tan et al., 2004; Wehr and Zador, 2003, 2005; Zhang et al., 2003; barrel cortex: Higley and Contreras, 2006; Wilent and Contreras, 2004, 2005; prefrontal cortex: Haider et al., 2006) has shown that functionally evoked excitatory and inhibitory synaptic responses are often associated with significant conductance modulations driven by reversal potentials near that for $GABA_A$ inhibition. Often these

modulations are sufficiently strong, thus from one to three times the neuron's resting input conductance, to fundamentally change the time scales and integrative properties of the involved circuits, as predicted by modeling studies (Bernander et al., 1991; Rapp et al., 1992; Destexhe and Paré, 1999; Rudolph and Destexhe, 2003). Taken together, these results support the idea that strong $GABA_A$-mediated inhibition plays an important non-linear role in functional synaptic integration.

Many experimental and theoretical studies have directly explored the impact of shunting inhibition with respect to basic I/O function at the cellular level. These studies typically have been made in the context of "background" synaptic activity, including those that employed dynamic-clamp-simulated synaptic input in vitro (Chance et al., 2002; Kreiner and Jaeger, 2003; Mitchell and Silver, 2003). These works have resulted in diverse interpretations: While some have presented evidence that $GABA_A$ inhibition affects I/O gain (Ingham and McAlpine, 2005), others have shown that at the spiking level the effect of shunting inhibition is mainly subtractive, thus linear, with respect to how many spikes are produced by a given level of excitatory input (Holt and Koch, 1997; Ulrich, 2003; Brizzi et al., 2004). Other studies have shown an explicit divisive effect of shunting inhibition, but only when the synaptic input is fluctuating, or "noisy" (Chance et al., 2002; Mitchell and Silver, 2003), or when dendritic non-linear integration is considered (Capaday and Van Vreeswijk, 2006), or with both conditions, thus fluctuating input in dendrites (Prescott and De Koninck, 2003).

To clarify these questions, we investigated the quantitative role of shunting inhibition in vivo on the I/O transfer function and on visual responses in rat and cat visual cortex, using the dynamic-clamp protocol. In particular, we wanted to establish the essential nature of the interaction between shunting inhibition and excitation, without making assumptions on the input dynamics. Our results confirmed that simulated shunting inhibition, at strengths consistent with that evoked during visual responses and with no a priori temporal structure (e.g. step inputs), has a significant non-linear as well as linear effect on the basic I/O transfer function of cortical neurons.

A large body of work has focused on the important question of how dynamical variability in the neuron state, broadly defined as "noise," affects I/O properties. For example, earlier studies have demonstrated the qualitative impact of membrane voltage fluctuations per se on the I/O relation of neurons, which may arise from distinct interactions with, on one hand, the conductance state of the cell and, on the other, the threshold characteristics of the spike mechanism (Fellous et al., 2003). In our experiments, we explicitly wanted to minimize the role of fluctuations in the effect of shunting inhibition. Not only does the use of simple inputs help establish a baseline for the effect of shunting inhibition, under some conditions tonic activation of $GABA_A$ receptors may have an important functional consequence (Stell et al., 2003; Semyanov et al., 2004). Our preliminary results also indicate that artificial shunting inhibition applied during the visual response has an effect that is more

complex than a simple reduction of spike output, and thus can modulate the timing of the response.

3 The BK Current and the Neuronal Response

The pattern of spike responses following a given input are determined in large part by the complex interaction of a neuron's intrinsic membrane channels. In particular, diverse potassium channels in a given cell type may span a large range of kinetic timescales, allowing the identification of specific dynamical characteristics of the spike output with specific channel types. As an example, the timing of spikes emitted by regular adapting, typically excitatory, neurons (following the physiological classification of neurons according to their firing patterns in response to sustained current inputs, e.g. McCormick et al., 1985) is characterized by three different time scales of adaptation of their firing frequency, roughly tens of milliseconds, hundreds of milliseconds, and one or more seconds. Furthermore, each time scale is associated primarily (but not exclusively) with specific K^+ currents with complementary kinetics, respectively the BK current (I_{BK}), the M current, and the after-hyperpolarization (AHP) current (reviewed in Storm, 1990). The M and AHP currents are increasingly activated with each additional spike, so that these hyperpolarizing K^+ currents act in the standard fashion to progressively counteract the depolarizing stimulation current.

The role of I_{BK}, in contrast, appears to be opposite to this classical action of K^+ current on spike firing. The large conductance BK channels (also called BKCa, KCa1.1, MaxiK, *Slo*) (Vergara et al., 1998) underlying I_{BK}, whose activation and inactivation are Ca^{2+} and voltage dependent, are found in different neuronal types including regular adapting cortical and hippocampal pyramidal cells. Various earlier studies have suggested that a downregulation of I_{BK}, either from experimental pharmacological manipulations or secondary to pathological conditions, is associated with increased excitability (reviewed in Gu et al., 2007). From our own theoretical modeling, we have proposed an explicit connection between this current and excitability, thus that fast firing adaptation in regular adapting neurons – the initial slowing of firing frequency over the first ten or so spikes – is due to the *removal*, not enhancement, of I_{BK} (Graham, 2006, 2007). First, we propose that the shortening of the spike by activation of I_{BK} during spike repolarization reduces the activation of other, slower, K^+ currents. Second, modeling (Borg-Graham, 1987, 1999) has predicted that at the end of spike repolarization I_{BK} inactivates extremely quickly, giving rise to the fast after-hyperpolarization (fAHP) in this cell type. This inactivation is much faster than that of other K + currents, thus when there is a prevalence of I_{BK} this allows a more rapid subsequent depolarization to continued stimulation, and thus more rapid firing of the next spike. Third, the local hyperpolarization caused by somatic I_{BK} is

immediately counteracted by dendritic charge, accounting in part for the depolarizing phase of the fAHP. In the case of a constant depolarizing current, this results in a faster charging of the soma membrane as compared to the response to the stimulus current alone (Borg-Graham, 1987, 1999; Storm et al., 1987). Fourth, the relatively hyperpolarized peak of the fAHP due to I_{BK} contributes to the removal of inactivation of the transient Na^+ current underlying the spike, and thus lowering spike threshold for the next spike. Finally, to account for the disappearance of the fAHP after several spikes, our model predicted that I_{BK} de-activates after several spikes, subsequently allowing other, slower, K^+ currents to dominate and to reduce the firing frequency (Borg-Graham, 1987, 1999). These ideas were supported by our earlier work measuring how I_{BK} modulates spike shape (Shao et al., 1999; specifically Figs. 3 and 6) in hippocampal pyramidal cells. This hypothesis was more explicitly explored in recent work by Storm and colleagues (Gu et al., 2007), who showed that pharmacological blocking of I_{BK} during in vitro recordings in hippocampal pyramidal cells strongly reduces the frequency of the first few spikes in a spike train evoked by a constant current step.

The experimental results to date, however, cannot establish a direct link between I_{BK} and spike frequency, simply because pharmacological manipulations may impact multiple mechanisms. We have therefore studied these predictions at the biophysical level, by combining pharmacological methods with dynamic-clamp, in order to show that I_{BK} alone can account for an acceleration of neuronal firing. Thus, we recorded from regular adapting cortical neurons with pipettes containing the fast Ca^{2+} buffer BAPTA. BAPTA prevents a sufficient increase of the intracellular Ca^{2+} concentration during a spike to activate I_{BK}, thus effectively reducing or even disabling this current (Velumian and Carlen, 1999). In our protocol we verified the control firing properties of the recorded cell immediately after whole-cell access before diffusion of BAPTA. We then continued to make f/I sequences to see if the expected disappearance of the fAHP, as an indication of a blocked I_{BK}, is correlated with a reduction of both fast adaptation and the peak firing rate. The next step was to restore a phenomenological I_{BK} by using a dynamic-clamp model inspired from that proposed from our earlier work (Borg-Graham, 1987, 1999; Shao, et al., 1999). In this manner, the fast adapting component of the recorded cell may be added or removed at will during subsequent protocols. We then explored how fast adaptation influences visual processing by comparing the spike response to a given visual stimulation with and without the dynamic-clamp I_{BK} model. Specifically, we propose that I_{BK} acts to both increase and to phase advance the response for stimulus durations – tens to one hundred milliseconds – that correspond to natural vision. Thus I_{BK}, and by extension pathways that modulate it in vivo, may dynamically adjust the response of excitatory neurons, perhaps qualitatively changing the receptive field type when considered with the dynamics of synaptic input tuning over the same timescales.

4 Methods

4.1 Animal Preparations

All experimental protocols described here were made in order to maximize the animal's well-being and comfort, and have been approved by the Direction Départementale des Services Vétérinaires. Sprague–Dawley Rats (male, 300–500 g) were anesthetized with urethane (1.5 g/kg i.p.). Young adult male cats (3.2–4.2 kg) were initially anesthetized with an injection of ketamine and xylazine (1 and 10 mg/kg, respectively, i.m.). Cats were intubated for artificial respiration and fitted with a urinary catheter. All surgical manipulations (incisions, pressure points) were preceded by local injections of lidocaine. After surgical preparation and anesthesia induction, animals were placed in a stereotaxic holder (Narishige model SN-3 N). In the case of cats, anesthesia was maintained by intravenous perfusion of propofol (5 mg/kg/h for anesthesia) and sufentanil (0.004 mg/kg/h for analgesia), delivered in Ringer 5% glucose. Rate and volume of the respiration pump was adjusted as necessary to maintain a relative PCO_2 between 3 and 4.5%. In order to eliminate natural eye movements, cats were paralyzed by an induction dose of pancuronium (0.3 mg/kg), followed by a continuous perfusion of pancuronium (0.3 mg/kg/h) delivered in Ringer 5% glucose solution. For cats, in order to reduce respiratory movement at the cortex, a bilateral pneumothorax was performed. For cats, gas-permeable contact lenses (Metro Optics) were used to prevent cornea degradation, with local application of atropine methyl nitrate (for pupil dilation) and neosenephrine (to retract the nictitating membrane), and correction lenses were chosen as appropriate to focus back-projections of the optic disc on the visual stimulus display. Rectal temperature was monitored and maintained in both rat and cat at 37.5 $\pm$ 0.5°C by a heating blanket (CWE Instruments). Heart rate was monitored to indicate the depth of the anesthesia, and as necessary supplemental urethane was injected i.p. (rat) or adjustment of propofol perfusion (cat). For whole-cell patch recordings, craniotomies were performed either above the somatosensory cortex (rat) or above the primary visual cortex (both animals). Experiments typically lasted for 5–6 h for rats and 2–3 days for cats. At the end of each experiment euthanasia was performed with an overdose injection of sodium pentobarbital (i.p. rat or i.v. cat).

4.2 Computational Implementation

Experiment control software (Surf Lab, in-house software) including visual response data acquisition and dynamic-clamp protocols was made with the LabVIEW system (v7.1, National Instruments). The dynamic-clamp software was based on the G-clamp system (v1.2, Kullmann et al., 2004), also written in LabVIEW. Data acquisition was made at 40 khz for both current and voltage, and update of the dynamic-clamp current command was also nominally at 40 khz.

The entire system (Fig. 1) consisted of three computers, including an "executive" computer running Windows XP (Dell Precision 650 – Intel Xeon 2.66 Ghz, 1.5 GB RAM) which ran the Surf Lab and G-clamp programs simultaneously, a real-time computer (generic computer based on an Intel Pentium 4 3.2 Ghz processor with 1 GB RAM) implementing the actual dynamic-clamp routines, and a second Windows XP computer dedicated to generating visual stimuli (Dell Optilex GX620 – Intel Pentium 4 3,2 Ghz, 1 GB RAM). Communication between the executive computer and the dynamic-clamp computer (commands from executive to dynamic-clamp; data from dynamic-clamp to executive), and between the executive and the visual computers (commands from the executive to the visual) was made by a TCP/IP serial link. Synchronization timing from the visual computer for the executive computer was made via a dedicated line

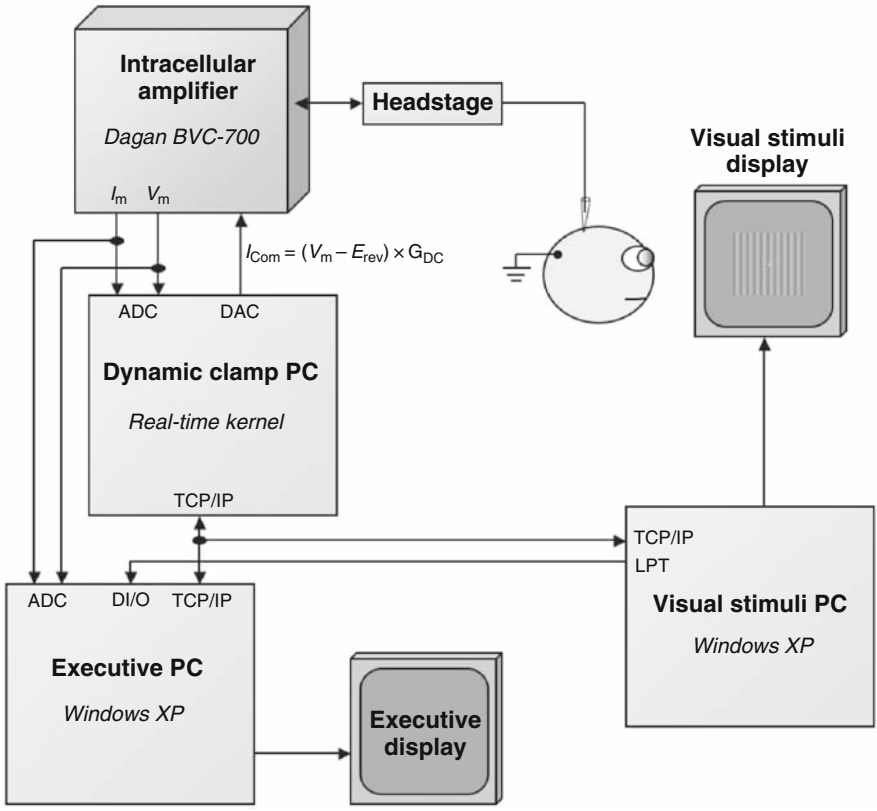

Fig. 1 System diagram of the in vivo dynamic-clamp system. ADC – analog–digital converter, DAC – digital analog converter, DI/O – digital input/output port, TCP/IP – TCP/IP serial port, LPT – parallel (line printer) port, I_m – membrane current amplifier output, V_m – membrane voltage amplifier output, I_{Com} – membrane current command amplifier input, G_{DC} – dynamic-clamp conductance model, E_{rev} – reversal potential of G_{DC}

from the parallel port (LPT) on the visual computer, and read on a digital I/O line on the data acquisition card of the executive computer.

The Surf Lab LabVIEW program controlled the visual experiments, and the G-clamp LabVIEW program controlled the dynamic-clamp routines. G-clamp has two components, one that includes the user and file system interface that runs on the executive computer, and one which runs on the real-time computer (under a real-time kernel, Pharlap), with a real-time version of LabVIEW. Surf Lab was used alone for running visual protocols under either current or voltage clamp. G-clamp was used alone for running current-clamp and dynamic-clamp protocols aimed primarily at measuring intrinsic properties, such as *f–I* and *f–G* curves. Finally, G-clamp was modified to include a continuous running mode, which allowed a particular dynamic-clamp conductance to be applied in the background while a visual protocol was simultaneously run under the control of Surf Lab.

Visual stimulation was generated using the VisionEgg software package (Straw et al., 2006). For a given protocol, stimulation parameters were sent to the visual stimulus computer from the executive computer running Surf Lab, followed by stimulus timing information sent in the opposite direction over the LPT line. Stimulus patterns typically consisted of moving sinusoidal gratings with a temporal frequency between 1 and 4 Hz, a spatial frequency typically between 0.1 and 0.8 cycles per degree, masked with a Gaussian window with width (sigma) between 10 and 40°. Orientation dependence was measured with gratings whose directions varied over 360° at increments of 45°, presented in random order for durations ranging from 0.5 to 2 s. The results presented here are from gratings with a contrast of 100%.

Whole-cell patch recordings were made with a Dagan Instruments BVC-700 intracellular amplifier. The membrane voltage output was low-pass filtered at 10 kHz with the amplifier's built-in filter, and the dynamic-clamp-calculated current was controlled via the amplifier's current command input in current-clamp mode.

4.3 Dynamic-Clamp Models for Shunting Inhibition and $\mathbf{I}_{BK}$

Our present study of how shunting inhibition affects firing properties uses the simplest possible model for the synapse, namely an imposed conductance with a reversal potential of –70 mV, applied either as a constant conductance step in the case of measuring firing rate in response to simultaneous excitatory conductance steps (reversal potential 0 mV), or as a continuous conductance during the measurement of visual responses.

Our study of I_{BK} employs dynamic-clamp to provide an intermediate channel model, specifically one that is not a conductance model in the standard sense. The native I_{BK} channel is co-localized with calcium channels (predicted by Borg-Graham, 1987, 1991, and subsequently verified by Marrion and Tavalin,

1998), allowing for a fast and sensitive dependence on calcium entry during the spike. In the I_{BK} model used here, this dependence on nearby calcium entry was implicit by turning on the current at the beginning of spike repolarization, defined solely in terms of the voltage trajectory. Once turned on, the I_{BK} model provided a fixed, predefined repolarizing current, typically on the order of 2–4 nA. The I_{BK} model was then turned off when the membrane voltage reached a fixed, predefined value, typically –60 mV, equivalent to the minimum value of the fAHP. As a final simplification, in the results presented here, there is no inactivation of the I_{BK} model, contrary to the real I_{BK}. Despite these simplifications, as shown in Fig. 5, the amplitude and duration of this basic model is consistent with the dynamics predicted by a biophysically detailed model.

An important motivation of this approach is that the resulting dynamic-clamp current is less susceptible to inevitable electrode artifacts. Thus, given the large current and fast dynamics of the biophysical model prediction, a true conductance model will be much more prone to "ringing" at onset and de-activation than the simple model. Future work will address these challenges to allow a more sophisticated and accurate I_{BK} dynamic-clamp model, e.g. by incorporating a predictive model of the electrode artifact (e.g. with the methods described in the chapter by Brette et al.) in the I_{BK} model to distinguish online the expected "true" membrane voltage from the signal arising from the incompletely compensated electrode circuit.

4.4 Electrophysiological Recordings

All recordings were done with the blind whole-cell patch-clamp technique in vivo, following protocols described previously (Borg-Graham, et al., 1998). We used both thick wall borosilicate glass capillaries with filaments and thin wall borosilicate glass capillaries without filaments to make the pipettes (respectively OD 1.5 mm, ID 0.84 mm and OD 1.5 mm, ID 1.12 mm, World Precision Instruments). Pipettes were pulled in a horizontal puller (Sutter Instruments model P-97) in three steps in order to have a small tip ($\sim$2 μm) and a long and thin taper. Pipette resistance prior to recording was kept to between 5 and 8 MΩ. Pipettes were filled with a solution containing (in mM) K-gluconate 140, KCl 4, Hepes 10, $MgCl_2$ 2, ATP 4, GTP 0.4, EGTA 0.5 and, depending on the case, 0.01% DMSO and 10 mM BAPTA. The osmolarity of the intracellular solution was adjusted to 285–295 mOsmol, and the pH was set to 7.2–7.5.

Whole-cell patch electrodes were introduced into the cortex under current-clamp mode, using a –1 nA amplitude, 10 Hz 50% duty cycle current pulse train to monitor the change in resistance as the electrode approached a cell, and with the amplifier bridge circuit balanced to compensate for the electrode resistance. For penetration of the cortical surface, the electrode was initially advanced using a motorized micromanipulator (Narishige model SM-21) in continuous

mode (~250 μm/s), with a positive pressure of 100–300 mmHg applied to the interior of the pipette. After penetration of the cortical surface was detected by a transient deflection of the measured voltage, the electrode was advanced until a predetermined depth (100–2,000 μm) was reached. The electrode was then retracted in continuous mode for 100–200 μm, and the positive pressure immediately reduced to 40–70 mmHg. The voltage offset was then adjusted according to the tip offset potential (–14 mV measured with our K-gluconate solution). The electrode was then advanced in 3–4 μm steps until a deflection of the voltage response equivalent to 5–10% of the unbalanced response was observed, reflecting contact with a cell membrane. At this point the positive pressure was removed and whole-cell access achieved by one of two methods. The first method maintained the 1 nA current pulse train, resulting in spontaneous electroporation of the membrane within several seconds as a result of large voltage fluctuations following giga-seal formation (Schramm and Graham, 2007). The second, more traditional, method was made by monitoring slow formation of the giga-seal with small (100 pA) current pulses, followed by brief application of suction on the pipette interior.

4.5 Bridge Balance – Estimation of Access Resistance

A fundamental challenge for single patch electrode dynamic-clamp protocols is the accurate online estimation and correction of the access resistance once in the whole-cell patch configuration. The first step for achieving this was to adjust the capacitance compensation on the amplifier during applied current pulses in current-clamp mode to the maximum degree without inducing oscillations. In our protocols we then used two criteria in current-clamp mode for the subsequent estimation of the bridge component (Borg-Graham et al., 1998): First, reasonable estimates of the bridge component are possible when there is a clear distinction of the electrode versus cell time constants during the response to a subthreshold hyperpolarizing or depolarizing current step (typically ±100 pA). Once the bridge is adjusted according to the differential time constants, the estimate was verified by noting any change in the height of the initial spike in response to a series of increasing suprathreshold current steps. Thus, a good estimate of the access resistance and subsequent stability of the compensation was contingent on a variation of spike height less than approximately 5 mV over a several hundred picoampere range of current step amplitudes. In our experience, adequate estimation and subsequent cancelation with the bridge balance adjustment of the amplifier necessitates an access resistance below 40–50 MΩ.

A typical example of the distinct bridge (electrode) and cell components that we find in the response to a current step is shown in Fig. 5, in the context of the I_{BK} dynamic-clamp protocols. In the center panels the voltage response (upper panel) is shown to a depolarizing 500 pA current pulse (lower panel), from a whole-cell patch recording made in rat somatosensory cortex in vivo. In this

trace the I_{BK} dynamic-clamp model is turned on, as indicated by the 4 nA hyperpolarizing pulse during the repolarizing phase of the action potential. In this example, the access resistance was estimated to be 26 MΩ, with a resting input resistance of the neuron of 55 MΩ. A small fast bridge component is seen at the start of the depolarizing current pulse, followed by larger but still very fast bridge components on the leading and trailing edges of the large model I_{BK} pulse. The much slower response component of the neuron's "linear" response – the linear membrane time constant of this cell was estimated at 9.5 ms – can be appreciated by the trajectory of the depolarizing voltage response over many milliseconds prior to the action potential.

5 Results

5.1 The Effects of Shunting Inhibition on the Input–Output Function and Visual Responses

To evaluate the quantitative effect of shunting inhibition on the I/O relation of a neuron, we applied conductance steps comprised of different combinations of artificial excitatory and inhibitory components, while measuring the resulting spike trains. Excitatory steps (reversal potential = 0 mV) and inhibitory steps (reversal potential = –70 mV) were calibrated relative to each neuron's resting input conductance, thus Gex(rel) and Ginh(rel). This procedure facilitated comparisons of firing properties across diverse cell populations, notably over a range of resting input resistances. Intrinsic noise was estimated by measuring the standard deviation of the membrane voltage at rest. Quantitative fits to *f–G* characteristics were made with a sigmoid expression, after excluding responses past firing saturation, if any, with gain defined as the maximum slope of the sigmoid fit. Saturation was estimated directly from the asymptotic maximum of the fitted sigmoid, whenever the fit showed a significant deceleration after the maximum slope.

Figure 2 shows *f–G* characteristics for increasing steps of constant dynamic-clamp excitatory "synaptic" conductance, with different levels of simultaneous shunting "synaptic" conductance. Increasing levels of shunting inhibition, Ginh(rel), tended to shift the *f–G* curve to the right – thus a linear interaction with the excitatory input – as well as reduce the slope or gain of the characteristic – thus a non-linear interaction with the excitatory input. This figure also shows two example traces, with excitation alone (bottom left) and with added shunting inhibition (bottom right), in the latter case with the excitation sufficient to give approximately the same number of spikes as the no inhibition condition. These traces show explicitly how shunting inhibition significantly diminishes the efficacy of a depolarizing current: In part because of the strongly amplified negative currents during each spike supplied by the inhibition, the average level of depolarizing current for evoking the same number of spike is significantly larger than when there is no inhibition.

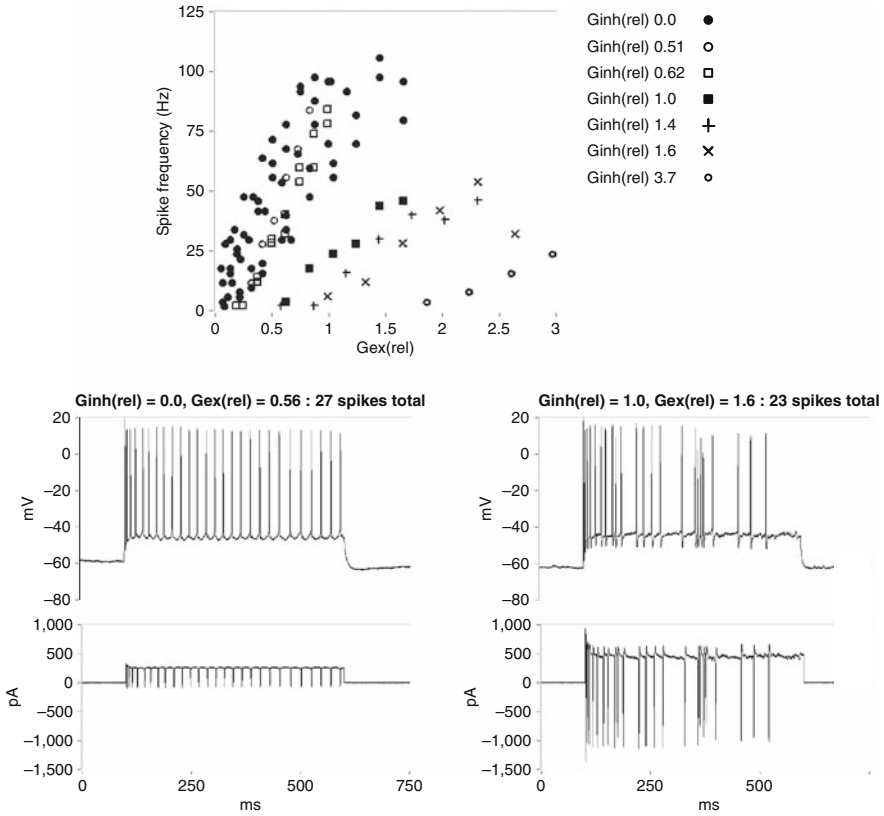

Fig. 2 The effect of dynamic-clamp "shunting inhibition" on the *f–G* characteristic of a regular adapting neuron recorded in rat cortex in vivo. *Top*: *f–G* characteristics measured with simultaneous steps of shunting inhibition ranging from 0 to 3.7 (values normalized to the neuron's resting conductance). *Bottom left*: Voltage and dynamic-clamp current in response to a pure excitatory "synaptic" conductance step, Gex(rel) = 0.56. *Bottom right*: Voltage and dynamic-clamp current in response to a conductance step combining an excitatory "synaptic", with Gex(rel) = 1.6, and shunting "synaptic" conductance with Ginh(rel) = 1.0, giving approximately the same number of evoked spikes as Gex(rel) = 0.56 with no inhibition

Figure 3 shows population results from a total of 27 regular adapting neurons recorded in vivo in rat and cat cortex, quantifying the effect of shunting inhibition on firing properties measured with *f–G* protocols. The dependence of *f–G* gain on inhibition (top left) and the dependence of Gex(rel) threshold on inhibition (top right) summarize the most basic non-linear and linear interactions, respectively, between excitation and inhibition, at least with respect to average firing over 500 ms of constant input. Quantitatively, the non-linear effect over the population is given by an average normalized sensitivity of –0.44 of the firing gain to shunting inhibition. This means that, on average, a shunting input equivalent to a neuron's resting conductance reduces the firing gain in

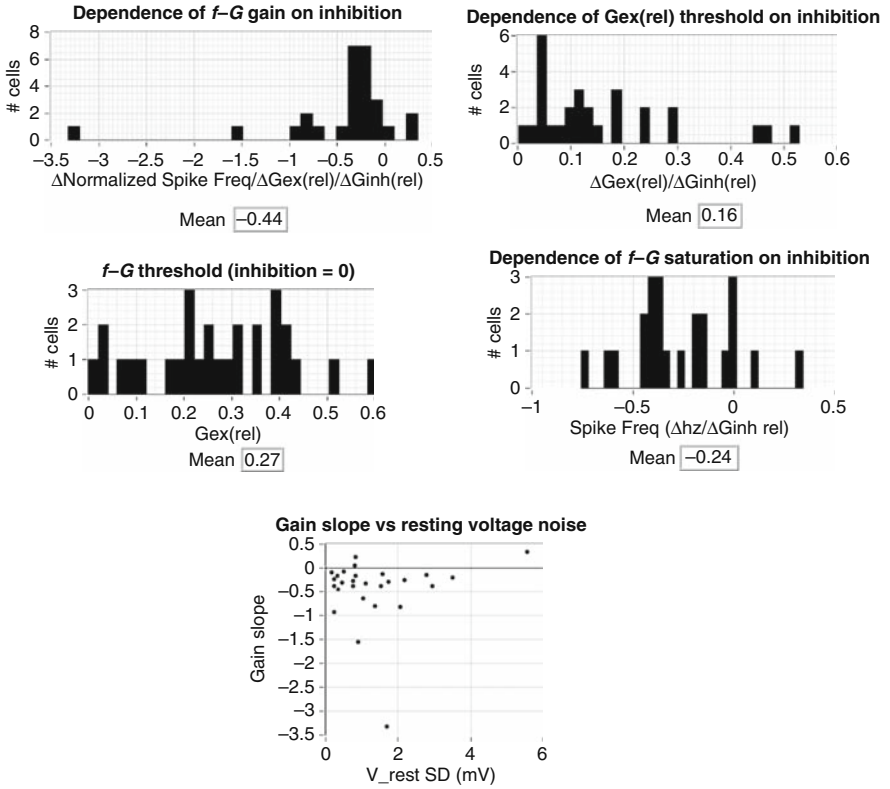

Fig. 3 Population results from 27 regular adapting neurons recorded in vivo in rat somatosensory and visual cortex ($N = 14$) and cat visual cortex ($N = 13$), quantifying the effect of artificial "shunting inhibition" on firing properties measured with *f–G* protocols. All values of excitatory and inhibitory "synaptic" dynamic-clamp conductance inputs are normalized to the resting input conductance of each neuron. Gain measures (e.g. ΔNormalized Spike Freq/ΔGex(rel)) are normalized with respect to the firing gain in the absence of artificial shunting inhibition. The "*f–G* threshold (inhibition = 0)" plot shows the distribution of minimum values of the normalized excitatory input (Gex(rel)) necessary to evoke spikes, while the "Dependence of Gex(rel) threshold on inhibition" plot shows the sensitivity of this value with simultaneous application of shunting inhibition. For the measure of "Dependence of saturation on inhibition," which shows how the measured (or in some cases extrapolated) maximum firing frequency is sensitive to shunting inhibition, a subset of 24 out of 27 neurons were analyzed which showed saturation for large values of excitation. The plot at bottom shows the lack of correlation between the gain sensitivity to inhibition ("gain slope") and the intrinsic fluctuations of the membrane potential at rest

response to synaptic excitation to 44% the gain when there is no inhibition. We also quantified the threshold excitatory synaptic input, analogous to the more classic measure of threshold current input, or rheobase. Over the population, the average minimum synaptic excitation for eliciting spikes with no inhibition was 0.27, again normalized to the resting conductance (middle left). The

sensitivity of this value with respect to the simultaneous presentation of shunting inhibition encapsulates the "linear" interaction between excitation and inhibition: Over the population the average normalized increase of the threshold excitatory input, e.g. the rightward shift of the *f–G* curve, with increasing inhibition (also normalized to the resting conductance) is 0.16 (top right). Thus, on average, for a shunting input equivalent to the resting conductance the threshold excitatory input increases by 16%.

Neuronal firing frequencies do not increase without limit for stronger inputs, and for realistic inputs the expected saturation may be relevant for coding. For those cells in our data set in for which saturation could either be measured directly or estimated (24 out of 27), we measured the effect of shunting inhibition on the saturation frequency. We found that, on average, shunting inhibition equivalent to the resting conductance of a neuron reduced the saturation firing frequency by 24% (middle right). Finally, in light of various reports describing a necessary role of noise for shunting inhibition to have a non-linear effect on firing gain, we measured the "intrinsic" voltage noise for each neuron in the resting state. From these measurements (bottom) we found no correlation between the sensitivity of firing gain to inhibition ("Gain Slope," as shown in the top left), indicating that for our experimental conditions, neither "noise" in the artificial inputs, nor "noise" intrinsic in the network are necessary to see a significant non-linear effect on firing rates between shunting inhibition and excitation.

Figure 4 illustrates the general suppression effect of artificial shunting inhibition on the visual response of a neuron in cat visual cortex. This cell showed a very tight selectivity to the orientation of a moving grating, giving a spike response only when the direction of motion was along the 90–270° axis (top right, tuning measured at 45° increments). This tuning was unchanged when a constant artificial shunting inhibitory input was added with the dynamic-clamp (middle right, Ginh(rel) = 1), whereas the number of spikes was significantly reduced by about half. Furthermore, shunting inhibition affected the coding of the response, tightening the temporal spread of the evoked spikes (compare spike times with and without the shunt, top left and middle left, respectively). Notably, the relatively strong inhibition (consistent with amplitudes evoked by visual stimuli, Borg-Graham et al., 1998; Monier et al., 2003) did not simply annihilate the response, but rather had a more nuanced effect.

5.2 *The Effects of* $\mathbf{I}_{BK}$ *on the Input–Output Function and Visual Responses*

Figure 5 illustrates the relationship between I_{BK} and spike repolarization as predicted by a biophysically detailed model (Borg-Graham, 1987, 1998), and recreated with a dynamic-clamp approximation during an in vivo recording of a rat cortical neuron with the native I_{BK} blocked with intracellular BAPTA.

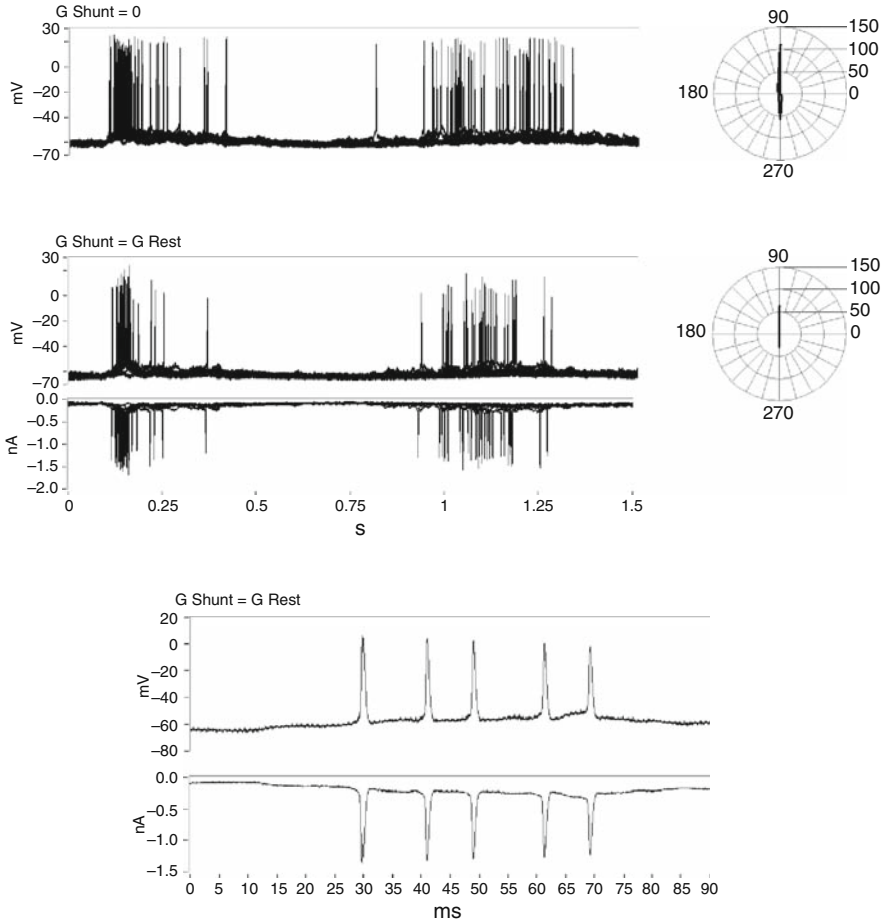

Fig. 4 The effect of artificial shunting inhibition during the visual response of a neuron in cat visual cortex in vivo. Top traces show superimposed voltage recordings of ten trials in response to a preferred stimulus (90° direction, 1 hz drifting sinusoidal grating) with the dynamic-clamp shunting inhibition turned off (G Shunt = 0) and on (G Shunt = G Rest), in the latter case showing the associated current traces supplied by the dynamic-clamp, thus the current through the "GABAA synapse." An expanded view of one response with shunting inhibition is shown in the lower traces

The simulated action potentials at the top left, in response to a short current pulse, shows the control condition with an active I_{BK} mediating the fAHP (thick trace), and the case with I_{BK} disabled (thin trace) by blocking calcium currents. The simulated membrane currents at bottom left show the principal repolarizing K^+ currents for the control condition, including I_A, I_{DR}, and I_{BK} (light gray, gray, and black traces, respectively) (adapted from Borg-Graham, 1999). The predicted repolarization trajectories with and without I_{BK} are well reproduced in the experimental recordings (right), demonstrating that the

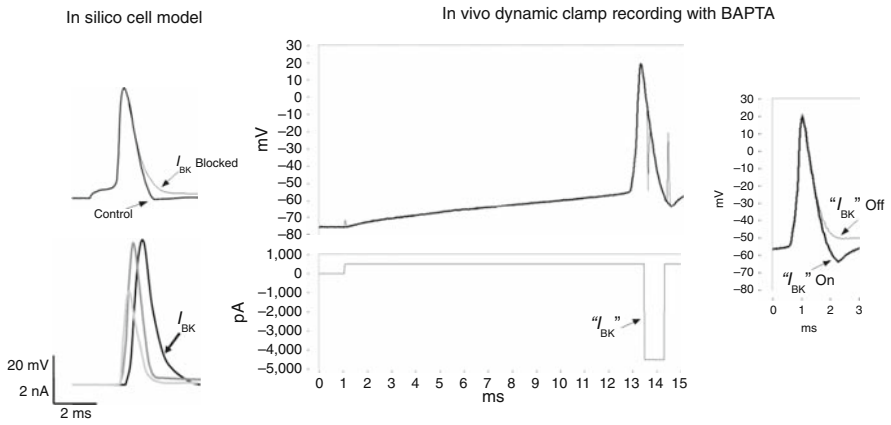

Fig. 5 Comparison of predictions of biophysically detailed model of hippocampal pyramidal cell with respect to the kinetics and voltage signature of I_{BK} (*left*), and electrophysiological dynamic-clamp recording with a simplified version of *I*BK injected during the repolarization of an action potential, of a regular adapting neuron recorded in rat somatosensory cortex in vivo (*middle and right*), with the calcium buffer BAPTA in the pipette acting to prevent full activation of the native I_{BK}. *Top middle* – Evoked action potential with I_{BK} dynamic-clamp model enabled. Thin trace is original voltage recording showing bridge artifacts from the current pulse transitions, while the thick trace has these artifacts removed by a simple algorithm that interpolates the voltage during a 200 μs interval whenever the current derivative exceeds a maximum value (here, 2nA/ms). *Bottom middle* – total clamp current supplied by recording amplifier, including a long 500 pA depolarizing step and a short "I_{BK}" pulse triggered by the repolarizing phase of the spike. Right – the same action potential from middle top (*thick trace*) superimposed with an action potential evoked by same depolarizing pulse, but with I_{BK} dynamic-clamp disabled (*thin trace*)

simple I_{BK} model captures the essential effect of this current at the level of the membrane voltage.

As mentioned earlier, the simple I_{BK} model shown here does not include a deactivation component that is seen over the first few spikes, and that we have explored in previous work (Borg-Graham, 1987, 1999; Shao et al., 1999). Therefore, this I_{BK} model provides a sort of upper bound of the effect of the native I_{BK} over a prolonged spike train. The augmentation of the overall *f–I* I/O relation by the artificial I_{BK} dynamic-clamp current is seen in Fig. 6, although the final impact on spike timing by the I_{BK} model is complex. Thus, for this cell the first interspike interval in the control case is shorter (i.e. the instantaneous frequency is higher) than that when the model I_{BK} is enabled, indicating a regime (possibly due in part to an incomplete block of the native I_{BK}) in which the extra hyperpolarizing current shows the classical effect of reducing excitability. Overall, though, for larger amplitudes of the artificial I_{BK} the interspike interval becomes shorter, being less than the control case for progressively earlier intervals (top right, for a current step of 350 pA). Again, this effect is probably larger than provided by the native I_{BK} because the model does

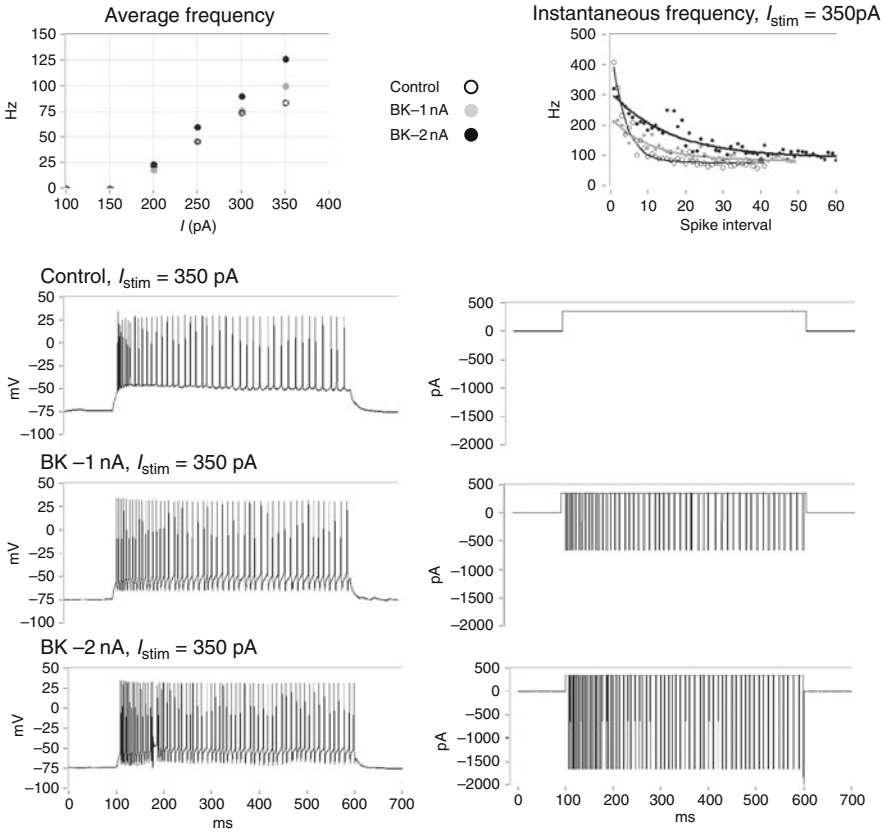

Fig. 6 I_{BK}-dependent *f–I* characteristics, measured in cat visual cortex in vivo with whole-cell patch recordings with the calcium buffer BAPTA in the pipette. The control case is with the dynamic-clamp I_{BK} disabled

not de-activate. Nevertheless, in the case of visual responses to moving gratings, as shown in Figs. 7 (rat visual cortex) and 8 (cat visual cortex), the evoked synaptic dynamics typically fluctuate to a large degree, as opposed to being steady and constant (cf. response to a current step), and therefore the lack of de-activation in the I_{BK} model is of secondary importance for these protocols. In Fig. 7, from rat visual cortex, the cell shows a relatively weak, but consistent, tuning preference for the 135–315° axis that is maintained when the overall response is increased with the dynamic-clamp I_{BK}. Figure 8, from cat visual cortex, compares the preferred response with the native I_{BK} blocked, and with the native I_{BK} replaced by the dynamic-clamp I_{BK}. The addition of I_{BK} not only increases the response, but, relevant to temporal coding, increases the "burstiness" of the evoked responses, i.e. tending to make the cell respond with a couplet or triplet of spikes, rather than just one, in response to a brief stimulus.

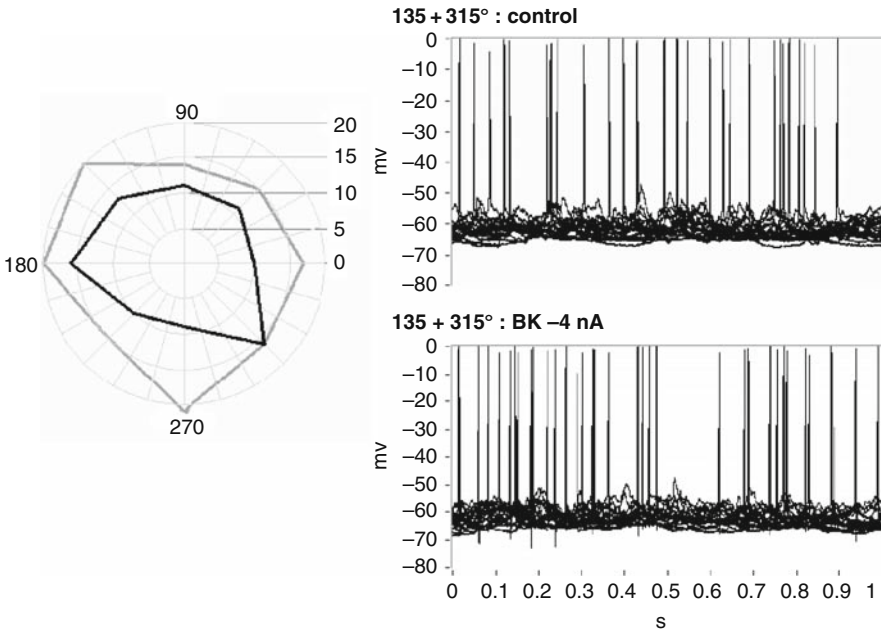

Fig. 7 I_{BK}-dependent visual response characteristics, measured in rat visual cortex in vivo with whole-cell patch recordings with the calcium buffer BAPTA in the pipette. *Left* – polar plot of total spike response over ten trials as a function of direction of drifting grating (Control, black; with dynamic-clamp I_{BK}, gray). *Right* – Preferred responses to oriented drifting grating with (*bottom*) and without (*top*) artificial I_{BK} (superimposed voltage responses of ten trials each of gratings moving toward 135 and 315°)

6 Discussion

Our results reveal that levels of shunting inhibition in the cortex, consistent with that evoked by functional stimuli, induces not only a linear shift in the spiking threshold, but also a reduction of the gain of the transfer function. This general effect holds as well for the case of visual responses. We are now working on a global quantification of this effect and on relating our findings with the previous studies. Particularly, in most previous work, the maximum shunt applied is less than or equal to the resting conductance, whereas in our protocols we test larger values of the relative shunt, which may account for some differences in the results. Moreover, we found no obvious relationship between intrinsics membrane voltage fluctuations and the sensitivity of firing gain on applied shunting inhibition, contrary to previous reports which have claimed a necessary role of "noise" in any non-linear effect of shunting inhibition. We also find that the saturation point of the transfer function is reduced with shunting inhibition. Finally, we found (Graham et al., 2007) that these effect are conserved among the various classical electrophysiological cell types in mammalian

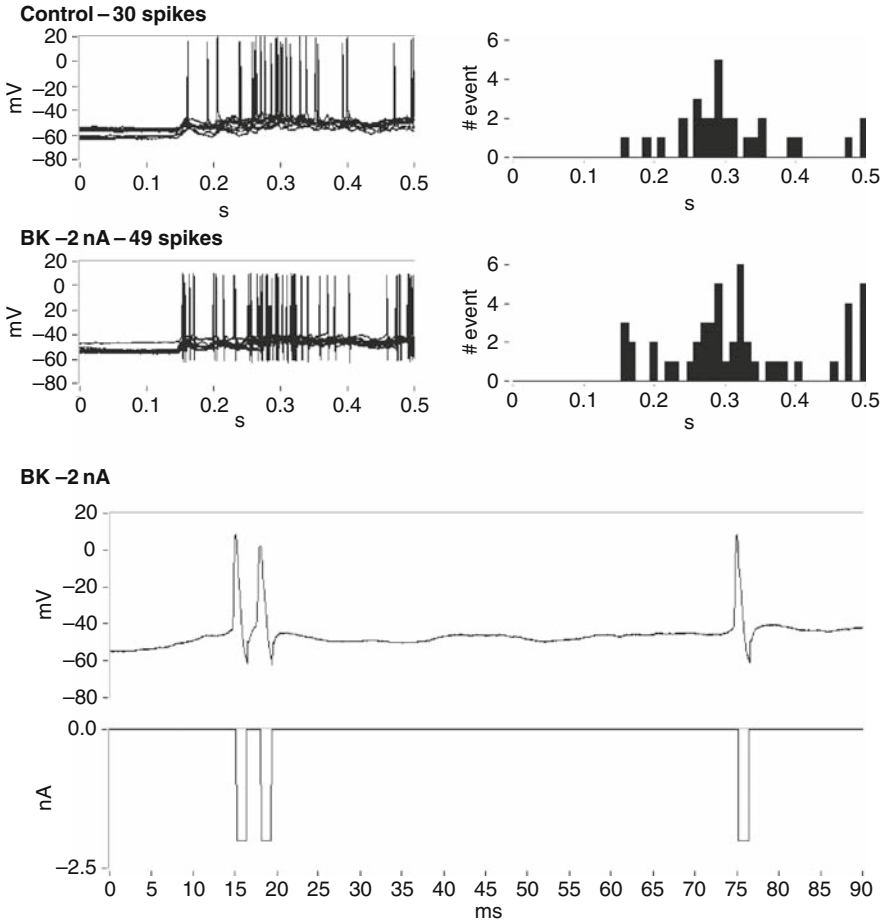

Fig. 8 I_{BK}-dependent visual response characteristics, measured in cat visual cortex in vivo with whole-cell patch recordings with the calcium buffer BAPTA in the pipette. *Top* – preferred responses to oriented moving grating without (control) and with (BK –2 nA) artificial I_{BK}. Left panels show superimposed voltage traces from ten trials, and right panels show post stimulus time histograms (PSTHs) of the evoked spike times. *Bottom* – Example voltage and dynamic-clamp current response with artificial I_{BK}. Compare with the similar hyperpolarizing spike currents supplied by artificial shunting inhibition in Fig. 4 (*bottom*)

cortex, thus regular adapting, fast spiking and bursting neurons (data not shown), which emphasizes the general importance of shunting inhibition control on neuronal information processing.

Our results on I_{BK} confirm previous hypotheses that this current, although hyperpolarizing, actually serves to accelerate the neuronal response. We verified this prediction at the biophysical level with our in vivo protocols by applying a minimal I_{BK} model with the native I_{BK} attenuated by the addition

of the calcium buffer BAPTA in the recording pipette. The simple I_{BK} model accelerated the response not only evoked by injected current steps, but also during "natural" visual responses.

It is interesting to contrast the complementary effects of shunting inhibition and I_{BK}, especially if we consider that, on one hand, in general both membrane currents act in opposition to depolarizing inputs, since both have reversal potentials near or below the resting potential. On the other hand, in particular as implemented in these experiments, the two mechanisms have completely complementary kinetics: The shunting inhibition model that we tested is essentially a tonic conductance input with no intrinsic kinetics, whereas the model I_{BK} kinetics are extremely precise, adjusted to exclusively sculpt the repolarizing phase of individual action potentials. The contrast can be appreciated by the example plots of the shunting inhibition current and I_{BK} at the bottom of Figs. 4 and 8, respectively. To a first approximation, the dynamic-clamp protocol supplies similar negative currents in the two cases, but indeed the fact that the kinetics are so different causes a qualitatively different effect on spiking. Thus, the divergent effects on spiking output underline the point that neuronal dynamics arise from a complex, and non-obvious, interaction of non-linear mechanisms in the single cell.

For shunting inhibition and I_{BK} our results suggest not only a general down- or upregulation, respectively, of the evoked response by these mechanisms, but also more subtle effects on the precise pattern of evoked spikes. The results have implications on how these extrinsic and intrinsic membrane mechanisms may impact the neural code, whether or not a rate-based code or timing-based code, or something in between, turns out to the be relevant language of the brain. In the final analysis it is essential to consider the fine details of various mechanisms such as these in order to establish the functional roles of the elements comprising the neuron's biophysical mosaic (Graham and Kado, 2002). The application of the dynamic-clamp method in vivo to address quantitative properties of biophysical mechanisms of neurons which are as close as possible to their natural state, and in the context of realistic functional responses, will be an essential tool toward this understanding.

Acknowledgments This work was supported by an HFSP grant (RGP0049/2002) and an Agence Nationale de Recherche grant (FUNVISYNIN) to Dr. Lyle J. Graham. We also gratefully acknowledge Thomas Gener for his help in developing the protocols and participating in early experiments. We also acknowledge the important contribution of the authors of the VisionEgg and the G-Clamp software packages.

References

Anderson J, Carandini M, Ferster D (2000) Orientation tuning of input conductance, excitation and inhibition in cat primary visual cortex. J Neurophysiol 84:909–26.

Anderson J, Lampl I, Gillespie D, Ferster D (2001) Membrane potential and conductance changes underlying length tuning of cells in cat primary visual cortex. J Neurosci 21:2104–12.

Bernander O, Douglas RJ, Martin KAC, Koch C (1991) Synaptic background activity influences spatiotemporal integration in single pyramidal cells. Proc Natl Acad Sci USA 88:11569–73.

Borg-Graham LJ (1987) Modelling the somatic electrical behaviour of hippocampal pyramidal neurons. MSEE Thesis, Massachusetts Institute of Technology.

Borg-Graham L, Monier C, Frégnac Y (1998) Visual input evokes transient and strong shunting inhibition in visual cortical neurons. Nature 389:369–73.

Borg-Graham LJ (1999) Interpretations of data and mechanisms for hippocampal pyramidal cell models. In Cerebral cortex, eds. Ulinski PS, Jones EG, & Peters A, pp. 19–138. Kluwer Academic/Plenum Publishers, New York.

Brizzi L, Meunier C, Zytnicki D, Donnet M, Hansel D, LaMotte D'Incamps B, Van Vreeswijk C (2004) How shunting inhibition affects the discharge of lumbar motoneurones. A dynamic clamp study in anaesthetised cats. J Physiol 558(Pt 2):671–83.

Capaday C, Van Vreeswijk C (2006) Direct control of firing rate gain by dendritic shunting inhibition. J Integr Neurosci 5:199–222.

Chance FS, Abbott LF, Reyes AD (2002) Gain modulation from background synaptic input. Neuron v35, 773–82.

Destexhe A, Paré D (1999) Impact of network activity on the integrative properties of neocortical pyramidal neurons in vivo. J Neurophysiol 81:1531–47.

Fellous J-M, Rudolph M, Destexhe A, Sejnowski TJ (2003) Synaptic background noise controls the input/output characteristics of single cells in an in vitro model of in vivo activity. Neuroscience 122:811–29.

Graham L, Kado R (2002) The neuron's biophysical mosaic and its computational relevance. In the Handbook for Brain Theory and Neural Networks, ed. Arbib M, 2nd edition, pp. 170–175. MIT Press.

Graham LJ (2006) Not what you'd expect: Paradoxical roles of Na+ and K+ currents on excitability. Paper presented at the Modelling the Brain's Labyrinth Meeting, Hieraklion, Greece.

Graham LJ (2007) Not what you'd expect: Paradoxical roles of Na+ and K+ currents on excitability. Paper presented at the Quantitative Neuron Modeling Meeting, EPFL, Lausanne, Switzerland.

Graham LJ, Schramm A, Gener T (2007) The modulation of firing gain and threshold by shunting inhibition in cortical neurons in vivo, Society for Neuroscience Annual Meeting Abstracts, San Diego, USA.

Gu N, Vervaeke K, Storm JF (2007) BK potassium channels facilitate high-frequency firing and cause early spike frequency adaptation in rat CA1 hippocampal pyramidal cells. J Physiol 580(3):859–82.

Haider B, Duque A, Hasenstaub A, McCormick D (2006) Neocortical network activity in vivo is generated through a dynamic balance of excitation and inhibition. J Neurosci 26:4535–45.

Haider H, Duque A, Hasenstaub AR, Yu Y, McCormick DA (2007) Enhancement of visual responsiveness by spontaneous local network activity in vivo. J Neurophysiol 4186–202.

Higley M, Contreras D (2006) Balanced excitation and inhibition determine spike timing during frequency adaptation. J Neurosci 26:448–57.

Hirsch JA, Alonso JM, Reid RC, Martinez LM (1998) Synaptic integration in striate cortical simple cells. J Neurosci 18:9517–28.

Holt G.R, Koch C (1997) Shunting inhibition does not have a divisive effect on firing rates. Neural Comput 9:1001–13.

Ingham NJ, McAlpine D (2005) GABAergic inhibition controls neural gain in inferior colliculus neurons sensitive to interaural time differences. J Neurosci 25(26):6187–98.

Kullmann PHM, Wheeler DW, Beacom J, Horn JP (2004) Implementation of a fast 16-bit dynamic clamp using LabVIEW-RT. J Neurophysiol 91:542–54.

Kreiner L, Jaeger D (2003) Synaptic shunting by a baseline of synaptic conductances modulates responses to inhibitory input volleys in cerebellar Purkinje cells. Cerebellum 3:112–25.

Manuel M, Meunier C, Donnet M, Zytnicki D (2005) How much afterhyperpolarization conductance is recruited by an action potential? A dynamic-clamp study in cat lumbar motoneurons. J Neurosci 25(39):8917–23.

Marino J, Schummers J, Lyon D, Schwabe L, Beck O, Wiesing P, Obermayer K, Sur M (2005) Invariant computations in local cortical networks with balanced excitation and inhibition. Nat Neurosci 8:194–201.

Marrion NV, Tavalin SJ (1998) Selective activation of Ca2 + -activated K + channels by co-localized Ca2 + channels in hippocampal neurons. Nature 395:900–5.

McCormick DA, Connors BW, Lighthall JW, Prince DA (1985) Comparative electrophysiology of pyramidal and sparsely spiny neurons of the neocortex. J Neurophysiol 54:782–806.

Mitchell SJ, Silver RA (2003) Shunting inhibition modulates neuronal gain during synaptic excitation. Neuron 38:433–45.

Monier C, Chavane F, Baudot P, Graham L, Frégnac Y (2003) Orientation and direction selectivity of excitatory and inhibitory inputs in visual cortical neurons: A diversity of combinations produces spike tuning. Neuron v37:663–80.

Prescott SA, De Koninck YD (2003) Gain control of firing rate by shunting inhibition: Roles of synaptic noise and dendritic saturation. Proc Natl Acad Sci USA 100(4):2076–81.

Priebe N, Ferster D (2005) Direction selectivity of excitation and inhibition in simple cells of the cat primary visual cortex. Neuron 45:133–45.

Priebe N, Ferster D. (2006) Mechanisms underlying cross-orientation suppression in cat visual cortex. Nat Neurosci 9:552–61.

Rapp M, Yarom Y, Segev I (1992) The impact of parallel fiber background activity on the cable properties of cerebellar Purkinje cells. Neural Comput 4:518–33.

Rudolph M, Destexhe A (2003) A fast-conducting, stochastic integrative mode for neocortical neurons in vivo. J Neurosci 23:2466–76.

Schramm A, Graham LJ (2007) Touch 'n Zap: A new technique for blind whole-cell patch recordings, 8e Colloque de la Société des Neurosciences, Montpellier, France.

Semyanov A, Walker MC, Kullmann DM, Silver RA (2004) Tonically active GABA A receptors: modulating gain and maintaining the tone. Trends Neurosci 27(5): 262–9.

Shao LR, Halvorsrud R, Borg-Graham L, Storm JF (1999) The role of BK-type Ca2 + -dependent K + channels in spike broadening during repetitive firing in rat hippocampal pyramidal cells. J Physiol v521.1:135–46.

Stell BM, Brickley SG, Tang CY, Farrant M, Mody I (2003) Neuroactive steroids reduce neuronal excitability by selectively enhancing tonic inhibition mediated by {delta} subunit-containing GABAA receptors. PNAS 100(24):1443.

Storm J F (1990). Potassium currents in hippocampal pyramidal cells. Prog Brain Res 83:161–87.

Storm J, Borg-Graham L, Adams P (1987) A passive component of the afterdepolarization (ADP) in rat hippocampal cells. Biophys J 51:65a.

Straw AD, Warrant EJ, O'Carroll DC (2006) A 'bright zone' in male hoverfly (*Eristalis tenax*) eyes and associated faster motion detection and increased contrast sensitivity. J Exp Biol 209(21):4339–54.

Tan AY, Zhang LI, Merzenich MM, Schreiner CE. (2004) Tone-evoked excitatory and inhibitory synaptic conductances of primary auditory cortex neurons. J Neurophysiol 92:630–43.

Ulrich D (2003) Differential arithmetic of shunting inhibition for voltage and spike rate in neocortical pyramidal cells. Eur J Neurosci 18:2159–65.

Velumian AA, Carlen PL (1999) Differential control of three after-hyperpolarizations in rat hippocampal neurones by intracellular calcium buffering. J Physiol 517:201–16.

Vergara C, Latorre R, Marrion NV, Adelman JP (1998) Calcium-activated potassium channels. Curr Opin Neurobiol 8:321–9.

Wehr M, Zador AM (2003) Balanced inhibition underlies tuning and sharpens spike timing in auditory cortex. Nature 426:442–6.
Wehr MS, Zador A (2005) Synaptic mechanisms of forward suppression in rat auditory cortex. Neuron 47:325–7.
Wilent W, Contreras D (2004) Synaptic responses to whisker deflections in rat barrel cortex as a function of cortical layer and stimulus intensity. J Neurosci 24:3985–98.
Wilent W, Contreras D (2005) Dynamics of excitation and inhibition underlying stimulus selectivity in rat somatosensory cortex. Nat Neurosci 8:1364–70.
Zhang LI, Tan AY, Schreiner CE, Merzenich MM (2003) Topography and synaptic shaping of direction selectivity in primary auditory cortex. Nature 424:201–5.

Functions of the Persistent Na^+ Current in Cortical Neurons Revealed by Dynamic Clamp

J.F. Storm, K. Vervaeke, H. Hu, and L.J. Graham

Abstract Many cortical neurons and other vertebrate nerve cells are equipped with a persistent Na^+ current, $I_{NaP,}$ which operates at membrane potentials near the action potential threshold. This current may strongly influence integration and transduction of synaptic input into spike patterns. However, due to the lack of pharmacological tools for selective blockade or enhancement of I_{NaP}, its impact on spike generation has remained enigmatic. By using dynamic clamp to cancel or add I_{NaP} during intracellular recordings in rat hippocampal pyramidal cells, we were able to circumvent this long-standing problem. Combined with computational modeling our dynamic-clamp experiments disclosed how I_{NaP} strongly affects the transduction of excitatory current into action potentials in these neurons. First, we used computational model simulations to predict functional roles of I_{NaP}, including unexpected effects on spike timing and current–frequency relations. We then used the dynamic-clamp technique to experimentally test and confirm our model predictions.

1 Introduction

The integration and transduction of synaptic input to patterns of action potentials involve a delicate and complex interplay between membrane currents operating at potentials near the spike threshold, and the larger currents underlying the action potential. The former, the "subthreshold currents" or "threshold currents" are often pivotal for determining spike pattern, timing, and frequency. Among the most enigmatic of the subthreshold currents operating in mammalian neurons is the persistent sodium current (I_{NaP}) (Crill, 1996). This current is likely to play important roles in mammalian cortical neurons, including synaptic integration and spike firing, as well as subthreshold oscillations and network

J.F. Storm (✉)
Department of Physiology at Institute of Basal Medicine, and Centre of Molecular Biology and Neuroscience, University of Oslo, pb 1103 Blindern, N-0317 Oslo, Norway
e-mail: j.f.storm@medisin.uio.no

A. Destexhe, T. Bal (eds.), *Dynamic-Clamp*, Springer Series in Computational Neuroscience 1, DOI 10.1007/978-0-387-89279-5_8,

rhythmicity, e.g., in the hippocampus, entorhinal cortex (EC), neocortex (Alonso & Llinas, 1989; French & Gage, 1985), and subcortical and cerebellar neurons (Llinas & Sugimori, 1980; Llinas, 1988; Taddese & Bean, 2002).

However, it has been particularly difficult to test the functional roles of I_{NaP} in firing behavior because it has proved virtually impossible to selectively manipulate this current with specific pharmacological tools. A likely reason for these difficulties is that I_{NaP} appears to arise from the same channel population that underlies the classical spike-generating transient Na^+ current (I_{NaT}). Thus, different states or gating modes of the same Na^+ channels may generate both I_{NaP} and I_{NaT} (Alzheimer et al., 1993; Crill, 1996; Taddese & Bean, 2002). Therefore, while functions of many other ionic currents have been determined by using specific pharmacological blockers and openers, or genetic manipulations, such approaches are problematic for I_{NaP} since manipulations that suppress this current will often suppress the spike-generating transient current, thus blocking firing and obscuring specific effects of I_{NaP}. In particular, blockers of I_{NaP} such as tetrodotoxin (TTX), riluzole, or phenytoin also directly affect I_{NaT}, reducing the amplitude of action potentials or eliminating them all together. Reduction of spike amplitude will in turn change the activation of voltage- and calcium-gated ion channels that mediate feedback regulation of spike frequency and spike pattern, thus distorting the effects of I_{NaP} (see below).

To circumvent these problems, we used dynamic clamp (Fig. 1) to study I_{NaP} both by the selective subtraction of this current (i.e. canceling out the native

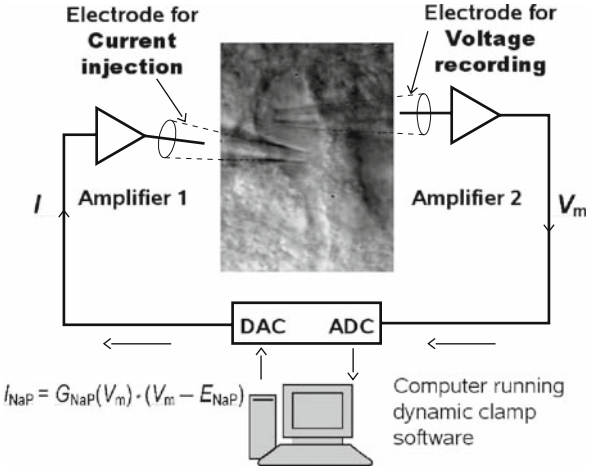

Fig. 1 Dynamic-clamp configuration for analysis of I_{NaP} functions in hippocampal pyramidal neurons. Diagram of the dynamic-clamp configuration, with two patch pipettes in whole-cell configuration at the soma of a CA1 pyramidal cell in a rat hippocampal slice: one pipette for voltage recording (*right*), the other for current injection (*left*). I_{NaP} it was calculated by the dynamic-clamp software, based on our I_{NaP} model and the measured membrane potential. To add the simulated I_{NaP}, the calculated current was injected into the cell in real time. To cancel the intrinsic I_{NaP} generated by the cell, a negative current equal to the simulated I_{NaP} was injected into the cell. (Modified from Vervaeke et al., 2006, with permission from *Cell Press, Elsevier*.)

current), as well as by the addition of a simulated I_{NaP} after the native I_{NaP} had been pharmacologically blocked. These tests were combined with other electrophysiological measurements from CA1 pyramidal neurons in hippocampal slices, and with simulations with a biophysically detailed compartmental model of this neuronal type.

2 Persistent Na^+ Current: History, Properties, and Functions

Many mammalian neurons show a noninactivating, TTX-sensitive sodium current component that begins to activate several millivolts negative to the spike threshold (Crill, 1996). The Hodgkin & Huxley (1952) (HH) equations for the fast inactivating Na^+ current (I_{NaT}) underlying action potentials imply that this conductance also gives rise to a noninactivating current component at a limited range of membrane potentials due to the overlap between the activation and in activation curves – a "window current" (see below, Fig. 5). Many neurons, however, show a distinct persistent Na^+ current, I_{NaP}, which is active far beyond the expected range of the classical HH window current and is thus apparently due to another mechanism (French & Gage, 1985; Crill, 1996). There is now good evidence that such an I_{NaP} can be caused wholly or partly by the same channel population as I_{NaT}, due to incomplete inactivation of these channels, or through some forms of modal gating (Aldrich et al., 1983; Alzheimer et al., 1993; Taddese & Bean, 2002). In addition, there is evidence that I_{NaP} may be caused partly by Na^+ channels that are biophysically and/or molecularly distinct from those underlying I_{NaT}, perhaps due to different subunit composition or modulation (Magistretti & Alonso, 1999; Magistretti & Alonso, 2002). Different mixtures of these mechanisms may contribute to various degrees in different cell types (Crill, 1996; Taddese & Bean, 2002).

Chandler & Meves (1966) found that the Na^+ current in squid axon shows incomplete inactivation, and Gilly & Armstrong (1984) identified a distinct population of Na^+ channels selectively activated by small depolarizations. However, the existence of a persistent Na^+ current in the brain was first inferred from intracellular current-clamp recordings from hippocampal and neocortical pyramidal neurons (Hotson et al., 1979; Connors et al., 1982) and cerebellar Purkinje cells (Llinas & Sugimori, 1980), revealing an increase in slope resistance – an "anomalous rectification" – starting ~10 mV negative to the spike threshold, apparently due to a noninactivating Na^+ current. Voltage-clamp measurements of such a current were first performed in cardiac Purkinje fibers (Attwell et al., 1979) and neocortical pyramidal neurons (Stafstrom et al., 1982). Subsequently, I_{NaP} has been studied in numerous neuronal types (Crill, 1996).

I_{NaP} typically turns on upon membrane depolarization positive to ~–65 mV, activates and deactivates fast (within ~5 ms), and shows either no or very slow inactivation (time constant ~2–6 s) (French et al., 1990; Magistretti & Alonso, 1999). It has for long been debated whether this current has a separate molecular identity from I_{NaT}. However, converging evidence now seems to support

the conclusion that I_{NaP} is caused by a separate, noninactivating or slowly inactivating gating mode and/or incomplete inactivation of the I_{NaT} channels, in pyramidal cells and at least some other neurons (Alzheimer et al., 1993; Taddese & Bean, 2002).

I_{NaP} has been shown to enhance both excitatory and inhibitory postsynaptic potentials (EPSPs and IPSPs) in neocortical (Stafstrom et al., 1985; Stuart & Sakmann, 1995; Stuart, 1999) and hippocampal pyramidal neurons (Lipowsky et al., 1996; Vervaeke et al., 2006). Furthermore, there is evidence that I_{NaP} amplifies the after-depolarization following a spike and can change the firing mode of CA1 pyramidal neurons from solitary spikes to spike bursts (Jensen et al., 1996; Yue et al., 2005). In addition, I_{NaP} drives spontaneous rhythmic firing in tuberomammillary neurons (Taddese & Bean, 2002).

In CA1 hippocampal pyramidal cells, we have shown that I_{NaP} engages in interesting interactions with the M-current (Kv7/KCNQ current), a persistent potassium current that is active in the subthreshold voltage range (Brown & Adams, 1980). Thus we found that I_{NaP} amplifies a form of subthreshold intrinsic neuronal resonance at theta frequencies (~8 Hz) that is mediated by M-current (called *M-resonance*) (Hu et al., 2002). In a later study we also showed how I_{NaP} amplifies after-hyperpolarizations (AHPs), how it affects the relation between injected depolarizing current (I) and the resulting discharge frequency (f/I relation), and how it has contrasting effects on spike timing in CA1 pyramidal neurons (Vervaeke et al., 2006).

3 Why Use Dynamic Clamp to Study I_{NaP}?

3.1 Lack of Specific Blockers of I_{NaP}

We used dynamic clamp for studying I_{NaP} functions in order to overcome the lack of specific pharmacological blockers. While some influential studies have used a low dose of TTX (~5 nM) to study I_{NaP} with only small effects on the spike shape (Jensen et al., 1996; Stuart, 1999), this approach is generally not suitable for studying the input–output relations in neurons, including repetitive firing and current-to-frequency transduction, since subtle changes in the spike shape can nevertheless have large consequences for these properties. Thus, a slight reduction in spike amplitude could strongly reduce the activation of voltage- and Ca^{2+}-dependent K^+ channels underlying the AHPs, which are among the main determinants of the input–output relations of a neuron (Madison & Nicoll, 1984; Peters et al., 2005; Vervaeke et al., 2006; Gu et al., 2007).

A drug that has been used as a more selective blocker of I_{NaP} is the neuroprotective agent riluzole (Urbani & Belluzzi, 2000). However, at higher concentrations riluzole can also block I_{NaT} in the inactivated state (Benoit & Escande, 1991) and also block various axonal K^+ currents (Benoit & Escande, 1993). However, the concentration necessary to substantially block I_{NaP} was

also found to affect the I_{NaT} amplitude (Urbani & Belluzzi, 2000). Moreover, riluzole has also potent effects on two-pore domain (2P) potassium channels (TREK-1 and TRAAK) (Duprat et al., 2000), which are major contributors to the resting K^+ leak current and thus important determinants of neuronal excitability throughout the central nervous system (Goldstein et al., 2001). Riluzole has also been reported to block high-voltage-activated Ca^{2+} channels at concentrations used to block I_{NaP} (Huang et al., 1997). Thus, although it has often been used for blocking I_{NaP}, riluzole is not selective.

The anti-epileptic drug phenytoin (Mattson et al., 1985) has also often been used as a blocker I_{NaP} (Chao & Alzheimer, 1995). It seems that phenytoin stabilizes I_{NaT} in the inactivated state at similar concentrations that blocks I_{NaP}, thus having an activity-dependent effect on I_{NaT} (Kuo & Bean, 1994). Fricker & Miles (2000) found that phenytoin dramatically reduced the amplitude of the later spikes during repetitive firing in CA1 pyramidal neurons, although it had little effect on the first spike. Phenytoin has also been reported to block high-voltage-gated Ca^{2+} channels at concentrations relevant for blocking I_{NaP} (Jeub et al., 2002). Thus, this blocker also seems unsuitable for studying the role of I_{NaP} in input–output relations of neurons.

3.2 *Perisomatic Localization of* I_{NaP} *in Cortical Pyramidal Neurons*

A major limitation of dynamic clamp is that it can fully cancel or mimic conductances only if they arise at the subcellular localization where the patch pipette(s) contact(s) the cell. Because the exact molecular identity of I_{NaP} channels is uncertain, their distribution has not been determined by immunohistochemistry. Nevertheless, converging evidence suggests that I_{NaP} in cortical pyramidal neurons originates near the soma, probably at the axon initial segment (Stuart & Sakmann, 1995; Astman et al., 2006). An elegant study by Stuart & Sakmann (1995), using dual somatic–dendritic and somatic–axonal recordings from neocortical layer V pyramidal neurons, provided the first evidence that I_{NaP} is likely to come from the soma or axon. Subsequently, several patch-clamp studies have supported a perisomatic distribution of I_{NaP} in layer 5 neocortical neurons of the somatosensory (Astman et al., 2006) and prefrontal cortex (Gonzalez-Burgos & Barrionuevo, 2001), and in CA3 (Urban et al., 1998) and CA1 pyramidal neurons (Andreasen & Lambert, 1999; Yue et al., 2005; Vervaeke et al., 2006).

However, dendritic exploration with patch-clamp electrodes revealed that I_{NaT} is also distributed along the apical trunk of pyramidal neurons at about the same density as in the soma membrane (Stuart & Sakmann, 1994; Magee & Johnston, 1995). The dendritic localization of I_{NaT}, together with the hypothesis that I_{NaP} and I_{NaT} arise from the same channel type, prompted groups to explore whether there is a functionally active I_{NaP} in the dendrites. Studies by Schwindt & Crill (1995) and Lipowsky et al. (1996) suggested such a dendritic localization in

both CA1 hippocampal and layer V neocortical pyramidal neurons. How can these results be explained in view of the abundant evidence for a perisomatic localization of I_{NaP}? Schwindt & Crill (1995) iontophoretically applied glutamate to the dendrites while recording EPSCs at the soma, and found that bath-applied TTX reduced the EPSC amplitude. Lipowsky et al. (1996) activated excitatory synapses impinging on the distal dendrites. Because local application of TTX to the dendrites reduced the somatic EPSPs, they proposed that I_{NaP} in the dendrites boosted the EPSPs. However, an alternative explanation of the results from these two groups may be that dendritic regenerative Na^+ spikes, carried by I_{NaT} in the dendrites, are caused by nearly synchronous synaptic activation of several dendritic spines onto a dendritic branch (Losonczy & Magee, 2006). Because these dendritic Na^+ spikes are strongly filtered on their way along the dendrite and mostly fail to invade the soma, they will merely produce larger somatic EPSPs, with a slightly steeper rising slope that can easily remain undetected (Losonczy & Magee, 2006). Therefore, dendritic application of TTX that blocks local dendritic Na^+ spikes will reduce the somatic EPSP amplitude. This scenario may explain why these two groups found a TTX-mediated decrease of synaptic potentials recorded at the soma.

Our work in CA1 pyramidal neurons further supports a perisomatic localization of I_{NaP} (Vervaeke et al., 2006). When we applied a voltage step that was just below the spike threshold (from –78 to –58 mV) during somatic whole-cell recording (Fig. 2B), thus activating I_{NaP} (Fig. 2A) but not I_{NaT}, we recorded a TTX-sensitive inward current (~35 pA) with very fast kinetics. Both the activation and deactivation could be fitted with single exponential functions with time constants of about 1 ms (Fig. 2B). These fast kinetics constrain the possible subcellular localization of I_{NaP}. Using detailed compartmental models of a CA1 pyramidal neuron based on reconstructed morphologies (Fig. 2C), we tested various possible subcellular localization of I_{NaP}, trying to reproduce the experimental results (Fig. 2D) (unpublished work). We found that I_{NaP} had to be localized in the immediate vicinity of the soma to reproduce the experimental results of Fig. 2B (Fig. 2D, dotted–dashed line). In comparison, distributing I_{NaP} (1) uniformly over soma and dendrites (Fig. 2D, continuous line), or (2) most of I_{NaP} at the axon initial segment and a much lower, uniform density in soma and dendrites (Fig. 2D, dashed line), or (3) most of I_{NaP} in the axon initial segment and a much lower density in the dendritic tuft (Fig. 2D, dotted line), all gave poor results. The model of I_{NaP} followed an activation curve as shown in Fig. 2A and had a voltage-independent time constant of 1 ms. In the model, fitting the I_{NaP} activation response with all I_{NaP} located in the axon initial segment (Fig. 2D, black trace) gave a somatic activation time constant of 1.07 ms, indicating a very good clamp control over I_{NaP}. These results strongly suggest that most of the channels underlying I_{NaP} are located very close to the soma.

Our results from hippocampal CA1 pyramidal cells are in good agreement with recent results from layer V pyramidal neurons by Astman et al. (2006), who provide strong evidence that I_{NaP} is specifically located at the axon initial segment. So why is the I_{NaP} conductance concentrated here, while there is hardly any

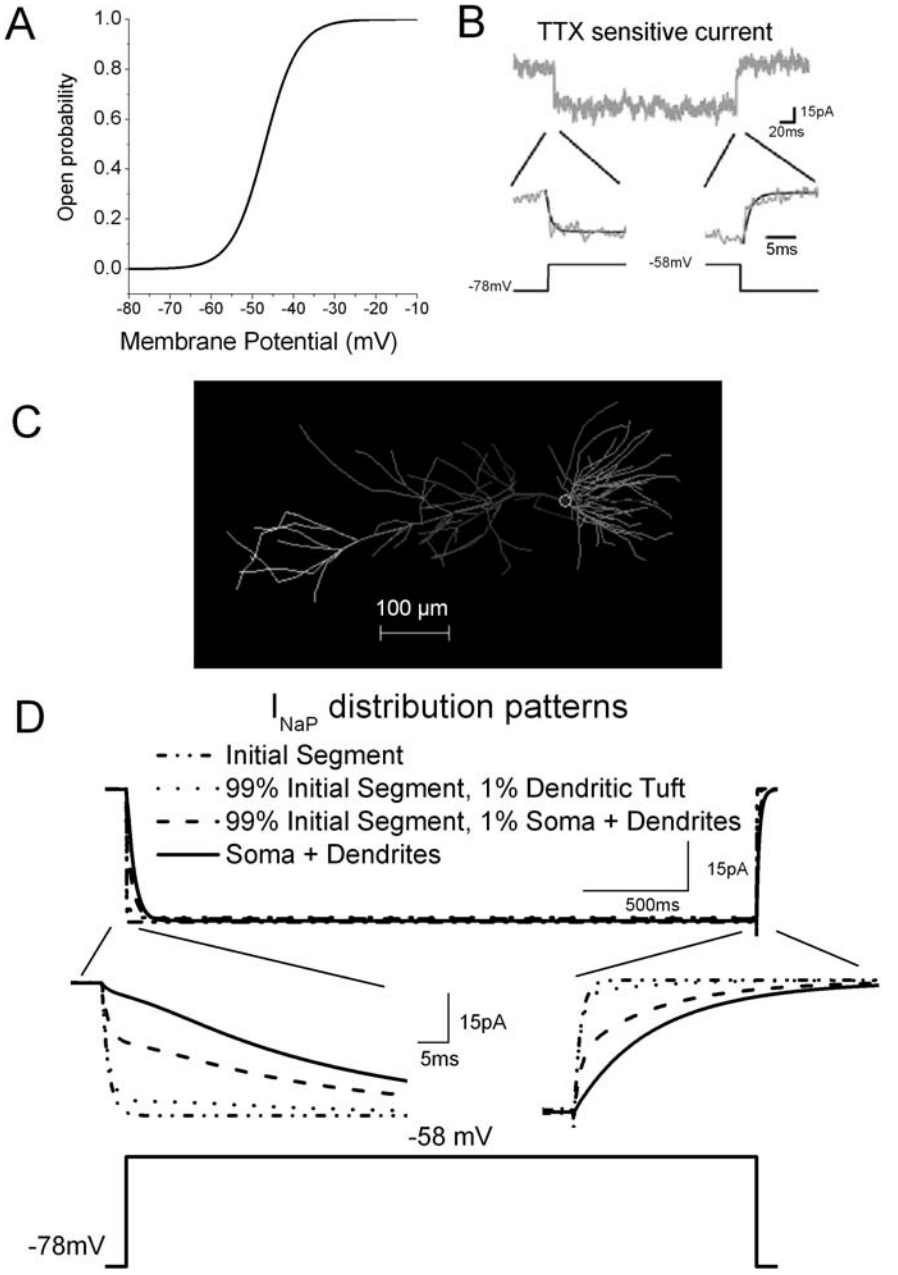

Fig. 2 Computer simulations support that I_{NaP} largely originates from the axon initial segment of CA1 pyramidal neurons. (**A**) I_{NaP} steady-state activation curve used in the model and dynamic-clamp experiments. (**B**) Experimental data from a somatic whole-cell recording. The membrane potential was stepped from −78 to −58 mV. The *gray trace* shows the TTX-sensitive current obtained by subtraction the resulting currents of before and after

in the dendrites? A plausible answer to this question may be obtained by combining resent results on the subcellular distribution of I_{NaT} in cortical pyramidal neurons, with data on the molecular identities of Na^+ channels in various parts of these cells. A recent elegant study by Kole et al. (2008) shows that the density of sodium channels underlying I_{NaT} is far higher (probably ~50 times) in the axon initial segment than in the soma and dendrites of layer V pyramidal neurons. Thus, the subcellular distribution of I_{NaT} seems to match that of I_{NaP}, both being highly concentrated at the axon initial segment. This fits nicely with the evidence that I_{NaP} is at least partially caused by the same channels as I_{NaT}, probably through incomplete inactivation and/or a modal gating (Alzheimer et al., 1993; Taddese & Bean, 2002). Because the I_{NaP} in pyramidal cells is usually only a small fraction (typically ~1%) of I_{NaT} (French et al., 1990; Hu et al., 2002; Yue et al., 2005), the channel states generating I_{NaP} must occur very infrequently. This, combined with the far lower density of Na^+ channels and I_{NaT} in the soma and dendrites compared to the axon, may partly explain why the density of I_{NaP} in the dendrites appears to be quite low. In addition, there is substantial evidence that that I_{NaT} in the axon initial segment and I_{NaT} in the soma and dendrites of pyramidal neurons are caused by channels of different molecular compositions (Kaplan et al., 2001; Boiko et al., 2001, 2003; Komai et al., 2006; Kole et al., 2008). Thus, in adult animals, axonal Na^+ channels contain α-subunits of the $Na_v1.6$ type, whereas somatodendritic Na^+ channels seem to be composed mainly of $Na_v1.2$ α-subunits, perhaps in combination with $Na_v1.1$ and $Na_v1.3$ (Kaplan et al., 2001; Boiko et al., 2001, 2003; Kole et al., 2008). This also seems to fit in with data from transgenic mice indicating that I_{NaP} in several neurons is to a large extent (~40–70%) mediated by $Na_v1.6$ α-subunits, e.g., in Purkinje and mesencephalic trigeminal neurons, although other α-subunit species can also contribute to I_{NaP} (Raman & Bean, 1999; Enomoto et al., 2007; Taddese & Bean, 2002). Thus, the I_{NaP} of pyramidal neurons may be largely caused by $Na_v1.6$-containing Na^+ channels concentrated at the axon initial segment, both because of the very high channel density here and the $Na_v1.6$ subunits are especially prone to the particular gating mode that generates I_{NaP}. In addition, certain Na^+ channel β-subunits may also enhance I_{NaP} (Qu et al., 2001).

Fig. 2 (continued) TTX application. (Modified from Vervaeke et al., 2006, with permission from *Cell Press, Elsevier*.) (**C**) Reconstructed neuron used for the simulations in (D). Different *shades of gray* indicate different membrane potentials during a simulation where the soma was clamped at −58 mV. (**D**) The experiment in (B) was simulated with various I_{NaP} distribution patterns, as indicated. *Continuous line*: I_{NaP} was uniformly distributed in soma and dendrites (0.325 pS/μm^2). *Dot–dash line*: all I_{NaP} (50 pS/μm^2) was located in the axon initial segment. *Dashed line*: most of I_{NaP} (99%) was located in the axon initial segment (20.5 pS/μm^2) while the density was 100 times lower (1%) in soma and dendrites (0.205 pS/μm^2). *Dotted line*: most of I_{NaP} (99%) was located in the axon initial segment (45 pS/μm^2) while the density was 100 times lower (1%) in the distal dendritic tuft (0.45 pS/μm^2). (K. Vervaeke, unpublished.)

3.3 Further Advantages of Dynamic Clamp

The fact that a dynamic-clamp system can cancel or restore I_{NaP} nearly instantaneously is a very important advantage compared to application of ion channel blockers or openers, which usually require several minutes to take full effect. During such a long delay, access resistance, neuronal, and/or network properties may change, thus complicating the interpretation of the results.

Furthermore, by using dynamic-clamp I_{NaP} can be increased or decreased in a arbitrary graded fashion, allowing the parameters of the I_{NaP} model to be varied freely, e.g., to resemble natural modulation (Astman et al., 1998; Cantrell & Catterall, 2001; Rosenkranz & Johnston, 2007). Also, because a given manipulation with dynamic clamp is instantaneous and does not require pharmacologic blockers, it is well suited for in vivo patch-clamp recordings. This would be especially important for studying I_{NaP} function in neurons embedded in an active network, e.g., during responses to sensory stimuli.

4 Methods Used for Studying I_{NaP} Functions by Dynamic Clamp

4.1 Characterization of I_{NaP} for Modeling and Dynamic Clamp

In order to establish our dynamic clamp for manipulating I_{NaP}, we first needed to determine its steady-state activation curve in CA1 hippocampal pyramidal cells, for building an accurate model of the current. For this purpose, we used two types of measurements (Hu et al., 2002), both obtained by whole-cell recording from the soma of this cell type in hippocampal slices from young male rats, under virtually identical experimental conditions as those used in the main study (Vervaeke et al., 2006).

We used voltage-clamp recording of the current (Hu et al., 2002) evoked by a slow voltage ramp (from ~–90 to ~–30 mV; Fig. 3A) before and after blockade of I_{NaP} by TTX. The TTX-sensitive current obtained by subtracting the two current recordings started to activate between −70 and −65 mV (Fig. 3B). A similar activation curve was obtained by a series of depolarizing voltage-clamp steps before and after TTX application (Fig. 3C–E). Both these methods yielded similar results (Hu et al., 2002), which also agree well with previous experimental reports from CA1 hippocampal pyramidal cells and other neurons (French et al., 1990; Crill, 1996).

To assess the time constants of I_{NaP} activation and deactivation in the subthreshold voltage range, somatic whole-cell voltage-clamp measurements were used (Fig. 2B). A 250-ms-long voltage step from −78 to −58 mV was applied and the clamp current before and after TTX application subtracted to obtain I_{NaP}. The activation and deactivation time courses of I_{NaP} were each

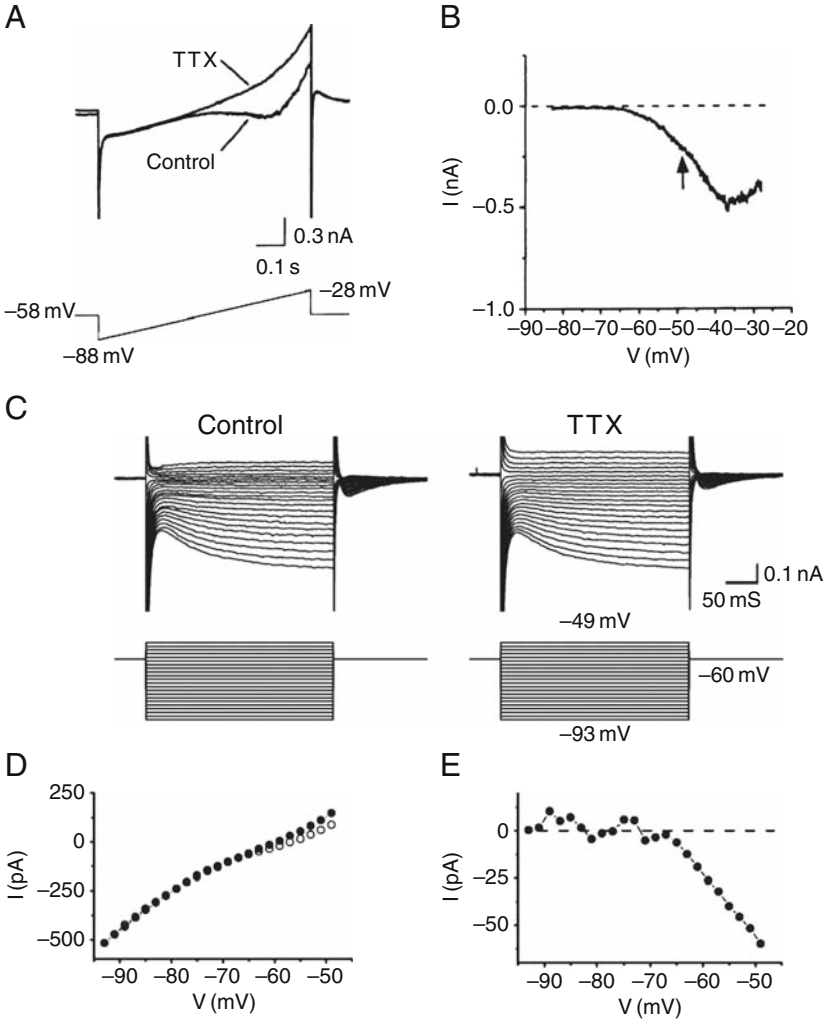

Fig. 3 Voltage-clamp measurents of I_{NaP} in of CA1 pyramidal neurons. (**A**) Membrane currents in response to a ramp voltage command (from −88 to −28 mV) before and after application of TTX (1 μM). (**B**) Voltage dependence of the TTX-sensitive current (I_{NaP}) obtained by subtracting the current in response the ramp command before and after TTX application. The *arrow* indicates the action potential threshold for this cell. (**C**) Membrane currents in response to voltage-clamp steps to different membrane potentials (from −93 mV to −40 mV) before and after TTX application. (**D**) Steady-state current–voltage (*I–V*) plot of the data from (C), measured at the end of the voltage steps. (**E**) TTX-sensitive current (I_{NaP}), calculated by subtracting the steady-state currents before and after TTX in (C). Note that the I_{NaP} started to activate at about −65 mV in both (B) and (E). (Modified from Hu et al., 2002, with permission from *The Journal of Physiology, Wiley-Blackwell*.)

fitted with a single exponential function. The best fits had time constants of ~1 ms (0.93.14 and 0.99±0.15 ms, respectively). Therefore, voltage-independent activation and deactivation time constants of 1 ms were used for our I_{NaP} model and dynamic clamp.

4.2 Na^+ Current Models Used for Our Dynamic Clamp and Computational Modeling

Next, we applied the model of I_{NaP} in a detailed model of a CA1 pyramidal cell that we have developed over the last decade, in agreement with the available voltage- and current-clamp data (Borg-Graham, 1999; Shao et al., 1999; Vervaeke et al., 2006). Like in these previous studies, we modeled the total Na^+ current as a sum of two components: I_{NaT} represented by a four-state Markov model and I_{NaP} represented by a HH model (Borg-Graham, 1999). For our dynamic clamp, we used the same HH model of I_{NaP}, which reproduced the main features of experimental voltage-clamp recordings of I_{NaP} in rat CA1 pyramidal cells (Figs. 3 and 4A,C) as well as those of I_{NaP}-dependent responses to subthreshold current ramps (Figs. 4B, 5, 6, and 7). The motivation for the use of the new Markov model, rather than the classical HH model of the entire Na^+ current was based on the following considerations.

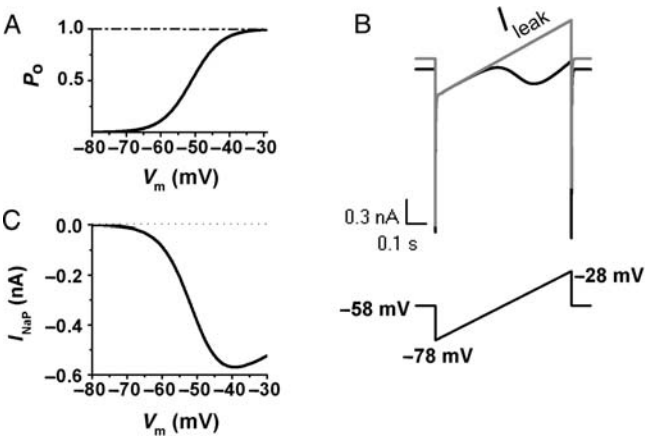

Fig. 4 Properties of the I_{NaP} model used for our dynamic clamp. Model simulations of I_{NaP} under voltage clamp. (**A**) Steady-state activation curve of the I_{NaP} model. P_o is the open probability. The voltage-independent activation and deactivation time constant was 1.0 ms. (**B**) I_{NaP} (*black*) compared to leak current (*gray*) in response to a voltage ramp command (lower trace) in the model. (**C**) I_{NaP} obtained by subtracting the current responses shown in (B). (Modified from Vervaeke et al., 2006, with permission from *Cell Press, Elsevier*.)

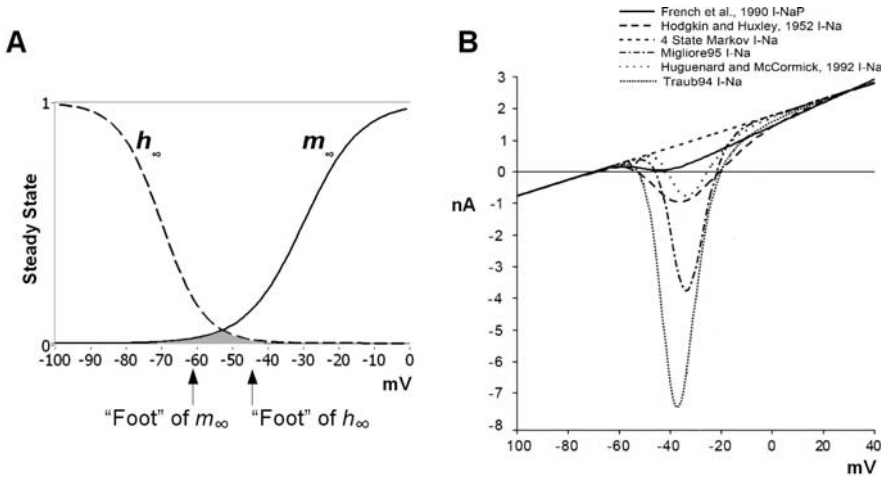

Fig. 5 Window current and steady-state characteristics of Hodgkin-Huxley (HH) Na^+ channel models. (**A**) The HH model of I_{Na} is defined in part by the voltage-dependent steady-state values of activation and inactivation (m_∞ and h_∞). Although the current is nominally transient, this model predicts a nonzero steady-state current for voltages where the two curves overlap (*gray region*), giving what is called the HH "window current." The positions on the voltage axis for the "feet" of these curves may be directly related to transient, e.g., firing, properties of I_{Na} including the span of spike thresholds and the minimum pre-hyperpolarization (PHP), before a spike that is required to remove inactivation. (**B**) Steady-state *I–V* characteristics of different Na^+ channel HH models (squid axon: Hodgkin & Huxley, 1952; hippocampal pyramidal cell: Traub et al., 1994, and Migliore et al., 1995; thalamic relay cell model adapted from cortical pyramidal cells: McCormick & Hugenard, 1992) inserted in a passive cell model, compared with the measured values of I_{NaP} (hippocampal pyramidal cell: French et al., 1990), showing that the steady-state inward rectification predicted by these models are much larger than the actual I_{NaP}. The modified four-state Markov model used in this study shows a negligible steady-state inward rectification

4.2.1 HH Models and I_{NaP}, and the Necessity of a New I_{Na} Model

The standard approach for modeling macroscopic neuron currents follows the paradigm established by Hodgkin & Huxley (1952) for Na^+ and K^+ currents in the squid axon. Nevertheless, this formalism fails to account for various properties of currents in other preparations, including hippocampal pyramidal cells (Borg-Graham, 1987; Kuo & Bean, 1994). Here we describe these limitations with respect to the Na^+ current, and how we addressed them in the theoretical foundation of our study of I_{NaP}.

The HH Na^+ channel model includes activation, m, and inactivation, h, "gating particles" whose voltage-dependent kinetics are defined in part by sigmoidal functions of their steady state, m_∞ and h_∞, respectively, parameterized by the position and steepness on the voltage axis. Any overlap of the m_∞ and h_∞ functions in the HH model predicts a steady state, or noninactivating,

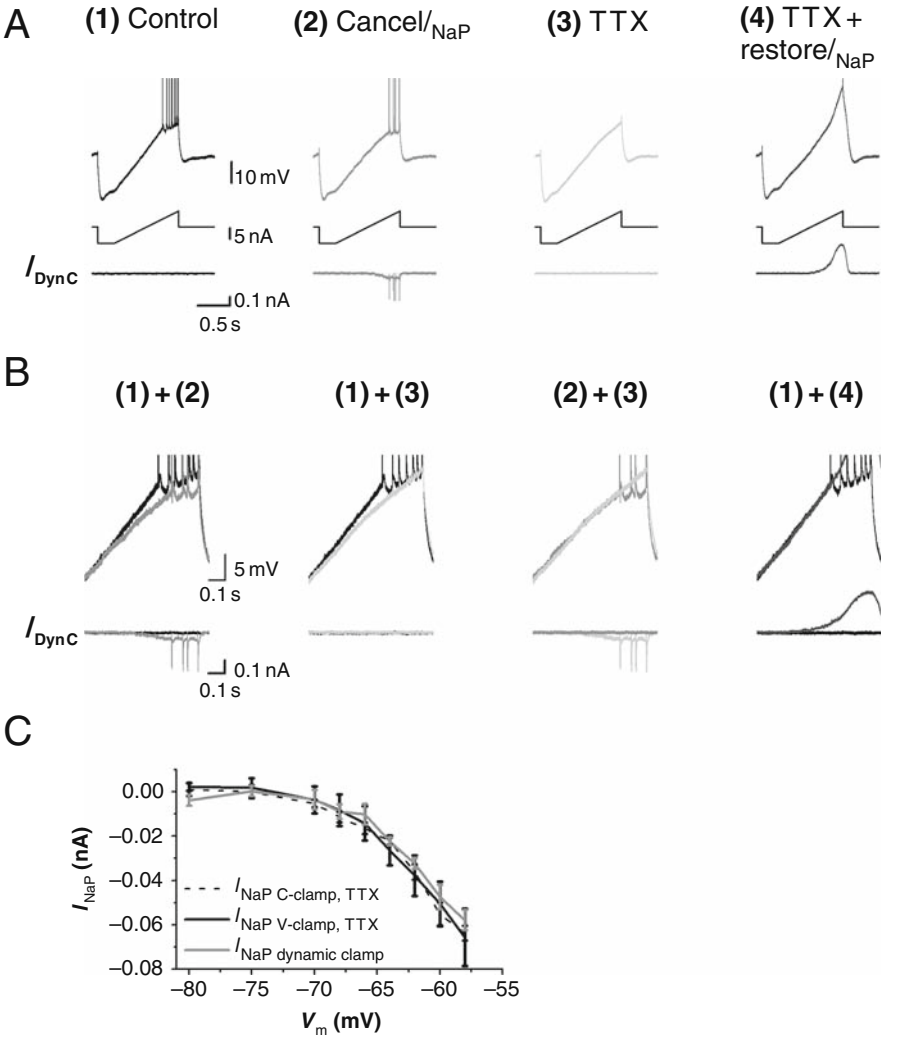

Fig. 6 Comparing the effects of effects of I_{NaP} subtraction by dynamic clamp with effects of I_{NaP} blocked by TTX. (**A**) voltage responses to a current ramp before (1) and after (2) canceling I_{NaP} with dynamic clamp, followed by application of 1 μM TTX and dynamic clamp turned off (3) and after restoring I_{NaP} with dynamic clamp in the presence of TTX (4). These four conditions were executed in sequence in each cell. The bottom traces show the current output from the dynamic clamp (I_{DynC}). (**B**) The same traces as in (A) shown superimposed on expanded scales. (**C**) Voltage dependence of I_{NaP}. Summary plots from three types of measurements: (1) the subthreshold TTX-sensitive current obtained in voltage clamp (V-clamp, TTX; $n = 5$; data from Hu et al., 2002), (2) the TTX-sensitive subthreshold current obtained from current-clamp recordings as shown in panel (B) and in Fig. 7 (C-clamp, TTX; $n = 5$), and (3) the artificial I_{NaP} produced by our dynamic clamp ($n = 5$). (Modified from Vervaeke et al., 2006, with permission from *Cell Press, Elsevier*.)

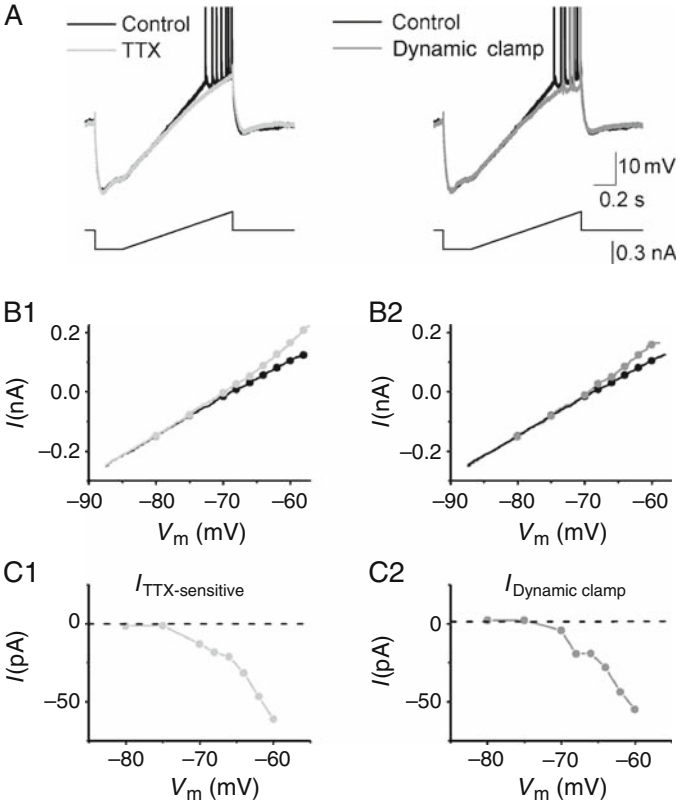

Fig. 7 Method for determining the voltage-dependence of I_{NaP} from current clamp data. (A) A current ramp (bottom traces) was injected into the cell and the voltage response recorded before and after application of TTX (left) or before and after applying dynamic clamp (right). During the subthreshold parts of the responses, every value of injected current (I) corresponds to a certain value of the membrane potential (V_m). **(B1, B2)** The values of injected current (I) and V_m, taken from (A) are re-plotted, by plotting I as a function of V_m. **(C1) and (C2)** show the differences of the plots within B1 and B2, respectively, thus revealing the voltage dependence of the TTX-sensitive sub-threshold current, I_{NaP} (C1) and dynamic clamp current (C2). (Modified from Vervaeke et al., 2006, with permission from *Cell Press, Elsevier*.)

component – or "window current" – of this nominally transient current (Fig. 5A), which is kinetically indistinguishable from a true persistent Na^+ current. Thus, measurement of a noninactivating Na^+ current sets an upper bound on the HH model window current, which in turn constrains the overlap of the m_∞ and h_∞ curves. At the same time, the positions and slopes of m_∞ and h_∞ are constrained by quantitative aspects of firing, and the key question is whether the HH model of the Na^+ current can satisfy all the constraints.

Here we focus on how two measures of spike firing in pyramidal neurons constrain m_∞ and h_∞, including the range of thresholds (roughly between −60 and −50 mV), and the maximum hyperpolarization between

spikes during repetitive firing (around −60 mV). To simplify matters, we can neglect any voltage dependence of the HH model time constants, as well as the number of m or h particles (for more than one particle, the relevant sigmoid function describes the steady-state value of the ensemble). Thus, the lowest spike threshold of around −60 mV imposes an upper bound on the "foot" of the m_∞ curve, since a sufficient number of I_{Na} channels must be activated for triggering an action potential (Fig. 5A). Next, I_{Na} channels are inactivated during a spike, and thus to allow a subsequent spike, such as during repetitive firing, the membrane voltage must become low enough to remove this inactivation. This means that the lowest voltage between spikes imposes a lower bound on the "foot" of the h_∞ curve. This potential was termed the "PHP," or "pre-hyperpolarization" in (Borg-Graham, 1987), in contrast to "AHP" since the PHP is functionally related to a spike which follows, not precedes, it.

These quantitative constraints are susceptible to the subcellular distribution of the channels, in that a given measured voltage (typically at the soma) may differ from the voltage "seen" by the channel. Nevertheless, as argued in our earlier work (Borg-Graham, 1987), the main point is that measured properties of hippocampal pyramidal cells constrain the m_∞ and h_∞ curves of the HH model to predict a window current that is at least an order of magnitude larger than direct measurements of I_{NaP}. This can be seen in Fig. 5B, where we compare the steady-state properties of I_{NaP} predicted by various published models of hippocampal pyramidal cells and other neurons, as well as the canonical HH squid axon parameters (adjusted for cell input impedance). In this comparison the maximum conductance of each I_{Na} model was adjusted so that they would give approximately the same spike current. Although this gives a relatively crude quantitative comparison (apart from amplitude, there was no detailed fitting of spike), it is clear that the HH-type I_{Na} models predict a wide range of persistent Na^+ currents, all of which overestimate the true I_{NaP}. This implies not only important differences between the models regarding synaptic integration and firing properties, but also, given our results with I_{NaP}, predictions at odds with the behavior of real neurons.

An Ad Hoc Markovian Model

Being more flexible, general Markov-type models can meet constraints which are impossible for the standard HH paradigm (ref. Kuo & Bean (1994) from hippocampus; Vandenberg & Bezanilla (1991) and Patlak (1991) from squid axon). A previous approach was to fit more than one HH-type model (Borg-Graham, 1987), each with relatively nonoverlapping activation and inactivation curves in order to limit the window current of I_{Na}, and whose voltage dependences spans a range sufficient to account for the observed range of spike thresholds. Note that this approach can be reduced to an equivalent, if complex, single Markov model; an advantage with considering "separate" channels is

that it can facilitate the initial fitting to desired kinetics. On the other hand, there is no data to support such kinetically distinct Na^+ channels.

Borg-Graham (1999) proposed a new ad hoc Markovian model for I_{Na} that was consistent with qualitative aspects of channel gating established from single-channel studies, and quantitative constraints inferred from macroscopic properties of the sodium current during action potentials. The model had two key predictions. First, the activation–inactivation sequence of the channel during and after a spike was dominated by a one-way path between an inactivated state, *I*, a closed state, *C*, an activated, open (conducting) state, *O*, and then back to the inactivated state. The implicit constraint that inactivation necessarily followed activation had been shown by single-channel studies (Armstrong, 1981; Patlak, 1991; Kuo & Bean, 1994). The second explicit predication of the model was that the voltage-dependent transition rate from the *C* state to the *O* state took into account the history of the membrane voltage. Thus, from the *C* state, as the membrane voltage increased, equilibrium increasingly favored the *O* state, following a monotonic function of voltage parametrized by a reference voltage V_{C-O}. On the other hand, if the membrane voltage decreased, the voltage dependence of *C–O* transition itself shifted to more hyperpolarized voltages, specifically, the value of V_{C-O} also decreased. In the basic form of the model the hyperpolarization of V_{C-O} with membrane hyperpolarization is irreversible (the time constant for any rightward shift of V_{C-O} with depolarization was infinite), though the scheme can easily incorporate, e.g., a slow adaptation of threshold following a slow depolarization of the membrane voltage. For convenience, the actual model used in the current study encapsulates the kinetics of the *C–O* transition described above with two distinct *C* states, but the qualitative behavior is similar. In sum, this model provides both a significant range of spike thresholds, where the dynamic spike threshold has an intrinsic memory of subthreshold potentials. Threshold is lower for lower previous membrane voltages, such as for the first spike of a train arising from rest, as compared to later spikes. Since the minimum membrane voltage, or PHP, between spikes in a train (for pyramidal cells) is many millivolts above rest, and since threshold depends on the PHP, the model predicts that thresholds for later spikes are higher than that for the first spike. Note that the proposed mechanism is not a *necessary* condition for a nonzero range of thresholds nor dependence on voltage history – even the original squid axon model of HH will show some degree of these characteristics. However, in principle the new Markov I_{Na} model can better account for the quantitative aspects of these characteristics, in part because it is explicit formulated to account for these properties, as opposed to a model where these properties are more emergent due to interactions between Na^+ and K^+ currents.

Unlike the HH formalism, this scheme allows essentially independent parameter fitting to the transient and steady-state properties of the Na^+ current. Specifically, realistic spike threshold dynamics can be reproduced given an essentially arbitrary steady-state value of the *O* state, that is a persistent

component of the Na^+ current. In the original version of the model, this aspect was adjusted to match published data on I_{NaP},, thus the defined I_{Na} accounted for all the Na^+ current, transient and persistent. Note that the HH model not only predicts a very large maximum window current: Since this model predicts complete inactivation with increased depolarization (h_∞ goes to zero), the HH window conductance approaches zero with increased depolarization. The experimentally measured persistent Na^+ current, however, shows a relatively constant conductance above the voltage for full activation. Although the functional effect of this relatively small current during the spike is unclear, the proposed Markov model of the entire Na^+ current can, in fact, reproduce this aspect. This result also confirms that an HH model, strictly speaking, cannot by itself account for the measured I_{NaP}.

As described earlier, for convenience and clarity in the present work, the original ad hoc Markov model was adjusted to have a negligible steady-state component, and a distinct I_{NaP} was explicitly modeled with a separate non-inactivating HH-type model. Nevertheless, from a kinetic standpoint, the complete Markov model and the hybrid Markov and HH model formulations are identical.

4.3 Dynamic-Clamp Configuration for Analysis of I_{NaP} Functions

Figure 1 shows a diagram of the dynamic-clamp configuration that we have used in our studies of I_{NaP} functions in rat CA1 pyramidal cells. We used two separate patch pipettes, both in whole-cell configuration at the soma of the same cell: one pipette for voltage recording, the other for current injection. The pipettes were coupled to a *DynClamp2* dynamic-clamp system (Pinto et al., 2001), which has an update rate of about 10 kHz ($\Delta t \sim 100$ μs) and was run on a *Pentium IV* computer with a *Digidata 1200* as ADC–DAC board (Molecular Devices). For every cycle, the expected amplitude of I_{NaP} was calculated by the dynamic-clamp software, based on our I_{NaP} model and the measured membrane potential. To cancel the intrinsic I_{NaP} generated by the neuron itself, a negative current equal to the simulated I_{NaP} was injected into the cell in real time. To add I_{NaP} after blocking the native persistent Na^+ current by TTX, a positive current equal to the simulated I_{NaP} was injected into the cell.

4.4 Advantages of Using Two Separate Electrodes for Dynamic Clamp

During dynamic clamp, it is necessary to measure the membrane potential very accurately and at the same time pass considerable amounts of current into the

cell. If the same patch pipette is used for both the voltage recording and current injection, a voltage error occurs due to the voltage drop caused by current flowing across the series or access resistance, (R_s), across the electrode. Thus, without compensation, the recorded voltage is the sum of the true membrane potential and the voltage drop across series resistance. Although most intracellular amplifiers use a subtraction technique known as "bridge balance" to eliminate the voltage drop caused by series resistance, this compensation is performed manually and is never perfect. Furthermore, the series resistance can often vary spontaneously during a recording, causing errors in the compensation. Thus, a series resistance that is not completely compensated may cause significant voltage errors, particularly when large currents are injected through the recording electrode, for instance, when using dynamic clamp to cancel or mimic the currents underlying action potentials (Ma & Koester, 1996). Since the reliability of dynamic clamp critically depends on the accuracy of the voltage measurements that are fed into the computer that calculates the output clamp current, and the clamp current often depends steeply and nonlinearly on the voltage, it is essential to avoid voltage recording errors. Therefore, we took special care to minimize the voltage recording error in our study of I_{NaP}, by using separate voltage recording and current injection pipettes (Fig. 1). We found that this was a significant advantage, because even though the amplitude of I_{NaP} in CA1 pyramidal is relatively small (~0.1–0.5 nA; Fig. 2) compared with the current underlying the action potential, it activates steeply over a narrow voltage range and has quite fast kinetics, so that even small voltage errors may have significant consequences.

For example, assuming that I_{NaP} is 0.5 nA (Fig. 3A), and the true series resistance $R_s = 20$ MΩ, a 10% error in the bridge balance, or a 10% change in R_s (2 MΩ), will give a voltage error of about 1 mV. This error in turn will cause an error in the injected I_{NaP}. Although small, this difference may still significantly affect spike timing in response to ramps and noisy inputs close to the spike threshold because of the regenerative nature of I_{NaP}, and the fact that the spike threshold is close to the half activation potential of I_{NaP}, thus where its activation curve is steepest (Fig. 2A). Furthermore, it is not uncommon that the series resistance is larger than 20 MΩ, and the bridge compensation error may exceed 10%, causing more severe distortions.

The same technique was also used in a recent paper to study the contribution of Kv3 channels to action potential repolarization and high-frequency firing in hippocampal interneurons (Lien & Jonas, 2003). Although powerful, the application of this multiple electrodes recording method is largely limited by the difficulty of obtaining two nearby (preferentially within about 20 μm) simultaneous recordings from same neuron (Williams, 2004).

In addition to the voltage drop error induced when the current is supplied with the same electrode that monitors the voltage, the series resistance, in combination with the capacitance of the recording pipette, acts as a low-pass filter, decreasing the amplitude of fast voltage signals (i.e., action potentials) even when the two-electrode configuration is used. Therefore, we constantly

compensated the series resistance of the voltage recording electrode during each recording, and rejected experiments on which the series resistance was too high.

Although there is a clear advantage of using two electrodes, it is also possible to use dynamic clamp in combination with single electrode recording, where the same pipette is used for both voltage recording and current injection. In a few of our experiments on I_{NaP} functions we also used this configuration (see Fig. 5 in Vervaeke et al., 2006). This possibility is of course essential for using dynamic clamp for in vivo experiments.

4.5 Testing and Adjusting Our Dynamic-Clamp Parameters

Before using our dynamic clamp for functional studies, we tested its performance in pilot experiments, starting with a maximal conductance for I_{NaP} (G_{max}) value of ~5 nS, which was determined from previous voltage-clamp data (Hu et al., 2002). Next, we adjusted this value after comparing the effects of I_{NaP} subtraction by the dynamic clamp, with the effects of blocking I_{NaP} with TTX (Fig. 6).

In these pilot experiments, we recorded responses of the cell to a slow, injected current ramp (Fig. 6A), and used the dynamic clamp to subtract I_{NaP}. G_{max} was then increased stepwise from the starting value, in steps of 0.4 nS, until we could reliably cancel the effect of the intrinsic I_{NaP} during the injected current ramp (Fig. 6A 1 − 2 and B 1 + 2) to the same extent as blockade by TTX (Fig. 6A 3 and B 2 + 3). We could then also fully restore the effect of the intrinsic I_{NaP} by dynamic clamp, after I_{NaP} had been blocked by TTX (Fig. 6A 4 and B 1 + 4). We found that the G_{max} value that could most reliably eliminate and restore I_{NaP} during our recordings was 4.8 nS. This value then was used for our subsequent experiments in this series (Vervaeke et al., 2006).

Figure 6C compares the voltage dependence plots of I_{NaP} obtained from the three different types of measurement: (1) the subthreshold TTX-sensitive current obtained in voltage clamp (V-clamp, TTX; data from Hu et al., 2002), (2) the TTX-sensitive subthreshold current obtained from current-clamp recordings as shown in Figs. 3B and 7, and (3) the artificial I_{NaP} produced by our dynamic clamp. The three types of measurement yielded virtually identical results.

To test the response speed of the dynamic-clamp system we applied a voltage step from −78 to −58 mV in the open loop configuration and fitted the response with single exponential functions, giving activation and deactivation time constants of 1.01 and 1.00 ms, respectively, as shown above (Fig. 3B).

To test the hypothesis that channels underlying I_{NaP} are localized near the soma, we used computational modeling, as already described above (Section 3.2; Fig. 2). To further test this hypothesis, we also used local application of TTX while giving subthreshold depolarizing voltage steps (from −78 to −58 mV, like in Fig. 2C) through a somatic recording electrode and monitoring the inward current. We then compared the effects of TTX applied locally to the soma with a micropipette (and a dye, 0.2 Vol% fast green, which showed that

the application spread ~100 μm perpendicular to the somatic layer), and subsequent bath application of TTX (1 μM). There was no significant difference between these effects, and local puffing of TTX occluded the effect of subsequent bath application of TTX (data not shown; Vervaeke et al., 2006). These tests strongly support the conclusion that I_{NaP} is confined to the perisomatic area, probably mainly at the axon initial segment (Astman et al., 2006).

4.6 Limitations of Our Dynamic-Clamp Approach

For our multicompartment model of a CA1 pyramidal cell (Vervaeke et al., 2006), we have modeled the total Na^+ current as a sum of two components, as described above: I_{NaT} represented by a four-state Markov model and I_{NaP} represented by a HH model (Borg-Graham, 1999), both I_{NaT} and I_{NaP} being confined to the soma, because there is good evidence for an extremely high Na^+ channel density in the axon initial segment of cortical pyramidal cells (Kole et al., 2008). Our dynamic clamp was based on the same HH model of I_{NaP}. This is obviously a great simplification compared to a fully realistic model of the Na^+ channels in this cell type, which is likely to comprise several molecular species, including the channels made by $Na_v1.6$ α-subunits in the axon, and $Na_v1.2$, perhaps in combination with $Na_v1.1$ and $Na_v1.3$ distributed over the somatodendritic membrane. Each of these may be further diversified by various β subunits and by modulation; each channel species may switch between more than ten different states, which may lead to a continuum of biophysical properties for each type rather than merely two distinct currents I_{NaT} and I_{NaP} (see, e.g., Taddese & Bean, 2002). Thus, by necessity, the Na^+ current models used in our CA1 cell model as well as in our dynamic clamp are obviously relatively simple approximations to the reality. Nevertheless, they reproduced and predicted important features of the cell's behavior, and our dynamic clamp was capable of both canceling and reproducing the main effects of the intrinsic I_{NaP} on somatic AHPs, f/I relation and, to some extent, spike timing. These observations suggest that these effects are fairly robust consequences of a subthreshold, voltage-dependent, persistent Na^+ conductance, and therefore tend to occur independently of the finer details in the properties of the Na^+ current.

Another major limitation of the HH model of I_{NaP} that we used for our dynamic clamp was that it did not include channel noise. Hence in our experiments we could not add noise caused by stochastic opening of simulated I_{NaP} channels. It has been suggested theoretically and supported by experimental evidence that ion channel noise can strongly affect spike time precision (Schneidman et al., 1998; White et al., 2000). Moreover, there is evidence that Na^+ channel noise caused by I_{NaP} channels is essential for subthreshold oscillations in entorhinal stellate neurons (Dorval, Jr. & White, 2005). However, our recent results suggest that subthreshold oscillations in CA1 hippocampal cells depend not only on intrinsic channel noise but also on I_{NaP} as an amplification mechanism (see Section 5.2).

4.7 Comparing Model Simulations and Dynamic-Clamp Manipulation of I_{NaP}

Throughout our study, we compared simulations performed by computational modeling of a CA1 pyramidal cell with results from dynamic-clamp experiments and other experimental manipulations. In most cases, we used a relatively simple computational model (8 compartments, 11 conductances; Vervaeke et al., 2006), but in order to check our results with the simple model we also employed far more complex and detailed models, comprising several hundred compartments (Fig. 2C, unpublished). Figure 8 shows the responses of the simple eight-compartment model cell to a ramp current injection, similar to those performed experimentally (Figs. 6 and 7). Omission of I_{NaP} in the model (Fig. 8, no I_{NaP}) had similar effects as canceling I_{NaP} with dynamic clamp or blocking it with TTX in real cells (Figs. 6 and 7).

4.8 Predictive Modeling

In our study of I_{NaP} functions in CA1 pyramidal cells (Vervaeke et al., 2006), we decided to test several of our ideas theoretically by computational modeling before testing the same ideas experimentally. Thus, we used our models to make predictions, before testing the predictions by intracellular recordings in brain slices with dynamic clamp, channel blockers, or other manipulations (Vervaeke et al., 2006). For example, our simulations led to the prediction that I_{NaP} would increase the amplitudes of AHPs (Fig. 9A). When we subsequently tested this prediction experimentally with dynamic clamp (Fig. 9B) or with TTX, the prediction was confirmed (Vervaeke et al., 2006); see Section 5.1, below). The

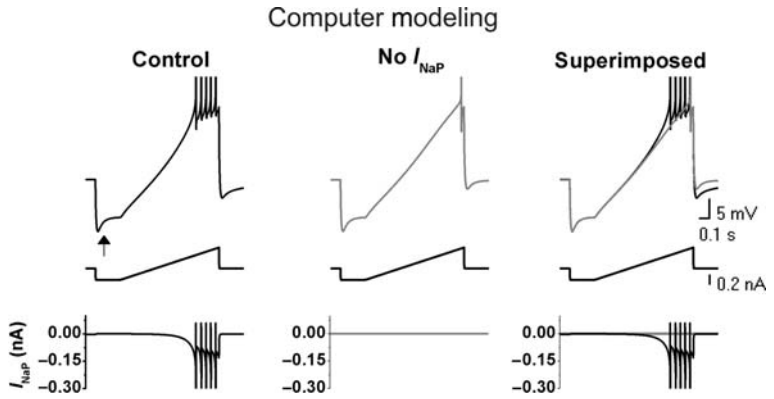

Fig. 8 Model simulations of I_{NaP} in current clamp. Voltage responses (upper traces) to a current ramp command with (*black*) and without I_{NaP} (*gray*). The time course of I_{NaP} is plotted below. (Modified from Vervaeke et al., 2006, with permission from *Cell Press, Elsevier*.)

model simulations also predicted that I_{NaP} would have contrasting effects on the excitability of the cell. As intuitively expected, the model predicted that I_{NaP} would reduce the minimal current necessary to evoke spiking (rheobase). In addition, however, the model also predicted that I_{NaP} would also reduce the slope (gain) of the f/I relation, which was intuitively quite unexpected. Nevertheless, when we tested these predictions experimentally by using dynamic clamp, the experiments confirmed both the model predictions (see Fig. 11 and Section 5.2, below).

5 I_{NaP} Functions in Hippocampal Pyramidal Neurons

5.1 *Effects of* I_{NaP} *on After-Hyperpolarizations*

In most kinds of neurons, single action potentials and spike bursts are followed by AHPs, mainly caused by activation of various voltage- and calcium-gated potassium conductances that outlast the spikes (Vogalis et al., 2003). These AHPs exert feedback regulation of neuronal excitability, shaping the spike pattern through spike frequency adaptation and other effects (Madison & Nicoll, 1984; Storm, 1989, 1990; Pedarzani & Storm, 1993; Peters et al., 2005; Gu et al., 2007). Since I_{NaP} is caused by a negative slope resistance that should be capable of amplifying any voltage deflection within its activation range (Crill, 1996; Stuart, 1999; Hu et al., 2002), we expected that I_{NaP} would enhance the AHP amplitudes in a voltage-dependent manner, just like it enhances subthreshold resonance and oscillations in these cells (Hu et al., 2002).

To test this idea, we first used our CA1 pyramidal cell model to simulate experiments (Fig. 9) (Vervaeke et al., 2006). Steady current injection (DC) was used to adjust the initial membrane potential to various levels, ranging from −58 to −80 mV, while action potentials were triggered by brief current pulses superimposed on the DC. As expected, the simulations showed that I_{NaP} enhanced the AHPs in a voltage-dependent manner in the model (Fig. 9A). In these simulations, we triggered more spikes when injecting a hyperpolarizing DC "holding current" than when using depolarizing DC, in order to be able to compare the impact of I_{NaP} on AHPs of similar amplitudes at different potentials, in spite of the voltage-dependent change in K^+ driving force. However, the spike number was always kept constant with and without I_{NaP}, and similar effects were seen also when the spike number was kept constant at different potentials.

To test whether I_{NaP} actually has such an amplifying effect also in real CA1 pyramidal cells, we repeated the same protocol during dual whole-cell recordings in rat hippocampal slices (Fig. 1) before and after canceling I_{NaP} with the dynamic clamp (Fig. 9B). Again, we used DC to adjust the initial membrane potential. We found that cancellation of I_{NaP} reduced the AHPs in a voltage-dependent manner, as predicted theoretically and by the model simulations (Fig. 9A). This implies that I_{NaP} ampifies the AHPs, as expected (Vervaeke et al., 2006).

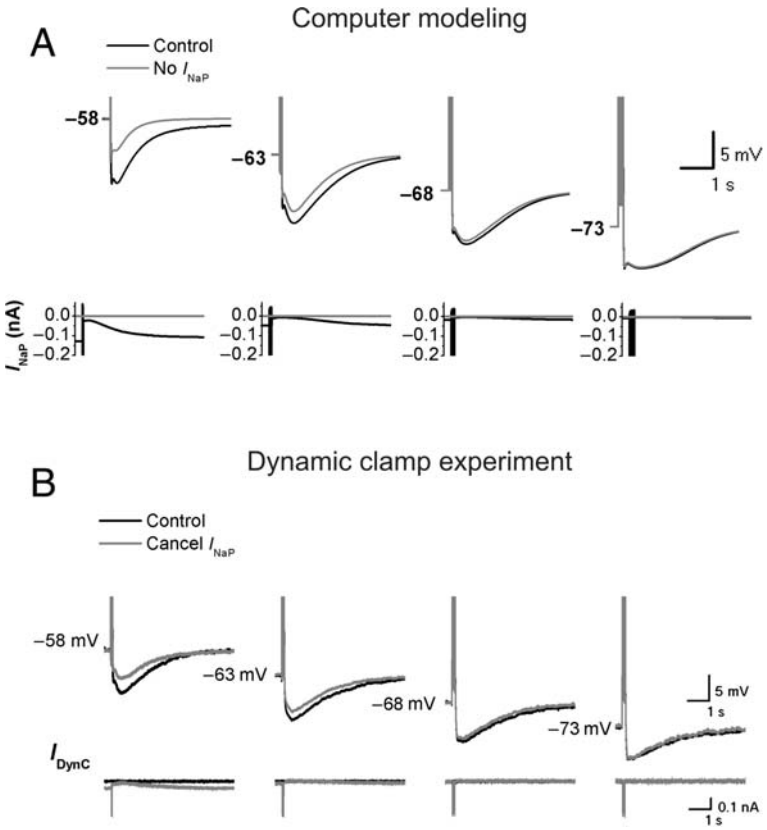

Fig. 9 Voltage-dependent amplification of after-hyperpolarizations (AHPs) by I_{NaP}: comparing computational model predictions with dynamic-clamp experiments. (**A**) Model simulations of AHPs evoked by spike trains, at different holding potentials (maintained by steady current injection), before (*black*) and after (*gray*) removing I_{NaP}. (**B**) AHPs evoked by action potentials before (*black*) and after (*gray*) canceling I_{NaP} by dynamic clamp. In both (A) and (B) each action potential was triggered by a brief, depolarizing current pulse (1–2 ms) and the spike number was adjusted to yield AHPs of similar amplitude for all holding potentials before eliminating I_{NaP}. In each case, I_{NaP} is plotted below the voltage traces. (Modified from Vervaeke et al., 2006, with permission from *Cell Press, Elsevier*.)

5.2 Effects of I_{NaP} *on Intrinsic Subthreshold Theta Oscillations*

Intrinsic, subthreshold membrane potential oscillations can be important determinants of neuronal integration, neuronal coding, and discharge patterns, and can support coherent network oscillations (Llinas, 1988; Singer, 1993; Steriade et al., 1993; Buzsaki, 2006). In the hippocampal formation, slow network oscillations in the theta frequency band (4–10 Hz) are prominent (Vanderwolf, 1988; Buzsaki, 2002). Even when isolated by synaptic blockade, spiny stellate

cells of the EC and hippocampal pyramidal neurons show subthreshold membrane potential oscillations and resonance within the theta frequency band, which are likely to support network theta and neuronal coding within this system (Alonso & Llinas, 1989; Leung & Yu, 1998; Pike et al., 2000; Buzsaki, 2002; Hu et al., 2002). By combining electrophysiology and modeling, we previously found that the subthreshold theta resonance in depolarized CA1 pyramidal cells is due to an interplay between I_{NaP} and the Kv7/KCNQ/M-type potassium current (I_M), while the theta resonance in hyperpolarized cells is due to h/HCN current (I_h) (Hu et al., 2002). Although the prominent perithreshold theta resonance and oscillations in depolarized EC stellate cells depend on I_h rather than I_M, these theta oscillations also depend on I_{NaP} (Alonso & Llinas, 1989). However, in the EC stellate neurons, there is evidence that not only I_{NaP} and I_h are needed for perithreshold oscillations; ion channel noise caused by persistent Na^+ channels also appears to be essential for these oscillations to appear (Dorval, Jr. & White, 2005).

To further examine the role of I_{NaP} in subthreshold membrane potential oscillations of hippocampal CA1 pyramidal neurons, we used dynamic clamp to cancel I_{NaP} in hippocampal CA1 pyramidal neurons in hippocampal slices from young rats (4–10 weeks of age) at 30°C (Fig. 10). The methods were identical to those used in our previous study (Vervaeke et al., 2006). In all neurons tested ($n = 5$), we found that cancellation of I_{NaP} strongly suppressed the subthreshold theta oscillations (Fig. 10B). The suppression by dynamic clamp was virtually as efficient as blockade of all Na^+ channels by bath application of 1.0 μM TTX (Fig. 10A). Since TTX blocks the macropscopic I_{NaP} as well as the ion channel noise caused by stochastic opening of Na^+ channels, these result suggest that subthreshold oscillations in CA1 pyramidal neurons depend on I_{NaP} as an amplification mechanism, probably in addition to intrinsic channel noise that is needed to trigger the depolarizing waves that constitute these oscillations.

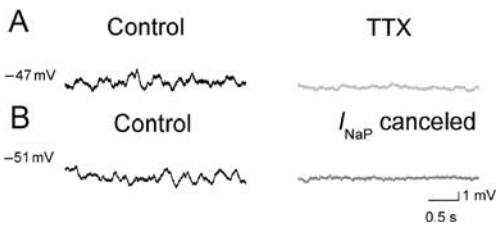

Fig. 10 I_{NaP} is necessary for subthreshold membrane potential oscillations in the theta frequency range in CA1 hippocampal pyramidal neurons. (**A**) Typical subthreshold membrane potential oscillations before and after blockade of I_{NaP} by bath application of 1 μM TTX. (**B**) Typical subthreshold membrane potential oscillations before and after canceling I_{NaP} with dynamic clamp. All traces were recorded at 30°C in the presences of synaptic blockers (10 μM DNQX (6,7-dinitroquinoxaline-2,3-dione) and 10 μM bicuculline free base, which block glutamatergic and GABAergic fast synaptic transmission). (H. Hu et al., unpublished data, 2006.)

5.3 *Effects of* I_{NaP} *on Current-to-Frequency Transduction*

Many neurons and sensory cells are capable of translating the intensity of a sustained excitatory synaptic barrage, sensory stimuli, or current injection (I) into a train of repetitive firing in which the action potential frequency (f) encodes the stimulus intensity – the so-called current-to-frequency transduction or frequency coding (Hodgkin, 1948; Kernell, 1965; Connor & Stevens, 1971). This function has been studied in CA1 hippocampal pyramidal cells, like in many other neurons, by injecting a depolarizing current (I) into the cell and plotting the spike frequency (f) as a function of the current intensity (f/I plot) (Lanthorn et al., 1984; Madison & Nicoll, 1984). These studies, as well as studies indicating that AHPs are important regulators of the f/I relation (Kernell, 1965; Madison & Nicoll, 1984; Storm, 1989; Pedarzani & Storm, 1993), suggested that I_{NaP} is likely to strongly affect the current-to-frequency transduction.

To test these ideas (Vervaeke et al., 2006), we first performed model simulations (Fig. 11A). Surprisingly, these simulations predicted that I_{NaP} would have two almost opposite or contrasting effects on the excitability of the cell. On one hand, the model predicted that I_{NaP} would reduce the minimal current necessary to evoke spiking (rheobase), as intuitively expected, because I_{NaP} naturally will help excite the cell, essentially by adding to the injected current, I. Thus, as shown in Fig. 11A (left), the base of the simulated f/I plot was shifted to the right when I_{NaP} was omitted from the model (gray curve). On the other hand, the model predicted that I_{NaP} would also reduce the steepness of the f/I relation (the f/I slope or gain), as shown by the superimposed f/I plots to the right in Fig. 11A. This result was surprising, because I_{NaP}, being an inward current activated by depolarization, might be expected to be activated more, and thus contribute more excitation, the more depolarizing current one injects. Nevertheless, when we tested these predictions experimentally by canceling I_{NaP} with dynamic clamp, the experiments confirmed both of the two model predictions: the foot of the f/I curve was shifted to the right, but the curve became steeper (Fig. 11B) (Vervaeke et al., 2006). The effect on the f/I slope is likely due to a complex interplay between, I_{NaP}, I_{NaT}, AHPs, and other factors.

5.4 *Effects of* I_{NaP} *on Firing Regularity*

The f/I experiments also showed that I_{NaP} strongly affected the regularity of repetitive firing in CA1 pyramidal cells (Fig. 12) (Vervaeke et al., 2006). Thus, canceling of I_{NaP} by dynamic clamp made the steady-state repetitive firing far less regular (Fig. 12, right), attenuated the peaks in the autocorrelation plots of spike timing (bottom), and significantly increase in the coefficient of variation of the interspike intervals, in all cells tested (data not shown here; Vervaeke et al., 2006).

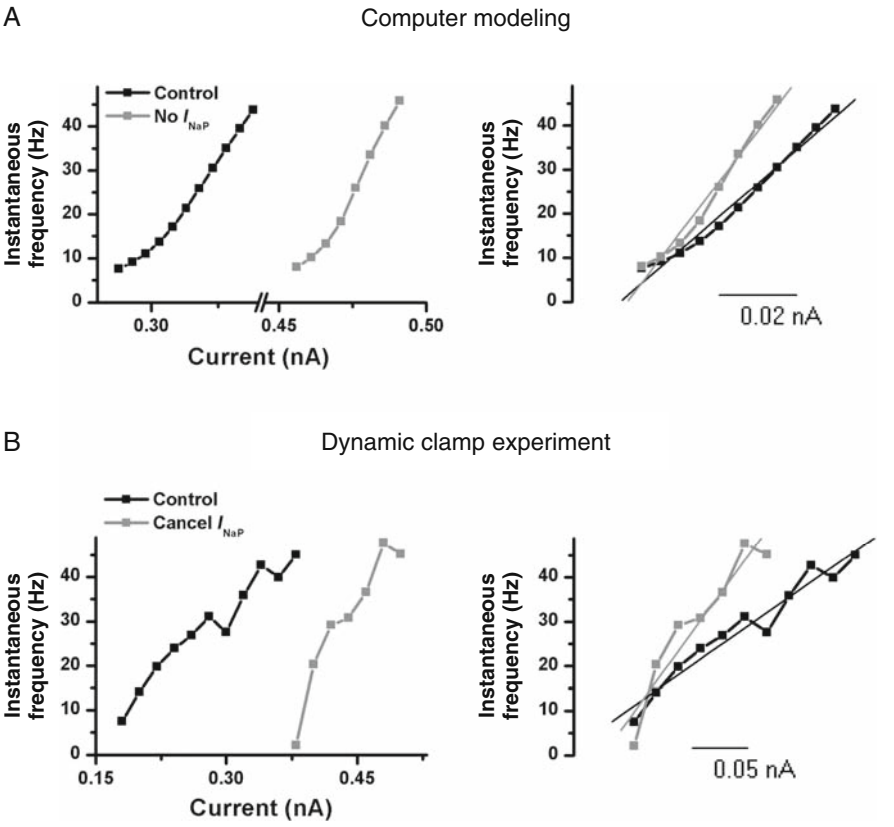

Fig. 11 Effects of I_{NaP} on the input–output relation in CA1 pyramidal neurons. Comparing model predictions with dynamic-clamp experiments of current (I)-to-spike frequency (f) transduction. (**A**) Frequency–current (f/I) plots with I_{NaP} (*black*: control) and without I_{NaP} (*grey*) of the average frequency of the first four spikes (range ~15–60 Hz) in response to injection of 1-s-long current pulses. The f/I slope for this range increased by 78 % when I_{NaP} was blocked, as shown by the fitted linear functions (*upper right*). (**B**) Experimental f/I plots obtained from a CA1 pyramidal cell according to the protocol described in (A), before (*black*) and after (*gray*) canceling I_{NaP} by dynamic clamp. Linear fits of the f/I curves (*right panels*) showed that canceling I_{NaP} increased the f/I slope, on average by 43% for all cells tested ($n = 7$, $p = 0.015$). (Modified from Vervaeke et al., 2006, with permission from *Cell Press, Elsevier*.)

We noted that cancellation of I_{NaP} caused the expected reduction in AHP amplitude between spikes (Fig. 9), but also a slightly higher spike threshold and lower spike amplitude and rate of rise. These observations suggest that in the absence of I_{NaP}, the shallower AHPs amplitudes allowed less than normal recovery from inactivation of the spike-generating Na^+ current, I_{NaT}, during each interspike interval. Under these conditions, the remaining active I_{NaT} channels may be so few that channel noise becomes more important for spike initiation, thus causing more irregular repetitive firing (Skaugen & Walløe, 1979; Schneidman et al., 1998).

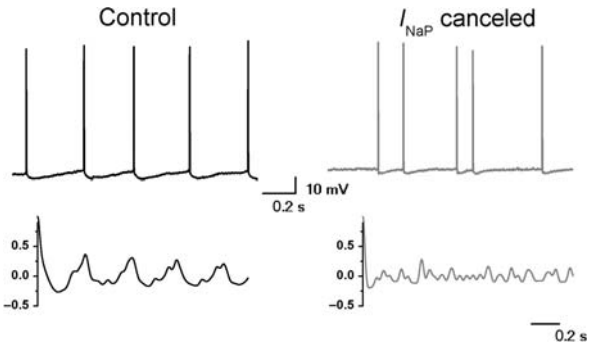

Fig. 12 I_{NaP} maintains regularity of repetitive firing in CA1 pyramidal neurons. (*Left*) Steady-state (fully adapted) repetitive firing of a CA1 pyramidal cell in response to a constant depolarizing current injection under normal conditions (*black trace*).When I_{NaP} was canceled by dynamic clamp (*right*, *gray trace*), the firing became less regular. The intensity of the injected steady current was adjusted to keep a constant average firing rate (~3 Hz) in both conditions The autocorrelation plots shown below (digitally filtered at 15 Hz) indicate that the regularity of firing was reduced when I_{NaP} was canceled ($\boldsymbol{n} = 6$). (Modified from Vervaeke et al., 2006, with permission from *Cell Press, Elsevier*.)

5.5 *Effects of* $\mathbf{I}_{NaP}$ *on Spike Timing Precision*

We also used dynamic clamp to tested how I_{NaP} affects the precision of spike timing in response to near-threshold excitatory synaptic input (EPSPs). Holding the CA1 cells at a slightly depolarized potential (~−60 mV), we evoked EPSPs by stimulating afferent glutamatergic axons in *stratum radiatum*, at just sufficient intensity to evoke an action potentials on about every other EPSP (50% probability). Under normal conditions, spike latency was highly variable (Fig. 13A, left), but this variability was strongly reduced as soon as we canceled I_{NaP} by dynamic clamp, readjusting the stimulus strength to achieve once again a 50% spike probability (Fig. 13A, right). Thus, these results support the conclusions of Fricker & Miles (2000) who suggested that I_{NaP} reduces spike precision. We also noticed that the subtraction of I_{NaP} by dynamic clamp reduced both the rise time and decay time of the EPSPs (Fig. 13B, left), and reduced the plateau potentials or prepotentials from which the spikes often arose in the presence of I_{NaP} (Lanthorn et al., 1984; Hu et al., 1992; Fricker & Miles, 2000). Naturally, loss of I_{NaP} also reduced the EPSP amplitude, but this was compensated in these experiments by increasing the stimulation intensity, in order to maintain ~50% firing probability both with and without cancellation of I_{NaP}. The sharper peak of the EPSP and the loss of plateau potentials in the absence of I_{NaP}, provides less room for random noise-triggered changes in spike latency. This is a likely cause of the increased spike timing precision when the effect of I_{NaP} was suppressed (Fig. 13A).

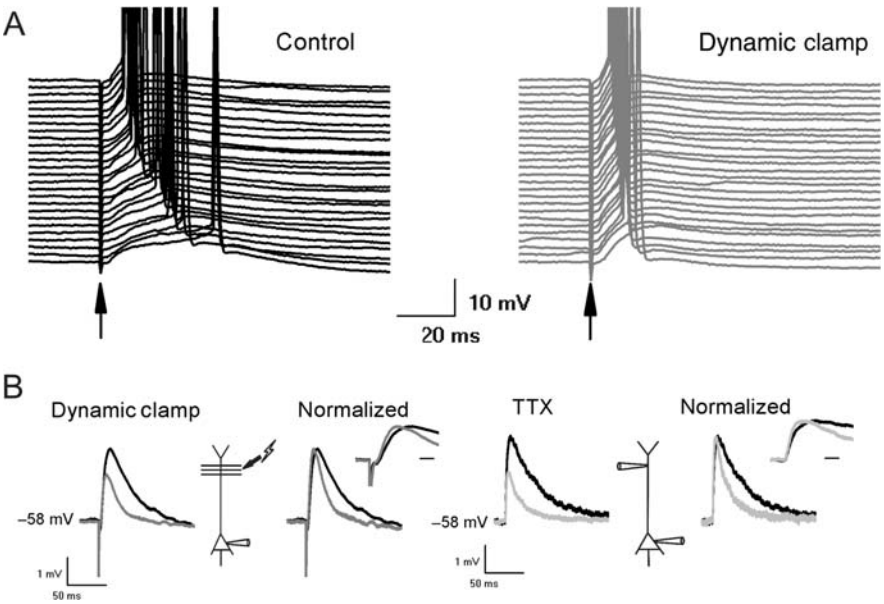

Fig. 13 I_{NaP} reduces spike timing precision in response to synaptic input. (**A**) Somatic recordings of excitatory synaptic potentials (EPSPs) evoked by stimulating dendritic excitatory synapses (axons in the middle of *stratum radiatum*). The EPSPs triggered a spike with a probability of 0.48. When I_{NaP} was canceled by dynamic clamp, the stimulation strength had to be increased to evoke spikes with a similar probability as before (0.41). (**B**, *left*) Subthreshold EPSPs were evoked by stimulating axons in *stratum radiatum* (100 μM APV (2- amino-5-phosphonovalerate) was present to block *N*-methyl-d-aspartate (NMDA)-type glutamate receptors). (**B**, *right*) A simulated EPSP current waveform was injected through a whole-cell patch pipette on the apical dendrite ~220 μm from the soma. Bicuculline free base (10 μM) was present throughout all experiments (Modified from Vervaeke et al., 2006, with permission from *Cell Press, Elsevier*.)

In order to compare the effects of dynamic clamp with complete Na^+ channel blockade with TTX, we also performed dual dendritic and somatic whole-cell recordings (Fig. 13B, right). After patching the apical dendrite 180–320 mm from the soma, an EPSP-like current waveform was injected into the dendrite to evoke an artificial somatic "EPSP" (aEPSP). Like the dynamic clamp, application of 1 μM TTX to the slice reduced both the rise time and decay time of the somatic aEPSP (Fig. 13B, right). These similarities indicate that our somatically applied dynamic "point" clamp was able to efficiently cancel the effects of I_{NaP} even on EPSPs of distal dendritic origin. Hence, the observed amplifying and slowing effects is entirely or largely due to an I_{NaP} that originates close to the soma since it is so well controlled by our somatic dynamic clamp. Thus, these results lend further, independent support to our conclusion that I_{NaP} in CA1 pyramidal cells is probably caused by Na^+ channels concentrated at the axon initial segment, which was part of the justification for using somatic dynamic clamp to study the functional roles of this current in the first place (Fig. 2).

6 Concluding Remarks

Based on the experiences described above, we conclude that somatic dynamic clamp is an extremely useful tool for studying the functions of the persistent sodium current, $I_{NaP.}$ Although the Na^+ current model that was used in our CA1 hippocampal pyramidal neuron model simulations contained only a simple HH model of I_{NaP} combined with a relatively simple four-state Markov model of the transient current, I_{NaT}, it successfully predicted and reproduced several key features of the Na^+ current-dependent response properties of the rat CA1 pyramidal cells. Our findings suggest that the main effects of I_{NaP} in these cells are quite robust, and therefore may be produced by any fast, persistent inward current with at least roughly the correct voltage dependence combined with a largely perisomatic subcellular distribution.

Considering the advantages of dynamic clamp over pharmacological manipulations for in vivo experiments, the use of this method for studying the functional roles of I_{NaP} and other currents in intact and active networks, holds great promise.

Acknowledgments Our work was supported by the Norwegian Research Council (NFR) through FUGE, NevroNor, and the Norwegian Centre of Excellence programs, and by HFSP for Research Grant RGP0049 to L.J.G. and J.F.S.

References

Aldrich RW, Corey DP, & Stevens CF (1983). A reinterpretation of mammalian sodium channel gating based on single channel recording. *Nature* **306**, 436–441.

Alonso A & Llinas RR (1989). Subthreshold Na + -dependent theta-like rhythmicity in stellate cells of entorhinal cortex layer II. *Nature* **342**, 175–177.

Alzheimer C, Schwindt PC, & Crill WE (1993). Modal gating of Na + channels as a mechanism of persistent Na + current in pyramidal neurons from rat and cat sensorimotor cortex. *J Neurosci* **13**, 660–673.

Andreasen M & Lambert JDC (1999). Somatic amplification of distally generated subthreshold EPSPs in rat hippocampal pyramidal neurones. *J Physiol* **519**, 85–100.

Armstrong CM (1981). Sodium channels and gating currents. *Physiol Rev* **61**, 644–683.

Astman N, Gutnick MJ, & Fleidervish IA (1998). Activation of protein kinase C increases neuronal excitability by regulating persistent Na + current in mouse neocortical slices. *J Neurophysiol* **80**, 1547–1551.

Astman N, Gutnick MJ, & Fleidervish IA (2006). Persistent sodium current in layer 5 neocortical neurons is primarily generated in the proximal axon. *J Neurosci* **26**, 3465–3473.

Attwell D, Cohen I, Eisner D, Ohba M, & Ojeda C (1979). The steady state TTX-sensitive ("window") sodium current in cardiac Purkinje fibres. *Pflugers Arch* **379**, 137–142.

Benoit E & Escande D (1993). Fast K channels are more sensitive to riluzole than slow K channels in myelinated nerve fibre. *Pflugers Arch* **422**, 536–538.

Benoit E & Escande D (1991). Riluzole specifically blocks inactivated Na channels in myelinated nerve fibre. *Pflugers Arch* **419**, 603–609.

Boiko T, Rasband MN, Levinson SR, Caldwell JH, Mandel G, Trimmer JS, & Matthews G (2001). Compact myelin dictates the differential targeting of two sodium channel isoforms in the same axon. *Neuron* **30**, 91–104.

Boiko T, Van Wart A, Caldwell JH, Levinson SR, Trimmer JS, & Matthews G (2003). Functional specialization of the axon initial segment by isoform-specific sodium channel targeting. *J Neurosci* **23**, 2306–2313.

Borg-Graham L (1987). Modelling the somatic electrical behavior of hippocampal pyramidal neuron. Massachusetts Institute of Technology. Ref Type: Thesis/Dissertation

Borg-Graham L (1999). Interpretations of data and mechanisms for hippocampal pyramidal cell models. In *Cerebral cortex*, eds. Ulinski PS, Jones EG, & Peters A, pp. 19–138. Kluwer Academic/Plenum Publishers, New York.

Brown DA & Adams PR (1980). Muscarinic suppression of a novel voltage-sensitive K+ current in a vertebrate neurone. *Nature* **283**, 673–676.

Buzsaki G (2002). Theta oscillations in the hippocampus. *Neuron* **33**, 325–340.

Buzsaki G (2006). *Rhythms of the brain buzsaki* Oxford University Press, Oxford.

Cantrell AR & Catterall WA (2001). Neuromodulation of Na+ channels: An unexpected form of cellular plasticity. *Nat Rev Neurosci* **2**, 397–407.

Chandler WK & Meves H (1966). Incomplete sodium inactivation in internally perfused giant axons from Loligo forbesi. *J Physiol* **186**, 121P–122P.

Chao TI & Alzheimer C (1995). Effects of phenytoin on the persistent Na+ current of mammalian CNS neurones. *neuroreport* **6**, 1778–1780.

Connor JA & Stevens CF (1971). Prediction of repetitive firing behaviour from voltage clamp data on an isolated neurone soma. *J Physiol* **213**, 31–53.

Connors BW, Gutnick MJ, & Prince DA (1982). Electrophysiological properties of neocortical neurons in vitro. *J Neurophysiol* **48**, 1302–1320.

Crill WE (1996). Persistent sodium current in mammalian central neurons. *Ann Rev Physiol* **58**, 349–362.

Dorval AD, Jr. & White JA (2005). Channel noise is essential for perithreshold oscillations in entorhinal stellate neurons. *J Neurosci* **25**, 10025–10028.

Duprat F, Lesage F, Patel AJ, Fink M, Romey G, & Lazdunski M (2000). The neuroprotective agent riluzole activates the two P domain K+ channels TREK-1 and TRAAK. *Mol Pharmacol* **57**, 906–912.

Enomoto A, Han JM, Hsiao CF, & Chandler SH (2007). Sodium currents in mesencephalic trigeminal neurons from Nav1.6 null mice. *J Neurophysiol* **98**, 710–719.

French CR & Gage PW (1985). A threshold sodium current in pyramidal cells in rat hippocampus. *Neurosci Lett* **56**, 289–293.

French CR, Sah P, Buckett KJ, & Gage PW (1990). A voltage-dependent persistent sodium current in mammalian hippocampal neurons. *J Gen Physiol* **95**, 1139–1157.

Fricker D & Miles R (2000). EPSP amplification and the precision of spike timing in hippocampal neurons. *Neuron* **28**, 559–569.

Gilly W & Armstrong CM (1984). Threshold channels[mdash]a novel type of sodium channel in squid giant axon. *Nature* **309**, 448–450.

Goldstein SAN, Bockenhauer D, O'Kelly I, & Zilberberg N (2001). Potassium leak channels and the KCNK family of two-p-domain subunits. *Nat Rev Neurosci* **2**, 175–184.

Gonzalez-Burgos G & Barrionuevo G (2001). Voltage-gated sodium channels shape subthreshold EPSPs in layer 5 pyramidal neurons from rat prefrontal cortex. *J Neurophysiol* **86**, 1671–1684.

Gu N, Vervaeke K, & Storm JF (2007). BK potassium channels facilitate high-frequency firing and cause early spike frequency adaptation in rat CA1 hippocampal pyramidal cells. *J Physiol* **580**, 859–882.

Hodgkin AL (1948). The local electric changes associated with repetitive action in a non-medullated axon. *J Physiol* **107**, 165–181.

Hodgkin AL & Huxley AF (1952). A quantitative description of membrane current and its application to conduction and excitation in nerve. *J Physiol* **117**, 500–544.

Hotson JR, Prince DA, & Schwartzkroin PA (1979). Anomalous inward rectification in hippocampal neurons. *J Neurophysiol* **42**, 889–895.

Hu GY, Hvalby O, Lacaille JC, Piercey B, Ostberg T, & Andersen P (1992). Synaptically triggered action potentials begin as a depolarizing ramp in rat hippocampal neurones in vitro. *J Physiol* **453**, 663–687.

Hu H, Vervaeke K, & Storm JF (2002). Two forms of electrical resonance at theta frequencies, generated by M-current, h-current and persistent Na + current in rat hippocampal pyramidal cells. *J Physiol* **545**, 783–805.

Huang CS, Song JH, Nagata K, Yeh JZ, & Narahashi T (1997). Effects of the neuroprotective agent riluzole on the high voltage-activated calcium channels of rat dorsal root ganglion neurons. *J Pharmacol Exp Ther* **282**, 1280–1290.

Jensen MS, Azouz R, & Yaari Y (1996). Spike after-depolarization and burst generation in adult rat hippocampal CA1 pyramidal cells. *J Physiol* **492(Pt 1)**, 199–210.

Jeub M, Beck H, Siep E, Ruschenschmidt C, Speckmann E-J, Ebert U, Potschka H, Freichel C, Reissmuller E, & Loscher W (2002). Effect of phenytoin on sodium and calcium currents in hippocampal CA1 neurons of phenytoin-resistant kindled rats. *Neuropharmacology* **42**, 107–116.

Kaplan MR, Cho MH, Ullian EM, Isom LL, Levinson SR, & Barres BA (2001). Differential control of clustering of the sodium channels Nav1.2 and Nav1.6 at developing CNS nodes of ranvier. *Neuron* **30**, 105–119.

Kernell D (1965). The limits of firing frequency in cat lumbosacral motoneurones possessing different time course of afterhyperpolarization. *Acta Physiol Scand* **65**, 87–100.

Kole MHP, Ilschner SU, Kampa BM, Williams SR, Ruben PC, & Stuart GJ (2008). Action potential generation requires a high sodium channel density in the axon initial segment. *Nat Neurosci* **11**, 178–186.

Komai S, Licznerski P, Cetin A, Waters J, Denk W, Brecht M, & Osten P (2006). Postsynaptic excitability is necessary for strengthening of cortical sensory responses during experience-dependent development. *Nat Neurosci* **9**, 1125–1133.

Kuo CC & Bean BP (1994). Slow binding of phenytoin to inactivated sodium channels in rat hippocampal neurons. *Mol Pharmacol* **46**, 716–725.

Lanthorn T, Storm J, & Andersen P (1984). Current-to-frequency transduction in CA1 hippocampal pyramidal cells: Slow prepotentials dominate the primary range firing. *Exp Brain Res* **53**, 431–443.

Leung LS & Yu HW (1998). Theta-frequency resonance in hippocampal CA1 neurons in vitro demonstrated by sinusoidal current injection. *J Neurophysiol* **79**, 1592–1596.

Lien CC & Jonas P (2003). Kv3 potassium conductance is necessary and kinetically optimized for high-frequency action potential generation in hippocampal interneurons. *J Neurosci* **23**, 2058–2068.

Lipowsky R, Gillessen T, & Alzheimer C (1996). Dendritic Na + channels amplify EPSPs in hippocampal CA1 pyramidal cells. *J Neurophysiol* **76**, 2181–2191.

Llinas R & Sugimori M (1980). Electrophysiological properties of in vitro Purkinje cell somata in mammalian cerebellar slices. *J Physiol* **305**, 171–195.

Llinas RR (1988). The intrinsic electrophysiological properties of mammalian neurons: insights into central nervous system function. *Science* **242**, 1654–1664.

Losonczy A & Magee JC (2006). Integrative properties of radial oblique dendrites in hippocampal CA1 pyramidal neurons. *Neuron* **50**, 291–307.

Ma M & Koester J (1996). The role of K + currents in frequency-dependent spike broadening in aplysia R20 neurons: A dynamic-clamp analysis. *J Neurosci* **16**, 4089–4101.

Madison DV & Nicoll RA (1984). Control of the repetitive discharge of rat CA 1 pyramidal neurones in vitro. *J Physiol* **354**, 319–331.

Magee JC & Johnston D (1995). Characterization of single voltage-gated Na + and Ca2 + channels in apical dendrites of rat CA1 pyramidal neurons. *J Physiol* **487(Pt 1)**, 67–90.

Magistretti J & Alonso A (1999). Biophysical properties and slow voltage-dependent inactivation of a sustained sodium current in entorhinal cortex layer-II principal neurons: A whole-cell and single-channel study. *J Gen Physiol* **114**, 491–509.

Magistretti J & Alonso A (2002). Fine gating properties of channels responsible for persistent sodium current generation in entorhinal cortex neurons. *J Gen Physiol* **120**, 855–873.

Mattson RH, Cramer JA, Collins JF, Smith DB, gado-Escueta AV, Browne TR, Williamson PD, Treiman DM, McNamara JO, & McCutchen CB (1985). Comparison of carbamazepine, phenobarbital, phenytoin, and primidone in partial and secondarily generalized tonic-clonic seizures. *N Engl J Med* **313**, 145–151.

McCormick DA, Huguenard JR (1992). A model of the electrophysiological properties of thalamocortical relay neurons. *J Neurophysiol* **68**, 1384–1400.

Migliore M, Cook EP, Jaffe DB, Turner DA, & Johnston D (1995). Computer simulations of morphologically reconstructed CA3 hippocampal neurons. *J Neurophysiol* **73**, 1157–1168.

Patlak J (1991). Molecular kinetics of voltage-dependent Na+ channels. *Physiol Rev* **71**, 1047–1080.

Pedarzani P & Storm JF (1993). PKA mediates the effects of monoamine transmitters on the K+ current underlying the slow spike frequency adaptation in hippocampal neurons. *Neuron* **11**, 1023–1035.

Peters HC, Hu H, Pongs O, Storm JF, & Isbrandt D (2005). Conditional transgenic suppression of M channels in mouse brain reveals functions in neuronal excitability, resonance and behavior. *Nat Neurosci* **8**, 51–60.

Pike FG, Goddard RS, Suckling JM, Ganter P, Kasthuri N, & Paulsen O (2000). Distinct frequency preferences of different types of rat hippocampal neurones in response to oscillatory input currents. *J Physiol* **529**, 205–213.

Pinto RD, Elson RC, Szucs A, Rabinovich MI, Selverston AI, & Abarbanel HDI (2001). Extended dynamic clamp: Controlling up to four neurons using a single desktop computer and interface. *J Neurosci Methods* **108**, 39–48.

Qu Y, Curtis R, Lawson D, Gilbride K, Ge P, DiStefano PS, Silos-Santiago I, Catterall WA, & Scheuer T (2001). Differential modulation of sodium channel gating and persistent sodium currents by the [beta]1, [beta]2, and [beta]3 subunits. *Mol Cell Neurosci* **18**, 570–580.

Raman IM & Bean BP (1999). Ionic currents underlying spontaneous action potentials in isolated cerebellar purkinje neurons. *J Neurosci* **19**, 1663–1674.

Rosenkranz JA & Johnston D (2007). State-dependent modulation of amygdala inputs by dopamine-induced enhancement of sodium currents in layer V entorhinal cortex. *J Neurosci* **27**, 7054–7069.

Schneidman E, Freedman B, & Segev I (1998). Channel stochasticity may be critical in determining the reliability and precision of spike timing. *Neural Comp* **10**, 1679–1703.

Schwindt PC & Crill WE (1995). Amplification of synaptic current by persistent sodium conductance in apical dendrite of neocortical neurons. *J Neurophysiol* **74**, 2220–2224.

Shao LR, Halvorsrud R, Borg-Graham L, & Storm JF (1999). The role of BK-type Ca2+-dependent K+ channels in spike broadening during repetitive firing in rat hippocampal pyramidal cells. *J Physiol* **521 Pt 1**, 135–146.

Singer W (1993). Synchronization of cortical activity and its putative role in information processing and learning. *Annu Rev Physiol* **55**, 349–374.

Skaugen E & Walløe L (1979). Firing behaviour in a stochastic nerve membrane model based upon the Hodgkin-Huxley equations. *Acta Physiol Scand* **107**, 343–363.

Stafstrom CE, Schwindt PC, Chubb MC, & Crill WE (1985). Properties of persistent sodium conductance and calcium conductance of layer V neurons from cat sensorimotor cortex in vitro. *J Neurophysiol* **53**, 153–170.

Stafstrom CE, Schwindt PC, & Crill WE (1982). Negative slope conductance due to a persistent subthreshold sodium current in cat neocortical neurons in vitro. *Brain Res* **236**, 221–226.

Steriade M, McCormick DA, & Sejnowski TJ (1993). Thalamocortical oscillations in the sleeping and aroused brain. *Science* **262**, 679–685.
Storm JF (1989). An after-hyperpolarization of medium duration in rat hippocampal pyramidal cells. *J Physiol* **409**, 171–190.
Storm JF (1990). Potassium currents in hippocampal pyramidal cells. *Prog Brain Res* **83**, 161–187.
Stuart G & Sakmann B (1995). Amplification of EPSPs by axosomatic sodium channels in neocortical pyramidal neurons. *Neuron* **15**, 1065–1076.
Stuart G (1999). Voltage-activated sodium channels amplify inhibition in neocortical pyramidal neurons. *Nat Neurosci* **2**, 144–150.
Stuart GJ & Sakmann B (1994). Active propagation of somatic action potentials into neocortical pyramidal cell dendrites. *Nature* **367**, 69–72.
Taddese A & Bean BP (2002). Subthreshold sodium current from rapidly inactivating sodium channels drives spontaneous firing of tuberomammillary neurons. *Neuron* **33**, 587–600.
Traub RD, Jefferys JG, Miles R, Whittington MA, & Toth K (1994). A branching dendritic model of a rodent CA3 pyramidal neurone. *J Physiol* **481**, 79–95.
Urban NN, Henze DA, & Barrionuevo G (1998). Amplification of perforant-path EPSPs in CA3 pyramidal cells by LVA calcium and sodium channels. *J Neurophysiol* **80**, 1558–1561.
Urbani A & Belluzzi O (2000). Riluzole inhibits the persistent sodium current in mammalian CNS neurons. *Eur J Neurosci* **12**, 3567–3574.
Vandenberg CA & Bezanilla F (1991). A sodium channel gating model based on single channel, macroscopic ionic, and gating currents in the squid giant axon. *Biophys J* **60**, 1511–1533.
Vanderwolf CH (1988). Synchronization of cortical activity and its putative role in information processing and learning. *Int Rev Neurobiol* **20**, 225–340.
Vervaeke K, Hu H, Graham LJ, & Storm JF (2006). Contrasting effects of the persistent Na + current on neuronal excitability and spike timing. *Neuron* **49**, 257–270.
Vogalis F, Storm JF, & Lancaster B (2003). SK channels and the varieties of slow after-hyperpolarizations in neurons. *Eur J Neurosci* **18**, 3155–3166.
White JA, Rubinstein JT, & Kay AR (2000). Channel noise in neurons. *Trends Neurosci* **23**, 131–137.
Williams SR (2004). Spatial compartmentalization and functional impact of conductance in pyramidal neurons. *Nat Neurosci* **7**, 904–905.
Yue C, Remy S, Su H, Beck H, & Yaari Y (2005). Proximal persistent Na + channels drive spike afterdepolarizations and associated bursting in adult CA1 pyramidal cells. *J Neurosci* **25**, 9704–9720.

Using "Hard" Real-Time Dynamic Clamp to Study Cellular and Network Mechanisms of Synchronization in the Hippocampal Formation

John A. White, Fernando R. Fernandez, Michael N. Economo, and Tilman J. Kispersky

Abstract We report on development and use of dynamic-clamp technology to understand how synchronous neuronal activity is generated in the hippocampus and entorhinal cortex. We find that "hard" real-time dynamic-clamp systems, characterized by very small maximal errors in timing of feedback, are necessary for cases in which fast voltage-gated channels are being mimicked in experiments. Using a hard real-time system to study cellular oscillations in entorhinal cortex, we demonstrate that the stochastic gating of persistent Na^+ channels is necessary for cellular oscillations, and that cellular oscillations lead to dynamic changes in gain for conductance-based synaptic inputs. At the network level, we review experiments demonstrating that oscillating entorhinal stellate cells synchronize best via mutually excitatory interactions. Next, we show that cellular oscillations are volatile in the hypothesized "high-conductance" state, thought to occur in vivo, and suggest alternate means by which coherent activity can be generated in the absence of strong cellular oscillations. We close by discussing future developments that will increase the utility and widespread use of the dynamic-clamp method.

1 Introduction

In the 15 years since its introduction to the neuroscience community (Robinson and Kawai, 1993; Sharp et al., 1993), the dynamic-clamp technique has made steady progress toward adoption as a standard technique in cellular electrophysiology. In neurophysiology, dynamic clamp is used for three main purposes:

1) Introducing "virtual" voltage-gated channels into the neuronal membrane (e.g., Dorval and White, 2005; Bettencourt et al., 2008).

J.A. White (✉)
Department of Bioengineering, Brain Institute, University of Utah, 20 S. 2030 E., Salt Lake City, UT 84112, USA
e-mail: john.white@utah.edu

A. Destexhe, T. Bal (eds.), *Dynamic-Clamp*, Springer Series in Computational Neuroscience 1, DOI 10.1007/978-0-387-89279-5_9,

2) Examining responses of neurons to artificial, conductance-based synaptic inputs (e.g., Dorval and White, 2006; Fernandez and White, 2008).
3) Constructing "hybrid" neuronal networks containing both biological and simulated virtual components (e.g., Netoff et al., 2005a, b; see also Canavier et al., this volume).

Our group's interest in the technique dates back a decade. We were collecting voltage-clamp data from stellate cells in entorhinal cortex and using those data to build and study computational models (White et al., 1998a). We argued that "channel noise" (White et al., 2000a; Kispersky and White, 2008), generated by stochastic flicker of voltage-gated persistent Na^+ channels between open and closed states, was necessary to generate robust subthreshold oscillations (White et al., 1998a).

The problem with our argument in 1998 was that we lacked the ability to perform the crucial, well-controlled experiment to prove our point: a direct comparison of current-clamp data with *noisy* and *noiseless* representations of persistent Na^+ channels. We recognized that the dynamic-clamp technique was the best way forward to perform these experiments. We built such a system around real-time extensions of the Linux operating system (Dorval et al., 2001) and used it to confirm our hypothesis (Dorval and White, 2005). The modern version of our system, developed in collaboration with David Christini of Weill Medical College of Cornell (Christini et al., 1999) and Robert Butera of Georgia Tech (Butera et al., 2001), is open-source and freely available for download (http://rtxi.org/).

In this chapter, we review some of the problems we have studied using the dynamic-clamp technique, encompassing all three uses of dynamic clamp mentioned at the beginning of this section. We first describe studies of how precisely timed dynamic-clamp manipulations must be before performance is compromised (Bettencourt et al., 2008). In *Probing Single-Cell Oscillations*, we review studies of how the properties of virtual Na^+ channels affect cellular membrane-potential oscillations (Dorval and White, 2005) and present new data demonstrating that "synaptic gain" (the PSP peak amplitude as a function of the amplitude of the underlying artificial synaptic conductance) changes dynamically during subthreshold voltage oscillations. In *Networks of Coupled Oscillators*, we discuss studies of synchronization in hybrid networks of periodically firing neurons (Netoff et al., 2005a, b). In *Evidence Against the "Cellular Oscillator" Hypothesis*, we present evidence that entorhinal stellate cells do not generate cellular oscillations under in vivo-like conditions (Fernandez and White, 2008). In *Network Oscillations Arising from Rate-Limiting Synaptic Inputs*, we describe how known coherent activity could arise and be stabilized by synaptic interactions rather than cellular oscillations. Finally, in the *Discussion and Conclusions*, we speculate on the future of the dynamic-clamp technique, in particular considering obstacles to be overcome to increase the general use of this powerful approach in neurophysiology.

2 "Hard" Versus "Soft" Real-Time Performance

In dynamic clamping, current is injected through a recording pipette to simulate the actions of voltage- or ligand-gated channels. Because the current through a membrane channel depends instantaneously on transmembrane potential, dynamic-clamp calculations must be performed in real time. The situation is only more complex if one is modeling channels for which the probability of opening or the open-channel conductance depends on membrane potential. In this case, one must determine the conductance and the transmembrane current in real time.

Our current dynamic-clamp system is built around RTAI (https://www.rtai.org/), a patch to the Linux kernel that allows one to construct processes that run in "hard" real time, without unexpected delays or interruptions. Relative to systems that require specialized hardware from commercial vendors (Robinson and Kawai, 1993; Kullmann et al., 2004), our solution gives excellent performance at substantially lower cost. The trade-off is that RTAI can be more difficult to install and use, because most end-users are less familiar with Linux than with commercial operating systems, and because hardware drivers for Linux are not always available and fully debugged. Faced with this problem, some developers have built their systems in the Windows operating system (e.g., Pinto et al., 2001; Hughes et al., 2008), sacrificing hard real-time performance for gains in ease of use for the community at large. Such "soft" real-time systems perform well on average, but do not guarantee real-time performance on every time step, because it is not possible in these systems to disable all interrupt requests from the operating system.

In a recent study (Bettencourt et al., 2008), we sought to understand just how problematic deviations from hard real-time performance are. To this end, we ran computational simulations of a dynamic-clamp system interacting with a neuron. These simulations allowed us to explore how errors in dynamic-clamp performance would be expected to affect recorded data. We also designed a dynamic-clamp protocol to allow us to degrade hard real-time performance in a controlled fashion in electrophysiological experiments. We studied the effects of the numerical solver, time step, and latency (the delay between the beginning of the time step and the moment that the injected current is updated; latency must be less than the time step to allow real-time performance). The numerical solver is crucial: in simulations with virtualized Na^+ channels, the forward Euler algorithm generated errors that were an order of magnitude larger than those seen with fourth-order Runge–Kutta or stiff algorithms for a given time step. In simulated dynamic-clamp experiments, we found that time steps or latencies above 100 μs disrupted spike shape, but did not affect average firing rate. The effect of time step was particularly deleterious for simulations of virtualized Na^+ channels. For simulations of randomly varying time step and/or latency, degradations in performance were bounded by the worst-case scenario (i.e., the largest errors corresponded to the largest observed values of time step and latency, and matched the errors seen with the same fixed values of time step and latency). This result is a bit surprising, because in our simulated experiments, average time step

was accounted for by the simulated dynamic-clamp algorithm, but jitter in timing was not. Our results imply that one can simply study worst-case delays and latencies to characterize the worst-case performance of the system. Of course, average and median performance depend on the entire distributions of latency and time step, not simply the worst-case values.

Interestingly, real-world experiments were substantially more sensitive to errors than simulations. In experiments, we measured evoked action potentials under control conditions (Fig. 1A), then blocked Na^+ channels with tetrodoxin (TTX) and replaced them under dynamic clamp (Fig. 1B, C, D). Even at our fastest time steps under dynamic clamp (Fig. 1B, $dt = 12.5$ μs, minimum possible latency for this calculation), the rising phase of the action potential was abnormally fast and oscillatory instability was evident near the peak of the spike. Several factors likely contribute to the differences between Fig. 1A, B, including inaccuracies of our modeled Na^+ channels and unaccounted for delays imposed by filtering in data acquisition. Inaccuracies grow dramatically with delays: a time step of 25 μs, with a latency 10 μs beyond the minimum possible value, leads to significant "ringing" of the action potential near the peak (Fig. 1C; for experiments, we do not know the exact value of latency, the part of the time step used to perform calculations, but we know in this case that latency is greater than 10 μs and less than 25 μs). With a time step of 100 μs and minimal latency, the action potential is drastically distorted (Fig. 1D). Overall, we found that delays in hard real-time processing of 10–100 μs led to substantial inaccuracies if they occurred during rapid events like Na^+-based action

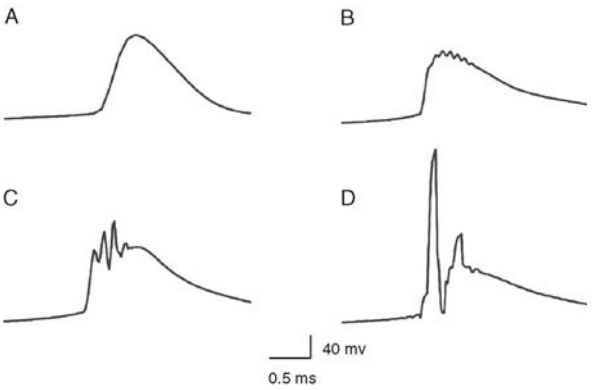

Fig. 1 Dynamic-clamp performance degrades with increased time step and latency. Under whole-cell patch clamp, we recorded depolarization-induced action potentials from a CA1 pyramidal cell. **A**: The action potential under control conditions. **B**: After blocking Na^+ channels with TTX, we replaced them using dynamic clamp. In this case, the time step was 12.5 μs. We solved the Na^+ channel gating equations and output current to the cell as quickly as possible. This implies that latency (the portion of the time step that elapses before current is updated) was the minimum possible value. **C**: The action potential with a time step of 25 μs and the latency increased to 10 μs above its minimal value. **D**: With a time step of 100 μs and minimal latency, the action potential is severely distorted. Adapted from Bettencourt et al. (2008)

potentials. However, for our simulations and experiments, the distortions were short lived: once real-time processing was regained, the system returned quickly to a more accurate solution (Bettencourt et al., 2008).

Is hard real-time performance necessary for effective dynamic clamping? The answer to this question depends on a number of factors:

- For a given soft real-time system and task, how often do uncontrolled interrupts lasting 10–100 μs occur? The answer to this question is likely to depend on the additional demands being placed on the computer and the dynamic-clamp task being performed. We encourage developers and users of soft real-time systems to explore this issue for their applications, as has been done in a recent case (Milescu et al., 2008).
- What sort of membrane mechanism is being simulated? If the timescale of the mechanism is slow compared with the longest uncontrolled interrupts, then hard real time is likely not necessary. Dynamic-clamp-based simulations of voltage-gated Na^+ channels (Fig. 1B, C, D) lie at the other extreme: even miniscule disruptions of hard real-time performance will likely lead to great distortion of results.
- For the hypothesis being tested, how critical is it that the data contain no distorted time steps, and can associated erroneous results be detected and removed before analyzing the data? For example, distortions in spike shape like those seen in Fig. 1C, D would not be difficult to detect in post hoc data analysis. Given our finding that disruptions due to long time steps or latencies are temporary, it should be possible to exclude short time windows around distorted results if they are indeed detectable.

3 Probing Single-Cell Oscillations

We have used dynamic-clamp techniques to study oscillatory behavior in single neurons and neuronal networks. Much of this work has focused on spiny stellate cells of the medial entorhinal cortex, which provide the great majority of the cortical input to the hippocampus (Gloor, 1997). In brain slice recordings, stellate cells generate intrinsic 3–8 Hz subthreshold oscillations in membrane potential (Alonso and Llinas, 1989; Alonso and Klink, 1993). Blocking Na^+ and HCN channels usually (Klink and Alonso, 1993; Dickson et al., 2000) eliminates these oscillations, suggesting that these two populations of channels are most important for generating the phenomenon. Some data (Haas et al., 2007) suggest that other channel populations may be involved as well.

In modeling work (White et al., 1995, 1998a, 2000a), we studied the emergence of subthreshold oscillations and found that the phenomenon was extremely sensitive to model parameters: deviations from ideal parameter values by a 1–5% disrupted the oscillations. Interestingly, accounting for "channel noise" (electrical noise generated by the stochastic opening and closing of membrane-bound ion channels) generated by voltage-gated, non-inactivating Na^+ channels

made modeled membrane-potential oscillations substantially more robust, in that they were supported over a much larger range of parameter space. A similar result was seen in a later study using a more complex model (Fransen et al., 2004).

To test the hypothesis that channel noise enhances 3–8 Hz subthreshold oscillations, we used dynamic clamp to compare control responses (Fig. 2A, B, black traces) with data collected under two experimental conditions: (1) with persistent Na^+ channels blocked (using the drug riluzole) and replaced by a dynamic-clamp representation including channel noise (Fig. 2A, B, dark gray traces) and (2) with persistent Na^+ channels blocked and replaced by a noiseless dynamic-clamp representation (Fig. 2A, B, light gray traces). In this example, stochastic dynamic-clamp results resemble the control case much more closely than noiseless dynamic-clamp results (Fig. 2A, B). Over a population of

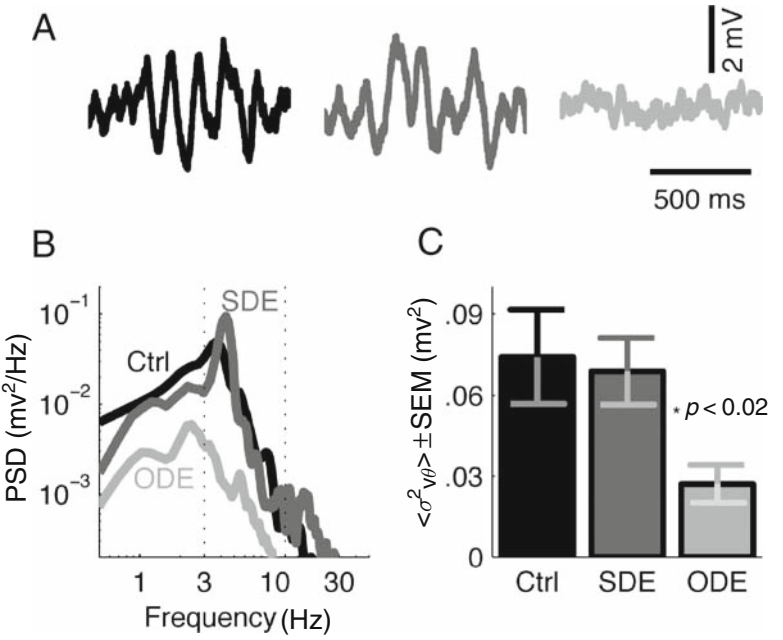

Fig. 2 Channel noise from persistent, voltage-gated Na^+ channels is essential for subthreshold oscillations in entorhinal stellate cells. A: Example subthreshold oscillations, recorded under whole-cell patch clamp from a stellate cell under three conditions. *Black*: control conditions. *Dark gray*: 6 μM riluzole (to block persistent Na^+ channels) plus a dynamic-clamp representation of stochastic differential equation representing the noisy persistent Na^+ channels. *Light gray*: 6 μM riluzole plus a dynamic-clamp representation of ordinary differential equation representing the noiseless persistent Na^+ channels. **B**: Power spectra of long data sets from one stellate cell under the same three conditions. Same color code as in panel A. **C**: Power (mean ± SEM, $n = 14$) in the theta (4–12 Hz) range of frequencies, measured across a population of 14 neurons in each of the three conditions. Same color code as in panel A. Control and stochastic differential equation (SDE) cases are statistically indistinguishable; the ordinary differential equation (ODE) case has substantially less power in the theta (4–12 Hz) band (pair-wise *t*-test, $n = 14$, $p < 0.02$). Adapted from Dorval and White (2005)

recordings, this result holds (Fig. 2C). We also demonstrated that channel noise is necessary to reproduce natural phase-locked responses of stellate cells to weak, 5–8 Hz inputs (Dorval and White, 2005). These results show directly that noise from persistent Na^+ channels has substantial effects on the integrative properties of entorhinal stellate cells. This kind of direct evidence could not be obtained without the benefit of a dynamic-clamp system.

In preliminary data, we have recently shown that subthreshold oscillations can alter the moment-by-moment "gain" describing excitatory postsynaptic potential (EPSP) magnitude for a given conductance input. In these experiments, we depolarized stellate cells to induce subthreshold oscillations, then used dynamic clamp to deliver artificial synaptic input at random times (and thus random phases with respect to the subthreshold oscillations). PSP amplitude clearly varies with the level of depolarization at that moment (Fig. 3A). This effect, which we call

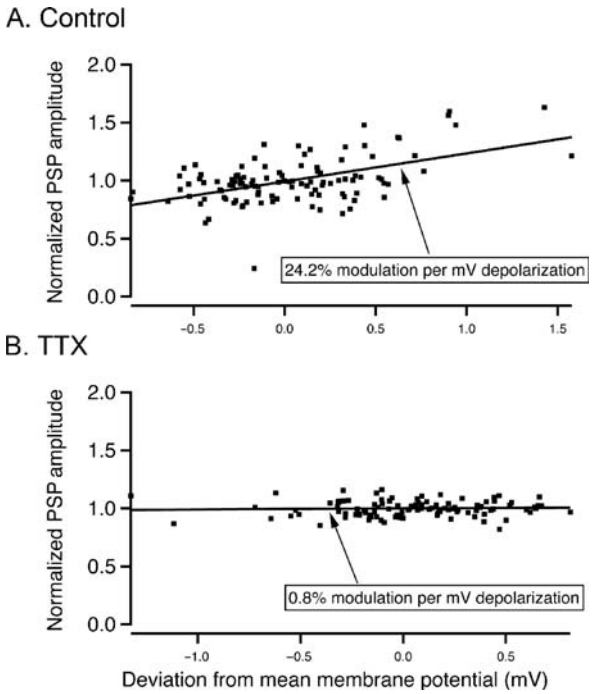

Fig. 3 Entorhinal stellate cells exhibit dynamic gain modulation over the voltage range of subthreshold oscillations. Under whole-cell patch clamp, we depolarized the stellate cell to generate subthreshold oscillations, then used dynamic clamp to deliver artificial "shunting" $GABA_A$-mediated inputs (reversal potential = –60 mV, corrected for junction potential) at random times to measure the effects of membrane potential on IPSP amplitude. **A**: Normalized IPSP amplitude (corrected for driving force) versus the deviation from resting potential, collected under control pharmacological conditions. Small deviations in membrane potential lead to large changes in IPSP amplitude, even with the effects of synaptic driving force accounted for. **B**: With voltage-gated Na^+ blocked using TTX, membrane potential has no effect on drive-corrected IPSP amplitude

dynamic gain modulation, is absent in the presence of the Na^+ channel blocker tetrodotoxin (Fig. 3B). Dynamic gain modulation is present for both inhibitory postsynaptic potentials (IPSPs) and EPSPs and appears independent of effects of synaptic driving force. We hypothesize that this result arises via effects of persistent Na^+ channels on the effective cellular input impedance: at more depolarized potentials, more persistent Na^+ channels are open, giving the appearance of a more resistive membrane because responses to depolarization or hyperpolarizing conductance inputs are larger.

4 Networks of Coupled Oscillators

Subthreshold membrane-potential oscillations in stellate cells have long been speculated to contribute to the theta rhythm, a 4–12 Hz EEG pattern that is believed to be generated by quasi-periodic, synchronized action potentials in the entorhinal cortex and hippocampus (Bland and Colom, 1993; O'Keefe, 1993; Buzsáki, 2002). Two implicit assumptions underlie this speculated mechanism: (1) action potential timing is determined by the subthreshold oscillations and (2) interactions between multiple neurons of this type are such that synchronization is stable. We used dynamic clamp to study the ability of stellate cells to synchronize at theta frequencies (Netoff et al., 2005a, b) via monosynaptic mutual excitation or disynaptic mutual inhibition. In these studies, we took advantage of *phase response analysis* (e.g., Ermentrout and Kopell, 1991; Hansel et al., 1995; Canavier et al., 1997), in which the effects of synaptic inputs to oscillating neurons is reduced to a simple effect on the timing of the next action potential. The main assumptions underlying phase response analysis are that the postsynaptic cell can be considered an oscillator, and that coupling is weak, allowing the effects of a given synaptic input or train of synaptic inputs to be determined via convolution (Ermentrout and Kopell, 1991). In the case that coupling is strong, the basic technique still applies (Acker et al., 2003), although the effect of changing the synaptic waveform (for example) cannot be determined by convolution.

Figure 4 shows results from dynamic-clamp experiments (Netoff et al., 2005b) in which we coupled two entorhinal stellate cells (labeled "E" for *excitatory*). We used two forms of network: one in which we assume mutual excitation via AMPAergic synapses (Fig. 4A) and one in which we assume that excitatory stellate cells communicate by driving inhibitory connections (labeled "I") to their neighbors (Fig. 4B). The depicted data are histograms of the time difference Δt between action potentials in the two stellate cells. The plots contain two peaks because we plotted, for each spike in cell 1, the time of the nearest spikes in cell 2 in both the past and the future. For mutual excitation (Fig. 4A), the two cells synchronize nearly exactly and with very little variance in timing from cycle to cycle (as indicated by the narrowness of the histograms). For mutual inhibition (Fig. 4B), the cells fire nearly out of phase, with

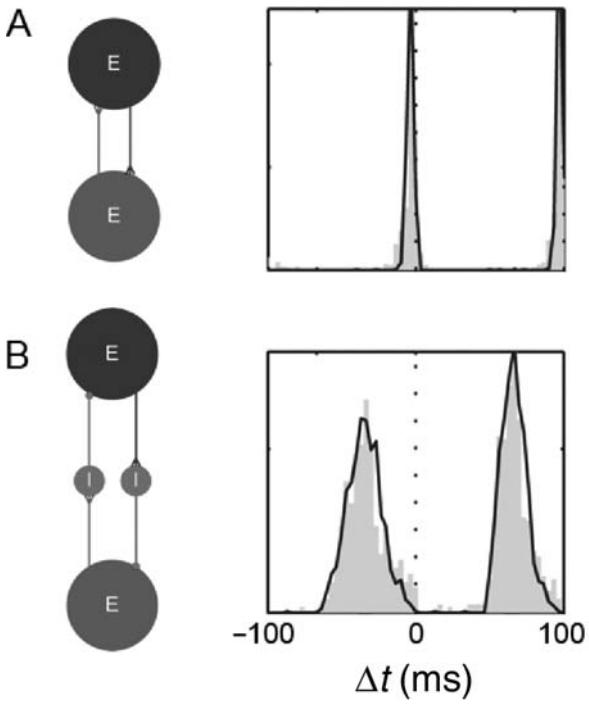

Fig. 4 Entorhinal stellate cells synchronize via mutual excitation but not via mutual inhibition. We recorded from two stellate cells simultaneously and connected them via virtual synapses under dynamic clamp. The diagrams show the two excitatory stellate cells (E) and the structure of the hybrid circuit. The gray bars in the histograms show observed difference in spike times between the two cells. The black lines show predicted time differences from phase response analysis (see text). For both cases, we plotted, for each spike in cell 1, the nearest spike times from cell 2 in both the past and the future. **A**: With virtual AMPAergic synapses between the two cells, they fire nearly synchronously and with small variance in the time difference Δt. Observations match predictions. **B**: With inhibitory interactions between the cells, carried by virtual interneurons giving rise to $GABA_A$-mediated inhibition, the cells do not synchronize and Δt has much larger variance. Again, observations match predictions. Adapted from Netoff et al. (2005b)

substantially more cycle-to-cycle variability. These results were quite consistent across a population of paired recordings (Netoff et al., 2005b).

It should be noted that each panel in Fig. 4 contains two histograms, not one. The gray bars represent observed values of Δt measured when the two stellate cells were connected via virtual synapses. The black lines represent predicted values, calculated based on phase-response measurements taken from each of the cells and combined using established theory. The close correspondence between predicted and observed results demonstrates that the underlying assumptions of phase response analysis hold for these recordings. Thus, we have here an all-too-rare instance in which neurons of immense complexity can

be described accurately as coupled oscillators that simply affect each other's timing. We can understand this system, and scale it to describe very large networks of interconnected neurons (White et al., 1998b), without being required to dissect the biophysical properties that give rise to the behavior.

5 Evidence Against the "Cellular Oscillator" Hypothesis

In the examples of the previous section, the neurons in question were treated as cellular oscillators, with the network frequency determined by the natural firing frequency of the individual cells. This natural firing frequency is in turn often assumed to be determined by the frequency of subthreshold oscillations. For networks involving entorhinal stellate cells, this view of subthreshold oscillations driving spiking behavior and thus network oscillations is prominent in recent modeling work (e.g., O'Keefe and Burgess, 2005; Burgess et al., 2007; Giocomo et al., 2007; Hasselmo et al., 2007). A host of data from recordings in brain slices has been interpreted as supporting this hypothesis (e.g., Alonso and Llinas, 1989; Alonso and Klink, 1993; Dickson et al., 2000; Haas and White, 2002; Fransen et al., 2004; Dorval and White, 2005; Netoff et al., 2005a, b; Haas et al., 2007).

Recent data from our group (Fernandez and White, 2008) call into question the notion that entorhinal stellate cells serve as cellular oscillators in either the subthreshold or suprathreshold regimes. In this work, we used dynamic clamp to flood recorded stellate cells with artificial excitatory and inhibitory synaptic input, effectively putting the neurons in the "high-conductance state" that has been reported from in vivo recordings (Borg-Graham et al., 1998; Destexhe and Pare, 1999; Destexhe et al., 2003). Summary data are shown in Fig. 5. Under control conditions in the brain slice (Fig. 5A), subthreshold oscillations are prominent, with a peak power around 5 Hz. Delivering current-based artificial synaptic input to the cells (Fig. 5B, gray traces) shifts the peak frequency of the subthreshold oscillations, but the cell remains oscillatory. These data are consistent with studies that demonstrate subthreshold resonance in stellate cells and tie this resonance to the intrinsic oscillations (Haas and White, 2002; Erchova et al., 2004; Schreiber et al., 2004; Haas et al., 2007). The situation with *conductance-based* inputs (Fig. 5B, black traces) is much different: responses in this condition are not resonant, containing no peak in the output power spectrum (black power spectral density [PSD] vs. frequency, Fig. 5B). Further study demonstrated that this loss of subthreshold oscillations and resonance was caused by the change in neuronal membrane resistance induced by more realistic conductance-based inputs (Fernandez and White, 2008). A similar effect was seen when we depolarized the stellate cells to induce action potentials in response to artificial synaptic inputs (Fig. 5C). Responses to current-based stimuli showed periodicity in output spike trains (Fig. 5C, gray traces), whereas responses to conductance-based inputs showed no such periodicity (Fig. 5C, black traces). In further dynamic-clamp experiments

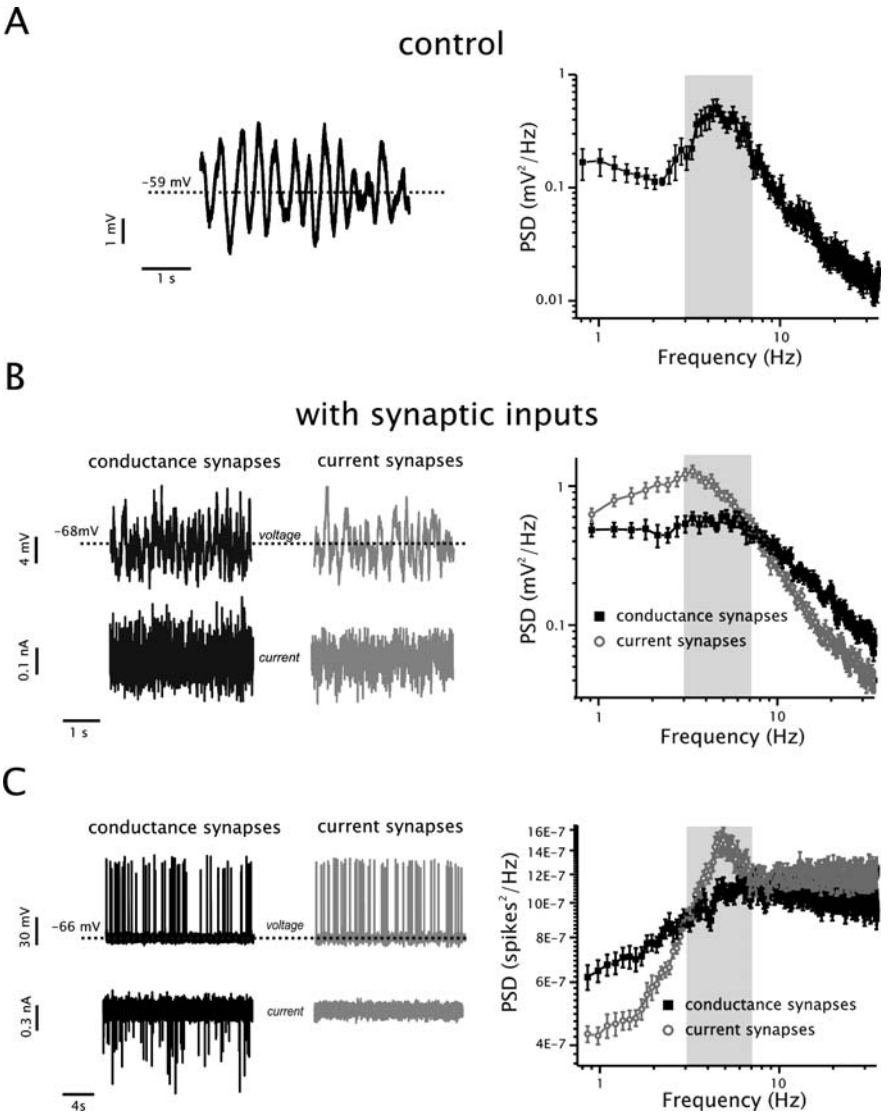

Fig. 5 Conductance-based inputs eliminate subthreshold oscillations, resonance, and intrinsic periodic spiking in entorhinal stellate cells. A: Example raw data (*left*) and power spectral density (PSD, mean ± SEM, $n = 10$) of stellate cell subthreshold voltage responses (average potential ~ –60 mV) under control conditions. **B**: Example responses and average PSD of subthreshold voltage responses under synaptic conductance-based (*black traces*) and current-based (*gray circles*) stimuli ($n = 14$ in each case). Stimuli in both cases were Poisson-process driven trains of artificial $GABA_A$-mediated inhibition and AMPA-mediated excitation. Conductance-based stimuli eliminate the resonance near 3.6 Hz. **C**: With more depolarization, input trains led to spikes. PSDs of spike trains (n = 15 for each case) showed periodic activity with current-based input but not conductance-based input. Adapted from Fernandez and White (2008)

(Fernandez and White, 2008), we demonstrated that conductance-based inputs obliterate periodic spiking in the postsynaptic cell by profoundly altering the shape of spike afterhyperpolarizations.

6 Network Oscillations Arising from Rate-Limiting Synaptic Inputs

The results of Fernandez and White (2008) call into question the widely held hypothesis (see citations above) that cellular oscillations in entorhinal stellate cells are responsible for pacing theta-rhythmic activity in the entorhinal cortex. But if cellular oscillations are not responsible for pacing network oscillations, what other factors might pace the coherent network activity? One attractive hypothesis is that the network is paced by the speed of recovery from chemical synaptic inhibition. Several years ago, we showed in modeling and theoretical work that the typical decay time constant of gamma-amino butyric acid $(GABA)_A$-mediated inhibition is ideal to support stable synchrony for the 40 Hz gamma rhythm (Chow et al., 1998; White et al., 1998b). This finding helped explain previous modeling results (Wang and Buzsáki, 1996). Studies since then have verified the power of mutual inhibition using dynamic clamp to couple neurons artificially, showing that inhibition-based gamma is stable for a wide variety of interneuron classes (Sohal and Huguenard, 2005) and that "shunting" inhibition ($GABA_A$-mediated inhibition with a chloride reversal potential near resting potential) increases the stability of gamma (Vida et al., 2006).

What of the 4–12 Hz theta rhythm? Slow $GABA_A$-mediated inhibition has been described in the hippocampus (Banks et al., 1998), and modeling studies show that slow inhibition could in principle contribute to the local generation of the theta rhythm (White et al., 2000b). More recent studies of theta activity in hippocampal brain slices implicate interactions among pyramidal cells, fast-spiking inhibitory interneurons, and *oriens-lacunosum moleculare* (O-LM) interneurons (Gillies et al., 2002; Gloveli et al., 2005b, a; Rotstein et al., 2005). In such models, two slow variables have been implicated: slow cellular oscillations in O-LM cells (Pike et al., 2000); and slowly decaying $GABA_A$-mediated inhibition from O-LM cells to postsynaptic targets (Maccaferri et al., 2000; Gillies et al., 2002).

We have begun studying the mechanisms by which the theta and gamma rhythms may arise in local hippocampal circuits. Our strategy in this work is to record from one or two neurons and use dynamic clamp to connect these biological neurons with simulated counterparts (Fig. 6A) to construct a "hybrid" network. Given that the high-conductance state disrupts cellular theta oscillations (Fernandez and White, 2008), we have focused on the hypothesis by which slow inhibition from O-LM cells may be the crucial factor pacing neuronal theta rhythms. Our preliminary hybrid network studies show that such a model is plausible. Depending on the level of inhibition from O-LM cells to pyramidal cells and fast-spiking interneurons, this hybrid microcircuit can support either

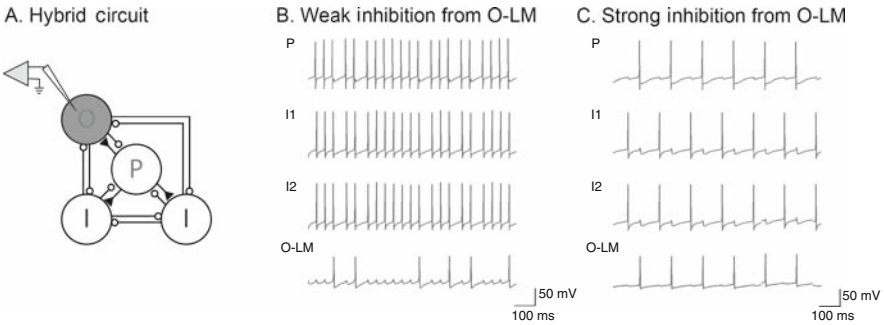

Fig. 6 Gamma and theta rhythms in a hybrid neuronal network. A: Under whole-cell patch-clamp, we recorded from an *oriens-lacunosum moleculare* (O-LM) interneuron and constructed a hybrid network around it based on published data and models (Gloveli et al., 2005b). O: biological O-LM cell. P: virtual pyramidal cell. I: virtual, fast-spiking inhibitory cell. **B**: With relatively weak inhibition from the O-LM cell to the other neurons, the P- and I-cells form a stable gamma rhythm, firing at ~ 40 Hz. The O-LM cell continues to fire slowly in this example. **C**: With strong, slow inhibition from the O-LM cell to the I-cells and P-cell, the network generates a stable theta rhythm

gamma (Fig. 6B) or theta (Fig. 6C) rhythms. The crucial factor in generating slow rhythmic activity in Fig. 6C is that the O-LM cell delivers strong, slow (decay time constant = 20 ms) inhibition to the other cells. In Fig. 6C and similar experiments and simulations, the theta period is roughly proportional to the sum of the decay time constant of O-LM inhibition and that induced by fast-spiking interneurons, which are the first to recover from O-LM inhibition.

7 Discussion and Conclusions

Since its independent introduction to the neurophysiology community by the groups of Marder (Sharp et al., 1993) and Robinson (Robinson and Kawai, 1993), the dynamic-clamp technique has grown steadily in popularity. Still, the technique is only used by a fairly small fraction of the labs that could profit from the technique. We believe that the fruition of the technique will require overcoming a number of barriers:

- The training barrier. Although electrophysiologists have embraced theoretical and mathematical approaches to a greater degree than have most biological and biomedical scientists, the power of the dynamic-clamp technique will likely remain underappreciated until the day when students in neuroscience receive more advanced training in applied mathematics. In particular, familiarity with differential equations and Hodgkin–Huxley style models is crucial for appreciating the power of the dynamic-clamp approach in allowing one to test quantitatively sophisticated hypotheses in living neurons.

- The implementation barrier. Each of the three kinds of dynamic-clamp systems have disadvantages. Linux-based systems still require relatively sophisticated users, particularly at the installation phase. Systems requiring specific real-time hardware are expensive, and do not to our knowledge include specific software for dynamic-clamp applications. Windows systems are the easiest to use and install, but do not include hard real-time performance. Support and documentation for most existing dynamic-clamp systems is not as strong as it should be.
- Barriers in performance. Although dynamic clamp makes entirely new kinds of experiments possible, there are of course limits. Three are worth mentioning here:
  - Modeled voltage- or ligand-gated channels are limited to the site of the recording pipette. This problem could potentially be mitigated by modeling spatially extended neural structures (e.g., dendrites) with the included channels, but doing so is both computationally expensive and difficult to achieve with any confidence of accuracy. For representations of ligand-gated channels, a more direct method would be to uncage the ligand optically, in real time and at the appropriate location(s) (Shoham et al., 2005). Although such uncaging techniques have not, to our knowledge, been tied to a dynamic-clamp system, we believe that this approach is technically feasible.
  - Any model of any membrane mechanism includes inaccuracies. Some, like the assumption of independent activation and inactivation in voltage-gated Na^+ channels, are known to be incorrect (Hille, 2001) but are used anyway. Even with the correct mathematical structure of the model, details of voltage-clamp-based models are wrong due to errors in space clamp and other difficulties. Worse yet, channel densities are often unidentified for a given case, and channel properties are quite sensitive to the neuromodulatory state (Hille, 2001), another unknown. In a recent paper, Milescu et al. (2008) take advantage of a very clever optimization strategy that automatically "tunes" the dynamic-clamp model to match data collected under control conditions. This approach could be extremely important for cases in which the control behavior is known.
  - Finally, dynamic clamp can at present only represent the electrical, not the electrochemical, actions of a given membrane mechanism. As a consequence, dynamic-clamp systems are of limited utility in studying calcium-dependent phenomena like synaptic plasticity. In principle, one could use calcium uncaging to begin to overcome this limitation. In practice, controlling intracellular calcium concentrations in real time is a very daunting challenge, made all the more difficult by the existence of calcium microdomains and fact that calcium indicators invariably distort the "true" calcium waveform. Of the three technical challenges mentioned here, this would seem to be the most daunting.

We do not wish to end on a pessimistic note. Although there is much work to do, we are firmly convinced that the dynamic-clamp approach has a bright

future, destined to assume its place beside current- and voltage-clamp techniques as a "standard" method in cellular electrophysiology.

Acknowledgments We thank past and present students and collaborators on dynamic-clamp work, including M.I. Banks, J.C. Bettencourt, M. Binder, R.J. Butera, D.J. Christini, A.D. Dorval, E. Idoux, K.P. Lillis, N. Kopell, L.E. Moore, T.I. Netoff, P. Randeria , and L. Stupin. This work was supported by grants from the National Institutes of Health (NCRR, NIMH, and NINDS).

References

Acker CD, Kopell N, White JA (2003) Synchronization of strongly coupled excitatory neurons: relating network behavior to biophysics. J Comput Neurosci 15:71–90.

Alonso A, Llinas RR (1989) Subthreshold Na^+-dependent theta-like rhythmicity in stellate cells of entorhinal cortex layer II. Nature 342:175–177.

Alonso A, Klink R (1993) Differential electroresponsiveness of stellate and pyramidal-like cells of medial entorhinal cortex layer II. J Neurophysiol 70:128–143.

Banks MI, Li TB, Pearce RA (1998) The synaptic basis of GABAA,slow. J Neurosci 18:1305–1317.

Bettencourt JC, Lillis KP, Stupin LR, White JA (2008) Effects of imperfect dynamic clamp: Computational and experimental results. J Neurosci Methods 169:282–289.

Bland BH, Colom LV (1993) Extrinsic and intrinsic properties underlying oscillation and synchrony in limbic cortex. Prog Neurobiol 41:157–208.

Borg-Graham LJ, Monier C, Fregnac Y (1998) Visual input evokes transient and strong shunting inhibition in visual cortical neurons. Nature 393:369–373.

Burgess N, Barry C, O'Keefe J (2007) An oscillatory interference model of grid cell firing. Hippocampus 17:801–812.

Butera RJ, Jr., Wilson CG, Delnegro CA, Smith JC (2001) A methodology for achieving high-speed rates for artificial conductance injection in electrically excitable biological cells. IEEE Trans Biomed Eng 48:1460–1470.

Buzsáki G (2002) Theta oscillations in the hippocampus. Neuron 33:325–340.

Canavier CC, Butera RJ, Dror RO, Baxter DA, Clark JW, Byrne JH (1997) Phase response characteristics of model neurons determine which patterns are expressed in a ring circuit model of gait generation. Biol Cybern 77:367–380.

Chow CC, White JA, Ritt J, Kopell N (1998) Frequency control in synchronized networks of inhibitory neurons. J Comput Neurosci 5:407–420.

Christini DJ, Stein KM, Markowitz SM, Lerman BB (1999) Practical real-time computing system for biomedical experiment interface. Ann Biomed Eng 27:180–186.

Destexhe A, Pare D (1999) Impact of network activity on the integrative properties of neocortical pyramidal neurons in vivo. J Neurophysiol 81:1531–1547.

Destexhe A, Rudolph M, Pare D (2003) The high-conductance state of neocortical neurons in vivo. Nat Rev Neurosci 4:739–751.

Dickson CT, Magistretti J, Shalinsky MH, Fransen E, Hasselmo ME, Alonso A (2000) Properties and role of I(h) in the pacing of subthreshold oscillations in entorhinal cortex layer II neurons. J Neurophysiol 83:2562–2579.

Dorval AD, White JA (2005) Channel noise is essential for perithreshold oscillations in entorhinal stellate neurons. J Neurosci 25:10025–10028.

Dorval AD, White JA (2006) Synaptic input statistics tune the variability and reproducibility of neuronal responses. Chaos 16:026105.

Dorval AD, Christini DJ, White JA (2001) Real-time Linux dynamic clamp: a fast and flexible way to construct virtual ion channels in living cells. Ann Biomed Eng 29:897–907.

Erchova I, Kreck G, Heinemann U, Herz AV (2004) Dynamics of rat entorhinal cortex layer II and III cells: characteristics of membrane potential resonance at rest predict oscillation properties near threshold. J Physiol 560:89–110.
Ermentrout B, Kopell N (1991) Multiple pulse interactions and averaging in systems of coupled oscillators. J Math Biol 29:195–217.
Fernandez FR, White JA (2008) Artificial synaptic conductances reduce subthreshold oscillations and periodic firing in stellate cells of the entorhinal cortex. J Neurosci 28:3790–3803.
Fransen E, Alonso AA, Dickson CT, Magistretti J, Hasselmo ME (2004) Ionic mechanisms in the generation of subthreshold oscillations and action potential clustering in entorhinal layer II stellate neurons. Hippocampus 14:368–384.
Gillies MJ, Traub RD, LeBeau FE, Davies CH, Gloveli T, Buhl EH, Whittington MA (2002) A model of atropine-resistant theta oscillations in rat hippocampal area CA1. J Physiol 543:779–793.
Giocomo LM, Zilli EA, Fransen E, Hasselmo ME (2007) Temporal frequency of subthreshold oscillations scales with entorhinal grid cell field spacing. Science 315:1719–1722.
Gloor P (1997) The temporal lobe and limbic system. New York: Oxford University Press.
Gloveli T, Dugladze T, Saha S, Monyer H, Heinemann U, Traub RD, Whittington MA, Buhl EH (2005a) Differential involvement of oriens/pyramidale interneurones in hippocampal network oscillations in vitro. J Physiol 562:131–147.
Gloveli T, Dugladze T, Rotstein HG, Traub RD, Monyer H, Heinemann U, Whittington MA, Kopell NJ (2005b) Orthogonal arrangement of rhythm-generating microcircuits in the hippocampus. Proc Natl Acad Sci USA 102:13295–13300.
Haas JS, White JA (2002) Frequency selectivity of layer II stellate cells in the medial entorhinal cortex. J Neurophysiol 88:2422–2429.
Haas JS, Dorval AD, II, White JA (2007) Contributions of Ih to feature selectivity in layer II stellate cells of the entorhinal cortex. J Comput Neurosci 22:161–171.
Hansel D, Mato G, Meunier C (1995) Synchrony in excitatory neural networks. Neural Comput 7:307–337.
Hasselmo ME, Giocomo LM, Zilli EA (2007) Grid cell firing may arise from interference of theta frequency membrane potential oscillations in single neurons. Hippocampus 17:1252–1271.
Hille B (2001) Ion channels of excitable membranes, 3rd Edition. Sunderland, Mass.: Sinauer.
Hughes SW, Lorincz M, Cope DW, Crunelli V (2008) NeuReal: An interactive simulation system for implementing artificial dendrites and large hybrid networks. J Neurosci Methods 169:290–301.
Kispersky TJ, White JA (2008) Stochastic models of ion channel gating. Scholarpedia 3:1327.
Klink R, Alonso A (1993) Ionic mechanisms for the subthreshold oscillations and differential electroresponsiveness of medial entorhinal cortex layer II neurons. J Neurophysiol 70:144–157.
Kullmann PH, Wheeler DW, Beacom J, Horn JP (2004) Implementation of a fast 16-Bit dynamic clamp using LabVIEW-RT. J Neurophysiol 91:542–554.
Maccaferri G, Roberts JD, Szucs P, Cottingham CA, Somogyi P (2000) Cell surface domain specific postsynaptic currents evoked by identified GABAergic neurones in rat hippocampus in vitro. J Physiol 524 Pt 1:91–116.
Milescu LS, Yamanishi T, Ptak K, Mogri MZ, Smith JC (2008) Real-time kinetic modeling of voltage-gated ion channels using dynamic clamp. Biophys J 95:66–87.
Netoff TI, Acker CD, Bettencourt JC, White JA (2005a) Beyond two-cell networks: experimental measurement of neuronal responses to multiple synaptic inputs. J Comput Neurosci 18:287–295.
Netoff TI, Banks MI, Dorval AD, Acker CD, Haas JS, Kopell N, White JA (2005b) Synchronization in hybrid neuronal networks of the hippocampal formation. J Neurophysiol 93:1197–1208.
O'Keefe J (1993) Hippocampus, theta, and spatial memory. Curr Opin Neurobiol 3:917–924.

O'Keefe J, Burgess N (2005) Dual phase and rate coding in hippocampal place cells: theoretical significance and relationship to entorhinal grid cells. Hippocampus 15:853–866.
Pike FG, Goddard RS, Suckling JM, Ganter P, Kasthuri N, Paulsen O (2000) Distinct frequency preferences of different types of rat hippocampal neurones in response to oscillatory input currents. J Physiol 529 Pt 1:205–213.
Pinto RD, Elson RC, Szucs A, Rabinovich MI, Selverston AI, Abarbanel HD (2001) Extended dynamic clamp: controlling up to four neurons using a single desktop computer and interface. J Neurosci Methods 108:39–48.
Robinson HP, Kawai N (1993) Injection of digitally synthesized synaptic conductance transients to measure the integrative properties of neurons. J Neurosci Meth 49:157–165.
Rotstein HG, Pervouchine DD, Acker CD, Gillies MJ, White JA, Buhl EH, Whittington MA, Kopell N (2005) Slow and fast inhibition and an H-current interact to create a theta rhythm in a model of CA1 interneuron network. J Neurophysiol 94:1509–1518.
Schreiber S, Erchova I, Heinemann U, Herz AV (2004) Subthreshold resonance explains the frequency-dependent integration of periodic as well as random stimuli in the entorhinal cortex. J Neurophysiol 92:408–415.
Sharp AA, O'Neil MB, Abbott LF, Marder E (1993) Dynamic clamp: Computer-generated conductances in real neurons. J Neurophysiol 69:992–995.
Shoham S, O'Connor DH, Sarkisov DV, Wang SS (2005) Rapid neurotransmitter uncaging in spatially defined patterns. Nat Methods 2:837–843.
Sohal VS, Huguenard JR (2005) Inhibitory coupling specifically generates emergent gamma oscillations in diverse cell types. Proc Natl Acad Sci USA 102:18638–18643.
Vida I, Bartos M, Jonas P (2006) Shunting inhibition improves robustness of gamma oscillations in hippocampal interneuron networks by homogenizing firing rates. Neuron 49:107–117.
Wang XJ, Buzsáki G (1996) Gamma oscillation by synaptic inhibition in a hippocampal interneuronal network model. J Neurosci 16:6402–6413.
White JA, Budde T, Kay AR (1995) A bifurcation analysis of neuronal subthreshold oscillations. Biophys J 69:1203–1217.
White JA, Klink R, Alonso A, Kay AR (1998a) Noise from voltage-gated ion channels may influence neuronal dynamics in the entorhinal cortex. J Neurophysiol 80:262–269.
White JA, Chow CC, Ritt J, Soto-Trevino C, Kopell N (1998b) Synchronization and oscillatory dynamics in heterogeneous, mutually inhibited neurons. J Comput Neurosci 5:5–16.
White JA, Rubinstein JT, Kay AR (2000a) Channel noise in neurons. Trends Neurosci 23:131–137.
White JA, Banks MI, Pearce RA, Kopell NJ (2000b) Networks of interneurons with fast and slow gamma-aminobutyric acid type A (GABAA) kinetics provide substrate for mixed gamma-theta rhythm. Proc Natl Acad Sci USA 97:8128–8133.

Unraveling the Dynamics of Deep Cerebellar Nucleus Neurons with the Application of Artificial Conductances

Dieter Jaeger and Risa Lin

Abstract In this chapter we demonstrate how dynamic clamping can be used to apply different types of conductances to neurons in the deep cerebellar nuclei (DCN) to explore how spiking in these neurons is controlled by the interaction of synaptic and intrinsic conductances. Besides the application of synaptic- and voltage-gated conductances, we introduce the modeling of an intracellular calcium pool in the real-time loop of the dynamic clamp in order to apply calcium-dependent conductances to DCN neurons in brain slices. Further, we report on our ongoing computer simulation studies, in which we compare the effects of focal somatic or distributed dendritic conductances on the spiking behavior of a full morphological DCN neuron model in order to better understand the limitations of dynamic clamping given by applying artificial conductances only at a single location.

1 Using Dynamic Clamping to Apply Backgrounds of Synaptic Input to Emulate the In Vivo Condition

Neurons in vivo receive a constant barrage of synaptic inputs, which can easily reach thousands of events per second. This condition results in a high-conductance state of these neurons, in which synaptic conductances are severalfold larger than the leak conductance (Destexhe, Rudolph and Pare 2003; Rudolph et al. 2005). This high-conductance state has important consequences for the dynamical behavior of neurons. Due to the higher membrane conductance, the time constant of the neuron is reduced, thus leading to a faster spread of dendritic signals (Bernander et al. 1991). At the same time, the amplitude of propagating dendritic signals is diminished because of synaptic shunting (Holmes and Woody 1989). Shunting has the general effect that the synaptic background pulls the neuron toward the weighted average of the reversal

D. Jaeger (✉)
Department of Biology, Emory University, Atlanta, GA 30322, USA
e-mail: djaeger@emory.edu

A. Destexhe, T. Bal (eds.), *Dynamic-Clamp*, Springer Series in Computational Neuroscience 1, DOI 10.1007/978-0-387-89279-5_10,

potential of excitatory and inhibitory conductance (Jaeger, DeSchutter and Bower 1997; Destexhe et al. 2003). This will dampen the dynamics of intrinsic currents, as well as provide a random bumpy baseline in V_m, which leads to spike initiation in an irregular pattern. Together, these factors result in a dynamical behavior of the neuron that is usually quite different from the intrinsic dynamics of the voltage-gated currents. One implication of these considerations is that data from brain slice recordings should not be taken to represent the in vivo condition. For instance, neurons such as the Purkinje cell in the cerebellum transition from a triphasic burst pattern in isolation (Llinás and Sugimori 1980; Womack and Khodakhah 2004) to irregular continuous spiking in vivo (Thach 1968; Lisberger and Fuchs 1978; Jaeger 2003). This transition can be mimicked and further analyzed by applying a background of random excitatory and inhibitory synaptic input to neurons in brain slices using the technique of dynamic clamping (Robinson and Kawai 1993; Sharp et al. 1993). When applied to Purkinje cells, dynamic clamping verified the transition from triphasic bursting to irregular continuous spiking just due to the presence of a mixed background of excitation and inhibition (Jaeger and Bower 1999). The same method also verified an interesting prediction stemming from a detailed compartmental Purkinje cell model (De Schutter and Bower 1994), namely that inhibitory input conductance in this cell type needs to be larger than excitatory ones (Jaeger et al. 1997). This modeling prediction was surprising, since Purkinje cells are dominated by about 180,000 excitatory inputs (Napper and Harvey 1988), but a careful examination of the statistics of Purkinje cell synaptology and the duration and amplitude of unitary excitatory and inhibitory conductance waveforms can account for this balance (Jaeger et al. 1997). This set of studies examining Purkinje cells also highlighted the value added by using a combined computer simulation and dynamic-clamp approach in the study of single-cell dynamics and in vivo spiking behavior.

2 The Deep Cerebellar Nuclei as a Key Junction in Cerebellar Processing

In the past 10 years our laboratory has continued using combined modeling and dynamic-clamp approaches. In particular, we have focused on the synaptic coding properties of neurons in the deep cerebellar nuclei (DCN), which provide the sole output of the cerebellum. An interesting characteristic of the cerebellar circuit is that the entire signaling pathway from the cerebellar cortex to the DCN is conveyed by gamma-amino butyric acid (GABA)ergic inhibition from Purkinje cells (Fig. 1). The statistics of this connection is noteworthy in that approximately 860 Purkinje cells are thought to converge onto a single DCN neuron (Palkovits et al. 1977), and Purkinje cells fire action potentials at high rates with a mean of 35 Hz in rodents (Stratton et al. 1988) and even higher rates in primates (Thach 1968; Lisberger and Fuchs 1978). This situation thus

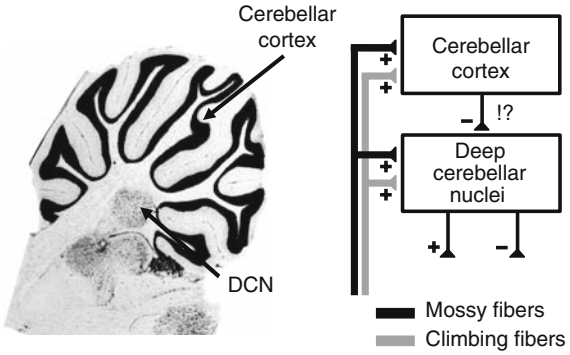

Fig. 1 Neurons in the deep cerebellar nuclei receive excitatory (+) inputs from mossy and climbing fiber collaterals and inhibitory (−) inputs from the cerebellar cortex via GABAergic synapses from Purkinje cells. The image on the left shows a parasagittal slice through rodent cerebellum (adapted from Paxinos and Watson, The Rat Brain in Stereotaxic Coordinates, Academic Press, 1998)

leads to a high tonic background of inhibitory conductance on DCN neurons despite small individual inhibitory post-synaptic potential (IPSP) sizes due to a 60% depression in amplitude at high-input frequencies (Telgkamp and Raman 2002), given that the quantal conductance is about 750 pS (Telgkamp and Raman 2002). Neurons in the DCN typically show a high baseline spike rate of 37–55 Hz in vivo (Thach 1968; LeDoux, Hurst and Lorden 1998; Rowland and Jaeger 2005), so obviously the Purkinje cell inhibition is not overwhelming the inward membrane currents of DCN neurons, despite the impressive numbers just listed. One factor that balances out inhibition is the intrinsic pacemaking behavior of DCN neurons, which results in a mean spike rate of 8 Hz in synaptic isolation in brain slices (Gauck and Jaeger 2000). However, this pacemaking can be shut off by small negative currents of 50–100 pA, and thus is unlikely to counter large GABAergic input from Purkinje cells by itself. The dominant source of excitation may instead be given by collaterals of mossy fibers and climbing fibers, which excite DCN neurons in addition to providing excitatory input to cerebellar cortex (Fig. 1). Thus, the cerebellum may consist of a direct loop of excitation of the DCN by mossy and climbing fibers, and an indirect loop through the cerebellar cortex, which can counteract the direct loop via inhibition by Purkinje cells (Fig. 1). The algorithm by which the cerebellar cortex evaluates mossy and climbing fiber input has been the subject of much debate (Bloedel 1992; Welsh and Llinas 1997). We approached the question of Purkinje cell function from a different angle by asking the question of how Purkinje cell output could affect spiking of DCN neurons. The consideration of input decoding in the DCN places constraints on the activity modulation of Purkinje cells that can be transmitted down the line. For example, if a single Purkinje cell action potential had a negligible effect on DCN spiking, it would be fruitless to look for codes in which information is encoded in the precise spike

timing of individual Purkinje cells upon detecting a specific input pattern (Steuber et al. 2007). Dynamic clamping presents an ideal tool to address the question of how inhibitory input controls spiking in DCN neurons. Any complex pattern of excitation and inhibition can be constructed as a stimulus and applied to DCN neurons in brain slices, where the input gets decoded by the natural properties of these cells. In contrast, synaptic input patterns in vivo can neither be precisely controlled nor measured.

3 Results

3.1 The Control of DCN Spiking by Inhibitory Purkinje Cell Inputs

3.1.1 Properties of In Vivo Like Inhibitory Input Conductance

We constructed a set of input conductances to probe the decoding properties of DCN neurons with respect to inhibitory Purkinje cell inputs. To approximate the in vivo situation of DCN inhibition, we chose to simulate a population of 400 $GABA_A$ synapses with the rise and fall time constants measured in Purkinje cells (Anchisi, Scelfo and Tempia 2001) and a frequency of 35 Hz as found for rodent Purkinje cells in vivo (Stratton et al. 1988). The combination of these 400 random input trains led to a fluctuating inhibitory input conductance with a mean of 32 nS, when the unitary conductance amplitude of a single inhibitory post-synaptic conductance (IPSC) was 138 pS (Fig. 2A). These fluctuations were small relative to the mean conductance when all Purkinje cells were activated independently from each other. To probe the consequences of synchronized Purkinje cell inputs to DCN neurons, we created stimuli with increasing numbers of Purkinje cells contributing to synchronized groups of input (Fig. 2B). With an increase in input synchronization, temporal fluctuations in the combined conductance of all Purkinje cell inputs increased. Further details of the stimulus construction are described in Gauck and Jaeger (2000).

To isolate influences of inhibitory inputs on DCN spike patterning, we used a constant baseline of excitatory conductance (Fig. 2B). The amplitude of this baseline was chosen so that the combined effect of inhibition and excitation would result in spike rates similar to in vivo recordings. The expected effect of a given balance of excitation and inhibition on the membrane potential can be derived from calculating the combined reversal potential (E_{syn}) of inhibition and excitation, which is given by the weighted average of the inhibitory and excitatory conductances (G_{in} and G_{ex}) multiplied by their respective driving forces:

$$E_{syn} = \frac{G_{ex} \times E_{ex} + G_{in} \times E_{in}}{G_{ex} + G_{in}} \quad (1)$$

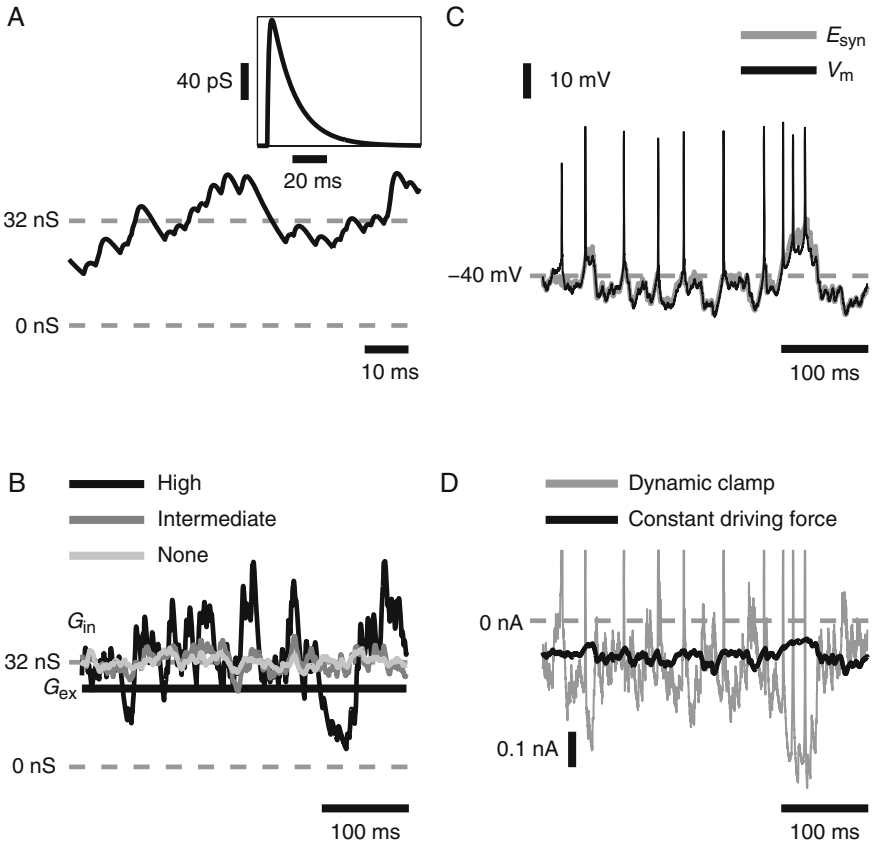

Fig. 2 (**A**) The timing of inputs is stochastic and composed of single inhibitory postsynaptic conductances (IPSCs) with a double-exponential time course and a peak of 138 pS (inset). The addition of the IPSCs from 400 synapses results in a fluctuating waveform (G_{in}) with a mean level of 32 nS. (**B**) G_{in} waveforms for higher levels of synchrony among inputs have larger transient fluctuations around the mean. In this study, the excitatory conductance (G_{ex}) is held constant with a mean of 3/4 that of inhibition. (**C**) When the input synchrony is high, the subthreshold membrane potential (*black*) closely follows the synaptic driving force (E_{syn}, gray). (**D**) The injected current waveform is much different when using dynamic clamping (*gray*) than when injecting a directly scaled version of G_{in} as current (*black*). The difference is due to the changing synaptic driving force during dynamic clamping. We used the mean driving force from (C) to scale G_{in} as current

The current that will be injected through the dynamic-clamp electrode is given by

$$I_{inj} = (G_{ex} + G_{in}) \times (V_m - E_{syn}) \quad (2)$$

This equation evaluates to zero if the membrane potential (V_m) equals the combined reversal potential E_{syn}. The larger the conductances G_{ex} and G_{in} are, the larger the current will be that ensues if $V_m \neq E_{syn}$. This current will always drive V_m back toward E_{syn}, since the current is depolarizing when V_m is negative to E_{syn}, and hyperpolarizing when V_m is positive to E_{syn}. If a neuron has a resting membrane potential negative to E_{syn}, V_m will tend to track slightly hyperpolarized to E_{syn} (Fig. 2C), and a mean inward synaptic current ensues (Fig. 2D). In contrast, if a neuron is a fast pacemaker and naturally sits depolarized to E_{syn}, then V_m will track slightly positive to E_{syn}, and a mean outward synaptic current results. This was found to be the case for Purkinje cells (Jaeger and Bower 1999). Thus, the inward or outward mean synaptic current is not solely a consequence of the synaptic conductances, but is also a result of intrinsic properties of neurons that drive V_m below or above E_{syn}. The large effect of changing synaptic driving forces due to fluctuations in V_m on the total synaptic current can be appreciated when the current flowing during dynamic clamping is compared to the current that would be injected if the driving force were constant (Fig. 2D). Generally the current during dynamic clamping showed larger and different fluctuations because the net synaptic driving force was changing dramatically as V_m was deflected away from E_{syn} due to active properties of the neuron. One such deflection was given by spike after-hyperpolarizations, which led to compensatory inward shunt current through the applied synaptic conductance. The largest transients in the dynamic-clamp current were associated with action potentials of the neuron, which led to momentary severalfold increases in driving force and to outward current spikes. In fact, the synaptic shunt current counteracting the inward action potential current sets an upper limit on the synaptic conductance amplitude that a neuron can tolerate; if the synaptic current shunting action potential currents becomes too large, the neuron is effectively prevented from firing action potentials.

3.1.2 Properties of DCN Neurons in Decoding Inhibitory Input

Neurons are generally thought to fire action potentials when their membrane potential exceeds spike threshold. In our DCN neuron recordings at 32°C in brain slices (see Gauck and Jaeger (2000) for experimental details), we found that spikes were initiated due to reductions in inhibitory input conductance and a concomitant depolarizing shift in E_{syn}, which was tracked by V_m (Fig. 2C). However, the potential at which spikes were initiated was not a constant threshold but increased when several spikes were fired at rapid intervals (Fig. 2C). This effect is likely due to accumulating sodium conductance inactivation in DCN neurons (Raman, Gustafson and Padgett 2000), which is known to raise spike threshold (Fleidervish, Friedman and Gutnick 1996).

We examined the dependence of DCN spiking on the total amount of synaptic input and synchronization between Purkinje cells. The total amount

was manipulated by a gain factor, which multiplied G_{ex} and G_{in} equally and thus did not affect the trajectory of E_{syn}. When the gain of synaptic input was low, the synaptic current due to differences between E_{syn} and V_m was small, and thus V_m was relatively more determined by intrinsic currents and did not track E_{syn} accurately (Fig. 3A). This led to a fairly regular spike train resembling spontaneous pacemaking of DCN neurons in brain slices.

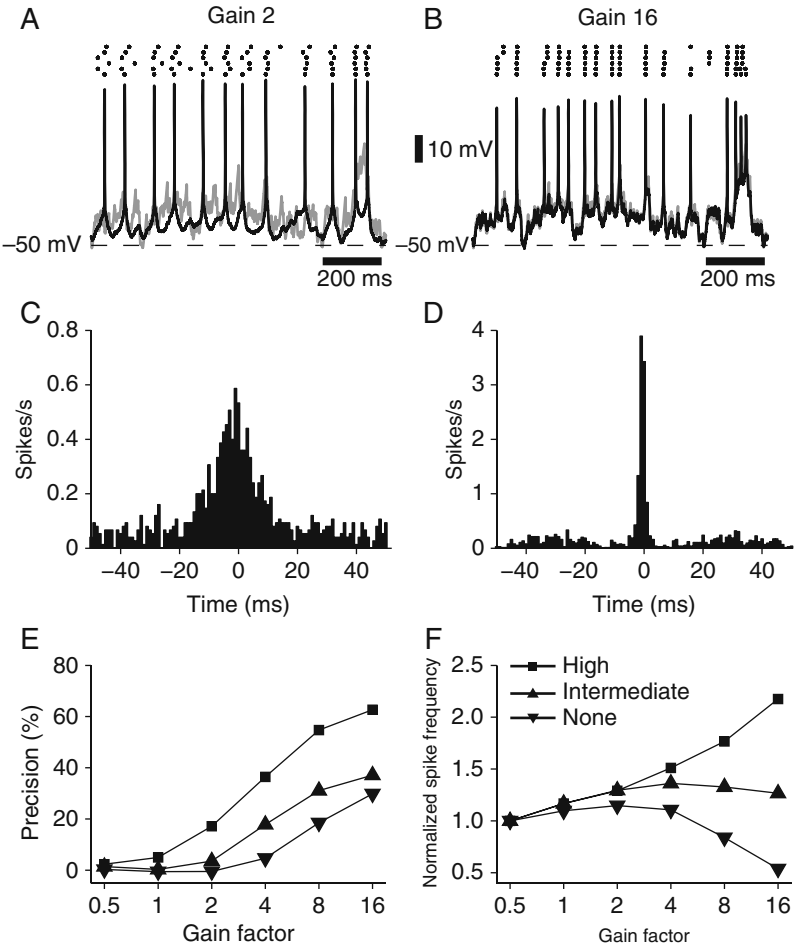

Fig. 3 Sample dynamic-clamp voltage traces are shown superimposed on E_{syn} for high-input synchronization and a gain of 2 (**A**), which corresponds to a mean conductance of 4 nS, and a gain of 16 (**B**). The spike-timing cross-correlograms between six different repetitions of the same 5 s stimulus waveform show that spikes are more precisely aligned for the gain of 16. (**E**) The average spike-timing precision for a criterion of ± 1 ms increases with both input gain and input synchronization. (**F**) The normalized mean spike frequencies for different gains and levels of synchronization. The mean frequencies for a gain of 0.5 were 10.0 Hz (high), 9.0 Hz (intermediate), and 10.2 Hz (no synchronization)

Individual spikes in this condition were not strongly constrained by the timing of input fluctuations (Fig. 3C). When the gain of inputs was increased to a level corresponding to a unitary inhibitory conductance of 138 pS, V_m followed the fast fluctuations in E_{syn} more faithfully, and spikes were precisely fired at the time of reduced inhibitory conductance (Fig. 3B and D). In fact, a majority of spikes in this condition were fired with a precision of ± 1 ms when the same conductance pattern was applied repeatedly, indicating that inhibitory Purkinje cell input in principle is capable of being represented by a precise spike time code in DCN neurons. However, this was only the case when the level of synchronization between populations of Purkinje cell input was high (10 groups of 40 synchronous Purkinje cell inputs each). The level of spike time precision correlated well with the amount of signal present in the spike-triggered average (STA) of the inhibitory input conductance (Fig. 4). When the input gain and the level of input synchronization increased, a clear trough of spike-triggered G_{in} emerged (Fig. 4), indicating that a 10 ms brief transient decrease in inhibition was associated with spike initiation. At low levels of Purkinje cell synchronization, spike timing was far less precise for any gain of input amplitudes (Fig. 3E), and the STA of G_{in} showed little relation to spike initiation (Fig. 4). This result indicates that single Purkinje cell inputs were not effective in controlling DCN spike times. In fact, high-input gains of fully desynchronized Purkinje cell input trains led to a near cessation of spiking (Fig. 3F) in the presence of a near constant level of G_{in} (Fig. 2B), indicating that temporal fluctuations in the input are vital to trigger DCN spikes. Thus, Purkinje cell synchronization not only induces precisely timed spiking, but also has a pronounced effect on the mean spike rate even when the total number and unitary amplitudes of Purkinje cell inputs remain identical (Fig. 3F). Changes in the mean rate of Purkinje cell inputs in the presence of an unchanged excitatory conductance also have a pronounced effect on DCN spike rate (Fig. 6 in Gauck and Jaeger, 2000). Overall, the spike rate shown by DCN neurons is a result of input rates as well as input synchronization.

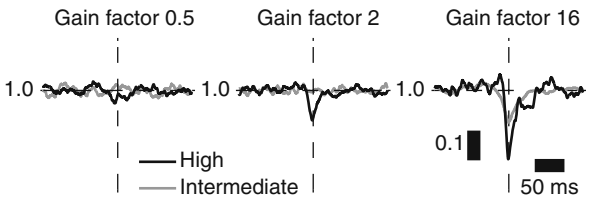

Fig. 4 Spike-triggered averages of inhibitory conductance show a transient decrease in inhibitory conductance preceding a spike. The magnitude of the trough increases with gain and the level of synchronization, corresponding with the greater spike-timing precision found for these stimulus conditions

3.2 *The Effect of Temporally Varying Excitation on Synaptic Coding in DCN Neurons*

DCN neurons receive time-varying excitatory inputs from mossy fibers and climbing fibers (Fig. 1). To determine the interaction between excitation and inhibition in controlling DCN spiking, we replaced the constant background of excitation described above with a random input of 100 excitatory synapses activated at 20 Hz (Gauck and Jaeger 2003). Excitatory input conductances to DCN neurons have a considerable NMDA component (Anchisi et al. 2001). Since NMDA conductances are voltage-dependent, the dynamic-clamp algorithm in this case is more complex and involves a voltage-dependent term gating the conductance amplitude (Gauck and Jaeger 2003). The effect on rate of a constant excitatory or inhibitory conductance (C) was compared with that of a randomly fluctuating conductance, in which the amplitude of the unitary event was scaled by a factor of 10 in order to simulate synchronized inputs (S). The value of the constant conductance was set equal to the average value of the randomly fluctuating conductance. The resultant rates were examined for three cases, one in which the neurons had the same inhibitory and excitatory inputs, one in which only inhibition was allowed to fluctuate randomly, one in which only excitation was allowed to fluctuate, and one in which they both were. In Fig. 5A, both AMPA and NMDA receptors were simulated for the excitatory input. If excitation was allowed to fluctuate then the rate was double when inhibition was allowed to fluctuate compared to when it was held constant, indicating that transients in the inhibitory input provide important spike triggers. On the other hand, if inhibition was allowed to fluctuate, the rate was the same whether excitation was allowed to fluctuate or not, indicating that excitatory transients were not an important spike trigger under these input conditions. This difference between inhibitory and excitatory fluctuations in controlling spike initiation was also borne out by STAs of the input conductances (Fig. 5A, bottom) which showed a dominant relation of spike initiation to transients reductions in inhibition. If only AMPA receptors were included in the excitatory input (Fig. 5B), then the case in which both inputs were allowed to fluctuate produced the greatest, followed by fluctuating excitation only, then fluctuating inhibition only. In this case, STAs (Fig. 5B, bottom) showed a dominant relation of AMPA conductance to spike initiation. Thus, the much larger fluctuations of a purely AMPA-based excitatory conductance (Fig. 6) have the ability to dominate over inhibition. For the purposes of examining the control of the temporal precision of spiking, two additional cases were examined, one in which the fluctuating excitation was common but the fluctuating inhibition was not, and the converse in which the fluctuating inhibition was common but the fluctuating excitation was not. These additional cases shown in Fig. 5A indicate that in the case of AMPA and NMDA receptors,

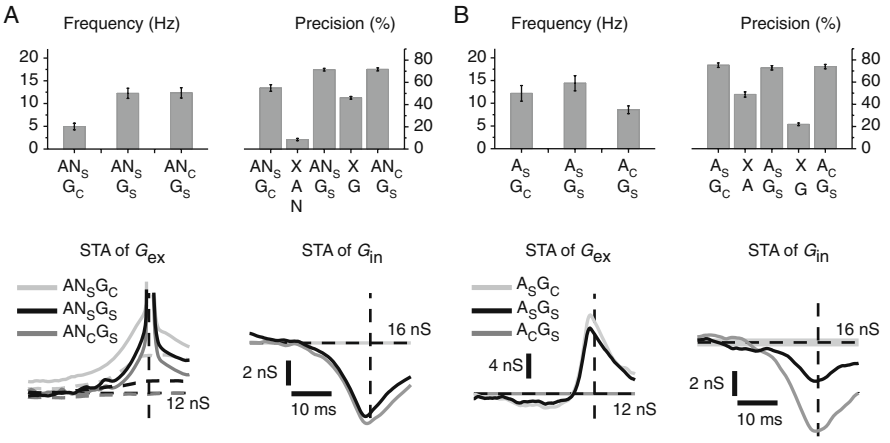

Fig. 5 (**A**) *Top left*: The mean spike frequency for three stimulus conditions composed of a combination of synchronized (AN_S) or constant AMPA and NMDA excitation (AN_C), and synchronized (G_S) or constant GABA inhibition (G_C). *Top right*: The spike-timing precision for the same stimulus combinations. In addition the spike-timing precision across different stimuli that either share only excitation (XAN) or only inhibition (XG) is shown. Stimuli that share the same synchronous inhibition but have different excitatory input result in near-identical spike timing, indicating that synchronous inhibition dominates in the control of spike initiation. *Bottom left*: The spike-triggered averages (STAs) of excitatory conductance increase before spikes, indicating a contribution of excitatory input to spike initiation. Most of the excitatory STA waveform is due to NMDA voltage dependence, as stimuli conditions containing a voltage-independent NMDA conductance (dashed lines) show very little increase preceding action potentials. *Bottom right*: The STA of inhibitory conductance shows a nearly identical transient decrease in G_{in} with and without excitatory input modulation, again indicating that inhibition plays a larger role in spike timing for these stimulus conditions. (**B**) The mean spike frequency and spike-timing precision for the analogous stimulus conditions as in (A) when the NMDA conductance is completely replaced by AMPA conductance. Bottom: The spike-triggered averages of G_{ex} and G_{in} for excitation with AMPA alone. The spike precision and the STAs in this condition are dominated by G_{ex}. All data shown is for a gain of 16

the common excitation (XAN) contributed much less than the common inhibition (XG) to the total precision compared to the case where both fluctuated (AN_S, G_S). In contrast, when only AMPA receptors were simulated (Fig. 5B), the relative contribution of common fluctuating excitation only (XA) to temporal precision was greater than that of common inhibition (XG) to the total (A_S, G_S). In both cases, fluctuating excitation by itself produced a larger temporal precision (much larger in Fig. 5A) when paired with a constant inhibitory conductance than when competing with inhibitory inputs that were not common.

Overall, the main finding of this study was that the presence of a strong NMDA component in excitatory DCN inputs is well suited to allow a faithful transmission of inhibitory Purkinje cell input patterns. This effect was actually enhanced by the voltage dependence of NMDA conductance,

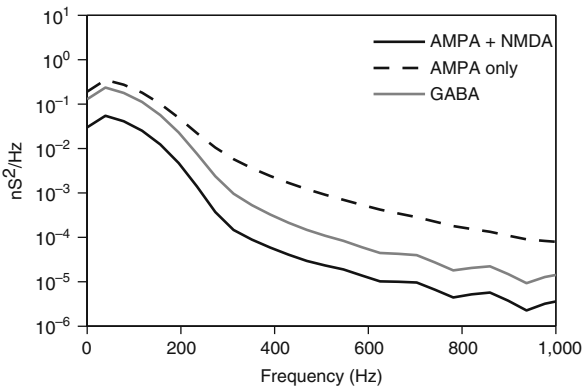

Fig. 6 Power spectra of 8 s of excitatory and inhibitory conductances resulting from synchronous AMPA and NMDA input (*solid black*), synchronous AMPA-only input (*dashed black*), and synchronous GABA input (*gray*). The power of GABA conductance is higher than that of NMDA and AMPA, but lower than that of AMPA-only. A good correspondence between power and the relative size of the spike triggered averages was found. The DC component of conductances was removed and was of equal amplitude for NMDA + AMPA and AMPA-only stimuli, since in the latter condition an equal mean conductance was created by increasing AMPA unitary EPSC amplitudes

which amplified periods of reduced inhibition through the addition of an inward NMDA current activated by the depolarization caused by disinhibition (Gauck and Jaeger, 2000, Fig. 7). The effect of different inputs on spike initiation can actually be predicted from the power spectrum of the synaptic conductances (Fig. 6) in that the conductance with the largest power determines spike timing most. In a dynamic-clamp study of cerebellar stellate cells, we found that the most important frequency range in the power spectrum determining the relation to spike initiation lies around 100 Hz (Suter and Jaeger 2004). This corresponds well to the 10 ms time course seen in our STA conductance waveforms preceding spike initiation (Fig. 5). This frequency selectivity is likely a consequence of the time constants of activation and inactivation of multiple voltage-gated conductances and has not been explored in detail. Different cell types with different time constants of voltage-gated conductances could thus show different selectivity to particular frequencies in the synaptic conductance.

3.3 A Novel Use of Dynamic Clamp: Using a Ca^{2+} *Pool Model to Obtain* Ca^{2+}*-Dependent* K^+ *Conductance Dynamics*

The dynamics of action potential spacing and initiation in DCN neurons is strongly influenced by the sk Ca^{2+}-dependent K^+ conductance (Aizenman and Linden 1999; Raman et al. 2000). When the sk conductance is blocked with

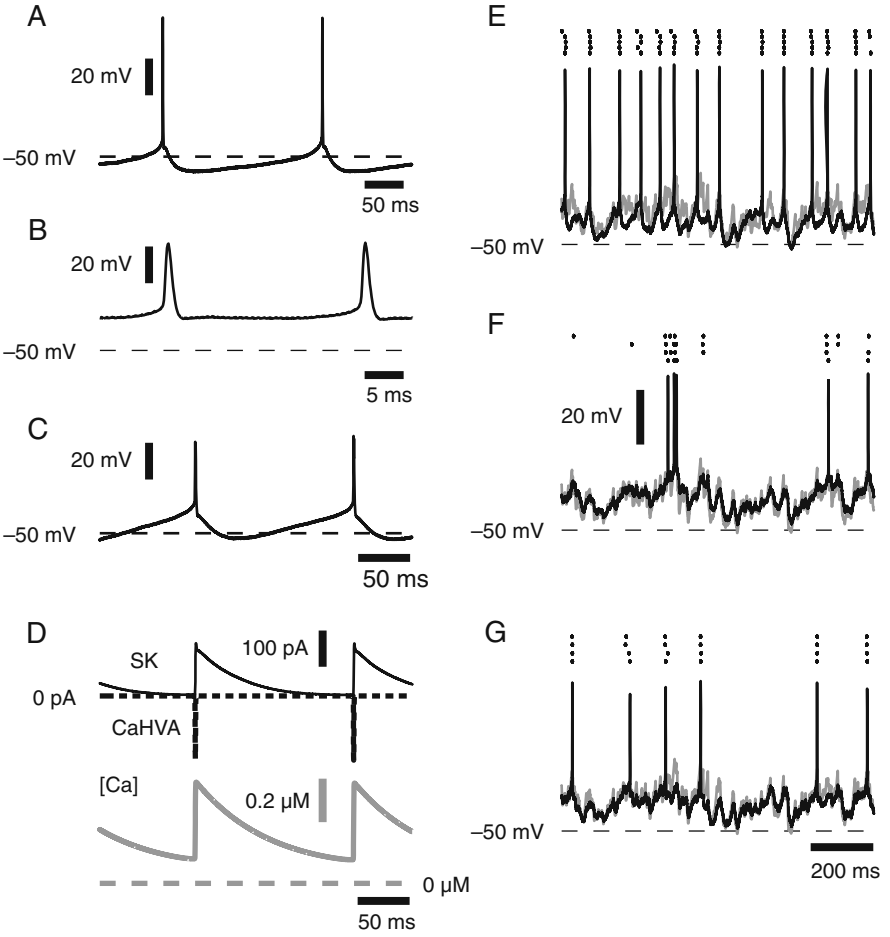

Fig. 7 The spontaneous activity of a DCN neuron recorded in slice under control conditions (**A**) and after apamin block (**B**). Note the 10× expanded timescale in (B). (**C**) When the sk conductance was reintroduced using dynamic clamp, the original spike pattern was rescued. (**D**) The simulated sk conductance was dependent on the intracellular calcium concentration, which was increased by a HVA Ca^{2+} current. (**E**, **F**) The spike pattern observed in dynamic clamp after sk block (F) shows short burst responses to strong depolarizing input fluctuations that were not observed using the same input before sk block (E). (**G**) When the sk conductance was added to the dynamic-clamp stimuli of background synaptic input, a spike pattern similar to pre-sk block conditions was obtained

apamin, DCN neurons start to show a pronounced bursting behavior (Aizenman and Linden 1999). Due to the loss of the sk-dependent spike after-hyperpolarization, spike firing during a burst is very rapid (Fig. 7A and B). We used dynamic clamping to determine whether re-introducing a sk conductance applied with dynamic clamping recovers the original activity. Since the sk

conductance is dependent on Ca^{2+} inflow through high-voltage-activated (HVA) Ca^{2+} conductance (Alvina and Khodakhah 2008), simulating a realistic sk conductance with dynamic clamping involves the simulation of not only HVA Ca^{2+} current but also intracellular Ca^{2+} concentration. We adopted the dynamics of HVA Ca^{2+} current and intracellular Ca^{2+} handling from a morphologically realistic DCN computer model (Steuber et al., unpublished) and added it to our dynamic-clamp algorithm. Our own implementation of dynamic clamping is carried out on a RT LabVIEW platform (National Instruments, Inc) using control-flow programming with forward Euler integration to add Ca^{2+} current and Ca^{2+} pool modeling (Feng and Jaeger, 2008). The program interface is designed such that conductance parameters such as time constants and maximal amplitude can be stepped through a hierarchical scheme to apply multiple settings of conductance kinetics in short succession. We found that by matching the Ca^{2+} pool decay to the spike after-hyperpolarization time course, we could recover most of the original dynamics of DCN neurons before sk conductance block (Fig. 7C and D). Ca^{2+} current flows into the neuron in a pulsatile fashion with each action potential, and the increased Ca^{2+} concentration slowly relaxes back to baseline (Fig. 7D). The speed of Ca^{2+} decay of 70 ms we used is slower than that of sk channel deactivation (Xia et al. 1998), and thus the sk conductance almost directly reflected the Ca^{2+} concentration. This approach is different from adding a fixed spike-triggered hyperpolarizing current to the neuron in that sk conductance is not saturated with a single spike. Fast spiking leads to a buildup of sk current, thus influencing the *FI* curve of the DCN neuron (not shown). When we blocked sk current with apamin but applied a background of synaptic conductances with dynamic clamping, we found that the spontaneous burst pattern seen with sk block was transformed into a deterministic pattern of spike encoding reflecting the applied synaptic conductances (Fig. 7F). Interestingly, the spike pattern obtained with a given synaptic input pattern was quite different from the spike pattern observed with the same input pattern prior to sk block (Fig. 7E and F). In particular, short burst spike responses were obtained with strong depolarizing input fluctuations after sk block but not before. In contrast, smaller depolarizing input fluctuations were better detected by DCN neurons before sk block (Fig. 7E and F). These findings show that the synaptic decoding function of DCN neurons and the specific generation of output spike patterns are dependent on both the synaptic input pattern and the combination of intrinsic conductances. When we added the simulated HVA Ca^{2+} current and Ca^{2+} pool to our dynamic-clamp stimuli of background synaptic conductances, we could recover a spike pattern more similar to the pre-sk block condition (Fig. 7G). Thus, we can show that a spike after-hyperpolarization dependent on Ca^{2+} inflow during spikes shapes the synaptic response pattern of DCN neurons. Since HVA conductances can undergo modulation that affects sk activation (Foehring 1996; Pineda, Waters and Foehring 1998), it might well be feasible that synaptic decoding is an adaptive process and could be fine-tuned in different DCN neurons.

3.4 Simulating Dynamic-clamp Application in a Full Morphological DCN Neuron Model: Comparison with Distributed Synaptic Input

An obvious limitation of dynamic clamping is that all applied conductances are directed focally to a single site of the recorded neuron, usually the soma. In contrast, natural conductances are typically distributed across the membrane surface of neurons. Synaptic input in particular is primarily dendritic in most cell types. The effect of focal somatic vs. distributed synaptic input can be investigated using computer simulations of morphological reconstructions of neurons containing a full set of membrane conductances. We constructed a model of a DCN neuron that replicated the spontaneous and current driven spiking behavior of DCN neurons recorded in brain slices (Steuber et al, unpublished, Fig. 8). We then applied the exact synaptic input patterns used in our previous dynamic-clamp study (Gauck and Jaeger 2000) either to a single summed conductance input at the soma or more realistically as synaptic input distributed across the dendrites. In order to simulate the random fluctuations in membrane potential found in biological recordings, we also added a noise term to the somatic membrane current. We find that the spike pattern induced with a simulated dynamic clamp at the soma in this model is quite similar to that found in our sample of brain slice recordings (Fig. 9A). Because the variability in spike patterns elicited with the same conductance waveform in different recorded

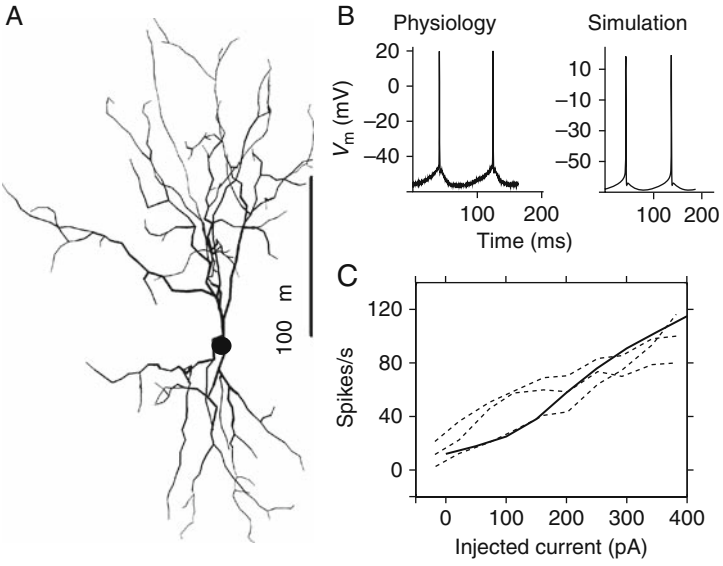

Fig. 8 (**A**) Morphological reconstruction of the DCN neuron used in simulations. (**B**) There is a good match in spike shape and after-hyperpolarization properties between a physiological slice recording (*left*) and a sample simulation (*right*). (**C**) The spike rate increases as a function of injected current for three recorded neurons (*dashed*) and the model neuron (*solid*)

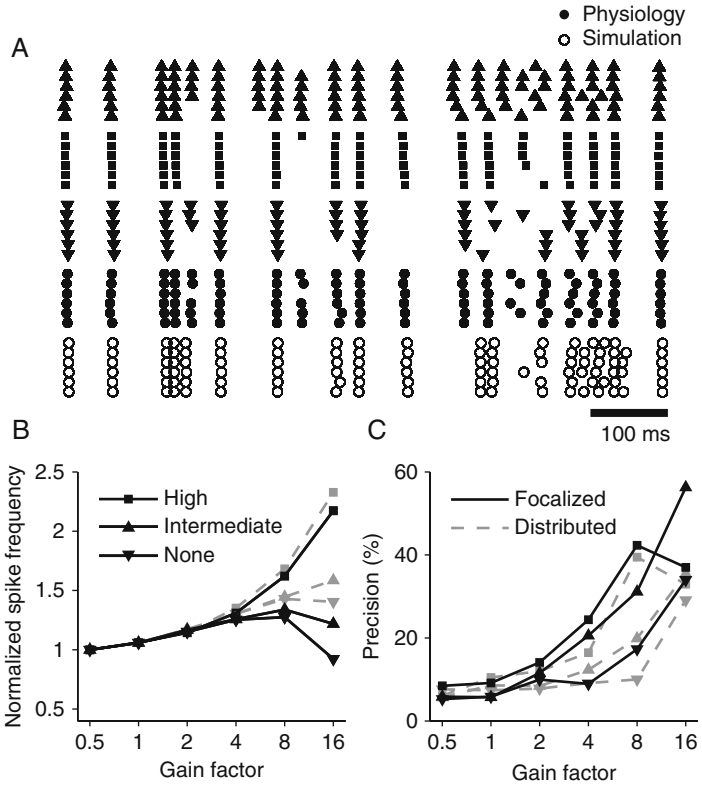

Fig. 9 (**A**) The spike patterns observed in the model neuron with simulated dynamic clamp (focalized inputs) follow the same pattern as the spike patterns observed in four different biological neurons using the same input. Different simulation trials were obtained by injecting a white noise current that reproduced biological subthreshold membrane potential fluctuations. Data are shown for a gain of 16 and high-input synchronization. (**B**) The dependence of normalized mean spike frequencies in the model on input gain and synchronization is similar to that of the physiology (Fig. 3F). When the focalized input conditions (*solid black*) are replaced with distributed inputs (*dashed gray*), the spike rate functions are still similar, but slightly higher spike frequencies are seen at high input gains. The mean frequencies for focalized inputs for a gain of 0.5 were 9.4 Hz (high), 9.5 Hz (intermediate), and 9.5 Hz (no synchronization). The mean frequencies for distributed inputs for a gain of 0.5 were 9.5 Hz (high), 9.6 Hz (intermediate), and 9.6 Hz (no synchronization). (**C**) The spike-timing precision for a criterion of ± 1 ms is also similar to that of the physiology (Fig. 3E). The focalized and distributed input conditions follow similar trajectories with the focalized input condition reaching slightly higher precisions. Note that at the highest gain, synchronized input causes a drop in spike precision for both focalized and distributed inputs. This effect was not observed in slice recordings, and is likely due to desynchronized high-frequency clusters of spikes in the model that are not observed in the biological neurons (see last segment of rasters in A)

neurons is quite high (Fig. 9A), the spike pattern found in our simulated neuron does in fact look indistinguishable from biological recordings. The close match holds up when the change of spike rate and precision with different input gains and synchronization levels are plotted (cf. Fig. 3E and

F vs Fig. 9B and C). When we switched to an application of the same synaptic conductance patterns through a set of distributed dendritic synapses, we achieved a very similar spike pattern and dependency of precision and rate on input conditions (Fig. 9B). Only in the case of low-input synchronization did we find that distributed inputs lead to a less-pronounced reduction in spike rate than focal somatic input. This similarity in the action of focal and distributed input can be explained by the relatively electrotonically compact structure of DCN neurons. We find that dendritic membrane voltage is fluctuating similarly for purely somatic or distributed dendritic inputs (Fig. 10A), and that dendritic voltage-gated currents are evoked in a very similar pattern in both input conditions (Fig. 10B). A small amount of reduction in dendritic currents with focal somatic input was seen (Fig. 10B), however, and was due to the dendritic voltage attenuation with purely somatic input. Overall, these simulation

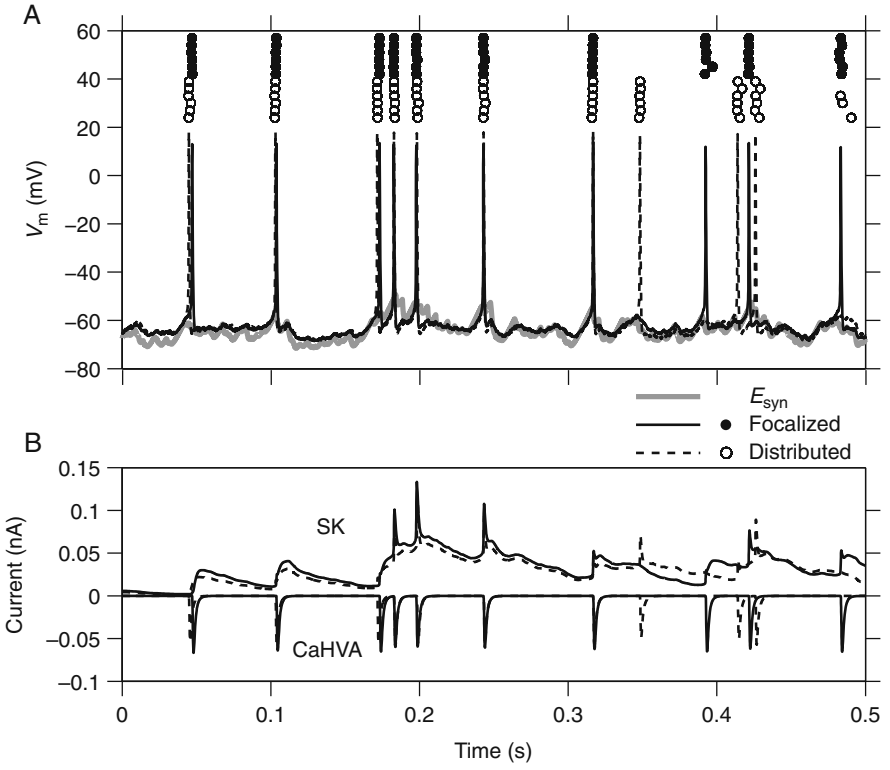

Fig. 10 (**A**) A very similar spike pattern is obtained when the same dynamic-clamp input is applied to the model neuron for focalized inputs at the soma (*solid*) and distributed inputs (*dashed*). (**B**) Dendritic voltage-gated currents are slightly smaller for distributed inputs than for focalized inputs, but are also evoked in a similar pattern

findings support the premise that dynamic clamping presents a valid approach to probe DCN neurons for their function of synaptic integration. Further, detailed compartmental simulations provide a valid tool to validate dynamic clamping approaches in different cell types, and should be used in more cases. While a membrane conductance of electrotonically compact neurons may be applied equally well at the soma or in a distributed fashion, this similarity will likely break down for large cell types such as cortical pyramidal neurons.

4 Conclusion

Dynamic clamping gave us a window of opportunity to study the effects of specific patterns of synaptic input on the spike generation of DCN neurons. Computer simulations showed that the approach of focalizing the synaptic input at the soma presented a valid approximation of distributed input for this electrotonically compact cell type. The main finding from our studies is that fluctuations in inhibitory and excitatory input are equally suited to control the rate, and even precision, of individual action potentials from a neuron subjected to a high continuous level of excitatory and inhibitory inputs. In this in vivo-like input regime, the amplitude of fluctuations of each conductance determined how much they contribute to spike initiation. Interestingly, when the NMDA component of excitatory input was set to a biological level for DCN neurons, fluctuations in excitatory conductance were smoothed out, and the impact of excitation on spike initiation was diminished. Generally, output spike rate was as much a function of the level of input synchronization as of the input rates, suggesting that temporal codes consisting of synchronous Purkinje spike patterns can be detected by DCN neurons. While DCN neurons showed temporally precise output spiking in response to synaptic input patterns in the presence of membrane noise, these patterns were nonetheless influenced to an important degree by specific voltage-gated conductances. This active filtering of input through voltage-gated conductances also explains how different neurons can react with different and yet individually precise output patterns to the same input conductance waveforms. With respect to neural coding in the cerebellum, our studies lead us to suggest that both rate and temporal codes could be conveyed through the inhibitory Purkinje cell–DCN pathway, and that synchronous events across a population of Purkinje cells are particularly well suited to steer output spiking in DCN neurons.

Acknowledgments The work described in this chapter was not solely carried out by the authors. Volker Gauck obtained the dynamic-clamp recordings with inhibitory and NMDA conductances, Steven Feng programmed the HVA, Ca^{2+} pool, and sk conductance simulation into our LabVIEW dynamic clamp package and obtained the dynamic clamp data using these conductances. The work was supported by RO1 MH065634.

References

Aizenman CD and Linden DJ (1999) Regulation of the rebound depolarization and spontaneous firing patterns of deep nuclear neurons in slices of rat cerebellum. J Neurophysiol 82:1697–1709.

Alvina K and Khodakhah K (2008) Selective regulation of spontaneous activity of neurons of the deep cerebellar nuclei by N-type calcium channels in juvenile rats. J Physiol 27:27.

Anchisi D, Scelfo B and Tempia F (2001) Postsynaptic currents in deep cerebellar nuclei. J Neurophysiol 85:323–331.

Bernander O, Douglas RJ, Martin KAC et al (1991) Synaptic background activity influences spatiotemporal integration in single pyramidal cells. PNAS 88:11569–11573.

Bloedel JR (1992) Functional heterogeneity with structural homogeneity: How does the cerebellum operate? Behav Brain Sci 15:666–678.

De Schutter E and Bower JM (1994) An active membrane model of the cerebellar Purkinje cell I. Simulation of current clamp in slice. J Neurophysiol 71:375–400.

Destexhe A, Rudolph M and Pare D (2003) The high-conductance state of neocortical neurons in vivo. Nat Rev Neurosci 4:739–751.

Feng S and Jaeger D (2008) The role of SK calcium-dependent potassium currents in regulating the activity of deep cerebellar nucleus neurons: A dynamic clamp study. Cerebellum 7:542–546.

Fleidervish IA, Friedman A and Gutnick MJ (1996) Slow inactivation of Na + current and slow cumulative spike adaptation in mouse and guinea-pig neocortical neurones in slices. J Physiol 493:83–97.

Foehring RC (1996) Serotonin modulates N- and P-type calcium currents in neocortical pyramidal neurons via a membrane-delimited pathway. J Neurophysiol 75:648–659.

Gauck V and Jaeger D (2000) The control of rate and timing of spikes in the deep cerebellar nuclei by inhibition. J Neurosci 20:3006–3016.

Gauck V and Jaeger D (2003) The contribution of NMDA and AMPA conductances to the control of spiking in neurons of the deep cerebellar nuclei. J Neurosci 23:8109–8118.

Holmes WR and Woody CD (1989) Effects of uniform and non-uniform synaptic 'activation-distributions' on the cable properties of modeled cortical pyramidal neurons. Brain Res 505:12–22.

Jaeger D (2003) No parallel fiber volleys in the cerebellar cortex: evidence from cross-correlation analysis between Purkinje cells in a computer model and in recordings from anesthetized rats. J Comput Neurosci 14:311–327.

Jaeger D and Bower JM (1999) Synaptic control of spiking in cerebellar Purkinje cells: Dynamic current clamp based on model conductances. J Neurosci 19:6090–6101.

Jaeger D, DeSchutter E and Bower JM (1997) The role of synaptic and voltage-gated currents in the control of Purkinje cell spiking: A modeling study. J Neurosci 17:91–106.

LeDoux MS, Hurst DC and Lorden JF (1998) Single-unit activity of cerebellar nuclear cells in the awake genetically dystonic rat. Neuroscience 86:533–545.

Lisberger SG and Fuchs AF (1978) Role of primate flocculus during rapid behavioral modification of vestiubloocular reflex. I. Purkinje cell activity during visually guided horizontal smooth-pursuit eye movements and passive head rotation. J Neurophysiol 41:733–763.

Llinás R and Sugimori M (1980) Electrophysiological properties of in vitro Purkinje cell somata in mammalian cerebellar slices. J Physiol 305:171–195.

Napper RMA and Harvey RJ (1988) Number of parallel fiber synapses on an individual Purkinje cell in the cerebellum of the rat. J Comp Neurol 274:168–177.

Palkovits M, Mezey E, Hamori J et al (1977) Quantitative histological analysis of the cerebellar nuclei in the cat. I. Numerical data on cells and synapses. Exp Brain Res 28:189–209.

Pineda JC, Waters RS and Foehring RC (1998) Specificity in the interaction of HVA Ca2+ channel types with Ca2+-dependent AHPs and firing behavior in neocortical pyramidal neurons. J Neurophysiol 79:2522–2534.
Raman IM, Gustafson AE and Padgett D (2000) Ionic currents and spontaneous firing in neurons isolated from the cerebellar nuclei. J Neurosci 20:9004–9016.
Robinson HP and Kawai N (1993) Injection of digitally synthesized synaptic conductance transients to measure the integrative properties of neurons. J Neurosci Meth 49:157–165.
Rowland NC and Jaeger D (2005) Coding of tactile response properties in the rat deep cerebellar nuclei. J Neurophysiol 94:1236–1251.
Rudolph M, Pelletier JG, Pare D et al (2005) Characterization of synaptic conductances and integrative properties during electrically induced EEG-activated states in neocortical neurons in vivo. J Neurophysiol 94:2805–2821.
Sharp AA, O'Neil MB, Abbott LF et al (1993) Dynamic clamp: computer-generated conductances in real neurons. J Neurophysiol 69:992–995.
Steuber V, Mittmann W, Hoebeek FE et al (2007) Cerebellar LTD and pattern recognition by Purkinje cells. Neuron 54:121–136.
Stratton SE, Lorden JF, Mays LE et al (1988) Spontaneous and harmaline-stimulated Purkinje cell activity in rats with a genetic movement disorder. J Neurosci 8:3327–3336.
Suter KJ and Jaeger D (2004) Reliable control of spike rate and spike timing by rapid input transients in cerebellar stellate cells. Neuroscience 124:305–317.
Telgkamp P and Raman IM (2002) Depression of inhibitory synaptic transmission between Purkinje cells and neurons of the cerebellar nuclei. J Neurosci 22:8447–8457.
Thach WT (1968) Discharge of purkinje and cerebellar nuclear neurons during rapidly alternating arm movements in the monkey. J Neurophysiol 31:785–797.
Welsh JP and Llinas R (1997) Some organizing principles for the control of movement based on olivocerebellar physiology. Prog Brain Res 114:449–461.
Womack MD and Khodakhah K (2004) Dendritic control of spontaneous bursting in cerebellar Purkinje cells. J Neurosci 24:3511–3521.
Xia XM, Fakler B, Rivard A et al (1998) Mechanism of calcium gating in small-conductance calcium-activated potassium channels. Nature 395:503–507.

Intrinsic and Network Contributions to Reverberatory Activity: Reactive Clamp and Modeling Studies

Jean-Marc Fellous, Terrence J. Sejnowski, and Zaneta Navratilova

Abstract Cortical cells belong to small interconnected ensembles. These ensembles have the potential of being activated in a reverberatory fashion in vitro and in vivo, spontaneously or in response to stimulation. We combined computer simulations and in vitro intracellular recording from prefrontal cortical neurons to explore the elicitation, modulation, and termination of these reverberations. In computer simulations, we studied the reverberating activity of small networks of neurons connected with realistic stochastic synaptic transmission and concluded that about 40 excitatory cells and a few interneurons were sufficient to reproduce the membrane and firing characteristics observed in vivo. Using a variant of the dynamic-clamp technique in vitro, we then stimulated the assembly and triggered self-sustained activity mimicking the activity recorded during the delay period of a working memory task in the behaving monkey. The onset of sustained activity depended on the number of action potentials elicited by the cue-like stimulation. Too few spikes failed to provide enough NMDA current to drive sustained reverberations; too many spikes activated a slow intrinsic hyperpolarizing current that prevented spiking; an intermediate number of spikes produced sustained activity. The firing rate during the delay period could be effectively modulated by the standard deviation of the inhibitory background synaptic noise without significant changes in the background firing rate before cue-onset. These results suggest that the balance between fast feedback inhibition and slower AMPA and NMDA feedback excitation is critical in initiating persistent activity, that intrinsic currents may determine which cell contributes to the onset or offset of reverberations and that the maintenance of persistent activity may be regulated by the amount of correlated background inhibition.

J.-M. Fellous (✉)
Department of Psychology and Program in Applied Mathematics, ARL Division of Neural Systems, Memory and Aging, University of Arizona, Tucson, AZ 85724, USA
e-mail: fellous@arizona.edu

A. Destexhe, T. Bal (eds.), *Dynamic-Clamp*, Springer Series in Computational Neuroscience 1, DOI 10.1007/978-0-387-89279-5_11,

1 Introduction

Groups of neurons are able to enter a state of self-sustained activity in response to stimuli. Such reverberatory activity is found in many parts of the mammalian brain including different subfields of the hippocampus (Hahn et al., 2007), in the monkey ventral premotor area (Graziano et al., 1997), and at several levels of the visual pathway and prefrontal cortices during working memory tasks (Goldman-Rakic, 1995; Pratt and Mizumori, 2001; Shadlen and Newsome, 2001; Casagrande et al., 2002; Hoffman et al., 2007). Reverberating activity also occurs spontaneously in vitro (Cossart et al., 2003). The fact that local reverberations are found both in vitro and in vivo point to a potentially essential feature of the cortex which is that neurons belong to small ensembles. Forming small ensembles of interconnected cells may increase the robustness of their co-activation (a few neurons misfiring would not affect the activity of the ensemble) and their postsynaptic impact (on a common target, an increase in near-synchronous inputs overcomes synaptic unreliability, and increases post-synaptic spatial integration). Other types of reverberatory activity can be found during sleep (natural or induced), and involve large, system-wide synchronization. These types of global up-states will not be considered here (El Boustani et al., 2007, but see Hughes et. al. "Using the Dynamic Clamp to Dissect the Properties and Mechanisms of Intrinsic Thalamic Oscillations" in this volume), although their underlying neural bases may share common features with that of local reverberations.

Optical recordings from cat cortex in vivo (Tsodyks et al., 1999) and calcium imaging from rat layer 5 neurons in vitro (Mao et al., 2001) have demonstrated that the activity of single cells can be strongly correlated with a spatial pattern of activity in neighboring neurons. This correlation results in part from local excitatory and inhibitory synaptic reverberations among groups of interconnected cells (Melchitzky et al., 1998; Gonzalez-Burgos et al., 2000; Okun and Lampl, 2008) and together with membrane currents is thought to be the basis for persistent activity observed in the prefrontal cortex during working memory tasks (Durstewitz et al., 2000; Wang, 2001). The exact nature of these reverberations and their dependence on a particular mixture of excitation and inhibition is under active investigation (McCormick et al., 2003; Hasenstaub et al., 2005; Haider et al., 2007). Neurons have a wide range of membrane currents that can potentially change the nature of their contribution to the reverberating ensemble. Intrinsic properties such as input resistance, threshold, burstiness, or spike frequency adaptation can determine the extent to which a given cell contributes to the initiation, termination, or maintenance of sustained activity, of which an 'up-state' is a special case (Luczak et al., 2007).

The goal here was to recreate the in vivo conditions of an elementary prefrontal cortical microcircuit in a computational model, and in an in vitro preparation by injecting simulated long-range synaptic background conductances and short-range excitatory and inhibitory feedback using a variant of the

dynamic-clamp technique. We studied some of the conditions that lead to the onset and offset of sustained reverberatory activity and we investigated the contribution of background synaptic noise to the level of activity during the reverberation.

2 Materials and Methods

2.1 Computer Simulations

All simulations were performed using the NEURON simulator (Hines and Carnevale, 1997). Two types of neurons were simulated: Excitatory, pyramidal-like neurons, and inhibitory gamma-amino butyric acid (GABA)ergic neurons (Navratilova and Fellous, 2008). The excitatory neurons were configured as 'ball and stick' and had a single somatic compartment, and a dendrite comprised of ten compartments. Passive leak currents adjusted to give an input resistance of 90 MΩ, were inserted in all compartments. Voltage-gated sodium and potassium currents were added to the soma (Golomb and Amitai, 1997) and adjusted to give an action potential generation threshold of −53 mV. To control the bursting properties of pyramidal neurons, a calcium-activated potassium channel (Destexhe et al., 1994) a calcium channel, a calcium pump, and intracellular calcium first order buffering (Destexhe et al., 1993) were added to the somatic compartment. Inhibitory neurons consisted of a single somatic compartment, and included voltage-gated sodium and potassium currents and passive leak currents adjusted to give an input resistance of 150 MΩ.

An Ornstein–Uhlenbeck background synaptic noise source (Destexhe et al., 2001) was added to the soma of each neuron to mimic long range inputs from neurons outside of the simulated network.

Briefly,

$$I_{\text{background}}(t) = G_{\text{e}}(t)(V(t) - E_{\text{GLU}}) + G_i(t)(V(t) - E_{\text{GABA}})$$

where E_{GLU} and E_{GABA} are the reversal potentials for AMPA and GABA_A conductances (0 and −80 mV, respectively) and V is the instantaneous membrane voltage of the recorded pyramidal cell. The fluctuating conductances $G_{\text{e}}(t)$ and $G_{\text{i}}(t)$ are given by two Ornstein–Uhlenbeck processes (Uhlenbeck and Ornstein, 1930):

$$\frac{\text{d}G_{\text{e}}(t)}{\text{d}t} = -\frac{1}{\tau_{\text{e}}}[G_{\text{e}}(t) - G_{\text{e0}}] + \sqrt{D_{\text{e}}}\chi_1(t)$$

$$\frac{\text{d}G_{\text{i}}(t)}{\text{d}t} = -\frac{1}{\tau_{\text{i}}}[G_{\text{i}}(t) - G_{\text{i0}}] + \sqrt{D_{\text{i}}}\chi_2(t)$$

where G_{e0} and G_{i0} are average conductances, τ_e and τ_i are time constants (2.7 and 10.7 ms, respectively), $\chi_1(t)$ and $\chi_2(t)$ are Gaussian white noise processes with unit standard deviation, and D_e and D_i are the "diffusion" coefficients. G_e and G_i are Gaussian variables with standard deviations $\sigma_e = \sqrt{D_e\tau_e/2}$ and $\sigma_i = \sqrt{D_i\tau_i/2}$, respectively. These standard deviations were adjusted so that membrane potential fluctuations of the simulated neurons resembled those during a down-state in vivo ($G_{e0} = 4$ nS, $G_{i0} = 35$ nS, $\sigma_e = 0.95$ nS, $\sigma_i = 3$ nS for excitatory neurons, and $\sigma_e = 0.54$ nS, $\sigma_i = 2.1$ nS for inhibitory neurons). Pyramidal neurons were connected to each other with AMPA/NMDA dynamic synapses showing facilitation and depression (Maass and Zador, 1999). These synapses were positioned onto a random dendritic compartment. There were approximately four times fewer inhibitory neurons than pyramidal neurons. Each inhibitory neuron received inputs from all the pyramidal neurons and output onto the somatic compartment of each pyramidal neuron to create shunting of the currents from the dendrite. GABAergic synapses were deterministic (Destexhe et al., 1996) and interneurons were not interconnected.

2.2 In Vitro Experiments

Regularly spiking layer 5 pyramidal cells from rat pre-limbic and infra-limbic areas of prefrontal cortex were recorded with the patch-clamp technique from 2 to 4-weeks-old Sprague–Dawley rats using standard techniques (Fellous and Sejnowski, 2003).

Data were acquired using two computers, one computer for standard data acquisition, current injection, and extracellular stimulation, and a second computer dedicated to real-time synaptic current injection (Fig. 1C). Programs for data acquisition were written using Labview 6.1 (National Instrument, Austin, TX), and data were acquired with a PCI16-E1 data acquisition board (National Instrument, Austin, TX). Data acquisition rate was either 10 or 20 kHz. Programs for conductance injection were written using a Dapview (Microstar Laboratory, Bellevue, WA) front-end and a language C backend. A variant of the dynamic-clamp technique (see below) was implemented using a DAP-5216a board (Microstar Laboratory, Bellevue, WA) at a rate of 10 kHz connected to the Axoclamp 2A amplifier in current-clamp mode.

2.3 Simulation of Synaptic Currents

To recreate in vivo conditions, simulated synaptic conductances were injected into the recorded cell. These conductances were divided into two groups:

The first group of conductances consisted of two Ornstein–Uhlenbeck processes (constructed as in model, see above) adjusted to mimic the arrival of 16,563 glutamatergic and 3,376 GABAergic synaptic inputs distributed on the

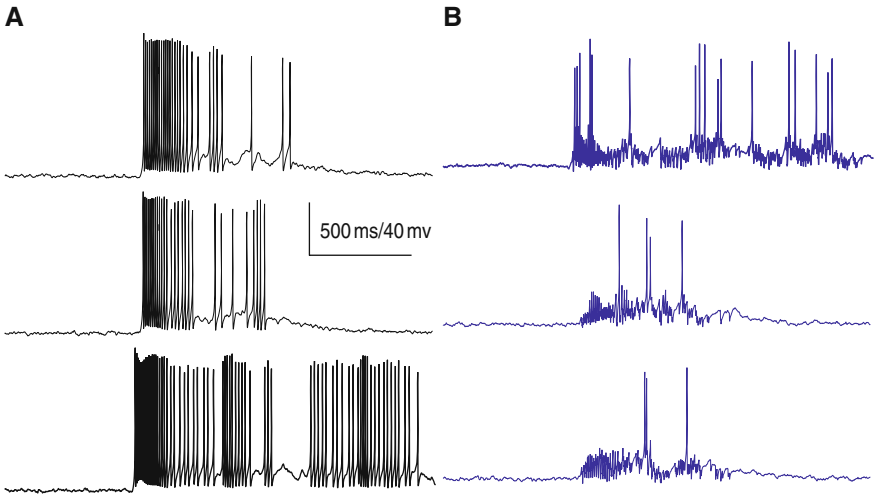

Fig. 1 Sample simulated voltage traces during reverberatory activity. A network of 26 pyramidal and 6 inhibitory cells was simulated and activated to generate reverberatory activity resembling 'up–states.' **A**: inhibitory neurons, **B**: excitatory neurons. Note the fast gamma-like fluctuations in the membrane potential of interneurons. Membrane levels, fluctuation, and firing characteristics were matched to that observed in vivo (see text)

dendritic tree of a reconstructed multi-compartmental cortical cell, measured at the soma. Because of the slow dynamics of NMDA channels, and the large number of glutamatergic synapses taken into consideration, their contribution was approximated by a change in the mean level of inputs (G_{e0} and G_{i0}). The adjustment of the different conductances of synaptic background activity was done in order to match various physiological aspects of the data. Direct conductance measurements in vivo are also possible (see Piwkowska et. al. "Testing Methods for Synaptic Conductance Analysis Using Controlled Conductance Injection with Dynamic Clamp" in this volume). These conductances were injected using the dynamic-clamp technique continuously throughout the duration of the recordings (see also Chance and Abbott "Simulating In Vivo Background Activity in a Slice with the Dynamic Clamp," Robinson "Synaptic Conductances and Spike Generation in Cortical Cells," and Jaeger and Lin "Unraveling the Dynamics of Deep Cerebellar Nucleus Neurons with the Application of Artificial Conductances" in this volume).

The second group of conductances was injected using dynamic clamp in 'a reactive mode' to simulate the activity of small reverberatory network in which the real cell is embedded (see Canavier et. al. "Dynamic-Clamp-Constructed Hybrid Circuits for the Study of Synchronization Phenomena in Networks of Bursting Neurons" in this volume for a two-neuron hybrid circuit and Sadoc et. al. "Re-Creating In Vivo-Like Activity and Investigating the Signal Transfer Capabilities of Neurons: Dynamic-Clamp Applications Using Real-Time NEURON" in this volume). The conductances were injected in response to

each action potential generated by the cell currently being recorded (hence 'reactive clamp').

$$I_{\text{feedback}}(t) = G_{\text{AMPA}}(t)(V(t) - E_{\text{GLU}}) + G_{\text{NMDA}}(t)(V(t) - E_{\text{GLU}}) + G_{\text{GABA}}(t)(V(t) - E_{\text{GABA}})$$

such that if $V(t) > 0$ (an action potential occurred) two Poisson sequences of synaptic release times were generated for glutamatergic and GABAergic synapses, respectively. Each sequence was computed such that

$$\forall n \in [1 \ldots N],\ t_n = t_{n-1} - a \ln(1 - r) \quad \text{with } t_0 = d$$

where N, a, and d are the number of synapses simulated, the mean inter-spike interval (ISI), and the dead time, respectively. The variable r is a random number uniformly distributed between 0 and 1. The feedback excitatory postsynaptic potentials (EPSPs) were modeled as the response of a single-cell representative of a population. Because each action potential of the recorded cell represented the synchronous firing of a small population of cells, it was assumed that the resulting postsynaptic effects were reliable rather than probabilistic. The synapses did not include short-term depression or facilitation. The conductance ratio of AMPA/NMDA excitatory synapses was 2–5 (McAllister and Stevens, 2000; Watt et al., 2000) so that AMPA and NMDA EPSPs typically had amplitudes of 1.5 and 0.5 mV, respectively.

The inhibitory postsynaptic potentials (IPSCs) were generated by interneurons simulating the activity of Calbindin D-28 k (CB) immunoreactive inhibitory cells that have local dendritic arbors and are believed to provide specific inhibition to the cortical module to which they belong (Conde et al., 1994; Gabbott and Bacon, 1996a, b; Gabbott et al., 1997; Krimer and Goldman-Rakic, 2001). The conductances of these synapses were adjusted to mimic the experimental observations, and to provide fast and reliable feedback inhibition after each action potential (Krimer and Goldman-Rakic, 2001).

When an action potential was detected, the conductance for each receptor type was modified in order to account for the new synaptic releases such that

$$G(t) = G_{\text{new}}(t) = G_{\text{old}}(t) + G_{\max} \sum_{n=1}^{N} g(t - t_n)$$

where $g(t)$ was an alpha function of time constant 2.7 ms for AMPA synapses, 70 ms for NMDA synapses, and 10 ms for $GABA_A$ synapses. Both AMPA and NMDA conductances shared the same t series (co-activation of NMDA and AMPA receptors). $G_{\max}$ was the maximal conductance for each respective receptor type and could be adjusted by the experimenter. In the text, this quantity was referred to as G_{AMPA}, G_{GABA}, and G_{NMDA}. In the case of

NMDA channels, however, G_{max} was voltage dependent (Jahr and Stevens, 1990) and was expressed as

$$G_{max} = \frac{G_{NMDA}}{1 + \frac{[Mg2+]}{3.57} e^{-0.062\,V}}$$

with [Mg2+] expressed in units of mM (here [Mg2+] = 2).

3 Results

The composition of a reverberatory network is currently unknown. Calcium imaging experiments in vitro indicated that a relatively small number of cells (5–20) could synchronously join a reverberatory ensemble (Cossart et al., 2003; Ikegaya et al., 2004). The first step in our studies was to determine the size of the reverberatory network under in vivo conditions. We explored this issue by comparing computational network models of varying size and by eliciting reverberatory activity using extracellular stimulation in vitro.

3.1 Network Size

To study network properties of reverberatory activity in a model, we started with a network of 26 pyramidal neurons and 6 inhibitory neurons, created as specified in Section 2. To generate sustained activity, a short (150 ms) current pulse was given simultaneously to a few (~30%) model pyramidal neurons to mimic excitatory inputs from the thalamus, another cortical region, or the hippocampus. The conductances of the synaptic inputs were adjusted to obtain firing rates and pyramidal neuron membrane potential (V_m) averages and fluctuations (standard deviation) similar to those measured during in vivo up-states (Fig. 1 and Table 1).

Table 1 Comparison of sustained activity generated by our model with in vivo up-state data (Isomura et al., 2006; Luczak et al., 2007; Haider et al., 2006; Waters and Helmchen, 2006; Rudolph et al., 2007)

	26 excitatory neuron model	In vivo data
Excitatory neuron firing rates	10.4 ± 1.3 Hz	8–15 Hz
Inhibitory neuron firing rates	34.5 ± 5.3 Hz	15–30 Hz
Average active state membrane potential	−59.7 ± 1.9 mV	−50 to −60 mV
Membrane potential fluctuations during active state	4.69 ± 0.52 mV	2–3 mV
Average 'down-state' membrane potential	−68.3 ± 0.5 mV	−65 to −75 mV
'Down-state' membrane potential fluctuations	1.03 ± 0.20 mV	0.6–2 mV
Duration of active state	1.168 ± 0.470 s	0.4–1.6 s

Because of the lack of intracellular data in the awake preparation during sustained activity, we used data obtained in vivo in the anesthetized animal to tune our model. The V_m fluctuations were the only statistic that did not fit to measured data levels if this network were to generate sustained activity, and therefore conductances were adjusted to make it as low as possible. The resulting model 'up-states' terminated spontaneously after 500–2,000 ms. Firing rates towards the end of the 'up-state' were constant until there was an abrupt end, indicating that activity did not just peter out.

Since the V_m fluctuations in this network were somewhat larger than those observed in vivo, we hypothesized that this network was smaller than those participating in reverberatory activity in vivo. To investigate how network size influences sustained activity statistics, the size was varied while keeping the proportion of excitatory and inhibitory neurons constant. Synaptic conductances were scaled proportionately to keep the overall synaptic inputs to each neuron approximately constant. This kept the average V_m of pyramidal neurons during sustained activity constant (Fig. 2A), but changed the V_m fluctuations (Fig. 2B), which were mainly determined by the conductances of single synaptic events. The V_m fluctuations reached the in vivo levels for networks with 39 excitatory neurons, and appeared to reach an asymptote within the in vivo measured range. The firing rates of both excitatory and inhibitory neurons were larger in small networks (Fig. 2C). This may be due to the larger size of each individual synaptic conductance, which may allow the neuron to cross threshold more often even though the average input is approximately the same. The average V_m of inhibitory neurons, unlike that of pyramidal neurons, increased as network size decreased (Fig. 2A). This increase may be due to the slightly higher pyramidal neuron firing rates in the smaller networks, which cause a non-balanced increase in the number of excitatory inputs to the inhibitory neurons. Another statistic that changed with network size was reverberatory activity duration, which increased for larger networks (Fig. 2D). These results show that a relatively small number of cells (39 pyramidal neurons and 9 interneurons) can generate and sustain reverberatory activity comparable to up-states observed in vivo. Smaller networks required larger individual synaptic events than those observed in vivo to generate sustained activity.

3.2 Properties of Reverberations In Vitro

To elucidate the amplitude and temporal dynamics of reverberations, reverberatory activity was elicited by stimulating the afferents to a neuron recorded intracellularly in vitro. The extracellular stimulating electrode was placed in layer 5, about 100 μm from the cell body of the recorded neuron. In the control medium, the stimulation elicited a monosynaptic compound EPSP of approximately 15 mV amplitude followed by a trail of multisynaptic EPSPs. These EPSPs were not affected by bath application of bicuculline (20 μM, not shown) but were greatly reduced by the application of DNQX (10 μM) that left only a

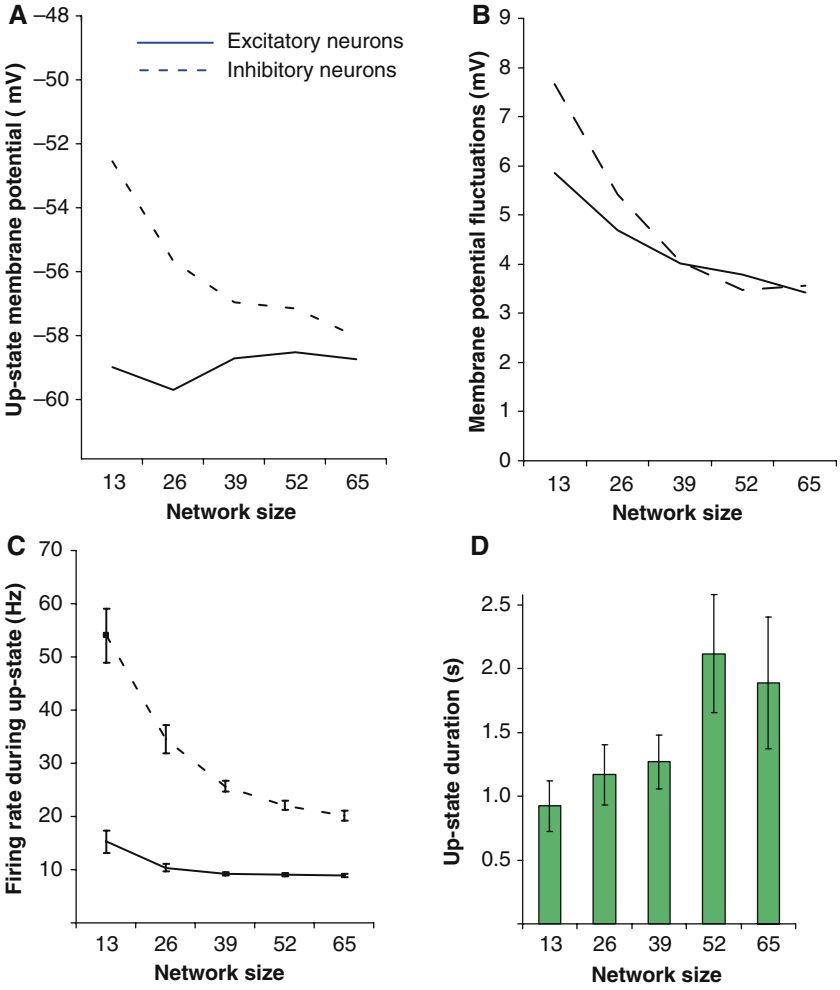

Fig. 2 Influence of network size on reverberatory activity characteristics. Network size was varied (*x*-axis is number of excitatory cells – inhibitory cells were varied proportionately) and several characteristics of the 'up-states' were measured. **A**: average membrane potential, **B**: Membrane fluctuations (standard deviation of V_m), **C**: firing rates, and **D**: duration of the sustained activity. Standard errors in panels A and B are within – the thickness of the lines and have been omitted. Adapted from Navratilova and Fellous (2008)

monosynaptic NMDA component (Fig. 3A middle). The application of APV (50 μM) abolished the response entirely (Fig. 3A, right). In 5/7 cells, afferent stimulation was followed by long latency excitatory inputs from neighboring pyramidal cells. These EPSPs could occur early and overlap with the repolarizing phase of the compound EPSP or could occur as late as 700 ms after stimulus onset, well after the compound EPSPs terminated. Some of these EPSPs may be

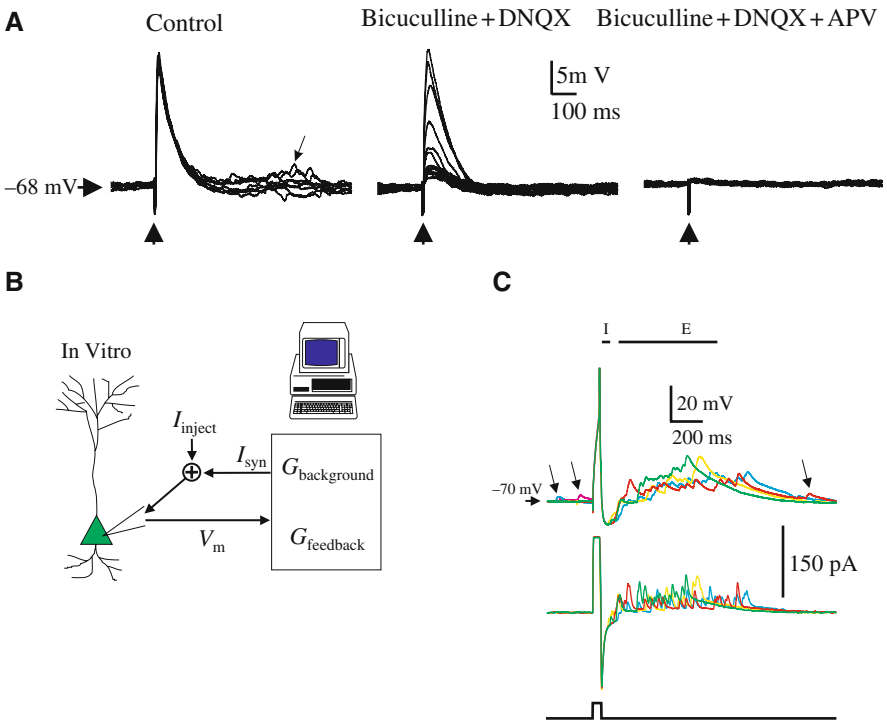

Fig. 3 Evidence for reverberatory activity in the in vitro preparation. A: Responses of a layer 5 pyramidal cell to a synaptic stimulation (*up arrow*) provided by an extracellular electrode placed about 100 μM from the soma in layer 5. *Left*: control condition (eight superimposed traces). Note the presence of a trail of EPSPs following the monosynaptic response (*arrow*). *Middle*: The wash-in of bicuculline (20 μM) and DNQX (10 μM) reduced the amplitude of the monosynatic response and suppressed the trail of EPSPs. *Right*: the remaining synaptic response was abolished by 50 μM APV indicating that it was mediated by NMDA receptor activation. **B**: schematic illustration of our hybrid system. At each time step (0.1 ms), a dedicated computer computed the values of two synaptic conductances. The first $G_{background}$ mimicked the continuous background activity of distant cells; the second $G_{feedback}$ was computed each time an action potential was emitted by the cell recorded in vitro (reactive clamp, see Section 2). **C**: Reactive clamp responses with mixed AMPA, NMDA, and $GABA_A$ conductances (four superimposed traces). Values for synaptic conductances were $G_{AMPA} = 2.1$ nS, $G_{NMDA} = 0.4$ nS, and $G_{GABA} = 7.1$ nS. Lower traces represent the current pulse injected to the cell to initiate a single action potential. The middle trace represents the sum of the current pulse, and the current computed and injected by the reactive clamp. The upper trace shows the membrane potential of the cell. Note the presence of spontaneous EPSPs (*arrows*). The horizontal bars labeled I and E indicate the average time course of the inhibitory and excitatory feedback inputs, respectively. Adapted from Fellous and Sejnowski (2003)

directly related to the cell's own spiking, but it is likely that most are due to multi-synaptic reverberations from other cells that have been simultaneously activated by the extracellular electrode. Feedforward inhibition was activated by the stimulation and was 'hidden' by the monosynaptic EPSP (Fellous and

Sejnowski, 2003). Because the onset times of the feedback IPSCs could not be directly measured, due to the monosynaptic response, we estimated their distribution (mean 40 $\pm$ 20 ms).

3.3 Reverberatory Ensemble Using Reactive Clamp

In order to study the impact of the reverberatory 'trail' on persistent activity, we used a variant of the dynamical clamp technique (Fig. 3B). A neuron was recorded intracellularly in current-clamp mode. A dedicated computer was programmed to detect the occurrence of an action potential (voltage crossing 0 mV) and to dynamically react to each action potential by generating a train of mixed IPSCs and EPSCs that was injected in the neuron. The time distribution of the simulated excitatory synaptic events was assumed to be Poisson with a mean and dead time matching the experimental data.

Compatible with the simulation results presented above, excitatory AMPA and NMDA components were generated by a population of 40 synapses together constituting a Poisson train of EPSPs with mean interval of 15 ms and a dead time of 100 ms. Because the average synaptic interval of 15 ms (66 Hz) corresponds to the discharge of 40 cells, each of these feedback cells is assumed to fire only once during $15 \times 40 = 600$ ms immediately following a single spike by the real cell. For each spike of the real cell, one and only one feedback EPSP/spike from each of the 40 cells is generated, so that in principle the firing rate of each of the simulated microcircuit feedback cells is always kept identical to the firing rate of the real cell (no matter what this firing rate is).

Feedback IPSPs were generated by a population of five GABAergic synapses with a mean interval of 10 ms and a dead time of 15 ms. In 6/21 exploratory experiments these values were set empirically so that excitatory mean intervals and dead times ranged from 12–18 and 90–150 ms, respectively, and inhibitory mean intervals and dead times ranged from 8–12 and 10–20 ms, respectively. The results obtained under these conditions were qualitatively similar to those obtained with the chosen standard intervals and dead times mentioned above.

The $GABA_A$ inhibitory feedback synaptic currents were distributed in time according to our experimental estimates above (Fellous and Sejnowski, 2003). Their mean discharge ISI was set to 10 ms with a deadtime of 15 ms. Fig. 3 shows the compound feedback injected by the reactive clamp in response to one elicited spike. A fast initial GABA component is followed by a slow NMDA-mediated component topped by AMPA EPSPs. Note that this curve is somewhat different from the data shown in Fig. 3. The EPSPs in Fig. 3C are lower in amplitude and the NMDA depolarization is smaller than the ones obtained with reactive clamp. The difference is due to the fact that the reactive clamp implements the in vivo situation where all the cells of the microcircuits are healthy and where all synaptic connections are functional. This is unlikely to be true in vitro. The fast GABA inhibition visible after the spike is more

pronounced than in Fig. 3 due to the fact that the experimental data included a powerful feedforward compound EPSP which partially masked inhibition.

Cells in vivo have large subthreshold membrane fluctuations (standard deviation of approximately 4 mV), a mean potential typically around –60 mV, spontaneous and irregular firing (0.3–2 Hz in prefrontal cortex with a coefficient of variation approaching 1.0), and a low input resistance (about 40 MΩ) (Paré et al., 1998; Destexhe and Paré, 1999; Fellous et al., 2003). These properties arise from the background synaptic inputs coming from other cells in the circuit. These aspects of in vivo activity can be effectively recreated in the in vitro preparation (Destexhe et al., 2001) by injecting the excitatory and inhibitory background synaptic activity as random conductance processes (see methods) into a neuron using a standard dynamical clamp protocol. The mean and standard deviation of these conductances were adjusted to yield in vivo-like activity.

3.4 Spontaneous Sustained Activity

Figure 4 shows an example of a cell recorded in vitro, to which synaptic background activity was added (G_{e0}= 10 nS, G_{i0}= 21 nS, σ_e = 3 nS, and σ_i=7.5 nS). The cell fired at 0.4 Hz (0.46 ± 0.1 Hz, n =19) with a CV of 0.71 (0.72 ± 0.1, n =16), its membrane potential was depolarized to −66 mV (−64.3 ± 1.53 mV, n =19), the membrane showed large fluctuations of 4.1 mV standard deviation (4.3 ± 0.8, n =19), and its input resistance was 42 MΩ (37.9 ± 6.4, n =19), without the noise the resting membrane potential was −71 mV (−69.8 ± 3.1, n =19) and its input resistance was 184 MΩ (157 ± 32, n =19). The lower trace shows the background synaptic current computed by the dynamic clamp. Note the presence of action potentials in the injected current trace, a hallmark of the dynamical clamp technique. The synaptic background noise represented the aggregate activity of a large population of pyramidal cells and interneurons located outside the cortical module where the cell was located. Unlike the feedback activity presented in Fig. 3, this activity was assumed to not depend on the specific firing pattern of the cell recorded, and its parameters (mean and standard deviation of excitatory and inhibitory processes) were typically kept constant. In this preparation, background synaptic activity alone was not sufficient to explain the high CV typically observed in vivo.

When the model of the cortical feedback was added along with synaptic background activity, the cell exhibited short and fast sequences of action potentials riding on a small NMDA-mediated feedback depolarization (G_{AMPA}= 1.5 nS, G_{NMDA}= 0.5 nS, and G_{GABA} = 6.0 nS). These sequences lasted typically less than 2 s (1.3 s ± 0.5 s, n =47, 4 cells, Fig. 4B lower trace, arrow) and the firing rate increased to in vivo-like values (1.2 ± .64 Hz, n =19). Because of the introduction of short ISIs, the CV increased to values typically observed in vivo (0.92 ± 0.2, n =16) (Softky and Koch, 1993; Holt et al., 1996; Shadlen and Newsome, 1998). These fast sequences were akin to in vivo 'up-states' and

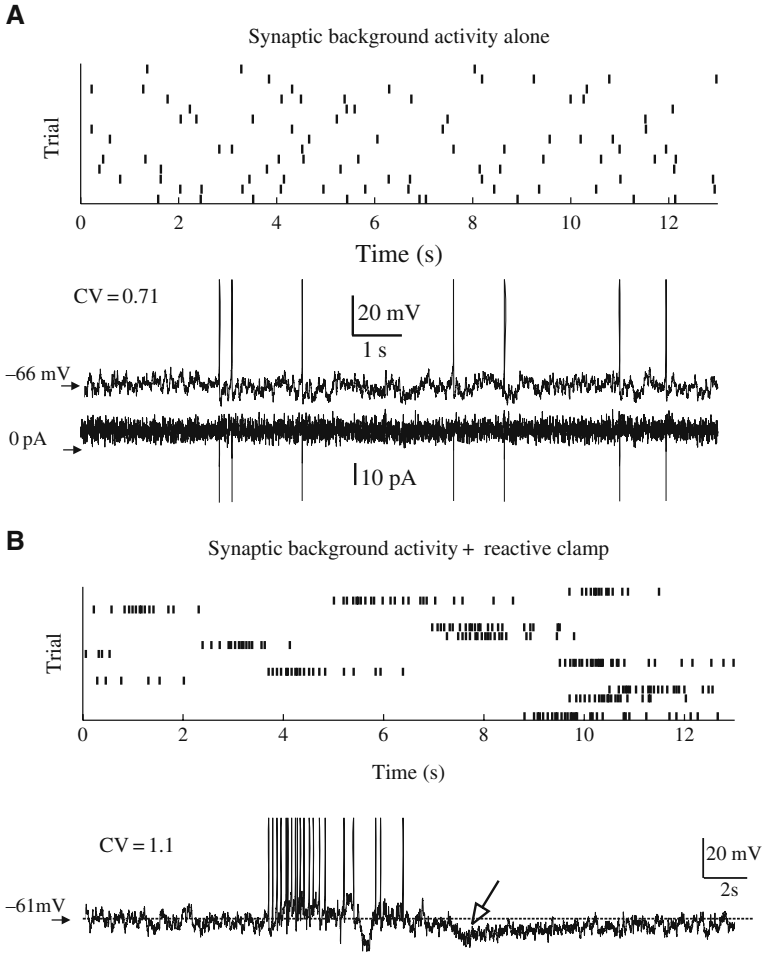

Fig. 4 Spontaneous spiking of a layer 5 pyramidal cell undergoing background and feedback synaptic noise. A: Example of a cell undergoing synaptic background noise only ($G_{e0} = 10$ nS, $G_{i0} = 21$ nS, $\sigma_e = 3$ nS, and $\sigma_i = 7.5$ nS). The rastergram shows the spiking activity of this cell during 182 s (represented as 14 trials of 13 s each). An example of the membrane voltage is shown below. The current computed by the dynamic clamp is shown below the voltage trace. In this condition, the CV of this cell was 0.71. **B**: Addition of reverberatory activity under reactive clamp. The cell now shows spontaneous bouts of sustained activity lasting typically longer than a second (see rastergram). A sample voltage trace is shown below the rastergram. Note the presence of a slow intrinsic hyperpolarizing current (not found in the computer-generated synaptic current trace, not shown) that terminates the reverberatory activity (*open arrow*). In this condition the CV was 1.1 due to the introduction of very fast ISIs. All panels are from the same cell. Adapted from Fellous and Sejnowski (2003)

were followed by long periods of spiking silence. Since the model of the synaptic background activity was derived from in vivo intracellular data in the anesthetized animal, the cells modeled here should reflect low levels of dopamine (Paré et al., 1998; Fellous et al., 2003). Recent in vitro studies demonstrated that

dopamine increased the excitability of prefrontal cortex (PFC) cells (Yang and Seamans, 1996; Shi et al., 1997; Henze et al., 2000) and increased the amount of NMDA current (Cepeda et al., 1993; Zheng et al., 1999; Seamans et al., 2001) elicited by extracellular stimulation. An increase in the average membrane potential (+5 mV) and an increase in the feedback NMDA current (+30%) mimicking the effect of higher, in vivo-behaving-like dopamine levels, yielded an increase in the occurrence and duration of the fast sequences (Fig. 4B). Typically, these sequences resembled spontaneous dopamine-dependent 'up-states' observed in vivo in prefrontal cortex (Lewis and O'Donnell, 2000), lasted substantially longer (3.2 ± 0.9 s, $n = 61$, five cells) than in baseline conditions and the CV increased slightly (1.1 ± 0.1, $n = 9$).

Reverberatory activity was initiated by a fast sequence of action potentials that recruited a large excitatory feedback. It was terminated by the activation of a slow hyperpolarizing intrinsic current (Fig. 4B, open arrow). Although this current was not pharmacologically characterized in this study it was primarily activated after a large amount of spiking,and likely included a calcium-activated potassium current. The parameters of the background and reactive components were then fixed for each cell recorded, and further explorations of the conditions of initiation of these reverberations were conducted.

3.5 Stimulus-Driven Elicitation of Sustained Activity

In a typical working memory task, cells in frontal cortices are transiently activated by the presentation of a cue, and continue to fire for several seconds after the cue has been removed, until the behavioral response is initiated. In order to assess the ability of a PFC cortical module to sustain activity, we simulated the cue and the behavioral response phases of a working memory task by positive and negative current injection, respectively. In Fig. 5, a PFC cell placed in realistic in vivo conditions fired in a sustained manner, long after the cue stimulus was turned off, until the simulated response was triggered ($G_{e0} =$ 12 nS, $G_{i0} = 20$ nS, $\sigma_e = 2.8$ nS, $\sigma_i = 7.1$ nS, $G_{AMPA} = 1.6$ nS, $G_{NMDA} = 0.5$ nS, and $G_{GABA} = 6.8$ nS). This behavior was elicited in 21 of the 32 cells tested. In these cells, the firing rate during the delay period was typically lower than during the presentation of the cue. Two of the 32 cells tested were strongly adapting and could not be stimulated to produce sustained activity while in a regime of spontaneous background similar to the ones observed in vivo. In nine cells, the short cue-depolarization failed to promote sustained spiking, and instead activated the slow hyperpolarization previously noted. In those cells, the firing rates during the delay period were decreased.

A detailed analysis of the trials during which sustained activity was not achieved revealed that sustained activity depended strongly on the number of action potentials generated during the cue period (Fellous and Sejnowski, 2003). For a low number of action potentials, or for action potentials sequences of

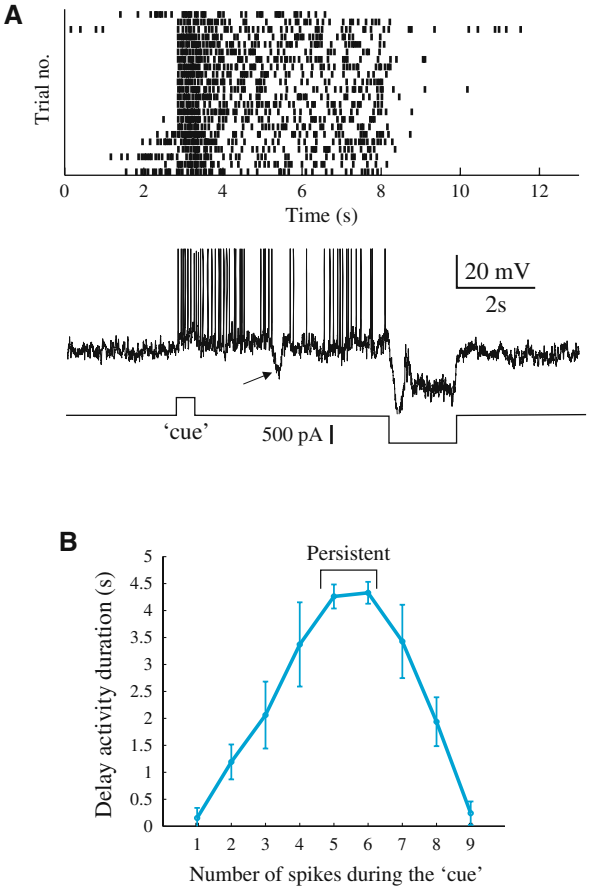

Fig. 5 Simulated delayed match-to-sample task in layer 5 pyramidal cells. **A**: A pyramidal cell was placed in in vivo like conditions by injecting background synaptic inputs ($G_{e0} = 12$ nS, $G_{i0} = 20$ nS, $\sigma_e = 2.8$ nS, $\sigma_i = 7.1$ nS, and 51 MΩ input resistance) and reactive feedback ($G_{AMPA} = 1.6$ nS, $G_{NMDA} = 0.5$ nS, and $G_{GABA} = 6.8$ nS). The cell was then injected a current pulse lasting 400 ms simulating the 'cue' and a hyperpolarizing current pulse lasting 1.8 s. The cell showed sustained firing for the duration of the delay period (4.5 s). Note the occurrence of large inhibitory events (*arrow*) resulting from the random synchronization between background and feedback inhibition. The background firing rate of the cell was 1.1 Hz, its firing rate during the delay period was 6.2 Hz, the rastergram shows 18 of 44 trials. **B**: Group data for five cells matched for their input resistance (40 ± 6 MΩ) and background firing rate (0.7 ± 0.4 Hz). The curve shows the average duration of the spiking activity after the cue offset, as a function of the number of action potentials generated during the cue. Persistent activity was most reliably achieved for five and six actions potentials. Adapted from Fellous and Sejnowski (2003)

large ISIs, the reverberatory activity was not sufficient to trigger additional spikes, as occurs during spontaneous activity. A large number of action potentials (7–8) activated an intrinsic slow hyperpolarizing current that kept the cells below threshold, despite a large amount of synaptic feedback. Intermediate

amounts of spiking (5–6 in Fig. 5B) could sustain the activity of the cell for several seconds. Group data on five cells matched for their input resistance (40 ± 6 MΩ with synaptic background) and background firing rate (0.7 ± 0.4 Hz) revealed that persistent activity optimally occurred when five or six action potentials were generated during the cue period (Fig. 5B). The inverted U-shape nature of the curve was qualitatively reproduced in most cells recorded, but its position and width on the *x*-axis varied greatly from cell to cell.

3.6 Regulation of Reverberatory Activity Level by Inhibition

Prefrontal cortical pyramidal cells recorded in vivo during working memory tasks show a wide range of firing rates during the delay period. In the same cell, firing rates might vary from baseline levels for non-preferred stimuli, to firing rates 10 times larger than control for preferred stimuli (Goldman-Rakic, 1995). Other cells modulate their firing rate in relation to the luminance of distracting stimuli (Constantinidis et al., 2001). The gain of a pyramidal cell depends on the standard deviation of the excitatory and inhibitory synaptic background noise that it receives (Chance et al., 2002; Fellous et al., 2003, Chance and Abbott "Simulating In Vivo Background Activity in a Slice with the Dynamic Clamp" in this volume). In prefrontal cortical cells, an increase in the standard deviation of the background inhibitory inputs (σ_i) mimicking an increase in inhibitory correlation was particularly effective in modifying the shape of the input/output curve of pyramidal cells recorded in vitro under in vivo like conditions (Fellous et al., 2003). Figure 6A shows an example of the influence of σ_i on the response of a cell that was placed in the nominal conditions of our experiments (Fig. 4, $G_{e0} = 23$ nS, $G_{i0} = 31$ nS, $\sigma_e = 2.5$ nS, $\sigma_i = 6.5$ nS, $G_{AMPA} = 1.2$ nS, $G_{NMDA} = 0.6$ nS, $G_{GABA} = 6.0$ nS, and the standard deviation of the membrane potential was 3.1 mV). As σ_i increased, the maximal value of the firing rate increased, and the slope of the frequency/current curve increased so that for low-input current the firing remained relatively unchanged, and for higher current intensity the firing rate in the two conditions became significantly different going from 20 Hz to about 40 Hz (the standard deviation of the membrane potential was increased to 5.3 mV, primarily in the hyperpolarizing direction). Firing rates were computed from 3-s-long current injections (excluding the first 500 ms). In the cue-elicited sustained activity experiments, with the low σ_i value (6.5 nS) the cell exhibited a background firing rate of 0.5 Hz, and a delay firing rate of about 8 Hz. When σ_i was increased to 25 nS, the background firing rate did not qualitatively change (0.9 Hz) but the firing rate during the delayed period increased to 31 Hz (Fig. 6B). The signal-to-noise ratio in this cell could therefore be tuned and was increased in this experiment by about 110% by increasing σ_i. Similar results were obtained for three other pyramidal cells with increases in signal-to-noise ratios of 20, 32, and 59%. These results suggest that the amount of correlation in the background inhibitory inputs might be key to determining

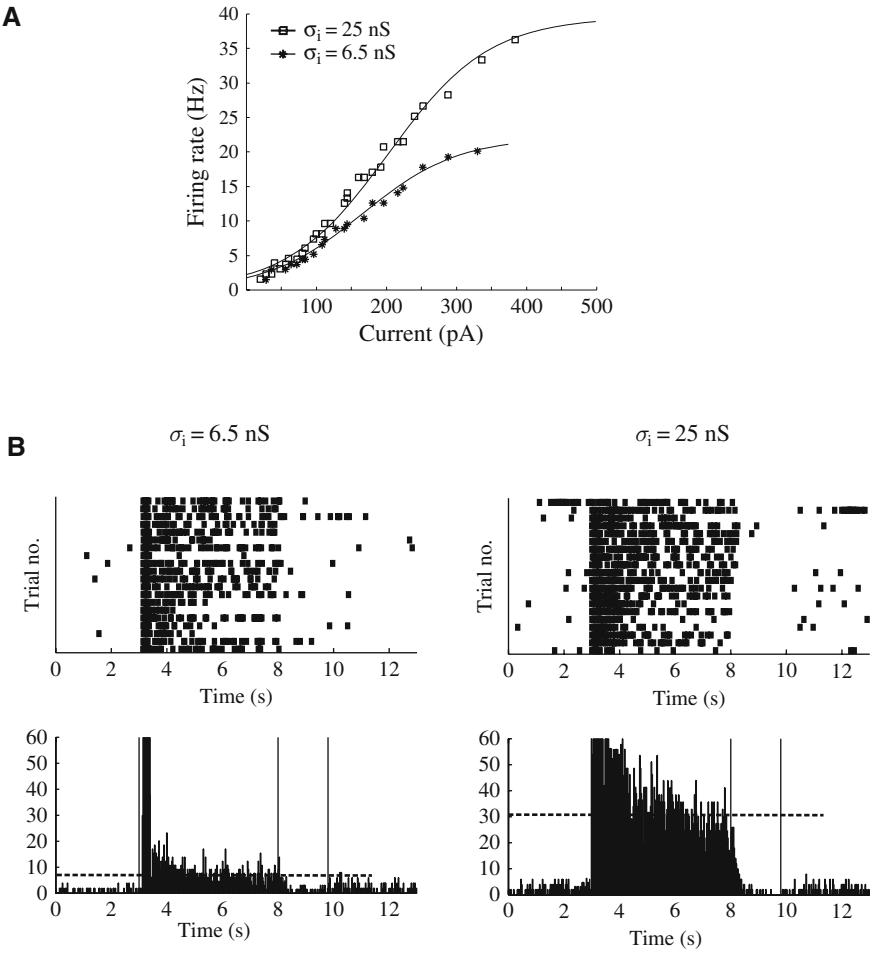

Fig. 6 The firing rate during the delay period activity can be modulated by the correlation of the background inhibitory synaptic noise. A: Average firing rate of a pyramidal cell in response to 3-s-long current pulses of varying amplitude for low ($\sigma_i = 6.5$ nS, stars) and high ($\sigma_i = 25$ nS, open squares) standard deviation of the background synaptic noise ($G_{e0} = 23$ nS, $G_{i0} = 31$ nS, $\sigma_e = 2.5$ nS, $G_{AMPA} = 1.2$ nS, $G_{NMDA} = 0.6$ nS, $G_{GABA} = 6.0$ nS, and 37 MΩ input resistance). This standard deviation corresponds to the amount of correlation in the background synaptic inputs (Fellous et al., 2003). **B**: The same cell was injected with cue and response pulses to elicit sustained activity as in Fig. 5. When σ_i was low, the cell sustained activity at 8 Hz during the delay period, and its background firing rate before the cue was 0.5 Hz. When σ_i was high, the cell sustained activity at 31 Hz and its background activity before the cue was 0.9 Hz. Adapted from Fellous and Sejnowski (2003)

the firing rate of the cell during the delay period (see also Jaeger and Lin "Unraveling the Dynamics of Deep Cerebellar Nucleus Neurons with the Application of Artificial Conductances" in this volume).

4 Discussion

Using computer simulations and a hybrid in vitro preparation we reproduced the reverberatory activity occurring in small cortical networks during self-sustained activity. Both studies indicated that about 40 excitatory cells were sufficient to mimic the membrane and firing statistics seen in vivo. Cells placed in such networks responded to a brief depolarization with an increase in firing rate that outlasted the depolarization, mimicking the activity of a cell responding to its preferred stimulus during the delay period of a working memory task in the behaving monkey. Some cells recorded with the reactive clamp technique showed 'off' responses and their firing rates decreased during the delay period due to the activation of a slow intrinsic hyperpolarizing current. Finally, we showed that background inhibition could change the input/output gain of single cells, and modulate the level of activity during sustained activity without significant changes in background baseline activity.

In modeling work we also showed that intrinsic currents such as the H-current could contribute to the initiation of sustained activity (Navratilova and Fellous, 2008). The H-current made the initiation of the reverberations more likely to occur following excitatory inputs. Also, since the H-current is activated at hyperpolarized potentials an inhibitory volley prior to excitatory inputs enhanced its activation and further increased the probability of generating sustained activity. The H-current did not have an effect on other properties of sustained activity, such as the firing rate or duration.

The simulation and in vitro results presented above suggest the following sequence of events bringing into play both intrinsic currents and network dynamics (see Tobin et. al. "Using the Dynamic Clamp to Explore the Relationship Between Intrinsic Activity and Network Dynamics," Sadoc et. al. "Re-Creating In Vivo-Like Activity and Investigating the Signal Transfer Capabilities of Neurons: Dynamic-Clamp Applications Using Real-Time NEURON," and White et al. "Using "Hard" Real-Time Dynamic Clamp to Study Cellular and Network Mechanisms of Synchronization in the Hippocampal Formation" in this volume for other examples). Reverberatory activity is initiated by brief depolarizations of a subset of neurons belonging to the ensemble. In cells containing an H-current, this depolarization is facilitated, especially if a short preceding hyperpolarization is present (Navratilova and Fellous, 2008). Provided that the level of depolarization is within a certain range, action potentials in the initiator cells will generate sufficient postsynaptic NMDA currents to recruit the other members of the assembly, including inhibitory cells. Background noise has been shown to modify the gain of the input/output curve (Chance et al., 2002; Fellous et al., 2003) and to make the cell more sensitive to transient inputs as short as 30 ms (Fellous et al., 2003). As noted anecdotally in previous work, inhibition, possibly due to its shunting nature, is more effective at controlling the gain than excitation (Fellous et al., 2003). We found that the amount of correlations in the inhibitory background

inputs (not belonging to the assembly, and modeled by the standard deviation of the inhibitory noise) controls the firing rate of individual cells in the assembly. Recent evidence has highlighted the predominant role of inhibition during reverberatory activity in vitro and in vivo (Piwkowska et al., 2008). The firing of the cells during the reverberation triggers slow intracellular calcium accumulation and activates calcium-dependent potassium currents. These currents build up and eventually shut down individual cells. A complementary role for calcium accumulation has been proposed elsewhere on theoretical ground (Mongillo et al., 2008). After a critical number of cells have shut down, the whole assembly shuts down due a lack of NMDA-dependent reverberatory drive, and the small network enters a quiet state. Our results could explain findings such as the increased duration of the reverberation by dopamine released from the ventral tegmental area (Lewis and O,Donnell, 2000). If, as our results suggest, reverberatory activity relies on prompt NMDA-dependent excitatory feedback within a small population of interconnected neurons, then modulation by dopamine depolarizes the cells, increases NMDA currents and results in an increase of the duration of sustained activity (Section 3 and Fig 4B).

These results and hypothetical mechanism are of course contingent on several assumptions made by the reactive clamp and computational models including the exact number of reverberatory synapses used and their dynamics. In light microscopy anatomical studies of the rat medial prefrontal cortex, a cortical module (50×50 μm) had about 80 pyramidal cells and about 16 interneurons (Gabbott and Bacon, 1996a, b; Gabbott et al., 1997). Since about 40 of these 80 pyramidal cells are in layer 5/6, and since most layer 5/6 cells are connected to other layer 5/6 cells, our population of synapses modeled the excitatory feedback within a single cortical module (Melchitzky et al., 1998). Further work is needed to compare the prefrontal cortex studied here with other cortical or subcortical areas that also exhibit persistent activity. While synapses in the model explicitly included stochasticity, the unreliability of the synapses in the reactive clamp experiments was captured by the Poisson nature of the feedback. However, the sizes of the individual e/ipsps were constant. Recent work has shown that short-term plasticity may be of functional relevance in removing or restoring temporal correlations within spike trains (Goldman et al., 2002) and further work is required to assess its impact on reverberatory activity.

Although this study focused on the spontaneous and stimulus-driven sustained activity in the PFC during a working memory task, it may apply to other systems and behaviors and can shed light on the functional nature of local microcircuits in other parts of the cortex. A cortical cell receives at least two functionally distinct kinds of inhibition: The first is a feedforward inhibition generated by the background synaptic noise from distant microcircuits. This input varies slowly and its standard deviation (amount of correlation) modulates the gain of the postsynaptic cell. The second kind of inhibition is feedback inhibition local to the microcircuit and its role is to control the amount of reverberation within the microcircuit. Recent experimental evidence supports

the presence of feedforward and feedback inhibition during working memory tasks (Constantinidis et al., 2002), and further experimental and theoretical studies should explore the consequences of this inhibition for the function of cortical microcircuits.

5 Glossary of terms

NMDA: N-methyl D-aspartate, AMPA: α-amino-3-hydroxyl-5-methyl-4-isoxazole-propionate, GABA: gamma-amino butyric acid, CB: Calbindin D-28k, DNQX: 6,7-Dinitroquinoxaline-2,3-dione, APV: (2R)-amino-5-phosphonovaleric acid, CV: Coefficient of variation.

References

Casagrande VA, Xu X, Sary G (2002) Static and dynamic views of visual cortical organization. Prog Brain Res 136:389–408.

Cepeda C, Buchwald NA, Levine MS (1993) Neuromodulatory actions of dopamine in the neostriatum are dependent upon the excitatory amino acid receptor subtypes activated. Proc Natl Acad Sci USA 90:9576–9580.

Chance FS, Abbott LF, Reyes AD (2002) Gain modulation from background synaptic input. Neuron 35:773–782.

Conde F, Lund JS, Jacobowitz DM, Baimbridge KG, Lewis DA (1994) Local circuit neurons immunoreactive for calretinin, calbindin D-28 k or parvalbumin in monkey prefrontal cortex: distribution and morphology. J Comp Neurol 341:95–116.

Constantinidis C, Franowicz MN, Goldman-Rakic PS (2001) The sensory nature of mnemonic representation in the primate prefrontal cortex. Nat Neurosci 4:311–316.

Constantinidis C, Williams GV, Goldman-Rakic PS (2002) A role for inhibition in shaping the temporal flow of information in prefrontal cortex. Nat Neurosci 5:175–180.

Cossart R, Aronov D, Yuste R (2003) Attractor dynamics of network UP states in the neocortex. Nature 423:283–288.

Destexhe A, Paré D (1999) Impact of network activity on the integrative properties of neocortical pyramidal neurons in vivo. J Neurophysiol 81:1531–1547.

Destexhe A, Babloyantz A, Sejnowski TJ (1993) Ionic mechanisms for intrinsic slow oscillations in thalamic relay neurons. Biophys J 65:1538–1552.

Destexhe A, Mainen ZF, Sejnowski TJ (1996) Kinetic models of synaptic transmission. In: Methods in neuronal modeling (Koch C, Segev I, eds). Cambridge: MIT Press.

Destexhe A, Contreras D, Sejnowski TJ, Steriade M (1994) A model of spindle rhythmicity in the isolated thalamic reticular nucleus. J Neurophysiol 72:803–818.

Destexhe A, Rudolph M, Fellous JM, Sejnowski TJ (2001) Fluctuating synaptic conductances recreate in vivo-like activity in neocortical neurons. Neuroscience 107:13–24.

Durstewitz D, Seamans JK, Sejnowski TJ (2000) Neurocomputational models of working memory. Nat Neurosci 3(Suppl):1184–1191.

El Boustani S, Pospischil M, Rudolph-Lilith M, Destexhe A (2007) Activated cortical states: experiments, analyses and models. J Physiol Paris 101:99–109.

Fellous JM, Sejnowski TJ (2003) Regulation of persistent activity by background inhibition in an in vitro model of a cortical microcircuit. Cerebral Cortex 13:1232–1241.

Fellous JM, Rudolph M, Destexhe A, Sejnowski TJ (2003) Synaptic background noise controls the input/output characteristics of single cells in an in vitro model of in vivo activity. Neuroscience 122:811–829.
Gabbott PL, Bacon SJ (1996a) Local circuit neurons in the medial prefrontal cortex (areas 24a,b,c, 25 and 32) in the monkey: I. Cell morphology and morphometrics. J Comp Neurol 364:567–608.
Gabbott PL, Bacon SJ (1996b) Local circuit neurons in the medial prefrontal cortex (areas 24a,b,c, 25 and 32) in the monkey: II. Quantitative areal and laminar distributions. J Comp Neurol 364:609–636.
Gabbott PL, Dickie BG, Vaid RR, Headlam AJ, Bacon SJ (1997) Local-circuit neurones in the medial prefrontal cortex (areas 25, 32 and 24b) in the rat: morphology and quantitative distribution. J Comp Neurol 377:465–499.
Goldman-Rakic PS (1995) Cellular basis of working memory. Neuron 14:477–485.
Goldman MS, Maldonado P, Abbott LF (2002) Redundancy reduction and sustained firing with stochastic depressing synapses. J Neurosci 22:584–591.
Golomb D, Amitai Y (1997) Propagating neuronal discharges in neocortical slices: computational and experimental study. J Neurophysiol 78:1199–1211.
Gonzalez-Burgos G, Barrionuevo G, Lewis DA (2000) Horizontal synaptic connections in monkey prefrontal cortex: an in vitro electrophysiological study. Cereb Cortex 10:82–92.
Graziano MS, Hu XT, Gross CG (1997) Coding the locations of objects in the dark. Science 277:239–241.
Hahn TT, Sakmann B, Mehta MR (2007) Differential responses of hippocampal subfields to cortical up-down states. Proc Natl Acad Sci USA 104:5169–5174.
Haider B, Duque A, Hasenstaub AR, McCormick DA (2006) Neocortical network activity in vivo is generated through a dynamic balance of excitation and inhibition. J Neurosci 26:4535–4545.
Haider B, Duque A, Hasenstaub AR, Yu Y, McCormick DA (2007) Enhancement of visual responsiveness by spontaneous local network activity in vivo. J Neurophysiol 97:4186–4202.
Hasenstaub A, Shu Y, Haider B, Kraushaar U, Duque A, McCormick DA (2005) Inhibitory postsynaptic potentials carry synchronized frequency information in active cortical networks. Neuron 47:423–435.
Henze DA, Gonzalez-Burgos GR, Urban NN, Lewis DA, Barrionuevo G (2000) Dopamine increases excitability of pyramidal neurons in primate prefrontal cortex. J Neurophysiol 84:2799–2809.
Hines ML, Carnevale NT (1997) The NEURON simulation environment. Neural Comput 9:1179–1209.
Hoffman KL, Battaglia FP, Harris K, MacLean JN, Marshall L, Mehta MR (2007) The upshot of up states in the neocortex: from slow oscillations to memory formation. J Neurosci 27:11838–11841.
Holt GR, Softky WR, Koch C, Douglas RJ (1996) Comparison of discharge variability in vitro and in vivo in cat visual cortex neurons. J Neurophysiol 75:1806–1814.
Ikegaya Y, Aaron G, Cossart R, Aronov D, Lampl I, Ferster D, Yuste R (2004) Synfire chains and cortical songs: temporal modules of cortical activity. Science 304:559–564.
Isomura Y, Sirota A, Ozen S, Montgomery S, Mizuseki K, Henze DA, Buzsaki G (2006) Integration and segregation of activity in entorhinal-hippocampal subregions by neocortical slow oscillations. Neuron 52:871–882.
Jahr CE, Stevens CF (1990) A quantitative description of NMDA receptor-channel kinetic behavior. J Neurosci 10:1830–1837.
Krimer LS, Goldman-Rakic PS (2001) Prefrontal microcircuits: membrane properties and excitatory input of local, medium, and wide arbor interneurons. J Neurosci 21:3788–3796.
Lewis BL, O'Donnell P (2000) Ventral tegmental area afferents to the prefrontal cortex maintain membrane potential 'up' states in pyramidal neurons via D(1) dopamine receptors. Cereb Cortex 10:1168–1175.

Luczak A, Bartho P, Marguet SL, Buzsaki G, Harris KD (2007) Sequential structure of neocortical spontaneous activity in vivo. Proc Natl Acad Sci USA 104:347–352.
Maass W, Zador AM (1999) Dynamic stochastic synapses as computational units. Neural Comput 11:903–917.
Mao BQ, Hamzei-Sichani F, Aronov D, Froemke RC, Yuste R (2001) Dynamics of spontaneous activity in neocortical slices. Neuron 32:883–898.
McAllister AK, Stevens CF (2000) Nonsaturation of AMPA and NMDA receptors at hippocampal synapses. Proc Natl Acad Sci USA 97:6173–6178.
McCormick DA, Shu Y, Hasenstaub A, Sanchez-Vives M, Badoual M, Bal T (2003) Persistent cortical activity: mechanisms of generation and effects on neuronal excitability. Cereb Cortex 13:1219–1231.
Melchitzky DS, Sesack SR, Pucak ML, Lewis DA (1998) Synaptic targets of pyramidal neurons providing intrinsic horizontal connections in monkey prefrontal cortex. J Comp Neurol 390:211–224.
Mongillo G, Barak O, Tsodyks M (2008) Synaptic theory of working memory. Science 319:1543–1546.
Navratilova Z, Fellous JM (2008) A biophysical model of cortical up and down states: excitatory-inhibitory balance and H-current. In: International School on Neural Nets – Dynamic Brain. Erice, Sicily: Springer.
Okun M, Lampl I (2008) Instantaneous correlation of excitation and inhibition during ongoing and sensory-evoked activities. Nat Neurosci 11:535–537.
Paré D, Shink E, Gaudreau H, Destexhe A, Lang EJ (1998) Impact of spontaneous synaptic activity on the resting properties of cat neocortical pyramidal neurons In vivo. J Neurophysiol 79:1450–1460.
Piwkowska Z, Pospischil M, Brette R, Sliwa J, Rudolph-Lilith M, Bal T, Destexhe A (2008) Characterizing synaptic conductance fluctuations in cortical neurons and their influence on spike generation. J Neurosci Methods 169:302–322.
Pratt WE, Mizumori SJ (2001) Neurons in rat medial prefrontal cortex show anticipatory rate changes to predictable differential rewards in a spatial memory task. Behav Brain Res 123:165–183.
Rudolph M, Pospischil M, Timofeev I, Destexhe A (2007) Inhibition determines membrane potential dynamics and controls action potential generation in awake and sleeping cat cortex. J Neurosci 27:5280–5290.
Seamans JK, Durstewitz D, Christie BR, Stevens CF, Sejnowski TJ (2001) Dopamine D1/D5 receptor modulation of excitatory synaptic inputs to layer V prefrontal cortex neurons. Proc Natl Acad Sci USA 98:301–306.
Shadlen MN, Newsome WT (1998) The variable discharge of cortical neurons: implications for connectivity, computation, and information coding. J Neurosci 18:3870–3896.
Shadlen MN, Newsome WT (2001) Neural basis of a perceptual decision in the parietal cortex (area LIP) of the rhesus monkey. J Neurophysiol 86:1916–1936.
Shi WX, Zheng P, Liang XF, Bunney BS (1997) Characterization of dopamine-induced depolarization of prefrontal cortical neurons. Synapse 26:415–422.
Softky WR, Koch C (1993) The highly irregular firing of cortical cells is inconsistent with temporal integration of random EPSPs. J Neurosci 13:334–350.
Tsodyks M, Kenet T, Grinvald A, Arieli A (1999) Linking spontaneous activity of single cortical neurons and the underlying functional architecture. Science 286:1943–1946.
Uhlenbeck GE, Ornstein LS (1930) On the theory of Brownian motion. Phys Rev 36:823–841.
Wang XJ (2001) Synaptic reverberation underlying mnemonic persistent activity. Trends Neurosci 24:455–463.
Waters J, Helmchen F (2006) Background synaptic activity is sparse in neocortex. J Neurosci 26:8267–8277.

Watt AJ, van Rossum MC, MacLeod KM, Nelson SB, Turrigiano GG (2000) Activity coregulates quantal AMPA and NMDA currents at neocortical synapses. Neuron 26:659–670.

Yang CR, Seamans JK (1996) Dopamine D1 receptor actions in layers V–VI rat prefrontal cortex neurons in vitro: modulation of dendritic-somatic signal integration. J Neurosci 16:1922–1935.

Zheng P, Zhang XX, Bunney BS, Shi WX (1999) Opposite modulation of cortical N-methyl-D-aspartate receptor-mediated responses by low and high concentrations of dopamine. Neuroscience 91:527–535.

Dynamic-Clamp-Constructed Hybrid Circuits for the Study of Synchronization Phenomena in Networks of Bursting Neurons

Carmen C. Canavier, Fred H. Sieling, and Astrid A. Prinz

Abstract Hybrid circuits comprised of one biological bursting neuron and one model bursting neuron were constructed using the dynamic clamp to create artificial synaptic conductances in both neurons. The strength and duration of reciprocal inhibitory and excitatory synaptic inputs were varied in a number of such circuits. The phase resetting curves (PRCs) for each component neuron were constructed for each isolated neuron using a pulse in postsynaptic conductance elicited by a single burst in the other neuron. The PRCs from the two component neurons were then used to predict whether a one to one phase-locked mode would be observed in the hybrid network, and if so, to predict the phase angle and network period. The predictions were qualitatively correct for 161 of 164 inhibitory networks and for 64 of 86 excitatory networks. The failures in the case of inhibition resulted from very weak coupling and in the case of excitation from two special cases, one in which the coupling becomes effectively continuous and another in which complex behavior results from a discontinuous PRC. The firing intervals and network period predictions were generally accurate within 10% of the values actually observed in the hybrid networks, a level similar to the level of variability observed in the measurement of the PRC and of the intrinsic period in the biological neuron.

1 Introduction

Phase resetting curves describe how an oscillator, such as a regularly spiking or bursting neuron, responds to perturbations, for example synaptic inputs, delivered at different phases of the ongoing oscillation. The phase resetting curves of individual neural oscillators have often been used to study the oscillators' synchronization tendencies in reciprocally connected networks. In general,

C.C. Canavier (✉)
Neuroscience Center of Excellence, Louisiana State University Health Sciences Center, New Orleans, LA, USA
e-mail: ccanav@lsuhsc.edu

A. Destexhe, T. Bal (eds.), *Dynamic-Clamp*, Springer Series in Computational Neuroscience 1, DOI 10.1007/978-0-387-89279-5_12,

the phase resetting curve (PRC) is generated for an isolated neuron (called the open-loop configuration), then applied to the analysis of the circuit which contains feedback from other neurons (the closed-loop configuration). There are two general approaches, one that assumes weak coupling such that inputs add linearly, and one that simply assumes that the effects of an input dissipate by the time the next one is received. In the weak coupling approach (Ermentrout 2002), the response of the neuron at each phase in its cycle to a stimulus that is infinitessimal in amplitude and duration is characterized in order to generate the infinitesimal PRC (iPRC). The response to any arbitrary stimulus is then calculated by decomposing the stimulus into a train of brief stimuli, scaling the iPRC by the amplitude of each of the brief stimuli, and then summing all the responses to produce the total resetting caused by the arbitrary stimulus. In other words, the arbitrary stimulus is convolved with the iPRC. This approach assumes that the trajectory never deviates significantly from the limit cycle, otherwise, the phase would be undefined and the phase resetting could not be calculated. In addition, the phase at which the later stimuli are received is not corrected for resetting by earlier inputs, so the resetting is assumed to be small in order for this approach to work. Together, these two constraints constitute the weak coupling assumptions.

In this study, we are interested in inputs that are more realistic in biological networks of bursting neurons, namely inputs that produce resetting that is a substantial fraction of the cycle period. We therefore use a second approach that is more general than weak coupling. This approach is to generate the PRC directly with the stimulus waveform that will be received by the neuron in the network (Canavier et al. 1997, 1999; Canavier 2005; Luo et al. 2004), usually the conductance waveform generated by an action potential (equivalent to the spike time response methods in Acker et al. 2003), or in our case a burst, in a neuron that in the closed-loop network configuration will be presynaptic to the neuron under study. The assumptions required in order to use this PRC for network analysis are that the stimulus waveform in the closed loop is not significantly altered from the open-loop stimulus used to generate the PRC, and that the effect of an input received in the closed loop has dissipated by the time the next input is received. We do not need to assume that the effect has dissipated by the time the next burst is generated. Any effect on the cycle containing the start of the perturbation is tabulated as the first-order resetting, and any effect on the next cycle is tabulated as second-order resetting.

We chose to generate the PRCs directly because the analysis of circuits comprised of rhythmically bursting neurons connected via reciprocal synapses is more complex than the analysis of circuits comprised of spiking neurons for several reasons. The main reason is that the active phase in one bursting neuron, and therefore the postsynaptic conductance in the neuron(s) to which it projects, lasts much longer than in neurons that produce single spikes. Therefore, the possibility that the active phase will overlap two cycles of the partner neuron, or that the trajectory will not have returned to the limit cycle by the time of the next burst, is significant. Calculating the first- and second-order

resetting separately ameliorates this difficulty. In addition, it is more likely that closing the loop will alter the active phase by prolonging or truncating the burst or changing the frequency. The latter difficulty has been addressed elsewhere (Oprisan and Canavier 2005), but did not cause severe complications in this study and was ignored here.

2 Methods

2.1 Hybrid Circuit Construction

Hybrid circuits comprised of one biological neuron and one model neuron (see Fig. 1b) were constructed using the dynamic clamp (Sharp et al. 1993). The open-loop PRC of the model neurons was found to be sufficient to completely predict the phase locking observed in closed-loop circuits comprised of these neurons. The dynamic-clamp technology allows us to incorporate a real neuron into the circuit and therefore to test the hypothesis that the phase resetting curve of a biological neuron can completely characterize the phase locking exhibited by this neuron in a network. The strength of the methodology is that all components of the network are completely under the control of the investigator except for the dynamics of a single biological neuron; therefore, we can test the hypothesis rigorously by comparing the activity predicted from the PRCs to that actually observed.

The biological neural oscillator was actually an oscillatory complex of three neurons that includes the pacemaker for the pyloric rhythm in the stomatogastric ganglion of the lobster or crab. The anterior burster (AB) neuron is thought to be the pacemaker, and it is electrically coupled to two pyloric dilator (PD) neurons. Together, these three neurons comprise the pacemaking kernel of the pyloric network (Fig. 1a). In general, recordings were made from the larger PD neurons. The only synaptic input to the AB/PD complex is from the lateral pyloric (LP) neuron, and LP is either killed or its synaptic input is blocked by application of picrotoxin. The model neuron was a bursting neuron intended to simulate the pacemaking kernel (Liu et al. 1998; Prinz et al. 2003). The synapses were of the form $I_{syn} = g_{syn}\ (V - E_{syn})$, where E_{syn} was -70 mV for some networks and 0 mV for others to generate artificial inhibitory or excitatory synapses. The open-loop PRCs (Fig. 1c) were generated using either the synaptic conductance waveform generated by a burst in the other neuron or a square conductance pulse with the duration of the burst in the other neuron. In the network, the synaptic activation variable m was described by a first-order differential equation, in some cases with different time constants for the rate of rise and for the decay and in others with a single time constant. The steady-state activation of m, indicated by the subscript ss, had a steep sigmoidal dependence ($m_{ss} = 1/(1 + \exp((V_{half} - V)/k))$ on presynaptic voltage with a slope factor k of 1 mV and a V_{half} preset with the intention that the conductance

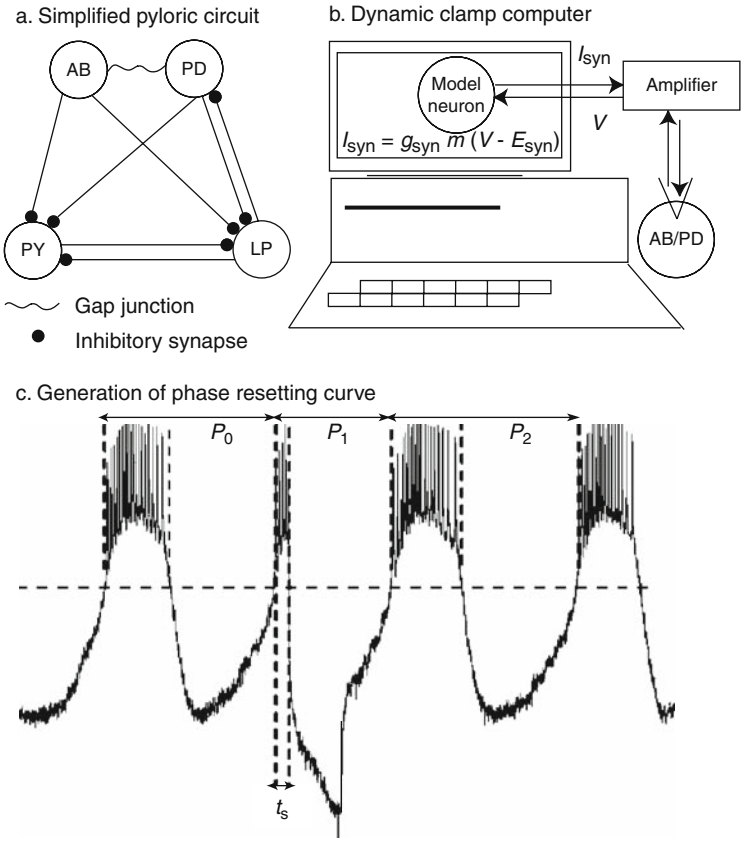

Fig. 1 Experimental setup. **a**. The pyloric circuit is comprised of one anterior burster (AB), two pyloric dilator (PD) neurons, eight pyloric (PY) neurons, and one lateral pyloric (LP) neuron. **b**. An isolated AB/PD complex was impaled with a sharp microelectrode, and the membrane potential (V) recorded through this electrode is used to determine how much current (I_{syn}) to inject for a given maximum artificial conductance (g_{syn}) whose fractional activation is given by m. **c**. Phase resetting in the AB/PD complex in response to an inhibitory pulse applied at an interval t_s after burst initiation. Upward and downward crossings (*vertical dashed line*) of the voltage threshold (*horizontal dashed line* at –45 mV) indicate burst initiation and termination, respectively. The unperturbed period is P_0, the length of the cycle containing the start of the perturbation is P_1, and the subsequent cycle length is P_2. Adapted from Oprisan, Prinz and Canavier (2004)

would only be on during a burst. The time constant for this variable was either held constant or had voltage dependence, with a maximum value of 10 ms. For analysis, the start of a burst is defined as the upward crossing of V_{half} (not counting any subsequent ones occurring between spikes during a burst) so that the start of the burst coincides with turning on the synaptic conductance in the other neuron. The conductance pulses were applied at various phases in order to tabulate the PRC. The stimulus time (t_s) is the time elapsed between the start

of the burst in the postsynaptic neuron and pulse onset (Fig. 1c). The phase (φ) was calculated as t_s/P_0, where P_0 was the average free-running period of the neuron. The first-order resetting $F_1(\varphi)$ is equal to the normalized change in the length of the cycle containing the pulse onset $(P_1 - P_0)/P_0$. Similarly, the second-order resetting $F_2(\varphi)$ is equal to the normalized change in the length of the cycle following the one containing the pulse onset $(P_2 - P_0)/P_0$. With these definitions, a positive phase resetting value corresponds to a delay of the burst following the stimulus, and a negative value corresponds to an advance of the following burst.

2.2 Theoretical Methods

In order to use the phase resetting curves generated in the open-loop condition as in Fig. 1c, the neuron must be back to its unperturbed oscillation, or limit cycle, by the time the next input is received. This is critical because otherwise the phase is not defined and the resetting calculated in the open loop cannot be applied to analysis of the closed-loop circuit. The resetting does not have to be complete by the time the next burst is initiated after an input is received, only by the time the next input is received.

Figure 2 shows the pulse coupled approximation upon which the theoretical method is based. The stimulus intervals (t_s) are defined as the elapsed time between the start of a burst (solid vertical bar aligned with the neuron firing) and the input onset (dashed vertical line aligned with burst start in the other neuron). Conduction delays are ignored. The recovery intervals (t_r) are defined as the time elapsed between the input onset and the start of the next burst in the neuron receiving the input. As an example, the effect of the first burst in the

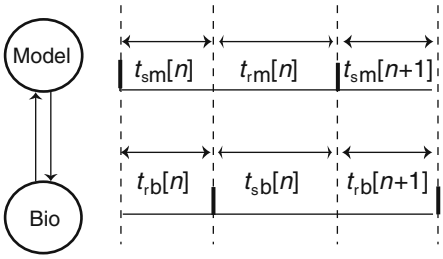

Fig. 2 Pulse-coupled approximation of bursting network. Burst start times for reciprocally coupled model (*top*) and biological (bio, *bottom*) neurons are shown as *thick vertical bars*. Since delays are ignored, each neuron is presumed to receive a synaptic input at the time its partner starts its burst (*vertical dashed lines*). The stimulus interval for the model neuron on cycle n ($t_{sm}[n]$) is by definition equal to the recovery interval in the biological neuron ($t_{rb}[n]$), and vice versa. Under the assumption that the resetting has only two components, one of which modifies the recovery interval following the input and the other of which modifies the subsequent stimulus interval, the resetting is complete by the time the next input is received and the phase resetting determines the interval lengths

biological neuron on the model neuron is felt by the model in the recovery interval $t_{rm}[n]$, which is equal to the fraction of the cycle remaining before the next burst would have occurred (calculated as one minus the phase at which the input is applied) plus the first-order phase resetting, all of which must be multiplied by the free-running intrinsic period for the model:

$$t_{rm} = P_{0,m}[1 - \varphi_m + F_1(\varphi_m)]$$

where the index for cycle number n has been dropped.

Since the next input is not received by the model until the stimulus interval $t_{sm}[n + 1]$ is complete, the central assumption is not violated if this interval is also altered by the previous input. Frequently, the subsequent burst in the model and biological neurons are shortened or lengthened by an input. This effect can be incorporated by defining the stimulus interval in the closed loop differently than in the open loop by adding the second-order resetting:

$$t_{sm} = P_{0,m}[\varphi_m + F_2(\varphi_m)]$$

The assumption is that the phase at the end of an altered burst is the same as the phase at the end of a free-running burst because the end of the burst corresponds to a specific point on the original limit cycle. Similar expressions ($t_{rb} = P_{0,b}\,[1 - \varphi_b + F_1(\varphi_b)]$), $t_{sb} = P_{0,b}\,[\varphi_b + F_2(\varphi_b)]$) apply to the biological neuron. The phase at which the input is received by each neuron uniquely determines the pairs of t_s and t_r intervals for that neuron, thus these quantities can be considered as functions of each other. Clearly in a steady one-to-one phase-locked mode, the recovery interval in one neuron is always equal to the stimulus interval in the other, hence, a simple graphical method can be used to find any periodic lockings that satisfy the conditions $t_{sm} = t_{rb}$ and $t_{sb} = t_{rm}$. Simply satisfying these criteria for periodicity is not sufficient to guarantee that a mode will be observed; it must also be robust to the inevitable perturbations caused by noise. We have previously established that the slopes of the PRCs at the phases φ_b and φ_m that correspond to lockings that satisfy $t_{sm} = t_{rb}$ and $t_{sb} = t_{rm}$ can determine the stability as follows. The roots of the characteristic equation

$$\lambda^2 - [(F'_{1,b}(\varphi_b) - 1)(F'_{1,m}(\varphi_m) - 1) - F'_{2,b}(\varphi_b) - F'_{2,m}(\varphi_m)]\lambda + F'_{2,b}(\varphi_b)F'_{2,m}(\varphi_m) = 0$$

where the prime symbols indicate the slope of the appropriate PRC must have an absolute value less than one in order for the discrete map derived from Fig. 2 to be stable (Oprisan and Canavier 2001; Oprisan, Prinz and Canavier 2004), implying stability for the corresponding locking in the hybrid circuit. In the case of synchrony, the characteristic equation must be evaluated twice, first assigning one neuron a phase of 0 and the other a phase of 1, using the left- or right-hand limit as appropriate, then switching the phases assigned to each neuron.

This accounts for perturbations from synchrony in which either neuron leads. However, exact synchrony was not encountered in the heterogeneous hybrid circuits constructed herein.

Note that the two intervals t_s and t_r for each neuron are equivalent to the two values of the time difference Δt between action potentials in stellate cell 1 and the previous and next spike in stellate cell 2 as described by White et al. "Using "Hard" Real-Time Dynamic Clamp to Study Cellular and Network Mechanisms of Synchronization in the Hippocampal Formation" in this volume.

3 Results

Typical phase resetting curves for both the biological (3A) and model (3B) neurons are shown in Fig. 3 for an inhibitory pulse. Predictions were made using all three curves (polynomial fit, upper and lower envelopes) to bracket the

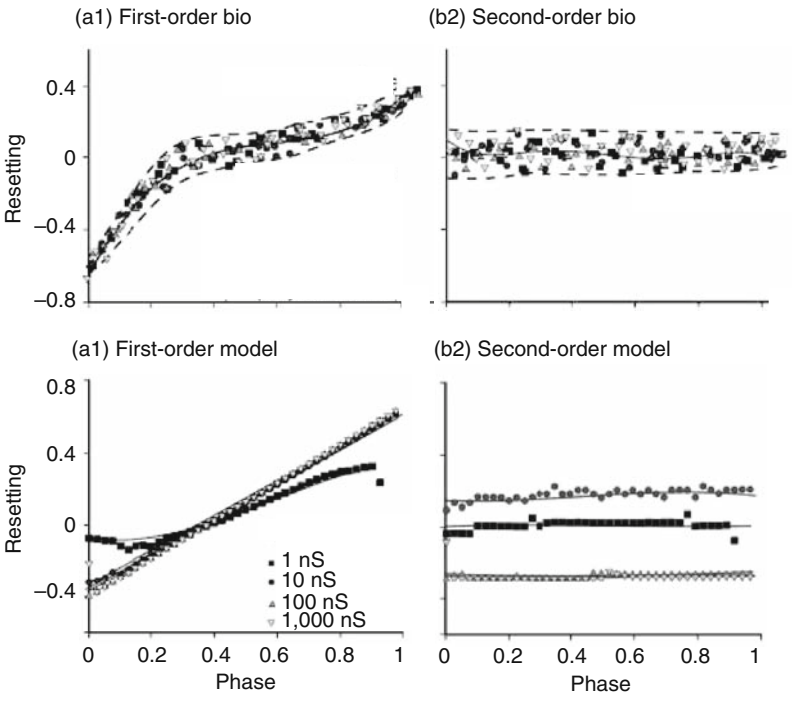

Fig. 3 Typical phase resetting curves. **a**. Biological neuron. The four different symbols (*square, circle, triangle, and inverted triangle*) indicate four separate trials on the same biological neuron. *The upper and lower dashed curves* represent the upper and lower envelope of the data, respectively, and the *solid curve* is the polynomial fit to the data. **a1**. First order. **a2**. Second order. **b**. Model neuron. Here the four different symbols show PRCs for four different stimulus conductance values. **b1**. First order. **b2**. Second order. Adapted from Oprisan, Prinz and Canavier (2004)

error in the prediction. The first-order PRC for the biological neuron (Fig. 3a1) was flattened in the middle such that inputs given at midcycle had the least effect (Oprisan et al. 2003). The second-order biological PRC (Fig. 3a2) was essentially flat, indicating a quick recovery to the limit cycle. The PRC for the model neuron is shown at several values of synaptic input conductance, but essentially saturated above 10 nS. At such stimulus conductances, the membrane potential was essentially clamped to the synaptic reversal potential such that there was a nearly constant time from perturbation offset until the next burst, resulting in a nearly linear first-order PRC (Fig. 3b1). The length of the subsequent burst was also altered in a consistent way, resulting in a nearly constant second-order PRC (Fig. 3b2).

Hybrid circuits were constructed using a variety of model and biological neurons. Depending on the model neuron chosen, hybrid circuits constructed using the same biological neuron could either lock in a one to one mode (Fig. 4a) with a firing pattern like the one assumed in Fig. 2, or not (Fig. 4b). Qualitatively, the presence or absence of one-to-one locking was correctly predicted by the theoretical method described above in 161 out of 164 inhibitory networks, with 140 of those exhibiting one-to-one locking. The failures all predicted one-to-one locking that was not observed at very weak values of the coupling from the biological neuron to the model neuron. Quantitatively, the predicted recovery and stimulus intervals fell within about 10% of the values actually observed in the hybrid networks, a level similar to the level of variability observed in the measurement of the PRC and of the intrinsic period in the biological neuron.

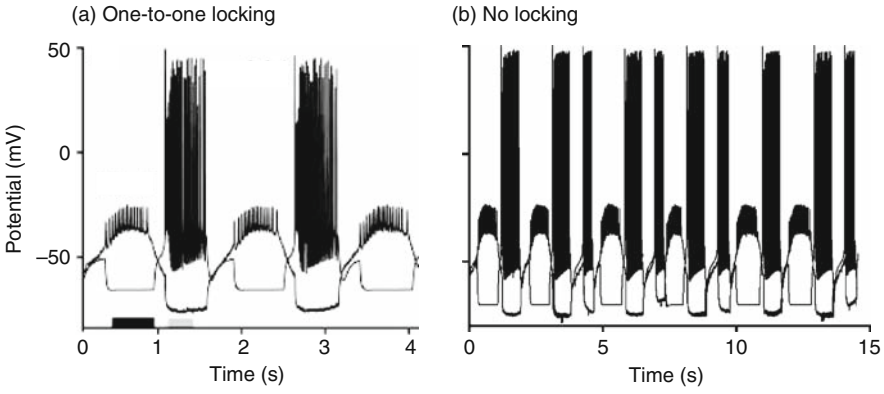

Fig. 4 Hybrid circuits constructed using mutual inhibition. The tall spikes indicate the model neuron and the small spikes were produced by the biological neuron. **a**. Here a stable one to one locking is seen. The *black horizontal bar* shows the unperturbed burst length in the biological neuron whereas the *gray bar* shows the unperturbed burst length in the model neuron. **b**. No stable locking pattern emerged in this circuit. Adapted from Oprisan, Prinz and Canavier (2004)

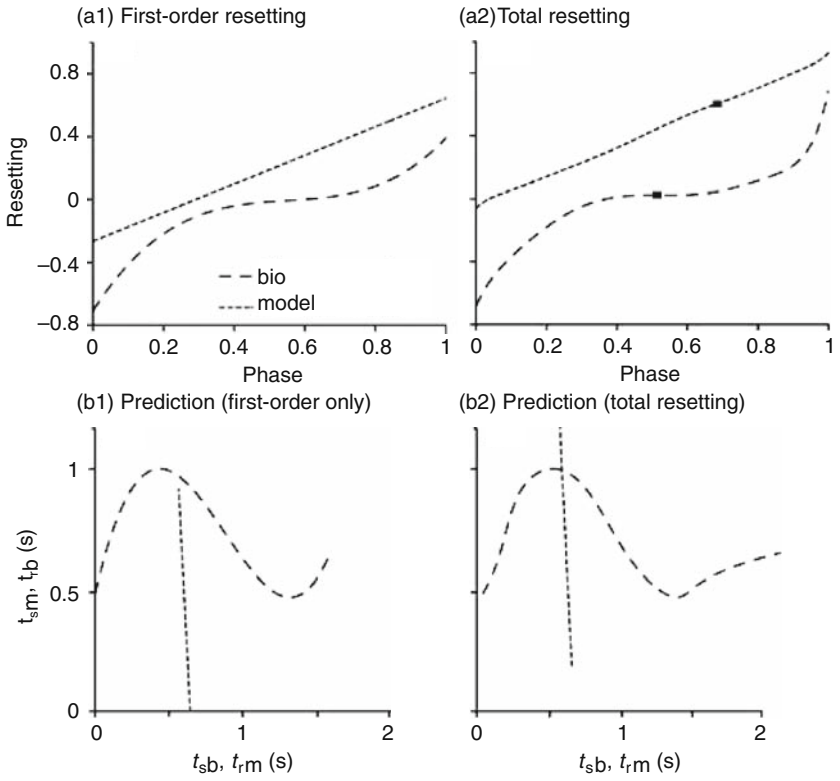

Fig. 5 Prediction of phase-locked modes. **a**. Phase resetting curves for biological and model neuron. **a1**. First order only. **a2**. The sum of first- and second-order resetting. **b**. Graphical prediction method. The recovery interval t_{rb} is plotted as a function of t_{sb} (*long dashes*) and t_{sm} is plotted as a function of t_{rm} (*short dashes*) such that the intersection gives the predicted mode. **b1**. In this example, ignoring second-order resetting gives an incorrect prediction of no one to one locking. **b2**. The same example, but now considering both first- and second-order resetting, correctly predicts the mode observed in Fig. 4a. The *squares* indicate the predicted phases (φ_b and φ_m) at which each neuron receives an input in the phase-locked mode. Adapted from Oprisan, Prinz and Canavier (2004)

An example prediction -corresponding to the phase-locked hybrid circuit in Fig. 4a is illustrated in Fig. 5. In this example, as in 21 of the 140 inhibitory lockings observed, the significant second-order resetting observed in the model neuron was required for a qualitatively correct prediction. In Fig. 5a1, the first-order phase resetting curves for the model neuron (short dashes) and the polynomial fit to the data for the biological neuron (long dashes) from Fig. 3a1 are shown. These phase resetting curves were used to construct t_{rb} as a function of t_{sb} and t_{sm} as a function of t_{rm}, as described in the theoretical methods, except that the second-order resetting term in the expression for the stimulus intervals was set to zero. The stimulus intervals for the model neuron

(short dashes) were too short to intersect the curve (Fig. 5b1) for the biological recovery intervals at the biological stimulus interval corresponding to the nearly constant model recovery interval. Fig. 5a2 shows that the total resetting (first plus second order) is nearly unchanged from the first-order resetting for the biological neuron, but the second-order resetting in the model neuron adds a nearly constant 200 ms at each phase. This lengthens the range of possible model stimulus intervals until an intersection does occur at which $t_{sm} = t_{rb}$ and $t_{sb} = t_{rm}$ (see Fig. 2), correctly predicting the one-to-one locking observed in Fig. 4a.

In addition to the inhibitory networks, 86 mutually excitatory networks (Sieling et al. 2008) were experimentally prepared using 5 biological neurons, 4 model neurons, and heterogeneous synapse strengths between 1 and 10,000 nS. We show that the method is robust to biological noise and accurate for 94% of the 72 excitatory networks we tested, after excluding the data from 14 experiments that fell into two special cases, one in which the coupling becomes effectively continuous and another in which complex behavior results from a discontinuous PRC. These two cases represent 16% of all networks tested. For the 26 networks where phase locking was both predicted and observed, phase relations were accurately predicted for all networks. Representative predictions from both inhibitory (Fig. 6a) and excitatory (Fig. 6b) hybrid circuits show that the PRC contains sufficient information to successfully predict the phasic relationships that component neurons will exhibit when coupled, despite the presence of noise in the biological neuron. In general, reciprocally inhibitory circuits locked in near antiphase (arrows pointing left) and excitatory networks locked near in phase synchrony (arrows pointing right).

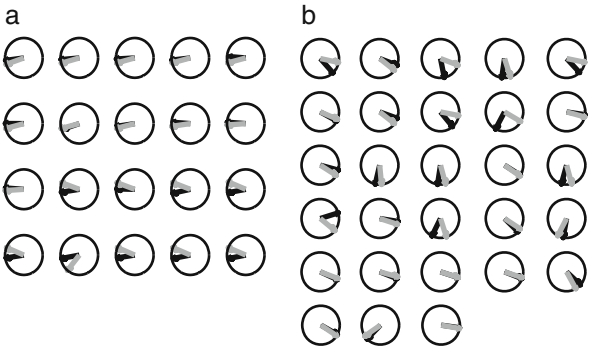

Fig. 6 Summary of predictions of phase-locking. Observed phase difference indicated by *black arrow*, predicted indicated by *gray*. An *arrow* that points to the *left* (nine o' clock position) indicates antiphase (phase of 180°) whereas an *arrow* pointing to the *right* (three o' clock position) indicates in phase synchrony with a phase difference of 0°. **a**. Representative predictions for hybrid circuits coupled via mutual inhibition. **b**. Representative predictions for hybrid circuits coupled via mutual excitation

4 Significance

The most important result presented herein is that the phase resetting curves of bursting neurons generated using the input that they will receive in a network are sufficient to predict whether phase locking will occur, as well as what the phase angle and network period of the locking will be. The prediction is based on an assumption of pulsatile coupling, which is not strictly true, but apparently the resetting is completed fast enough for the method to work, that is largely by the time the next input is received. The predictions are robust to the noise inevitably encountered in a biological system, at least for the examples we examined. We have also shown previously that the method can easily be extended to networks with short synaptic delays, and works equally well in that case (Oprisan, Prinz and Canavier 2004). Furthermore, the method is robust to some change in burst duration as a result of completing the circuit compared to the open-loop condition used to generate the PRCs. Additionally, the large number of special cases encountered in the excitatory network results lead us to believe that excitatory synaptic connections are ill-suited to mediate reliable 1:1 phase locking. This may help to explain why we see few excitatory synapses utilized in biological central pattern generators (CPGs), e.g. invertebrate CPGs such as those in the stomatogastric ganglion have no excitatory synapses.

The dynamic clamp is a valuable tool for constraining the unknown part of the circuit to a manageable level, in this case only the intrinsic dynamics and noise attributable to the biological neuron were not under the direct control of the experimentalist. In contrast, the equations and parameters characterizing the model neuron as well as the two reciprocal synapses were exactly known. The advantage of using PRC-based methods is that they can be applied to biological neurons without knowledge of the equations underlying the intrinsic dynamics because useful PRCs can be obtained experimentally despite the presence of biological noise, as we have seen in this study. Another source of noise is the dynamic clamp itself. The method is limited by transient instabilities that occur when conductances of large magnitude or fast rate of change are injected (Preyer and Butera 2007, see Brette et al. "Dynamic Clamp with High-Resistance Electrodes Using Active Electrode Compensation In Vitro and In Vivo" and Butera and Lin "Key Factors for Improving Dynamic Clamp Performance" in this volume), e.g. we cannot inject a typical fast sodium conductance due to its large magnitude and fast dynamics; however, nominal synaptic conductances such as those presented here are well within these limits.

Neurons that burst endogenously in the neuromodulatory context of their particular CPG have been shown to be critical components of many such circuits (Selverston et al. 1997) including respiration in neonatal rodents (Smith et al. 1991), the heartbeat of crustacea (Tasaki and Cooke 1990), the feeding and swimming CPGs of mollusks (Arshavsky et al. 1991), swimming in the lamprey (Wallen and Grillner 1987), and flight in locusts (Ramirez and

Pearson 1991). Therefore, this analysis of circuits of bursting neurons may be useful in deciphering the operation of CPGs generally.

Acknowledgments Some of the work presented here was supported by NIH NS54281 grant which was awarded under the CRCNS program. Sorinel Oprisan performed some of the analyses presented herein. We also acknowledge Eve Marder for her support.

References

Acker CD, Kopell N, White JA (2003) Synchronization of strongly coupled excitatory neurons: relating network behavior to biophysics. J Comput Neurosci 15:71–90

Arshavsky Y, Grillner S, Orlovsky G et al. (1991) Central pattern generators and the spatiotemporal pattern of movements. In: Fagard J and Wolff P (eds) The Development of Timing Control, Elsevier, Amsterdam, pp 93–115

Canavier CC, Butera RJ, Dror RO et al. (1997) Phase response characteristics of model neurons determine which patterns are expressed in a ring circuit model of gait generation. Biol Cybernetics 77:367–380

Canavier CC, Baxter DA, Clark JW et al. (1999) Control of multistability in ring circuits of oscillators. Biol Cybernetics 80:87–102

Canavier CC (2005) The application of phase resetting curves to the analysis of pattern generating circuits containing bursting neurons. In: Coombes S and Bressloff P (eds) Bursting: The Genesis of Rhythm in the Nervous System. Series in Mathematical Neuroscience, World Scientific, Singapore, pp 175–200

Ermentrout B (2002) Simulating, Analyzing, and Animating Dynamical Systems: A Guide to XPPAUT for Researchers and Students. SIAM, Philadelphia

Liu Z, Golowasch J, Marder E et al. (1998) A model neuron with activity-dependent conductances regulated by multiple calcium sensors. J Neurosci 18:2309–2320

Luo C, Canavier CC, Baxter DA et al. (2004) Multimodal behavior in a four neuron ring circuit: mode switching. IEEE Trans Biomed Eng 51:205–218

Oprisan SA, Canavier CC (2001) Stability analysis of rings of pulse-coupled oscillators: The effect of phase resetting in the second cycle after the pulse is important at synchrony and for long pulses. Differ Equations Dyn Syst 9:242–259.

Oprisan SA, Canavier CC (2005) Stability criterion for a two-neuron reciprocally coupled network based on the phase and burst resetting curves. Neurocomputing 65–66:733–739

Oprisan SA, Prinz AA, Canavier, CC (2004) Phase resetting and phase locking in hybrid circuits of one model and one biological neuron. Biophysical J 87:2283–2298

Oprisan SA, Thirumalai V, and Canavier CC (2003) Dynamics from a time series: Can we extract the phase resetting curve from a time series? Biophysical J 84:2919–2928

Preyer AJ, Butera RJ (2007) The effect of residual electrode resistance and sampling delay on transient instability in the dynamic clamp system. Conf Proc IEEE Eng Med Biol Soc 2007:430–433

Ramirez J, Pearson K (1991) Octopominergic modulation of interneurons in the flight system of the locust. J Neurophys 66:1522–1537

Prinz AA, Thirumalai V, Marder E (2003) The functional consequences of changes in the strength and duration of synaptic inputs to oscillatory neurons. J. Neurosci 23:943–954

Selverston A, Panchin YV, Arshavsky et al. (1997) Shared features of invertebrate pattern generators. In Stein SG, Grillner S, Selverston AI and Stuart DG (eds) Neurons, Networks, and Motor Behavior. MIT Press, Cambridge, pp 105–117.

Sharp AA, O'Neil MB, Abbott LF et al. (1993) Dynamic clamp – computer-generated conductances in real neurons. J Neurophysiol 69:992–995

Sieling FH, Canavier CC, Prinz AA (2008). Predicting phase-locking in excitatory hybrid circuits, BMC Neurosci 9: P133.
Smith J, Ellenberger H, Ballanyi K et al. (1991) PreBotzinger complex: A brainstem region that may generate respiratory rhythm in mammals. Science 254:726–729
Tasaki K, Cooke M (1990) Characterization of Ca current underlying burst formation in lobster cardiac ganglion motorneurons. J Neurophysiol 63:370–364
Wallen P and Grillner S (1987) N-methyl D-aspartate receptor-induced, inherent oscillatory activity in neurons active during fictive locomotion in the lamprey. J Neurosci 7:2745–2755

Using the Dynamic Clamp to Explore the Relationship Between Intrinsic Activity and Network Dynamics

Anne-Elise Tobin, Rachel Grashow, Lamont S. Tang, Stefan R. Pulver, and Eve Marder

Abstract Our goal is to understand how neural network dynamics depend on the properties of the component neurons and their synaptic connections. To that end, we propose a novel method using the dynamic clamp to evaluate the intrinsic properties of isolated neurons that replaces conventional methods such as measuring input impedance. Secondly, we construct novel circuits using the dynamic clamp by electrically coupling pairs of pacemakers of rhythmically active pyloric networks from stomatogastric ganglia. We determine whether we can synchronize pacemakers with different intrinsic frequencies and how the coupled network frequency depends on the frequencies of the isolated pacemaker kernels.

Our aim is to understand how the dynamics of neuronal circuits depend on the properties of circuit neurons and the synaptic connections among them. To measure the intrinsic properties of individual circuit neurons, it is often necessary to isolate them from their synaptic partners before measuring properties of their activity. It is then inferred how the isolated-cell activity, or properties such as response to current injection, would relate to the activity of the neurons in a network. In the first part of this chapter, we propose a novel method that uses the dynamic clamp (Sharp et al. 1993a, b) to evaluate the intrinsic properties of neurons in a way that may be more appropriate to understanding how they will act in a network than conventional measures. In the second part of this chapter we use the dynamic clamp to couple two biological networks to understand how the frequency of the new network depends on the starting frequencies of the individual networks and the coupling strength.

A.-E. Tobin (✉)
Volen Center and Biology Department, Brandeis University, Waltham, MA 02454-9110, USA
e-mail: atobin@brandeis.edu

A. Destexhe, T. Bal (eds.), *Dynamic-Clamp*, Springer Series in Computational Neuroscience 1, DOI 10.1007/978-0-387-89279-5_13,

1 Using the Dynamic Clamp as a Novel Assay of a Neuron's Functional Intrinsic Properties

It is often important to measure the intrinsic properties of neurons isolated from circuits. It is unclear, however, what are the most appropriate measures of intrinsic properties. Typically, researchers synaptically isolate cells and use single-cell measures such as input resistance and *FI* curves (spike frequency as a function of injected current) to evaluate the cellular activity. Such artificial measures, however, may not necessarily predict the biologically relevant activity of a neuron in its network.

We propose a novel method for evaluating intrinsic properties of a neuron that involves constructing networks using the dynamic clamp. By evaluating the activity of different individual neurons within a constant, user-defined network, it is possible to compare the activity of neurons under conditions that should predict their behavior better than artificial measures such as input resistance. We illustrate the proof of concept using model neurons, and demonstrate the application to living neurons using dynamic clamp.

We constructed model neurons and compared their isolated intrinsic properties and their activity in a network to see whether cells that had similar activity in the same network would also have similar intrinsic properties. We chose six tonically spiking models with spike frequencies between 0.5 and 5 Hz from a database of stomatogastric neurons (Prinz et al. 2003a). The isolated models were evaluated based on four conventional criteria: input resistance, spike threshold, intrinsic spike frequency, and spike frequency with 0.1 nA injected current (Fig. 1). Figure 1 shows how these neurons would be rank ordered by each of these conventional measures. Since the rank ordering of these six models is different in each of the conventional measures, it is unclear which measure would best describe the similarities or differences among individual neurons of the same class, or which would best describe the effect of a given treatment on the intrinsic properties of the neurons.

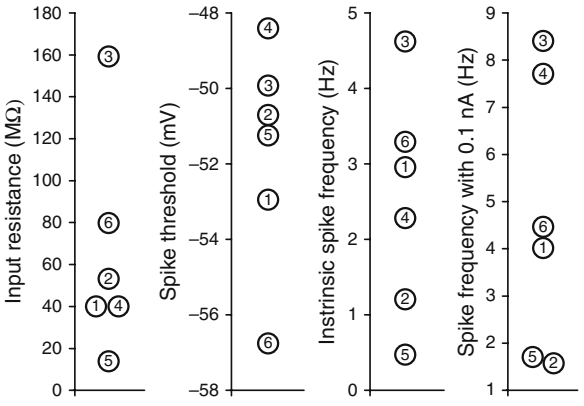

Fig. 1 Measurements of intrinsic properties of six model neurons. Models are identified by number

We created model networks by pairing each model with another tonically spiking model (Model #1) in a reciprocally inhibitory network. The network activity was mapped over a range (0–100 nS in 10 nS increments) of synaptic conductance, g_{syn}, and conductance of the hyperpolarization-activated cation current, g_h (Fig. 2). For all values of g_h and g_{syn} tested, the network of Models #1 to #1 showed no spiking, while the network of Models #1 to #2 exhibited alternating, half-center oscillations. The network of Models #1 to #3 was "asymmetric," where one model was silent for all values, while the other spiked tonically. The network with Models #1 to #4 was also asymmetric, although which model was silent varied across conductance values. The networks with Models #1 to #5 and Models #1 to #6 exhibited half-center oscillations for most values of the conductances, and asymmetric activity elsewhere. Based on their activity in these networks (Fig. 2), Models #3 and #4 were most similar to each other, and Models #5 and #6 were most similar to each other.

Do any of the isolated cell measures best predict the similarity of the models in the network? Models #3 and #4 were most similar to each other in spike threshold and spike frequency with injected current (Fig. 1), thereby suggesting that these measures might predict network activity. However, in no single isolated cell measure were Models #5 and #6 most similar to each other (Fig. 1). Thus, the network activity maps highlight similarities between models that are not evident from isolated cell measures.

We have done preliminary experiments to extend this method to biological neurons using the dynamic clamp to construct an artificial network from a defined model neuron and the biological neuron to be evaluated. In the rhythmic pyloric network that controls food filtering in the lobster (*Homarus americanus*) stomach, the pacemaker kernel is composed of three neurons, one anterior burster, and two pyloric dilator (PD) neurons. We constructed reciprocally inhibitory networks between a PD neuron and a tonically spiking model cell. The activity of the hybrid network was classified into one of six categories of observed activity (Fig. 3) and was mapped across varying values of synaptic strengths of the model-to-neuron synapse and the neuron-to-model synapse (0–300 nS). When networks were constructed between PD neurons from different animals and the same model neuron, the activity maps were somewhat different (Fig. 4). Although PD neurons in their native pyloric networks have very similar activity from animal to animal, this new method of evaluating intrinsic properties of neurons suggests that the PD neurons themselves may have different activity from each other when taken out of their native networks. Previous studies have demonstrated that PD neurons from different animals have different levels of the conductances that shape their activity, despite similar activity in their native networks (Schulz et al. 2006). It is possible that the pyloric networks compensate for the variability of their component neurons, for example by altering synaptic strength, to produce dependable network activity (Marder and Goaillard 2006).

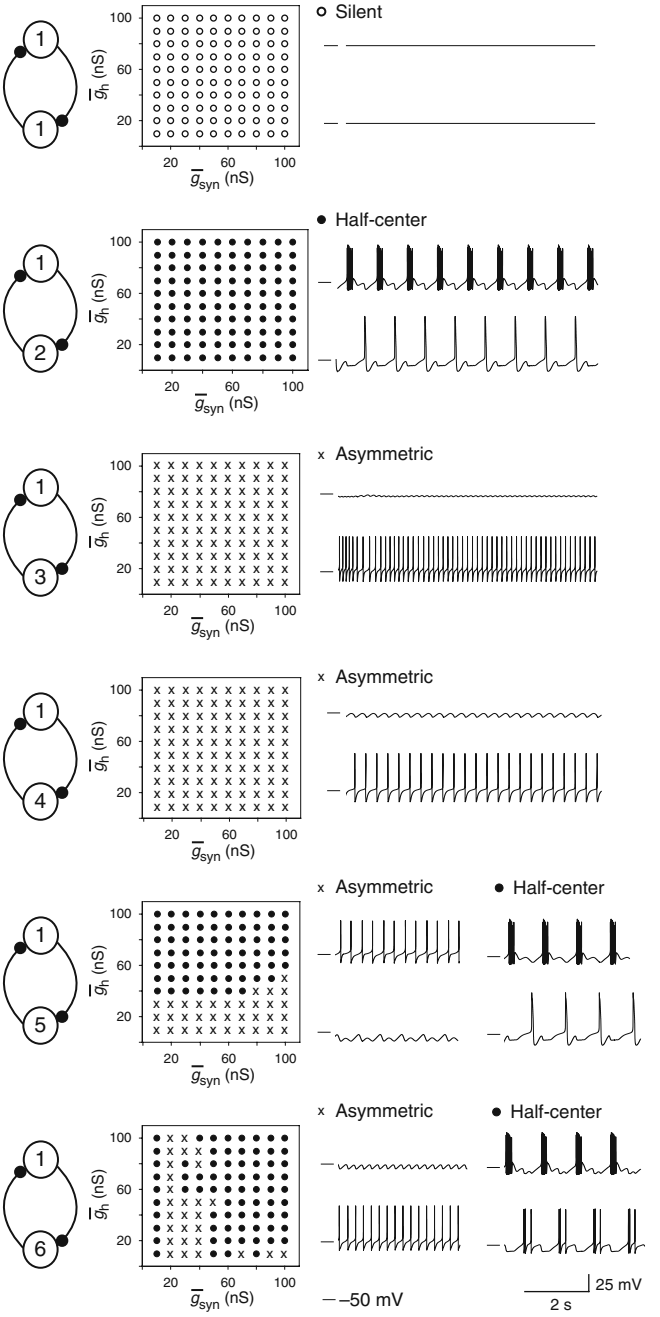

Fig. 2 Activity maps from reciprocally inhibitory networks of Model #1 and Models #1 to #5. H conductance, g_h, and synaptic conductance, g_{syn}, are varied from 0 to 100 nS. For all networks, activity is classified as "silent" (*open circles*) where neither model produces action potentials, "asymmetric" (*black x's*) where one model spikes, while the other is silent, and "half-center," (*filled circles*) where the models exhibit alternating activity

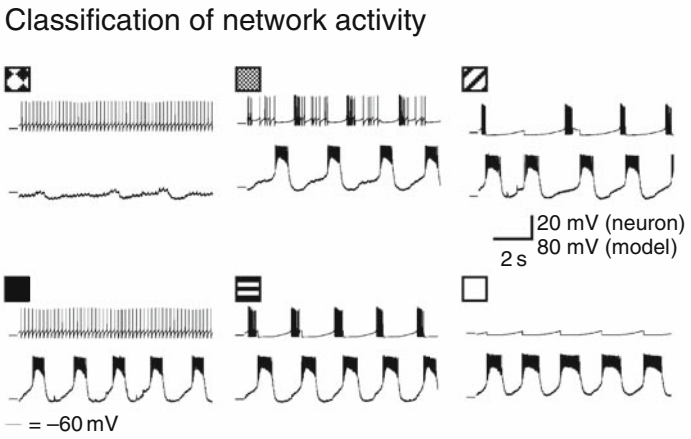

Fig. 3 The activity of a reciprocally inhibitory hybrid network (one living neuron, one model neuron) is classified according to the six activity patterns observed

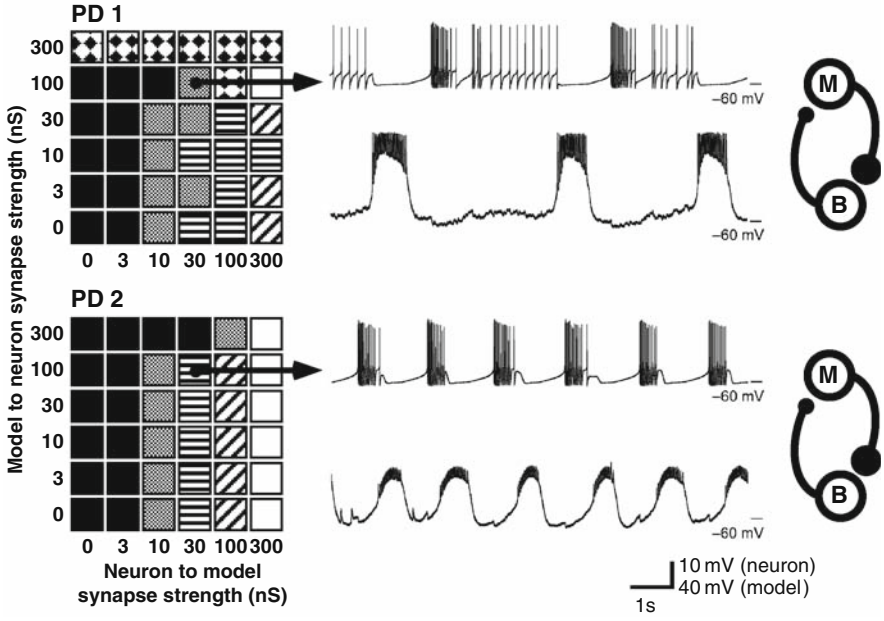

Fig. 4 Two PD neurons produce different activity maps when coupled in the hybrid network. Example activity is shown for 30 nS of synaptic conductance from the neuron to the model and 100 nS synaptic conductance from the model to the neuron

2 Using the Dynamic Clamp to Study the Coupling of Non-identical Neural Oscillators

In many systems, networks of oscillators and chains of segmentally coupled oscillators drive rhythmic motor activity (Bal and McCormick 1993; Buchanan 1996; Kristan et al. 2005; Murchison et al. 1993; Roberts et al. 1998). It has been a focus in these systems to determine how the dynamics of the coupled oscillatory network depend upon the intrinsic oscillatory properties of its component neurons (Del Negro et al. 2008; Masino and Calabrese 2002; Matsushima and Grillner 1992; Mulloney 1997; Pena 2008). Do the fastest oscillators drive the system, does the system oscillate at the mean of the intrinsic periods of the component neurons, or do other factors play into determining the final network period? To study how non-identical neural oscillators would entrain to produce an oscillatory network, we use the dynamic clamp to couple pacemaker neurons from two different preparations into a single rhythmic network.

Using dynamic clamp, we coupled the pacemaker kernels from two different pyloric networks from crab (*Cancer borealis*) stomatogastric ganglia (STGs), using an artificial electrical synapse, to study how the pacemaker kernels would entrain each other. We coupled the pacemakers in two ways. In some preparations, a single PD neuron from each pacemaker kernel was coupled via an artificial electrical synapse, whereby the current injected into each neuron was equal to the product of the gap junctional conductance and the voltage difference between the two neurons. In other preparations, the current calculated from this single artificial electrical synapse was injected into both PD neurons in each pacemaker kernel. Because the PD neurons within each pacemaker kernel have very similar activity, this latter technique approximates coupling each of the PD neurons from one preparation to each of the PD neurons from the other preparation. We increased the gap junctional conductance in 20 nS increments until the pacemakers were synchronized. The pacemakers were considered synchronized when the cycle periods of each pacemaker were not statistically different from each other (paired *t*-test, $p < 0.01$). The coupled network period presented is the average of the cycle periods of each pacemaker when synchronized.

To explore the effect of the period differences of the uncoupled pacemakers on the coupled network period, we manipulated the cycle period of each pacemaker by independently manipulating the bath temperature of each ganglion. With a single preparation (consisting of two STGs), we paired the pacemakers multiple times with different intrinsic cycle periods for each pacemaker. The data thus comprise 5 preparations and 11 pacemaker pairings.

The minimum gap junctional conductance required to synchronize the two pacemakers increased as the period difference of the uncoupled oscillators increased (Fig. 5). Comparing the coupled network period to the periods of the uncoupled oscillators revealed that neither the fast nor the slow pacemaker drove the coupled network; the coupled network period was a compromise between the individual cycle periods of the uncoupled pacemakers (Fig. 6). In eight of ten

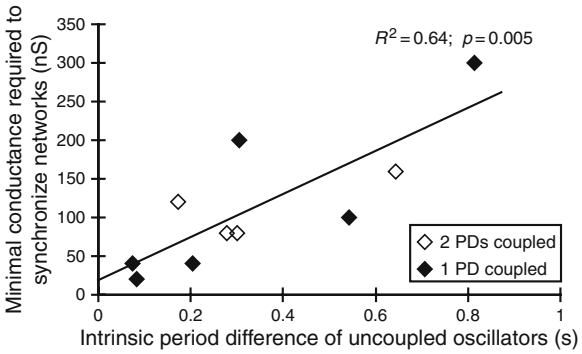

Fig. 5 As the intrinsic period difference between the uncoupled oscillators increases, more gap junctional conductance is required to couple the oscillators. The gap junctional conductance plotted reflects the total conductance injected into each pacemaker kernel; i.e. for the same gap junction strength, when both PD neurons in each pacemaker kernel were injected with current, the gap junctional conductance is double that when a single PD neuron from each pacemaker kernel is injected with current

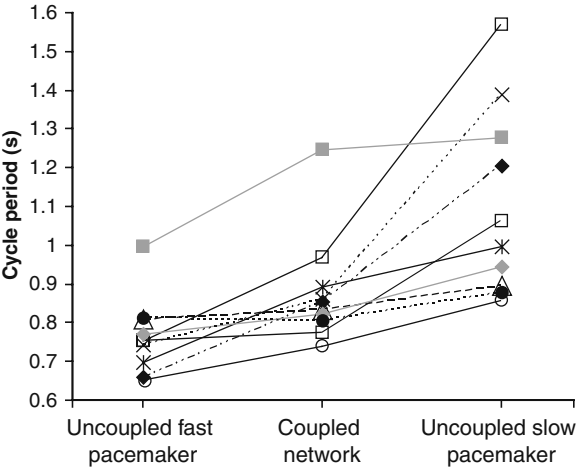

Fig. 6 The period of the coupled network reflects a compromise between the periods of the uncoupled fast pacemaker and the uncoupled slow pacemaker

pacemaker pairings, the coupled network period was faster than the arithmetic mean of the fast and slow intrinsic pacemaker periods; averaging over all preparations, the coupled network period was 7.0% faster than the arithmetic mean.

There is no standard rule for how the intrinsic cycle periods of uncoupled neural oscillators will determine the period of the coupled network. In a system of simple phase-coupled oscillators with symmetric coupling, K:

$$\theta_1' = \omega_1 + K \sin(\theta_2 - \theta_1),$$
$$\theta_2' = \theta_2 + K \sin(\theta_1 - \theta_2),$$

where θ_1 and θ_2 are the phases of the oscillators and ω_1 and ω_2 are the natural frequencies (Strogatz 1994). The steady-state compromise frequency, ω^*, is the arithmetic mean of the individual frequencies

$$\omega^* = \frac{\omega_1 + \omega_2}{2}.$$

In more complicated neural networks, one oscillator can predominantly determine the frequency of the coupled network. In the leech heartbeat network, two segmental oscillators are coupled by synaptic interactions with coupling interneurons. The cycle period of the intact timing network is established by the faster segmental oscillator (Masino and Calabrese 2002). Similarly, manipulating the excitability of different segments of the lamprey spinal cord suggested that the ensemble cycle period can be determined by the cycle period of the fastest segment (Matsushima and Grillner 1992). These examples, however, involve chemical as well as electrical coupling, in configurations that are not purely bidirectional.

In a system of biological oscillators with symmetric coupling, the final frequency is neither the arithmetic mean, nor purely driven by the faster oscillator, but somewhere in between. Early studies of the pacemaker cells in the sino-atrial node of the rabbit heart attempted to identify how the intrinsically rhythmic myocytes created a cohesive rhythm when coupled by electrical synapses (Jalife 1984). By reversibly uncoupling portions of the sino-atrial node into two populations of myocytes with different cycle periods, it was demonstrated that the period of the coupled network was not determined entirely by the faster or slower myocyte populations. Similar to our findings, the coupled sino-atrial node network cycled somewhat faster than the arithmetic mean of the periods of the uncoupled networks.

The dynamics of how each oscillator contributes to the compromise period of the coupled network may be understood by considering the phase response curves of the neurons. Prinz et al. (2003b) used dynamic clamp to inject conductance pulses in PD neurons at different phases in its cycle and measured the phase delay or phase advance of the subsequent cycle. The use of the dynamic clamp to inject conductance, rather than current pulses, ensures that the voltage remains within biologically meaningful values, and better approximates the effect of synaptic conductance on the activity of the neurons. These phase response curves (Fig. 7) illustrate how the cycle period of PD neurons responds to conductance inputs. To understand how the phase response curves could determine the coupled network period of the pacemaker kernels, consider the effects of each PD neuron on the other during the beginning and end of each burst. Just before the beginning of each burst (phase ~ 0.9), the fast neuron receives hyperpolarizing current from the more hyperpolarized slow neuron. According to the phase response curves, the phase of the fast neuron would be delayed, thus increasing its period (Fig. 7A). The slow neuron, however, receives depolarizing current from the more depolarized

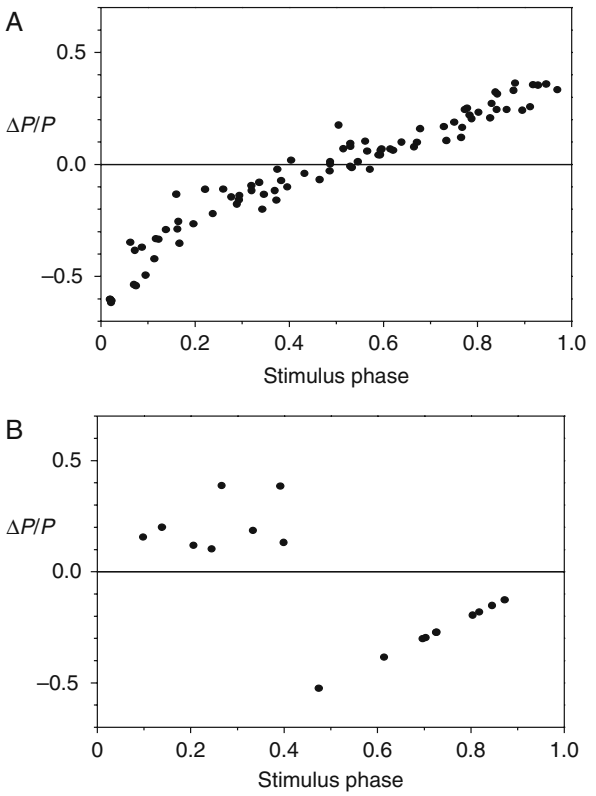

Fig. 7 Response of PD neurons to conductance pulses at different phases of the PD cycle. The change in period, ΔP, is normalized by the period, P. **A**. The phase response of PD neurons to inhibitory conductance pulses of 500 ms duration and 200 nS amplitude. The reversal potential of the conductance is –90 mV. **B**. The phase response of PD neurons to excitatory conductance pulses of 500 ms duration and 200 nS amplitude. The reversal potential of the conductance is 0 mV. (A and B modified from Prinz et al. 2003b, with permission.)

fast neuron, advancing its phase and decreasing period (Fig. 7B). These opposite effects on the fast and slow neurons would work to synchronize the neurons' activities toward a compromise period that is faster than the slow neuron's and slower than the fast neuron's period. At the end of its burst (phase $\sim$0.2 – 0.5, depending on duty cycle), the fast neuron receives depolarizing current from the slow neuron, which is still in the process of its plateau potential. Depending on the phase when this occurs, the result is either a moderate slowing or a dramatic speeding of the period (Fig. 7B). At the end of its burst, the slow neuron receives inhibitory input from the already hyperpolarized fast neuron. Depending on the phase when this occurs, this input would either have little effect, or would slightly speed the period (Fig. 7A).

Because the duty cycle of each neuron determines where in the phase response curve the bursts end, it is not straightforward to determine what effect the neurons would have on each other at the end of each burst. This may explain why we see a compromise period that can be both faster and slower than the arithmetic mean. However, the phase response curves are weighted more heavily in the direction of phase advance, or speeding of cycle period. This may explain why overall the compromise period is faster than the average of the natural periods.

3 General Conclusions

Using the dynamic-clamp technique, we created novel networks to compare the activity of neurons outside of and within networks. We created hybrid networks between a neuron and a model to demonstrate that the activity of different neurons in a constant network can be used as a tool to highlight similarities and differences between neurons that might not be evident from single-cell measures or from comparing neurons in their native networks. We also created novel networks between pacemaker neurons from two different animals to study how oscillators with different cycle periods couple together to form a cohesive rhythmic network. We demonstrated that a larger gap junctional conductance is needed to couple networks with greater disparity in their intrinsic cycle periods. We also showed that, when coupled with a bidirectional gap junction, the coupled network cycle period is not solely driven by the faster or slower oscillator, but is a compromise between the two intrinsic periods. An investigation of the phase response curves demonstrated that the compromise period may depend not only on the intrinsic cycle periods of the uncoupled oscillators, but also their duty cycles. Overall, the dynamic clamp has enabled us to study the properties of neurons in isolation and in carefully controlled networks to elucidate how intrinsic and synaptic properties and activity of neurons relate to network dynamics.

Acknowledgments This work was supported by NIH NS059255 (AET), NIH NS581102 (RGG), and NIH 46742 (EM).

References

Bal T and McCormick DA. Mechanisms of oscillatory activity in guinea-pig nucleus reticularis thalami in vitro: a mammalian pacemaker. *J Physiol* 468: 669–691, 1993.

Buchanan JT. Lamprey spinal interneurons and their roles in swimming activity. *Brain Behav Evol* 48: 287–296, 1996.

Del Negro CA, Pace RW, and Hayes JA. What role do pacemakers play in the generation of respiratory rhythm? *Adv Exp Med Biol* 605: 88–93, 2008.

Jalife J. Mutual entrainment and electrical coupling as mechanisms for synchronous firing of rabbit sino-atrial pace-maker cells. *J Physiol* 356: 221–243, 1984.

Kristan JWB, Calabrese RL, and Friesen WO. Neuronal control of leech behavior. *Prog Neurobiol* 76: 279, 2005.

Marder E and Goaillard JM. Variability, compensation and homeostasis in neuron and network function. *Nat Rev Neurosci* 7: 563–574, 2006.

Masino MA and Calabrese RL. Period differences between segmental oscillators produce intersegmental phase differences in the leech heartbeat timing network. *J Neurophysiol* 87: 1603–1615, 2002.

Matsushima T and Grillner S. Neural mechanisms of intersegmental coordination in lamprey: local excitability changes modify the phase coupling along the spinal cord. *J Neurophysiol* 67: 373–388, 1992.

Mulloney B. A test of the excitability-gradient hypothesis in the Swimmeret system of crayfish. *J Neurosci* 17: 1860–1868, 1997.

Murchison D, Chrachri A, and Mulloney B. A separate local pattern-generating circuit controls the movements of each swimmeret in crayfish. *J Neurophysiol* 70: 2620–2631, 1993.

Pena F. Contribution of pacemaker neurons to respiratory rhythms generation in vitro. *Adv Exp Med Biol* 605: 114–118, 2008.

Prinz AA, Billimoria CP, and Marder E. Alternative to hand-tuning conductance-based models: construction and analysis of databases of model neurons. *J Neurophysiol* 90: 3998–4015, 2003a.

Prinz AA, Thirumalai V, and Marder E. The functional consequences of changes in the strength and duration of synaptic inputs to oscillatory neurons. *J Neurosci* 23: 943–954, 2003b.

Roberts A, Soffe SR, Wolf ES, Yoshida M, and Zhao FY. Central circuits controlling locomotion in young frog tadpoles. *Ann N Y Acad Sci* 860: 19–34, 1998.

Schulz DJ, Goaillard JM, and Marder E. Variable channel expression in identified single and electrically coupled neurons in different animals. *Nat Neurosci* 9: 356–362, 2006.

Sharp AA, O'Neil MB, Abbott LF, and Marder E. The dynamic clamp: artificial conductances in biological neurons. *Trends Neurosci* 16: 389, 1993a.

Sharp AA, O'Neil MB, Abbott LF, and Marder E. Dynamic clamp: computer-generated conductances in real neurons. *J Neurophysiol* 69: 992–995, 1993b.

Strogatz SH. *Nonlinear Dynamics and Chaos*: Addison-Wesley Publishing Company, 1994.

Re-Creating In Vivo-Like Activity and Investigating the Signal Transfer Capabilities of Neurons: Dynamic-Clamp Applications Using Real-Time Neuron

Gerard Sadoc, Gwendal Le Masson, Bruno Foutry, Yann Le Franc, Zuzanna Piwkowska, Alain Destexhe, and Thierry Bal

Abstract Understanding the input–output transfer properties of NEURONs is a complex problem which requires detailed knowledge of the intrinsic properties of neurons, and how these intrinsic properties influence signal integration. More recently, it became clear that the transfer function of neurons also highly depends on the activity of the surrounding network, and in particular on the presence of synaptic background activity. We review here different in vitro techniques to investigate such problems in cortex, thalamus, and spinal cord, along three examples: First, by constructing "hybrid" networks with real and artificial thalamic neurons using dynamic clamp, it was possible to study how the state of the circuit influences spike transfer through the thalamus. Second, the dynamic clamp was used to study how the state of discharge of spinal neurons influences their information processing capabilities. Third, the dynamic-clamp experiments could re-create "in vivo-like" background synaptic activity by injection of stochastic excitatory and inhibitory conductances, and we showed that this activity profoundly modifies the input–output transfer function of thalamic and cortical neurons. We also illustrate how such applications are greatly facilitated by the use of a neuronal simulator to run the dynamic-clamp experiments, as shown here for RT-NEURON.

1 Introduction

Central neurons have complex intrinsic properties which are responsible for a variety of electrical behaviors such as oscillations or bursting activity (Llinas 1988). These properties are due to the presence of specific voltage- and calcium-dependent conductances in neuronal membranes. The presence of these conductances also determines the responsiveness of the neurons, which will be very

G. Sadoc (✉)
Unité de Neurosciences Intégratives et Computationnelles (UNIC), CNRS, Gif sur Yvette, France
e-mail: sadoc@unic.cnrs-gif.fr

A. Destexhe, T. Bal (eds.), *Dynamic-Clamp*, Springer Series in Computational Neuroscience 1, DOI 10.1007/978-0-387-89279-5_14,

different according to the type of intrinsic properties expressed by a given neuron. In the particular case of the thalamus, it was shown that the typical rebound bursting properties of relay cells are conferred by a low-threshold calcium current (the T-type current), which is responsible for setting the thalamic neuron in either tonic or bursting mode according to its level of polarization (Jahnsen and Llinas 1984). Similarly, in the dorsal horn of the spinal cord, relay neurons (DHN) express a wide variety of intrinsic membrane properties (Morisset and Nagy 1998), responsible for output patterns ranging from single spiking to plateau and intrinsic bursting. Whether thalamic or DHN relay neurons are in burst or tonic mode has a dramatic effect on their input–output transfer properties (McCormick and Feeser 1990; Timofeev et al. 1996; Steriade et al. 1997; Debay et al. 2004; Derjan et al. 2003).

More recently, it was shown that neuronal responsiveness depends not only on the intrinsic properties of the neuron, but also on the state of the network to which the neuron belongs (reviewed in Destexhe and Contreras 2006). The presence of sustained and seemingly random synaptic inputs ("synaptic bombardment") may set neurons in high-conductance states, which, in turn, may have a profound influence on neuronal responsiveness (Destexhe et al. 2003). This modulation of neuronal responsiveness by a form of synaptic "noise" was long studied in theoretical neurosciences (Tuckwell 1988), and since the membrane potential of central neurons in vivo is characterized by fluctuations due to strong, sustained, and apparently random synaptic activity (Azouz and Gray 1999; Bringuier et al. 1997; Steriade, 2001), the presence of this synaptic noise must be taken into account to study neuronal responsiveness. Indeed, simulating this activity in model cortical neurons predicted a major impact on their input–output functions (Hô and Destexhe 2000), which was later tested in real neurons using the dynamic-clamp technique (Destexhe et al. 2001; Chance et al. 2002 and Chance and Abbott "Simulating In Vivo Background Activity in a Slice with the Dynamic Clamp" in this volume; Shu et al. 2003).

In a recent paper, the combined effect of intrinsic properties and synaptic noise was explicitly considered for the first time by injection of stochastic synaptic conductances in thalamic neurons (Wolfart et al. 2005). One of the discoveries of this investigation was that the duality of modes (tonic or bursting) is no longer present in the presence of synaptic background noise, but bursts and tonic activity (single spikes) are mixed, in response to additional excitatory inputs, at all membrane potentials. Moreover, it was shown that the T-type current could compensate for hyperpolarization and yield a responsiveness which is less dependent on the level of polarization. Since this property may require the T-type current, and is only seen in the presence of synaptic noise, we conclude that understanding the "input–output" transfer function of neurons requires knowledge of both intrinsic properties and the properties of background synaptic inputs.

In this chapter, we review some of these results. We show that the understanding of the transfer properties of neurons is a problem which can be studied in vitro using dynamic clamp, which enables a fine control of the type of input and of synaptic background noise received by the cell. We illustrate this

approach with three examples. First, by constructing "hybrid" networks with real and artificial thalamic neurons using dynamic clamp, it is possible to study how the state of the circuit influences spike transfer through the thalamus (Le Masson et al. 2002). Second, the dynamic clamp can be used to study how the state of intrinsic properties of spinal cord relay neurons influences their information processing capabilities (Derjan et al. 2003). Third, the dynamic-clamp experiments can re-create "in vivo-like" background synaptic activity by injection of stochastic excitatory and inhibitory conductances, and this activity profoundly modifies the input–output transfer function of neurons, as we illustrate on thalamic and cortical neurons.

Another particularity of the work we describe here is that the dynamic-clamp experiments were run using a neuronal simulator, in which the computational models of conductances are easily implemented using standard techniques. This simulator, NEURON (Hines and Carnevale 1997), was initially modified by Gwendal Le Masson and colleagues to be interfaced in real time with the electrophysiological setup (Le Franc et al. 2001). We describe this "RT NEURON" tool in detail in an appendix.

2 Experimental Applications of Dynamic Clamp: Hybrid Networks and Synaptic Noise

2.1 Thalamic Hybrid Networks

2.1.1 The Gating of Input Signals During Sleep-Like Oscillations

More than a decade ago, we and others have shown that intracellular and extracellular multiple unit recordings from slices of the dorsal lateral geniculate nucleus (LGNd) of ferrets revealed the spontaneous occurrence of sleep-like oscillations, the so-called spindle waves. We then demonstrated that spindle waves were endogenously generated in the network by synchronized rebound burst firing in thalamic relay cells. This rebound burst firing resulted from inhibitory postsynaptic potentials arriving from the perigeniculate nucleus (PGN or RE for reticular nucleus), the cells of which were activated by burst firing in relay neurons (von Krosigk et al. 1993; Steriade et al. 1993, Bal et al. 1995; Debay et al. 2004). Spindle waves occur in humans and animals at the onset of sleep, when sensory perception drops. These synchronized sleep oscillations may participate in gating incoming inputs through several mechanisms: the presence of rhythmic synaptic inhibition could block the detection of the sensory excitatory postsynaptic potentials (EPSPs) and the slow kinetics of recovery of the T current act as a low-pass filter (Debay et al. 2004; Steriade et al. 1997; Timofeev et al. 1996; McCormick and Feeser 1990). A particularity of the synapses that form the intra-thalamic loop is the relative efficiency with which a single PGN cell is able to trigger a spiking response in the postsynaptic relay cell (Kim et al. 1997, McCormick and Bal 1997; Le Masson et al. 2002).

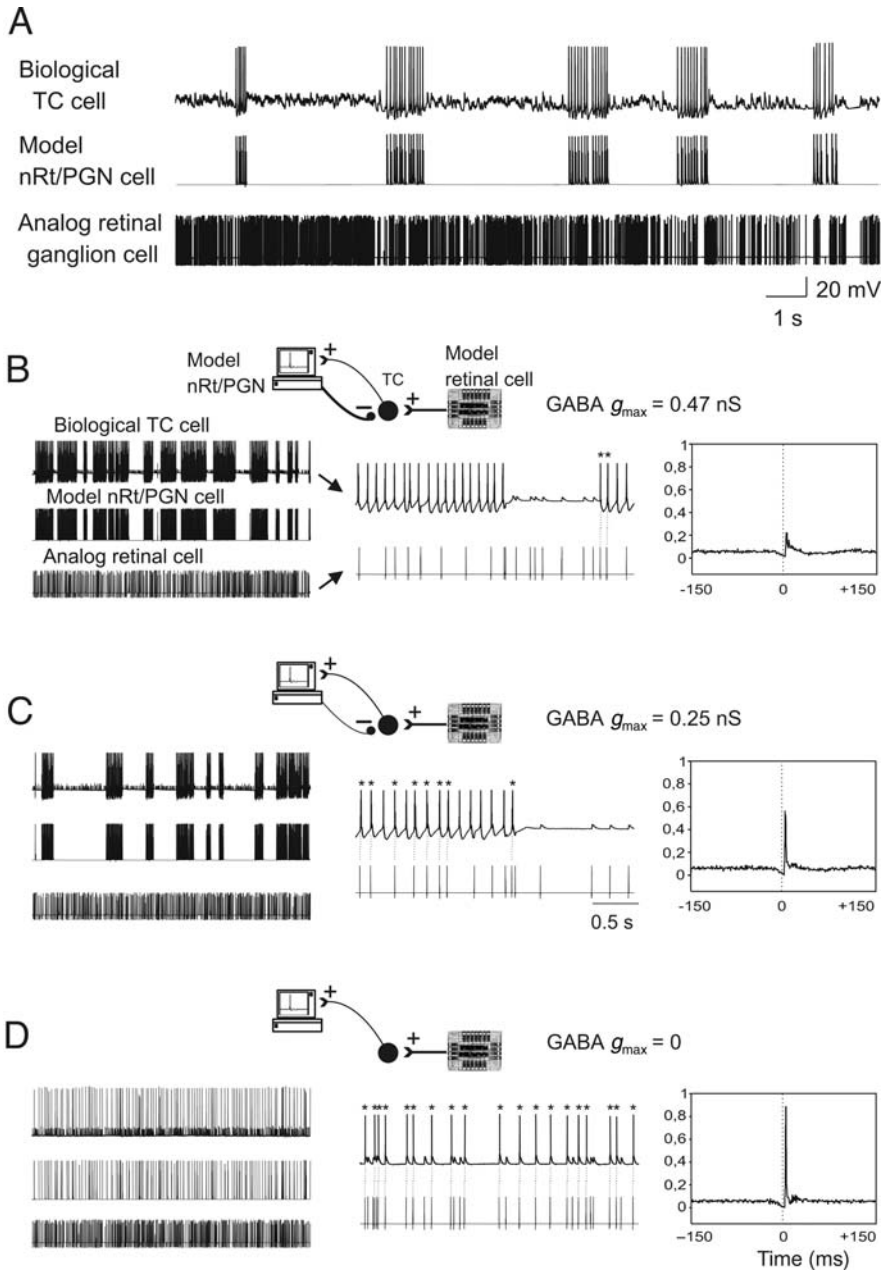

Fig. 1 The strength of inhibition regulates temporal correlation between input retinal and output TC cell spikes. **A**. Patterned firing (mean rate 42 Hz; $\gamma = 1.5$) of the analog retinal neuron generates an artificial synaptic bombardment in the biological TC cell (top trace), resulting in generation of recurrent spindles waves by the hybrid thalamic circuit. The duration of spindles and interspindle periods are emergent properties resulting from the

A post-hyperpolarization rebound burst of action potentials (AP) evoked in a single thalamocortical neuron (TC) following the somatic injection of a brief hyperpolarizing current pulse can trigger the firing of a target PGN neuron which in turn generates fast feedback inhibition in the recorded TC neuron (Fig. 1b in Le Masson et al. 2002). In the intact network during spindle waves, synaptic interaction between PGN and TC neurons leads to repetitive bursts in the TC cell. Modeling studies have clarified the interplay of synaptic and intrinsic conductances in generating spindles and other types of oscillations at the cellular and network levels (reviewed in Destexhe and Sejnowski 2003).

In order to explore the gating properties of the thalamic circuit, we have reproduced these basic properties in hybrid circuits consisting of a biological TC neuron recorded in vitro reciprocally connected with a conductance-based modeled GABAergic RE/PGN neuron (these results were obtained using an earlier version of our dynamic-clamp system, which was not based on RT-NEURON; Le Masson et al. 2002). Dynamic clamp was used to insert synaptic conductances in the TC cell, allowing full control of the conductances modulating synaptic strength. Indeed, the properties of the synaptic connections could be selectively and quantitatively controlled throughout their dynamic range, in a systematic manner which is impossible during spontaneous or stimulus-evoked dynamics passively observed using classical recording methods. Progressive increase of the maximal conductance (G_{max}) of the RE-to-TC GABAergic synapse, mediated via both $GABA_A$ and $GABA_B$ receptor subtypes, led to an increasing probability of rebound burst generation in the TC neuron. Sustained oscillations, resembling spindle waves, were obtained for a critical threshold value of total GABA G_{max} of approximately 30 nS.

The reconstruction of the retinothalamic hybrid circuit was then completed with the addition of a modeled retinal synapse connected to the biological TC neuron. We evaluated the accuracy with which such artificial synaptic current could reproduce voltage-dependent responses to retinal synaptic inputs. We compared the response of the biological cell to retinal EPSPs, either resulting from optic tract stimulations or using dynamic clamp, across a wide range of membrane potentials (Le Masson et al. 2002; Debay et al. 2004). As expected, as inputs from retinal ganglion cells are located near the soma, on the proximal

Fig. 1 (continued) interaction of intrinsic membrane properties in real and artificial cells with synaptic influences. **B**. Control temporal correlation (*right panels*; normalized cross-correlograms) between input retinal spikes and output TC spikes in the presence of a strong RE/PGN to TC inhibitory synaptic conductance. Middle traces show expanded detail from left panels. Stars and vertical dotted lines in middle panels indicate TC spikes triggered within a delay <10 ms following a retinal spike. **C**, **D**. Decreasing the strength of the inhibition increases the input/output temporal correlation. Modified from Le Masson et al. (2002). Data obtained in guinea pig LGNd slices

dendrites of thalamocortical cells, artificial somatic injection using dynamic clamp was found to be a realistic procedure for mimicking such retinal inputs.

In order to further explore the gating properties of rhythmic inhibition associated with synchronized spindle oscillations, we used a structured input activity that would better mimic real retinal ganglion cell activity. We reproduced the temporal structure of the firing activity of an input retinal cell (Fig. 1) using either computer simulations or analog silicon integrated circuits (ASICs). The latter perform real-time processing independently of the model's complexity and could be programmed to generate Hodgkin–Huxley-type models (Le Masson et al. 1999). The analog implementation of model neurons on programmable micro-electronic VLSI (very large-scale integration) circuits will not be detailed here. We have used the statistics of cat retinal ganglion cell discharge to re-create the synaptic bombardment simulating the effect of a single retinal input to the circuit. In the cat in vivo, in darkness or under constant illumination of the retina, ganglion cells discharge irregularly, with a mean rate ranging from 5 to 50 Hz. The interspike interval distribution of the ganglion cell action potential train can be accurately described by a renewal process, where the degree of regularity is set by the gamma order. Renewal processes with gamma orders within the physiological range ($\gamma = 3$–8) were used to generate ISIs for our artificial retinal cells. Remarkably, hybrid thalamic circuits receiving this physiologically patterned simulated synaptic bombardment spontaneously generated short bursts of approximately 10 Hz oscillations, recurring periodically in a manner very similar to biological spindle waves occurring during sleep (Fig. 1A).

We hypothesized that transitions from the sleeping to the waking state necessitate the intervention of mechanisms able to tune up or down the sampling rate or the sensitivity of retinal event detection, increasing or decreasing in turn the amount of sensory information reaching the cortex. We therefore used the hybrid circuit to test whether the degree of inhibition produced by RE/PGN interneurons could directly tune the time windows of sensory transfer in TC cells. The strength of inhibition was systematically screened and at each step we calculated the temporal coincidence of input/output signals using cross-correlation analysis of retinal and TC spikes (Fig. 1B–D), which gave us the probability, for a retinal spike, to trigger a thalamic spike. In the presence of inhibitory feedback sufficiently strong to produce rhythmic oscillations, the input–output cross-correlation was low (Fig. 1B) indicating that the thalamus was not transferring spikes in a one-to-one manner. However, as the inhibitory synaptic strength was decreased, the spike-to-spike correlation gradually increased (Fig. 1C–D). Thus, intra-thalamic inhibition can shift in a graded way the mode of signal transmission, from slow integration where only marked changes in retinal firing (for instance, a burst or a period of silence in the input) produce thalamocortical outputs in the form of bursts (Sherman 2001a, b; Debay et al. 2004) to a fast integration mode where single retinal spikes are faithfully transmitted to the cortex.

2.2 *Re-creating in Vivo-Like Nociceptive Input and its Processing in Spinal Cord Dorsal Horn*

Nociceptive signals originating from peripheral receptors are conveyed through A∂ and C fibers, which project onto relay neurons located in the dorsal part of the spinal cord. One of the major types of relay cells is the deep DHN of layer V. Their axons project to the thalamus through the spinothalamic tract (STT). DHNs can express a wide variety of intrinsic membrane properties (Morisset and Nagy 1998), responsible for output patterns ranging from single spiking to plateau and intrinsic bursting. In acute slices, the nature of the intrinsic activity they express depends on the balance between their mGluR and $GABA_B$ receptor stimulation. In control experiments, where no extrinsic pharmacological agent is used, most of the recorded DHNs display regular spiking activity when stimulated. In the presence of an mGluR agonist, they tend to express plateau properties, while when mGluRs are stimulated together with $GABA_B$ receptors blockade, many DHNs express spontaneous bursting activity.

Using hybrid spinal networks in a similar way as presented above in the thalamus, we have explored the influence of the intrinsic state of firing of DHNs (tonic, plateau, or bursting firing) on the filtering capacity of these cells (Derjan et al. 2003). We used a model of an afferent fiber A∂, firing action potentials with a slow adaptation when stimulated by a square current input (Fig. 2A, B) to mimic a transient nociceptive stimulus. This model was simulated with RT-NEURON and connected to the biological cell via a synaptic excitatory glutamatergic conductance using dynamic clamp.

DHNs were recorded in acute slices of the rat spinal cord using patch-clamp electrodes. Each AP of the model fiber triggers an excitatory synaptic potential in the recorded DHN and can elicit an AP depending on temporal summation (Fig. 2B). Pharmacological modulation was applied to control the firing state of DHNs. For each state, the filtering process of the network was evaluated using both correlation and contribution coefficients. Results are illustrated in Fig. 2C and quantification of coefficients shown in Fig. 2D, E. When in tonic state, DHNs respond to an afferent discharge by sparse firing and the ratio between incoming APs and produced APs (correlation) is low (around 0.1). This demonstrates a rather high level of filtering, where most of the sensory information is not transmitted, but when it does the signal is highly informative because each produced AP is indeed strictly related to an afferent AP (high contribution coefficient). When excitability of the DHN is increased by application of either a glutamatergic agonist or a GABAergic antagonist, the DHN neuron tends to switch into the plateau state. In this state, the response to an afferent volley is different. The correlation coefficient is dramatically increased, resulting in much less filtering, i.e. incoming APs have a higher probability of being transmitted, but because of the generation of plateau potentials, extra APs are produced at all times during and after the afferent stimulation, lowering the correspondence between incoming APs and produced APs (low contribution

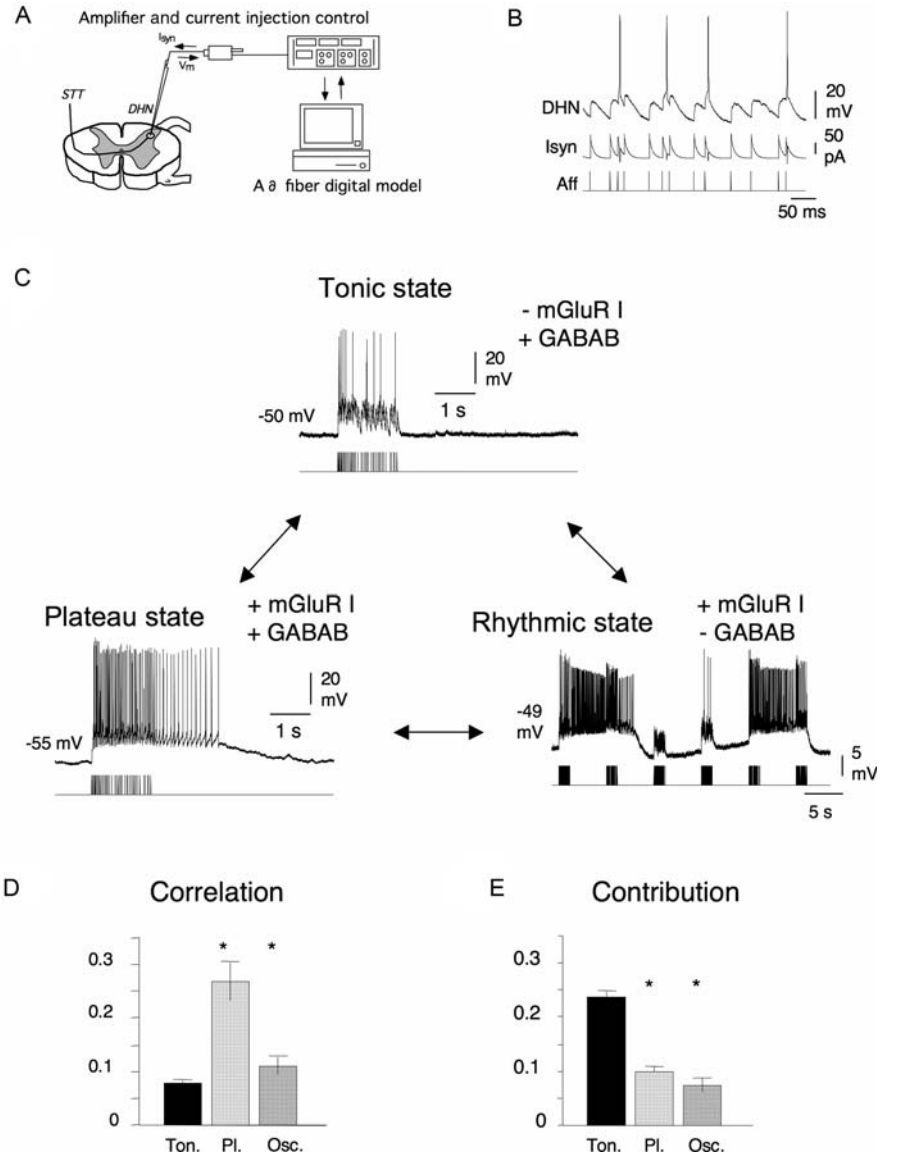

Fig. 2 Hybrid reconstruction of nocicepive transfer through the spinal cord dorsal horn. **A**. A model A∂ fiber is modeled and connected using patch recording of deep dorsal horn neuron (DHN) in acute dorsal horn slices. **B**. Each action potential (AP) in the afferent model (Aff) leads to a model AMPA synaptic current (I_{syn}) and an artificial excitatory synaptic potential in the DHN. Temporal summation can occur and trigger APs in the DHN. **C**. Depending on the modulation of both metabotropic glutamatergic (mGluR I) and gabaergic (GABAB) receptors using application of agonists (+) or antagonists (–), the recorded DHN can switch between different intrinsic properties, leading to different firing regimes (tonic, plateau or bursts). **D**. These different electrical responses to a transient volley from the afferent model

coefficient). Finally, when a glutamatergic agonist and a GABAergic antagonist are applied simultaneously, DHNs produce spontaneous bursts. This bursting state decreases AP transmission, leading to a low correlation coefficient together with a low contribution coefficient (Fig. 2E), effectively decoupling the relay neuron from the sensory input.

In summary, DHNs can switch their firing regime from regular spiking (tonic state) to plateau firing (plateau state) and spontaneous bursts production (bursts state) depending upon the balance between glutamatergic and GABAergic metabotropic modulation. Each regime corresponds to a different functional state of sensory transmission. These states can be related to different pain integration modalities, from acute nociception to long-lasting central sensitization.

2.3 Re-creating In Vivo-Like Activity in Cortical Neurons

Another application of the dynamic clamp is to re-create in vivo-like conditions in slices, by providing artificial synaptic inputs to the neuron, in order to simulate the conditions of "synaptic bombardment" as seen in vivo. We successively consider below the model used to inject in vivo-like inputs and applications of this model to cortical neurons. In the Section 2.4 we review its application to the study of thalamic neurons.

2.3.1 The "Point-Conductance" Model of Stochastic Synaptic Activity

Analysis of intracellular recordings of cortical neurons in vivo revealed that the synaptic bombardment can be faithfully reproduced by assuming a large number of randomly occurring weakly correlated excitatory and inhibitory synaptic inputs of small amplitude (Paré et al. 1998; Destexhe and Paré 1999). Instead of explicitly simulating a large number of such weakly correlated synaptic inputs, which may require important computation time, a simple model was proposed which was more adequate for dynamic-clamp experiments. This "fluctuating point-conductance" model (Destexhe et al. 2001) consists of two effective synaptic conductances varying stochastically in a manner similar to random walk processes:

$$dg_x dt = -1/\tau_x(g_x - g_{x0}) + \sqrt{(2\sigma_{x^2}/\tau_x)}\xi_x(t)$$

Fig. 2 (continued) correspond to different functional filtering properties. The tonic regime corresponds to a low correlation and low contribution state. The plateau regime corresponds to a high correlation but low contribution state, and rhythmic bursting to a low correlation with low contribution state

where g_x stands for either g_e (the excitatory conductance) or g_i (the inhibitory conductance), g_{x0} is the mean conductance, τ_x is the time constant of conductance variations, σ_{x^2} is the variance of the conductance, and $\xi_x(t)$ is a Gaussian white noise source (zero mean, unit variance). The total synaptic current is given by

$$I_{syn} = g_e(t)(V - E_e) + g_i(t)(V - E_i)$$

where E_e and E_i are the reversal potentials for excitation and inhibition, respectively.

The advantage of this model is that these parameters have a clear correspondence with biological parameters: the intensity of synaptic bombardment affects the average conductance, the correlation between inputs of the same type affects its variance and the time constant equals the decay time constant of the synaptic current (see details in Destexhe et al. 2001).

In this initial study, the parameters $\tau_e = 3$ ms and $\tau_i = 10$ ms were chosen to match the power spectrum of synaptic conductances seen at the soma and resulting from thousands of randomly releasing synapses distributed on the dendritic tree of a multicompartmental, morphologically realistic model cell. The mean and variance of conductances were adjusted to match the input resistance and membrane potential fluctuations observed in vivo. The values of the time constants can be fit to experimental data using analytic expressions for the power spectral density of the V_m (Rudolph et al. 2005), although such fits may be subject to large errors (Piwkowska et al. 2008; see also Piwkowska et al. "Testing Methods for Synaptic Conductance Analysis Using Controlled Conductance Injection with Dynamic Clamp" in this volume).

An important advantage of the point-conductance model is that the mean and the variance of the conductances can be controlled independently, which is equivalent to controlling the intensity and the correlation of the synaptic bombardment, respectively (Destexhe et al. 2001). As we will see below, these parameters modulate the gain and sensitivity of cortical neurons (see also Chance and Abbott "Simulating In Vivo Background Activity in a Slice with the Dynamic Clamp" in this volume; Prescott and De Koninck "Impact of Background Synaptic Activity on Neuronal Response Properties Revealed by Stepwise Replication of In Vivo-Like Conditions In Vitro" in this volume; Robinson "Synaptic Conductances and Spike Generation in Cortical Cells" in this volume).

2.3.2 Synaptic Noise Enhances the Responsiveness of Cortical Neurons

The fact that the synaptic "noise" can have drastic influence on the responsiveness of cortical neurons was first predicted by computational models (Hô and Destexhe 2000). In these models, the response of the simulated neuron to excitatory synaptic inputs (arrow in Fig. 3A) was

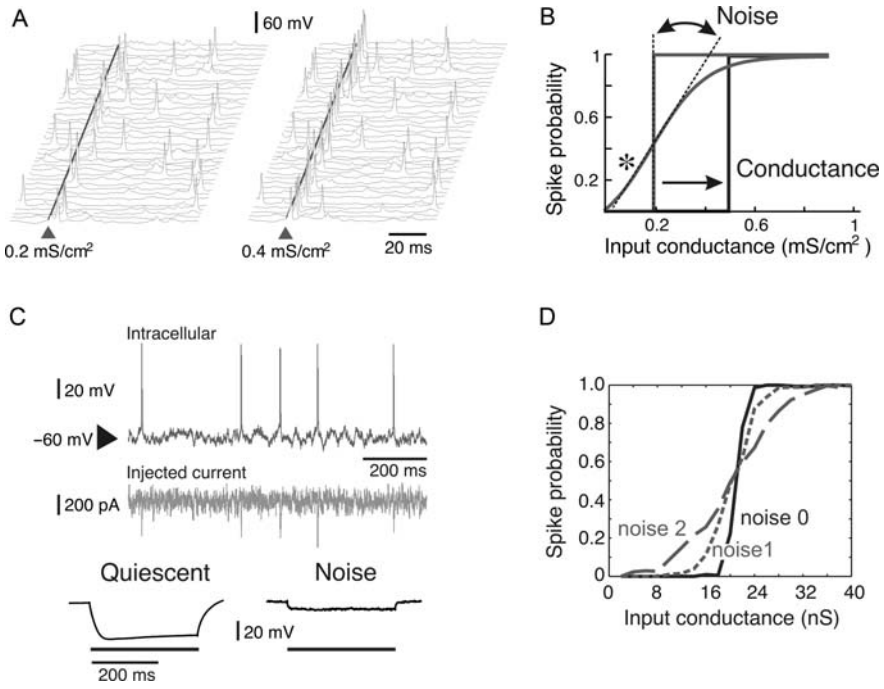

Fig. 3 Synaptic noise modulates the responsiveness of cortical neurons. **A**. Computational model to calculate the responsiveness in the presence of synaptic background activity. Repeated trials are performed in the presence of background activity and an additional single excitatory stimulus (arrow). **B**. Transfer function of the model neuron, calculated from the probability of evoked spikes represented as a function of input amplitude. The effect of the conductance is to shift the transfer function while the effect of the "noise" changes the slope ("gain") of the transfer function. **C**. Dynamic-clamp re-creation of in vivo-like activity in cortical neurons. High-conductance states similar to in vivo measurements are re-created by injection of stochastic synaptic conductances. **D**. Effect of noise on responsiveness. Controlling the amount of noise affects the slope of the transfer function in a living cortical neuron, as predicted by models (B). Modified from from Hô and Destexhe 2000 (A, B), Destexhe et al. 2001 (C), and Shu et al. 2003 (D)

investigated in the presence of background activity, and in particular the probability of inputs to generate a spike was computed. When represented as a function of input amplitude, this measure yields the response curves shown in Fig. 3B. By dissecting the conductance effect from the effect of fluctuations (which were monitored by correlation changes), it was found that the conductance shifts the response curve (Fig. 3B, "Conductance"), while the fluctuations affect the shape of the response curve (Fig. 3B, "Noise"). Thus two parameters, the intensity and correlation of the background activity, modulate the position and shape of the response curve. As we have seen above, these parameters can be controlled by the mean and variance of conductances in the point-conductance model.

Computational models also predicted a number of other computational consequences of synaptic noise (reviewed in Destexhe et al. 2003). In addition to its effect on responsiveness, background activity also affects dendritic integration by enabling distal inputs to be almost as efficient as proximal inputs, leading to a "democratization" of the dendritic tree. This "stochastic integrative mode" (Rudolph and Destexhe 2003) is only possible in the presence of large amounts of synaptic noise. Background activity also affects the temporal resolution of the cell due to the resulting high membrane conductance and the associated effect on the time constant. Finally, background activity modifies the integrative mode of the cell, enabling neurons to function as coincidence detectors or integrators at the same time (Rudolph and Destexhe 2003). Some of these consequences were predicted by early models (Bernander et al. 1991). It is interesting to confront these theoretical predictions on the impact of extrinsic conductances on the dendrosomatic propagation of signals with intrinsic mechanisms like the I_H, I_{NaP} conductances and dendritic spikes (Williams 2004; reviewed in Williams "Dendritic Dynamic Clamp – A Tool to Study Single Neuron Computation" in this volume).

The modulation of integrative properties by noise was investigated by dynamic-clamp experiments performed with different hardware systems, using the "point-conductance" model described above (Destexhe et al. 2001; Shu et al. 2003; Prescott and De Koninck 2003). In a first study, stochastic synaptic conductances were injected in rat prefrontal cortex cells in vitro (Fig. 3C) (Destexhe et al. 2001). For the first time, these experiments successfully re-created the most salient properties of neurons recorded intracellularly in vivo, such as a depolarized membrane potential, the presence of high-amplitude membrane potential fluctuations, a low-input resistance, and irregular spontaneous firing activity, suggesting that many of the characteristics of cortical neurons in vivo can be explained by fast glutamatergic and GABAergic conductances varying stochastically. In another study, the effect of conductance and the effect of "noise" were dissociated, demonstrating that the conductance shifts the response curve while the noise affects its slope (Fig. 3D) (Shu et al. 2003), in agreement with model predictions. Related effects of "gain modulation" were also demonstrated by other authors using similar methods (Chance et al. 2002; Prescott and De Koninck 2003; Chance and Abbott " Simulating In Vivo Background Activity in a Slice with the Dynamic Clamp" in this volume; Prescott and De Koninck "Impact of Background Synaptic Activity on Neuronal Response Properties Revealed by Stepwise Replication of In Vivo-Like Conditions In Vitro" in this volume).

In conclusion, the principal neurons of the cerebral cortex, pyramidal neurons, seem to be strongly affected by the synaptic background activity present in vivo. Not only their basic electrophysiological properties but also their input–output transfer function seems to depend on background activity. A number of computational advantages can be delineated in the presence of

synaptic noise, such as enhanced responsiveness and sensitivity, larger coding range, and sharper temporal resolution (reviewed in Destexhe et al. 2003).

2.3.3 Re-creating Up-states in Dynamic Clamp

Another application of the dynamic clamp was to re-create up-states in cortical slices. To this end, one must analyze the real up-states generated by cortical slices, in order to extract the conductance parameters, which are then re-injected in the neuron using dynamic clamp. This procedure, illustrated in Fig. 4A, consists of using the "VmD method" to extract the mean and variance of conductances from intracellular recordings (Rudolph et al. 2004; Piwkowska et al. "Testing Methods for Synaptic Conductance Analysis Using Controlled Conductance Injection with Dynamic Clamp" in this volume). The conductance parameters estimated from real network activity are then used to simulate artificial synaptic noise using the point-conductance model. This model of synaptic noise is then injected in the same neuron using dynamic clamp (this injection is done in quiescent states). The comparison of real and artificial up-states obtained by this procedure is shown in Fig. 4B. This procedure was used to test the VmD method and verify that the estimated conductance parameters were consistent with the activity recorded experimentally (see details in Rudolph et al. 2004). A similar testing was also realized (also using RT-NEURON) for a recent method to extract spike-triggered averages of conductances from V_m activity (Pospischil et al. 2007; reviewed in Piwkowska et al. 2008 and in Piwkowska et al. "Testing Methods for Synaptic Conductance Analysis Using Controlled Conductance Injection with Dynamic Clamp" in this volume).

Another way of comparing the real and the re-created up-states is to evaluate their transfer function. This was realized in dynamic clamp by comparing the response to injected excitatory conductances in natural up-states (spontaneously generated by the cortical slice), and up-states re-created using injection of stochastic synaptic conductances (with manually adjusted parameters in this case; Shu et al. 2003). The agreement between the two methods is remarkable (Fig. 4C). In these experiments, the natural network activity was recorded from a somatic location where the intracellular recording was performed. The re-injection of this "apparent" background synaptic activity at the same somatic site yielded similar responsiveness, suggesting that only the "apparent" synaptic activity reaching the axon hillock near the soma is relevant for action potential generation. However, extracting the "true" parameters of the background noise would imply to perform the recordings at dendritic sites. Likewise, re-injection of the artificial synaptic background using dynamic clamp should be performed at the dendritic sites using a double patch electrode approach (Williams and Mitchell 2008) or more conveniently, using the active electrode compensation (AEC) single-electrode approach (Brette et al. 2008; Brette et al. "Dynamic Clamp with High-Resistance Electrodes Using Active Electrode Compensation In Vitro and In Vivo" in this volume).

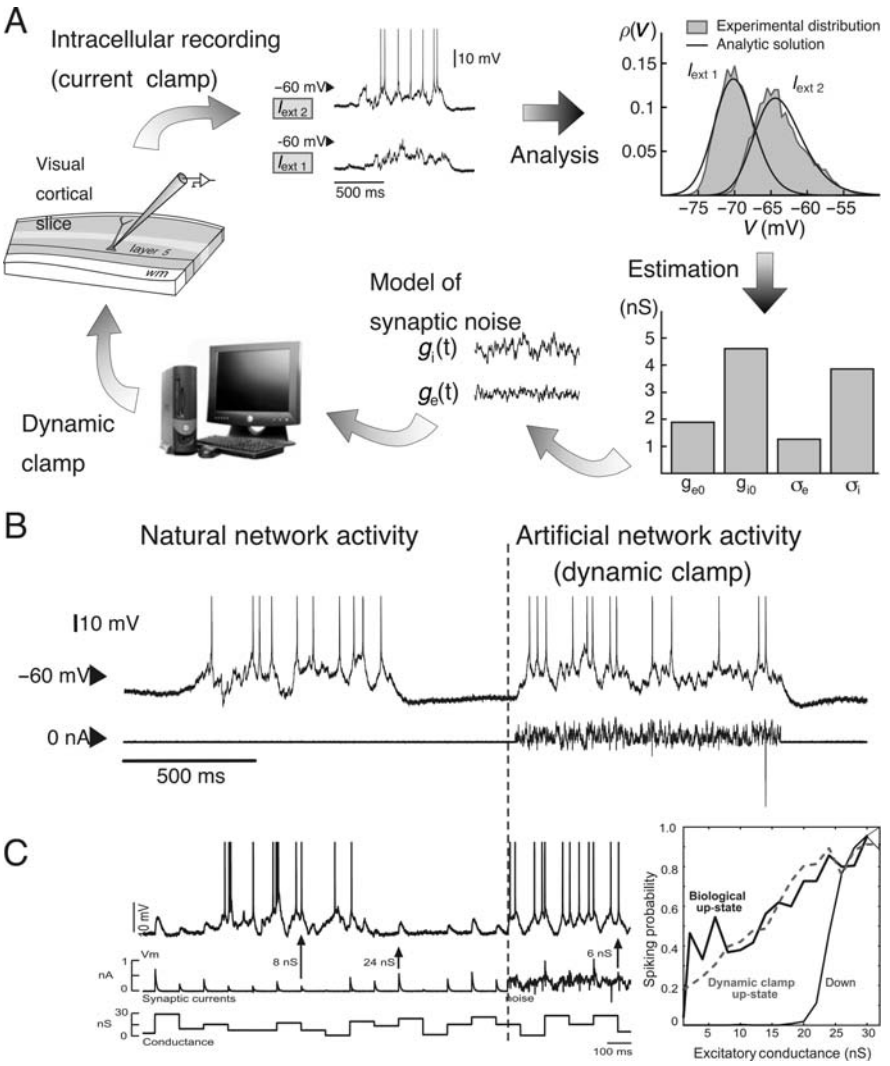

Fig. 4 Comparing natural and dynamic clamp re-created synaptic activity in cortical slices. **A**. Online analysis of up-states and dynamic-clamp test procedure. Network activity was recorded in the slice (*top left*), then analyzed with the VmD method to yield estimates of the conductance parameters (*right*). These estimates were then used to re-inject artificial synaptic noise in the same neuron using dynamic clamp (*bottom*). **B**. Comparison of the natural and artificial network activities obtained. **C**. Comparison of responsiveness to discrete, randomly varying amplitude AMPA synaptic conductances, during the natural and artificial network activities (here the parameters were not extracted using the VmD method, but adjusted manually). The graph represents the probability of spiking in the absence of synaptic noise (Down) and in the presence of synaptic background activity either biological (Up-state, continuous line) or generated using dynamic clamp (*dashed line*). Modified from Rudolph et al. (2004) (A, B) and Shu et al. (2003)(C)

2.4 Dynamic-Clamp Injection of Stochastic Conductances in Thalamic Neurons

2.4.1 A Fast Cortical Control of the Thalamic Gate?

The function of the corticothalamic pathway during natural states of vigilance in the awake animal has remained elusive despite appealing theories on attentional processes (see Section 3). It has been proposed that corticothalamic feedback could control, in a global manner, the transmission state of the LGN (Sherman and Koch 1986; Koch 1987, Steriade et al. 1993; McClurkin et al. 1994, Contreras et al. 1996a, Montero 1999, Sherman 2001), and/or that it could control, in a more specific manner, the processing of sensory stimuli such as moving visual targets (Murphy and Sillito 1987; Sillito et al. 1993; Montero 1999; Przybyszewski et al. 2000; Sillito and Jones 2002) or moving whiskers (Temereanca and Simons 2004).

Thalamocortical cells recorded extracellularly in unanesthetized animals show irregular firing patterns dominated by the tonic firing mode mixed with a small proportion of burst firing (Guido and Weyand 1995; Ramcharan et al. 2000a, b; Swadlow and Gusev 2001), indicating that their membrane potential is depolarized and fluctuates near spike threshold. Intracellular recordings from thalamic cells in awake behaving animals show such depolarization (Hirsch et al. 1983) but are rare due to the technical difficulties involved. The "active" state of thalamic neurons during waking may, in fact, resemble the state of cells recorded intracellularly during paradoxical sleep in chronic unanesthetized animals (Hirsch et al. 1983) and the state seen during "up-states" of thalamic cells in anesthetized animals (Contreras et al. 1996b; Steriade 2001). In up-states, TC neurons are depolarized and present irregular firing patterns, high membrane potential variability and decreased input resistance (Contreras et al. 1996b; Steriade 2001), similar to what has been described as the high-conductance state in cortical neurons (Bringuier et al. 1999; Destexhe et al. 2003). Most likely, the main source of these fluctuations in V_m and input resistance of TC cells is the glutamatergic projection from cortical layer VI cells, generating mixed monosynaptic excitation and disynaptic inhibition (reviewed in Wolfart et al. 2005).

Using a similar approach as described above for cortical neurons, we have recreated the "active," high-conductance state in thalamocortical neurons recorded in vitro in order to test potential mechanisms of corticothalamic modulation of signal integration in TC cells.

We have interfaced thalamocortical neurons recorded in slices of the guinea pig LGN with a large population of artificial excitatory and inhibitory synaptic inputs using point-conductance models, thus mimicking, in a simplified manner, the impact of corticothalamic connectivity. The resulting, noisy high conductance state of the recorded thalamocortical cell resembled the activity reported in vivo (Contreras et al. 1996b; Steriade 2001). The responsiveness of the cell was tested by dynamic clamp-injection of simulated input conductances with AMPA (alpha-amino-3-hydroxy-5-methtyl-4-isoxazolepropionic acid) receptor kinetics

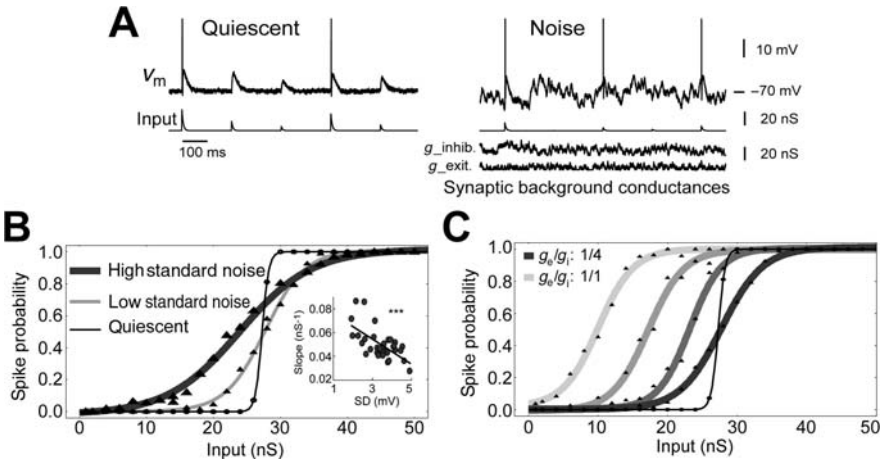

Fig. 5 The influence of synaptic conductance noise changes the transfer function of thalamocortical cells recorded in vitro. **A**. V_m recorded during injection of AMPA input conductance alone (Quiescent) and with additional inhibitory plus excitatory stochastically fluctuating synaptic conductance (Noise). **B**. Probabilities of input strengths to evoke 1 spike, fitted to sigmoid functions. Noise induced a gain (slope) reduction of the response curve compared to quiescent. Decreasing the variance of noise values (high standard, low standard) increased the input–output slope (multiplicative effect). The response gain was correlated with the noise-induced V_m variance (SD). Error bars, SEM. Modified from Wolfart et al. (2005) (A, B). **C.** Increasing the g_e/g_i ratio shifts the response curve to higher responsiveness (additive effect). Input value at 0.5 probability 1/4: 53.5 ± 10.8 versus 1/1: 37.6 ± 10.3 nS ($n = 4$, $p = 0.034$ one-sided non-parametric Wilcoxon rank-sum test)

of randomly varying amplitude. The probability that evoked excitatory postsynaptic potentials trigger a spike was plotted against the strength of the corresponding input conductance, where the slope of such response curves corresponds to the gain of the neuron's input–output transfer function (Fig. 5).

2.4.2 Noise Precisely Tunes the Transfer Function of Thalamic Neurons

We found that the presence of synaptic background activity decreased the slope (gain) of the input–output function of thalamocortical neurons in such a way that it increased the responsiveness to small inputs and reduced that to larger inputs (Fig. 5B). This means that synaptic noise (such as it could be produced by corticothalamic feedback) could shift the nature of input detection of thalamocortical neurons from deterministic (all-or-none) to probabilistic (graded), transmitting more faithfully the parameters of sensory input to cortex.

In addition, the effect of corticothalamic feedback is expected to vary considerably according to the vigilance state of the animal and the signals that are processed. Therefore, we explored two different strengths of variance of fluctuating conductances. In a strong noise condition (Fig. 5B; high standard noise),

variance for excitatory and inhibitory noise was 3 and 12 nS, respectively. A decrease in noise variances (to 1 and 4 nS, respectively; "low std noise"), leading to a reduced V_m variance, increased the input–output gain (see change in the slope of the curve in Fig. 5B). In addition, the gain in the various noise conditions correlated with the actual degree of V_m variance induced by the noise (Fig. 5B, *inset*). Thus, these results show that background synaptic activity is able to modify the response curve of TC neurons in a multiplicative manner. Next, we tested several ratios of excitatory to inhibitory conductances, namely 1/1, 1/2, 1/3, and 1/4, respectively (Fig. 5C). Again, in accordance with what was observed in cortical neurons, with an increasing inhibitory component in the fluctuating conductances the input–output probability curve is shifted to higher input values.

2.4.3 Noise Mixes Burst and Single-Spike Responses

Subsequent results showed that not only the synaptic conductance background modulates the input/output gain – in other terms, the "transfer properties" – by increasing the sensitivity to small inputs, but that it also changes dramatically the influence of the T current, a powerful calcium current involved in the generation of action potential bursting in thalamic cells. In addition, noise increases the occurrence of burst firing at resting and depolarized potentials, making the cell's response paradoxically more reliable in regard to the sensory input characteristics. We figured that if the number of spikes in the response grew proportionally to the strength of the input, spike count could be used to reliably encode sensory information. Without synaptic background, such a reliable transfer function does not exist at resting and depolarized states, the cell behaving as a high-pass filter detecting only strong inputs with no discrimination of strength passed a threshold (see the step-like response in Fig. 5B, thin trace). We found that noise made cells fire on average a number of spikes proportional to input strength (not shown), providing a more linear transfer function at all potentials. Thus, in the presence of synaptic background activity, probabilistic "mixing" of single-spike and burst responses potentially endows TC cells with interesting encoding capabilities (see details in Wolfart et al. 2005).

2.4.4 Noise Abolishes Voltage and Frequency Dependences of Spike Transfer

We also performed stimulations with Poisson-distributed physiologically realistic inputs, as previously described in Section 2.1. The magnitude of a single retinogeniculate EPSP may vary little, but the "effective" postsynaptic retinogeniculate EPSPs depend on variable degrees of temporal summation, such that the effective input has a larger magnitude range. In the experiments described so far, the variability of "effective" input was achieved by randomizing the input conductances while fixing the input frequency, thereby separating magnitude from frequency and allowing better control and comparison with cortical neurons (Shu et al. 2003). Here, though the retinogeniculate input conductance was fixed, Poisson-rate stimulation led to variable "effective" input EPSP magnitudes due to summation (Fig. 6).

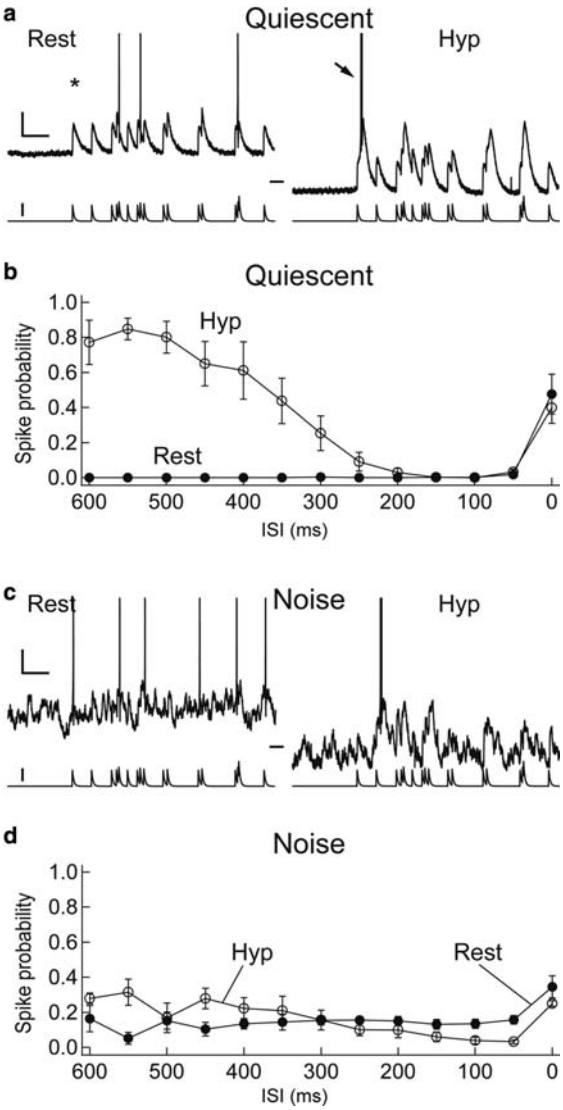

Fig. 6 Physiologically realistic Poisson-distributed inputs: noise abolishes voltage and frequency dependencies. **A**, **B** Comparison of the response properties of thalamocortical cells during stimulation with Poisson-distributed "retinal" input using a mean frequency of 10 Hz, in the absence of noise (Quiescent) and **C**, **D** in the presence of two stochastic conductances (g_e, g_i) injected in a thalamocortical cell. In addition to this background synaptic activity, the excitatory (AMPA) "retinal" stimuli were injected at random time intervals (I). Graphs represent spike probability as a function of the ISI (interstimulus interval). In Quiescent conditions, the spike probability was boosted at hyperpolarized levels (Hyp) compared to rest (Rest), because of the presence of calcium-mediated bursts. In the presence of synaptic background activity (Noise), single spikes and bursts were mixed at all V_m levels, and the probabilities were approximately equal, as well as only weakly dependent on ISI. Modified from Wolfart et al. (2005)

At resting potential, with subthreshold input magnitude, spikes were only evoked by summed inputs at smaller interstimulus intervals (ISIs) (Fig. 6A, B): ISIs in the range of 50–600 ms were related to spike probabilities up to 0.02, whereas ISIs shorter than 50 ms were associated with a spike probability of approximately 0.5. In contrast, at hyperpolarized potentials, spike response could be evoked not only by input summation, but also by long ISIs in the range of 300–600 ms with spike probabilities in the range of 0.25–0.85. These long ISIs were responsible for the activation of the low-threshold Ca^{2+} conductance (I_T) that in turn evoked spikes. Thus, spike probabilities induced by Poisson rate input had an all-or-none character at resting potential, but were very dependent on input frequency and activation kinetics of I_T, adopting intermediate values at hyperpolarized potentials.

We repeated the Poisson rate experiment described above in the presence of noise (Fig. 6C, D). With noise, input summation increased the spike probability at resting and hyperpolarized potentials. However, unlike in the quiescent condition, larger ISIs did not lead to different spiking probabilities at hyperpolarized compared to resting potential. Although no direct comparison between fixed rate and Poisson rate experiments (such as comparing the gain) is feasible, these results match: in both experimental conditions voltage and frequency dependencies (as represented by the various ISIs) were abolished with synaptic background noise.

In conclusion, the injection of in vivo-like background synaptic activity resulted in marked changes of neuronal responsiveness in thalamocortical neurons. Background synaptic activity is able to 1) linearize the response curve via probabilistic "mixing" of single-spike and burst responses, endowing TC cells with linear encoding capabilities and 2) tune the responsiveness of the TC cells via different properties of the fluctuating conductances (amplitude of noise and g_i/g_e ratio). Although it remains to be explored in vivo, it is then tempting to hypothesize that cortical activity could exert a fast control of the thalamic gate, via rapid changes in the balance of the inhibitory and excitatory corticothalamic pathways, resulting in shifts in the response curve (additive effects) as well as by changes in the level of synchrony in both inputs, resulting in amplitude changes of the noise and slope modifications in the response curve (multiplicative effect) (see details in Wolfart et al. 2005).

3 Discussion and Outlook

In this chapter, we have reviewed several approaches to study the integrative properties of central neurons. In particular, we have employed a real-time combination of models and experiments to probe how intrinsic neuronal properties and extrinsic (synaptic) background inputs shape neuronal responsiveness. These techniques include "hybrid" systems connecting real and artificial neurons via dynamic-clamp-based synapses, or dynamic-clamp injections of

artificial input and background noise channels in neurons. We have reviewed applications of such techniques to the study of cortical, thalamic and spinal neurons in vitro.

3.1 Probing Sensory Gating in Intrinsically Active Neurons

The notion that the activity of relay cells is governed by a combination of state-dependent intrinsic membrane properties and synaptic inputs has been the subject of many review articles and hypotheses in the thalamus (Steriade et al. 1993, 1997; Sherman 2001, Sherman and Guillery 2002). Surprisingly, only little direct data has been published concerning the mechanisms at the cellular level by which thalamic circuits might operate as a gate, nor how this gate might be controlled by top-down corticothalamic inputs (McCormick and Feeser 1990; Steriade et al. 1997). The relative rarity of intracellular data to support these hypotheses is due to the technological difficulties of recording thalamic neurons intracellularly in the behaving animal during sensory processing. It has been hypothesized that feedback inhibition within the thalamic circuitry could be a means for decoupling the brain from sensory inputs at the onset of sleep (Yingling and Skinner 1977; Ahlsen et al. 1985; Steriade et al. 1997). Firing intensity in the intrathalamic feedback loop modulates the strength of the inhibitory feedback to the target TC cells (Kim et al. 1997). This mechanism has been generalized as a "variable gain regulator" hypothesis for modulating the transmission of sensory information from retina to the cortex according to the level of arousal (Ahlsen et al. 1985). It should be noted that the variable gain regulator hypothesis was inspired by earlier work in circuits of the brainstem, which involve feedback loop inhibitions by Renshaw cells for the gating of sensory inputs (Hultborn et al. 1979).

We have shown in a very simple hybrid network that a varying strength of intrathalamic inhibition can shift in a graded way the mode of signal transmission from a complete decoupling between input and output, to a fast integration mode where single spikes are faithfully transmitted to the cortex (Le Masson et al. 2002). The importance of the combination of intrinsic properties such as I_H and I_T with the synaptic feedback was subsequently demonstrated in this function involving network oscillation (Debay et al. 2004), but the role of other properties such as the intrinsic bistability of TC cells leading to the slow (<1 Hz) oscillation (Hughes et al. "Using the Dynamic Clamp to Dissect the Properties and Mechanisms of Intrinsic Thalamic Oscillations" in this volume) could in the future also be tested in regards to sensory processing, using the hybrid network approach.

Interestingly, the results we have obtained using dynamic clamp in relay neurons located in the dorsal part of the spinal cord show that switching between bistability, rhythmic oscillation, and tonic firing results in profound changes in signal transfer capabilities. The three firing modes of the DHNs

correspond to specific states of information transfer in which dorsal horn circuitry can faithfully transmit, greatly enhance, or block the transfer of nociceptive information. From a functional point of view, these three states may correspond to different pain integration modalities ranging from acute nociception to long-lasting central sensitization. Extrinsic modulation through mGlu and $GABA_B$ receptors controls the switch between these different functional states (Derjan et al. 2003).

3.2 A Coherent View of the State-Dependent Thalamic Transfer Function

Similarly in the thalamus, activation of ascending neurotransmitter systems modulates intrinsic properties of thalamocortical cells and leads to considerable changes at the level of the network, underlying the transition from sleep to arousal (reviewed in Steriade and McCarley 1990; McCormick 1992). We have tested directly the effect of noradrenaline on the hybrid retinothalamic circuit, and found that the neuromodulated circuit transmits retinal input with a one-to-one transfer ratio, resulting in increased signal transfer (Le Masson et al. 2002).

However, the effects of ascending neuromodulator systems are rather slow and spatially widespread. These characteristics are not compatible with the precision and rapidity of attentional mechanisms, which have been hypothesized to enable the brain to process the overwhelming amount of sensory information that reaches our senses. One likely candidate to mediate such fast modulation of thalamic gating is the corticothalamic feedback. Cognitive studies propose that the massive corticothalamic feedback plays a supervising role in the processing of incoming sensory information: the "searchlight," "active blackboard," and "focal attention" hypotheses (Crick 1984; Mumford 1991; Montero 1999). Thus, at the level of the thalamus, cortical influence could be able to "focus the appropriate circuitry on the most relevant characteristics of the visual stimulus" (Sillito et al. 1994; Sillito and Jones 2002; Temereanca and Simons 2004). We have proposed in Section 2.4 how the influence of corticothalamic inputs on GABAergic interneurons and relay thalamic neurons could implement this function at the cellular level.

The present work and that of others on the transfer function of thalamocortical relay neurons leads to a coherent view based on the principles summarized in Fig. 7. The decrease of conscious sensory perception at the onset of sleep and during absence seizures may result in part from a functional decoupling of the sensory flow during slow synchronous oscillations reverberating in thalamocortical networks. The genesis of these oscillations and their large-scale synchronization critically depends upon the bursting properties of the thalamocortical cell membrane and the recurrency of synaptic connections within the thalamus and between thalamus and cortex.

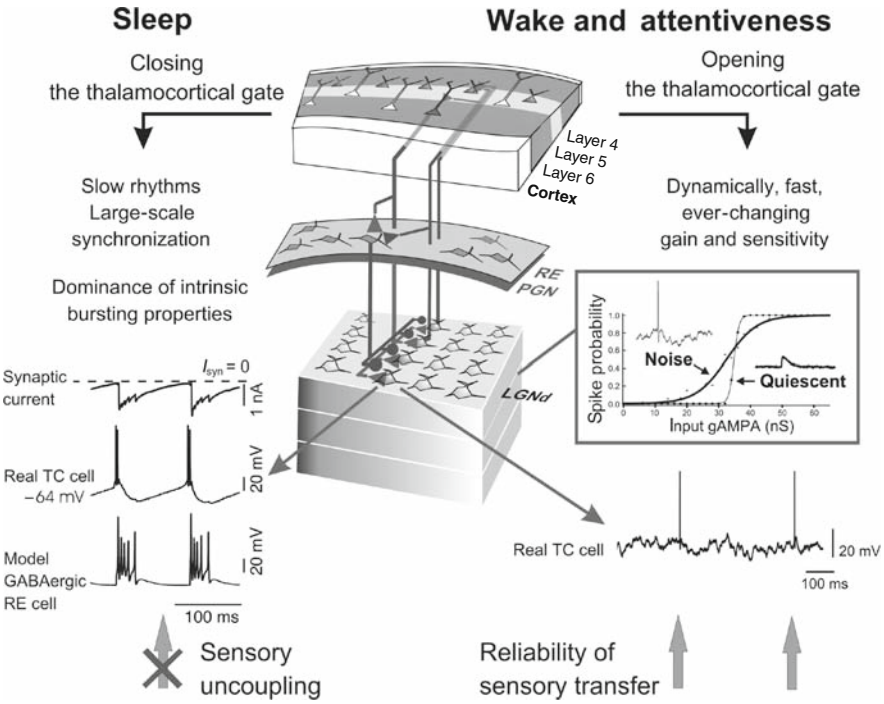

Fig. 7 Two functional facets of the thalamic gate. Center: a schematic synaptic organization of the thalamocortical network. *Circles*: inhibitory synapses, *triangles*: excitatory synapses, LGNd: dorsal lateral geniculate nucleus, PGN: perigeniculate nucleus, a sub-nucleus of the reticular thalamic nucleus (RE). During sleep, the activity of thalamic cells is dominated by intrinsic membrane properties and robust synchronized slow oscillation symbolized here by a detail of spindle wave produced in an hybrid network (*bottom* recordings on the *left*). In vivo, these phenomena are associated with a significant drop of conscious sensory perception. Upon arousal, thalamic cells are in high conductance states that change drastically their integrative properties. These "active" states are due to the presence of background synaptic bombardments resulting from the activity of recurrent synaptic networks in cortical and corticothalamic networks. Modeled synaptic bombardment is injected in the TC cell using dynamic clamp. Graph represents the input–output response in presence or absence of noise, see text. (Modified from Le Masson et al. 2002, Wolfart et al. 2005.)

Upon awakening, the function of top-down corticothalamic inputs could switch to precisely controlling the transfer function of thalamocortical neurons. The demonstration by dynamic-clamp experiments that the transmitting properties of TC cells are dependent on the stochastic nature of the contextual synaptic feedback needs further confirmation in vivo, but it already suggests that computation exerted by thalamic relay cells should not be entirely defined on the basis of intrinsic conductances. Rather, thalamic operations could be under a graded control exerted by global network recurrency. Therefore, it is remarkable that sleep is dominated by the impact of intrinsic oscillation-promoting membrane properties in thalamic cells, while this impact could be

lessened upon awakening by the combined influences of ascending neuromodulatory systems and that of background synaptic activity produced by descending cortical inputs. The cortical control of thalamic transfer function by a tunable mixed excitatory and inhibitory synaptic background activity presents several advantages over the modulation by slow neuromodulators: it is dynamic, fast, and topographically precise.

The model used here in thalamic and cortical neurons describes excitatory and inhibitory conductance fluctuations as independent stochastic processes, which is equivalent to assume that the influence of the cortical circuit on cortical cells or relay cells is a mixture of uncorrelated EPSPs and IPSPs. In the thalamus, this seems to contrast with the fact that corticothalamic feedback activates in relay cells strong feedforward IPSPs (Steriade et al. 1997), which would tend to correlate the direct cortical EPSPs and the feedforward IPSPs. However, the latter are mediated by the bursts of thalamic reticular cells which are likely to be much reduced in activated states. In addition, EPSPs and IPSPs result from different cortical presynaptic neurons through direct excitation and diffuse feedforward inhibition via the reticular nucleus and intrinsic interneurons, and these different cortical populations are unlikely to be synchronized during activated states. Moreover, the reticular neurons also send inhibitory synapses to interneurons as well as within the reticular nucleus, which would also tend to "blur" correlations. Thus, correlations are not likely to be large in activated states, and in the absence of experimental data, excitatory and inhibitory conductances were considered as uncorrelated. Including correlations in the model of background activity is currently being considered (work in progress; Marre et al. 2007; Piwkowska et al. 2008).

3.3 Revisiting Dynamic Clamp: The Combination of Real-Time NEURON with Active Electrode Compensation

Dynamic-clamp (or "conductance injection") experiments consist of real-time interactions between computer-generated conductances and a living neuron, in which the current corresponding to the modeled conductances is injected through the intracellular recording electrode. Coupling conductance-based models of neurons, populations of synapses or isolated neuronal compartments (i.e. a dendritic tree, Hughes et al. "Using the Dynamic Clamp to Dissect the Properties and Mechanisms of Intrinsic Thalamic Oscillations" in this volume) or even artificial networks (Hughes et al. "Using the Dynamic Clamp to Dissect the Properties and Mechanisms of Intrinsic Thalamic Oscillations" in this volume) to living neurons enables to create small "hybrid" cells or networks. In this type of "neuronal cyborgs," synaptic-like interactions between the recorded biological neuron and model neurons run in real-time, following the natural dynamics of the biological cell.

To set up a dynamic-clamp system, two technical problems must be resolved: (1) establishing a real-time dialog between the computer and the recorded neuron, which presents a number of technical difficulties as discussed below and (2) programming the desired model equations and simulating them in real time. These equations can be complex to implement; for example, injecting a voltage-dependent conductance described by the Hodgkin and Huxley (1952) model requires solving this model numerically, which in turn requires to use adequate integration methods as these equations are highly nonlinear. Thus, a dynamic-clamp system must incorporate ways to integrate ordinary differential equations, and possibly more complex types of models. A way to circumvent the latter difficulty is to make use of an existing neural simulation environment, in which these aspects have been taken care of.

In the appendix, we review such a system running under the Windows operating system and based on the widely-used NEURON simulation environment (Hines and Carnevale 1997), which was re-designed for real time (Le Franc et al. 2001) to run dynamic-clamp experiments. The main technical difficulty is to force NEURON to run in real time and communicate with the amplifier for reading the V_m and sending the value of the current to be injected. This technical obstacle was solved here using a DSP board (see also Robinson 2008; Robinson "Synaptic Conductances and Spike Generation in Cortical Cells" in this volume), but other solutions exist (reviewed in Prinz et al. 2004), such as using a real-time operating system (NEURON running in RT-LINUX, M. Hines, personal communication; Dorval et al. 2001, White et al. "Using "Hard" Real-Time Dynamic Clamp to Study Cellular and Network Mechanisms of Synchronization in the Hippocampal Formation" in this volume), or using software which enables real-time applications under Windows (NeuReal, Hughes et al. 2008; Hughes et al. "Using the Dynamic Clamp to Dissect the Properties and Mechanisms of Intrinsic Thalamic Oscillations" in this volume; Milescu et al. 2008) – an example of such software is the INtime kernel (Tenasys; http://www.tenasys.com/products/intime.php). Using the latter framework should greatly facilitate the realization of a very reliable real-time system, which could coexist with other materials and applications running under Windows; it should also enable the use of different data acquisition boards while keeping a user-friendly graphical interface. We are presently testing this possibility.

Another recent application of the dynamic clamp has been to enhance the precision of the recording by using a computational model of the electrode, which corrects online for electrode artifacts. This method, called "AEC" was recently set up and its precision was demonstrated using the RT-NEURON version of the dynamic clamp (Brette et al. 2008). AEC was tested in particularly demanding recording conditions such as injection of conductance noise in vivo and in vitro (see details in Brette et al. "Dynamic Clamp with High-Resistance Electrodes Using Active Electrode Compensation In Vitro and In Vivo" in this volume and in the Appendix below). The combination of AEC with any of the dynamic-clamp platforms described in this volume is likely to enhance the

precision of dynamic clamp when using sharp electrodes, and may become a convenient alternative to dual patch recording at dendritic sites (see Williams "Dendritic Dynamic Clamp – A Tool to Study Single Neuron Computation" in this volume).

4 Appendix: The Real-Time Neuron Simulator

4.1 Real-Time Implementation of NEURON

From the point of view of the NEURON simulation environment (Hines and Carnevale 1997), the inclusion of a real-time loop is relatively straightforward. In NEURON, the state of the system at a given time is described by a number of variables (V_m, I_m, etc.). The value of some of these variables is externally imposed ("input" variables), whereas other variables must be calculated ("output" variables). Their values not only depend on the other variables at present time, but also on the values of all variables in the past.

In a conventional NEURON simulation (not real time), if a fixed-step integration method such as Backward Euler or Crank–Nicholson is chosen the system is first initialized (function *finitialize*), then the state of the system is calculated at each time step, at time $n \times \mathrm{d}t$, where n is an integer and $\mathrm{d}t$ is the fixed time step. The function which performs this integration is called *fadvance* in NEURON and calculates the state of the system at time $n \times \mathrm{d}t$ from the values at preceding times, $(n-1) \times \mathrm{d}t$, $(n-2) \times \mathrm{d}t$, $(n-3) \times \mathrm{d}t \ldots$

To realize a real-time system, we must (1) Associate some input variables of NEURON to the analog inputs of an external device; (2) Associate some output variables of NEURON to analog outputs of this device; and (3) Make sure that the sequence (read input variables, calculate new state, write output variables) is done at each instant $n \times \mathrm{d}t$. As a consequence, such a system necessarily requires a fixed-step integration method.

These steps are easily implemented using the recent multifunction data acquisition boards available for PCs. The card must possess analog and digital input and output (I/O) channels, as well as a clock to set the acquisition frequency – these characteristics are relatively standard today. The card must also be able to send an interrupt to the PC at each acquisition, so that computations can be initiated, as well as reading input variables and writing to output variables. This latter requirement is more restrictive, and guides the choice of the data acquisition board.

4.1.1 Real-Time Implementation with a DSP Board

We use a data acquisition card with a digital signal processor (DSP) on board (card DSP M67, Innovative Integration). This card is equipped with an analog module A4D4, with four analog inputs, four analog outputs, and a very

efficient interrupt procedure. This interruption procedure is critical to the system, as we detail below.

A first and obvious possibility is to use the DSP to program the computational part of the dynamic-clamp system (see also Robinson "Synaptic Conductances and Spike Generation in Cortical Cells" in this volume; Robinson, 2008). However, this solution would require the compilation of the NEURON simulator on the DSP board, which is very difficult technically, and also not flexible because the source code of NEURON would have to be profoundly modified, thus making difficult any upgrade with most recent versions of NEURON. Instead, the solution chosen was to run NEURON on the operating system (Windows NT, 2000, or XP), and have a minimal program running on the DSP to handle the timing of I/O events. This minimal program receives simple commands from the PC (such as "Start," "Stop," and "Set Clock") and implements a procedure triggered by the DSP clock at each dt. This procedure: (1) reads in inputs and stores the values in a mailbox; (2) triggers an interrupt on the PC; and (3) receives the output values in a mailbox and refreshes the analog outputs. In practice, the operation (3) is executed first – the output values of the preceding circle are processed, which introduces a systematic delay equal to the time step dt.

On the PC, in NEURON, the interrupt procedure reads the inputs from the mailbox and stores the values to the variables associated to these entries. The interrupt procedure then calls the procedure *nrn_fixed_step* (which is a low-level version of *fadvance*). It then sends the calculated values of the output variables to the mailbox.

Thus, the mechanism chosen was to have a data acquisition board that sends an interrupt at every time step dt, and this interrupt triggers the execution of a particular I/O procedure linked to NEURON. This procedure enabled us to run real-time applications under Windows. Other solutions are also possible, such as using a real-time operating system (such as RT-LINUX). Such a solution is under investigation by M. Hines. The Windows-based RT-NEURON was first implemented in 2001 using version 4.3.1. of NEURON, and running on the Windows NT operating system. This version has now been ported to version 6.0 of NEURON, and runs on all versions of Windows (Fig. 8).

To manage the DSP in Neuron, we created a new C++ class directly linked to the tools developed on the board. In order to make these functions accessible to the HOC level, NEURON was recompiled while registering a corresponding HOC class with methods allowing the direct control and set up of the DSP board.

These new HOC class allow to load software on the DSP board, to initialize the internal clock with the chosen integration time step dt, to initialize the gain of the AD/DA converters, to set the model's variables which will be used as input and output, to determine the priority level of the interruption request and finally to start or stop the real-time experiment.

Despite these new tools, the link between NEURON and the acquisition system is not complete. Most of NEURON objects, and more precisely the

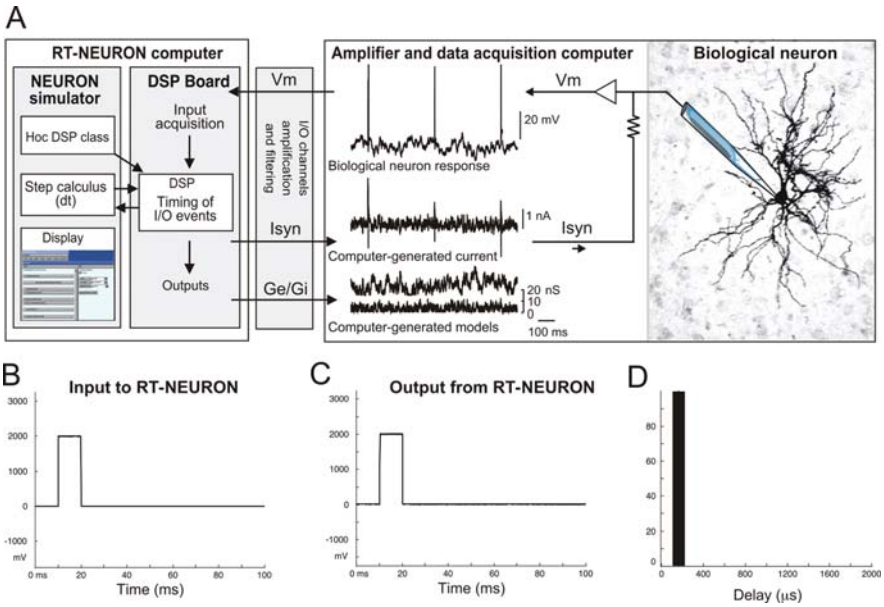

Fig. 8 The real-time-NEURON (RT-NEURON) system architecture. **A**. Software-generated model neuron and conductances run in real-time in the RT-NEURON Windows-based computer (*left box*). A DSP board paces the operations of the Pentium processor(s) and controls the input/output data transfer between the model and biological cells. Input variables such as the biological neuron membrane potential (V_m) are sent to the NEURON simulator through the DSP at each dt. In return, output variables such as the command current (I_{syn}) corresponding to the excitatory and inhibitory conductances (G_e/G_i) in this exemple, are sent to the amplifier or the acquisition system. Here I_{syn} is injected in discontinuous current clamp in a thalamocortical neuron through the same pipette that collects the V_m. **B**. Test of the real time in RT-NEURON-based dynamic clamp. RT-NEURON was used to copy an analog input to an analog output while simultaneously running a simulation. B. Test rectangular signal sent as input to RT-NEURON via the DSP. RT-NEURON was running simultaneously the G_e/G_i stochastic conductance model such as in A. **C**. Signal recorded on the output channel. **D**. Histogram of delays between B and C, showing a single peak at the value of 100 μs, which was the value of the cycle dt, thus demonstrating that the system strictly operates in real time

mechanisms as synapse models or ionic channels, must be linked to an object compartment, which represents a volume of membrane. Thus, in order to calculate the injected current, it is crucial to link the model to a "ghost compartment" which should have a negligible participation to the calculation. This compartment, which acts as an anchoring point for the mechanisms, will be the buffer for the data transfer during the real time, receiving the measured membrane potential of the biological neuron for example. This "ghost compartment" is a simple cylinder with a total area of 1 cm^2 to avoid any scaling effect on the calculated injected current, as the current is expressed in NEURON in units of ampere per cm^2. We added a simple numerical variable attached to the compartment on which the DSP will point to send the measured membrane potential.

In addition to these HOC tools, we developed a graphical interface that allows to access all these functions and starts the real-time sequence (see Section 4.2.2 below).

4.1.2 Windows and Real Time

It is clear that the version presented above is in contradiction with the principles of Windows, which was conceived for multitasking, which by definition does not respect the timing of interrupts. No process can pretend to have the absolute priority over another process, or over processes triggered by the operating system. Nevertheless, on present PCs and given a few precautions, RT-NEURON works correctly with a dt of 100–60 μs (10–15 kHz) using the system described above. In this case, the interrupts generated by the DSP board must be given maximum priority. To achieve this, the normal interrupts must be deactivated, such as network cards, USB handling, and all programs that are susceptible to be started at any time (such as Windows updates and anti-virus software). Second, the RT-NEURON software must be given the maximum priority level allowed in MS-Windows. This function called *real time* (task manager/Process/neuron.exe/define priority/real time) however does not give to RT-Neuron the absolute priority over all processes but it allows better performances. It can be conveniently acceded by creating a text file named nrngui.bat containing the following command line (start/real time c:\nrn\bin\-neuron c:\nrn\lib\hoc\nrngui.hoc) that will automatically launch RT-NEURON in the real-time configuration of Windows. If necessary, another way to enhance the real-time performance is to run Windows in the diagnostic mode (start menu/execute/msconfig) – note that this is not necessary in recent multicore computers.

Finally it should be noted that, independent of the type of the dynamic-clamp system used, the time resolution is limited to approximately 3 kHz when using sharp glass pipettes, as it is commonly the case for dynamic clamp in vivo (Brette et al. 2008) or in some cases in vitro (Shu et al. 2003). Until recently, it was necessary to discretize the injection/recording of current using the discontinuous current-clamp (DCC) method. We have introduced a new method of electrode compensation, AEC, that suppresses this limitation and we have incorporated this innovation in the RT-NEURON system (see Section 3.3 and Brette et al. "Dynamic Clamp with High-Resistance Electrodes Using Active Electrode Compensation In Vitro and In Vivo" in this volume).

4.1.3 Testing RT-NEURON

To validate the real-time system, we have conceived the following test procedure. A program is run on NEURON, and in addition, one asks NEURON at each cycle to copy a supplementary analog input to an analog output. A rectangular periodic signal is sent to the analog input. A second computer, equipped with a data acquisition board (100 kHz), acquires inputs and outputs

at high frequency. By comparing these two channels, one can directly evaluate the real time by computing the distribution of measured delays between the input and the output channels. If the real time was perfect, the histogram obtained should have a single peak at the value of the dt (100 μs in this case). This is in general observed, as shown in Fig. 8B, D. Note that in most recent multicore processors, it was not necessary (although recommended) to deactivate system processes, the test was successful in all circumstances.

4.2 RT-NEURON at Work

In this section, we illustrate the use of RT-NEURON, and in particular the new procedures that have been added to run the dynamic-clamp experiments. We will illustrate the steps taken in a typical dynamic-clamp experiment using RT-NEURON.

4.2.1 Specificities of the RT-NEURON Interface

To start a dynamic-clamp experiment, the procedure consists, as in the classical Neuron, in loading the DLL (nrnmech.dll) and the HOC files of the chosen models and protocols from the *File* menu in the NEURON main menu.

A novel *DspControl* box was added in the Neuron *Tools* menu, it contains the new commands to run the simulations in real time via the control of the DSP (Fig. 9A).

4.2.2 A Typical Conductance Injection Experiment Combining RT-NEURON and AEC

In order to test a protocol for conductance injection in a biological cell (and also to build the RT-NEURON platform), it is convenient to first simulate the experiment in an electronic RC-circuit (the "model cell" available with some commercial current-clamp amplifiers).

In the illustration of the practical utilization of RT-NEURON (Fig. 9), a stochastic "point-conductance" model was used to re-create synaptic background activity in a real neuron in the form of two independent excitatory and inhibitory conductances (G_e and G_i) using a point conductance model (Destexhe et al. 2001). In fact, any type of conductance models or current waveforms programmed in the HOC file can be simultaneously injected in a neuron. The complexity of the model is only limited by the speed of the computer. The On/Off command for injecting the command current corresponding to the modeled ionic currents, and the parameters such as the amplitude of the conductance (G_{max}) can be modified online during the recording using the interface (Fig. 9D).

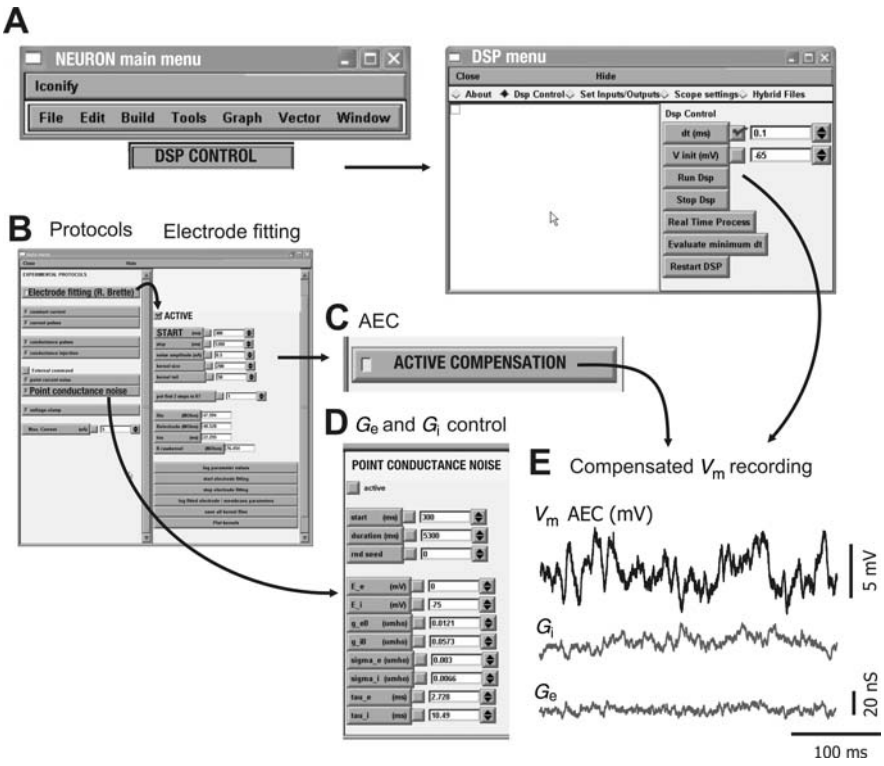

Fig. 9 Conductance injection using RT-NEURON and active electrode compensation (AEC). **A**. Modified "Tools" menu for real-time commands and settings. *Dsp Control* submenu allows to start and stop the DSP and to set the calculation d*t*. *Set inputs/outputs* allocates the destination of the input (Membrane voltage, triggers) and output (command current, conductance models, etc.) variables to input and output channels of the DSP, which are connected to various external devices (amplifier, oscilloscope, acquisition system). Sessions containing predefined experimental protocols can be loaded from the menu *Hybrid Files*. **B–D**. Examples of programmable display windows for controlling conductance models injection (B, D) and AEC (C, D). **E**. Top trace: error-free membrane potential of a biological cortical neuron recorded in vitro (V_m AEC) in which synaptic conductance noise (lower traces G_i and G_e) is injected via a sharp glass micropipette (modified from Brette et al. 2008)

Mimicking the electrical activity of ionic channels using dynamic clamp relies on the injection of high-frequency currents in the neuron via a glass pipette. However, injection of such high-frequency currents across a sharp microelectrode or a high-impedance patch electrode (such as those used in vivo) is known to produce signal distortions in the recording. These recording artifacts can be traditionally avoided by using the discontinuous current-clamp method but with the disadvantage of a limited sampling frequency. Recently, Brette and colleagues have introduced a novel recording method named AEC that eliminates all distortions by subtracting online in real time a model of the

electrode contribution from the voltage recording (see Brette et al. 2008; Brette et al. "Dynamic Clamp with High-Resistance Electrodes Using Active Electrode Compensation In Vitro and In Vivo" in this volume). The dual use of AEC and RT-NEURON allows high temporal resolution dynamic clamp with the sampling frequency only limited by the speed of the computer.

Acknowledgments This work was supported by Centre National de la Recherche Scientifique, European Commission (IST-2001-34712), Action Concertée Incitative "Neurosciences intégratives et computationnelles" and ANR grants T-State and HR-cortex. We thank Michelle Rudolph, Paul Galloux, Leonel Gomez, and José Gomez for help with computation, Jakob Wolfart, Damien Debay, and Mathilde Badoual for testing RT-NEURON experimentally, and Charlotte Deleuze for comments on the manuscript.

References

Ahlsen G, Lindstrom S and Lo FS (1985) Interaction between inhibitory pathways to principal cells in the lateral geniculate nucleus of the cat. Exp Brain Res 58: 134–143.

Azouz R and Gray CM (1999) Cellular mechanisms contributing to response variability of cortical neurons in vivo. J Neurosci 19:2209–23.

Bal T, Von Krosigk M and Mccormick DA (1995) Synaptic and membrane mechanisms underlying synchronized oscillations in the ferret lateral geniculate nucleus in vitro. J Physiol 483: 641–663.

Bernander O, Douglas RJ, Martin KAC and Koch C (1991) Synaptic background activity influences spatiotemporal integration in single pyramidal cells. Proc Natl Acad Sci USA 88:11569–11573.

Brette R, Piwkowska Z, Monier C, Rudolph-Lilith M, Fournier J, Levy M, Frégnac Y, Bal T and Destexhe A (2008) High-resolution intracellular recordings using a real-time computational model of the electrode. Neuron 59:379–391.

Bringuier V, Frégnac Y, Baranyi A, Debanne D and Shulz D (1997) Synaptic origin and stimulus dependency of neuronal oscillatory activity in the primary visual cortex of the cat. J Physiol (Lond) 500:751–74.

Bringuier V, Chavane F, Glaeser L and Frégnac Y (1999) Horizontal propagation of visual activity in the synaptic integration field of area 17 neurons. Science 283:695–699.

Chance FS, Abbott LF and Reyes AD (2002) Gain modulation from background synaptic input. Neuron 35:773–782.

Contreras D, Destexhe A, Sejnowski TJ and Steriade M (1996a) Control of spatiotemporal coherence of a thalamic oscillation by corticothalamic feedback. Science 274:771–774.

Contreras D, Timofeev I and Steriade M (1996b) Mechanisms of long-lasting hyperpolarizations underlying slow sleep oscillations in cat corticothalamic networks. PG – 251–64. J Physiol 494:251–64.

Crick F, (1984) Function of the thalamic reticular complex: The searchlight hypothesis. Proc Natl Acad Sci USA 81:4586–4590.

Debay D, Wolfart J, Le Franc Y, Le Masson G and Bal T (2004) Exploring spike transfer through the thalamus using hybrid artificial-biological neuronal networks. J Physiol Paris 98:540–558.

Derjan D, Bertrand B, Le Masson G, Landry M, Morrisset V and Nagy F (2003) Multiple states in spinal dorsal Horn neurons : switch under a dynamic balance of metabotropic controls. Nat Neurosci 6:274–281.

Destexhe A and Contreras D (2006) Neuronal computations with stochastic network states. Science 314:85–90.

Destexhe A and Paré D (1999) Impact of network activity on the integrative properties of neocortical pyramidal neurons in vivo. J Neurophysiol 81:1531–1547.
Destexhe A, Rudolph M and Pare D (2003), The high-conductance state of neocortical neurons in vivo. Nat Rev Neurosci 4:739–751.
Destexhe A, Rudolph M, Fellous JM and Sejnowski TJ (2001) Fluctuating synaptic conductances recreate in-vivo-like activity in neocortical neurons. Neuroscience 107:13–24.
Destexhe, A and Sejnowski, TJ (2003) Interactions between membrane conductances underlying thalamocortical slow-wave oscillations. Physiol Rev 83:1401–1453.
Dorval AD, Christini DJ and White JA (2001) Real-time Linux dynamic clamp: a fast and flexible way to construct virtual ion channels in living cells. Ann Biomed Eng 29:897–907.
Guido W and Weyand T (1995) Burst responses in thalamic relay cells of the awake behaving cat. J Neurophysiol 74:1782–1786.
Hines ML and Carnevale NT (1997) The NEURON simulation environment. Neural Comput 9:1179–1209.
Hirsch JC, Fourment A and Marc ME (1983) Sleep-related variations of membrane potential in the lateral geniculate body relay neurons of the cat. Brain Res 259:308–312.
Hô N and Destexhe A (2000) Synaptic background activity enhances the responsiveness of neocortical pyramidal neurons. J Neurophysiol 84:1488–1496.
Hodgkin AL and Huxley AF (1952) A quantitative description of membrane current and its application to conduction and excitation in nerve. J. Physiol. 117:500–544.
Hughes SW, Lõrincz ML, Cope DW et al. (2008) NeuReal: An interactive simulation system for implementing artificial dendrites and large hybrid networks. J Neurosci Methods 169:290–301.
Hultborn H, Lindstrom S and Wigstrom H (1979) On the function of recurrent inhibition in the spinal cord. Exp Brain Res 37:399–403.
Jahnsen H and Llinas R (1984) Electrophysiological properties of guinea pig thalamic neurones: an in vitro study. J Physiol (London) 349:205–226.
Kim U, Sanchez-Vives MV and McCormick DA (1997) Functional dynamics of GABAergic inhibition in the thalamus. Science 278:130–134.
Koch C (1987) The action of the corticofugal pathway on sensory thalamic nuclei: a hypothesis, Neuroscience 23:399–406.
Le Franc Y, Foutry B, Nagy F and Le Masson G (2001) Nociceptive signal transfer through the dorsal horn network: hybrid and dynamic-clamp approaches using a real-time implementation of the NEURON simulation environment. Soc Neurosci Abstracts 927:18.
Le Masson G, Renaud-Le Masson S, Debay D and Bal T (2002) Feedback inhibition controls spike transfer in hybrid thalamic circuits. Nature 417:854–858.
Le Masson S, Laflaquière A, Bal T and Le Masson G (1999) Analog circuits for modeling biological neural networks: Design and applications. IEEE Trans Biomed Eng 45:638–645.
Llinas R (1988) The intrinsic electrophysiological properties of mammalian neurons: insights into central nervous system function. Science 242:1654–1664.
Marre O, El Boustani S, Baudot P, Levy M, Monier C, Huguet N, Pananceau M, Fournier J, Destexhe A. Fregnac Y. (2007) Stimulus-dependency of spectral scaling laws in V1 synaptic activity as a read-out of the effective network topology. Abstr Soc Neurosci 33:790.6.
Mcclurkin JW, Optican LM and Richmond BJ (1994) Cortical feedback increases visual information transmitted by monkey parvocellular lateral geniculate nucleus neurons. Vis Neurosci 11:601–617.
McCormick DA and Bal T (1997) Sleep and arousal: thalamocortical mechanisms. Annu Rev Neurosci 20:185–215.
McCormick DA and Feeser HR (1990) Functional implications of burst firing and single spike activity in lateral geniculate relay neurons. Neuroscience 39:103–113.
McCormick DA (1992) Neurotransmitter actions in the thalamus and cerebral cortex and their role in neuromodulation of thalamocortical activity. Prog Neurobiol 39:337–388.

Milescu LS, Yamanishi T, Ptak K, Mogri MZ and Smith JC (2008) Real-time kinetic modeling of voltage-gated ion channels using dynamic clamp. Biophys J 95:66–87.
Montero VM (1999) Amblyopia decreases activation of the corticogeniculate pathway and visual thalamic reticularis in attentive rats: a 'focal attention' hypothesis. Neuroscience 91:805–817.
Morisset V and Nagy F (1998) Nociceptive integration in the rat spinal cord: role of nonlinear membrane properties of deep dorsal horn neurons. Eur J Neurosci 10:3642–3652.
Mumford D (1991) On the computational architecture of the neocortex. I. The role of the thalamo-cortical loop. Biol Cybern 65:135–145.
Murphy PC and Sillito AM (1987) Corticofugal feedback influences the generation of length tuning in the visual pathway. Nature 329:727–729.
Paré D, Shink E., Gaudreau H, Destexhe A and Lang, EJ (1998) Impact of spontaneous synaptic activity on the resting properties of cat neocortical neurons in vivo. J. Neurophysiol. 79:1450–1460.
Piwkowska Z, Pospischil M, Brette R, Sliwa J, Rudolph-Lilith M, Bal T and Destexhe A (2008) Characterizing synaptic conductance fluctuations in cortical neurons and their influence on spike generation. J Neurosci Methods 169(2):302–22.
Pospischil M, Piwkowska Z, Rudolph M, Bal T and Destexhe A (2007) Calculating event-triggered average synaptic conductances from the membrane potential. J Neurophysiol 97:2544–2552
Prescott SA and De Koninck Y (2003) Gain control of firing rate by shunting inhibition: roles of synaptic noise and dendritic saturation. Proc Natl Acad Sci USA 100:2076–2081.
Prinz AA, Abbott LF and Marder E (2004) The dynamic clamp comes of age. Trends Neurosci 27:218–224.
Przybyszewski AW, Gaska JP, Foote W and Pollen DA (2000) Striate cortex increases contrast gain of macaque LGN neurons. Vis Neurosci 17:485–494.
Ramcharan EJ, Cox CL, Zhan XJ, Sherman SM and Gnadt JW (2000a) Cellular mechanisms underlying activity patterns in the monkey thalamus during visual behavior. J Neurophysiol 84:1982–1987.
Ramcharan EJ, Gnadt JW and Sherman SM (2000b) Burst and tonic firing in thalamic cells of unanesthetized, behaving monkeys. Vis Neurosci 17:55–62.
Robinson, HPC (2008) A scriptable DSP-based system for dynamic conductance injection. J Neurosci Methods 169:271–281.
Rudolph M, Piwkowska Z, Badoual M, Bal T and Destexhe A (2004) A method to estimate synaptic conductances from membrane potential fluctuations. J Neurophysiol 91: 2884–2896.
Rudolph M and Destexhe A (2003) A fast-conducting, stochastic integrative mode for neocortical neurons in vivo. J Neurosci 23:2466–2476.
Rudolph M, Pelletier J-G, Pare D and Destexhe A (2005) Characterization of synaptic conductances and integrative properties during electrically-induced EEG-activated states in neocortical neurons in vivo. J Neurophysiol 94:2805–2821.
Sherman SM and Guillery RW (2002) The role of the thalamus in the flow of information to the cortex. Philos Trans R Soc Lond B Biol Sci 357:1695–1708.
Sherman SM and Koch C (1986), The control of retinogeniculate transmission in the mammalian lateral geniculate nucleus. Exp Brain Res 63:1–20.
Sherman SM (2001a) Tonic and burst firing: dual modes of thalamocortical relay. Trends Neurosci 24:122–126.
Sherman SM (2001b) A wake-up call from the thalamus. Nat Neurosci 4:344–346.
Shu Y, Hasenstaub AR, Badoual M, Bal T and McCormick DA (2003) Barrage of synaptic activity control the gain and sensitivity of cortical neurons. J Neurosci 23: 10388–10401.
Sillito AM and Jones HE (2002) Corticothalamic interactions in the transfer of visual information. Philos Trans R Soc Lond B Biol Sci 357:1739–1752.

Sillito AM, Cudeiro J and Murphy PC (1993) Orientation sensitive elements in the corticofugal influence on centre-surround interactions in the dorsal lateral geniculate nucleus. Exp Brain Res 93:6–16.
Sillito AM, Jones HE, Gerstein GL and West DC (1994) Feature-linked synchronization of thalamic relay cell firing induced by feedback from the visual cortex. Nature 369:479–482.
Steriade M (2001) Impact of network activities on neuronal properties in corticothalamic systems. J Neurophysiol 86:1–39.
Steriade M, Mccormick DA and Sejnowski TJ (1993), Thalamocortical oscillations in the sleeping and aroused brain. Science 262:679–685.
Steriade M and McCarley RW (1990) Brainstem Control of Wakefulness and Sleep. New York: Plenum Press.
Steriade M, Jones, EG and McCormick DA (1997) Thalamus (eds. Steriade, M, Jones, EG & McCormick, DA) (Elsevier Science Ltd, Amsterdam, Lausanne, New York, Oxford, Shannon, Tokyo).
Swadlow HA and Gusev AG (2001) The impact of 'bursting' thalamic impulses at a neocortical synapse. Nat Neurosci 4:402–408.
Temereanca S and Simons DJ (2004) Functional topography of corticothalamic feedback enhances thalamic spatial response tuning in the somatosensory whisker/barrel system. Neuron 41:639–651.
Timofeev I, Contreras D and Steriade M (1996) Synaptic responsiveness of cortical and thalamic neurones during various phases of slow sleep oscillation in cat. J Physiol 494:265–278.
Tuckwell HC (1988) Introduction to Theoretical Neurobiology. Cambridge University Press, Cambridge UK.
von Krosigk M, Bal T and McCormick DA (1993) Cellular mechanisms of a synchronized oscillation in the thalamus. Science 261: 361–364.
Williams SR (2004) Spatial compartmentalization and functional impact of conductance in pyramidal neurons. Nat Neurosci 7:961–967.
Williams SR and Mitchell SJ (2008) Direct measurement of somatic voltage clamp errors in central neurons. Nat Neurosci 11:790–798.
Wolfart J, Debay D, Le Masson G, Destexhe A and Bal T (2005) Synaptic background activity controls spike transfer from thalamus to cortex. Nat Neurosci 8:1760–1767.
Yingling CD and Skinner JE (1977)Gating of Thalamic Input to Cerebral Cortex by Nucleus Reticularis Thalami, vol. 1, Karger, Basel.

Using the Dynamic Clamp to Dissect the Properties and Mechanisms of Intrinsic Thalamic Oscillations

Stuart W. Hughes, Magor Lörincz, David W. Cope, and Vincenzo Crunelli

Abstract During different stages of vigilance, the thalamus engages in a range of rhythmic activities from the slow (<1 Hz), delta (δ) (1–4 Hz) and spindle (7–14 Hz) waves that permeate the brain during sleep and anaesthesia to the faster oscillations in the alpha (α) and beta/gamma (β/γ) (>15 Hz) bands that occur during wakefulness. In recent years, it has been shown that several of these oscillations are associated with intrinsic rhythmic activity in individual thalamocortical (TC) neurons, with these intrinsic oscillations also being readily observable in recordings of TC neurons from thalamic slice preparations. In this chapter we will show how the dynamic-clamp technique provides an extremely useful means for studying the intricate cellular mechanisms and key properties of some of theses intrinsic oscillations. We will mainly focus on the intrinsic δ or so-called pacemaker ($\sim$1–2 Hz) oscillation and the slow (<1 Hz) oscillation but will also briefly discuss how the dynamic-clamp technique can be utilized to study additional important oscillatory phenomena in the thalamus.

1 Introduction

The thalamus is one the most diverse and powerful oscillatory machines in the mammalian brain. During different stages of arousal this structure engages in a range of rhythmic activities from the slow (<1 Hz), delta (δ) (1–4 Hz) and spindle (7–14 Hz) waves that permeate the brain during sleep and anaesthesia (Steriade, Contreras and Curro Dossi 1993; von Krosigk, Bal and McCormick 1993; Contreras and Steriade 1995, Steriade, Amzica and Contreras 1996; Achermann and Borbély 1997; Amzica and Steriade 1998; Hughes et al. 2004) to the faster oscillations in the alpha (α) and beta/gamma (β/γ) (>15 Hz) bands that occur during wakefulness (Lopes da Silva et al. 1973; Rougeul-Buser and Buser 1997; Steriade et al. 1991, 1996). Over the last 25 years it has been noted that many of these oscillations are related to intrinsic rhythmic activity in

S.W. Hughes (✉)
School of Biosciences, Cardiff University, Cardiff CF10 3US, UK
e-mail: hughessw@Cardiff.ac.uk

A. Destexhe, T. Bal (eds.), *Dynamic-Clamp*, Springer Series in Computational Neuroscience 1, DOI 10.1007/978-0-387-89279-5_15,

thalamocortical (TC) neurons, with these intrinsic oscillations also being readily observable in recordings of TC neurons from thalamic slice preparations maintained in vitro (Leresche et al. 1990, 1991; McCormick and Pape 1990; Pedroarena and Llinás 1997; Hughes et al. 2002, 2004). However, due in part to the lack of selective pharmacological tools, but also more generally to an inability to finely manipulate individual membrane conductances, the properties and mechanisms of these oscillations have not always been straightforward to decipher. In this chapter we will describe how the dynamic-clamp technique (Robinson and Kawai 1993; Sharp et al. 1993a, b) provides a highly effective means for studying the intricate cellular mechanisms and key properties of some of the intrinsic oscillatory events expressed by TC neurons. Whilst our main focus will be on the intrinsic δ ($\sim$1–2 Hz) oscillation (Leresche et al. 1990, 1991; McCormick and Pape 1990) and the so-called slow (<1 Hz) sleep oscillation (Hughes et al. 2002; Zhu et al. 2006; Destexhe et al. 2007), we will also briefly discuss how the dynamic-clamp technique can be harnessed to study additional important oscillatory phenomena in the thalamus. Our primary aim is to bring attention to two underappreciated aspects of thalamic physiology: (1) that all TC neurons possess a non-negligible T-type Ca^{2+} 'window' current that is essential for the generation of the slow oscillation and (2) that whilst the effect of various modulatory neurotransmitters that are thought to be involved in maintaining wakefulness is to depolarize TC neurons and therefore move the membrane potential of these cells away from the voltage region where δ and slow oscillations naturally occur, the basic biophysical changes induced by these neurotransmitters otherwise enhance the intrinsic capacity to generate slow rhythmic activities. For the sake of clarity, we will restrict our discussion to the most salient aspects of the results obtained during our recent studies. An appendix providing a brief summary of our methods is included with this chapter but for a more detailed explanation of methods and in-depth description of numerical data the reader is directed towards our original research papers (Hughes, Cope and Crunelli 1998; Hughes et al. 1999, 2002, 2008; Blethyn et al. 2006). All data described here was obtained from in vitro slices of the cat and rat lateral geniculate nucleus (LGN) and ventrobasal thalamus (VB).

2 Validating the Use of the Dynamic Clamp for Studying the Main Ionic Conductances in TC Neurons

2.1 Introduction of Artificial I_h and I_T Following Their Pharmacological Block Reinstates the Original Properties of TC Neurons

Apart from the Na^+ and K^+ currents that are responsible for generating action potentials the intrinsic electrophysiological properties of TC neurons are essentially dominated by two distinct voltage-dependent ionic currents: the

non-inactivating, hyperpolarization-activated mixed cation current, I_h (McCormick and Pape 1990; Soltesz et al. 1991) and the inactivating low-threshold T-type Ca^{2+} current, I_T (Hernandez-Cruz and Pape 1989; Coulter, Huguenard and Prince 1989; Crunelli, Lightowler and Pollard 1989). As in many neuronal types, I_h plays an important role in setting the resting membrane potential of TC neurons (Hughes, Cope and Crunelli 1998). However, the main electrophysiological manifestation of this current is a slow sag-like depolarization that occurs in response to brief hyperpolarizing current pulses elicited from around –60 mV (Fig. 1A, top; B) (McCormick and Pape 1990; Soltesz et al. 1991; Williams et al. 1997b; Turner et al. 1997). This sag-like depolarization is abolished by the selective I_h blocker, ZD7288 (Fig. 1A, middle) (BoSmith, Briggs and Sturgess 1993; Williams et al. 1997b), but can be subsequently 'rescued' by using the dynamic-clamp technique to introduce an artificial I_h with properties that are based on voltage-clamp measurements from TC neurons (Fig. 1A, bottom; B) (Soltesz et al. 1991; see also Tóth and Crunelli 1992).

The dominant manifestation of I_T in TC neurons on the other hand is the production of a transient rebound depolarization (Fig. 2A–D) (Deschenes et al. 1984; Jahnsen and Llinás 1984a, b). This depolarization is commonly referred to as a low-threshold Ca^{2+} potential (LTCP) or low-threshold spike (LTS), can lead to a high-frequency burst of action potentials and typically occurs following a transient hyperpolarizing voltage excursion that is elicited from around –60 mV and that is of sufficient duration and amplitude to de-inactivate T-type Ca^{2+} channels (Fig. 2A, top; D, top). The LTCP can be eliminated by the non-selective Ca^{2+} channel blocker Ni^{2+} (Fig. 2A, middle; B and C) (Crunelli, Lightowler and Pollard 1989) but as with the I_h-mediated sag potential can be reinstated by introducing a biophysically realistic, artificial I_T using the dynamic-clamp system (Fig. 2A, bottom; B and C) (Hughes, Cope and Crunelli 1998; Hughes et al. 2008).

An obvious advantage of the dynamic-clamp technique is that the artificial conductances being introduced are under the complete and instantaneous control of the experimenter. This fine level of control allows the effects of intrinsic currents which have been pharmacologically blocked to be reproduced with a high degree of fidelity. It also enables the possibility of bringing about an 'electronic block' whereby the effects of an intrinsic current are negated by introducing a closely matched replica with opposite sign (Sharp et al. 1993a, b). Indeed, for the specific case of I_T in TC neurons, this aspect of the dynamic-clamp approach has not only allowed us to produce a highly precise reproduction of the LTCP following Ni^{2+} application (Fig. 2B and C) (Hughes et al. 1999, 2002, 2008), but also to achieve a reliable elimination of the LTCP via an effective 'electronic block' of the endogenous current (Fig. 2D) (Hughes et al. 1999). Such accuracy and 'blocking' ability were typically only possible to realize by allowing an immediate and fine control of not only the maximal conductance (i.e. g_T), but also the activation and inactivation kinetics (Fig. 2D) (Hughes et al. 2008). Thus, the dynamic clamp provides an effective and

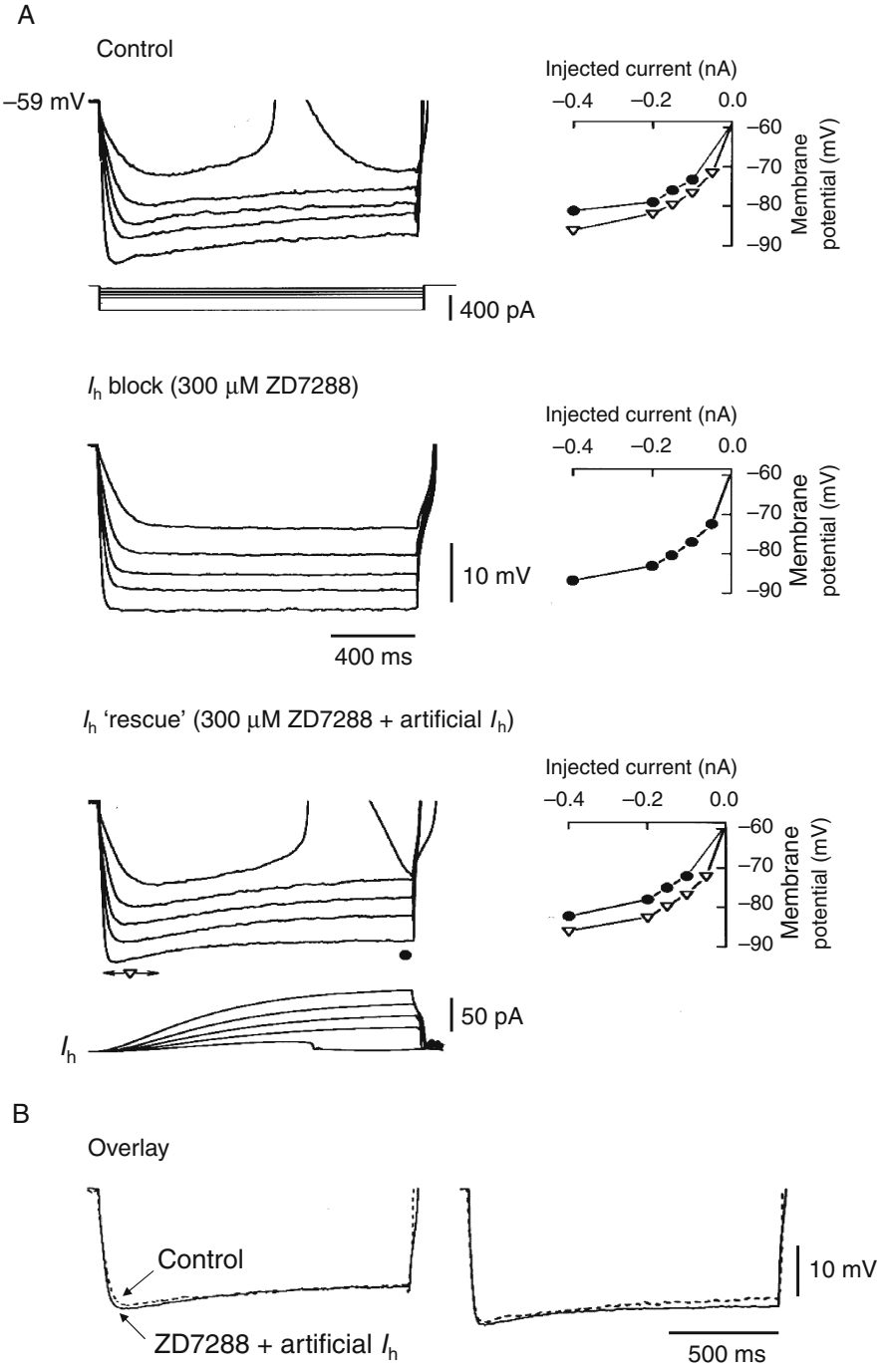
A
Control
–59 mV
400 pA
Injected current (nA)
–0.4
–0.2
0.0
–60
–70
–80
–90
Membrane potential (mV)
I_h block (300 μM ZD7288)
10 mV
400 ms
I_h 'rescue' (300 μM ZD7288 + artificial I_h)
50 pA
I_h
B
Overlay
Control
ZD7288 + artificial I_h
10 mV
500 ms

adaptable means to manipulate and study the effects of the major ionic components of TC neuron electrophysiology.

3 Role of I_h and I_T in Intrinsic δ (~1–2 Hz) Oscillations in TC Neurons

3.1 *Confirmation that* I_h *is Essential for Intrinsic* δ *Oscillations*

In addition to the basic effects of I_h and I_T that are observed following the injection of predetermined current pulses (i.e. Figs. 1 and 2), these ionic currents can also combine to generate spontaneous intrinsic membrane potential oscillations at ~1–2 Hz (Fig. 3A) (Leresche et al. 1990, 1991; McCormick and Pape 1990). These oscillations are often referred to as δ or pacemaker oscillations and consist of rhythmic LTCPs separated by a slow I_h-dependent depolarization (Fig. 3A and B, top; Fig. 4A, top left). The fundamental importance of I_h in generating δ oscillations can be readily demonstrated by first abolishing this activity with the I_h blocker, ZD7288 (Fig. 3B, middle), and then showing that the subsequent introduction of an artificial I_h using the dynamic clamp is sufficient to reinstate it (Fig. 3B, bottom) (Hughes, Cope and Crunelli 1998).

3.2 *Mimicking the Neuromodulation of* I_h *Alters the Propensity of TC Neurons to Generate Intrinsic* δ *Oscillations*

The capacity to selectively block endogenous I_h with ZD7288 and then recreate δ oscillations with an artificial analogue is extremely useful because it enables us to examine how the ability of TC neurons to generate these oscillations is affected by altering various properties of I_h. This is important because I_h in

Fig. 1 Introduction of artificial I_h accurately reproduces the depolarizing 'sag' potential in TC neurons. A. Voltage responses of a TC neuron from the cat LGN to negative current steps in control conditions (*top*), in the presence of ZD7288 (*middle*) and following the introduction of artificial I_h (g_h = 2 nS) (*bottom*). The block of I_h by ZD7288 was accompanied by a 3 mV hyperpolarization that was offset by steady current injection in the middle panel. The artificial I_h used to reinstate the typical depolarizing 'sag' response is shown in the lower traces of the bottom panel. Note that during the smallest voltage responses in the top and bottom panel an LTCP (truncated for clarity) is evoked. The plots to the right demonstrate the accuracy of the dynamic clamp in reconstructing the peak (∇) and steady-state ($\bullet$) voltage–current relationships. **B**. Overlay of the voltage responses from **A** to the two largest negative current steps during control conditions (*continuous line*) and in ZD7288 and artificial I_h (*dashed line*) indicates the ability of the dynamic clamp to accurately reproduce the effects of endogenous I_h. (Note: in this and subsequent figures the amplitude of action potentials may have been truncated for clarity.) Reproduced from Hughes, Cope and Crunelli 1998 with permission

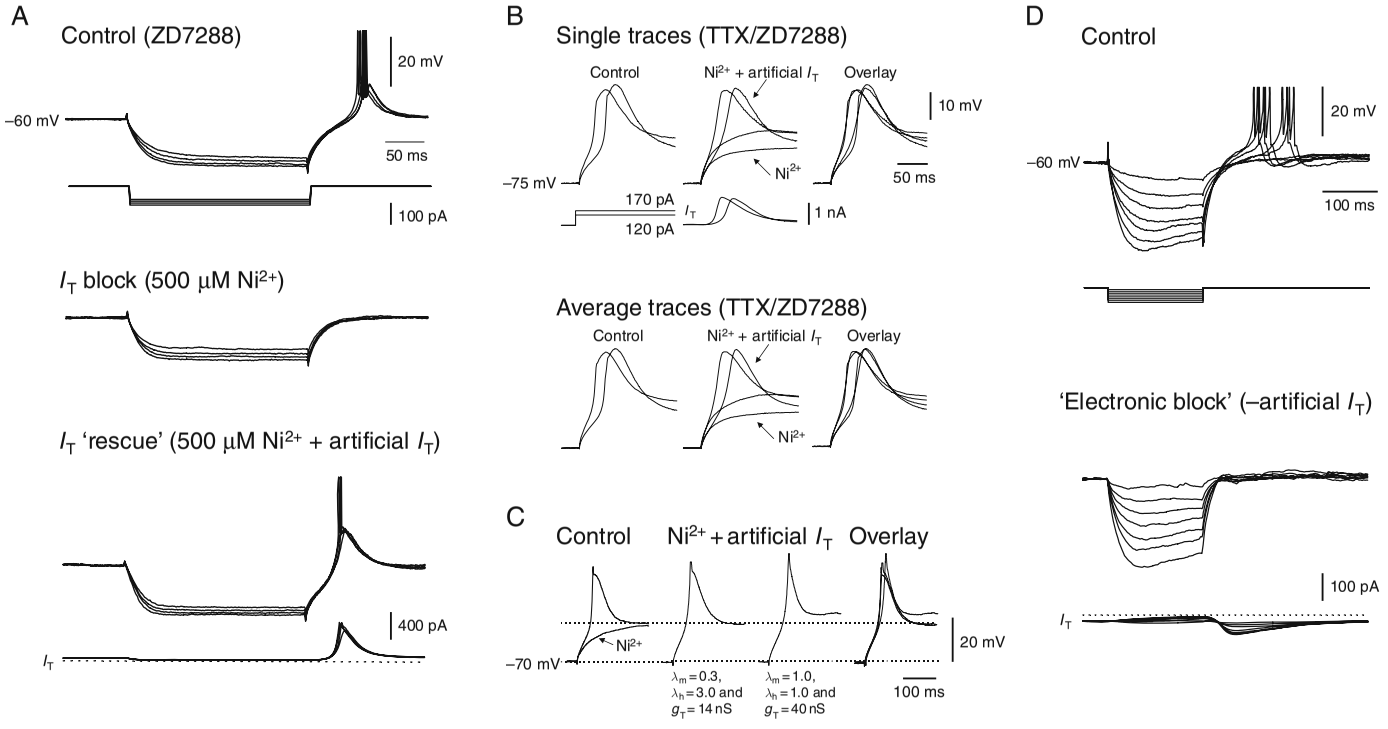

Fig. 2 Accurate reproduction and 'electronic block' of the LTCP with artificial I_T. A. Voltage responses of a TC neuron in the cat LGN show a characteristic LTCP and associated burst of action potentials at the offset of negative current steps, i.e. a rebound burst (*top traces*). This LTCP is blocked by 0.5 mM Ni^{2+} (*middle trace*) but can be reinstated following the introduction of an artificial I_T (g_T = 50 nS, *bottom traces*). ZD7288 was

TC neurons is a common postsynaptic target of several modulatory neurotransmitters that are thought to be involved in maintaining brain activation and wakefulness such as 5-HT, noradrenaline and histamine (McCormick 1992). These neurotransmitters typically act by shifting the steady-state activation curve of I_h in the depolarizing direction. As such, there is a prevailing assumption that because this leads to a steady depolarization of the membrane potential towards single spike activity (i.e. tonic firing), it has a simplistic anti-oscillatory effect. However, because TC neurons can be subject to simultaneous hyperpolarizing influences it is important to determine not only the effect of I_h modulation on steady membrane potential but also its effect on the basic ability of TC neurons to generate oscillations. To do this, we performed a series of experiments in the presence of ZD7288 where we introduced an artificial I_h with various physiological values of the maximal conductance (i.e. g_h) and half-activation voltage ($V_{½}$) into TC neurons. Then, as a basic measure of their stability, we examined the range of steady current values for which δ oscillations were present for these various values (Figs. 3C and D) (Hughes, Cope and Crunelli 1998). In doing so we found that (1) δ oscillations are most stable when the $V_{½}$ value of I_h is towards the upper end of the physiological range (i.e. –60 to –55 mV) (Fig. 3C and D), and (2) for all values of $V_{½}$ where oscillations are present there is an optimal value of g_h (around 10 nS) for which they occur over the largest current range (Fig. 3C and D). Thus, although positive shifts in the steady-state activation curve of I_h move the membrane potential away from the range of voltages where δ oscillations spontaneously occur, the stability of these oscillations, as induced by the subsequent injection of steady hyperpolarizing current, is in the main increased.

Fig. 2 (continued) present during this experiment. **B**. Removal of the LTCP in a cat LGN TC neuron following Ni^{2+} and its 'rescue' with artificial current (g_T = 45 nS). In this example the experiment was performed in the presence of TTX (1 μM) and ZD7288 (300 μM) to minimize contamination of the LTCP by other currents. The *top panel* shows single traces whereas the *bottom panel* depicts averages of three traces. Each set of traces was generated by applying the same current step protocol. **C**. Voltage response of a different cat LGN TC neuron to a positive current step of amplitude 100 pA in control conditions, and following the application of Ni^{2+} and introduction of artificial I_T. Although not necessary in all cases, the most accurate reproduction of the LTCP in this cell was achieved by altering kinetic scaling factors, λ_m and λ_h (*third trace from the left*, as indicated), rather than simply increasing g_T (*second trace from the left*) (see Hughes et al. 2008). Again, this experiment was performed in the presence of TTX (1 μM) and ZD7288 (300 μM). **D**. Voltage response of a rat LGN TC neuron to negative current steps in control conditions (*top*), and following the introduction of artificial negative I_T (*bottom*) (g_T = –25 nS). The applied current step protocol was the same in both panels. Note how application of reverse I_T in the bottom panel blocks LTCP generation for all current steps. **A** and **C** modified from Hughes et al. (2008). **B** and **D** modified from Hughes et al. (1999)

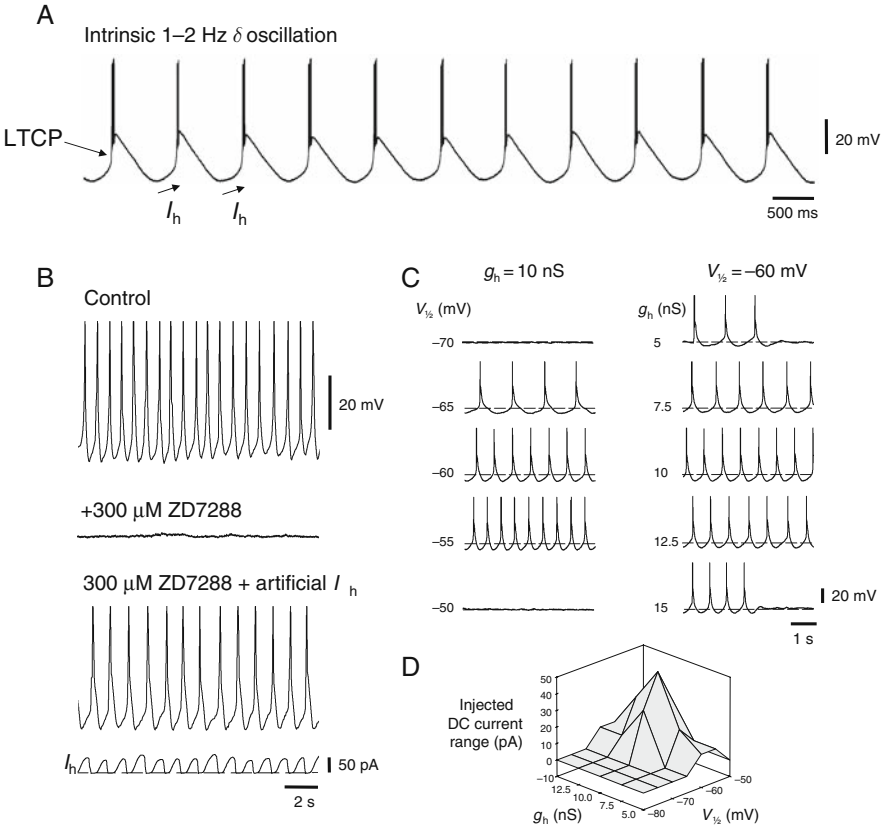

Fig. 3 Role of I_h, and its modulation, in shaping intrinsic δ oscillations. A. Example of the intrinsic δ oscillation in a cat LGN TC neuron recorded in vitro. **B**. The intrinsic δ oscillation in another cat LGN TC neuron (*top*) is abolished by ZD7288 (*middle*) but is reinstated following the introduction of artificial I_h (g_h = 10 nS) (*bottom*). **C**. *Left column*: traces showing the activity of a cat LGN TC neuron in the presence of ZD7288 and following the introduction of an artificial I_h, where g_h is kept constant at 10 nS but $V_{½}$ is varied from −70 to −50 mV. *Right column*: same neuron but with an artificial I_h, where $V_{½}$ is kept constant at −60 mV but g_h is varied from 5 to 15 nS. **D**. Plot showing the range of steady current values for which δ oscillations were present for different physiological values of $V_{½}$ and g_h. Modified from Hughes, Cope and Crunelli 1998

3.3 *The Amplitude of I_T is Critical in the Generation of δ Oscillations*

The dynamic-clamp technique can also be used to demonstrate the essential role of I_T in δ oscillations. For example, these oscillations can be readily abolished by introducing an artificial negative I_T into TC neurons in order to bring about an effective suppression of endogenous I_T (Fig. 4A$_2$). Again, a beneficial aspect of this type of experiment is the ability to finely control the amount of negative

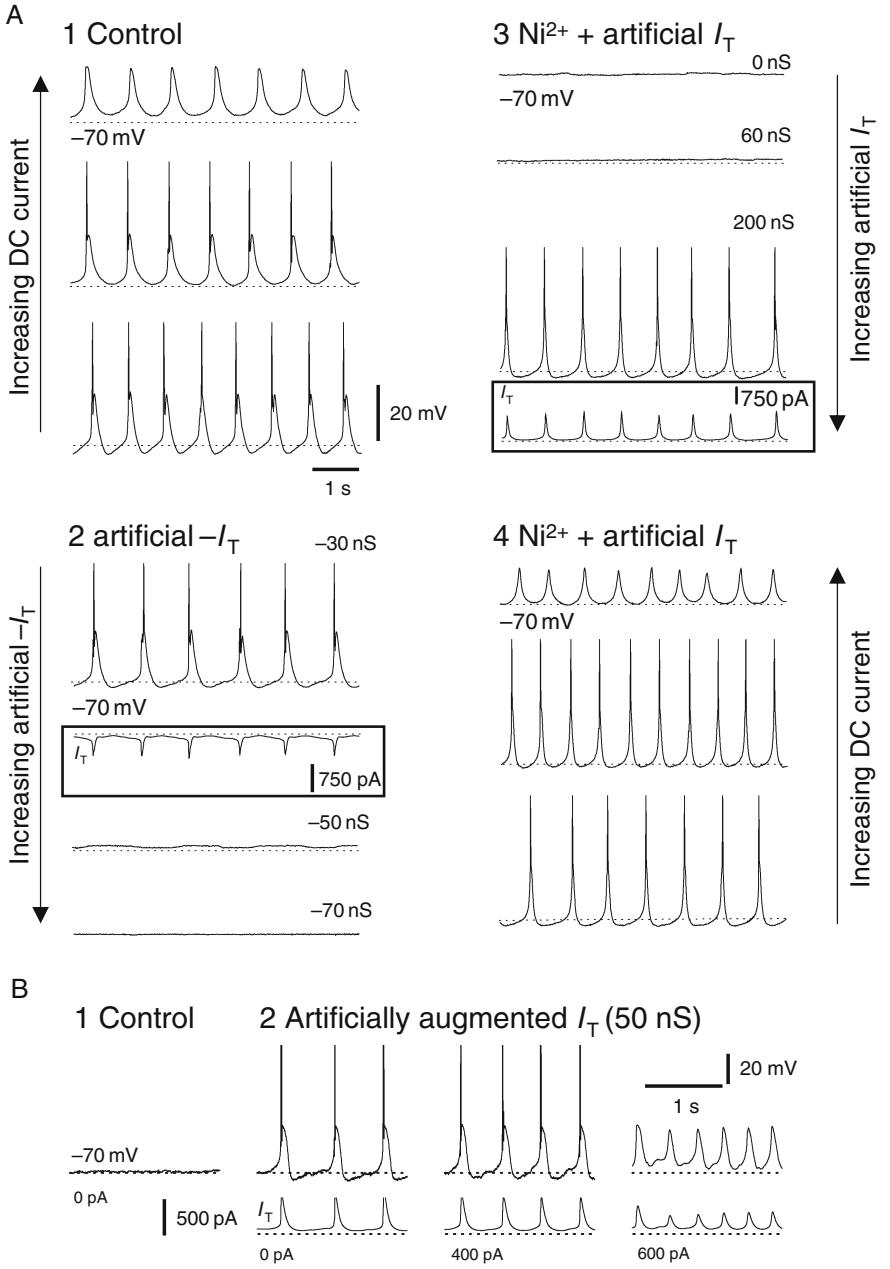

Fig. 4 Using the dynamic clamp to probe the essential role of I_T in δ oscillations. A. **1**: Intrinsic δ oscillations in a cat LGN TC neuron at various levels of steady injected current (increasing from *bottom to top* as indicated). 2: Suppression of δ oscillations following the introduction of increasing amounts of artificial reverse I_T as indicated. **3**: δ oscillations are also abolished following the application of Ni^{2+} (*top trace*) but can be reinstated following an introduction

I_T being introduced as this allows us to assess the amount of artificial conductance needed to 'just abolish' oscillations (Fig. $4A_2$). After a full block of endogenous I_T with Ni^{2+} we can then compare this value with the amount of artificial positive I_T needed to fully reinstate δ oscillations (Fig. $4A_3$ and A_4). Typically, we find that the amount of artificial reverse I_T needed to prevent δ oscillations is approximately 25% of that needed to bring about realistic δ oscillations in the presence of Ni^{2+} (Fig. $4A_3$ and A_4). This type of experiment clearly indicates that for δ oscillations to occur, the conductance of I_T must exceed a certain threshold and suggests that in TC neurons that are unable to exhibit this form of spontaneous rhythmic activity, boosting I_T should bring it about. Indeed, we find that artificially enhancing endogenous I_T through the addition of ~30–50 nS artificial I_T provides a reliable way to convert non-oscillating TC neurons into oscillating cells (Fig. 4B).

4 Role of the T-type Ca^{2+} 'Window' Current in the Slow (<1 Hz) Oscillation and Intrinsic Bistability in TC Neurons

4.1 The Slow (<1 Hz) Oscillation and Intrinsic Bistability in a Subset of TC Neurons

During our investigations into the intrinsic electrophysiological properties of TC neurons we have noted that, in addition to generating conventional δ oscillations, a subset of cells also exhibit a slow (<1 Hz) oscillation comprising rhythmic LTCPs that are followed by a pronounced 'shoulder' (Fig. 5A) (Williams et al. 1997a; Hughes et al. 1999). Interestingly, in these cells, blocking I_h with ZD7288 converts this oscillation into membrane potential bistability whereby neurons are able to exhibit two distinct membrane potentials for the same level of steady injected current (Fig. 5B) (Williams et al. 1997a). These two levels typically reside at around –80 and –60 mV and can be switched between by inducing small voltage perturbations through the injection of brief current steps. Through a combination of experiments (Williams et al. 1997a) and modelling work (Tóth, Hughes and Crunelli 1998), we have been able to deduce that this unusual form of bistability is generated by an interaction between the

Fig. 4 (continued) of sufficient artificial I_T as indicated. **4**: The variation in frequency and appearance of δ oscillations with respect to different levels of steady current injection during introduction of artificial I_T are similar to those observed in control conditions. Increasing steady current is from *bottom to top*. In this panel, for voltage traces the *dotted line* represents –70 mV whereas for current traces (i.e. I_T) the *dotted line* represents 0 pA. **B**. Following the introduction of a small amount of artificial I_T, the activity of a non-oscillating rat LGN TC neuron (1) is mod∞ified to include δ oscillations (2). The *dotted line* represents 0 pA. In 2, increasing steady current is from *left to right*

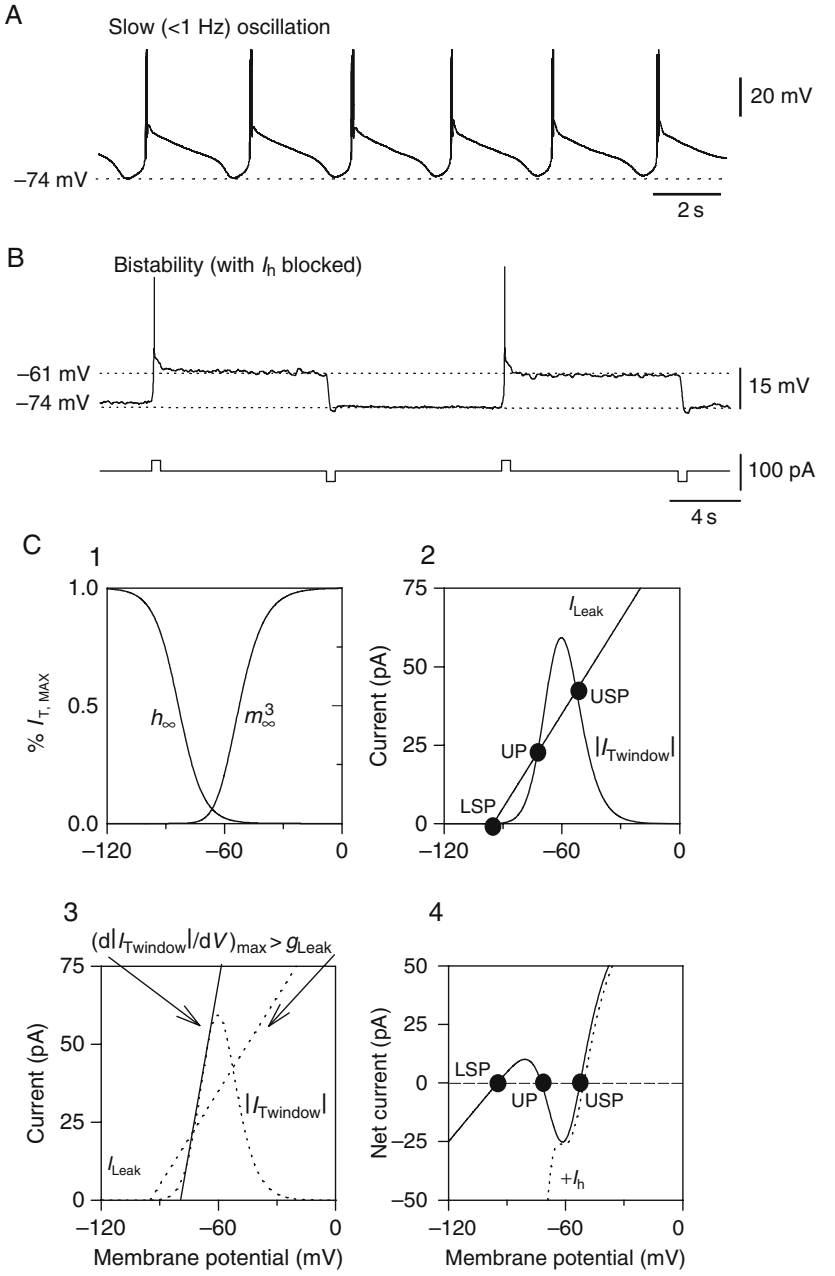

Fig. 5 The slow (<1 Hz) oscillation and membrane potential bistability in TC neurons. A. Example of the slow (<1 Hz) oscillation recorded from a TC neuron in the cat LGN in vitro. **B**. Following a block of I_h with ZD7288 the slow oscillation is converted into membrane potential bistability. **C**. **1**: Steady-state activation (m_∞^3) and inactivation (h_∞) curves for I_T

leak K^+ current, I_{Leak}, and the 'window' component of I_T (i.e. the current that is formed by the overlap in the steady-state activation and inactivation curves and denoted as $I_{Twindow}$) (Fig. $5C_1$ and $5C_2$). In mathematical terms, this bistability will exist for some value of steady injected current if, and only if, the maximal gradient with respect to membrane potential (V) of the absolute magnitude of $I_{Twindow}$ exceeds the leak conductance, g_{Leak}, i.e. $(d|I_{Twindow}|/dV)_{max} > g_{Leak}$ (Fig. $5C_3$) (Tóth, Hughes and Crunelli 1998; Hughes et al. 1999; Crunelli et al. 2005). An alternative way to view this condition is to note that bistability will exist when the ratio of I_T to I_{Leak} conductance (i.e. g_T/g_{Leak}) exceeds $1/[d(\theta|(V-E_T)|)/dV]_{max}$, where θ is the product of steady-state inactivation and the nth power of activation for I_T and E_T is the reversal potential of I_T. In theory, any neuron that expresses a T-type Ca^{2+} current that meets this simple condition should be able to exhibit membrane potential bistability or some form of bistability-associated phenomenon (see Izhikevich 2007). More importantly, however, it suggests that the reason why the majority of TC neurons do not display a slow oscillation and bistability is either because they express a fundamentally different I_T which exhibits negligible overlap between its steady-state activation and inactivation curves (i.e. lack of appreciable $I_{Twindow}$), or simply that they possess an insufficiently large g_T or excessively large g_{Leak} (Fig. 5C).

4.2 *Artificially Augmenting I_T or Reducing I_{Leak} Brings About the Slow (<1 Hz) Oscillation and Intrinsic Bistability in all TC Neurons*

To determine conclusively whether the majority of TC neurons do not exhibit the slow (<1 Hz) oscillation and membrane potential bistability because of a

Fig. 5 (continued) (Crunelli, Lightowler and Pollard 1989). $I_{T\infty}$ exists as the result of an area of overlap between the two curves. **2**: Plot of $|I_{T\infty}|$ and I_{Leak} vs. membrane potential. **3**: same plot as in **B** showing the tangent $(d|I_{T\infty}|/dV)_{max}$ to $I_{T\infty}$ as a continuous line. **4**: Plot of net current ($I_{T\infty} + I_{Leak}$, *continuous line*; $I_{T\infty} + I_{Leak} + I_h$, *dotted line*) vs membrane potential. If the value of g_{Leak} is smaller than $(d|I_{T\infty}|/dV)_{max}$ then, in the absence of I_h, for some steady current value there will exist three points at which the net current is zero. The upper (USP) and lower (LSP) of these equilibrium points are stable attractors since following small perturbations around them, the system will be returned to these points. The remaining equilibrium point (UP) however is unstable. The mechanism is easily illustrated by considering hyperpolarizing voltage deviations elicited from USP. For those deviations that are too small to reach UP the membrane potential will return to USP since the balance of membrane current remains inwards. In contrast, voltage excursions of sufficient amplitude to cross UP will activate a further hyperpolarization towards LSP owing to a net outward current. The membrane potential is only prevented from reaching (or remaining at) LSP by the activation of I_h (*dashed line*). In **D**, the *dotted line* indicating the net current in the presence of I_h has been slightly offset to the right for clarity. Modified from Hughes et al. (1999)

fundamentally distinct I_T or because they express a g_T/g_{Leak} ratio that is simply below the appropriate threshold, we used the dynamic-clamp technique to introduce either an artificial I_T in order to augment the total effective g_T, or an artificial negative I_{Leak} so that we could decrease the overall effective g_{Leak}. In all cases, sufficient injection of positive artificial I_T (above that required to induce δ oscillations) or negative I_{Leak} brought about a slow oscillation (Fig. 6A and B) (Hughes et al. 1999). Furthermore, when I_h was blocked, these manipulations led to membrane potential bistability (Fig. 6C and D). Overall, in order to bring about a slow oscillation or membrane potential bistability by introducing a positive artificial I_T or a negative artificial I_{Leak}, an approximate doubling of the g_T/g_{Leak} ratio was consistently required (Hughes et al. 1999). In

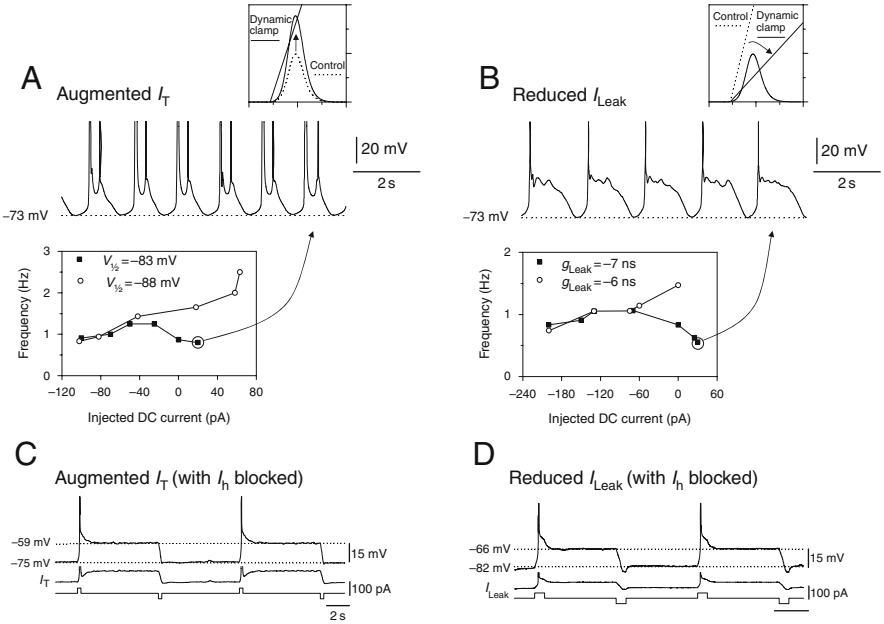

Fig. 6 Inducing the slow (<1 Hz) oscillation in TC neurons by artificially manipulating the effective g_T/g_{Leak} ratio. A. Slow oscillation induced in an LGN TC neuron following an artificial enhancement of I_T (g_T = 100 nS, schematically depicted in the *top right* corner of this panel). The atypical form of the frequency–current relationship (i.e. initial increase in frequency followed by a decrease) can be transformed to the conventional pattern for δ oscillations (i.e. steady increase in frequency) (Williams et al. 1997) by reducing $I_{T\infty}$ via a small negative shift (−5 mV) in the half-inactivation voltage ($V_{½}$) of artificial I_T. **B**. Slow oscillation unveiled in the same TC neuron shown in A following addition of artificial reverse I_{Leak} (g_{Leak} = −7 nS, schematically depicted in the top right corner of this panel). Following injection of a slightly smaller amount of artificial inward I_{Leak} (g_{Leak} = −6 nS) the neuron displayed δ oscillations with a characteristic frequency–current relationship. **C** and **D**. Membrane potential bistability induced in two different TC neurones in the presence of ZD7288 (300 ¼M) following the addition of artificial I_T (g_T = 100 nS), and artificial reverse I_{Leak} (g_{Leak} = −7 nS), respectively. Modified from Hughes et al. (1999)

other words, we either needed to artificially double the effective g_T or artificially halve the effective g_{Leak}. Importantly, for the introduction of artificial I_T, the attainment of a slow oscillation and membrane potential bistability could not be attributed merely to the interaction of artificial $I_{Twindow}$ and endogenous I_{Leak}. Thus, both types of experiments indicate that all TC neurons express a substantial endogenous $I_{Twindow}$ that under appropriate conditions can underlie a slow oscillation or membrane potential bistability (Hughes et al. 1999). Such a suggestion is also supported by recent molecular cloning and expression studies showing that recombinant channels formed by the alpha subunit responsible for the pore forming domain of T-type Ca^{2+} channels in TC neurons, i.e. α1G or CaV3.1, exhibit a substantial 'window' component (Perez-Reyes 2003; see also Crunelli et al. 2005; Crunelli, Cope and Hughes 2006). Lastly, it should also be noted in this section that whilst the slow oscillation waveform brought about by artificially reducing the effective g_{Leak} (Fig. 6A) was very similar to that observed in a small proportion of TC neurons in control conditions (i.e. Fig. 5A), the waveform of the oscillation brought about by artificially increasing the effective g_T (Fig. 6B) was notably different. This suggests that cells which exhibit a slow oscillation without any artificial manipulation probably express a lower than normal inherent g_{Leak} rather than a larger than average endogenous g_T (Hughes et al. 1999).

4.3 Accurate Prediction of Bistable Voltage Levels in TC Neurons Using a Simple Mathematical Model

Because the two stable voltage levels exhibited during membrane potential bistability correspond directly to the upper and lower stable equilibrium points shown in Fig. $5C_4$, in cases where artificial I_T is used to replace entirely the endogenous I_T that has been blocked by Ni^{2+}, it should be possible to accurately predict these levels based on the amount of artificial I_T, the steady injected current and an estimate of the endogenous g_{Leak} (taken as the reciprocal of the apparent input resistance). This is indeed the case (Fig. 7) (Hughes et al. 1999) and confirms that the $I_{Twindow}$-based model of intrinsic bistability in TC neurons depicted in Fig. 5C correctly and realistically describes the subthreshold behaviour of these cells (Tóth, Hughes and Crunelli 1998).

4.4 Activation of mGluRs on TC Neurons also Brings About the Slow (<1 Hz) Oscillation and Membrane Potential Bistability

During deep sleep and some types of anaesthesia, TC neurons in the intact brain also exhibit a slow (<1 Hz) oscillation (Steriade, Contreras and Curro Dossi 1993; Contreras and Steriade 1995; Steriade, Amzica and Contreras 1996; Hughes et al. 2004). Furthermore, this oscillation is virtually indistinguishable

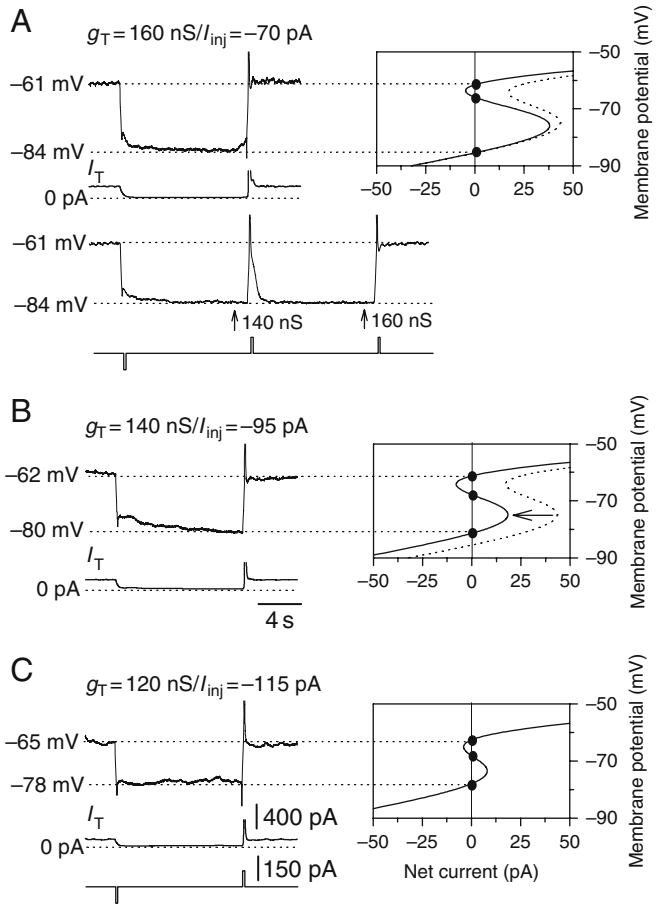

Fig. 7 Accurate prediction of bistable voltage levels in TC neurons. A, **B** and **C**. Voltage traces obtained from a cat LGN TC neuron in the presence of Ni^{2+} (0.5 mM) and ZD7288 (300 ¼M) show the two resting membrane potentials to match accurately the points of which the net current is zero in the voltage vs. net current plot (*continuous line* in plot), constructed using this neuron's g_{Leak}, the indicated artificial I_T and injected steady current (I_{inj}). Note that a decrease in artificial I_T from 160 to 140 nS without an accompanying change in I_{inj} failed to elicit bistability (*left arrow* in bottom voltage record) since only one equilibrium point was present for this combination of g_{Leak}, artificial I_T and I_{inj} (*dashed line* in plots in **A** and **B**). Membrane potential bistability could be reinstated for an artificial I_T of 140 nS when I_{inj} was changed from −70 to −95 pA (*continuous line* in **B**), or for an even smaller I_T and I_{inj} of −115 pA (**C**). Current calibrations in **C** also apply to **A** and **B** and time calibration in **B** applies to **A** and **C**. Reproduced from Hughes et al. (1999) with permission

from the one induced by artificially reducing I_{Leak} in vitro using the dynamic clamp (i.e. Fig. 6B) (Hughes et al. 1999). Interestingly, the slow oscillation in the intact brain is abolished by removing cortical input (Timofeev and Steriade 1996). This is striking because this input is known to activate metabotropic glutamate receptors (mGluRs) on TC neurons which are negatively coupled to

I_{Leak} (Godwin et al. 1996; von Krosigk et al. 1999; Turner and Salt, 2000; Hughes et al. 2002; Zhu et al. 2006). This led us to hypothesize that reactivation of the mGluR component of cortical input to TC neurons would, by virtue of sufficiently reducing I_{Leak}, bring about a slow oscillation in TC neurons in vitro (Hughes et al. 1999). Indeed, bath application of either of the mGluR agonists 1-Aminocyclopentane-trans-1,3-dicarboxylic acid (*trans*-ACPD) or 3,5-dihydroxyphenylglycine (DHPG) brings about a slow oscillation in more than 70% of TC neurons recorded in vitro (Fig. 8A) (Hughes et al. 2002; Zhu et al. 2006; see also Blethyn et al. 2006). Furthermore, blocking I_h in these cells with ZD7288 reveals membrane potential bistability in all cases (Fig. 8B) (Hughes et al. 2002).

In most TC neurons, in order to observe a slow oscillation following mGluR activation (or for that matter after introducing negative I_{Leak}) it is necessary to counteract the tonic depolarization brought about by this manipulation by

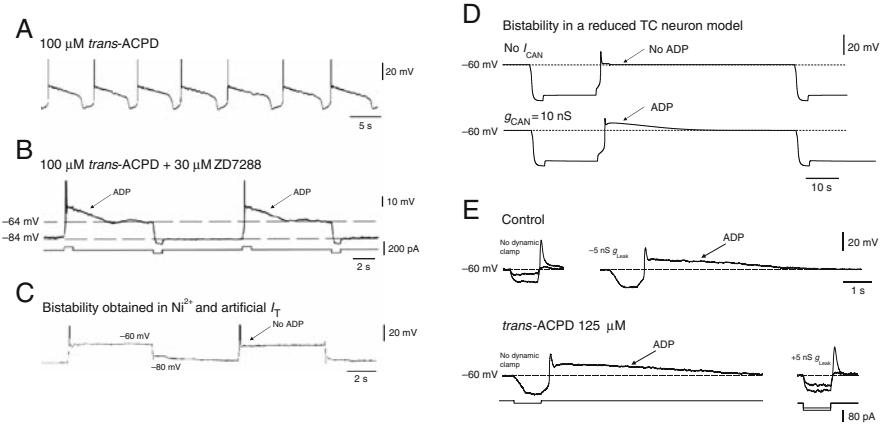

Fig. 8 An mGluR-induced reduction in I_{Leak} also causes a slow (<1 Hz) oscillation and membrane potential bistability and reveals a prominent ADP. A. Slow oscillation brought about in an LGN TC neuron by the mGluR agonist, *trans*-ACPD (100 μM). **B**. Membrane potential bistability observed in a cat LGN TC neuron in the presence of *trans*-ACPD and ZD7288. Note the presence of a pronounced ADP following the LTCPs which occur at the transition from the lower to upper stable voltage level. **C**. ADPs are not present during bistability that is brought about solely by artificial I_T injection during a block of endogenous current with Ni^{2+}. **D**. *Top*: bistability in a simplified TC neuron model possessing only I_T and I_{Leak} does not exhibit an ADP. Bottom: the addition of I_{CAN} to the model gives rise to an ADP. **E**. *Top left trace*: voltage responses of an LGN TC neuron to small hyperpolarizing current steps (−20 and −40 pA) in control conditions. *Top right trace*: following an artificial reduction in I_{Leak} using the dynamic clamp (artificial $g_{Leak} = -5$ nS), the neuron displays an increase in apparent resistance and a prominent ADP (response shown is to a −20 pA current step). *Bottom left trace*: following *trans*-ACPD application the same neuron exhibits identical behaviour as during the dynamic-clamp-induced I_{Leak} reduction (response shown is to a −20 pA current step). *Bottom right trace*: a subsequent artificial increase in g_{Leak} (artificial $g_{Leak} = 5$ nS) causes the neuron to revert to activity identical to that observed in control conditions. TTX (1 μM) was also present in the recording medium during this experiment. Part E modified from Hughes et al. (2002)

injecting steady hyperpolarizing current (Hughes et al. 2002, 2004; Zhu et al. 2006). This means that as with the effect of positively shifting the activation curve of I_h (see above), although reducing I_{Leak} moves the membrane potential of TC neurons away from the region where the slow oscillation occurs, it increases the basic capacity of these cells to exhibit this activity.

5 A Ca^{2+}-Activated Non-selective Cation Current Generates a Prominent After-Depolarization that Stabilizes the Slow (<1 Hz) Oscillation in TC Neurons

5.1 mGluR Activation Reveals a Pronounced ADP that is Generated by a Ca^{2+}-Activated Non-selective Current

During experiments where we induced membrane potential bistability with either artificial negative I_{Leak} (Hughes et al. 1999) or mGluR agonists (Hughes et al. 2002), we noted that the LTCP that is present at the transition from the lower to upper stable voltage level was followed by prominent after-depolarization (ADP) lasting several seconds (Fig. 8B). Interestingly, however, this ADP was not present in cases where bistability was brought about solely with artificial I_T (Fig. 8C) (Hughes et al. 1999). It was also absent from simulations performed with a reduced TC neuron model possessing only I_{Leak} and I_T (Fig. 8D, top). Because artificial I_T provides a good replica of endogenous current except that it obviously does not involve any real Ca^{2+} influx, we hypothesized that the ADP is generated by some type of Ca^{2+}-dependent current. Indeed, through a series of voltage-clamp experiments and pharmacological manipulations we were able to show that the ADP is produced by a Ca^{2+}-activated non-selective (CAN) cation current (Hughes et al. 2002).

Importantly, regardless of whether an ADP is brought about by an artificial reduction in I_{Leak} or through an equivalent mGluR-induced reduction in I_{Leak} (matched by their respective effects on apparent input resistance), its duration and amplitude are indistinguishable (Fig. 8E) (Hughes et al. 2002). This strongly suggests that the I_{CAN}-generated ADP is a latent property of TC neurons that is unmasked by a simple mGluR-mediated reduction in I_{Leak} rather than being 'switched on' or facilitated by a cascade of mGluR-initiated intracellular events.

5.2 The CAN Current is Critical for Stabilizing the Slow (<1 Hz) Oscillation in TC Neurons

As would be expected, addition of I_{CAN} to the reduced TC neuron model introduces a realistic ADP to simulations of membrane potential bistability (Fig. 8D, bottom). More importantly, however, it transpires that in a more

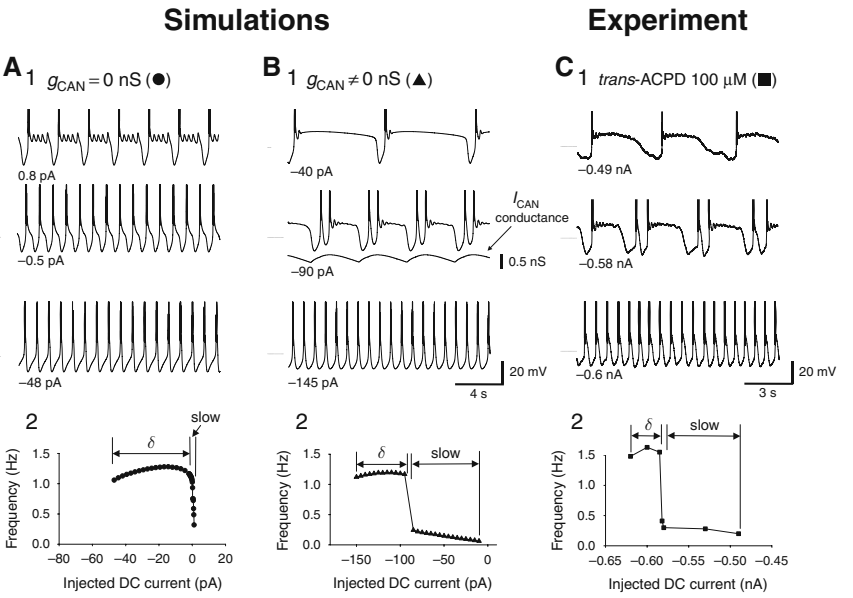

Fig. 9 I_{CAN} **is essential for stablizing the slow(<1 Hz) oscillation. A**. In the absence of I_{CAN} (i.e. $g_{CAN} = 0$ nS), a model TC neuron with $g_{Leak} = 1.5$ nS exhibits a slow oscillation (**1**), but only for a very narrow range of DC current inputs ('slow' in **2**). **B**. With $g_{CAN} = 10$ nS, the model exhibits a slow oscillation over a much greater range of steady current inputs (**1** and **2**). Furthermore, in this condition the model displays oscillations that closely match those observed in experiments (**C**). Reproduced from Hughes et al. (2002) with permission

realistic TC neuron model which also possesses Na^+ and K^+ action potential generating currents and I_h, the presence of I_{CAN} is crucial for stabilizing the slow (<1 Hz) oscillation (Hughes et al. 2002). Specifically, in the absence of this current a slow oscillation can be observed in the model but for such a narrow range of steady current levels that it is essentially a theoretical concept only (Fig. 9A). Also, the slow oscillation in this condition does not closely mimic the qualitative properties of experimentally observed oscillations (i.e. Fig. 9C). However, following the addition of I_{CAN}, the model exhibits a slow oscillation over a wide range of steady current levels and has an appearance and general properties which closely match those observed in experiments (Fig. 9B).

6 Future Directions

Thus far, most investigators have used the dynamic-clamp technique to introduce small numbers of 'virtual' ion channels to the soma of single cells, i.e. along the lines described above, or to construct small hybrid neuronal circuits comprising a limited number of cells. However, this approach largely ignores two

obvious and fundamental aspects of the architecture of real neurons and neuronal networks: (1) that neurons are spatially extended structures that possess complex branching dendritic trees and (2) that neurons are embedded in networks of many thousands of cells. In our view, the challenge for the next generation of dynamic-clamp tools and experiments is therefore to more realistically take these factors into account. Recently, we performed a group of experiments in TC neurons which demonstrated the viability of extending the normal operation of the dynamic-clamp technique in two strategic ways. Firstly, we showed how the dynamic clamp can be used to 'attach' artificial, i.e. simulated, dendritic tree structures, comprising multiple compartments and various active ionic conductances, to real neurons (Fig. 10) (Hughes et al. 2008; Dorval, Christini and White 2001; Debay et al. 2004). Specifically, we showed how action potentials that are generated in real TC neurons differentially backpropagate down an artificial dendritic tree in the absence and presence of specific active conductances (Fig. 10A). We also showed how realistic somatic δ oscillations (see Fig. 4) can be be brought about by attaching multiple artificial

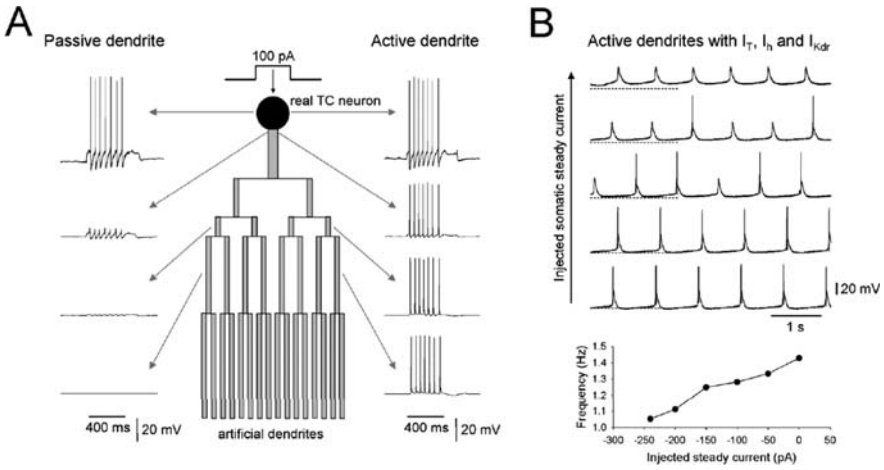

Fig. 10 Adding artificial dendrites to real TC neurons. A. *Left column*: series of traces at different locations, as indicated by the *grey arrows*, showing the response of a TC neuron following the attachment of the illustrated artificial dendritic tree to a 100 pA positive current pulse injected at the soma. Note how action potentials are rapidly attenuated in the dendritic tree. *Right column*: same experiment but following the addition of an inactivating Na^+ current (I_{Na}, 25 mS/cm^2) and delayed rectifier K^+ current (I_{Kdr}, 12 mS/cm^2) to the dendrites action potentials show a minimal decline in amplitude even at fairly distal sites. **B**. Attachment of eight identical artificial dendritic trees (same geometry as in **A**) possessing I_T (2 mS/cm^2), I_h (0.5 mS/cm^2) and I_{Kdr} (2 mS/cm^2) to a TC neuron which did not show any oscillatory activity in control conditions brings about realistic somatic δ oscillations. The conventional pattern in the change in frequency of these oscillations with respect to varying steady current injection at the soma is shown below. Modified from Hughes et al. (2008)

dendritic trees with a high density of I_T, moderate density of I_h and small amount of delayed rectifier K^+ current, i.e. I_{Kdr} (Fig. 10B) (see Emri et al. 2000). Secondly, we demonstrated the feasibility of constructing hybrid neuronal networks that can contain large quantities of biophysically realistic simulated cells (Hughes et al. 2008) (Fig. 11). In particular, we showed how a

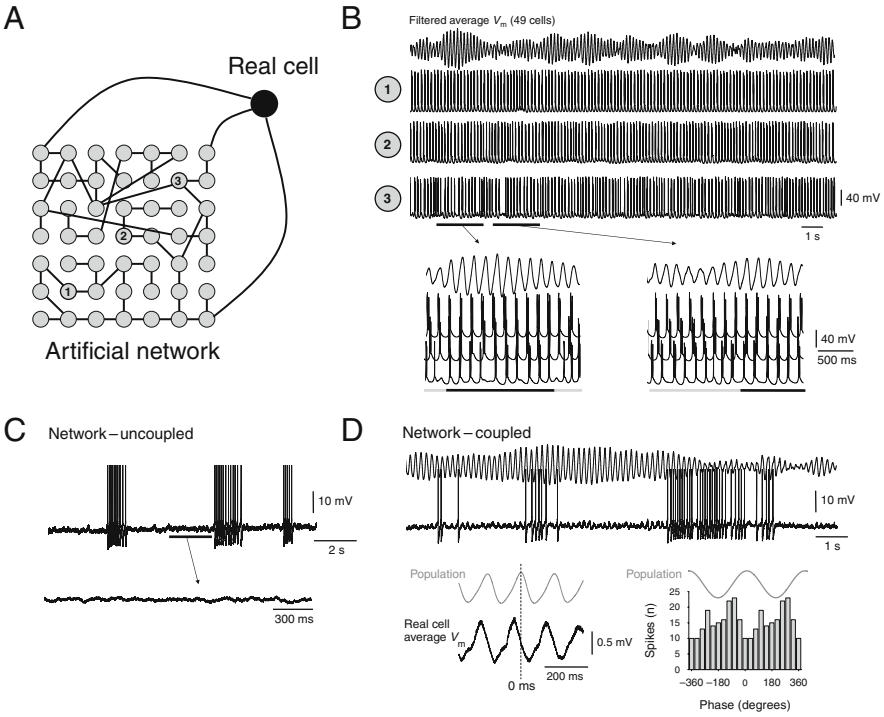

Fig. 11 Implementation of a large hybrid network using the dynamic clamp. A. Schematic representation of a large hybrid network implemented using the dynamic clamp. The simulated part consists of 49 HT burst cells (*filled grey circles*) connected randomly by electrical synapses as indicated. The real TC neuron (*filled black circle*) is connected to three distinct HT burst cells, also by electrical synapses. The conductance of all electrical synapses was 500 pS. **B**. Examination of the isolated HT burst cell network shows the population output (taken as the 2–15 Hz band-pass filtered average membrane potential of all cells) to be a waxing and waning oscillation at ~8 Hz (*top trace*). The three traces below show the activity of HT burst cells 1, 2 and 3. The enlarged sections further below show how periods of high-amplitude population activity are related to increased synchrony between HT burst cells (denoted by *a black bar* underneath the traces). **C**. Activity of a real tonic firing TC neuron in the absence of hybrid network input. **D**. Activity of the same cell when the hybrid network is attached. The population output is shown at the *top*. Note how the membrane potential of the real TC neuron is now modulated by the network input which is further demonstrated by the population triggered subthreshold membrane potential average shown to the *bottom left*. Note also how this modulation influences action potential timing as indicated by the histogram shown to the *bottom right*. Reproduced from Hughes et al. (2008) with permission

randomly connected network of high-threshold (HT) bursting TC neurons can generate a waxing and waning population rhythm in the α band (8–13 Hz) and modulate the firing of a real TC neuron that is connected to a small number of these HT bursting cells via electrical synapses (Hughes et al. 2004, 2008; Lőrincz, Crunelli and Hughes 2008). In short, broadening the dynamic-clamp concept in these ways is important because it provides a potentially novel avenue for investigating two technically demanding questions: (1) How does dendritic structure, and how do active dendritic conductances, affect the integrative properties of individual neurons? and (2) How are the properties of single neurons shaped by large-scale neuronal network activity?

7 Concluding Remarks

We have discussed how the dynamic clamp provides a useful means to gain an insight into the mechanisms and properties of certain forms of intrinsic oscillatory activity in TC neurons (Hughes, Cope and Crunelli 1998; Hughes et al. 1999, 2002, 2008; Blethyn et al. 2006). Specifically, we have illustrated how this technique can be used to (1) confirm that both I_h and I_T are essential for the generation of δ oscillations, (2) show that δ oscillations are optimally supported by a moderate conductance of I_h (around 10 nS), (3) indicate that in order for δ oscillations to be present, the conductance of I_T must be above a sizeable threshold, (4) demonstrate that all TC neurons possess the ability to exhibit the slow ($<$1 Hz) oscillation and membrane potential bistability given an appropriate setting of the g_T/g_{Leak} ratio, (5) show that such a setting can be achieved physiologically through an mGluR-induced reduction of I_{Leak}, an effect that probably occurs naturally in the intact brain through corticothalamic feedback and (6) reveal that TC neurons possess a CAN current that is critical for stabilizing the expression of the slow oscillation. We have also shown how the dynamic-clamp concept can be extended to more realistically take into consideration the spatial complexity of individual neurons and networks. Most fundamentally, our studies have demonstrated that all TC neurons express a non-negligible I_T 'window' current without which these cells would be unable to generate an intrinsic slow ($<$1 Hz) oscillation. We have also stressed the important distinction between the membrane potential region where TC neurons may be spontaneously positioned and the basic ability of these cells to generate oscillations. In conclusion, we believe the dynamic clamp to be an extremely valuable tool for probing the function and properties of neurons and other types of excitable cells and one which facilitates a whole range of experiments that would not be possible to carry out by other means.

Acknowledgements Our ongoing work is supported by the Wellcome Trust, grants 71436, 78403 and 78311.

Appendix

The majority of the work (i.e. Figs. 1, 2, 3, 4, 5, 6, 7, 8, 9) described in this chapter was carried out on a personal computer with MS-DOS based software written in a combination of C++ and assembler and using an Axon Instruments Digidata 1200 ADC/DAC system (Hughes, Cope and Crunelli 1998; Hughes et al. 1999, 2002). These experiments were typically performed at sampling/update rates of 10–20 kHz although rates of up to 50 kHz could be achieved. The experiments depicted in Figs. 10 and 11 were carried out with the NeuReal software system (Hughes et al. 2008). NeuReal is an interactive system that runs on Windows XP, is also written in a combination of C++ and assembler, and uses the Microsoft DirectX application programming interface (API) to achieve high-performance graphics. Whilst not being a hard real-time system, NeuReal offers reliable performance and tolerable jitter levels up to an update rate of 50 kHz. A key feature of NeuReal is that rather than being a simple dedicated dynamic clamp, it operates as a fast simulation system within which neurons can be specified as either real or simulated. By using the Digidata 1200 hardware-based representation of membrane potential at all stages of computation and by employing simple look-up tables (see also Butera et al. 2001), on a modern personal computer (PC) NeuReal can typically simulate over 1,000 independent Hodgkin and Huxley (Hodgkin and Huxley 1952)-type conductances in real-time. For example, on a PC possessing a 2.26 GHz Intel Pentium processor and 2 GB of RAM and for an integration step size of 0.1 ms, equivalent to an update/sampling rate of 10 kHz in a dynamic-clamp experiment, NeuReal can compute 2,070 independent activation/inactivation variables and, therefore, simulate 690 inactivating and 690 non-inactivating conductances at sub-real-time speeds.

References

Achermann P, Borbély AA (1997) Low-frequency (<1 Hz) oscillations in the human sleep electroencephalogram. Neuroscience 81:213–22.

Amzica F, Steriade M (1998) Cellular substrates and laminar profile of sleep K-complex. Neuroscience 82:671–86.

Blethyn KL, Hughes SW, Tóth TI et al. (2006) Neuronal basis of the slow (<1 Hz) oscillation in neurons of the nucleus reticularis thalami in vitro. J Neurosci 26:2474–86.

BoSmith RE, Briggs I, Sturgess NC (1993) Inhibitory action of zeneca ZD 7288 on whole-cell hyperpolarization activated inward current (I_f) in guinea-pig dissociated sinoatrial cells. Br J Pharmacol 110:343–49.

Butera RJ Jr, Wilson CG, Delnegro CA et al. (2001) A methodology for achieving high-speed rates for artificial conductance injection in electrically excitable biological cells. IEEE Trans Biomed Eng 48:1460–70.

Contreras D, Steriade M (1995) Cellular basis of EEG slow rhythms: A study of dynamic corticothalamic relationships. J Neurosci 15:604–22.

Coulter DA, Huguenard JR, Prince DA (1989) Calcium currents in rat thalamocortical relay neurones: kinetic properties of the transient, low-threshold current. J Physiol (London) 414:587–604.

Crunelli V, Cope DW, Hughes SW (2006). Thalamic T-type calcium channels and NREM sleep. Cell Calcium 40:175–90.

Crunelli V, Lightowler S, Pollard CE (1989) A T-type Ca^{2+} current underlies low-threshold Ca^{2+} potentials in cells of the cat and rat lateral geniculate nucleus. J Physiol (London) 413:543–61.

Crunelli V, Tóth TI, Cope DW et al. (2005) The 'window' T-type calcium current in brain dynamics of different behavioural states. J Physiol 562:121–29.

Debay D, Wolfart J, Le Franc Y et al. (2004) Exploring spike transfer through the thalamus using hybrid artificial-biological neuronal networks. J Physiol (Paris) 98:540–58.

Deschenes M, Paradis M, Roy JP et al. (1984) Electrophysiology of neurons of lateral thalamic nuclei in cat: resting properties and burst discharges. J Neurophysiol 51: 1196–219.

Destexhe A, Hughes SW, Rudolph M et al. (2007) Are corticothalamic 'up' states fragments of wakefulness? Trends Neurosci 30:334–42.

Dorval AD, Christini DJ, White JA (2001) Real-Time linux dynamic clamp: a fast and flexible way to construct virtual ion channels in living cells. Ann Biomed Eng 29:897–907.

Emri Z, Antal K, Tóth TI et al. (2000) Backpropagation of the delta oscillation and the retinal excitatory postsynaptic potential in a multi-compartment model of thalamocortical neurons. Neuroscience 98:111–27.

Godwin DW, Van Horn SC, Erisir A et al. (1996) Ultrastructural localization suggests that retinal and cortical inputs access different metabotropic glutamate receptors in the lateral geniculate nucleus. J Neurosci 16:8181–92.

Hernandez-Cruz A, Pape HC (1989) Identification of two calcium currents in acutely dissociated neurons from the rat lateral geniculate nucleus. J Neurophysiol 61:1270–83.

Hodgkin AL, Huxley AF (1952) A quantitative description of membrane current and its application to conduction and excitation in nerve. J Physiol (London) 117:500–44.

Hughes SW, Cope DW, Blethyn KL et al. (2002) Cellular mechanisms of the slow (<1 Hz) oscillation in thalamocortical neurons in vitro. Neuron 33:947–58.

Hughes SW, Cope DW, Crunelli V (1998) Dynamic clamp study of I_h modulation of burst firing and delta oscillations in thalamocortical neurons in vitro. Neuroscience 87:541–50.

Hughes SW, Cope DW, Tóth TI et al. (1999) All thalamocortical neurones possess a T-type Ca^{2+} 'window' current that enables the expression of bistability-mediated activities. J Physiol (London) 517:805–15.

Hughes SW, Lőrincz M, Cope DW et al. (2004) Synchronized oscillations at alpha and theta frequencies in the lateral geniculate nucleus. Neuron 42:253–68.

Hughes SW, Lőrincz ML, Cope DW et al. (2008) NeuReal: an interactive simulation system for implementing artificial dendrites and large hybrid networks. J Neurosci Methods 169:290–301.

Izhikevich EM (2007) Dynamical Systems in Neuroscience. The Geometry of Excitability and Bursting. MIT Press, Cambridge MA.

Jahnsen H, Llinás R (1984a) Electrophysiological properties of guinea-pig thalamic neurones: an in vitro study. J Physiol (London) 349:205–26.

Jahnsen H, Llinás R (1984b) Ionic basis for the electro-responsiveness and oscillatory properties of guinea-pig thalamic neurones in vitro. J Physiol (London) 349:227–47.

Leresche N, Jassik-Gerschenfeld D, Haby M et al. (1990) Pacemaker-like and other types of spontaneous membrane potential oscillations of thalamocortical cells. Neurosci Lett 113:72–7.

Leresche N, Lightowler S, Soltesz I et al. (1991) Low-frequency oscillatory activities intrinsic to rat and cat thalamocortical cells. J Physiol (London) 441:155–74.

Lopes da Silva FH, van Lierop TH, Schrijer CF et al. (1973) Organization of thalamic and cortical alpha rhythms: spectra and coherences. Electroencephalogr Clin Neurophysiol 35:627–39.

Lőrincz ML, Crunelli V, Hughes SW (2008) Cellular dynamics of cholinergically induced alpha (8–13 Hz) rhythms in sensory thalamic nuclei in vitro. J Neurosci 28: 660–71.
McCormick DA (1992) Neurotransmitter actions in the thalamus and cerebral cortex and their role in neuromodulation of thalamocortical activity. Prog Neurobiol 39:337–88
McCormick DA, Pape HC (1990) Properties of a hyperpolarization-activated cation current and its role in rhythmic oscillation in thalamic relay neurones. J Physiol (London) 431:291–318.
Pedroarena C, Llinás R (1997) Dendritic calcium conductances generate high-frequency oscillation in thalamocortical neurons. Proc Natl Acad Sci USA 21:724–8.
Perez-Reyes E (2003) Molecular physiology of low-voltage-activated t-type calcium channels. Physiol Rev 83: 117–161.
Robinson HP, Kawai N (1993) Injection of digitally synthesized synaptic conductance transients to measure the integrative properties of neurons. J Neurosci Methods 49:157–65.
Rougeul-Buser A, Buser P (1997) Rhythms in the alpha band in cats and their behavioural correlates. Int J Psychophysiol 26:191–203.
Sharp AA, O'Neil MB, Abbott LF et al. (1993a) Dynamic clamp: computer-generated conductances in real neurons. J Neurophysiol 69:992–5.
Sharp AA, O'Neil MB, Abbott LF et al. (1993b) The dynamic clamp: artificial conductances in biological neurons. Trends Neurosci 16:389–94.
Soltesz, I, Lightowler S, Leresche N et al. (1991) Two inward currents and the transformation of low-frequency oscillations of rat and cat thalamocortical cells. J Physiol (Lond) 441:175–97.
Steriade M., Curro Dossi R, Paré D et al. (1991) Fast oscillations (20–40 Hz) in thalamocortical systems and their potentiation by mesopontine cholinergic nuclei in the cat. Proc Natl Acad Sci USA 88:4396–400.
Steriade M, Amzica F, Contreras D (1996) Synchronization of fast (30–40 Hz) spontaneous cortical rhythms during brain activation. J Neurosci. 16:392–417.
Steriade M., Contreras D, Amzica F et al. (1996) Synchronization of fast (30–40 Hz) spontaneous oscillations in intrathalamic and thalamocortical networks. J Neurosci 16: 2788–808.
Steriade M., Contreras D, Curro Dossi R (1993) The slow (<1 Hz) oscillation in reticular thalamic and thalamocortical neurons: Scenario of sleep rhythm generation in interacting thalamic and neocortical networks. J Neurosci 13:3284–99.
Timofeev I, Steriade M (1996) Low-frequency rhythms in the thalamus of intact-cortex and decorticated cats. J Neurophysiol 76:4152–68.
Tóth TI, Crunelli V (1992) Computer simulation of the pacemaker oscillations of thalamocortical cells. Neuroreport 3:65–8.
Tóth TI, Hughes SW, Crunelli V (1998) Analysis and biophysical interpretation of bistable behaviour in thalamocortical neurons. Neuroscience 87:519–523.
Turner JP, Anderson CM, Williams SR et al. (1997) Morphology and membrane properties of neurones in the cat ventrobasal thalamus in vitro. J Physiol (London) 505:707–726.
Turner JP, Salt TE (2000) Synaptic activation of the group I metabotropic glutamate receptor mGlu1 on the thalamocortical neurons of the rat dorsal lateral geniculate nucleus in vitro. Neuroscience 100:493–505.
von Krosigk M, Bal T, McCormick DA (1993) Cellular mechanisms of a synchronized oscillation in the thalamus. Science 261:361–64.
von Krosigk M, Monckton JE, Reiner PB et al. (1999) Dynamic properties of corticothalamic excitatory postsynaptic potentials and thalamic reticular inhibitory postsynaptic potentials in thalamocortical neurons of the guinea-pig dorsal lateral geniculate nucleus. Neuroscience 91:7–20.
Williams SR, Tóth TI, Turner JP et al. (1997a) The 'window' component of the low threshold Ca^{2+} current produces input signal amplification and bistability in cat and rat thalamocortical neurones. J Physiol 505:689–705.

Williams SR, Turner JP, Hughes SW et al. (1997b) On the nature of anomalous rectification in thalamocortical neurones of the cat ventro-basal complex in vitro. J Physiol 505:727–47.

Zhu L, Blethyn KL, Cope DW et al. (2006) Nucleus- and species-specific properties of the slow (<1 Hz) sleep oscillation in thalamocortical neurons. Neuroscience 141:621–36.

Dynamic Clamp with High-Resistance Electrodes Using Active Electrode Compensation In Vitro and In Vivo

Romain Brette, Zuzanna Piwkowska, Cyril Monier, José Francisco Gómez González, Yves Frégnac, Thierry Bal, and Alain Destexhe

Abstract The active electrode compensation (AEC) consists of an online correction of the recorded membrane potential based on a computational model of the electrode. This technique may be particularly useful for situations where high-frequency components (such as noise) must be injected. This is particularly important for dynamic-clamp applications because of the real-time feedback between injected current and recorded voltage, since any artifact is amplified and may cause instabilities. We show here that such problems are greatly limited by the AEC, and this technique enables dynamic-clamp injection at high feedback frequencies (>10 kHz) and in demanding conditions. We illustrate AEC with applications such as injection of conductance noise in vivo and in vitro.

1 Introduction

1.1 Dynamic Clamp with a Single High-Resistance Electrode

The dynamic clamp or "conductance injection" (Robinson and Kawai, 1993; Sharp et al., 1993; Prinz et al., 2004), consists of injecting a current $I(t)$ that depends on the value of the membrane potential $V(t)$, according to Ohm's law $I(t) = g(t)\,[V(t) - E]$, where $g(t)$ is the conductance injected and E is the reversal potential. In many situations, especially in vivo, current injection and voltage measurement are performed with the same electrode. In vivo, this electrode is either a high-resistance sharp microelectrode with low capacitance (Steriade et al., 2001; Wilent and Contreras, 2005a; Crochet et al., 2006; Higley and Contreras, 2007; Haider et al., 2007; Paz et al., 2007) that is also used in some adult in vitro preparations (Thomson and Deuchars, 1997; Shu et al., 2003), or a patch electrode that can display a whole range of resistances and capacitances

R. Brette (✉)
Equipe Audition (ENS/CNRS), Département d'Études Cognitives, Ecole Normale Supérieure, F-75230 Paris Cedex 05, France
e-mail: romain.brette@ens.fr

A. Destexhe, T. Bal (eds.), *Dynamic-Clamp*, Springer Series in Computational Neuroscience 1, DOI 10.1007/978-0-387-89279-5_16,

depending on the age and species of the animal (Margrie et al., 2002, Borg-Graham et al., 1998, Monier et al., 2008, Pei et al., 1991, Hirsch et al., 1998, Anderson et al., 2000, Wehr and Zador, 2003, Mokeichev et al., 2007). The problem inherent to such single-electrode recordings is that the injected current biases the measurement because of the voltage drop through the electrode.

In a typical current-clamp recording with a single electrode, where current is simultaneously injected, the recorded potential is $V_r = V_m + U_e$, where V_m is the membrane potential (which is the variable we are interested in) and U_e is the voltage across the electrode. As a first approximation, the electrode acts as a resistance: $U_e \approx R_e I$, where R_e is the electrode resistance and I is the injected current. Thus a first estimation, known as *bridge compensation*, is $V_m \approx V_r - R_e I$. However, this is too crude an approximation because the electrode has a non-zero charge time and is better modeled by a RC circuit (resistance + capacitance). Amplifiers include a capacitance neutralization circuit which amounts to inserting a negative capacitance in the circuit (Thomas, 1977). Again, this model is too simple because there is always a residual capacitance, which appears as capacitive transients in recorded responses to current pulses (Fig. 1a). In dynamic clamp, the artifacts are injected back and can be amplified by the control loop, which leads to oscillatory instabilities (Fig. 1b; see Appendix 2 for a mathematical analysis). An option is to use a discontinuous mode (Fig. 1c), alternatively injecting current and recording the V_m (Brennecke and Lindemann, 1971, 1974a, b; Finkel and Redman, 1984) with a frequency set by the electrode time constant (typically 1.5–3 kHz with sharp electrodes in our experiments in cortical neurons in vitro and in vivo). Unfortunately, the alternation method is valid only when the electrode response is at least two orders of magnitude faster than the recorded phenomena (Finkel and Redman, 1984), because the membrane response must be quasi-linear in the sampling interval. Moreover, recordings in discontinuous modes are very noisy and sampling frequency is limited, which makes the precise recording of fast phenomena like spikes impossible (Fig. 1d).

We developed a method named active electrode compensation (AEC) based on a digital model of the electrode seen as an unknown linear filter, which allows sampling the V_m during current injection with a frequency only limited by the speed of the computer simulating the electrode model (Brette et al., 2007, 2008). In this chapter, we review this method and its application to dynamic-clamp experiments.

1.2 Active Electrode Compensation

The AEC method consists in using a more complex model of an electrode, by assuming that the electrode can be seen as an arbitrarily complex circuit of resistances and capacitances, which can be represented by a linear time-invariant filter, i.e., the response of the electrode to a current $I(t)$ is expressed as a convolution

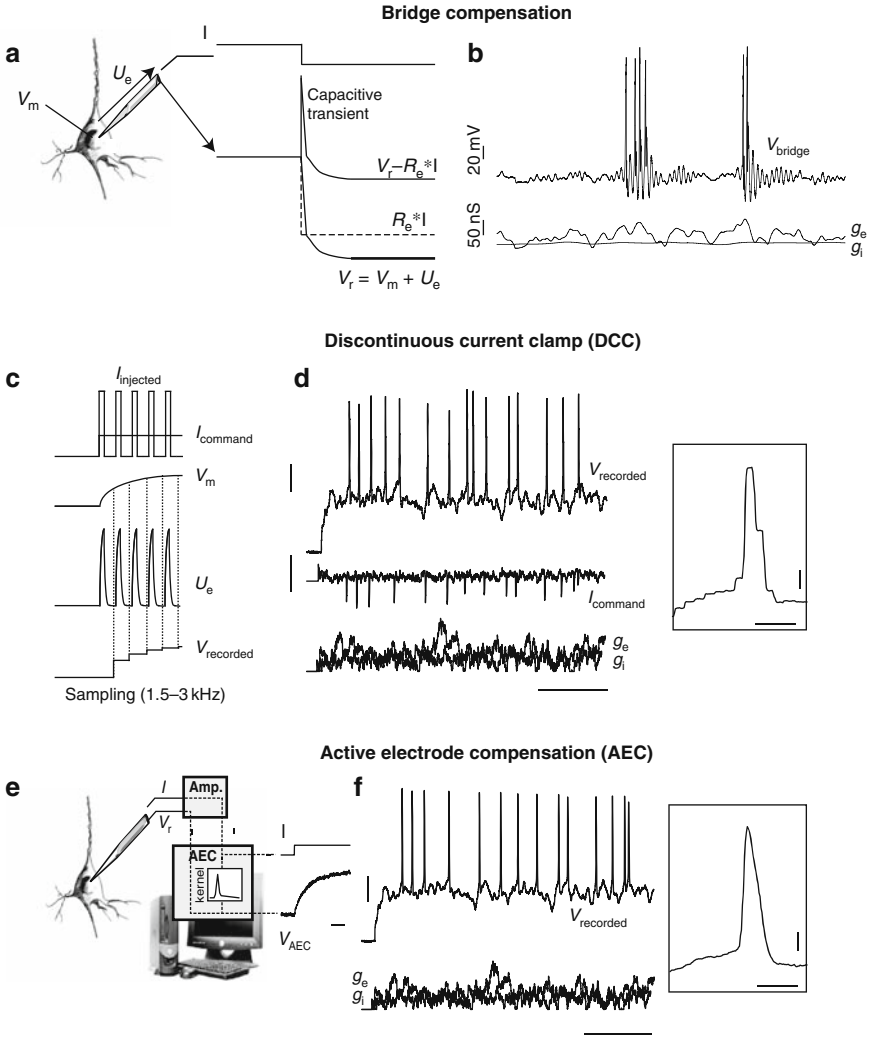

Fig. 1 Dynamic clamp with high-resistance electrodes. (**a**) When recording with a single electrode and injecting current at the same time, the recorded potential is $V_r = V_m + U_e$, where V_m is the membrane potential and U_e is the voltage across the electrode. Bridge compensation consists in modeling the electrode as a pure resistance: $U_e = R_e I$, where R_e is the electrode resistance and I is the injected current, and subtracting the estimated electrode voltage from the recording V_r. Because the electrode is not a pure resistance, a capacitance transient appears on the compensated trace. (**b**) In dynamic clamp (here excitatory and inhibitory conductances g_e and g_i), capacitive transients are injected back and induce instabilities. If the conductances are too high or too fast (here they were low-pass filtered), the recording is unstable (no meaningful signal). (**c**) The discontinuous current clamp (DCC) consists in alternating current injection and voltage recording, so that the potential is recorded at times when the electrode voltage U_e has vanished. Thus the sampling frequency is limited by the response speed of the electrode. (**d**) Stable dynamic clamp is possible with DCC (here: fluctuating excitatory and inhibitory conductances), but the temporal resolution is limited: the

$$U_e(t) = (K_e * I_e)(t) = \int_0^{+\infty} K_e(s) I_e(t-s) ds$$

where $K_e(\cdot)$ is named the *electrode kernel* (Fig. 1e, f). Thus the voltage across the electrode depends linearly on all past values of the injected current. This formulation encompasses any linear model, e.g., a circuit with a resistor and a capacitor (the kernel K_e is then an exponential function). The technique consists in identifying the electrode kernel by observing the response of the electrode to a known noisy current. In practice, the electrode kernel can only be estimated when the electrode impales the neuron (because electrode properties change after impalement). In this case, we first remove the membrane kernel from the full measured kernel (see the next section).

Once the electrode kernel has been estimated, we use the expression above to estimate the voltage across the electrode during current injection and subtract it from the recording $V_r(t)$. In practice, the recordings are digitized and the formula reads:

$$U_e(n) = \sum_0^{+\infty} K_e(p) I_e(n-p)$$

and the digital convolution is performed in real time by a computer.

We first describe the implementation of AEC in detail (Section 2), then we examine the influence of various aspects on AEC recordings, such as time constants and electrode nonlinearities (Section 3), and finally we show some practical examples of recordings in vitro and in vivo (Section 4). The appendixes contain more details about typical errors using AEC (Appendix 1) and dynamic-clamp instabilities with standard bridge compensation (Appendix 2). Sample code is available at the following URL: http://www.di.ens.fr/~brette/HRCORTEX/AEC/.

2 Theory and Implementation

The algorithm to estimate the electrode kernel (Fig. 2) consists in (1) finding the kernel of the full system neuron + electrode (+ amplifier) from the voltage response to a known input current and (2) extracting the electrode kernel from the full kernel (see Fig. 2). Indeed, the electrode kernel cannot be measured in isolation because the electrode properties change after it penetrates the

Fig. 1 (continued) shape of action potentials cannot be captured. (**e**) Active electrode compensation is used in continuous mode, with a computer running both the dynamic-clamp protocol and the electrode compensation. (**f**) Stable dynamic clamp is possible with AEC with high temporal resolution

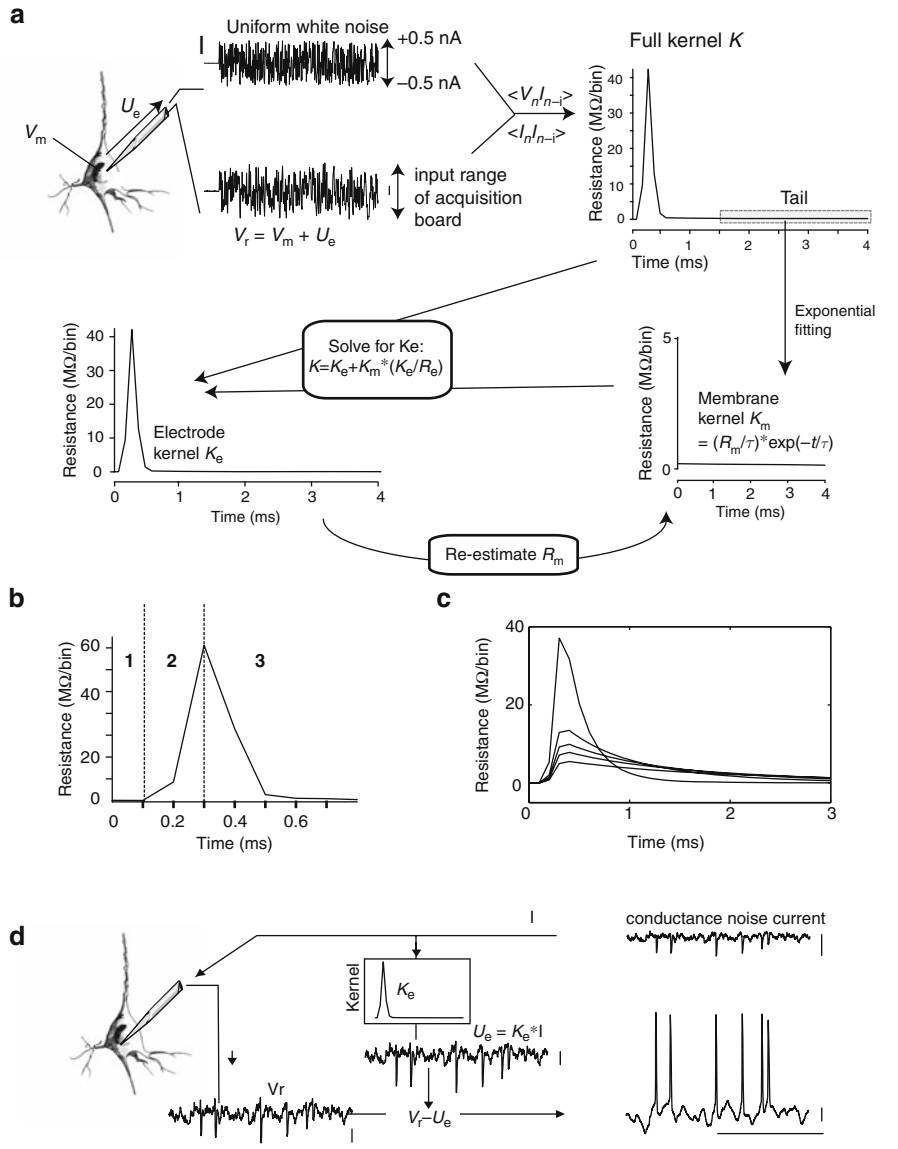

Fig. 2 AEC algorithm. (**a**) Non-Gaussian white noise current (scale bar: 0.5 nA) is injected into the neuron, as a series of independent random current steps uniformly distributed in −0.5 nA. . .0.5 nA. The total response V_r, corresponding to the sum of the membrane potential V_m and the voltage drop across the electrode U_e, is recorded (scale bar: 10 mV). The cross-correlation between the input current and the output voltage and the autocorrelation of the current give the kernel K (or impulse response) of the neuronal membrane + electrode system (full kernel K, *right*). The tail of the kernel is fit to an exponential function, which gives a first estimation of the membrane kernel K_m (note: the resistance of each bin is very small since the

membrane. Once the electrode kernel is measured, the electrode response can be calculated online by convolving the kernel with the injected current; then it is subtracted from the voltage recording to obtain the membrane potential.

2.1 Finding the Kernel

We assume that the neuron and the electrode respond linearly to the injected currents we use. We will discuss this hypothesis later (Sections 3.4 and 3.5). Then the recorded potential V in response to an input current I is the linear convolution:

$$V(t) = V_0 + (K * I)(t) = V_0 + \int_0^{+\infty} K(s)I(t-s)ds$$

where K is the impulse response of the system (neuron + electrode), also named the *kernel*, and V_0 is the resting potential. In the digital domain, the formula reads

$$V_n = V_0 + \sum_0^{+\infty} K_p I_{n-p}$$

Note that both the continuous and the discrete formulas express the linearity of the response and $V(t_n) = V_n$, but the continuous and discrete kernels are generally not identical (they only agree in the limit of small sampling steps). In fact, the kernel contains not only the neuron and the electrode, but also everything else that is between the output of the computer and the electrode, including all the filters and circuits in the amplifier (e.g., the capacitance neutralization circuit).

If the time-varying current I is known and V is measured over a long enough period of time, then it is possible to calculate the kernel K. Assuming that the measure is corrupted by Gaussian noise, the best estimation of K is the solution of the linear least-squares problem, i.e., $(\mathbf{K}, V_0)$ minimizes

Fig. 2 (continued) kernel is distributed over a long duration). The electrode kernel K_e is recovered from K and K_m by solving the equation $K = K_e + K_m{}^*(K_e/R_e)$ (convolution). The process is iterated several times to obtain a better estimation of the membrane kernel. (**b**) A typical electrode kernel (cortical cell in vitro), consisting of three phases: (1) the first two time steps are zero, representing the feedback delay of the system; (2) a fast rise (most likely representing the electrical characteristics of the amplifier or acquisition filters); and (3) a slower decay. (**c**) The electrode kernel also captures all the filters on the amplifier: here, five kernels measured in the electronic model cell with different settings for the low-pass filter of the amplifier (0.1–10 kHz). (**d**) Once the electrode kernel has been calibrated, it is then used in real time for electrode compensation: the injected current (scale bar: 5 nA) is convolved with the electrode kernel to provide the electrode response U_e to this current. U_e is then subtracted from the total recorded voltage V_r (scale bars: 100 mV) to yield the V_m (V_{AEC}; scale bars: 10 mV, 100 ms)

$$E = \sum_{n=0}^{N-1} \left(V_n - V_0 - \sum_{p=0}^{+\infty} K_p I_{n-p} \right)^2$$

where N is the number of measurements, i.e., $N\Delta$ is the duration of the stimulation, where Δ is the sampling step ($\Delta = 0.1$ ms in our experiments). Typically, the stimulation lasts 5–20 s, which corresponds to 50,000–200,000 measurements.

From $\frac{\partial E}{\partial V_0} = 0$ and $\frac{\partial E}{\partial K_i} = 0$ for all i we find

$$\forall i \geq 0, \sum_{n=0}^{N-1} V_n I_{n-i} = \sum_{p=0}^{+\infty} K_p \sum_{n=0}^{N-1} I_{n-p} I_{n-i} + V_0 \sum_{n=0}^{N-1} I_{n-i}$$

$$\sum_{n=0}^{N-1} V_n = \sum_{p=0}^{+\infty} K_p \sum_{n=0}^{N-1} I_{n-p} + NV_0$$

with the convention $I_k = 0$ when $k < 0$ (no input current before time 0). In the following we define $\langle x_n \rangle = \frac{1}{N} \sum_{n=0}^{N-1} x_n$ (average over all samples).

In practice, we consider only the first M steps of the kernel K, so that the equations above can be expressed as a matrix problem $\mathbf{AX} = \mathbf{B}$, where $\mathbf{A}$ is a square matrix with coefficients $a_{i,j} = \langle I_{n-j} I_{n-i} \rangle$ for $i, j \in \{0 \ldots M-1\}$, $a_{i,M} = \langle I_{n-i} \rangle$ for $i \in \{0 \ldots M-1\}$, $a_{M,j} = \langle I_{n-j} \rangle$ for $j \in \{0 \ldots M-1\}$ and $a_{M,M} = 1$; $\mathbf{X}$ is a column vector with $X_i = K_i$ for $i \in \{0 \ldots M-1\}$ and $X_M = V_0$; $\mathbf{B}$ is a column vector with $B_i = \langle V_n I_{n-i} \rangle$ for $i \in \{0 \ldots M-1\}$ and $B_M = \langle \mathrm{V_n} \rangle$. Solving this linear equation for $\mathbf{X}$ gives the coefficients of the kernel K and the resting potential V_0.

Although there is no theoretical problem in solving the linear problem described above, the matrix $\mathbf{A}$ can be large and each coefficient is a sum over all samples. But we note that in the limit $N \to +\infty$ (infinite number of samples) $\langle I_{n-i} I_{n-j} \rangle = \langle I_n I_{n+i-j} \rangle$ for a stationary current. In this case the matrix $\mathbf{A}$ has only $M + 1$ distinct coefficients. However, in practice, the number of samples is finite, so that for $j > i$,

$$\langle I_{n-i} I_{n-j} \rangle = \frac{1}{N} \sum_{n=-i}^{N-1-i} I_n I_{n+i-j}$$

$$= \langle I_n I_{n+i-j} \rangle - \frac{1}{N} \sum_{n=N-i}^{N-1} I_n I_{n+i-j}$$

In general, the correction term vanishes only when $N \to +\infty$, but we can ensure that it also vanishes for finite N by enforcing $I_n = 0$ for all $n \in \{N-M+1 \ldots N-1\}$, i.e., there is no input current at the end of the stimulation. In the same way, $\langle I_{n-i} \rangle = \langle I_n \rangle$ for all $i \in \{0 \ldots M-1\}$. It follows that the matrix has a special form known as a *Toeplitz matrix*, and solving a linear problem for a such a matrix can be done very quickly with the use of the Levinson–Durbin algorithm (which is

documented, e.g., in Press et al., 1993). Besides, it is not necessary to store all the values of V_n and I_n, since the averages $< V_n I_{n-j} >$ can be computed online in real time (M additions at each time step). More details about expressing the problem with a Toeplitz matrix can be found in Appendix 3.

2.2 Choosing the Input Signal

The input signal I must be chosen so that

1. it is zero at the end of the stimulation (last M steps, where M is the kernel size) in order to use the Levinson–Durbin algorithm, as shown in the previous section;
2. the neuron response is essentially linear;
3. it makes the best possible use of the D/A converters of the acquisition board.

Constraint 2 is satisfied by letting (I_n) be a sequence of independent random numbers with appropriate variance, as explained below. Constraint 3 is satisfied by letting each current step I_n be a random number with uniform distribution in the range of the D/A converter. Thus, the input current is a stationary non-Gaussian white noise (digitally sampled). We discuss this choice in the following.

2.2.1 Membrane Response During Injection

In general, the membrane potential does not respond linearly to the input current. However, it can be considered as locally linear around a given value of the potential; our strategy is thus to inject a signal that has a small effect on the membrane and a large effect on the electrode. Because the electrode time constant is much smaller than the membrane time constant, the choice of a white noise input signal ensures that the membrane potential will not vary much while the electrode potential will vary much more. Indeed, the standard deviation of the response of a membrane with time constant τ_m and resistance R_m to a white noise is proportional to $R_\mathrm{m}/\sqrt{\tau_\mathrm{m}}$. Thus, if the electrode has time constants τ_e and resistance R_e then the ratio of electrode response over membrane response is

$$\frac{R_\mathrm{e}}{R_\mathrm{m}}\sqrt{\frac{\tau_\mathrm{m}}{\tau_\mathrm{e}}}$$

For a sharp electrode, the electrode and membrane resistances have the same magnitude and with a properly adjusted recording setup, $\tau_\mathrm{m} \approx 100\tau_\mathrm{e}$, so that the electrode voltage response is about 10 times larger than the membrane response. Thus it is possible to ensure that the membrane potential remains within about 1 mV of its resting potential while the recorded potential varies by 10 mV on average.

Besides, linearity of the membrane response is not so crucial in the estimation procedure because in cases when the response is non-linear, the algorithm finds the best linear approximation (in the least-squares sense; see Figs. 5e, f and 7a).

2.2.2 Choosing the Level of Noise Injection

To estimate the kernel K, we inject a noisy current consisting of a sequence of independent random current steps at sampling resolution Δ, with amplitude uniformly distributed between $-I_{\max}$ and $+ I_{\max}\cdot$ $I_{\max}$ is chosen so that the membrane potential remains close to its resting level, while the electrode response is large enough so as to maximize the signal/noise ratio. For an ideal electrode (i.e., very fast compared to the membrane), the membrane response is piecewise exponential, it is a low-pass filtered version of $R_m I(t)$ with time constant τ_m, where R_m is the membrane resistance, $I(t)$ is the injected current, and τ_m is the membrane time constant. The standard deviation σ_V of the membrane potential is then given by the following formula:

$$\sigma_V = \sqrt{\frac{1 - e^{-\frac{\Delta}{\tau_m}}}{1 - e^{-\frac{\Delta}{\tau_m}}}} R_m \sigma_I \approx \sqrt{\frac{\Delta}{6\tau_m}} R_m I_{\max}$$

where σ_I is the standard deviation of the injected current and assuming that the sampling step Δ is small compared to the membrane time constant τ_m. With the values $\Delta = 0.1$ ms, $\tau_m = 10$ ms, $R_m = 40$ MΩ, and $I_{\max} = 0.5$ nA, we obtain $\sigma_V = 0.8$ mV, which is small enough. The expression we derived applies to an ideal electrode; for nonideal electrodes (which filter the injected current), it gives an upper bound for σ_V (approximately, τ_m is replaced by $\tau_m + \tau_e$, where τ_e is the electrode time constant). The electrode time constant has the same magnitude as the sampling step, therefore the electrode response can occasionally be close to the upper bound $R_e I_{\max}$, where R_e is the electrode resistance. It is crucial to estimate the range of the measured signal in order to adjust the acquisition system correctly. With $R_e = 50$ MΩ and $I_{\max} = 0.5$ nA, the range is ±25 mV, which was appropriate for our acquisition system.

2.3 Isolation of Electrode Kernel

Once the kernel of the system neuron + electrode has been determined, the electrode kernel remains to be extracted. The idea is that the membrane is much slower than the electrode, so that we can distinguish the two contributions in the full kernel. As a first approximation, we can write $K = K_m + K_e$, where K_m is the membrane kernel and K_e is the electrode kernel. We suppose that, in the regime in which the kernel was obtained (i.e., small white noise injection), the membrane responds approximately as a first order low-pass linear filter (i.e., a resistor–capacitor circuit), so that

$$K_{\mathrm{m}}(t) = \frac{R}{\tau} e^{-t/\tau}$$

The electrode kernel is supposed to decay much faster, so that for large t, $K(t) \sim K_{\mathrm{m}}(t)$. This suggests the idea of estimating K_{m} by fitting an exponential function to the tail of K and subtracting it ($K_{\mathrm{e}} = K - K_{\mathrm{m}}$).

However, a more careful examination of the circuit shows that the assumption $K = K_{\mathrm{m}} + K_{\mathrm{e}}$ is a crude approximation. Indeed, the recorded potential can be more precisely written as

$$\begin{aligned} V_{\mathrm{r}} &= V_{\mathrm{m}} + U_{\mathrm{e}} \\ &= V_0 + K_{\mathrm{m}} * I_{\mathrm{m}} + K_{\mathrm{e}} * I \end{aligned}$$

where V_{m} is the membrane potential (which is the quantity we want to recover), U_{e} is the potential across the electrode, and I_{m} is the current entering the membrane. The electrode filters the command current I; a reasonable approximation is to set $I_{\mathrm{m}} = U_{\mathrm{e}}/R_{\mathrm{e}}$, where R_{e} is the electrode resistance (defined as the ratio U_{e}/I for a constant injected current I). It follows that the full kernel reads

$$K = K_{\mathrm{m}} * \frac{K_{\mathrm{e}}}{\int K_{\mathrm{e}}} + K_{\mathrm{e}} \quad (*)$$

Thus the membrane kernel cannot be simply subtracted from the total kernel. However we can still use the tail of K to estimate the membrane time constant. Indeed, if $K_{\mathrm{e}}(t) = o(e^{-t/\tau})$ with $\tau_{\mathrm{e}} < \tau_{\mathrm{m}}$, then for large t, we have

$$\begin{aligned} K_{\mathrm{m}} * \frac{K_{\mathrm{e}}}{R_{\mathrm{e}}} &= \frac{R}{R_{\mathrm{e}}\tau} \int_0^t e^{\frac{s-t}{\tau}} K_{\mathrm{e}}(s) ds \\ &\sim \frac{R}{R_{\mathrm{e}}\tau} e^{-\frac{t}{\tau}} \int_0^{+\infty} e^{\frac{s}{\tau}} K_{\mathrm{e}}(s) ds \end{aligned}$$

(where the convergence of the integral is guaranteed by the dominated convergence theorem). Thus, fitting an exponential function to the tail of the kernel gives the correct membrane time constant, but not the correct membrane resistance (it overestimates the resistance).

In practice, we need to split the kernel K at some point T (the tail parameter) and to fit an exponential function to the right part (the "tail" of the kernel). The choice and sensitivity to this parameter is discussed in Section 3.1 (typical values in our experiments were $T \approx 3$–5 ms).

2.3.1 Removing the Membrane Kernel

We use equation (*) to extract the electrode kernel K_{e} from K. Here we assume that the membrane kernel K_{m} has already been recovered, i.e., the parameters

R_m and τ_m are known. In the next section we explain how to obtain good estimates for these parameters, but for the moment we can assume that we have obtained the correct parameters.

First, we need to estimate the electrode resistance. We have $R_e = \int_0^{+\infty} K - R_m$. In practice only the first M steps of the kernel are known, so that the formula we need is actually

$$R_e = \int_0^{M\Delta} K - R_m + R_m^0 e^{-M\Delta/\tau_m}$$

where Δ is the sampling step and $R_m{}^0$ is the estimate from fitting an exponential function to the tail of the full kernel K (which would be the first guess for R_m). Once R_e and K_m are known, we invert the relationship (*) by using the Z-transform (see Appendix 4 – in the end it simply amounts to applying a low-pass filter).

The difficulty in using the procedure above is that only τ_m can be estimated from the tail of the kernel K, while it is hard to estimate R_m reliably. If R_m is not estimated correctly, then the estimated electrode kernel K_e includes a residual slow component (e^{-t/τ_m}) from the membrane kernel. Therefore we can use the following strategy to obtain a better estimate of R_m: for each value R_m^* of the membrane resistance, the procedure gives an estimate of the electrode kernel $K_e(R_m^*)$; for the true value $R_m{}^* = R_m$ we expect the residual slow component to vanish, so that we search the resistance value which minimizes the tail of $K_e(R_m^*)$:

$$R_m = \underset{R_m^*}{\operatorname{argmin}} \int_T^{+\infty} K_e(R_m^*)^2 dt$$

Since the variable to be adjusted is only one-dimensional, we simply use the golden search algorithm to find the optimal resistance. Note that the formula above is exact in the limit of large T. In some practical cases when the electrode resistance is very small compared to the membrane resistance (typically with patch electrodes), there can be several local minima and the golden search algorithm can lead to the wrong value. A simple way to avoid this problem is to isolate the first minimum (which is the correct one) by calculating the error measure for a small value of $R_m{}^*$ and increase $R_m{}^*$ in logarithmic steps (i.e., multiplying by a constant factor at every step) until the error starts to grow; then the first minimum is bracketed by the last two values of $R_m{}^*$.

2.4 Implementation

The computer implementation should follow easily from the algorithms we have previously described. In this section we outline a few important points and the general procedure. The programs must run on a real-time computer system connected to the amplifier.

2.4.1 Estimation Procedure

The estimation procedure lasts about 10 s and must be performed when the electrode is impaled in the neuron (because the properties of the electrode are not the same as in the extracellular medium). During this time, a uniform white noise current (in the form of a sequence of independent random numbers) is injected in the neuron. The signal is sent through an acquisition board to the amplifier. The amplifier should be properly set, with the capacitance neutralization circuit set at a high level (so as to reduce the time constant of the electrode). The bridge compensation circuit must be off. The range of the uniform noise must be the same as the range of the D/A converters of the acquisition board. The range of the input A/D converters, which relay the voltage recording to the computer, must be large enough to avoid clipping (it is best to check on an external oscilloscope). Although the membrane potential does not vary much, the electrode voltage is much more variable. For example, if the range of the uniform current is ± 1 nA and the electrode is very fast (i.e., faster than the acquisition rate) and its resistance is 100 MΩ (sharp electrode), then the potential would vary between -100 and 100 mV. Note that it can be useful to change the offset of the voltage output of the amplifier so that the resting potential is close to 0 mV.

The computer program does not need to store the whole sequence of measures (I and V). It is enough so store in memory the running averages of $I_n I_{n-i}, V_n I_{n-i}, I_n$, and V_n. At the end of the stimulation, the program applies the Levinson–Durbin algorithm to find the full kernel and extract the electrode kernel with the algorithms described previously (exponential fitting of the tail followed by suppression of the membrane kernel). This part of the algorithm is not required to run in real time. Subsequently, only the electrode kernel needs to be stored. Typically, the resulting kernel is short and only the first tens of steps are non zero.

2.4.2 Online Compensation

Once the electrode kernel has been calculated, it can be used in real time to estimate the electrode voltage and subtract it from the recording. Again, the bridge compensation circuit must be turned off on the amplifier. Then it must be remembered that the potential actually recorded by the system is the sum of the membrane and the electrode responses and therefore it can be much larger than the membrane potential. The electrode voltage is subtracted in real time by a convolution, the input current I being known:

$$V_{\mathrm{m}}(n) = V_{\mathrm{r}}(n) - \sum_{p=0}^{l-1} K_{\mathrm{e}}(p) I(n-p)$$

where l is the number of steps in the electrode kernel (typically 30–50). Thus, the value of the previous l steps of the injected current must be held in memory (using, e.g., a circular array).

3 Practical Aspects

The quality of AEC recordings depends on a number of parameters and assumptions. In this section we examine the influence of AEC parameters such as the duration and amplitude of the white noise injection (Section 3.1), the instabilities that may arise from the feedback delay of the acquisition system (Section 3.2), and the robustness of the method with respect to the main three hypotheses we made: the electrode time constant is short compared to the membrane time constant (Section 3.3), the membrane response is essentially exponential (Section 3.4), and the electrode is linear (3.5). In practice, these hypotheses are only approximations but fortunately it generally has a mild effect on the quality of electrode estimation.

3.1 Estimation Parameters

The kernel estimation algorithm relies essentially on the following parameters: the parameters of the noise injection (duration and amplitude) and the parameters of the kernels (size and the tail parameter).

In theory, in a noise-free system, observing the response to a current injection with same duration as the kernel is enough to determine the kernel, that is, about 10–20 ms. However real systems are noisy and recording noise can be averaged out by using longer durations. We found (using high-resistance sharp electrodes) that 5 s was enough to obtain reliable and smooth kernels in vitro (we found no difference with 10 and 20 s stimulations; see Fig. 3c, d). A shorter duration is generally sufficient but 5 s is safer (in one case we found a significant difference with an injection lasting only 1 s). In vivo, recordings are noisier because of the network activity; in our experience, reliable estimates could be found with stimulations lasting 20 s. The amplitude of the noise current should be set so that the membrane response is small, as explained in Section 2.2; we found no significant impact of this parameter in the experiments. A constant current can also be applied in addition to the white noise, e.g., to avoid spikes. In this case the kernel estimation can be sensitive to the amount of DC current if the electrode is significantly nonlinear. This issue is addressed in detail in Section 3.5.

The size of the kernel (neuron + electrode) is essentially determined by the speed of the hardware, since the computational cost of online operations is directly proportional to the number of values in the kernel. We used 150–200 points with a 10 kHz sampling rate (i.e., the kernel size was 15–20 ms). A rule of thumb is that the kernel should contain about one membrane time constant

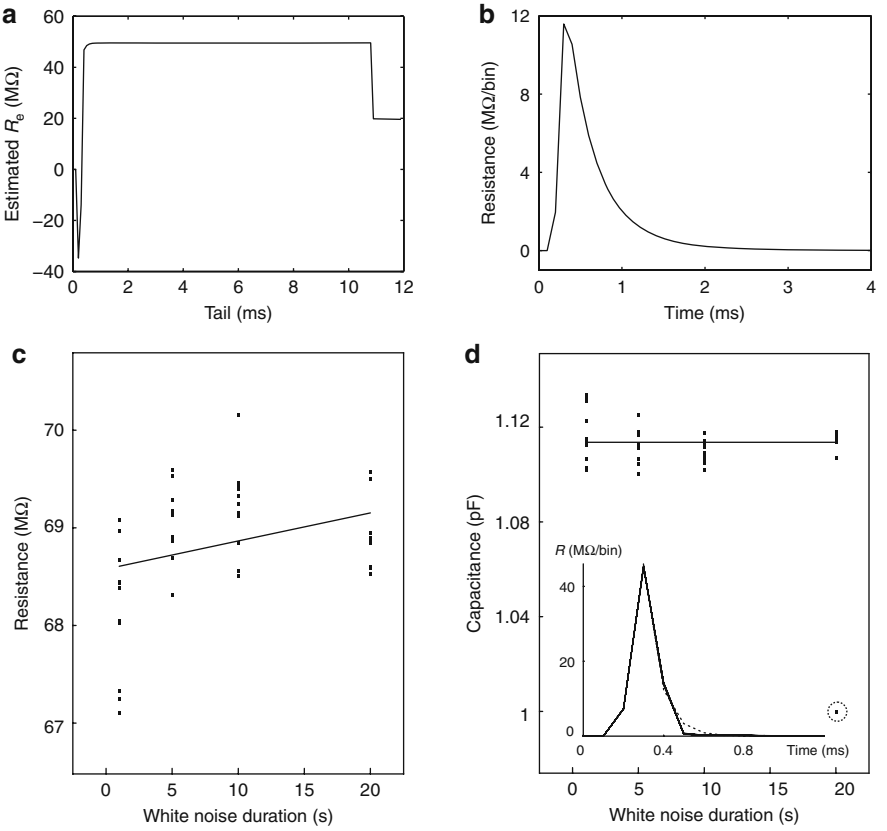

Fig. 3 Sensitivity of AEC to estimation parameters. (**a**) Numerical simulations show that there is a broad plateau of values of the tail parameter for which the kernel estimation is correct, as shown in this plot of estimated electrode resistance R_e vs. tail parameter (target $R_e = 50$ MΩ, electrode time constant $\tau_e = 0.2$ ms, membrane time constant $\tau_m = 15$ ms). If the parameter is too small, part of the electrode kernel is removed together with the membrane kernel and estimated R_e is too small (*left*). If it is too close to the total size of the full kernel (15 ms in this case), the fit of the membrane response by an exponential fails and this also leads to a wrong estimation (*right*). (**b**) An example of a real electrode, showing that the estimated kernels are very similar for three different values of the tail parameter (5, 7, and 10 ms), confirming the existence of a broad plateau (regular spiking cortical cell). (**c**, **d**) For one cortical cell recorded in vitro, parameters of the estimated electrode kernel for different durations of white noise (WN) injection used for the estimation (interleaved durations of 1, 5, 10, and 20 s were used). The electrode resistance (c) is the sum of all the kernel coefficients. The electrode capacitance (d) is obtained by dividing τ by the resistance, where τ is the decay time constant of an exponential fit to the decaying part of the kernel. All the 44 kernels are shown, superimposed, as an inset in the *right panel*. One of the kernels (*dashed line*) appears as an outlier, the corresponding point on the right panel is indicated by a *dashed circle*. ANOVA tests showed that only the 1 s WN duration produced resistance estimates significantly different from the other durations ($p < 0.01$), whether or not the outlier was included in the analysis. For the capacitance, ANOVA tests showed that there was no significant difference between the different durations, or a significant difference between 1 and 10 s when the outlier was removed

(although this is not a crucial requirement). In fact, the kernel size should not be too large (i.e., many times the membrane time constant), otherwise a large part of the kernel is nonsignificant (close to zero) and dominated by noise.

The tail parameter is used for extracting the electrode kernel; it corresponds to the time from which the full kernel is considered as corresponding to the membrane response only, and it has to be chosen prior to the separation of the full kernel into a membrane kernel and an electrode kernel. The membrane time constant is estimated from the tail of the kernel and the electrode kernel is assumed to vanish from that point. There is clearly a trade-off in the choice of this parameter: it must be large enough so that the electrode kernel does indeed vanish after that point, but small enough so that there are enough remaining points to estimate the membrane time constant. Fortunately, there is a broad plateau of parameter values for which the kernel estimation is correct (see simulation results in Fig. 3a, confirmed by in vitro experiments in Fig. 3b).

3.2 Feedback Delay

In a digital dynamic clamp operated by a computer (as opposed to an analog dynamic-clamp system), the feedback delay is a source of instability – which is not specific to AEC. A computer or a digital signal processor records and injects at sampling rate f. At time $t_n = n/f$, the membrane potential $V_n = V(t_n)$ is sampled, then the computer calculates the current to inject $I_n = g(E - V_n)$ during the interval $[t_n, t_{n+1}]$, and the current is injected during the next interval $[t_{n+1}, t_{n+2}]$ (hence the feedback delay is $2/f$). Assuming perfect electrode compensation (i.e., in effect, no electrode), the dynamics of the sampled membrane potential is given by the following recurrence equation:

$$\begin{aligned} V_{n+2} &= \lambda V_{n+1} + (1-\lambda) R I_n \\ &= \lambda V_{n+1} + (1-\lambda) g R (E - V_n) \end{aligned}$$

where $\lambda = \exp(-1/\tau f) \in]0,1[$ ($\tau = RC$ is the membrane time constant). In general, the sampling step is at least two orders of magnitude smaller than the membrane time constant, so that $\lambda \approx 1 - 1/(\tau f)$. This is a second-order linear recurrence equation, and the solutions are determined by the roots of the polynomial $X^2 - \lambda X + (1-\lambda) gR$. Oscillations can arise if the discriminant is negative, i.e., $\lambda^2 - 4(1-\lambda) gR < 0$, which is approximately (using $1/f << \tau$):

$$gR > \frac{\tau f}{4}$$

In this case the real part of the roots is $-\lambda/2$, which is smaller than one, so that the solution of the recurrence equation is a damped oscillation, i.e., ringing.

If the discriminant is positive, then there are two real roots a and b, such that $a + b = \lambda \in]0,1[$ and $ab = (1-\lambda)gR > 0$. The latter inequality means that a and b have the same sign, and $a + b > 0$ implies that this sign is positive. From the inequality $a + b < 1$, it follows that a and b are both in $]0,1[$, therefore, the solutions of the recurrence equation are stable.

Thus, in the case of perfect compensation, the feedback delay induces ringing if $gR > \tau f/4$ but does not destabilize the system for constant conductances. In our experiments, $\tau f \approx 100$, so that the maximum clamp conductance is about 25 times the membrane conductance.

Note that this inequality also applies to the maximal feedback gain of a digital voltage-clamp system (the expression we obtained is very similar to the formula derived by Finkel and Redman (1984) in the analysis of the discontinuous voltage clamp: $g_c = \tau f/(RD)$, where D is the duty cycle).

3.3 Time Constants

To separate the membrane kernel and the electrode kernel, we use the assumption that the electrode kernel is shorter than the membrane kernel, so that the membrane time constant can be estimated from the tail of the full kernel. This estimation can still be done if the electrode time constant is only slightly shorter than the membrane time constant. However, the quality of the electrode kernel estimation degrades with larger ratios τ_e/τ_m, so that the electrode should be as fast as possible (this is one reason why it is still useful to use the capacitance neutralization circuit on the amplifier – which is a feedback rather than a compensation method). Numerical simulations (Fig. 4a) show that the quality degrades continuously with larger ratios and starts to degrade seriously when this ratio is greater than 1/10 (the rule of thumb is that the error in signal reconstruction grows as τ_e/τ_m), so that AEC should be useful when the electrode time constant is about one order of magnitude shorter than the membrane time constant (in our somatic recordings with sharp microelectrodes, the electrode time constant was about 0.1 ms, so that the minimum membrane time constant for a good kernel estimation should be about 1 ms).

When the electrode time constant is large, the quality of recordings is impaired but the technique is still usable (in continuous mode) as shown in Fig. 4b–d (numerical simulations), where the ratio of time constants is about 1/10. The situation is quite different with discontinuous current clamp (DCC), which also has a constraint on time constants: proper operation of the DCC requires ratios lower than 1/50–1/100, but the technique does not give a meaningful signal if the ratio is higher (first because the optimal clock frequency is very low, second because it is impossible to accurately determine the optimal frequency).

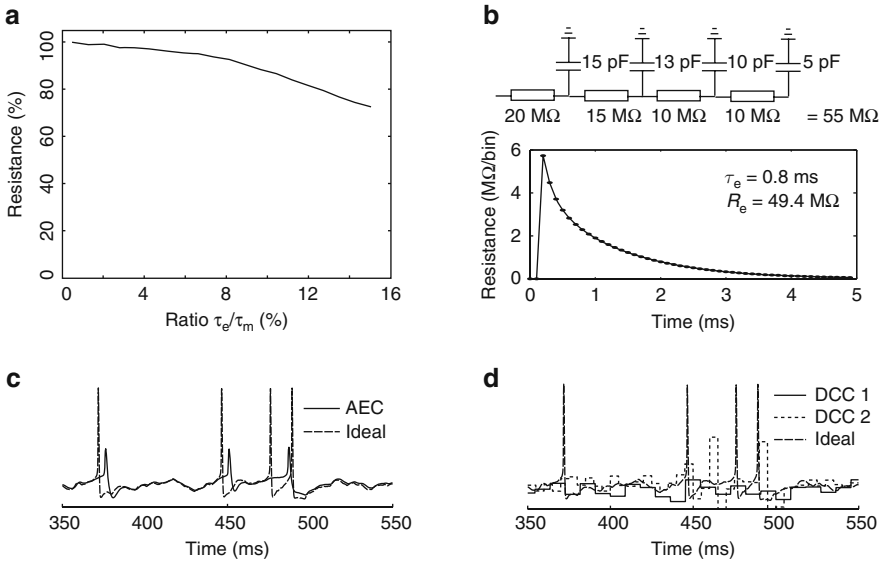

Fig. 4 Role of electrode and membrane time constants on electrode compensation. (**a**) We simulated a model including a passive membrane (R_m = 50 MΩ, τ_m = 20 ms) and a simple RC electrode with resistance R_e = 80 MΩ and varying time constant. Applying the AEC estimation procedure to this model shows that the quality of the electrode kernel degrades continuously when the ratio of electrode time constant and membrane time constant increases. The plot shows the estimated resistance with AEC, relative to the actual resistance (80 MΩ). The error on estimated resistance with AEC was less than 10% for τ_e/τ_m <9%. (**b**) We simulated a dynamic-clamp protocol with conductance noise and a slow electrode made of four resistors and capacitors (time constant 0.8 ms), impaled into a cortical cell modeled as a single-compartment Hodgkin–Huxley-type model (equations and parameters in Destexhe et al., 1998), and connected to a model amplifier (emulating DCC, bridge compensation and an acquisition board; we used a model of the electrode previously published in a conference proceedings – Brette et al., 2007). The electrode time constant is much slower than our typical measurements in vitro (about 0.1 ms with sharp electrodes). The electrode kernel measured by AEC underestimates the total resistance (49.4 MΩ instead of 55 MΩ). (**c**) With AEC, the subthreshold response is good and spikes are recorded, but in a filtered version (which is to be expected since AEC only compensate for the bias induced by injected currents). (**d**) With DCC, no meaningful signal can be recorded (DCC 1: optimal setting of the sampling frequency; DCC 2: higher setting). Increasing the DCC frequency leads to unstable oscillations like in bridge (not shown). Thus, dynamic-clamp recordings are possible with AEC when the electrode time constant is large and no other technique can be used

All single-electrode compensation methods have a requirement on the ratio of time constants (τ_e/τ_m): setting the bridge resistance requires separating electrode and membrane responses, while the discontinuous current clamp is valid when the ratio is about 1/100 or better. In this respect, AEC has a better critical ratio, so that it can be used in more situations than either bridge or DCC.

3.4 Dendrites

To extract the electrode kernel from the full kernel (neuron + electrode), we assume that the membrane kernel is a single exponential function and estimate the time constant from the tail of the kernel. In fact, due to the dendritic tree, there are additional exponential modes with faster time constants, some of which are similar to the electrode time constant, as shown in Fig. 5 (simulation of a pyramidal cell). With a single electrode (for any method), there is no way to distinguish fast dendritic contributions from electrode contributions at the same timescale. In fact, for any linear time-invariant system, such as a linear electrode and a passive neuron with a dendritic tree, the relationship between the current injected at a given point and the potential recorded at another (or the same) point is fully characterized by the kernel, so that there is no more information that we may have on the system. Therefore, an electrode compensation system must rely on the fact that the fast dendritic contributions to the kernel are relatively small in amplitude. This might not be always the case (and if so, a second electrode would be necessary), but at least in numerical simulations of morphologically reconstructed pyramidal cells, the dendrites contribute not more than a few megaohms of the total resistance (the resistance of typical sharp electrodes are around 80 MΩ).

Because the fast dendritic contribution to the kernel is included in the electrode kernel, and therefore subtracted by electrode compensation, there is a little less high-frequency power in the compensated trace than in the real membrane potential. However, this is a constant subtraction and not a low-pass filtering, so that fast active changes in membrane properties (e.g., spikes) are not filtered out by the method, as shown in Fig. 5 f.

3.5 Nonlinearities

The crucial hypothesis underlying the AEC technique is that the electrode is linear. However, it is known that high-resistance electrodes can be nonlinear, which is characterized by the fact the electrode resistance can change with strong currents. Physical modeling of nonlinearities (Purves, 1981) indicates that these are slow processes due to redistribution of ions near the electrode tip. Nonlinearities are stronger for electrode tips with a small radius (which is inversely correlated with the resistance) and when the concentrations of the two solutions (intracellular and inside the electrode) differ. However, in practice, the amount of electrode nonlinearity is highly variable and unfortunately cannot be assessed before the electrode is impaled into the cell – although electrodes with an unusually high resistance in the slice can be discarded from the start. This nonlinearity problem is not different with AEC than with standard bridge compensation, however AEC provides a simple way to measure it, and possibly discard the recordings if the nonlinearity is too important. We first note that nonlinearities are too slow to affect the stability of dynamic-clamp recordings, so that the issue is rather the quality of voltage estimation.

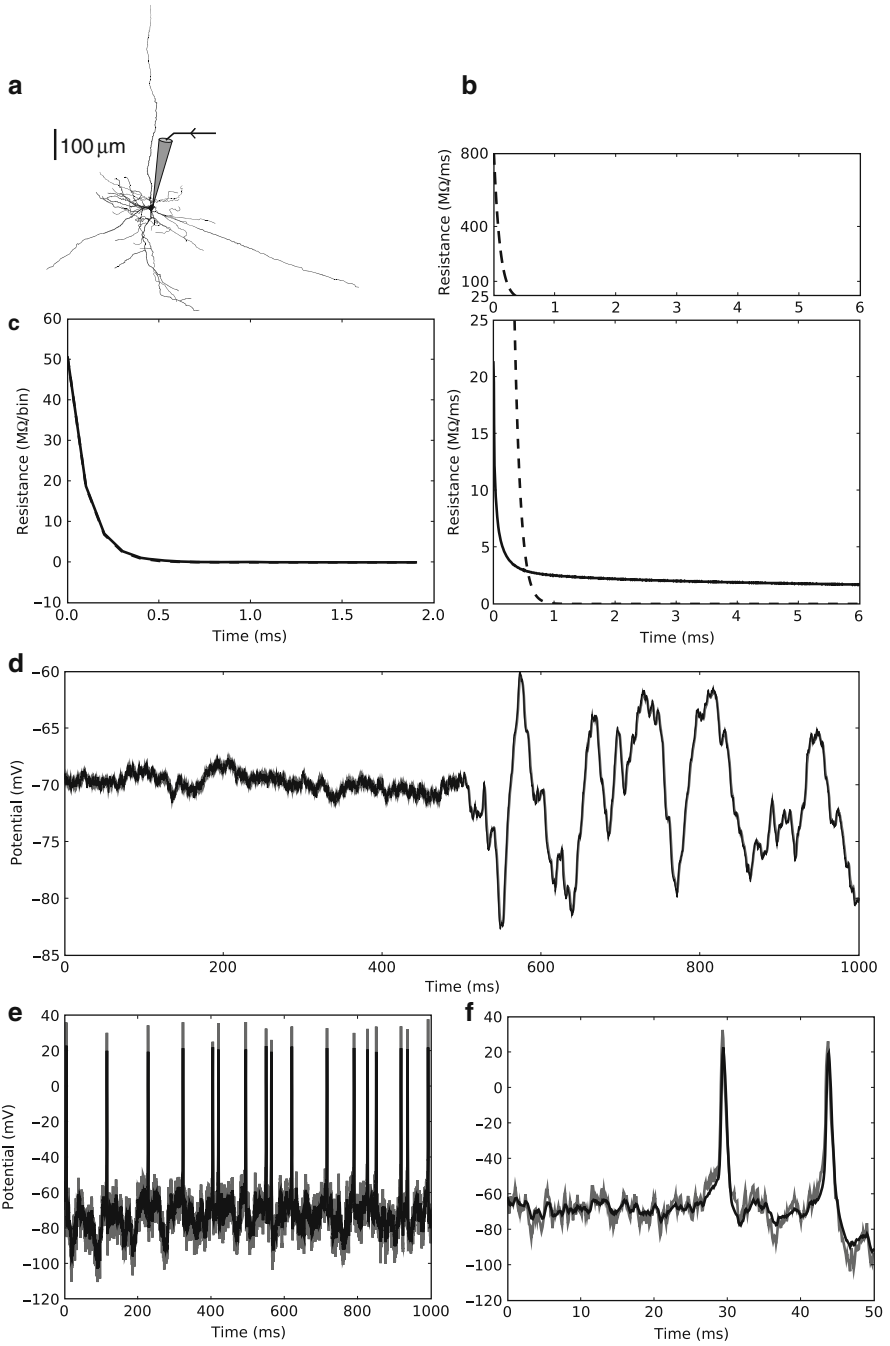

Fig. 5 Impact of dendrites on electrode compensation. We simulated a morphologically reconstructed layer VI pyramidal cell (Contreras et al., 1997) using Neuron, (Hines and Carnevale,

Electrode nonlinearities are usually measured before impalement from the *I–V* curve of the electrode, but it is not possible to use the same approach intracellularly because the *I–V* curve of the electrode could be confused with the *I–V* curve of the neuron. AEC can be used to measure the electrode resistance by running the kernel estimation procedure intracellularly with different levels of constant injected current (Fig. 6), corresponding to the typical (average)

1997) with passive properties **Fig. 5** (continued) (b–g) as in Destexhe and Paré (1999), compatible with whole-cell patch recordings: leak conductance $g_l = 0.0155\,\mathrm{mS/cm^2}$ (range tested: 0.015–0.03 $\mathrm{mS/cm^2}$), resting potential $V_{rest} = -80$ mV, intracellular axial resistivity $R_a = 70\ \Omega$.cm (Stuart and Spruston (1998); range tested: 65–280 Ω.cm), specific membrane capacitance $c_m = 1\ \mu\mathrm{F/cm^2}$. In the simulations of panel e, voltage-dependent Na^+ and K^+ currents were inserted in the soma, dendrites, and axon (parameters in Destexhe and Pare, 1999). A high-resistance electrode, modeled as a resistor and a capacitor, was located into the soma ($R_e = 80\ \mathrm{M\Omega}$ and $\tau_e = 0.1$ ms). An additional leak conductance of 10 nS was inserted in soma to model the impalement. White noise and colored noise currents were injected through the electrode and AEC was used to correct the recording. AEC and subsequent analysis were done off-line using custom Python code (http://www.di.ens.fr/~brette/HRCORTEX/AEC/) and the Brian simulator (http://brian.di.ens.fr/). Recordings were sampled at 10 kHz (neuron simulations use a 0.01 ms integration time step). (**a**) Dendritic tree of the simulated neuron, reconstructed from a layer VI pyramidal cell (Contreras et al., 1997). (**b**) The kernel of the cell, as measured by direct somatic injection (*solid line*) is not a pure exponential function. Fitting to a sum of three exponential functions shows however that the slower one accounts for 56 MΩ of the total resistance $R = 57.8\ \mathrm{M\Omega}$. The electrode kernel (*dashed line*) is concentrated on the first ms and is two orders of magnitude larger than the membrane kernel on that timescale (note the change of scale in the upper part of the figure). The neuron and electrode kernels were calculated separately, i.e., the neuron kernel was estimated with no electrode resistance, and the electrode kernel was calculated without the neuron (therefore, it is a single exponential function with time constant 0.1 ms); thus, these calculations did not rely on AEC. (**c**) The electrode kernel measured by AEC (*solid line*) was very close to the real one (*dashed line*); the estimation gave $R_e = 81\ \mathrm{M\Omega}$ instead of 80 MΩ. (**d**) White noise (first half) and colored noise (second half; time constant 5 ms) currents were injected through the electrode, and the voltage compensated with AEC using the measured electrode kernel shown in (c). The AEC compensated trace (*black line*, foreground) is compared to real somatic potential of the model (*grey line*, background). (**e**) This figure shows a very challenging situation for electrode compensation: nonlinear voltage-dependent conductances in the cell, electrode kernel estimated during spiking activity, large dendritic contributions to the membrane kernel, high ratio electrode resistance/membrane resistance, short membrane time constant, and white noise injection. Voltage-dependent conductances were inserted, so that the cell was able to produce action potentials. As a result, the membrane resistance (and thus the time constant) at rest was halved (and even more reduced during spiking), giving a large ratio $R_e/R_m = 2.5$ (even larger during spiking activity: R_e/R_m). Suprathreshold white noise was injected through the electrode, inducing spiking activity. The electrode kernel was estimated with the same suprathreshold white noise injection, i.e., there were spikes during the estimation. The estimated electrode resistance was 82.6 MΩ, which was very close from the same estimation with subthreshold white noise injection (estimated $R_e = 82\ \mathrm{M\Omega}$). The *black trace* shows the result of AEC compensation during the injection (*gray* = real somatic potential). Even though the subthreshold activity looks filtered by AEC because the fast dendritic contribution to the membrane kernel is large (10% at rest), the technique does not act as a low-pass filter: measured action potentials look very similar to the real ones

levels that will be used subsequently, and check that the amount of nonlinearity is acceptable (in our experiments, about half the electrodes were not significantly nonlinear). This raises the issue of estimating the kernel when the membrane has a nonlinear, possibly spiking, response. Although in principle,

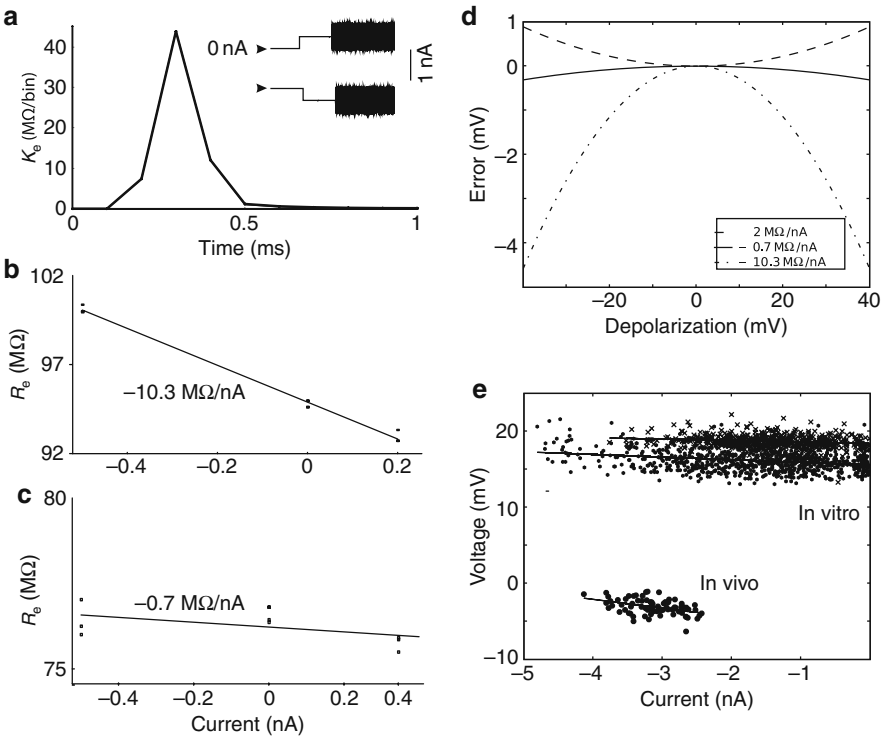

Fig. 6 Electrode nonlinearities. (**a**) Electrode nonlinearities can be measured intracellularly by running the AEC estimation procedure with different levels of additional constant currents, and comparing the resulting electrode kernels. (**b**, **c**) The electrode resistance R_e (sum of all values of the electrode kernel) is plotted vs. the constant injected current for a very nonlinear electrode (b) and an essentially linear electrode (c). The slope of the linear regression measures the nonlinearity. The first electrode (b) should be discarded. (**d**) The voltage error resulting from electrode nonlinearities can be expressed as quadratic function of the membrane depolarization, as shown on this plot for the electrode in (c) (*solid line*, typical of about half the electrodes in our experiments), the electrode in (b) (*mixed line*), and another nonlinear electrode (*dashed line*). (**e**) We analyzed the spikes produced by two cells during injection of colored conductance noise in vitro and one cell in vivo. Because of the dynamic-clamp protocol, a very large negative current was injected during spikes. Any error ΔR_e in the estimation of the electrode resistance, which could be caused by electrode nonlinearities during these large current injections, would result in an error $\Delta R_e * I$ in the voltage estimation. For these cells, the voltage peak was not very variable (standard deviations 0.9–1.4 mV), and the estimated resistance errors from linear regression between the injected current and the voltage at peaks were all smaller than 1 MΩ, which indicates an absence of fast nonlinearities. Electrode resistances ranged between 63 and 68 MΩ (estimated at rest with AEC)

the response of the whole system (membrane + electrode) should be linear during the estimation of the electrode kernel, this is not a strong requirement for the membrane, because the method calculates the best linear approximation to that response. The full kernel is, to a first approximation, $K_e + K_m$, and if the membrane behaves nonlinearly (e.g., spiking), the impact will mainly be on K_m, therefore, the main issue in that case is whether the estimated K_m differs significantly from an exponential function, so that it can be properly subtracted. Numerical simulations show that moderate spiking activity has a small impact on kernel estimation; we were also able to estimate electrode kernels during moderate spiking activity in vivo (see the next section).

In dynamic clamp, the injected current can be transiently very high: e.g., during an action potential, the injected current becomes typically very large and negative (e.g., for a current of the form $I = g(E - V_m)$ where E is low). These transients would be a big problem for electrode compensation if nonlinearities were fast. Fortunately, we confirmed that transients do not trigger significant nonlinearities. Fig. 6e shows the measured compensated voltage and current at the peaks of action potentials during conductance noise protocols (in vitro and in vivo). Those two quantities were very weakly correlated (the slopes of linear regressions ranged from -0.1 to -0.6 MΩ), which indicates that the electrode resistance could not have changed much during spikes (any error ΔR_e in the estimation of the electrode resistance would result in an error $\Delta R_e * I$ in the voltage estimation.).

Electrode nonlinearity can be approximated by a quadratic dependence of voltage on current or equivalently as a linear change in resistance with injected current (MΩ/nA). The voltage error resulting from an error ΔR_e in the estimation of the electrode resistance can be described simply as follows (see Fig. 6d). The resistance error (compared to infinitesimal current injection) is $\Delta R_e = \lambda * I$, where λ (in MΩ/nA) quantifies the nonlinearity (measured with AEC as in Fig. 6a–c). If the membrane resistance is R_m, then the voltage error resulting from the nonlinearity is $\lambda * I^2 = (\lambda / R_m^2) * \Delta V^2$, where ΔV is the depolarization of the membrane induced by the injection ($= V_m$ – resting potential). For example, if the electrode nonlinearity is 2 MΩ/nA and the membrane resistance is 60 MΩ, then the voltage error is 0.0005 mV/mV^2 (e.g., 0.5 mV for 30 mV depolarization). This analysis applies to linear depolarizations induced by constant subthreshold currents, not, e.g., for action potentials, which are transient.

4 AEC Recordings in Vitro and in Vivo

4.1 Practical Issues

There are two main important practical issues in experiments, especially in vivo: whether the electrode kernel can change over the time course of an experiment, and whether the technique can be easily used given unavoidable perturbations such as recording noise and synaptic activity.

It is known that the electrode resistance can change from time to time over the time course of an experiment. It is then necessary to recalibrate the technique (e.g., balance the bridge). The same applies for AEC, but not more often than with other techniques. In practice, one should run the estimation procedure from time to time and check that the kernel has not changed. Fortunately, it only takes a few seconds and it is fully automatic. In vivo, we found that electrode properties could remain stable for up to 2 h, as assessed with kernel estimations obtained repetitively, also when using different constant current injections and different durations of white noise injection (Fig. 7b). Regarding stability, an important point is that AEC allows the use of high-resistance sharp electrodes, which are more stable in vivo than patch electrodes.

The second practical issue is the problem of ongoing synaptic activity and recording noise. Recording noise is not a very big problem for the technique because the number of measurements (50,000 points for 5 s estimations at 10 kHz) is much larger than the number of points in the kernel (typically around 150), so that noise is averaged out. Important variations of the membrane potential during estimation, such as spiking activity, could be more problematic. However, as we mentioned earlier, the linearity hypothesis is crucial for the electrode but not so much for the membrane, because the method finds the best linear kernel and the membrane part is removed – the fact that the membrane kernel is not accurate is not an issue as long as the electrode kernel is correctly recovered. Membrane nonlinearities can affect the electrode kernel only if they introduce a systematic current–voltage relationship at the timescale of the electrode; otherwise, the perturbations are averaged out. We checked in numerical simulations that electrode kernel estimation is possible during spiking activity, with a small impact on the estimated kernel. We were indeed able to run the procedure in vivo while the neuron was spiking and use the resulting electrode kernel for subsequent dynamic-clamp experiments (Fig. 7a). In vivo, we used longer injections (20 s) to make sure that all sources of noise are averaged out.

4.2 Examples

Here we show a number of examples of dynamic-clamp experiments using AEC in vitro and in vivo.

4.2.1 Square Conductance Waves

We injected a square wave of alternating "excitatory" ($E_{\text{excitation}} = V_{\text{rest}} + 10$) and "inhibitory" ($E_{\text{inhibition}} = V_{\text{rest}} - 10$) conductance pulses with different conductance amplitudes (range 10–100 nS) and frequencies (range 10–1,000 Hz) in vitro, with sharp electrodes (Fig. 7c). This is a challenging protocol if the conductance or the frequency is large. In particular, bridge compensation can

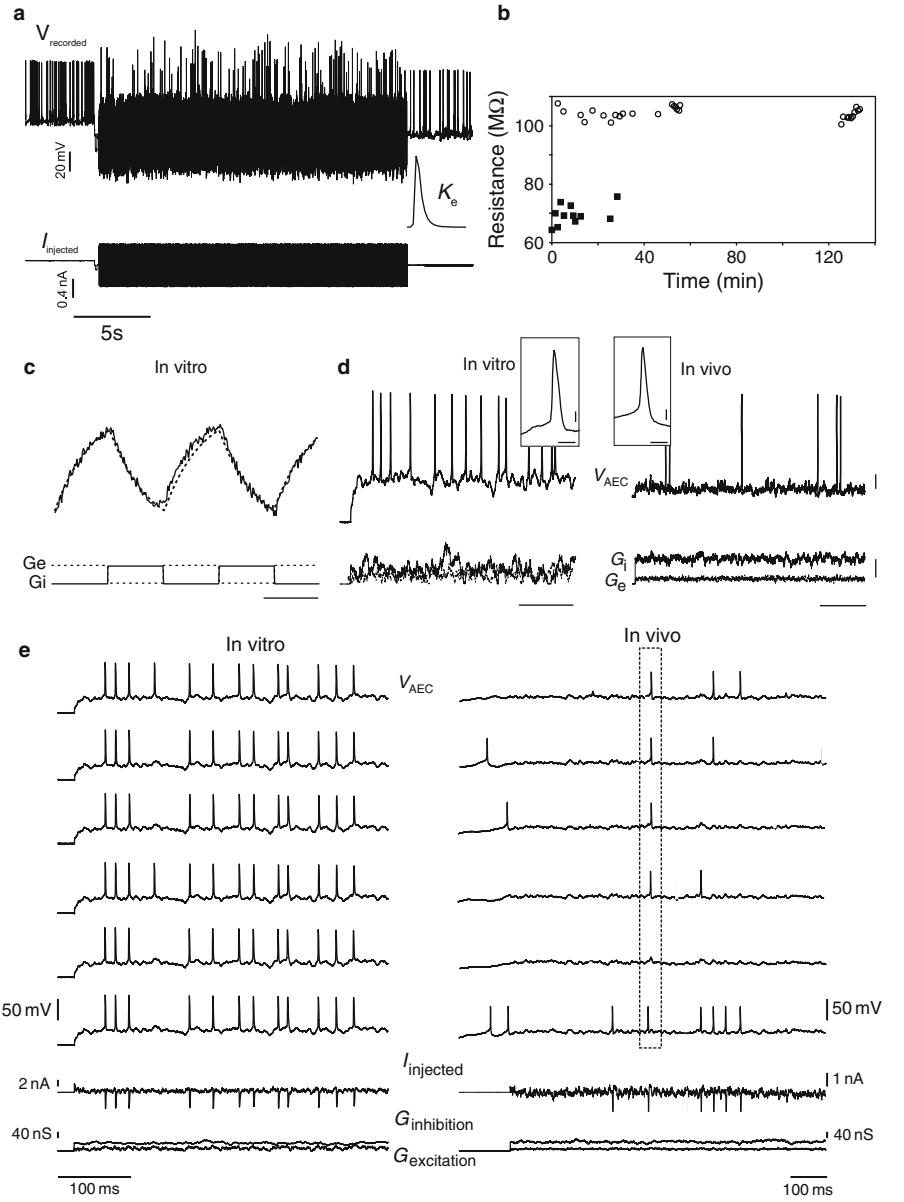

Fig. 7 AEC recordings in vitro and in vivo. (**a**) This trace is an example of a kernel estimation in vivo: in this case, there were spikes occurring during the white noise current injection; however, the electrode kernel was very similar to a previous one obtained in the absence of spikes (measured electrode resistances were $R_e = 105\ M\Omega$ in the absence of spikes and $R_e = 103\ M\Omega$ in the presence of spikes). (**b**) Temporal stability of the electrode properties in vivo for two regular spiking cells. The kernel was estimated using 5 or 20 s white noise current injections. In addition different constant current levels (DC) were injected, preventing spiking activity during the estimation. (**c**) Dynamic-clamp protocol with 50 nS square conductance

be used only for very small conductances (see Appendix 2), and DCC shows strong artifacts at high frequencies. The responses with AEC correspond to what would be expected from a passive cell model.

4.2.2 Conductance Noise

We injected a colored conductance noise consisting of two stochastic variables, $g_e(t)$ for excitation and $g_i(t)$ for inhibition (Fig. 7d), mimicking cortical synaptic background activity as seen in vivo (Destexhe et al., 2001). This protocol could not be performed with bridge compensation (recordings are unstable). With AEC we could easily inject synaptic noise of high total conductance (5 times the leak conductance). The spikes can be recorded with excellent precision (while they would be reduced to a few sampling points with DCC). We performed this protocol both in vitro and in vivo.

4.2.3 Reliability of Spike Timing with Recreated Synaptic Activity

The precision of dynamic-clamp recordings with AEC allowed us to evaluate the reliability and precision of spike timing in cortical neurons with recreated synaptic activity, instead of current noise (Mainen and Sejnowski, 1995). Figure 7e shows the responses of cortical neurons to repeated dynamic-clamp injections of frozen conductance noise, mimicking synaptic activity (as described above). In cortical neurons in vitro (left), the repetition of such a realistic, fluctuating conductance stimulus can lead to highly precise and reliable spiking patterns (as has also been shown by others, e.g., Harsch and Robinson, 2000; Tateno and Robinson, 2006). In a cortical neuron in vivo, however (right), due to real synaptic inputs from the network and possibly to different intrinsic properties of the recorded cell (note the V_m close to threshold at the beginning of the shown traces, before any conductance injection), the situation is more complex: on the example shown, one particular spike (box) appears as precise and reliable from

Fig. 7 (continued) waves in vitro (alternation of excitation and inhibition; scale bar: 5 ms; R_e = 71 MΩ). The recording with AEC is very close to the prediction (from a passive model). (**d**) Dynamic-clamp protocol with fluctuating inhibitory and excitatory conductances using AEC, in vitro and in vivo. Recordings are stable and action potentials are measured with high temporal resolution. (**e**) Dynamic-clamp protocol with repeated injections of frozen synaptic conductance noise using AEC, in a guinea pig visual cortical RS neuron in vitro (*left*) and in a cat visual cortical RS neuron in vivo (*right*). The injected inhibitory and excitatory conductances, $G_{inhibition}$ and $G_{excitation}$, identical for each trial, are shown at the *bottom*. The injected current, $I_{injected}$, is displayed on top of the conductances, for only one trial; the corresponding response of the cell, V_m is displayed directly on top of the current. Subsequent V_m responses to the same conductance pattern are displayed above. Conductance noise parameters: in vitro, g_{e0} = 15 nS, g_{i0} = 50 nS, s.d.$_e$ = 8 nS, s.d.$_i$ = 6 nS; in vivo, g_{e0} = 12 nS, g_{i0} = 57 nS, s.d.$_e$ = 3 nS, s.d.$_i$ = 7 nS

trial to trial, but this is not the case for the other spikes. This example illustrates that future dynamic-clamp experiments in vivo, enabled by the AEC method, would be useful in identifying the conditions for spike-timing precision and reliability in functioning cortical networks.

5 Discussion

In this chapter, we have reviewed the recent developments of a technique to perform dynamic-clamp experiments at high resolution using single electrodes. We have described the theory behind AEC and its implementation (Section 2), as well as some practical aspects such as how to estimate compensation parameters, and the effect of electrode nonlinearities and of the dendrites (Section 3). We also reviewed practical examples of demanding conditions, such as injection of conductance noise and dynamic-clamp experiments in vivo (Section 4). We now discuss the AEC technique in reference to other compensation techniques, as well as future perspectives.

The AEC technique is based on a nonparametric linear model of the electrode which is automatically calibrated. It allows accurate intracellular recordings at a high sampling frequency during simultaneous current injection, uncontaminated by capacitive transients, which makes it especially appropriate for dynamic-clamp protocols, especially with high-resistance electrodes. Previous techniques suffered from either instability issues (bridge compensation) or limited temporal resolution (DCC). Another advantage of model-based electrode compensation is that the technique provides the precise characteristics of the electrode along with the recording, which can be useful to estimate the recording quality. It should be noted that AEC compensates for the electrode voltage, but does not modify the injected current. Thus, the injected current remains filtered by the electrode, although the true injected current can be approximately estimated off-line from the knowledge of the electrode kernel.

The main condition that has to be met for the method to work accurately is the linearity of the electrode and of the whole recording chain between the electrode and the computer (amplifiers and filters), for the range of expected currents. The technique provides a fast and automated way to measure electrode nonlinearities intracellularly, which was previously difficult, if not impossible. One can then estimate the resulting errors in subsequent recordings, and possibly discard the recordings if the nonlinearity is too important. These nonlinearities are due to slow processes, so that large currents that are only transiently injected should not degrade the quality of electrode compensation.

Another requirement, which is also shared by previous techniques, is that the electrode and membrane time constants should be well separated, which means that the capacitance neutralization provided by the amplifier should be used optimally like in the other methods. However, admissible results can be obtained if the electrode is only 10 times faster than the membrane, while

DCC requires electrodes about 100 times faster than the membrane. Thus AEC should extend the applicability of single-electrode dynamic clamp to neurons with much shorter time constants.

We are now investigating several extensions of the AEC technique. In particular, we are currently working on using our compensation method for the single-electrode voltage clamp. The development of this "AEC-VC" technique represents a considerable interest because it would enable recording in voltage-clamp mode using sharp electrodes and without using a discontinuous mode, therefore, enabling continuous voltage-clamp recordings with sharp electrodes in vivo. We are presently testing this technique on sharp electrode recordings in vivo and in vitro, and compare it with discontinuous voltage-clamp (DVC) methods. Other possible extensions include dendritic patch-clamp recordings which use electrodes with higher series resistance compared to somatic patch recordings, as well as applications of the AEC to model electrode nonlinearities.

Acknowledgments This work was supported by CNRS, ANR (HR-CORTEX grant), ACI, HFSP, the European Community (FACETS grant FP6 15879) and the FRM. More information is available at http://www.di.ens.fr/~brette and http://cns.iaf.cnrs-gif.fr.

Appendix 1: Typical Sources of Errors

Here we enumerate a number of anomalous situations that can occur during the estimation or compensation stages that may produce unwanted biases in the electrode kernel estimate. Many of these errors can be easily noticed as anomalies in the electrode kernel, as is illustrated in Fig. 8.

The bridge compensation is on: in this case the program can still capture a kernel but it has a strange shape (Fig. 8a) with a total resistance close to 0 (if it is well adjusted), which makes the membrane suppression procedure fail.

Input or output ranges on the acquisition board are not correctly set: if the ranges are too large, the method only loses some accuracy; however if the ranges are not large enough, then clipping occurs, which can be disastrous both at the estimation stage and at the compensation stage. It can remain unnoticed at the estimation stage because it only results in errors in the estimated kernel. At the compensation stage it results in large compensation errors which can be seen as noise on the compensated output in current clamp. It is more serious in dynamic clamp because it can result in losing the cell because of oscillatory instabilities.

The kernel is too large: if the number of steps M in the full kernel is very large, then during the estimation procedure the program may not have enough time to compute all the running averages within one time step. Depending on the real-time system, this can result in freezing the program or in errors in the kernel (Fig. 8b). The latter is more problematic because it can remain unnoticed: in this case, the program sometimes takes more than one step to do all the required

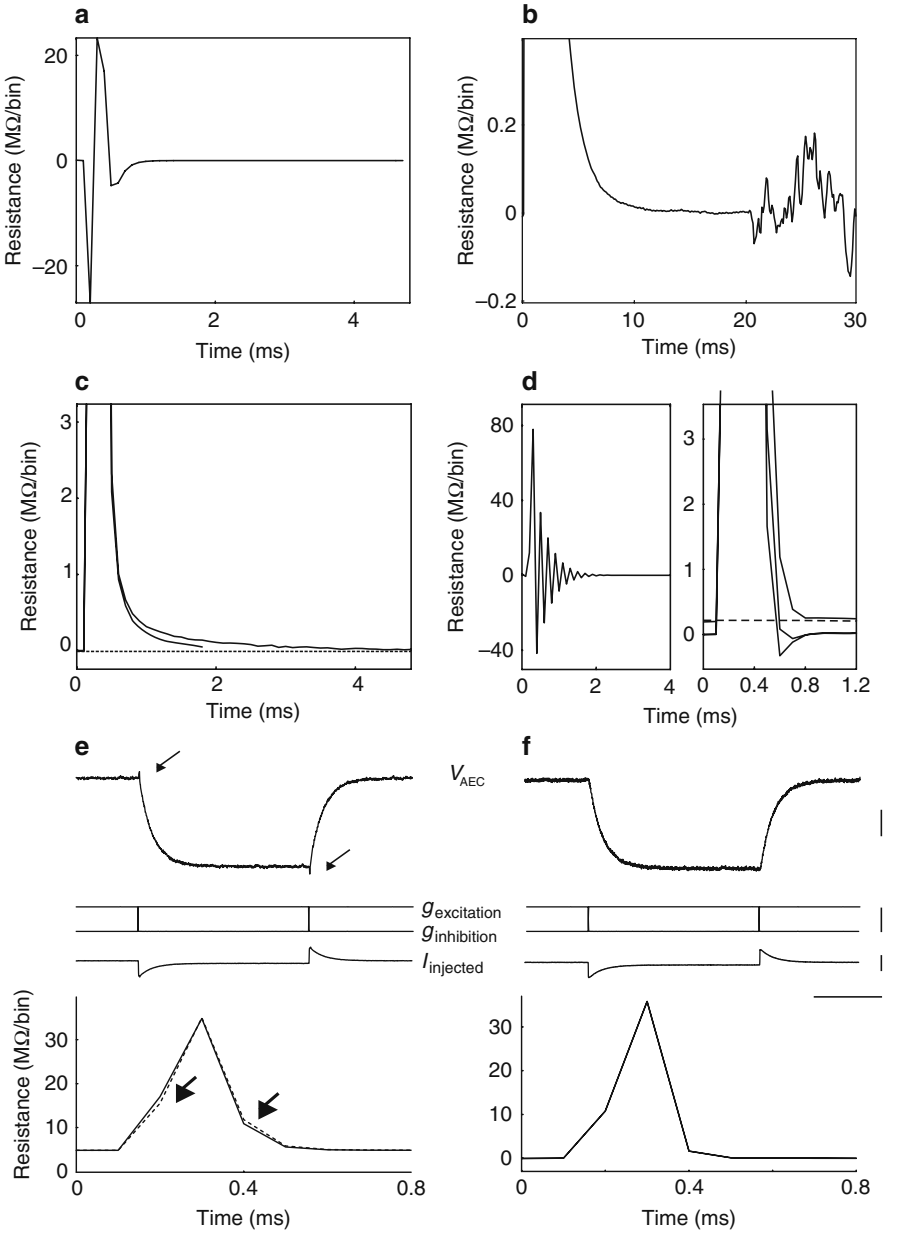

Fig. 8 Electrode kernels resulting from typical errors (Appendix 1). (**a**) Appearance of the estimated electrode kernel if bridge compensation was erroneously on during white noise injection. (**b**) If the size of the raw kernel is too big, the real-time estimation procedure might not follow. Here, an example of raw kernel obtained in this case, with noise dominating the kernel after 20 ms. Note that this error might manifest itself differently depending on the real-time system used. (**c**) If the chosen tail parameter is too small, the electrode kernel might not

operations and it can be an important source of error. Therefore, it is important to check that the kernel is not too large for the system.

The tail parameter is too small: one must specify what part of the kernel (which we called the tail) is used for estimating the membrane contribution. If the splitting time is too small, then the tail contains part of the electrode kernel, which makes the procedure fail. This can sometimes be seen as the electrode kernel not vanishing at the end (Fig. 8c) or as a negative part appearing in the electrode kernel (usually the kernel is entirely positive).

The tail parameter is too large: if the splitting time is too large, then remaining tail is too small to estimate the membrane kernel reliably. This also results in errors in the electrode kernel (although not as serious). There is however a broad range of values of this parameter for which there is no significant error in the kernel.

The capacitance neutralization has changed: it must be remembered that the electrode kernel captures in fact not only the electrode properties, but the properties of the whole recording setup, including the amplifier. Therefore if any circuit is used on the amplifier, their setting must remain unchanged as long the same electrode kernel is used, otherwise the estimation procedure should be run again.

The capacitance neutralization is too high: instability problems can appear if the capacitance neutralization circuit is set at a high value. This is not specific to AEC, but it can be identified in the electrode kernel as damped oscillations (Fig. 8d). The oscillations should disappear if the capacitance neutralization is set at a slightly lower value.

The electrode properties have changed: it happens that the electrode properties change during an experiment for some reason (e.g., small movements of the electrode). It results in compensation errors which can be seen as abnormal noise on the traces (with current noise injection). In this case the estimation

Fig. 8 (continued) contain the whole electrode response, which can manifest itself as the kernel not converging to 0 (*dashed line*) at its last point. In this case, the correct kernel is shown as a *thick line* (note that the electrode has an exceptionally slow component in this case). (**d**) Ringing due to capacitance overcompensation is readily seen as a damped oscillation at the level of the estimated kernel (*left*). While reducing capacitance neutralization, it is important to carefully monitor that no residual oscillation remains in the kernel, i.e., that the kernel always remains positive, as is the case for the kernel shown with the *thick line* (*right*), but not for the two kernels shown with *thin lines*. (**e**) Manifestations of fast nonlinearities in the recording circuitry, when using an electronic model cell + electrode. During conductance pulse injection in dynamic-clamp, artifacts (*arrows*) can be seen during fast current transients (*top panel*). Under these recording conditions, electrode kernels obtained using white noise injections of different amplitude (*bottom panel*; *solid line*: 0.5 nA; *dashed line*: 1.5 nA) are not identical (*arrows*). (**f**) After replacing one element in the recording circuitry, there are no artifacts left during conductance pulse injection. Under these recording conditions, electrode kernels obtained during white noise injections of different amplitude (as in e) are identical (perfectly superimposed on the graph). (Scale bars for e and f, *top panels*: vertical 5 mV, 100 nS, 2 nA, horizontal 200 ms)

procedure must be run again (just like with the standard bridge compensation method). The best practice is to run the estimation once in a while in order to check that the electrode properties have not changed.

The amplifier or filters are nonlinear: normally good electrical circuits in amplifiers and acquisition boards should be linear. However there can be small fast electrical nonlinearities if some components are faulty. This can be identified as small changes in the kernels for different noise amplitudes, as small transients in response to current pulses or as abnormal noise on compensated traces with fluctuating inputs (Fig. 8e, f). Searching for electrical nonlinearities should be done using an electronic circuit modeling the cell + electrode.

Appendix 2: Dynamic-Clamp Errors with Bridge Compensation

Steady-State Errors Resulting from Poor Electrode Compensation

At equilibrium, the recording potential before compensation is $V_\mathrm{r} = V_\mathrm{m} + R_\mathrm{e}^I$ (by definition of the electrode resistance, independently of its properties). If the estimated electrode resistance is $R_\mathrm{e} + \Delta R_\mathrm{e}$ (whether by bridge compensation or AEC), then the estimated potential is $V = V_\mathrm{m} + \Delta R_\mathrm{e}^I = (R + \Delta R_\mathrm{e})g(E - V)$, thus

$$V = \frac{(R + \Delta R_\mathrm{e})gE}{1 + (R + \Delta R_\mathrm{e})g}.$$

which can be expressed as follows: the dynamic clamp interprets the residual electrode resistance as part of the membrane resistance. The membrane resistance is

$$V_\mathrm{m} = RI = gR(E - V) = \frac{gRE}{1 + (R + \Delta R_\mathrm{e})g}$$

Therefore the relative error (compared to the case $\Delta R_\mathrm{e} = 0$) is

$$\begin{aligned}\frac{V_\mathrm{m}}{V_\mathrm{m}^*} - 1 &= \frac{1 + gR}{1 + (R + \Delta R_\mathrm{e})g} - 1 \\ &= -\frac{\Delta R_\mathrm{e} g}{1 + (R + \Delta R_\mathrm{e})g} \\ &\approx -\Delta R_\mathrm{e} g\end{aligned}$$

(for small error ΔR_e). For large clamp conductance g, the relative error tends to $-\Delta R_\mathrm{e}/(R + \Delta R_\mathrm{e})$.

Instabilities with Bridge Compensation

We consider a dynamic-clamp protocol with ideal bridge compensation, i.e., $V = V_r - R_e^I$, where R_e is the (perfectly estimated) electrode resistance. The dynamic clamp is analog, so that there is no feedback delay. The electrode is modeled as a resistor (R_e) and a capacitor (C_e). In the absence of the capacitor, the bridge estimation is perfect, i.e., $V = V_m$, otherwise it differs from the real membrane potential because of the capacitive current through the electrode. The dynamic-clamp current is $I = g\,(E - V_r - Re_I)$, thus:

$$I = \frac{g(E - V_r)}{1 - gR_e} = \alpha(E - V_r)$$

where α is a definition. We already note that $\alpha < 0$ if and only if $gR_e < 1$, which, as we will see, is the stability condition. In the following we consider Laplace transforms of the time-dependent variables. With the Laplace variable s, the impedance of a capacitor is $1/(Cs)$. The current flowing through the electrode is the command current minus the current flowing through the electrode capacitance:

$$I_e = I - C_e s V_r = \alpha(E - V_r) - C_e s V_r \tag{1}$$

It also equals the transmembrane current

$$I_e = (R_m^{-1} + Cs)V_m = (R_m^{-1} + Cs)(V_r - R_e I_e)$$

and thus

$$I_e = \frac{(R_m^{-1} + Cs)V_r}{1 + (R_m^{-1} + Cs)R_e} \tag{2}$$

From Eqs. (1) and (2), it follows:

$$(R_m^{-1} + Cs)V_r = (\alpha(E - V_r) - C_e s V_r)(1 + (R_m^{-1} + Cs)R_e)$$

The solutions are stable if and only if the roots of the following polynomial have a negative real part:

$$R_m^{-1} + Cx + (\alpha + C_e x)(1 + (R_m^{-1} + Cx)R_e)$$

This is equivalent to the statement that the sum of the roots is negative and their product is positive, that is:

$$C(\alpha R_e + 1) + C_e(1 + R_m^{-1} R_e) > 0$$
$$R_m^{-1} + \alpha(1 + R_m^{-1} R_e) > 0$$

If $\alpha > 0$, this is clearly true. Conversely, the second inequality can be re-expressed as $1 + \alpha (R_m + R_e) > 0$, and using the formula for α:

$$\frac{1 + gR_m}{1 - gR_e} > 0$$

which is true if and only if $gR_e < 1$ (i.e., $\alpha > 0$).

Thus, the condition for stability with ideal bridge compensation is $gR_e < 1$. There is no ringing in this case (only non-oscillatory instability), it only occurs when feedback delays are introduced (see next paragraph). To compare with the stability condition in the next section, it is useful to write this condition as follows:

$$gR < \frac{R}{R_e}$$

In our experiments (with high-resistance electrodes), this ratio was between 0.3 and 1, and in that case only conductances smaller than the membrane conductance can be injected. When the electrode is correctly compensated, the limiting factor is the feedback delay, as explained below, and the critical clamp conductance is much higher.

In the derivation of the critical conductance, we modeled the electrode resistance as a simple RC circuit, with the capacitor on the amplifier side. If the capacitance is distributed, the result would change slightly; e.g., if the capacitor is moved to the middle of the resistor, then the critical conductance will be twice higher (because half of the resistance if fully compensated).

Appendix 3: Fast Implementation of Kernel Estimation

In Section 2.1, we saw that the least-squares estimation of the kernel is a matrix problem $\mathbf{AX} = \mathbf{B}$, where $\mathbf{A}$ is a square matrix with coefficients $a_{i,j} = \langle I_{n-j} I_{n-i} \rangle$ for $i,j \in \{0 \ldots M-1\}$, $a_{i,M} = \langle I_{n-i} \rangle$ for $i \in \{0 \ldots M-1\}$, $\alpha_{M,j} = \langle I_{n-j} \rangle$ for $j \in \{0 \ldots M-1\}$, and $\alpha_{M,M} = 1$; $\mathbf{X}$ is a column vector with $X_i = K_i$ for $i \in \{0 \ldots M-1\}$ and $X_M = V_0$; $\mathbf{B}$ is a column vector with $B_i = < V_n I_{n-i} >$ for $i \in \{0 \ldots M-1\}$ and $B_M = < V_n >$.

The matrix has a special form if the signal I vanishes in the last M steps, so that $<I_{n-i}I_{n-j}> = <I_nI_{n+i-j}>$. Then we define $a_k = <I_nI_{n-k}>$ for all $k \in \{0 \ldots M-1\}$, and $y = <I_n>$, so that the matrix $\mathbf{A}$ can be written as follows:

$$A = \begin{pmatrix} a_0 & a_1 & a_2 & \cdots & a_{M-1} & y \\ a_1 & a_0 & a_1 & \cdots & a_{M-2} & y \\ a_2 & a_1 & a_0 & \cdots & a_{M-3} & y \\ \cdots & \cdots & \cdots & \cdots & \cdots & y \\ a_{M-1} & a_{M-2} & a_{M-3} & \cdots & a_0 & y \\ y & y & y & \cdots & y & 1 \end{pmatrix} = \begin{pmatrix} \tilde{A} & Y \\ Y^T & 1 \end{pmatrix}$$

We also define $\mathrm{X} = \begin{pmatrix} \mathbf{K} \\ V_0 \end{pmatrix}$ and $\mathrm{B} = \begin{pmatrix} \tilde{\mathbf{B}} \\ \langle V_n \rangle \end{pmatrix}$ and $\mathrm{Y}^T = (y\, y \ldots\, y)$.

Solving the matrix equation by block gives

$$V_0 = \langle V_n \rangle - Y^T \mathrm{K} = \langle V_n \rangle - \langle I_n \rangle \sum_{p=0}^{M-1} K_p$$

$$(\tilde{\mathrm{A}} - YY^T)K = \tilde{B} - \langle V_n \rangle Y$$

The coefficients of the matrix $\mathrm{U} = \tilde{\mathrm{A}} - \mathrm{YY}^T$ are $u_{i,j} = a_{|i-j|} - \langle I_n \rangle^2$. The coefficients of the vector $\tilde{B} - \langle V_n \rangle Y$ are $<V_nI_{n-i}> - <V_n><I_n>$. The matrix $\mathbf{U}$ is a Toeplitz matrix, and solving a linear problem for a Toeplitz matrix can be done very quickly with the use of the Levinson–Durbin algorithm (which is documented, e.g., in Press et al., 1993). It is not necessary to store all the values of V_n and I_n, since the averages $<V_nI_{n-j}>$ can be computed online in real time (M additions at each time step).

Appendix 4: Extraction of the Electrode Kernel

To extract the electrode kernel (Section 2.3), we need to solve the following equation for K_e:

$$K = K_\mathrm{m} * \frac{K_\mathrm{e}}{\int K_\mathrm{e}} + K_\mathrm{e} \tag{3}$$

where K_m is a known exponential function representing the membrane kernel (resistance R_m, time constant τ_m). We use the Z-transform to transform convolutions into products

$$\mathcal{Z}[K_\mathrm{e}] = \mathcal{Z}[K]\left(\frac{\mathcal{Z}[K_\mathrm{m}]}{R_\mathrm{e}} + 1\right)^{-1}$$

We have

$$\mathcal{Z}[K_\mathrm{m}] = R_\mathrm{m}\frac{\Delta}{\tau_\mathrm{m}}\frac{1}{1-\lambda z^{-1}}$$

with $\lambda = e^{-\Delta/\tau_m}$. We define $\alpha = \frac{R_\mathrm{m}\Delta}{R_\mathrm{e}\tau_\mathrm{m}}$ and after a little algebra, we obtain

$$\mathcal{Z}[K_\mathrm{e}] = \mathcal{Z}[K]\left(1 - \frac{\alpha}{\alpha+1}\frac{1}{1-\frac{\lambda}{\alpha+1}z^{-1}}\right)$$

The second term corresponds to a first-order low-pass filter which can be implemented recursively as follows:

$$\begin{cases} Y_0 = & \frac{\alpha}{\alpha+1}K_0 \\ Y_n = & \frac{\alpha}{\alpha+1}K_n + \frac{\lambda}{\alpha+1}Y_{n-1} \quad \text{for } n>0. \end{cases}$$

then $K_\mathrm{e} = K - Y$.

References

Anderson, J.S., Carandini, M., and Ferster, D. (2000). Orientation tuning of input conductance, excitation, and inhibition in cat primary visual cortex. J Neurophysiol *84*:909–26.

Borg-Graham, L. J., Monier, C., and Frégnac, Y. (1998). Visual input evokes transient and strong shunting inhibition in visual cortical neurons. Nature *393*:369–373.

Brennecke, R., and Lindemann, B. (1971). A chopped-current clamp for current injection and recording of membrane polarization with single electrodes of changing resistance. TI–TJ Life Sci *1*:53–58.

Brennecke, R., and Lindemann, B. (1974a). Theory of a membrane-voltage clamp with discontinuous feedback through a pulsed current clamp. Rev Sci Instrum *45*:184–188.

Brennecke, R., and Lindemann, B. (1974b). Design of a fast voltage clamp for biological membranes, using discontinuous feedback. Rev Sci Instrum *45*:656–661.

Brette, R., Piwkowska, Z., Rudolph, M., Bal, T., and Destexhe, A. (2007). A non-parametric electrode model for intracellular recording. In Proceedings of CNS 2006 (Edinburgh, UK). Neurocomputing *70(10–12)*:1597–1601.

Brette, R., Piwkowska, Z., Rudolph-Lilith, M., Bal, T., and Destexhe, A. (2007). High-resolution intracellular recordings using a real-time computational model of the electrode. ARXIV preprint. http://arxiv.org/abs/0711.2075

Brette, R., Piwkowska, Z., Monier, C., Rudolph-Lilith, M., Fournier, J., Levy, M., Frégnac, Y., Bal, T., and Destexhe, A. (2008). High-resolution intracellular recordings using a real-time computational model of the electrode. Neuron *59*(3):379–391.

Contreras, D., Destexhe, A., and Steriade M. (1997). Intracellular and computational characterization of the intracortical inhibitory control of synchronized thalamic inputs in vivo. J Neurophysiol *78*(1):335–350.

Crochet, S., Fuentealba, P., Cisse, Y., Timofeev, I., and Steriade, M. (2006). Synaptic plasticity in local cortical network in vivo and its modulation by the level of neuronal activity. Cereb Cortex *16*:618–631.

Destexhe, A., Contreras, D., and Steriade, M. (1998) Mechanisms underlying the synchronizing action of corticothalamic feedback through inhibition of thalamic relay cells. J Neurophysiol *79*(2):999–1016.

Destexhe, A., and Paré, D. (1999). Impact of network activity on the integrative properties of neocortical pyramidal neurons in vivo. J Neurophysiol *81*(4):1531–47.

Destexhe, A., Rudolph, M., Fellous, J. M., and Sejnowski, T. J. (2001). Fluctuating synaptic conductances recreate in vivo-like activity in neocortical neurons. Neuroscience *107*:13–24.

Finkel, A. S., and Redman, S. (1984). Theory and operation of a single microelectrode voltage clamp. J Neurosci Methods *11*:101–127.

Haider, B., Duque, A., Hasenstaub, A. R., Yu, Y., and McCormick, D. A. (2007). Enhancement of visual responsiveness by spontaneous local network activity in vivo. J Neurophysiol 97:4186–4202.

Harsch, A., and Robinson, H. P. (2000). Postsynaptic variability of firing in rat cortical neurons: the roles of input synchronization and synaptic NMDA receptor conductance. J Neurosci *20*(16):6181–6192.

Higley, M. J., and Contreras, D. (2007). Cellular mechanisms of suppressive interactions between somatosensory responses in vivo. J Neurophysiol *97*:647–658.

Hines, M. L., and Carnevale, N. T. (1997). The NEURON simulation environment. Neural Comput *9*:1179–1209.

Hirsch, J. A., Alonso, J. M., Reid, R. C., and Martinez, L. M. (1998) Synaptic integration in striate cortical simple cells. J Neurosci *18*:9517–9528.

Mainen, Z. F., and Sejnowski, T. J. (1995). Reliability of spike timing in neocortical neurons. Science *268*(5216):1503–1506.

Margrie, T.W., Brecht, M., and Sakmann, B. (2002) In vivo, low-resistance, whole-cell recordings from neurons in the anaesthetized and awake mammalian brain. Pflugers Arch *444*(4):491–498.

Mokeichev, A., Okun, M., Barak, O., Katz, Y., Ben-Shahar, O., and Lampl, I. (2007). Stochastic emergence of repeating cortical motifs in spontaneous membrane potential fluctuations in vivo. Neuron *53*:413–425.

Monier, C., Fournier, J., and Frégnac, Y. (2008). In vitro and in vivo measures of evoked excitatory and inhibitory conductance dynamics in sensory cortices. J Neurosci Methods, *169*(2):323–365.

Paz, J. T., Chavez, M., Saillet, S., Deniau, J. M., and Charpier, S. (2007). Activity of ventral medial thalamic neurons during absence seizures and modulation of cortical paroxysms by the nigrothalamic pathway. J Neurosci *27*:929–941.

Pei, X., Volgushev, M., Vidyasagar, T. R., and Creutzfeldt, O. D. (1991). Whole-cell recording and conductance measurements in cat visual cortex in vivo. NeuroReport *2*:485–488.

Press, W. H., Flannery, B. P., Teukolsky, S. A., and Vetterling, W. T. (1993). Numerical Recipes in C: The Art of Scientific Computing (Cambridge; New York, Cambridge University Press).

Prinz, A. A., Abbott, L. F., and Marder, E. (2004). The dynamic clamp comes of age. Trends Neurosci *27*:218–224.

Purves, R. D. (1981). Microelectrode methods for intracellular recording and ionophoresis (London ; New York, Academic Press).

Robinson, H. P., and Kawai, N. (1993). Injection of digitally synthesized synaptic conductance transients to measure the integrative properties of neurons. J Neurosci Methods *49*:157–165.

Sharp, A. A., O'Neil, M. B., Abbott, L. F., and Marder, E. (1993). The dynamic clamp: artificial conductances in biological neurons. Trends Neurosci *16*:389–394.

Shu, Y., Hasenstaub, A., Badoual, M., Bal, T., and McCormick, D. A. (2003). Barrages of synaptic activity control the gain and sensitivity of cortical neurons. J Neurosci *23*:10388–10401.

Steriade, M., Timofeev, I., and Grenier, F. (2001). Natural waking and sleep states: A view from inside neocortical neurons. J Neurophysiol *85*:1969–1985.
Stuart, G., and Spruston, N. (1998) Determinants of voltage attenuation in neocortical pyramidal neuron dendrites. J Neurosci *18*(10):3501–10.
Tateno, T., Robinson, H.P. (2006) Rate coding and spike-time variability in cortical neurons with two types of threshold dynamics. J Neurophysiol *95*(4):2650–2663.
Thomas, M. V. (1977). Microelectrode amplifier with improved method of input-capacitance neutralization. Med Biol Eng Comput *15*:450–454.
Thomson, A. M., and Deuchars, J. (1997). Synaptic interactions in neocortical local circuits: dual intracellular recordings in vitro. Cereb Cortex *7*:510–522.
Wehr, M., and Zador, A. M. (2003). Balanced inhibition underlies tuning and sharpens spike timing in auditory cortex. Nature *426*:442–446.
Wilent, W. B., and Contreras, D. (2005a). Dynamics of excitation and inhibition underlying stimulus selectivity in rat somatosensory cortex. Nat Neurosci *8*:1364–1370.

Key Factors for Improving Dynamic-Clamp Performance

Robert Butera and Risa Lin

Abstract The dynamic-clamp technique has been recognized and used by electrophysiologists for over 15 years. Nevertheless, only a small number of papers have been written focusing on the performance and reliability of this protocol and how the accuracy of a dynamic-clamp system can be assessed. Here we review the published literature to date, focusing on how experimental, computational, and algorithmic factors contribute to the reliability of the dynamic-clamp protocol. Several of these papers point towards a common and technologically realizable solution – the need for dynamic-clamp systems that run at computational rates much faster (100–200 kHz) than currently available. At present, dynamic-clamp rates are limited by the use of desktop computers and rationalized by the kinetics of the model simulated. Recent results show that faster and lower latency systems would result in a greater range of conductances that could be utilized, improved stability, and more accurate real-time model simulations.

1 Introduction

The dynamic-clamp protocol (Robinson and Kawai 1993, Sharp et al. 1993) is an increasingly popular tool in cellular electrophysiology. Applications have expanded from the study of intrinsic single neuron properties to the control of small neural networks and even the creation of hybrid networks that combine biological and simulated neurons. The application of such methods has been covered in numerous review articles and reference material (Preyer and Butera 2005, Prinz 2004, Prinz et al. 2004) as well as other articles in this volume.

R. Butera (✉)
Laboratory for Neuroengineering, School of ECE, Georgia Institute of Technology, Atlanta, GA 30332-0250, USA
e-mail: rbutera@gatech.edu

A. Destexhe, T. Bal (eds.), *Dynamic-Clamp*, Springer Series in Computational Neuroscience 1, DOI 10.1007/978-0-387-89279-5_17,

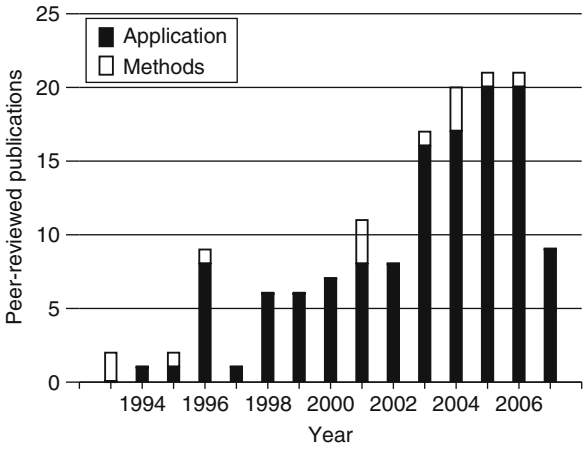

Fig. 1 Number of peer-reviewed publications using the dynamic-clamp technique (*black*) or developing or evaluating methodologies for implementing the dynamic clamp (*white*)

The dynamic clamp is seeing increasing usage. Figure 1 illustrates the number of peer-reviewed journal articles published by year. Nevertheless, very few papers have discussed factors affecting dynamic-clamp performance. Limitations on dynamic-clamp performance include experimental considerations, numerical and algorithmic issues, and hardware platform-specific issues. The first section of this chapter will discuss the experimental performance of dynamic clamp and how experimental design and techniques affect the accuracy of voltage measurements as well as the stability and dynamic range of the entire system. The second section will focus on the numerical performance of dynamic clamp and discuss factors that affect the computation of the membrane model and therefore, the speed, accuracy, and real-time reliability of the system. The final section will suggest benchmarks that can be used to quantify these measures of performance and determine the limits of acceptable accuracy and reliability for dynamic-clamp experiments.

2 Experimental Performance

A typical dynamic-clamp system includes an electrophysiology amplifier for measuring membrane potential and injecting current, a multifunctional data acquisition system (DAQ), and a computation platform for computing the membrane model, such as a PC or dedicated hardware. The multifunctional DAQ is the key link between the computer and the electrophysiology amplifier, and includes a digital-to-analog converter (DAC) to generate an output voltage that controls the current injected into the cell and an analog-to-digital converter (ADC) to convert the measured membrane voltage to a binary number to be read by the computational platform. Most multifunctional DAQs have many more input (measurement) channels than output channels.

2.1 ADC and DAC Resolution and Conversion Issues

DAQ systems operate by converting measured voltages to digital values and digital values to output voltages on a regular basis. Commercial DAQ hardware specify an overall conversion rate, typically in kilosamples per second. This rate is the total number of samples that can be converted per second across all channels. For many dynamic-clamp applications, only one channel is used if only measuring from one cell. However, a growing number of applications in the future may involve the use of multiple input channels. In such cases, many commonly used DAQ systems have only one ADC and it must multiplex ("take turns") each channel one by one for conversion. For example, if a board specifies a conversion rate of 200 ksamples/s and a dynamic-clamp application requires four ADC channels, the conversion rate for each channel is 50 ksamples/s. Another important consideration here is that for more than one input channel, *not all of the channels are read at the same time*. The one sample delay in reading each channel may or may not be critical, depending on the application. If such delays are critical, manufacturers sell more expensive DAQ systems which feature simultaneously sampling ADCs. Such systems can sample multiple channels simultaneously prior to conversion.

The magnitude of voltages that will be measured and of currents that will be injected must be considered for optimal dynamic-clamp performance. It is extremely important to match the conversion range of the ADC and DAC to the measured voltage and injected currents. The *input* (*or output*) *range* describes the range of voltages that are converted to a digital representation, while the *resolution* is the number of bits of the digital representation. These two factors, along with the *accuracy* (described further below) specified by the manufacturer, determine the smallest change of voltage (ΔV) that can be measured or output. For example, if the input range is ± 10 V and the resolution is 12 bits, the smallest measurable increment of voltage will be the voltage range (20 V, from –10 to + 10 V) divided by 4,096 (2^{12}), or about 4.88 mV.

Using this example range, a typical electrophysiology amplifier outputs a "$10V_m$" voltage, which is 10 times the measured membrane potential. Practically speaking, the dynamic-clamp system only needs to measure a voltage range of ± 100 mV; over this range, the electrophysiology amplifier will output a range of ± 1 V. Thus the raw membrane potential signal has a gain of 10 applied to it by the amplifier. If this voltage were connected to a DAQ board with an input range of ± 10 V, then ΔV would be about 0.488 mV. This does not sound too bad, but the measurement range of 1–10 V is not being utilized, resulting in a lower effective resolution. If the $10V_m$ output were scaled by an external amplifier by a factor of 10 (or the dynamic range of the ADC were changed from ± 10 to ± 1 V), the raw signal would have a net gain of 100 applied to it (10 from the electrophysiology amplifier and 10 from the external amplifier). Under such conditions, the theoretical ΔV would be 0.0488 mV.

In practice, most commercial multifunction DAQ boards have a programmable gain, which allows the input gain to be selected by software from a rather wide range, from ±10 mV to ±10 V. Therefore, with appropriate consideration of the scaling of the measured membrane potential, it is rather simple to maximize the usable input range of the ADC.

However, DAQ boards also have a specified *accuracy* of the conversion to/from a voltage. The accuracy represents an uncertainty in the data conversion process, and is often expressed in terms of a voltage (at a given input range) or, more commonly, in terms of *least-significant bits* (*lsb*). To revisit the example above, if the ADC has an accuracy of ±2 lsbs, then there exist two bits of measurement noise and the ΔV in terms of the membrane potential would be 1.95 mV or 0.195 mV (without and with the additional gain to improve the input range), respectively. In practice, due to the well-defined range of the membrane potential for all electrically excitable cells and the gains on this measured signal provided by electrophysiology amplifiers, ΔV is typically in the same range or much better than the amount of noise typically encountered in a membrane potential recording. As a result, 12 bits is common and adequate for most voltage measurements.

The effects of precision and accuracy on the output current are much more profound, however. Excitable cells respond to a wide range of currents from picoamperes to nanoamperes. The output range of the DAC should ideally be as small as possible to maximize the precision of the currents injected, yet as large as possible to accommodate the magnitude of currents to be injected into the cell. For example, consider an electrophysiology amplifier with an input current conversion of 1 V/nA (typically, the injected current is controlled by an analog voltage converted to a current). If the DAC is 12 bits with an output range of ±10 V, the range of currents that can be output is ±10 nA with a precision of 4.88 pA. If the DAC only had an accuracy of ± 2 lsb, then the real precision would only be about 19.5 pA. Such accuracy may be acceptable in some cases (e.g., invertebrate neurons or spiking currents in mammalian neurons), but would be unacceptable for many mammalian neurons. Similar to the earlier example for input gain, the output gain can be maximized by altering the current conversion gain (V/nA) by choice of appropriate headstage or via the electrophysiology amplifier. Unlike input range, however, the output range on many commercial DAC boards cannot be selected via software. It is either fixed at ±10 V or can be user-supplied by a voltage source (e.g., battery or power supply) which is used as a reference for the output voltage range.

Maximizing the output range for injected currents becomes particularly problematic if the currents to be injected span a wide range. For example, consider a dynamic-clamp experiment that may wish to inject a low-amplitude subthreshold current as well as spike-related current. Figure 2 illustrates an extreme example of this, where a modeled bursting neuron was implemented on an RC (resistor–capacitor) cell model connected to an electrophysiology amplifier via dynamic clamp. Bursting neuron models have rather small currents underlying the burst and large currents for generating the spiking. When the

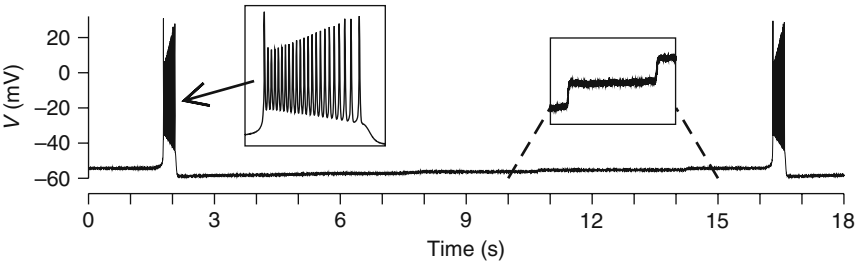

Fig. 2 Intrinsically bursting neuron model implemented via an RC cell and an electrophysiology amplifier and a dynamic clamp. The dynamic clamp provided all the dynamic ionic currents for the membrane potential dynamics. The insets highlight the ability to generate spikes during the burst (*left*) and the discretization of membrane potential during the interburst interval (*right*). Modified from Butera et al. (2001)

voltage range of the interburst interval is examined, stepwise changes in the membrane potential can be seen. These are due to 1-bit changes in the very small output current being injected to the neuron. We were only able to even make this modeled example work by providing an external reference voltage to the injected current so that the largest equivalent current that could be generated via the DAC was about the largest necessary for this RC-cell-based experiment. The parameters utilized also demonstrated a mismatch from the known simulated values; further simulations revealed that the different dynamics found were also due to this quantization error.

2.2 Dynamic-Clamp Stability

The stability of the dynamic clamp is limited by factors related to single-electrode recording as well as the delay caused by the sampling of the DAQ and the entire computational loop. The use of a single electrode requires recording in bridge mode or discrete current clamp (DCC). The DCC also imposes strict limitation on the sampling rate, thus this discussion is primarily concerned with recording in bridge mode, though the effects are similar. Lack of complete compensation in either method results in an offset in the membrane potential measurement proportional to the injected current.

Instabilities in the measured membrane potential have been observed in a variety of dynamic-clamp implementations. While whole system stability is readily obvious, we and other labs (T. Netoff, R. Calabrese, A. Prinz, personal communications) have often observed transient instabilities that appear as a transient ringing artifact in the action potential (Fig. 3AB). These instabilities often occur when a dynamic-clamp conductance is increased beyond a specific value. These values are often well below realizable conductance values and impede some experiments where larger conductances are desirable. These

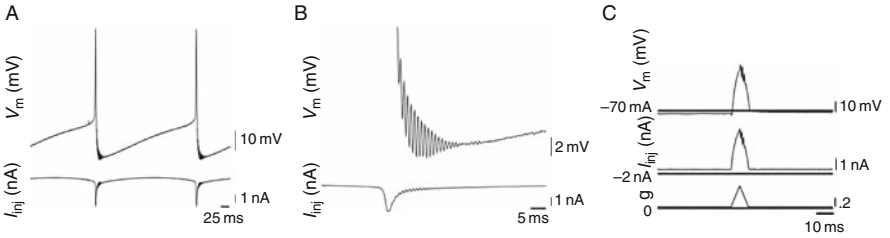

Fig. 3 An example of a transient instability (**A**) in a spiking neuron, which appears as a ringing artifact in the afterhyperpolarization of the action potential. The instability appeared as the maximal conductance of a slow potassium current, I_M, was increased. Panel **B** is a closeup of the instability. Panel **C** illustrates a similar instability at subthreshold potentials in response to an up/down ramp of injected conductance into a neuron. Modified from Preyer and Butera (2009)

instabilities are not due to numerical integration, as they can also occur when an up/down ramp of conductance is injected via dynamic clamp into the neuron (Fig. 3C). Instabilities have also been reported when the artificial conductance became significantly larger than the resting input conductance of the cell (Brette et al. 2008, Brizzi et al. 2004). In that particular study, they eliminated the instability by low-pass filtering the membrane potential before sampling. Such a solution is only viable for particular applications with lower sampling rates and where there is no significant effect on the membrane potential trajectory.

Further investigation by us showed that the transient instabilities illustrated in Fig. 3 are not due to saturation of the electronic equipment or the numerical methods used in the model. Rather, they occur when the electrode is insufficiently compensated (both series resistance and capacitance), even at compensation values that are generally considered acceptable by experimentalists (e.g., 80–90% compensation of series resistance). Simulations also showed that significantly faster dynamic-clamp rates (100–200 kHz) result in much greater stability at higher conductances. At present, dynamic-clamp rates are rationalized based on the time constants of the integrated gating variables; our recent work (Preyer and Butera 2009) shows that higher rates would enable the use of much higher conductance values without losing stability. An alternative approach for stability at higher conductance values would to use online estimation techniques to estimate a general electrode model, rather than statically setting the resistance/capacitance parameters as is done with current amplifiers. Such a method has been recently demonstrated (Brette et al. "Dynamic Clamp with High-Resistance Electrodes Using Active Electrode Compensation In Vitro and In Vivo" in this volume, Brette et al. 2007, 2008), in which a kernel is estimated for the electrode and instrumentation prior to the experiment and implemented in real time. This technique captures the electrical characteristics of not only the electrode, but also of any other hardware between the computer and the electrode.

3 Numerical Performance

The computational performance of dynamic clamp suffers from a trade-off between the speed of computation and numerical accuracy. After acquiring each sample, the computational hardware must compute a step of numerical integration of the gating variables as well as calculate output currents and any other quantities that require calculation. The dynamic-clamp sampling rate determines how much time is in a given computational cycle for these operations to be performed, and the duration of the computational cycle restricts the types of numerical methods that may be used to integrate the gating variables. Higher rates dictate that less time is available per cycle to perform computations. Besides numerical integration methods, other factors that can affect numerical performance include jitter, latency, and quantization error.

3.1 Numerical Integration Methods

The choice of numerical integration method has a significant effect on the numerical performance of the dynamic clamp. Unlike traditional applications of numerical integration, it is often not possible in real-time systems to simply decrease the time step and wait longer for the model result. Two of the simplest methods are the Euler method (direct forward integration) and a method commonly referred to as the Exponential Euler method (Moore and Ramon 1974, Rush and Larsen 1978), which is a direct solution of the relaxation of the gating variable to steady state with the voltage fixed at its current measurement value. Both methods are quick and easy to implement, and with the use of lookup tables, each only requires a single multiply and a single add operation per integration (Butera et al. 2001). It is often thought that the Exponential Euler method offers a higher level of accuracy, but recent numerical analysis suggests that Exponential Euler has a larger theoretical error bound than Euler in terms of the time step and time constant (Butera and McCarthy 2004). Higher order explicit methods will achieve greater accuracy, but at the expense of increasing the minimum possible time step due to higher computational demands. Iterative methods, usually based on implicit solution schemes, offer higher promise, but are limited by a variable amount of computation time for a required level of accuracy.

Given that the membrane potential measurement often has a certain amount of noise (typically 0.5–2 mV), it is reasonable to ask "is all of this accuracy necessary?" We recently performed a numerical analysis of the Euler and Exponential Euler methods in the case of a dynamic clamp (Butera and McCarthy 2004). Assuming the measured voltage V has a given uncertainty (noise) level of δ, we show that the error bound for one step of the Euler method is bounded by

$$|\text{Error}| = \left(e^{\Delta t/\tau} - 1\right)\left(\frac{\delta}{4|d|} + \frac{\Delta t}{\tau}\right)$$

where Δt is the integration time step, τ is the time constant of the gating variable, and d is the slope factor of the sigmoidal steady-state voltage-dependent activation curve; a smaller value of d corresponds to a steeper curve. Several things are evident from the form of this error bound. First, it is a common "rule of thumb" for Δt to be several times smaller than τ, and an ideal value is for $\Delta t/\tau$ to be 0.1 or less; such assumptions are consistent with the error term above. However, notice that there are two additive terms – one related to the measured voltage error and a second related to the time step. The voltage term highlights that the slope of the steady-state activation curve has a major role in determining how acceptable the amount of measurement noise is. Depending on noise levels and the integration time step, the effects of these terms vary. Figure 4 illustrates the error bound as a function of $\Delta t/\tau$ and δ/d. When noise levels are low, the error scales with Δt^2, when the noise term dominates the error scales with Δt. Likewise, in low-accuracy situations where $\Delta t/\tau$ is larger than ideal, improvement in measurement error will not significantly improve the error bound.

3.2 Jitter

Jitter is the variability in the actual duration of a computational cycle. For example, if a dynamic-clamp system is to run at 10 kHz, the nominal period is 100 μs. However, some cycles may occur after 97 or 103 μs. Jitter is barely existent in hardware-based dynamic clamp where a microprocessor is directly programmed, but cannot be avoided with any system that uses an operating system. Issues with jitter are especially evident on systems based on desktop operating systems, though recent multicore processes and advanced programming methods may alleviate these concerns. One approach to minimizing jitter is to utilize real-time operating systems designed for the well-timed operation of

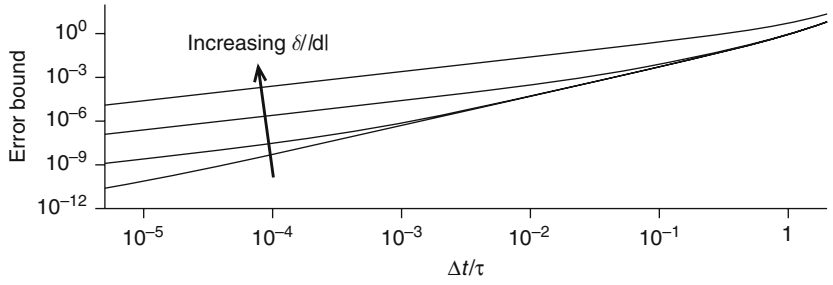

Fig. 4 Error bound as a function of $\Delta t/\tau$ and δ/d according to the error bounds for the Euler method. See text for details. Modified from Butera and McCarthy (2004)

periodic real-time tasks (Butera et al. 2001, Dorval et al. 2001, Raikov et al. 2004). Another approach is to recognize the presence of jitter and incorporate a measurement of the actual time step into the numerical computation. One system (Nowotny et al. 2006, Pinto et al. 2001) uses Microsoft Windows to run as fast as possible, as opposed to periodically, and at each time step calculates the length of the previous cycle and estimates the duration of the next cycle. While this puts the jitter out of the control of the user, if well bounded it still yields usable results. NEURON has also been ported to run in a similar mode under Windows (Sadoc et al. "Re-Creating In Vivo-Like Activity and Investigating the Signal Transfer Capabilities of Neurons: Dynamic-Clamp Applications Using Real-Time NEURON" in this volume).

Jitter can also simply arise from the demands of other concurrently running programs on the processor as well as asynchronous requests for data from peripheral devices such as network cards and hard disk drives. Simple precautions to take during an experiment include minimizing the number of running processes, minimizing graphics intensive applications that require rapid screen updates, disconnecting the computer from a network, and buffering data to memory instead of writing to a hard disk during real-time operations (Butera et al. 2001). Jitter increases with the dynamic-clamp nominal cycle rate, as a greater fraction of the cycle period is dedicated to solving the computations of the model (and a lesser fraction to system resources). Figure 5 illustrates performance of an earlier dynamic-clamp system of ours for a given model as the nominal computational rate is increased. The panels illustrate the fraction of computational cycles that were more than 10% longer than the nominal specified cycle period, and the worst-case (longest) cycle period, plotted in terms of frequency. Performance was worst with constant disk drive or ongoing network activity during the real-time process. Recent advances in multicore processors may reduce the effects of such issues, and we have observed less jitter on dual processor machines, even when all computational tasks were running on one processor (i.e. the other processor is free to service device requests).

The numerical effects of jitter have recently been studied. Simulations of dynamic clamp show that for a time step modeled as a uniformly distributed random variable, the maximum error for a random time step is equal to the error of the fixed worst-case time step. This result suggests that if the worst-case time step provides satisfactory accuracy, then the effect of jitter can be ignored (Bettencourt et al. 2008).

3.3 Latency

Latency refers to the time it takes for the system to produce an output on the DAC from the time an input arrives at the ADC. Thus, the system cannot have a computational cycle period smaller than the overall latency, which determines the upper limit of the sampling rate. Some latencies are fixed, such as the delay associated with the measurement and conversion of each ADC measurement

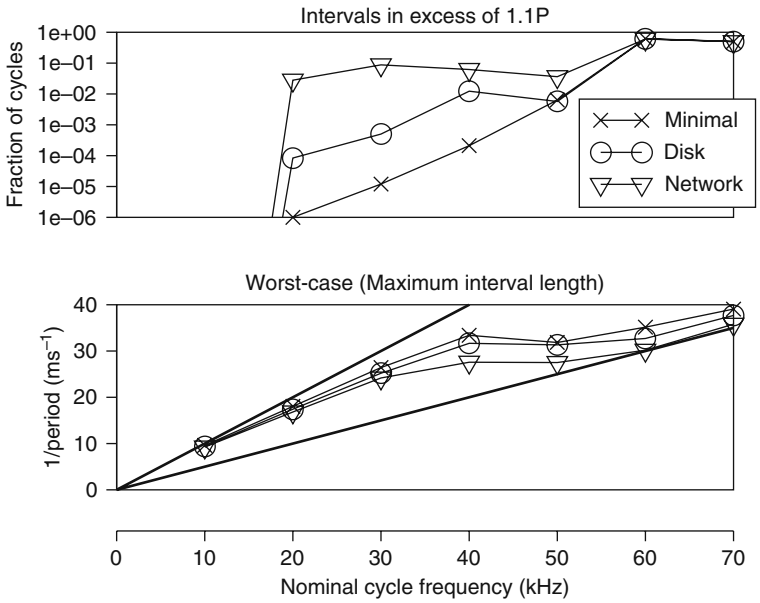

Fig. 5 Effects of nominal cycle rate and peripheral hardware demands on jitter for a Hodgkin–Huxley model simulated at various nominal cycle rates. Legend indicates results with the network card removed and disk drive asleep (minimal), constant background network activity (network), and constant hard drive reading activity (disk). *Top panel* illustrates fraction of measured periods more than 10% longer than the specified period. *Bottom panel* illustrates the worst-case measured period, plotted as a reciprocal of period (ms^{-1}). The upper solid line is the identity line, representing the ideal case where worst-case period is the specified period. The lower solid line is the identity/2 line, which the perfomance approaches when the computational cycle becomes so short that every-other calculation is essentially missed (i.e., not computed). Modified from Butera et al. (2001)

and DAC output. The computational component is model dependent, as more complex models will require longer computations.

System latency can also affect the numerical solution, as it introduces a fixed delay into the system. The timing of the ADC input and DAC output can vary from implementation to implementation, depending on the coding of the periodic computational process. Recently, Bettencourt et al. (2008) showed that the solution of a system can vary significantly with latency, even when the latencies are less than the duration of a single computational cycle period.

4 Performance Benchmarks

In order to compare the performance of different dynamic-clamp setups composed of a variety of hardware and software implementations, a set of objective performance benchmarks is needed that assesses experimental and numerical performance, especially at high sampling rates. It is likely that a complete panel

of performance benchmarks will include both computational and experimental protocols. These benchmarks should include not only the sampling rate of the system, but also statistics that reflect the system's measurement accuracy and real-time reliability (Fig. 6).

4.1 System-Wide Performance

In Raikov et al. (2004), we described how a measure of the overall system performance, including latencies, jitter, quantization errors, and

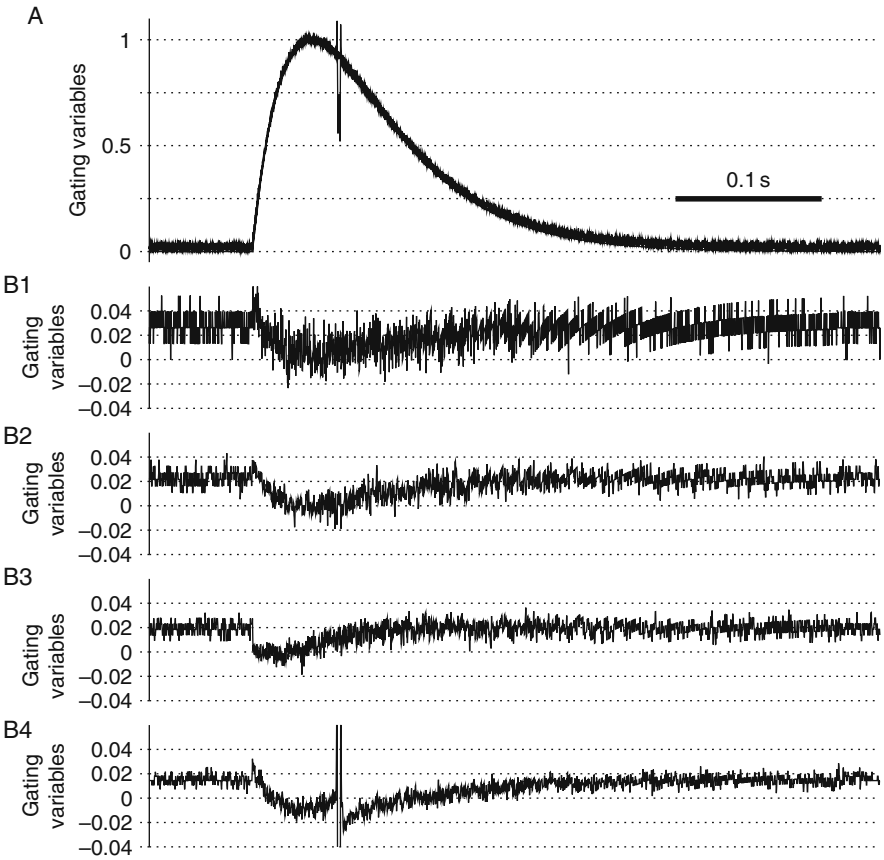

Fig. 6 Stimulus reconstruction of an artificial conductance. *Upper panel* (**A**) illustrates the reconstructed synaptic conductance; the vertical spike indicates a divide-by-zero error in the reconstruction where the measured current is near zero, but so is the $(V - E)$ term (see text). Panels **B1**–**B4** illustrate the error signal between the reconstructed and specified stimulus for increasing conductance magnitudes (B4 corresponds to the reconstruction shown in A). At lower magnitudes, the effects of quantization noise on the output (e.g., B1) are quite evident. Modified from Raikov et al. (2004)

electrophysiological factors such as bridge balance can easily be made (this will not assess numerical issues related to integration). The process is to apply a known conductance time course to a neuron via dynamic clamp. The resulting voltage trajectory as well as the true injected current (output by the electrophysiology amplifier) is recorded. The measured current and voltage, along with the specified reversal potential of the modeled injected current, can be used to reconstruct the stimulus. For example, let $g(t)$ represent a specified conductance time-course, $V(t)$ is the measured voltage in response to the application of $g(t)$, $I(t)$ is the measured current injected into the neuron, and E_{rev} is the reversal potential. The injected current specified by the dynamic clamp is $g(t)(V(t) - E_{\text{rev}})$. The reconstructed conductance $g_{\text{est}}(t)$ is calculated as

$$g_{\text{est}}(t) = \frac{I(t)}{V(t) - E_{\text{rev}}}$$

This method is illustrated in Fig. 4 as the same conductance waveform is repeatedly applied to a neuron scaled by different magnitudes. The difference between the actual waveform and the reconstructed waveform yields a residual error conductance waveform that may contain a baseline offset. In this particular example, the offset is due to quantization error that produces a small 1-bit offset in the DAC output driving current injection, which results in a small DC current. When this offset is taken into account, the magnitude of the residual error compared with the reconstructed stimulus waveform gives a measure of the magnitude of the system error. This analysis can indicate whether the primary source of noise in measurements is due to experimental conditions, such as resistance and capacitance compensation, or quantization. Similar analyses can be conducted by using a model RC circuit cell or a simulated neuron, where the exact output is known, in place of a biological neuron and quantifying errors in the shape of the action potential and channel currents (Bettencourt et al. 2008, Dorval et al. 2001). Experimenters can go further by introducing additional latencies in the hardware or software, adding jitter, or changing the numerical methods to determine the sensitivity of their system to these factors.

4.2 Input/Output Assessment

A complementary approach to that in the previous section that is particularly useful for assessing quantization and latency measures is a simple input/output test. A dynamic-clamp model is run to provide a computational load on the system; however, the input and output are not used for an actual dynamic-clamp experiment. Instead, a sinusoidal voltage waveform is provided at the input and the model simply copies the waveform to the output. By comparing the simultaneous traces of the input and output waveform on an oscilloscope,

latencies and quantization errors are easily observed (Fig. 7). Varying the amplitude of the waveform allows the dynamic range of the ADC and DAC to be observed and varying the computational rate of the dynamic clamp as well as the period of the sinusoid allow sampling rate and latency issues to be assessed.

4.3 Timing Statistics

All microprocessors have an on-board counter that is incremented with every count of the microprocessor clock. With microprocessor clock rates routinely in excess of 1 GHz today, this counter provides nanosecond level precision. Such measurements can be incorporated into the computational cycle of a dynamic clamp. By measuring the time stamp at the start and end of each cycle for a sufficiently long time (e.g., at a commonly used 10 kHz rate 100,000 cycles can be measured in 10 s), statistics on the cycle period as well as the duration of the computation required in a single cycle can be collected (Butera et al. 2001, Raikov et al. 2004). Useful statistics include the mean, standard deviation, and maximal value; the latter two are ideal measures of jitter and latency.

In Raikov et al. (2004), we proposed a simple heuristic to estimate the maximum speed at which a given computational model can be run. The dynamic-clamp system is run at an arbitrarily low rate prior to the experiment, and the duration of the computation component of a single cycle is measured repeatedly. This estimate of cycle duration plus a constant representing system latencies was used to reliably estimate the minimal period (maximum frequency) at which the system will stably run.

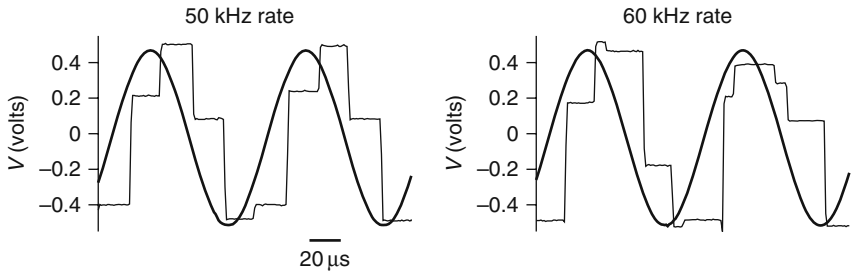

Fig. 7 Input/output test. A 10 kHz sine wave was applied to a dynamic-clamp system that was programmed to copy the input to the output. *The thick trace* is the applied waveform and the thin trace is the measured output of the DAC. Results are shown for dynamic-clamp rates of 50 and 60 kHz, respectively. Note the effects of jitter (variable length outputs) at 60 kHz not evident at 50 kHz. The latency can be measured as the duration from the sine wave at a given time point to the output of the DAC at the same voltage

5 Future Outlook

The performance considerations for dynamic-clamp point immediately to the need for faster dynamic-clamp systems. Preyer and Butera (2009) show that faster systems will allow a greater range of conductance magnitudes that can be implemented without losing stability. Bettencourt et al. (2008) show that latencies even less than one sampling period can affect simulated waveforms, pointing to a need for the computational time of a dynamic clamp to be as short as possible to minimize the time from input to output. These concerns are primarily relevant for fast processes and large currents – there are many examples (e.g., synaptic coupling of invertebrate bursting neurons) where the current magnitudes and conductance time scales are slow enough that many systems will perform reliably.

Such speed improvements may be realized on multicore multiprocessor PCs, as recent operating system advances may allow less jitter than previously allowed. However, for critical solutions, some labs have resorted to dedicated real-time computational hardware, such as LabView RT (Kullmann et al. 2004) and dedicated digital signal processing boards (Lien and Jonas 2003, Preyer 2002). Field programmable gate arrays have also been demonstrated as a viable real-time computational solution for neuron models (Graas et al. 2004), though we are currently unaware of their use in a dynamic-clamp application.

Finally, more advanced dynamic-clamp protocols could come about through greater integration of electrophysiology amplifiers, computers used for data acquisition and online monitoring of the experiment, and computers/hardware used for implementing the dynamic clamp. In most labs, all three of these items are separate and distinct. For example, protocols where a dynamic clamp could implement a high-gain voltage-clamp-like protocol may be desirable, but the current-clamp circuitry is typically slower and of lower amplitude than what is required to maintain a reliable voltage clamp (which is one reason why the voltage clamp uses distinctly separate circuitry). It is technologically feasible to design a software-based electrophysiology amplifier where many aspects of the control of a current-clamp, voltage-clamp, and dynamic-clamp circuit could be implemented via software controlling appropriately designed analog components – the question remains whether an appropriate market exists for the development of such a product.

Acknowledgments This work was supported by grants from the National Institutes of Health (PI: Christini, R01-RR020115; PI: Canavier, R01-NS054281) and previously by the National Science Foundation (PI: Butera, DBI-9987074). Many investigators have contributed to this work and the discussions within, including Ivan Raikov, Amanda Preyer, Maeve McCarthy, John White, David Christini, and Jonathan Bettencourt.

References

Bettencourt JC, Lillis KP, Stupin LR, et al. (2008) Effects of imperfect dynamic clamp: Computational and experimental results. J Neurosci Methods 169:282–289
Brette R, et al. CHAPTER In This Volume
Brette R, Piwkowska Z, Monier C, et al. (2008) Higher-resolution intracellular recordings using a real-time computational model of the electrode. Neuron 59:379–391
Brette R, Piwkowska Z, Rudolph M, et al. (2007) A non-parametric electrode model for intracellular recording. Neurocomputing 70:1597–1601
Brizzi L, Meunier C, Zytnicki D, et al. (2004) How shunting inhibition affects the discharge of lumbar motoneurones: A dynamic clamp study in anaesthetized cats. J Physiol 558:671–683
Butera RJ, Jr., Wilson CG, Delnegro CA, et al. (2001) A methodology for achieving high-speed rates for artificial conductance injection in electrically excitable biological cells. IEEE Trans Biomed Eng 48:1460–1470
Butera RJ and McCarthy ML (2004) Analysis of real-time numerical integration methods applied to dynamic clamp experiments. J Neural Eng 1:187–194
Dorval AD, Christini DJ and White JA (2001) Real-Time linux dynamic clamp: A fast and flexible way to construct virtual ion channels in living cells. Ann Biomed Eng 29:897–907
Graas EL, Brown EA and Lee RH (2004) An FPGA-based approach to high-speed simulation of conductance-based neuron models. Neuroinformatics 2:417–435
Kullmann PH, Wheeler DW, Beacom J, et al. (2004) Implementation of a fast 16-Bit dynamic clamp using LabVIEW-RT. J Neurophysiol 91:542–554
Lien CC and Jonas P (2003) Kv3 potassium conductance is necessary and kinetically optimized for high-frequency action potential generation in hippocampal interneurons. J Neurosci 23:2058–2068
Moore JW and Ramon F (1974) On numerical integration of the Hodgkin and Huxley equations for a membrane action potential. J Theor Biol 45:249–273
Nowotny T, Szucs A, Pinto RD, et al. (2006) StdpC: A modern dynamic clamp. J Neurosci Methods 158:287–299
Pinto RD, Elson RC, Szucs A, et al. (2001) Extended dynamic clamp: controlling up to four neurons using a single desktop computer and interface. J Neurosci Methods 108:39–48
Preyer AA (2002) A hardware implementation of the dynamic clamp. Master of Science in Electrical and Computer Engineering, Georgia Institute of Technology.
Preyer A and Butera R (2005) Neuronal oscillators in Aplysia californica that demonstrate weak coupling in vitro. Phys Rev Lett 95:138103
Preyer A and Butera R (2009) Causes of transient instabilities in the dynamic clamp. IEEE Trans Neural Sys Rehab Eng. In Press.
Prinz AA (2004) Neural networks: Models and neurons show hybrid vigor in real time. Current Biology 14:R661–R662
Prinz AA, Abbott LF and Marder E (2004) The dynamic clamp comes of age. Trends Neurosci 27:218–224
Raikov I, Preyer A and Butera RJ (2004) MRCI: a flexible real-time dynamic clamp system for electrophysiology experiments. J Neurosci Methods 132:109–123
Robinson HP and Kawai N (1993) Injection of digitally synthesized synaptic conductance transients to measure the integrative properties of neurons. J Neurosci Methods 49:157–165
Rush S and Larsen H (1978) A practical algorithm for solving dynamic membrane equations. IEEE Trans Biomed Eng 25:389–392
Sadoc, et al. CHAPTER in This Volume
Sharp AA, O'Neil MB, Abbott LF, et al. (1993) Dynamic clamp: computer-generated conductances in real neurons. J Neurophysiol 69:992–995

Development of a Genetically Engineered Cardiac Pacemaker: Insights from Dynamic Action Potential Clamp Experiments

Arie O. Verkerk, Jan G. Zegers, Antoni C.G. van Ginneken, and Ronald Wilders

Abstract In this chapter, we briefly review the use of dynamic clamp in cardiac cellular electrophysiology and present novel results obtained with the 'dynamic action potential clamp' (dAPC) technique. This is a technique that we recently developed to study the effects of long-QT syndrome-related ion channel mutations by effectively replacing the associated native ionic current of a cardiac myocyte with wild-type or mutant current recorded from a HEK-293 cell that is voltage clamped by the free-running action potential of the myocyte. Here we demonstrate that the dAPC technique can also be used as a powerful tool in the development of a 'biological pacemaker' or 'bio-pacemaker,' i.e. a genetically engineered cardiac pacemaker. We record 'pacemaker current' from an HCN4-transfected HEK-293 cell and inject this current into a model of a human atrial cell of which the free-running membrane potential is used to voltage clamp the HEK-293 cell. Thus we explore the conditions under which this HCN4-based pacemaker current turns the atrial cell into a pacemaker cell.

1 Introduction

In this chapter, we first briefly review the use of dynamic clamp in cardiac cellular electrophysiology with particular emphasis on the 'dynamic action potential clamp' (dAPC) technique that we developed to study the effects of ion channel mutations by effectively replacing a native ionic current of a cardiac myocyte with wild-type (WT) or mutant current expressed in cells of the HEK-293 cell line. The dAPC technique allowed us to assess changes in the ventricular action potential due to ion channel mutations found in patients with the heritable long-QT syndrome (Berecki et al. 2005, 2006). These patients show a

R. Wilders (✉)
Department of Physiology, Academic Medical Center, University of Amsterdam, 1105 AZ Amsterdam, The Netherlands
e-mail: r.wilders@amc.uva.nl

A. Destexhe, T. Bal (eds.), *Dynamic-Clamp*, Springer Series in Computational Neuroscience 1, DOI 10.1007/978-0-387-89279-5_18,

long-QT interval on the electrocardiogram and may suffer from ventricular arrhythmias resulting in syncope and sudden death.

Next, we present data from recent dAPC experiments that are helpful in the development of a genetically engineered 'biological pacemaker' or 'biopacemaker.' One of the approaches in this rapidly emerging field is to turn intrinsically quiescent myocardial cells, i.e. atrial or ventricular cells, into pacemaker cells by making them express the cardiac hyperpolarization-activated 'pacemaker current' (I_f, known in neurophysiology as I_h), which is encoded by the hyperpolarization-activated cyclic nucleotide-modulated (HCN) gene family (Robinson et al. 2006; Boink et al. 2007; Rosen et al. 2007; Marbán and Cho 2007; Spaan et al. 2007; Marbán and Cho 2008).

We carried out dAPC experiments in which we record current from a HEK-293 cell transfected with HCN4, i.e. the dominant HCN isoform in the sinoatrial (SA) node (Moosmang et al. 2001). This HCN4-transfected HEK-293 cell is voltage clamped by the action potential generated in a real-time simulation of a human atrial cell. In a continuous feedback loop, this current is injected into the atrial cell, so that we have effectively expressed an HCN4-based pacemaker current in this atrial cell. With sufficiently high 'expression levels' of HCN4 current the atrial cell is turned into a pacemaker cell with an SA nodal like action potential. Lower expression levels are sufficient if the inward rectifier potassium current (I_{K1}), which is largely responsible for the stable resting potential of atrial cells, is 'downregulated' by 50%. We have also carried out dAPC experiments with a rabbit SA nodal pacemaker cell model. Data from these experiments demonstrate that the HCN4 expression levels that are required to turn the atrial cell into a pacemaker cell have similar functional effects on the SA nodal action potential as the native I_f of the SA nodal cell.

2 Dynamic Clamp in Cardiac Electrophysiology

In neurophysiology, 'dynamic clamp' was introduced by Sharp and coworkers (Sharp et al. 1992, 1993a, b), whereas similar techniques were introduced by Robinson and Kawai (1993), named 'conductance injection,' and by Hutcheon et al. (1996), named 'reactive current clamp,' all with the purpose to introduce artificial conductances into biological neurons, thus simulating synaptic input, additional membrane ionic current or an electrical synapse. At that time, related techniques had already been applied in cardiac electrophysiology by Scott (1979) and by Joyner and coworkers (Tan and Joyner 1990; Joyner et al. 1991). Scott had designed an 'Ersatz Nexus' to create a physical connection between two clusters of spontaneously beating embryonic chick ventricular cells, each impaled with a sharp microelectrode, thus simulating intercellular electrical coupling through gap junctions. Joyner and coworkers independently developed a similar 'coupling clamp' circuit that could be used to simulate gap junctional coupling between two single isolated myocytes. The 'Ersatz Nexus'

and 'coupling clamp' setups are illustrated in Fig. 1. In Scott's setup (Fig. 1a) an analog circuit is used to generate positive and negative command potentials proportional to the difference in membrane potential between the two clusters. These command potentials (V_N and $-V_N$) are sent to the main amplifiers to let them inject a 'nexus current' into each of the clusters such that these are effectively coupled by a nexus resistance R_N. The setup includes an HP 2116A 'minicomputer,' but its role is limited to recording the membrane potential of each cluster.

Figure 1b illustrates a PC-controlled version of the 'coupling clamp' circuit. Electrical recordings are made from two isolated myocytes, both in current-clamp mode, thus requiring two patch-clamp amplifiers. The membrane potentials $V_{m,1}$ and $V_{m,2}$ of the two myocytes are sampled into a PC, which then computes the coupling current I_c flowing from myocyte 1 to myocyte 2, which is

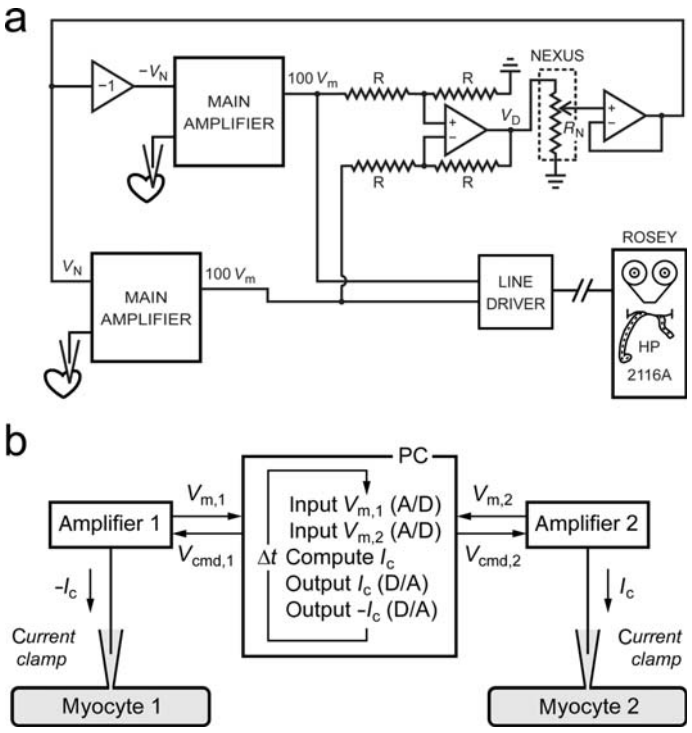

Fig. 1 Dynamic-clamp configurations in cardiac electrophysiology. **a** 'Ersatz Nexus' introduced by Scott (1979) to study the mutual synchronization of two small clusters (≈100 μm in diameter) of spontaneously beating embryonic chick ventricular cells by electrical coupling through a simulated gap junction (or 'nexus') with resistance R_N. Redrawn from Fig. 6 of chapter 2 of Scott (1979). **b** PC-controlled version of the 'coupling clamp' circuit introduced by Joyner and coworkers (Tan and Joyner, 1990; Joyner et al. 1991) to simulate gap junctional coupling between two isolated rabbit ventricular myocytes by injecting an ohmic 'coupling current' I_c (positive or negative) into each of the myocytes. See text for further details

proportional to $V_{m,1}$ minus $V_{m,2}$ in case of an ohmic conductance, and sends command potentials ($V_{cmd,1}$ and $V_{cmd,2}$) to the amplifiers such that the appropriate current is injected into each of the myocytes, where it contributes to the net membrane current and thus affects the membrane potential. The time step for updating input and output values is Δt. The PC-controlled dynamic-clamp implementation of Fig. 1b is much more flexible than the analog circuitry of Fig. 1a, but comes with the disadvantage of discretization errors and latency in the feedback loop between voltage and current.

Although dynamic clamp exists in cardiac electrophysiology for 30 years now, it is less common than in neurophysiology. Recent applications of dynamic clamp in cardiac electrophysiology include the simulation of stretch-activated current in rat atrial myocytes (Wagner et al. 2004), transient outward current in guinea pig and canine endocardial ventricular myocytes (Sun and Wang 2005; Dong et al. 2006), and gap junctional current between two mouse ventricular myocytes (Wang et al. 2006). In these recent years we developed a novel dynamic-clamp technique that we named dynamic action potential clamp (dAPC) (Berecki et al. 2005, 2006). It differs from 'traditional' dynamic clamp and action potential clamp in that it combines current clamp, as used in dynamic clamp, and voltage clamp, as used in action potential clamp. Below we will first discuss traditional action potential clamp and then dAPC.

3 Action Potential Clamp

3.1 Traditional Action Potential Clamp

Essentially, action potential clamp is a particular refinement of the voltage-clamp technique. Instead of the traditional step protocols a prerecorded action potential waveform is used as voltage-clamp command potential. In the early 1990s, several neurophysiologists independently developed the dynamic-clamp technique, with some debate on who was first (see Wilders 2005, 2006), while the technique had already been used in cardiac electrophysiology in the late 1970s. The opposite holds for the action potential clamp technique, which among cardiac electrophysiologists is commonly believed to have been developed by Doerr and coworkers (Doerr et al. 1989, 1990) while it had already been used in neurophysiology in the late 1970s to study sodium current during the action potential in the giant axon of *Loligo pealei* (Starzak and Starzak, 1978), but also in the 1980s, e.g. by de Haas and Vogel (1989) to study sodium and potassium current during the action potential in single nerve fibers of *Xenopus laevis*. Furthermore, the technique had already been applied to cardiac cells by Mazzanti and DeFelice (1987) and by Anderson and Patmore (1988) before Doerr and coworkers published their 'new method.'

Figure 2 shows a recent application of traditional action potential clamp by Bellocq et al. (2004) to investigate differences in kinetics of WT and A561P mutant ion channels encoded by the human ether-a-go-go-related gene (HERG), i.e. the gene encoding the pore-forming α-subunit of the channels underlying the cardiac rapid delayed rectifier current (I_{Kr}). To this end both WT + A561P mutant HERG channels, representing heterozygous carriers of the long-QT syndrome associated A561P mutation, and WT HERG channels, representing non-carriers, are expressed in a cell line expressing little or no endogenous membrane current. A previously recorded human ventricular action potential (Fig. 2a) is used as voltage-clamp command potential and applied to HERG channel expressing COS-7 cells at a rate of 1 Hz. The

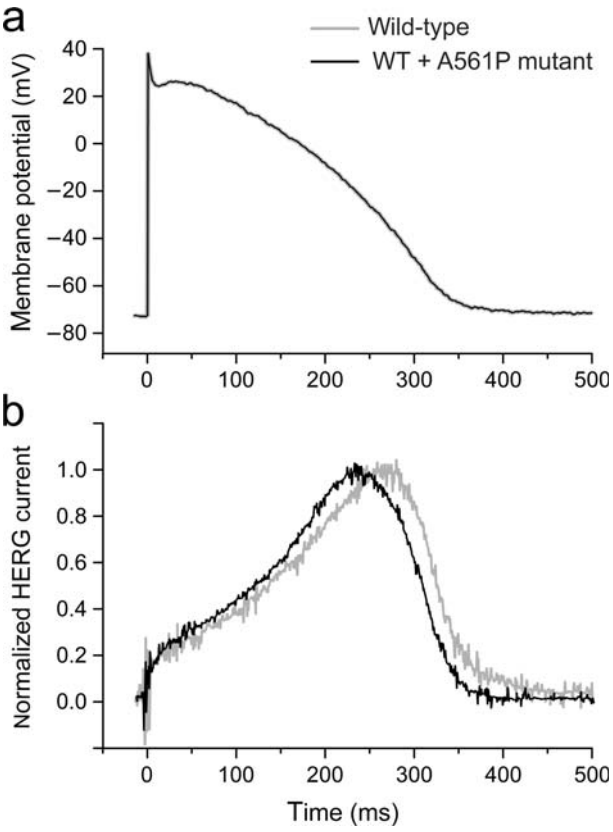

Fig. 2 Traditional action potential clamp experiment on African green monkey kidney (COS-7) cells that were either transfected with human wild-type (WT) HERG cDNA or co-transfected with WT and A561P mutant HERG cDNA. **a** Action potential recorded from a human ventricular myocyte used as command voltage to clamp HERG-transfected COS-7 cells (identical for WT and WT + A561P mutant). **b** Normalized HERG current in response to the command voltage of **a**. Data from Bellocq et al. (2004)

associated normalized HERG current is shown in Fig. 2b. The current traces demonstrate a more rapid activation of WT + A561P current (black trace) compared to WT (gray trace), which would increase action potential duration, but also a more rapid deactivation, which would decrease action potential duration. From these data, it is difficult to predict the net effect of these changes in kinetics on the action potential. This is where dAPC can provide a direct and unambiguous answer.

3.2 Dynamic Action Potential Clamp

The diagram of Fig. 3a illustrates the concept of dAPC. Again, WT or mutant HERG channels are expressed in a cell line, in this case HEK-293 cells, and subjected to voltage clamp to investigate differences in kinetic properties of these channels. However, the voltage-clamp command potential is not a

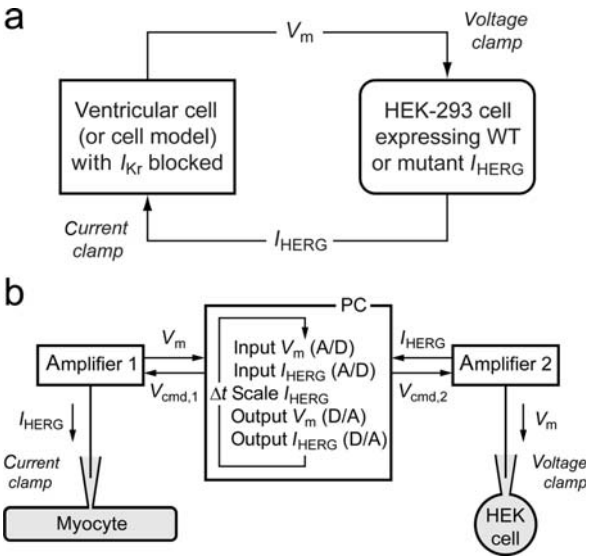

Fig. 3 Dynamic action potential clamp (dAPC) technique. **a** Diagram of the dAPC technique when used to effectively replace the native HERG-encoded cardiac delayed rectifier potassium current (I_{Kr}) of a ventricular cell (or cell model) with the HERG current (I_{HERG}) recorded from a HEK-293 cell transfected with wild-type (WT) or mutant HERG cDNA. **b** Diagram of the dAPC experimental setup. I_{HERG} is recorded from the voltage-clamped HEK-293 cell, appropriately scaled, and then applied as external current to the ventricular myocyte, which is in current-clamp mode and has its native I_{Kr} blocked pharmacologically (or set to zero in case of a model cell). The free-running action potential of the myocyte, co-shaped by the input I_{HERG}, is applied as voltage-clamp command potential to the HEK cell, thus establishing dAPC

prerecorded action potential, but is the free-running membrane potential of a freshly isolated, patch-clamped ventricular cell (or cell model) with its native HERG-encoded current, i.e. I_{Kr}, blocked by a pharmacological agent (or set to zero in case of a model cell). The measured HERG current is injected into the ventricular myocyte in real time. Thus, there is continuous feedback between action potential and HERG current. The WT or mutant HERG channels are allowed to follow the natural time course of the ventricular action potential (through the voltage clamp), upon being simultaneously allowed to contribute current for the generation of this action potential as if they were incorporated into the membrane of the myocyte (through injection of the HERG current into the myocyte).

The experimental setup is diagrammed in Fig. 3b. The central desktop PC is connected to two patch-clamp amplifiers, one in current clamp and one in voltage-clamp mode. It tells amplifier 2 to make the HEK-293 cell follow the membrane potential of the myocyte. At the same time, it tells amplifier 1 to inject the HERG current recorded from the HEK-293 cell into the myocyte. This is typically done with an update rate of 20 kHz, i.e. with the time step Δt set to 50 μs. Given the relatively high expression level of HERG channels, the HERG current is scaled down to achieve an appropriate current amplitude. Any endogenous current included in the current recorded from the HEK-293 cell – both small (Zhou et al. 1998) and relatively large (Yu and Kerchner 1998) endogenous current has initially been reported – is then also scaled down, so that this endogenous current becomes negligible. However, if the expressed current needs to be scaled up, precautions should be made to avoid distortion by endogenous current (see Berecki et al. 2006).

Figure 4 shows data from a dAPC experiment with HERG current carried out by Berecki et al. (2005). Figure 4a shows action potentials from the same isolated rabbit ventricular myocyte generated with the contribution of either WT or R56Q mutant HERG current (Fig. 4b), obtained by subsequently coupling the myocyte to a HEK-293 cell expressing WT current and a HEK-293 cell expressing R56Q mutant current (gray and black traces, respectively). The experiment of Fig. 4 directly demonstrates that the R56Q mutation results in significant action potential prolongation. Notably, this action potential prolongation occurs despite the larger initial HERG current in the mutant case, which demonstrates that the change in action potential profile is not only the result of changes in HERG current but also of changes in other membrane currents through their dependence on membrane potential. In this experiment, WT and mutant HERG current were both scaled down to produce a HERG current density comparable to the native I_{Kr} density of the real isolated myocyte, as estimated using the I_{Kr} blocker E-4031. This scaling procedure seemed appropriate because the R56Q mutation is associated with altered gating properties rather than impaired trafficking from the endoplasmic reticulum to the cell membrane.

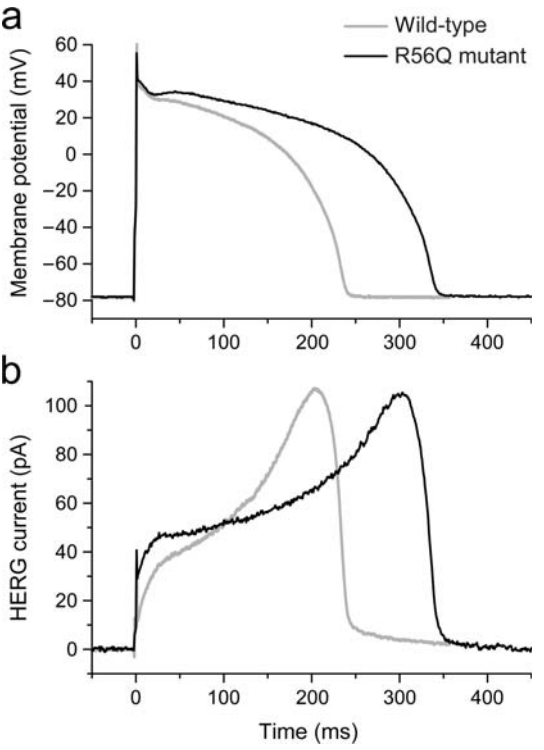

Fig. 4 Dynamic action potential clamp (dAPC) experiment, exploring the effect of a mutation in HERG. **a** Superimposed action potentials of a single isolated rabbit ventricular myocyte successively coupled to a HEK-293 cell expressing wild-type HERG current (*gray line*) and a HEK-293 cell expressing R56Q mutant HERG current (*black line*). **b** Associated HERG current traces. The myocyte had its native I_{Kr} blocked by E-4031 and was paced at 1 Hz. Data from Berecki et al. (2005)

As already indicated in Fig. 3a, the real isolated myocyte of Fig. 3b may be replaced with a real-time simulation of a ventricular myocyte. In this case, V_m is not acquired from a real cell through the A/D-converter on the data acquisition board, but computed in the PC through integration of a comprehensive mathematical model, with the current recorded from the HEK-293 cell as an additional transmembrane current. We have previously used such hybrid configuration with the Priebe and Beuckelmann (1998) human ventricular cell model to study the effects of mutations in the HERG gene (Berecki et al. 2005) and the SCN5A gene (Berecki et al. 2006), the latter encoding the pore-forming α-subunit of the channels underlying the cardiac fast sodium current (I_{Na}).

3.3 Setting up a dAPC System

As long as real-time simulations are not required, dAPC experiments can be carried out using analog circuitry, but if ease of use and high flexibility are important, the use of dedicated software running on a PC equipped with a multifunction data acquisition board is the best option. We have made our

dAPC software publicly available through our institutional website (URL: www.amc.nl/index.cfm?pid=4922). It requires a standard PC that can run the real-time variant of the Linux operating system (RT-Linux; Barabanov and Yodaiken 1997) and a data acquisition board that is supported by the open-source Control and Measurement Device Interface (Comedi) software library (URL: www.comedi.org/). In the process of setting up a PC-controlled dAPC system, the public resources of the 'Real-Time eXperiment Interface' (RTXI) project may be very helpful (URL: www.rtxi.org/).

4 Dynamic Action Potential Clamp with HCN4 Current

One approach in the field of creating a bio-pacemaker is the implant of exogenous cells that are engineered to sustain pacemaker activity, once electrically connected to the intrinsically quiescent host myocardium. Another approach is the induction of pacemaking in intrinsically quiescent myocardial cells by modification of their expression pattern of membrane currents. This requires genetic modification at the site of interest, typically by gene transfer aimed at downregulation of I_{K1} and/or upregulation of I_f in atrial or ventricular myocardium (Robinson et al. 2006; Boink et al. 2007; Rosen et al. 2007; Marbán and Cho 2007; Spaan et al. 2007; Marbán and Cho 2008). In a series of dAPC experiments, we have tested whether expression of HCN4 current in a human atrial cell model, either per se or in combination with downregulation of I_{K1}, induces SA nodal-like pacemaker activity in this intrinsically quiescent cell type.

4.1 HCN4 Current in HEK-293 Cells

Figure 5b shows the current recorded from an HCN4-transfected HEK-293 cell in response to the traditional voltage-clamp step protocol of Fig. 5a. Recordings were made in the whole-cell configuration of the patch-clamp technique at a temperature of 36°C and recording conditions were similar to those in recent studies on HCN-encoded currents by Verkerk and coworkers (Verkerk et al. 2007; Boink et al. 2008), except for the NaCl concentration in the patch pipette solution, which was increased to 10 mM.

While non-transfected HEK-293 cells do not express significant endogenous I_f current (Varghese et al. 2006), the HCN4-transfected HEK-293 cell exhibits a slowly developing I_f like inward current with an amplitude of ≈3.1 nA upon a hyperpolarizing step to −100 mV from a holding potential of −30 mV (all potentials corrected for liquid junction potential). Stepping back from −100 to +10 mV results in (1) current reversal due to the membrane potential now becoming positive to the HCN4 reversal potential, (2) fast deactivation of the HCN4 current, and (3) the emergence of a steady outward current with an

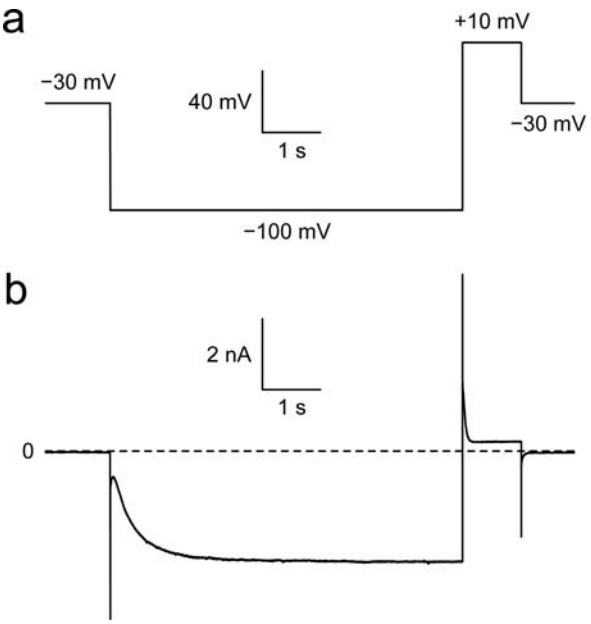

Fig. 5 Voltage-clamp experiment on a HEK-293 cell expressing wild-type HCN4 channels. Voltage-clamp protocol (**a**) and associated current trace (**b**). *Dashed line* indicates zero-current level

amplitude of ≈260 pA (Fig. 5b). The nature of this steady outward current is unclear and requires further investigation. We exclude a major contribution of the delayed rectifier (I_K) like endogenous current reported by Yu and Kerchner (1998) since our recordings were made in presence of the I_{Kr} blocker E-4031 (5 μM). It may result from K_V channels that are not blocked by E-4031 (Jiang et al. 2002), but one may also speculate that this outward current reflects a fraction of HCN4 channels that remain open at positive potentials.

4.2 Type of Experiments

We used the HCN4-transfected HEK-293 cell of Fig. 5 in two types of dAPC experiments, which are both diagrammed in Fig. 6. In the first type of experiment, we used the HEK-293 cell in combination with the Wilders et al. (1991) model of a rabbit SA nodal pacemaker cell with its native I_f set to zero (Fig. 6a). Thus, we were able to test whether the current of the HCN4-transfected HEK-293 cell could replace the I_f of the model cell. In the second type of experiment, we used the HEK-293 cell in combination with the Courtemanche et al. (1998) model of a human atrial cell with its I_{K1} set to 50–100% of control (Fig. 6b). Thus, it could be tested whether the atrial cell developed SA nodal like pacemaker activity upon the inclusion of HCN4 current per se or upon the inclusion of HCN4 current in combination with downscaling of I_{K1}.

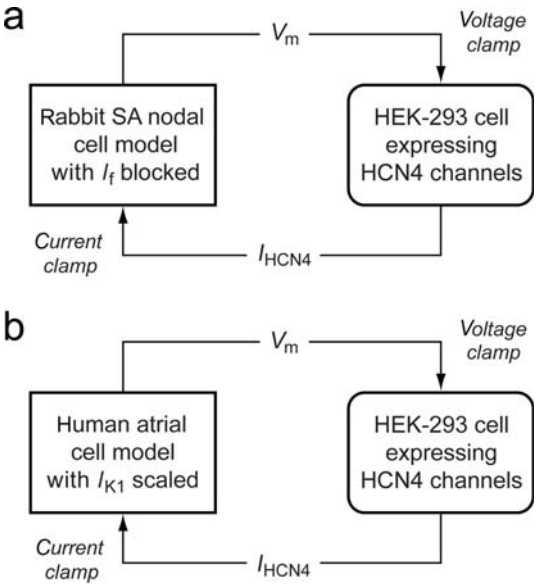

Fig. 6 Dynamic action potential clamp (dAPC) configurations used in experiments on HEK-293 cells expressing wild-type HCN4 channels. **a** A sinoatrial (SA) nodal pacemaker cell is simulated in real time using the Wilders et al. (1991) model of a rabbit SA nodal myocyte. The HCN-encoded hyperpolarization-activated current I_f, also known as 'pacemaker current' or 'funny current,' is replaced with HCN4 current recorded from the HEK-293 cell (I_{HCN4}). **b** A human atrial cell is simulated in real time using the Courternanche et al. (1998) model of such cell. The inward rectifier potassium current of the model (I_{K1}) is scaled down and HCN4 current recorded from the HEK-293 cell is added to the net membrane current of the model cell, thus mimicking the gene therapy strategy to create a biological pacemaker by downregulation of I_{K1} and (over)expression of I_f

4.3 Can HCN4 Current Replace I_f *in SA Nodal Pacemaker Cells?*

In accordance with experimental data (see Wilders et al. 1991), the cycle length of the SA nodal model cell increases by 22% upon blockade of I_f, which is largely due to a decrease in the rate of diastolic depolarization (Fig. 7a). We used the action potential of the model cell – with its I_f set to zero – to voltage clamp the HEK-293 cell and fed the recorded HCN4 current back into the current-clamped model cell (dAPC configuration of Fig. 6a). Given the large current expressed in the HEK-293 cell (cf. Fig. 5b), we applied scaling factors of 0–0.01, i.e. 0–1%, to this HCN4 current before adding it to the model. With the scaling factor set to zero (Fig. 7b, trace labeled '0.0'), the resulting action potential is identical to that of the model cell with its I_f set to zero (Fig. 7a, solid line). With a scaling factor of 1.0% (Fig. 7b, trace labeled '1.0'), the cycle length becomes considerably shorter and almost identical to that of the original

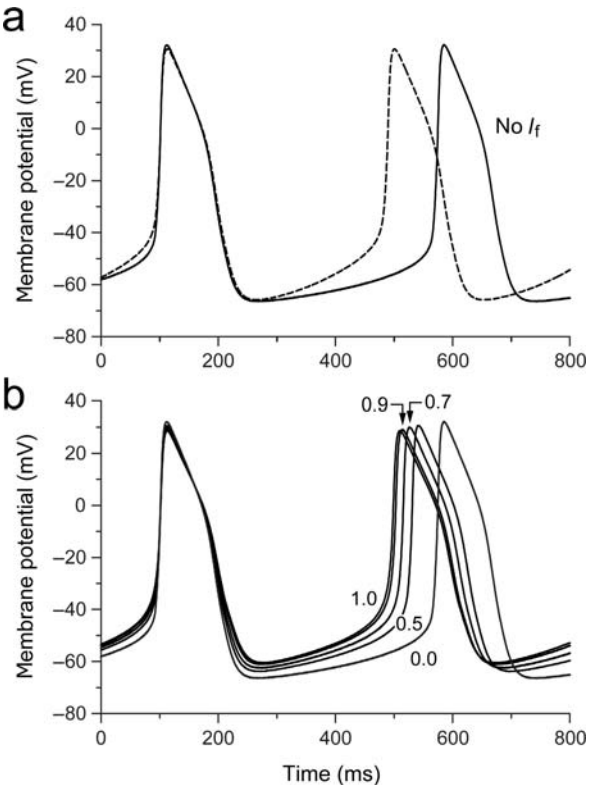

Fig. 7 Dynamic action potential clamp (dAPC) experiment with a real-time simulation of an SA nodal pacemaker cell and a HEK-293 cell expressing HCN4 channels (cf. Fig. 6a). **a** Effect of removing I_f on the action potential of the model SA nodal cell. **b** Effect of adding increasing amounts of HCN4 current to the SA nodal cell with its native I_f set to zero. Numbers near traces indicate the percent scaling factor applied to the HCN4 current recorded from the HEK-293 cell of Fig. 5

model with its default I_f (Fig. 7a, dashed line). Recordings with intermediate values for the scaling factor demonstrate that the cycle length decreases with increasing 'expression level' of the HCN4 current (Fig. 7b, traces labeled '0.5,' '0.7,' and '0.9').

Functionally, in terms of modulating pacemaker frequency, the HCN4 current can replace the native I_f. However, unlike I_f, increasing the HCN4 current not only increases the rate of diastolic depolarization, but also clearly depolarizes the maximum diastolic potential to less negative values. This underscores that the kinetics of HCN4 channels are not identical to those of native I_f channels (Qu et al. 2002) and that HCN4 channels should not simply be regarded as a replacement of I_f 'pacemaker channels' in gene therapy strategies. In addition, it stresses that the behavior of HCN channels is more complex than reflected in the description of I_f in currently available SA nodal cell models (Wilders 2007). A caveat that should be put in place here is that the depolarization of the maximum diastolic potential may, at least to some extent, be due to inward 'leakage current' of the HEK-293 cell, although the scaling factor of 0.01 or less also applies to this current.

4.4 Creating a Biological Pacemaker Using HCN4

Figure 8a illustrates the effect of a reduction in I_{K1} on the resting potential of the human atrial cell model. With decreasing I_{K1} this resting potential depolarizes from its control value of −81 mV (Fig. 8a, trace labeled '100%') to −75 mV at 50% I_{K1}, with intermediate values of −80, −79, and −77 mV at 80, 70, and 60% I_{K1}, respectively. Application of short stimuli every 800 ms (Fig. 8a, slanted arrows) to the model with 50% I_{K1} elicits action potentials with the typical shape of the Courtemanche et al. (1998) model cell. A further decrease in I_{K1} results in further depolarization of the resting potential (data not shown).

Figure 8b shows traces obtained with the same I_{K1} settings as in Fig. 8a, i.e. 100, 80, 70, 60 or 50% of control, but now with the inclusion of HCN4 current

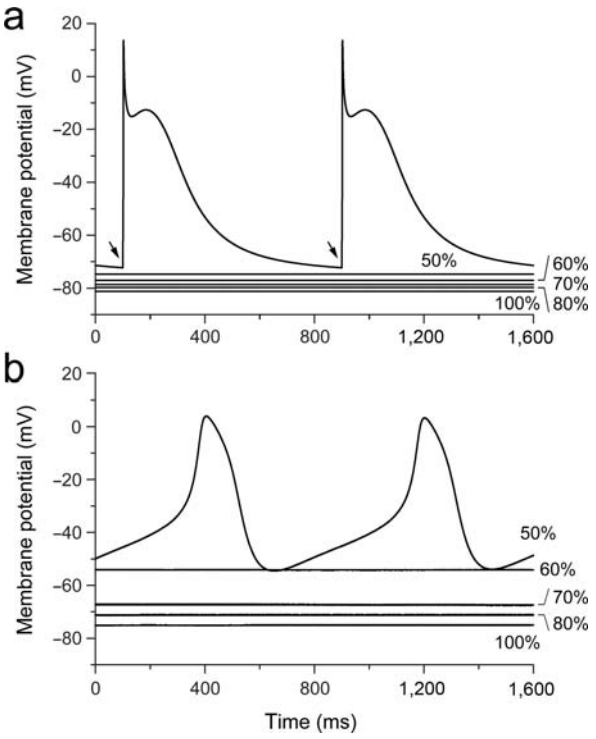

Fig. 8 Dynamic action potential clamp (dAPC) experiment with a real-time simulation of a human atrial cell and a HEK-293 cell expressing HCN4 channels (cf. Fig. 6b). **a** Effect of downregulation of I_{K1} on the resting potential of the non-stimulated model cell. Percentages indicate the amount of I_{K1} channels present. Also shown are action potentials of the model cell with 50% I_{K1} elicited by stimuli delivered at an interpulse interval of 800 ms (*arrows*). **b** Effect of adding HCN4 current to the atrial cell with different amounts of I_{K1} present (50–100% as indicated). HCN4 current was recorded from the HEK-293 cell of Fig. 5 and applied to the atrial cell with a constant scaling factor of 1.0%

with a constant scaling factor of 1.0%, i.e. the highest value used in Fig. 7b. At 100% I_{K1}, the resting potential is now −75 mV, resulting from a steady HCN4 inward current at this potential. This resting potential again depolarizes with decreasing I_{K1}, to −71, −67, and −54 mV at 80, 70, and 60% I_{K1}, respectively, all less negative than the corresponding resting potential values of Fig. 8a due to the inward HCN4 inward current. However, in contrast with Fig. 8a, a further decrease in I_{K1} to 50% now leads to spontaneous SA nodal-like activity of the atrial cell with a cycle length of ≈800 ms.

The bio-pacemaker activity at the single-cell level of Fig. 8b occurs on the background of a 'downregulated' I_{K1} (50% of control). We also tested whether this bio-pacemaker activity could be achieved without downscaling of I_{K1}. Therefore, we increased the scaling factor for the injected HCN4 current from 1.0%, as used in Fig. 8b, to 2.0 or 3.0%. With a scaling factor of 2.0%, the resting potential depolarizes from its value of −75 mV at 1.0% (Fig. 9, trace labeled '1.0') to −69 mV (Fig. 9, trace labeled '2.0'). However, bio-pacemaker activity develops if the scaling factor is further increased to 3.0% (Fig. 9, trace labeled '3.0'). It differs from that in Fig. 8b in that the maximum diastolic potential is now more negative (−66 vs. −54 mV) and that the cycle length is considerably longer (≈1,450 vs. ≈800 ms). The experiments of Figs. 8 and 9 demonstrate that engineering of a single cell bio-pacemaker is facilitated by downregulation of I_{K1}, but that such downregulation is not a prerequisite.

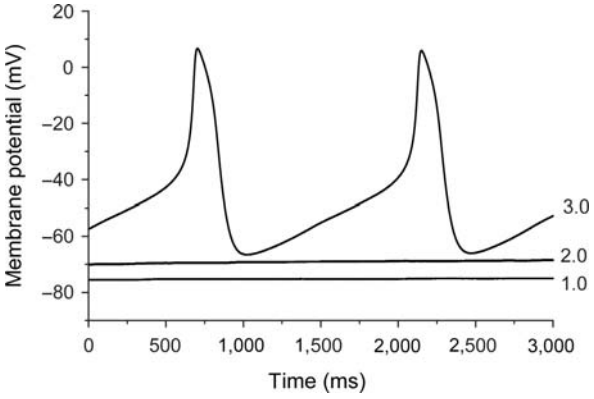

Fig. 9 Dynamic action potential clamp (dAPC) experiment with a real-time simulation of a human atrial cell and a HEK-293 cell expressing HCN4 channels (cf. Fig. 6b). I_{K1} is set to 100% (no downregulation) and increasing amounts of HCN4 current are added to the non-stimulated atrial cell. Numbers near traces indicate the percent scaling factor applied to the HCN4 current recorded from the HEK-293 cell of Fig. 5

5 Concluding Remarks

In this chapter we have shown that the dAPC technique provides direct insights into the effects of introducing HCN4 current into an atrial cell. This is of particular importance when screening a number of candidate genes – or different combinations of genes, e.g. in transfections with different relative amounts of HCN1–HCN4 cDNA aimed at producing pacemaker channels with different time- and voltage-dependent properties – for the creation of a bio-pacemaker. Thus, dynamic action potential clamp may prove a powerful tool in the process of developing a genetically engineered cardiac pacemaker.

Acknowledgment We thank Berend de Jonge for expert biotechnical assistance.

References

Anderson AJ, Patmore L (1988) Calcium currents evoked in embryonic chick myocytes during depolarization with an action potential voltage waveform. J Physiol 407:126P.

Barabanov M, Yodaiken V (1997) Introducing real-time Linux. Linux J 34:19–23

Bellocq C, Wilders R, Schott J-J, Louérat-Oriou B, Boisseau P, Le Marec H, Escande D, Baró I (2004) A common antitussive drug, clobutinol, precipitates the long QT syndrome 2. Mol Pharmacol 66:1093–1102

Berecki G, Zegers JG, Verkerk AO, Bhuiyan ZA, de Jonge B, Veldkamp MW, Wilders R, van Ginneken ACG (2005) HERG channel (dys)function revealed by dynamic action potential clamp technique. Biophys J 88:566–578

Berecki G, Zegers JG, Bhuiyan ZA, Verkerk AO, Wilders R, van Ginneken ACG (2006) Long-QT syndrome-related sodium channel mutations probed by the dynamic action potential clamp technique. J Physiol 570:237–250

Boink GJJ, Seppen J, de Bakker JMT, Tan HL (2007) Gene therapy to create biological pacemakers. Med Biol Eng Comput 45:167–176

Boink GJJ, Verkerk AO, van Amersfoorth SCM, Tasseron SJ, van der Rijt R, Bakker D, Linnenbank AC, van der Meulen J, de Bakker JMT, Seppen J, Tan HL (2008) Engineering physiologically controlled pacemaker cells with lentiviral HCN4 gene transfer. J Gene Med. 10:487–497

Courtemanche M, Ramirez RJ, Nattel S (1998) Ionic mechanisms underlying human atrial action potential properties: insights from a mathematical model. Am J Physiol 275:H301–H321.

de Haas V, Vogel W (1989) Sodium and potassium currents recorded during an action potential. Eur Biophys J 17:49–51

Doerr T, Denger R, Trautwein W (1989) Calcium currents in single SA nodal cells of the rabbit heart studied with action potential clamp. Pflügers Arch 413:599–603

Doerr T, Denger R, Doerr A, Trautwein W (1990) Ionic currents contributing to the action potential in single ventricular myocytes of the guinea pig studied with action potential clamp. Pflügers Arch 416:230–237

Dong M, Sun X, Prinz AA, Wang H-S (2006) Effect of simulated I_{to} on guinea pig and canine ventricular action potential morphology. Am J Physiol Heart Circ Physiol 291:H631–H637

Hutcheon B, Miura RM, Puil E (1996) Models of subthreshold membrane resonance in neocortical neurons. J Neurophysiol 76:698–714

Jiang B, Sun X, Cao K, Wang R (2002) Endogenous K_V channels in human embryonic kidney (HEK-293) cells. Mol Cell Biochem 238:69–79

Joyner RW, Sugiura H, Tan RC (1991) Unidirectional block between isolated rabbit ventricular cells coupled by a variable resistance. Biophys J 60:1038–1045

Marbán E, Cho HC (2007) Creation of a biological pacemaker by gene- or cell-based approaches. Med Biol Eng Comput 45:133–144

Marbán E, Cho HC (2008) Biological pacemakers as a therapy for cardiac arrhythmias. Curr Opin Cardiol 23:46–54

Mazzanti M, DeFelice LJ (1987) Regulation of the Na-conducting Ca channel during the cardiac action potential. Biophys J 51:115–121

Moosmang S, Stieber J, Zong X, Biel M, Hofmann F, Ludwig A (2001) Cellular expression and functional characterization of four hyperpolarization-activated pacemaker channels in cardiac and neuronal tissues. Eur J Biochem 268:1646–1652

Priebe L, Beuckelmann DJ (1998) Simulation study of cellular electric properties in heart failure. Circ Res 82:1206–1223

Qu J, Altomare C, Bucchi A, DiFrancesco D, Robinson RB (2002) Functional comparison of HCN isoforms expressed in ventricular and HEK 293 cells. Pflügers Arch 444:597–601

Robinson HPC, Kawai N (1993) Injection of digitally synthesized synaptic conductance transients to measure the integrative properties of neurons. J Neurosci Meth 49:157–165

Robinson RB, Brink PR, Cohen IS, Rosen MR (2006) I_f and the biological pacemaker. Pharmacol Res 53:407–415

Rosen MR, Brink PR, Cohen IS, Robinson RB (2007) Biological pacemakers based on I_f. Med Biol Eng Comput 45:157–166

Scott S (1979) Stimulation Simulations of Young Yet Cultured Beating Hearts. Dissertation, State University of New York at Buffalo

Sharp AA, Abbott LF, Marder E (1992) Artificial electrical synapses in oscillatory networks. J Neurophysiol 67:1691–1694

Sharp AA, O'Neil MB, Abbott LF, Marder E (1993a) Dynamic clamp: Computer-generated conductances in real neurons. J Neurophysiol 69:992–995

Sharp AA, O'Neil MB, Abbott LF, Marder E (1993b) The dynamic clamp: Artificial conductances in biological neurons. Trends Neurosci 16:389–394

Spaan JAE, Coronel R, de Bakker JMT, Zaza A (eds) (2007) Biopacemaking. Springer, Heidelberg

Starzak ME, Starzak RJ (1978) An action potential clamp to probe the effectiveness of space clamp in axons. IEEE Trans Biomed Eng 25:201–204

Sun X, Wang H-S (2005) Role of the transient outward current (I_{to}) in shaping canine ventricular action potential – a dynamic clamp study. J Physiol 564:411–419

Tan RC, Joyner RW (1990) Electrotonic influences on action potentials from isolated ventricular cells. Circ Res 67:1071–1081

Varghese A, TenBroek EM, Coles J Jr, Sigg DC (2006) Endogenous channels in HEK cells and potential roles in HCN ionic current measurements. Prog Biophys Mol Biol 90:26–37

Verkerk AO, Wilders R, van Borren MMGJ, Peters RJC, Broekhuis E, Lam KY, Coronel R, de Bakker JMT, Tan HL (2007) Pacemaker current (I_f) in the human sinoatrial node. Eur Heart J 28:2472–2478

Wagner MB, Kumar R, Joyner RW, Wang Y (2004) Induced automaticity in isolated rat atrial cells by incorporation of a stretch-activated conductance. Pflügers Arch 447:819–829

Wang Y, Cheng J, Joyner RW, Wagner MB, Hill JA (2006) Remodeling of early-phase repolarization: a mechanism of abnormal impulse conduction in heart failure. Circulation 113:1849–1856

Wilders R, Jongsma HJ, van Ginneken ACG (1991) Pacemaker activity of the rabbit sinoatrial node: a comparison of mathematical models. Biophys J 60:1202–1216

Wilders R (2005) 'Dynamic clamp' in cardiac electrophysiology. J Physiol 566:641

Wilders R (2006) Dynamic clamp: a powerful tool in cardiac electrophysiology. J Physiol 576:349–359

Wilders R (2007) Computer modelling of the sinoatrial node. Med Biol Eng Comput 45:189–207

Yu SP, Kerchner GA (1998) Endogenous voltage-gated potassium channels in human embryonic kidney (HEK293) cells. J Neurosci Res 52:612–617

Zhou Z, Gong Q, Ye B, Fan Z, Makielski JC, Robertson GA, January CT (1998) Properties of HERG channels stably expressed in HEK 293 cells studied at physiological temperature. Biophys J 74:230–241

Index

A
AB/PD complex, 263–264
Access resistance estimation, 150–151, 182
Accuracy
  data acquisition system (DAQ), 384
Action potential clamp
  dynamic action potential clamp, 404–406
  traditional action potential clamp, 402–404
Action potential waveform
  of pyramidal neurons, 66
  stereotyped presynaptic, 62
Activation of mGluRs
  in TC neurons, 334–337
Active electrode compensation (AEC), 14–15, 24, 348–350
  algorithm, 350
  conductance injection using RT-NEURON and, 315–317
  parameters
    dendrites, 364
    estimation parameters, 359–361
    feedback delay, 361–362
    nonlinearities, 364–368
    time constants, 362–363
  recordings *in vitro*, 368–372
  recordings *in vivo*, 368–372
ADC, *see* Analog-to-digital converter (ADC)
Ad hoc Markovian model, of I_{NaP}, 179
  C–O transition kinetics, 180
  spike threshold dynamics, 180–181
ADP, *see* Afterdepolarization (ADP)
AEC, *see* Active electrode compensation (AEC)
Afterdepolarization (ADP), 337
After-hyperpolarizations (AHPs)
  voltage-dependent amplification by I_{NaP}, 186–187
α-Amino-3-hydroxy-5-methyl-4-isoazoleprionic acid
  conductance, 225–226
  receptor, 49, 51
    conductance, spike-triggered average, 54
    dominated conductance, 56, 57
    excitation, spike-triggered averages of, 58
    transients, Poisson train of, 54
AMPA, *see* α-Amino-3-hydroxy-5-methyl-4-isoazoleprionic acid
AMPA/NMDA excitatory synapses, 242
Amplifiers, 348
Amplitude of I_T
  in generation of δ oscillations, 328–330
Analog systems
  for dynamic clamp calculations, 11
Analog-to-digital converter (ADC), 384, 406
Andronov–Hopf bifurcations, 60
Anterior burster (AB) neuron, 263
Artificial shunting inhibition
  effect on visual response, 143–144, 154–155
Asymmetric trapping block, 67
ATB, *see* Asymmetric trapping block

B
Background synaptic activity, *see* Synaptic background activity
BAPTA and fAHP, 145
Biological neural oscillator, 263
Biological pacemaker creation
  HCN4 current, 407–408
Bistable voltage levels
  in TC neurons, 334
BK current
  dynamic-clamp models for, 148–149

BK current (*cont.*)
and neuronal response
BAPTA and fAHP, 145
local hyperpolarization, 144–145
potassium channels, 144
in rat and cat cortex *in vivo*, 142
anesthesia and surgical manipulations, 146
capacitance compensation, 150
data acquisition, 146
electrophysiological recordings, 149–150
extrinsic and intrinsic membrane mechanisms, 160
input–output function, 154–158
visual experiments, 148
visual responses, 154–158, 159
in vivo dynamic-clamp system for, 147
voltage response, 150–151
Bridge compensation, 348
Bursting network, pulse-coupled approximation of, 265

C
Ca^{2+}-activated non-selective (CAN) cation, 337
in TC neuron, 337–338
Ca^{2+}-dependent K^+ conductance dynamics, 227
bursting behavior, 228
high-voltage-activated, 229
sk conductance, 229
CA1 hippocampal pyramidal neurons
current-to-frequency transduction in, 189
dynamic-clamp configuration in, for I_{NaP} analysis
selective subtraction, 166–167
steady-state activation curve, 171
firing regularity in, 189–191
impact of noise on
firing rate modulation, *see* Firing rate modulation, impact of noise on
repetitive spiking, *see* Repetitive spiking
impact of shunting on
passive membrane properties, *see* Passive membrane properties, impact of shunting
repetitive spiking, *see* Repetitive spiking
pyramidal morphology, 91
spike rate in, 96
Calcium-dependent potassium channels, 50
CAN, *see* Ca^{2+}-activated non-selective (CAN) cation
Cardiac electrophysiology
dynamic clamp, 400–402
Cardiac fast sodium current (I_{Na}), 406
Cellular neurobiology, 142
Cellular oscillators, *see* Coupled oscillators
Central neurons, intrinsic properties of, 287–288
Central pattern generators (CPGs), 271
Cerebellum transition, 218
Channel models
calcium channels, 148
HH model of I_{NaP}, 175
limitation of, 184
PHP and, 179
properties of, 176
in squid axon, 176, 179–180
subcellular distribution of channels, 179
window current and steady-state characteristics of, 176
Channel noise, 15
from persistent Na^+ channels, 204–205
Computer modeling, 190
Conductance analysis techniques
advantages and limitations of, 131–132
limitations of dynamic clamp in testing of, 130–131
Conductance compartmentalization, 39–42
Conductance injection, 6–7, 400
experiment, RT-NEURON and AEC, 309–311, 315–317
Conductance noise, 371
Cortex
dynamic-clamp study in, 15, 19, 22, 24
Cortical neurons, 49
AP waveform, 65
in awake state, 116
excitatory input, 57–58
fast-spiking inhibitory, 52
decision, complexity of, 53
simulation of, 52, 53
membrane potential recordings, *see* Membrane potential (V_m) recordings, of cortical neurons
re-creating *in vivo*-like activity in point-conductance model for, 295–296
synaptic noise and responsiveness, 296–299
RS/FS, 59

synaptic input, 52
unitary synaptic conductance transients
typical time courses of, 51
See also Pyramidal neurons, cortical
Cortical slices, re-creating up-states in
natural and dynamic clamp, synaptic activity, 300
VmD method and real up-states, 299
Corticothalamic pathway, function of, 301
COS-7 cells, 403
Coupled network
frequency of, 282
period of, 280–281
Coupled oscillators
entorhinal stellate cells as
implicit assumptions in, 206
mutual excitation, 206
mutual inhibition, 206–207
in subthreshold/suprathreshold regimes, 208–209
virtual synapses, 207
from rate-limiting synaptic inputs
$GABA_A$-mediated inhibition, 210
O-LM inhibition, 210
Coupling clamp, 12
PC-controlled version of, 393

D

DAC, *see* Digital-to-analog analog converter (DAC)
D/A converters, 354
dAPC, *see* Dynamic action potential clamp (dAPC)
DAQ, *see* Data acquisition system (DAQ)
Data acquisition card, 311–312
Data acquisition system (DAQ), 384
accuracy, 386
DCC, *see* Discontinuous current clamp (DCC)
DC current, 359
DCN, *see* Deep cerebellar nuclei (DCN)
Deep cerebellar nuclei (DCN)
synaptic coding properties of neurons in
GABAergic inhibition, 219
inhibitory conductance and quantal conductance, 219
spiking, 219–220
Deep cerebellar nuclei (DCN) neurons
bursting behavior, 228–229
decoding properties, inhibitory Purkinje cell inputs
combined reversal potential, 220
high-input synchronization, 223
IPSCs, 221
spike threshold, 222
STA of inhibitory input conductance, 224
synaptic current, 223
synaptic shunt current, 222
dynamic clamping
focal and distributed input, 230
morphological reconstructions, 229
spike pattern, 229–230
dynamics of action potential spacing and initiation in, 227–228
effect of temporally varying excitation on synaptic coding in
AMPA and NMDA receptors, 225–227
mean spike frequency, 226
spike initiation, 227
intrinsic pacemaking behavior of, 219
in slice under control conditions, spontaneous activity of, 228
synaptic decoding function of, 229
Dendrites
impact on AEC recordings, 364
Dendritic dIPSPs (inhibitory postsynaptic potentials), 16, 32–33, 34
impact on action potential output, 39, 40
somatic time course of, 38, 39
voltage dependence of, 37, 38
Dendritic dynamic clamp, 34
Dendritic signals, 217
Dendritic spikes
forward propagation of, 43, 44
generation of, 50
Dendritic whole-cell patch clamp, 50
Dendrosomatic attenuation of synaptic potentials, 36–39
Depolarizing inhibition, 16–17
DHN, *see* Dorsal horn neuron (DHN)
Digital dynamic clamp, 361
Digital signal processing (DSP) board, 10–13
Digital-to-analog analog converter (DAC), 384
dIPSPs, dendritic, *see* Dendritic dIPSPs (inhibitory postsynaptic potentials)
Discontinuous current clamp (DCC), 349, 362, 387
Discontinuous voltage clamp (DVC), 373
Divisive modulation, of firing rate, 104–110
Dorsal horn neuron (DHN)
in acute slices of rat spinal cord

Dorsal horn neuron (DHN) (*cont.*)
filtering process, 293
spontaneous bursts, 295
intrinsic membrane properties, 293
Driving force, for currents, 4
DSP board, RT-NEURON
analog modules, 311–312
"ghost compartment", 313
interrupt procedure, 312
source code of, 312
Dual somatic recording approach, 33
DVC, *see* Discontinuous voltage clamp (DVC)
Dynamic action potential clamp (dAPC) technique, 399, 404–406
experiments, 408–409
with HCN4 current, 407–412
system set up, 406–407
Dynamic clamp, 1–2, 6–10
applications, 12–24
in cardiac electrophysiology, 400–402
dendritic, 34
for dendritic IPSPs, *see* Dendritic dIPSPs (inhibitory postsynaptic potentials)
experimental performance, 384
ADC and DAC resolution, 385–387
stability, 387–388
in generation of δ oscillations, 328–330
implementation, 10–13
implementation of a large hybrid network, 340
for main ionic conductances in TC, 322–325
numerical performance, 389–392
jitter, 390–391
latency, 391–392
numerical integration method, 389–390
performance benchmark, 392–395
input/output assessment, 394–395
system-wide performance, 393–394
timing Statistics, 395
principles of, 2–9
equivalent electrical circuit of membrane, 2–5
with a single high-resistance electrode, 347–348
synaptic integration in central neurons, 32–46
implementaion, 32–36
methodological concerns, 32–36
Dynamic-clamp background activity
multiplicative gain modulation, 77–81
Dynamic-clamp configuration, for I_{NaP} analysis
activation and deactivation time courses of, 173–174
ad hoc Markovian model for, 179–181
C–O transition kinetics, 180
spike threshold dynamics, 180–181
advantage of using two electrodes in, 181–183
in CA1 hippocampal pyramidal neurons
selective subtraction, 166–167
steady-state activation curve, 171
HH model of I_{NaP}, 176
limitation of, 184
PHP and, 176
properties of, 175
in squid axon, 176, 179–180
subcellular distribution of channels, 179
window current and steady-state characteristics of, 178
intrinsic and simulated I_{NaP}, 181
membrane potential measurement, 181–182
reasons of
natural modulation, 173
perisomatic localization, 169–172
pharmacological blockers, lack of, 168–169
testing and adjusting, 183–184
Dynamic clamp input, 73
background synaptic input
conductance effects of, 74
dendritic arbor, 76
electrophysiological properties, 83–84
gain modulation effect, 75
neuron depends, 75
generation, 75–77
generic conductance, 81
membrane potential, 76
mimic background synaptic input, 74
simulating *in vivo* background activity, 74
synapses distribution, 76
with white-noise input
autocorrelation function of, 82–83
synaptic conductance, 82
Dynamic-clamp models
for I_{BK}, 148–149
for shunting inhibition, 145–149
Dynamic-clamp protocols, 141
Dynamic-clamp software, 146–147
Dynamic-clamp technique, 50

Dynamic-clamp tests
coupling of non-identical neural oscillators
final frequency, 282
gap junctional conductance, 280
pacemaker kernels, 277
PD neurons, cycle period of, 277–279
hard *vs.* soft real-time performance, 201–203
implementation barrier associated with, 212
intrinsic properties of circuit neurons estimation by, *see* Intrinsic properties, circuit neurons
limitations, in conductance analysis techniques, 130–131
of models of synaptic input to cell, 133
in neurophysiology, 199–200
oscillatory behavior in single neurons
channel noise, Na^+ channels, 203
dynamic gain modulation, 206
stellate cells, 203, 206
performance issues, 212
phase response analysis, 206
in rat and cat cortex *in vivo*, 142
anesthesia and surgical manipulations, 146
data acquisition, 146
visual experiments, 148
in vivo dynamic-clamp system for, 147
re-creating up-states in, 299–300
stochastic conductances in thalamic neurons
burst and single-spike responses, 303
corticothalamic pathway, 301
ISIs, 305
Poisson-distributed physiologically realistic inputs, 303–305
synaptic conductance noise, 302–303
in vivo-like background synaptic activity, 305
synaptic inputs, neurons *in vivo*
excitatory and inhibitory conductance, 218
high-conductance state, 217
inhibitory inputs, 220–222
shunting, 217–218
sk Ca^{2+}-dependent K^+ conductance, 227–229
spike after-hyperpolarizations, 222
synaptic coding properties, 218
thalamic hybrid networks
intra-thalamic inhibition, 292
renewal processes, 292
spindle waves, 289
TC cell, 290
training barrier associated with, 211
in vivo-like activity in cortical neurons, recreating
fluctuating point-conductance model, 295–296
synaptic noise, 296–299
in vivo-like nociceptive input
DHNs and $GABA_B$ receptors, 293
hybrid reconstruction of, 294
See also Synaptic conductance analysis, V_m

E
Electrical coupling, 282
Electrode kernel, 350
finding, 352–354
implementation, 350–359
isolation of, 355–357
online compensation, 358–359
Electrode model, *see* Active electrode compensation (AEC)
Electrode nonlinearities, 364
Entorhinal cortex, 166
Entorhinal stellate cells
channel noise in, 203
as coupled oscillators
implicit assumptions in, 206
mutual excitation, 206
mutual inhibition, 206–207
in subthreshold/suprathreshold regimes, 208–209
virtual synapses, 207
mutual excitation via AMPAergic synapses, 206–207
network oscillations in, 208
subthreshold oscillations in, 203, 206
EPSP, *see* Excitatory postsynaptic potential
Equivalent electrical circuit of membrane, 2–5
Ersatz nexus, 12, 400
Estimation parameters, AEC, 359–361
Estimation procedure, 358
Euler integration
for updating kinetic variables, 54
Euler method
error, 389–390
Excitable cells, 386
Excitatory input conductance
fundamental property of, 55, 56

Excitatory input conductance (*cont.*)
input bursts, 55
Excitatory postsynaptic potential, 65
Excitatory synaptic conductance, 218
fluctuating point-conductance model and, 121, 136
Experimental performance, dynamic clamp, 384
ADC and DAC resolution, 385–387
stability, 387–388

F
fAHP and I_{BK}, 145
Fast-spiking inhibitory, 52
neurons
firing rate, plots of, 60
low-latency inhibition, 64
resonance/optimum level, 58
Feedback delay, 361–362
f–G characteristics, regular adapting neuron
effect of artificial "shunting inhibition" on firing properties, 154
effect of dynamic-clamp "shunting inhibition" on, 152–153
Firing-rate curve
of neurons, 77
nonzero portion of, 76, 77
Firing rate modulation, impact of noise on
divisive effects, 109–110
mixed divisive/subtractive modulation, 109
subtractive modulation, 107
voltage fluctuation, 109–110
voltage noise, 108
Fluctuating point-conductance model, 129
advantage of, 132
cortical activity *in vivo* and, 133
limitation of, 131–132
of recurrent cortical activity, 116
Forward propagation
of dendritic spikes, 43, 44
FS inhibitory, *see* Fast-spiking inhibitory

G
$GABA_A$-mediated inhibition, 210
$GABA_A$ receptor, *see* Gamma-amino butyric acid receptor
GABAergic-like conductance, 17
GABAergic synapses, 240, 247
Gamma-amino butyric acid receptor
conductance, 49, 52, 58
compound conductance, 62
FS cell firing, gap-junctional, 62
gap junctional, 61
like conductance, 53
Gamma phase encoding, 63
Gaussian-distributed variables, 116
Gaussian distribution, 82
Gaussian noise, 352
G-clamp, 148
Golden search algorithm, 357

H
Half-center oscillations, 277–278
HCN, *see* Nucleotide-modulated (HCN) gene
HCN4-based pacemaker, 400
HCN4 channels
dynamic action potential clamp experiments in, 404, 407, 410, 411, 412
HCN4 currents
creating a biological pacemaker, 411–412
in HEK-293 cells, 407–408
in SA nodal pacemaker cells, 409–410
HEK-293 cell, 399, 400, 404
HCN4 current in, 407–408
voltage-clamp experiment in, 408
HERG, *see* Human ether-a-go-go-related gene (HERG)
HH model of I_{NaP}, 175
limitation of, 184
PHP and, 176
properties of, 176
in squid axon, 176, 179–180
subcellular distribution of channels, 179
window current and steady-state characteristics of, 176
High-conductance state, neurons, 217
High-threshold (HT) bursting
in TC neuron, 337
Hippocampal formation, 54
Hippocampal pyramidal cells, I_{NaP} in, 168
Histamine, 327
History
dynamic-clamp technique, 12
Human ether-a-go-go-related gene (HERG), 403
effect of mutation, 406
encoded current, 405
HVA conductances, 229
Hybrid circuits
construction of, 263–265

inhibitory circuits and excitatory networks, 270
intra-thalamic inhibition, 292
phase-locked, 266
physiologically patterned simulated synaptic bombardment, 292
Hybrid networks, 18–19
Hyperpolarization-activated current, 409

I
I_{BK}, *see* BK current
I_{K1}, *see* Inward rectifier potassium current (I_{K1})
I_{Na}, *see* Cardiac fast sodium current (I_{Na})
I_{NaP}, 166
computational modeling of
ad hoc Markovian model, 179–181
in current clamp, 185
eight-compartment model cell, 185
dynamic-clamp configuration for analysis of, *see* Dynamic-clamp configuration, for I_{NaP} analysis
functions, in hippocampal pyramidal neurons, 168
after-hyperpolarizations, 186–187
EPSPs and IPSPs, 168
intrinsic subthreshold theta oscillations, 187–188
repetitive firing, 189–190
spike timing, 191–192
history of, 167
predictive modeling of, 185–186
voltage dependence plots of, 183
Infinitesimal PRC (iPRC), 262
Inhibitory conductance inputs
diagrammatic representation of, 59
excitation, level of, 59
gain modulation, 59
Inhibitory neuron, 240
Inhibitory postsynaptic potentials (IPSCs), 242
Inhibitory synaptic conductance, 218
fluctuating point-conductance model and, 120, 132
Input conductance bursts
structure of, 57
Input/output assessment, 394–395
Input retinal cell, temporal structure of the firing activity of, 292, 294
Input signal, 354
isolation of electrode kernel, 355–356
level of noise injection, 355
membrane response, 354–355
removing membrane kernel, 356–357
Intra-thalamic inhibition, 292
Intrinsically active neurons, sensory gating in, 306–307
Intrinsic bistability in TC neuron, 330–334
artificially augmenting I_T or reducing I_{Leak}, 332–334
Intrinsic channel manipulations in single cells, 13–16
Intrinsic currents, 237
H-current, 254
slow hyperpolarizing, 250
Intrinsic δ oscillations, 325–328
amplitude of I_T in, 328–330
neuromodulation of I_h alters the propensity, 325–328
Intrinsic noise, 151
Intrinsic properties, circuit neurons
biological neurons
gap junctional conductance, 280
PD neurons, 277, 279
coupled oscillatory network, 280
measurement of, 276
model neurons
activity maps, reciprocally inhibitory networks of, 278
network activity, 277
spiking models, 276–277
In vivo dynamic-clamp system, 147
Inward rectifier potassium current (I_{K1}), 400, 409
Ion channel synapse, 32, 36, 38
I/O transfer function
membrane voltage fluctuations and, 143
IPSPs, dendritic, *see* Dendritic dIPSPs (inhibitory postsynaptic potentials)

J
Jitter, 390–391
Just abolish oscillations, 330

K
Kernel
estimation procedure, 358
finding, 352–354
online compensation, 358–359
parameters, 359–361
removing membrane kernel, 356–357
theory, 350–359
Kv3 channels, 182

L
Labview 6.1, 240
LabVIEW program and visual experiments, 148
Latency, time, 391–392
Lateral geniculate nucleus (LGN), 322
Lateral pyloric (LP) neuron, 263
Least-significant bits (lsb), 386
Levinson–Durbin algorithm, 358
LGN, *see* Lateral geniculate nucleus (LGN)
Linear convolution, 352
Loligo pealei, 402
Low-threshold Ca^{2+} potential (LTCP), 323
  electronic block, 326
Low-threshold spike (LTS), 323
lsb, *see* Least-significant bits (lsb)
LTCP, *see* Low-threshold Ca^{2+} potential (LTCP)
LTS, *see* Low-threshold spike (LTS)

M
M current, 144
Measurement error, 390
Membrane conductance
  Ohm's law, 79–80
Membrane potential, 52
  bistability, 334–337
Membrane potential (V_m) recordings, of cortical neurons
  synaptic conductance analysis, *see* Synaptic conductance analysis, V_m
  during "up-" and "down-" states, 116
  using dynamic clamp and VmD method
    fluctuating conductance noise, 118–119
    leak conductance and cell capacitance, 119
    real up-states, 119–120
    V_m distributions, 120–121
  V_m fluctuations
    PSD of, 116, 121–122
    steady-state distribution of, 117
Membrane properties
  DHNs and intrinsic, 293
  passive
    depolarization, 94
    impact of shunting on, *see* Passive membrane properties, impact of shunting on
    input resistance and membrane time constant, 93–94
    subthreshold responses to noisy stimulation, 94–95
Metabotropic glutamate receptors (mGluRs)
  agonist, 293
  induced reduction in I_{Leak}, 336
mGluRs, *see* Metabotropic glutamate receptors (mGluRs)
Mixed divisive/subtractive modulation, 107
Multiple synaptic inputs' manipulations, 20–23
Multiplicative gain modulation
  in slice, 77–81

N
Natural firing frequency, 208
Neocortex
  dendrosomatic spread of synaptic potentials in, 36, 43
Nernst–Planck electrodiffusion, 51
Nernst potential, *see* Reversal potential (E_{rev})
Neural responses, modulating, 75
Neural simulations, 310
NeuReal, 23
Neuromodulation of I_h alters the propensity, 325–328
Neuronal circuits
  dynamics of, 275
Neuronal firing
  effect of shunting inhibition, 151
Neuronal response properties
  effects of membrane conductance on, 93
Neuronal responsiveness
  modulation of, 288
Neuron dynamic-clamp system, 11
Neurons
  background activity, 79
    effects of, 80
    firing-rate curves, 80
  firing rate, 75
    additional conductance, effect of, 81
    curve of, 80
    vs. input current, 78
  membrane potential of, 76
  spatial processing in, 50
  synaptic inputs, 217–218
  synaptic integration
    conduction injection, technique of, 55
    dynamics of, 49
NEURON simulator, 239, 289
  applications of

conductance injection
using, 315–317
DspControl box, 315
real-time implementation of
DSP board, 311–314
Windows and real time, 314
specificities of, 315
validating, 314–315
Neurons integrate network, 51
Neuron's spike generation mechanisms, 52
Neurophysiology, 400
Nexus current, 401
NMDA, *see N*-methyl-D-aspartate
NMDA-mediated feedback
depolarization, 248
NMDA-R conductance signal, 55
NMDA-R-dominated conductance
burst time, 56
intrinsic kinetics of, 57
spike-time reliability, 56
NMDA synapses, 242, 247
N-methyl-D-aspartate
conductance, 225–226
receptors, 225–226
asymmetric trapping block model of, 68
pyramidal neurons, excitatory drive of, 67
spike shape coding, 67–69
voltage dependence of, 67, 68
voltage-dependent block of, 49
Nociceptive signals, in spinal cord dorsal horn
in acute slices of rat spinal cord, 293
hybrid reconstruction of, 294
intrinsic activity, 293
spontaneous bursts, 295
Noise
channel, 15
synaptic, 20, 21, 24
Noise injection parameter, 359–361
Noisy current, 350
Noisy fluctuating conductance signal, 53
Non-Gaussian white noise, 351
Nonlinearities, in AEC recordings, 364–368
Noradrenaline, 327
Nucleotide-modulated (HCN) gene, 400
Numerical integration method, 389–390
Numerical performance, dynamic clamp, 389–392
jitter, 390–391
latency, 391–392
numerical integration method, 389–392

O

Ohm's law, 79, 347
O-LM inhibition, 210
Online compensation, 358–359
Open-loop PRC
definition of, 261–262
of model neurons, 263–264
phase resetting curves generated in, 265, 271
Ornstein–Uhlenbeck background synaptic noise source, 239–240
Oscillatory firing, 60

P

Pacemaker
HCN4-based, 400
Pacemaker kernels
gap junctional conductance required to synchronize, 280–283
Partial voltage clamp, 9
Parvalbumin-expressing inhibitory neurons, 53
Passive leak currents, 239
Passive membrane properties, impact of shunting on
depolarization, 94
input resistance and membrane time constant, 93–94
subthreshold responses to noisy stimulation, 94–95
See also Synaptic background activity
Patch-clamp technique
on HCN-encoded currents, 407
Performance benchmark, dynamic clamp, 392–395
input/output assessment, 394–395
system-wide performance, 393–394
timing statistics, 395
Persistent sodium current, *see* I_{NaP}
Pharmacological block
of thalamocortical (TC) neurons, 322–325
Phase-locked hybrid circuit, prediction of, 269–270
Phase resetting curves
for biological neurons
first order and second order, 262–263
phase-locked modes, 268–269
pulse-coupled approximation, 265
recovery interval, 266
definition of, 261–263
dynamic clamp and, 271

Phase resetting curves (*cont.*)
generation of, 262–263
for model neurons, 268
stimulus intervals for, 269–270
in open-loop condition
pulse coupled approximation for, 265
unperturbed oscillation, 265
Phase response curve, 61
Point-conductance model, of stochastic synaptic activity
biological parameters, 296
expression for, 296
Poisson model, 76, 82
Power spectral density, of V_m
frequency scaling of, 122–124
parameter estimation, 121–122
procedure for evaluating analytic expression of, 122, 123
time constants, 121–122
PRCs, *see* Phase resetting curves
Predictive modeling, I_{NaP} functions, 185–186
Prefrontal cortical microcircuit
in vitro preparation, reverberatory activity
data acquisition, 240
reverberatory network size, 243–244
temporal dynamics of reverberations, 244–245
in vivo conditions, computational model
CV, 250
GABA inhibition, 247
membrane potential fluctuations, 240–241, 245, 248
PFC cell in, 250
pyramidal cells, 252–253
reverberatory network size, 243–244
synaptic currents, 240–243
Processor speed issues
in dynamic clamp implementation, 10–11
Purkinje cells
cerebellum transition and dynamic clamping, 218
Pyloric circuit, 263–264
Pyloric dilator (PD) neurons, 263
Pyramidal neurons
CA1 hippocampal, *see* CA1 hippocampal pyramidal neurons
cortical, 65
dendritic synaptic integration in, 42–45
dendrosomatic attenuation of dIPSPs in, 38
Pyramidal neurons encode
action potential waveforms of, 66

R
Rat somatosensory cortex
5 pyramidal neuron, 77
slice of, 77
RC-cell, 387
model, 387
RC circuit, 348
Real-time neuron simulator, *see* NEURON simulator
Real-time simulation, 406
Real-time synaptic current injection, 240
Reciprocally inhibitory hybrid network, activity of, 278–279
Recordings *in vitro*, AEC, 368–372
Recordings *in vivo*, AEC, 368–372
Regular-spiking neurons
excitatory postsynaptic potential, 65
gamma-modulation, 64
gamma threshold frequencies, 61
re-creating gamma oscillations in, 63
resonance/optimum level, 58
Regular-spiking pyramidal neuron, 54
Relay cells
rebound bursting properties of, 288
Repetitive spiking
in high-conductance state, 96
impact of shunting on, *see* Repetitive spiking, impact of shunting on
in quiet *vs.* noisy conditions, 101–103
stimulus-driven voltage fluctuations, 103
subthreshold activation, 103–104
Repetitive spiking, impact of shunting on
adaptation, computational modeling
CA1 pyramidal cells, 97
depolarizing shift in voltage threshold, 100–101
E_{shunt} and I_M, 101
Morris–Lecar model, 96–97, 98–99
RE/PGN interneurons, intra-thalamic inhibition by, 292
Retinothalamic hybrid circuit, reconstruction of, 291
Reverberatory activity
influence of network size on, 243–244
in mammalian brain, 238
sustained activity, 243–244
in vitro preparation, 246
V_m fluctuations and, 244
See also Prefrontal cortical microcircuit

Reverberatory ensemble, using reactive clamp, 247–248
Reversal potential (E_{rev}), 3–4
RS, *see* Regular-spiking

S
SA, *see* Sinoatrial (SA) node
SA nodal model cell, 409
SCN5A gene, 406
Shunting, 217–218
  impact of noise on firing rate modulation by
    divisive effects, 106–107
    mixed divisive/subtractive modulation, 107
    subtractive modulation, 104
    voltage fluctuation, 109–110
    voltage noise, 108
  and passive membrane properties
    depolarization, 94
    input resistance and membrane time constant, 93–94
    subthreshold responses to noisy stimulation, 94–95
Shunting effect, 8–9
Shunting inhibition
  dynamic-clamp models for, 148–149
  and neuronal response
    $GABA_A$ inhibition, 142–143
    I/O function, 143
  non-linear effect of, 158
  in rat and cat cortex *in vivo*, 142
    anesthesia and surgical manipulations, 146
    data acquisition, 146
    extrinsic and intrinsic membrane mechanisms, 160
    input–output function, 151–152
    visual experiments, 148
    visual responses, 151–154, 159
    in vivo dynamic-clamp system for, 147
SIF, *see* Synaptic interaction function
Simple phase-coupled oscillators, 281
Single-cell oscillations
  channel noise, Na^+ channels, 203–204
  dynamic gain modulation, 205–206
  stellate cells, 203
Single patch electrode dynamic-clamp protocols, 150
Single synaptic inputs' manipulations, 16–17
Sinoatrial (SA) node, 400
sk conductance
  blocking of, 227–228
Sleep-like oscillations, gating of input signals during
  gating properties of
    rhythmic inhibition, 292
    thalamic circuit, 291–292
  spindle waves, 289
  synaptic and intrinsic conductances, 291
  TC cell spikes, 290–291
Sleep rhythm, 334
Somatic recording electrode, 183–184
Somatic voltage clamp
  errors, 35
  synaptic integration in central neurons's study and, 33–36
Spectral analysis, 117
Speed, dynamic clamp system, 396
Spike generation, 54
Spike-rate coding, 57
Spike shape encoding
  of conductance input, 66
Spike-time coding, 57
Spike timing precision, effects of I_{NaP} on, 191–192
Spike timing with recreated synaptic activity, 371–372
Spike-triggered averages (STAs)
  AMPAconductance, 54
  of conductance input signals, 58
  reverse correlation, 53
Spike-triggered averages (STAs), V_m
  effective "leak" conductance estimation, 128–129
  estimation with dynamic clamp, 124–127
Spiking neurons
  membrane potential of, 77
  types of, 60
Spontaneous activity, 75
Square conductance waves, 369–371
Stability
  dynamic clamp, 387–388
Start of burst, definition of, 261
Steady-state compromise frequency, 282
Stimulus time, 264–265
Stochastic synaptic input
  excitatory conductance drive, 53–57
  inhibitory conductance drive, 57–59
  noisy fluctuating conductance signal, 53
Stomatogastric ganglion, 263, 271
Subthreshold currents
  in mammalian neurons, 165–166
Subthreshold membrane fluctuations, 248

Subthreshold membrane potential oscillations
importance of, 187–188
role of I_{NaP} in, 188
Subthreshold oscillations
conductance-based inputs role in, 208
in entorhinal stellate cells, 204, 207
Subtractive modulation, of firing rate, 104–105
Sustained activity
spontaneous, 248–250
stimulus-driven elicitation of, 250–252
Synapse models, 313
Synaptic background activity
in acute brain slices, 90
brains of adult male Sprague–Dawley rats
membrane conductance, 91–92
noisy stimulus waveforms, 92
dopamine levels, 249–250
gain modulation effect, 75
impact of shunting on passive membrane properties, *see* Passive membrane properties, impact of shunting on
integrative properties, neurons, 90
neocortical pyramidal neurons and, 89–90
synaptic background noise, 248
Synaptic conductance analysis, V_m, 217
assumptions in, 116–117, 128
based on current-clamp data, 127–128
fluctuating point-conductance model, 131–132
at soma of cortical neuron, 116
STAs estimation
dynamic-clamp injections, 124–125
population analysis, 126–127
probabilistic method for, 125
time constants, evaluation of
dynamic clamp and, 122
PSD, 121–122
V_m fluctuations, 122–124
VmD method for extracting parameters of
dynamic-clamp technique and, 118–121
stochastic conductance variables, 117
Synaptic conductance inputs
electrical nature of, 51–53
membrane potential, 84
neuron
stereotypical transient, 51
spike shape encoding of, 65–67
Synaptic current
DCN neurons, 222–223
Synaptic inhibition
and excitation, interaction between, 142
Synaptic inputs' manipulations
multiple, 20–23
single, 16–17
Synaptic integration
compartmentalized, 42–45
Synaptic integration, in central neurons, 31–32
dynamic clamp to study, 32–45
implementaion, 32–36
methodological concerns, 32–36
Synaptic integration function
in cortical neurons, 50
cortical slice, 52
Synaptic interaction function
in cortical neurons, 50
phase delay, 61
Synaptic noise, 20, 21, 24, 371
effect on burst and single-spike responses, 303
and responsiveness of cortical neurons
background activity, 297–298
computational models for, 298
conductance, 298
response to excitatory synaptic inputs, 296–299
retinogeniculate EPSP, spike transfer of
background synaptic activity, 305
physiologically realistic Poisson-distributed inputs, 303–304
retinogeniculate input conductance, 303
and transfer function of thalamocortical cells, 302–303
Synchrony, 221, 266–267, 270
System-wide performance, 393–394

T

TC, *see* Thalamocortical (TC) neurons
Thalamic gate
cortical control of, 301–302, 309
functional facets of, 308
Thalamic hybrid networks, dynamic clamp of
intra-thalamic inhibition, 292
renewal processes, 292
spindle waves, 289
TC cell, 291
Thalamocortical (TC) neurons, 322
activation of mGluRs, 334–337

bistable voltage levels, 334
Ca^{2+}-activated non-selective cation current, 337
CAN current, 337–338
dynamic clamp for studying main ionic conductances in, 322–325
high-threshold (HT) bursting, 341
intrinsic bistability, 330–332
intrinsic δ oscillations, 325–330
noisy high-conductance state in, 301–302
pharmacological block, 322–325
role of I_h and I_T, 325–330
transfer function of, 307
EPSPs and IPSPs, 309
top-down corticothalamic inputs, 308
T-type Ca^{2+} current, 330–337
Thalamus
DHN axons and, 293
excitatory and inhibitory conductance fluctuations, 309
role of neurotransmitter activation in, 307
spike transfer through, 289, 292
Theta resonance, 188
Time constants, AEC, 362–363
Time-varying excitatory inputs
from mossy and climbing fiber collaterals, 219
Timing Statistics, 395
Toeplitz matrix, 353–354
Tonic bursting, 288
Traditional action potential clamp, 402–404
Transient Na^+ current (INaT)
and I_{NaP}, 167
TTX-sensitive current, 171
TTX-sensitive subthreshold current, 183
T-type Ca^{2+} current
in TC neurons, 330–337
T-type current, 288
Type 2 threshold, 60

U
Unitary conductance parameters, 59

V
VB, *see* Ventrobasal thalamus (VB)
Ventrobasal thalamus (VB), 322
Virtual pharmacology, 13–16
Visual cortex, 143
adapting neurons recorded *in vivo* in, 152–153
artificial shunting inhibition effect on visual response of neuron in, 154–155
I_{BK}-dependent f–I characteristics, 157
Visual stimulation
generated using VisionEgg software package, 148
shunting inhibition role in, 142
spike response to, 144
VmD analysis method
real cortical neurons using dynamic clamp
fluctuating conductance noise, 118–119
real up-states, 119–120
V_m distributions, 120–121
V_m fluctuations, steady-state distribution of, 117
Voltage clamp, somatic
errors, 35
synaptic integration in central neurons's study and, 33–36
Voltage-clamp experiment
on HEK-293 cell, 408
Voltage fluctuations and firing rate modulation, 109–110
Voltage noise, 106

W
White-noise-driven model, 84
White-noise input, 82
Whole-cell patch-clamp technique, 204, 205, 211
in cat visual cortex *in vivo*, 153, 155
craniotomies in, 146
instruments used for, 148
in rat somatosensory cortex *in vivo*, 150–151
in rat visual cortex *in vivo*, 157
Working memory
prefrontal cortical pyramidal cells recorded *in vivo* during, 255
simulation of, 252

X
Xenopus laevis, 402

Z
ZD7288, 327